# The University of Nottingham

## UNITED KINGDOM · CHINA · MALAYSIA
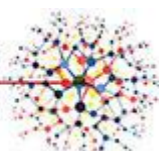
**School of Pharmacy**

# Aggregation Prone Region analogues: synthetic excipients for protein formulation

**Ruggero Foralosso, Msc**

Thesis submitted to the University of Nottingham for the degree of Doctor of Philosophy

September 2018

CDT in Advanced Therapeutics and Nanomedicines

# Abstract

In the last few decades, protein therapeutics have become a relevant segment of the pharmaceutical industry. However, clinical use of biotherapeutics can be limited by poor stability of proteins in the different steps of manufacturing, storage and formulation, with subsequent formation of protein aggregates. Aggregation affects not only therapeutics proteins, with detrimental effects on production costs, final product yields and therapeutic efficacy, but also endogenous proteins, as it leads to the formation of large aggregates deposits which have been correlated to different neurodegenerative diseases. Consequently, a range of stabilisers have been developed to increase the stability of biotherapeutics in formulations, or prevent the aggregation of endogenous proteins. Among the different strategies employed, excipients that stabilise proteins through non-covalent interactions have been reported.

This thesis focusses on the stabilisation of proteins through hydrophobic interactions: here, the synthesis of short, hydrophobic, stabilisers is reported. These stabilisers were tested on different proteins, to interact with hydrophobic patches on proteins primary strucures, and block these patches from mutual, self-interactions that may lead to proteins aggregation.

In the first part of this work, peptides analogous of hen egg lysozyme Aggregation Prone Region (APR), were synthesised, and tested on lysozyme to verify any potential interaction between these synthetic peptides and their homologous sequence on lysozyme, to block its site from self-interactions that

lead to aggregation. For improved solubility and to enhance its stabilising effect, the APR peptide fragment was finally copolymerised with monomer *N*-hydroxyethylacrylamide, to generate a peptide-polyacrylamide copolymer stabiliser. Pleasingly, the copolymer proved to be able to delay the onset of lysozyme aggregation, which was induced in strong basic conditions.

Encouraged by these results, in the second experimental chapter this strategy was expanded by developing a library of amphiphilic block copolymers, comprising hydrophobic amino acid-like moieties, potentially able to non-covalently interact with hydrophobic, self-aggregating protein domains, and prevent protein aggregation/denaturation. Three moieties were chosen, indole 3-acetic acid, phenyl acetic acid and methylisobutiric acid, to mimic the side chains of three amino acids, tryptophan, phenylalanine and isoleucine, respectively. The copolymers were tested on two different proteins, hen egg lysozyme, bovine pancreatic insulin, and the antimicrobial peptide IDR 1018. Potential interaction between the proteins and the copolymers was evaluated under stressful conditions, which induced proteins aggregation, measured by turbidity and solubility studies. Promising stabilising effects were shown by some of the indole-contaning copolymers, which proved to be able to prevent the aggregation and to increase the solubility of both insulin and peptide IDR 1018. Hydrophobic Indole-based oligomers were further tested to evaluate their efficacy in encapsulating the antimicrobial peptide IDR 1018. The peptide was first ion paired with the antimicrobial molecule usnic acid, to develop a hydrophobic complex for enhanced IDR 1018 encapsulation and potential co-delivery of two antimicrobial drugs.

In the fourth experimental chapter of this thesis, cholanic-polyacrylamides conjugates were synthesised for potential non-covalent protein conjugation. Cholanic acid has been previously investigated for its ability to interact with proteins hydrophobic patches. In particular, a series of PEG-cholanes of different molecular weight were used to efficiently complex two different proteins, the recombinant human growth hormone (rh-GH) and the recombinant human granulocyte colony stimulating factor (rh-G-CSF). improving their bioavailability and extending their half-life. Here, cholanic acid was incorporated into a RAFT agent and used to mediate the polymerization of *N*-hydroxyethylacrylamide, to develop cholanic-polyacrylamides of different length. The polymers were successfully employed as protein complexing agents for two model proteins, bovine serum albumin and bovine pancreatic insulin.

Finally, the last chapter is presented in a form of a draft paper, and is part of a collaborative work started by a former PhD student in our group, Joao Madeira do O.  A series of linear and 4-arm glycopolymers, were previously prepared by copper azide alkyne cycloaddition (CuAAC) functionalisation of preformed poly(propargyl methacrylate)s with different sugar azides. In this thesis, the reversible, non-covalent interaction between the small hydrophobic molecule Nile Red and linear and 4-arm glycopolymers was evaluated. Results suggest that the interaction occurs between the dye molecule and single polymer chains, suggesting that these glycopolymers do not self-assemble in supramolecular aggregates and act instead as unimolecular micelles.

# Acknowledgments

It has been a complicated journey, and I can't say that I always enjoyed it. My first thought goes to my parents, who have been so patient and supportive during my PhD.

Surely, without the help of many other people around me I could have never made it. In first place my supervisors, Snow, Beppe and Cameron, whose guidance has been essential through all these years. I won't forget my long meetings with Snow, spent discussing about science and European History. I am so grateful to Beppe for putting up with my writing style, this thesis was surely a long journey for him as well.

For everyone in BSB and B15: I thank you for your help and support. My thanks go to Francesca, first of all. And then to Rosa, Patricia and Emanuele, for your friendship and support whenever I felt blue (more or less always). Finally, to Ines, Nora, Alejandro, Benoit, Akosua, Vasiliki, Marco, Catherine, Gokhan, Lucy, Federica, Chiara, Marina, Rebeca…apologies if I have missed anyone. I would like to thank two people that have been really important for my professional and personal development, Professor Steve Brocchini and Dr Alessandro Canacci.

Finally, my special thanks go to my girlfriend, Alessandra, for her patience and sweetness. I know I am like a baby sometimes, messy and moody (pretty much most of the times). You are the best gift from these four years of PhD.

# Table of Contents

# List of Figures

# List of Schemes

# List of Tables

# Abbreviations

AIBN Azobiisobutyronitrile

Ala Alanine

AMP Antimicrobial Peptide

APR Aggregation Prone Region

Arg Arginine

$CHCl_3$ Chloroform

CHO Chinese Hamster Ovary

CMC Critical Micelle Concentration

Con A Concanavalin A

$D_2O$ Deuterium oxide

DCM Dichloromethane

DMF Dimethylformammide

DCVJ 9-(2,2-Dicyanovinyl)julolidine

DLS Dynamic Light Scattering

DLVO Boris Derjaguin and Lev Landau, Evert Verwey and Theodoor Overbeek

DMF N,N-Dimethylformamide

DMSO Dimethylsulfoxide

DP Degree of polymerisation

ESI MS Electrospray ionization Mass Spectroscopy

$Et_2O$ Diethylether

$Et_3N$ Triethylamine

EtOAc Ethyl acetate

FTIR Fourier transform infrared spectroscopy

HPLC High Performance Liquid Chromatography

Gly Glycine

Ile Isoleucine

IPOH Isopropanol

Leu Leucine

Lys Lysine

MALDI MS Matrix-assisted laser desorption/ionization Mass Spectroscopoy

MeOH Methanol

$M_n$ Number Average Molecular Weight

mN/m milliNewton per metre

$M_w$ Weight Average Molecular Weight

MW Molecular weight

NMR Nuclear magnetic resonance

PDI Polydispersity index

PEG Poly(ethylene glycol)

Ppm Parts per million

RAFT Reversible Addition Fragmentation Chain Transfer

SEC Size exclusion chromatography

Ser Serine

SiO2 Silicon dioxide

THF Tetrahydrofuran

$T_g$ Glass Transition Temperature

TGA Thermo-gravimetric analysis

TLC Thin Layer Chromatography

Trp Tryptophan

Val Valine

λem Emission wavelength

λex Excitation wavelength

# Chapter 1

**Literature review**

_____

## 1.1. The relevance of protein therapeutics

In the last decades, the use of protein therapeutics for the treatment of a range of different diseases has been constantly increasing[1]. The first and arguably most known biotherapeutic is insulin. Insulin was isolated for the first time in 1922 from beef pancreas[2], and technologies for its production and formulation have been continuously improving from the 70s onwards. Current insulin formulations use different types of human biosynthetic analogues, each with different pharmacokinetic properties[3]. Following the development of therapeutic insulin, an increasing number of proteins and peptides have been explored and eventually reached the market. FDA approved 91 protein therapeutics between 1980 and 2013 and this number is exponentially increasing[4]. Today more than 130 protein therapeutics are routinely clinically prescribed[3]. These are commonly divided in four groups, according to their function[1]:

- group I: protein therapeutics with enzymatic or regulatory activity (e.g. hormones);

- group II: proteins with special targeting activity (e.g. antibodies);

- group III: vaccines;

- group IV: protein diagnostics[1].

Compared to the majority of the small molecule drugs, biotherapeutics stand out for their higher specificity and lower toxicity[5]. Moreover, using modern molecular biology techniques they can be produced recombinantly, with higher

potency and/or low immunogenicity compared to the corresponding wild types[1].

For all these reasons, the global protein therapeutics market, which was valued at $140,109 million in 2016, is predicted to reach $217,591 million by 2023[6].


## 1.2. Incidence of protein aggregation in biotherapeutics and endogenous proteins

The use of biotherapeutics is often limited by their low stability to aggregation in solution[7, 8]. It should be noticed that also many endogenous proteins show propensity for aggregation, which has been related to different diseases[9, 10].

As a definition of protein aggregation, one can use a following statement. "Protein aggregation is the process by which misfolded proteins adopt a conformation that cause its polymerization into aggregates and organized fibrils"[11].

### 1.2.1. Aggregation of biotherapeutics and its immunogenic effects

During the protein therapeutics production, aggregation can occur at different stages of protein expression and purification processes and typically requires additional steps to re-solubilise the insoluble aggregate or separate it from native, non-aggregating protein. Hence, aggregation results in increase of production costs and reduced yields[7, 12].

For example, protein aggregation and accumulation of such aggregates has been observed in *E. coli*, bacterial expression host for protein therapeutics. In

this case, aggregation is ascribed to the large amount of protein that bacteria are forced to produce to generate the highest yield possible. Over-expression results in very high concentration of recombinant protein in the cytoplasm, too high to be stabilised and folded through bacterial chaperones and post-translational modifications, or to be subjected to proteolytic degradation[13-15].

Following expression, protein aggregation can occur also during purification steps. Antibodies are usually purified *via* Protein A Chromatography. This technique generally requires low pH for protein elution, which may induce proteins structural changes leading to aggregation[16]. Agitation, mixing or shaking, applied to achieve homogeneity of the protein solution, can also induce protein aggregation. The underlying mechanisms are not fully understood, but are believed to involve the air-water interface which forms upon agitation[17]. The air-water interface is relatively hydrophobic and may hypothetically induce substantial modifications of protein secondary structure[18]. Freeze-thaw cycles can also induce protein denaturation and aggregation, believed to be a result of cold-induced protein misfolding and by cryo-concentration of solutes when the water crystallizes[19].

Undesired aggregation can further occur when the dried protein powder is re-solubilised into an aqueous medium prior to administration. Most of clinically approved protein therapeutics are delivered in a form of liquid injections. As IM and SC injections do not allow the administration of more than around 1 mL of volume *per* dose, proteins are usually dissolved at very high concentrations, which favours the formation of protein aggregates[8].

Accidental exposure of protein formulation to elevated temperature that may occur during shipping or storage is another stress factor capable of inducing protein aggregation. Elevated temperature can induce partial-to-complete protein conformational destabilization[20]. Aggregation during storage, transport, upon or after administration may have an impact on protein immunogenicity[8, 21], manifested as reduced protein efficacy, cytokine release syndrome and anaphylaxis[22]. Aggregates can activate the production of specific Anti Drug Antibodies (ADA) - which bind the protein, causing a reduction of its biological activity and alteration of its pharmacokinetic profile. Importantly, complexation with ADAs typically results in much faster protein clearance.[23, 24] A number of therapeutic proteins have been shown to undergo aggregation and consequently inducing an immune response. For example, the human growth hormone (hGH) induced antibody responses in clinical trials which was directly correlated with the proportion of aggregates present in the formulations[24]. Interferon β, clinically utilised in the treatment of multiple sclerosis, induces the production of Interferon β-binding ADA in around 25% of patients, resulting in impaired receptor binding and consequent drastic reduction of therapeutic efficacy[25].

### 1.2.2. Aggregation of endogenous proteins and their relevance in neurodegenerative diseases

Aggregation into highly ordered protein aggregates called amyloids has been linked to neurodegenerative diseases, including Huntington's, Parkinson's and Alzheimer's disease[26, 27]. Alzheimer's is a progressive and irreversible disease that affects the brain, slowly hampering memory and cognitive skills. The brain

of patients affected by Alzheimer is characterised by high accumulation of amyloid plaques, which mainly contain the protein fragment Aβ. Aβ is believed to play a crucial role in inducing Alzheimer's disease, as one of its isoforms, $Aβ_{42}$, can induce ordered self-assembly of Aβ into amyloid plaques which will ultimately cause neuronal damage[28]. Parkinson's disease is characterised by progressive loss of dopaminergic neurons in the *substantia nigra* in the brain. The neuronal damage has been associated with the accumulation within the neurons of protein aggregates, called Lewy bodies, formed of different proteins, in particular aggregates of the pre-sinaptic proteins α-ynuclein[29, 30]. Similarly, a mutation of huntingtin protein leads to its aggregation and formation of large intraneuronal aggregates, called inclusion bodies, that are hallmarks of Huntington disease, a neurodegenerative disorder which causes impaired motor movements, impaired cognitive skills, and early death[31].

## 1.3. Mechanisms the induce, regulate and control proteins aggregation

### 1.3.1. The four different levels of proteins structure

Proteins are large macromolecules consisting of one or more polypeptide chains.

Protein structure can be considered at 4 levels (Fig. 1.1)[32]:

- The primary structure of a protein considers its amino acids sequence.

- The secondary structure refers to local folded areas that forms within the protein molecule through non-covalent interactions between atoms of the protein amino acid sequence. The most common secondary

structures are the α-helix and the β-sheet. In the α-helix the polypeptide chain adopts a helical conformation, stabilised by H-bonds between the carbonyl (C=O) of one amino acid and the NH of the amino acid which is four down in the chain, such that each turn of the helix contains 3.6 amino acids[33]. The β-sheet is characterised by two peptide strands running in the same (parallel β-sheet) or opposite direction (antiparallel β-sheet), kept together by hydrogen bonding between the strands. The H-bonds are established between carbonyl and amino groups of amino acid chain, while the side chains locate above and below the plane of the sheet[34].

- The tertiary structure is determined by non-covalent interactions between amino acids side chains within the protein backbone. These interactions can be hydrophobic, electrostatic, H-bonds and disulphide linkages[35].

- Some proteins comprise different polypeptide chains, called subunits, which are held together by weak interactions. The association of these subunits forms the quaternary structure[35].
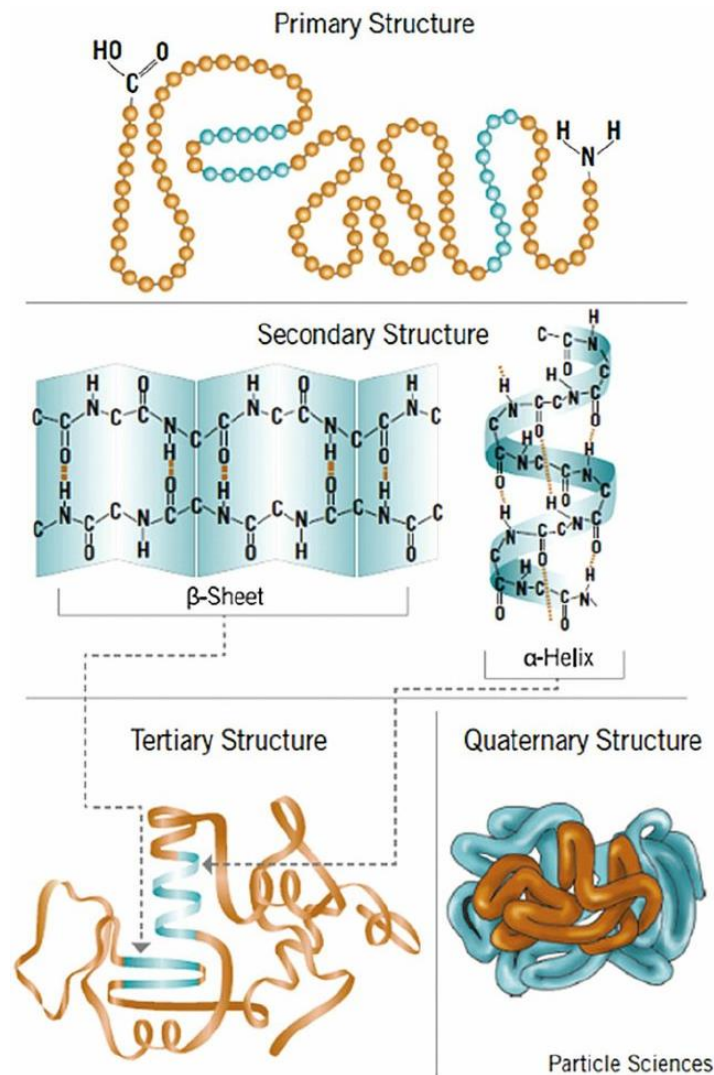
Figure 1.1: The four different levels of proteins structure. Image taken from reference [36].

## 1.3.2. The main stages of proteins aggregation

Protein folding is the process by which a protein acquires its most stable, i.e. the lowest energy, 3-dimensional conformation, which is called the native form[37]. In this conformation the protein is properly operative and functional[38]. The native form is stabilised by intramolecular interactions, such as hydrogen bonds and electrostatic interactions, although the studies have highlighted the hydrophobic effect as the major driving force for protein folding: the burying of hydrophobic residues into protein inner space, allows intramolecular

interactions between water molecules and with the protein surface in a less ordered manner, thus increasing the general entropy of the system[39].

The conformation adopted by the protein in its native state cannot be considered as a completely rigid and stable condition. Indeed, the protein conformation is constantly fluctuating around its native state. This flexibility helps the protein to adapt to environmental changes and exert its physiological function[40, 41].

In normal conditions in aqueous environment, there is an equilibrium between the protein in a native state, and small amounts of partially unfolded intermediates, further in equilibrium with the completely unfolded/denatured states. These unfolding intermediates are generally considered the main trigger of protein aggregation, as they are more flexible and expose hydrophobic patches capable of self-interacting. Under stress conditions, or due to genetic mutations, the protein may undergo conformational changes that alter the equilibrium between folded protein and partially unfolded intermediates. Increased population, and subsequent self-assembly of these intermediates will lead to formation of protein aggregates[42].

The aggregation process and its rate can vary considerably according to the particular protein and the conditions at which aggregation occurs. However, three distinct phases are usually identified: a lag phase, a growth phase and a plateau phase (Fig. 1.2).
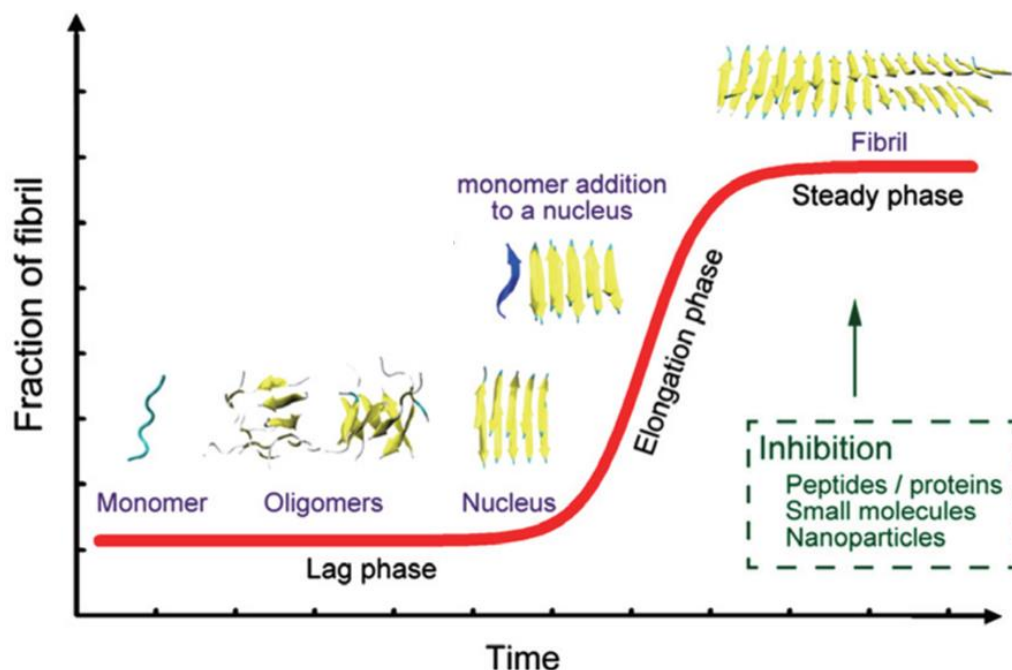
Figure 1.2: Sigmoidal curve typical of protein aggregation process. Soluble protein monomers begin to form oligomers, which gradually evolve into growth competent nuclei. The initial lag phase is followed by a phase of fast growth of aggregates, due to addition of soluble protein monomers to the nucleus surface. The aggregates growth reaches plateau as the number of protein monomers in solution decreases. Meanwhile, aggregates can further associate into complex structures, for example fibrils. Image taken from reference[43].

During an initial lag-phase nuclei (or nucleation seeds) are formed from single monomeric, partially unfolded protein/peptide molecules. Initial monomers association results in reversible oligomers (prenuclei). Further association generates the smallest irreversible aggregates, the *x*-mer nucleus. This is followed by a second, faster phase, called elongation, where monomers are added to the nucleated aggregates, now growth-competent. The addition, initially reversible, is followed by conformational changes in the aggregate that make it irreversible. The aggregates may then further self-associate, to generate fibrils or more amorphous precipitates[7, 44-46]. The elongation phase can be influenced by so-called secondary nucleation mechanisms. For example, fibrils fragmentation increases the number of fibrils ends where soluble protein

molecules can attach. Nucleation at the surface of the growing aggregate may also occur. The aggregation will ultimately reach a plateau phase, as its rate depends on the number of soluble monomers still present in solution, which gradually decreases during the elongation process[47, 48].

Protein aggregates can be classified using different parameters, such as size, reversibility, conformation and morphology[49]. In particular, they are usually divided into two groups: amorphous and fibrillary (Fig. 1.3).
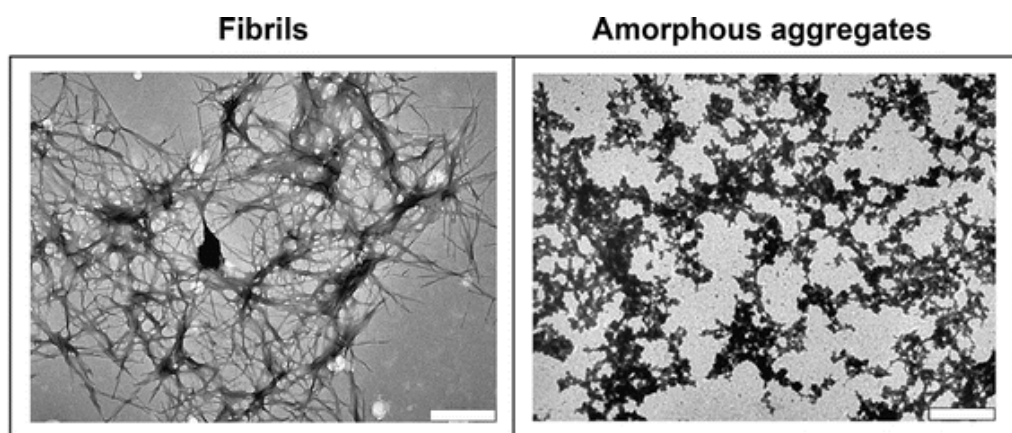


Figure 1.3: TEM images of lysozyme fibrils (left) and amorphous aggregates (right). Image taken from reference[50].

Amorphous aggregates are characterised by a lack of high-order structure[7] and are often observed, for example, in inclusion bodies formed in recombinant bacteria during the expression and purification steps of recombinant proteins. Their aggregation is often reversible, but solubilisation and refolding procedures can be time-consuming and do not always guarantee an acceptable recovery yield[51].

By contrast, fibrillary aggregates are characterised by highly-ordered structure. They are rich in β-sheet and lack α-helix domains. It has been shown that the

fibrils originate from two continuous β-sheet strands, whose side chains interact tightly, forming a zipper[7]. Fibrils are usually the main component of amyloids plaques, which, as mentioned above, are protein aggregates deposits that characterise several neurodegenerative diseases[52].

Protein aggregation and folding can be considered as competitive processes, both regulated by the same forces, such as electrostatic and hydrophobic interactions, together with more specific interactions such as salt bridges and disulphide bonds[53].

Hydrophobic interactions are generally considered to be a key factor that may trigger proteins aggregation, inducing protein molecules self-assembly through mutual interactions[42]. In amyloid-like aggregates, they contribute to the stability of the β-sheet strands. On the contrary, electrostatic interactions generally have an anti-aggregation effect: polar amino acid residues are usually not evenly distributed on the protein backbone, but preferentially organised in patches which can be highly charged, especially in conditions away from the isoelectric point, and normally enhance protein repulsion and decrease the rate of aggregation[53].

### 1.3.3. The role of Aggregation Prone Regions (APRs) and gatekeepers in proteins aggregation

Recently, an increasing body of literature has been focusing on the role that specific sequences on proteins backbone have on aggregation: they are known as Aggregation Prone Regions (APRs).

These sequences are usually 5-15 amino acids long, with a high degree of hydrophobicity and a low net charge. They have been shown to be sufficient to induce protein aggregation: their covalent conjugation induced aggregation of otherwise un-aggregating proteins[7, 54]. Most of the proteins possess one or more APRs, but they are typically buried into proteins hydrophobic inner space (core) or positioned in the groves of the protein active site. Aggregation is led by exposure of these segments to the solvent. Protein unfolding and subsequent denaturation, caused for example by external stress factors (e.g. temperature or pH), or intrinsic factors (e.g. destabilisation of the native structure by genetic mutation) will expose these sequences and allow their self-assembly[7]. APRs start self-interacting and self-assemblying through mutual β-sheet interactions, forming β-sheet-containing aggregates that may vary from amorphous aggregates into ordered amyloid fibrils (Fig.4).
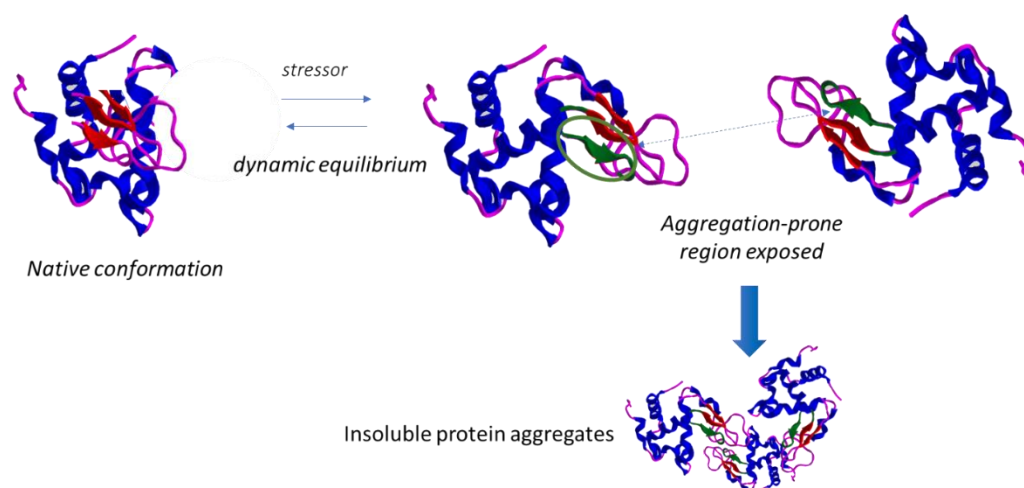


Figure 1.4: Importance of Aggregation Prone Regions APRs on protein aggregation. In the native state, APRs are usually buried inside the protein core. The native state is always in equilibrium with small population of partially unfolded intermediates. Different external stress factors (in case of biotherapeutics) or genetic mutations (in case of endogenous proteins) may induce protein misfolding, shifting the equilibrium towards partially unfolded protein intermediates, where Aggregation Prone Regions (shown in green), may be exposed to the external solvent. APRs from different protein molecules can start mutual interactions which lead to protein aggregation and ultimately to the formation of large, insoluble protein aggregates.

Interestingly, a strong preference of APRs for self-interaction over hetero-interactions was observed when two different APR sequences were mixed; self-interaction was by far more preferable[54, 55].

The aggregation propensity of APR sequences is directly correlated with their tendency to establish β-sheet-like interactions. Usually, charged amino acids show the lowest incidence of β-sheet formation, while on the contrary, aliphatic and aromatic hydrophobic amino acids are the most common components of the β-sheet strands. Aromatic aminoacids residues are believed to stabilise the β-sheet secondary structure through π-C and hydrophobic interactions and APRs are usually rich in hydrophobic residues and possess a very low net charge[56-58].

Different computational tools have been developed to predict the aggregation propensity of different peptide sequences and thus identify potential APRs within a protein structure. An early example is TANGO, a statistical thermodynamic algorithm which locates β-nucleation sequences on the protein backbone[7]. Other increasingly complex algorithms have been developed, which take into consideration on a combination of different amino acidic properties such as hydrophobicity, charge and β-sheet propensity[59, 60]. One of these algorithms was developed and tested by Pawar et *al.*[61] to predict the intrinsic propensities for the aggregation of individual amino acids. The highest aggregation propensity was found for the aromatic hydrophobic amino acids Tryptophan, Phenylalanine and Tyrosine, followed by aliphatic hydrophobic amino acid such as leucine, isoleucine and valine[61].

The model was further expanded by Tartaglia *et al*. to predict APRs in different proteins: a high aggregation potential for the 12-residue N-terminal region and for residues 18–19 and 27–28 of salmon calcitonin was predicted in this way. Same predictions were made for residues 6–10 and 23–27 of hormone glucagone. In the case of Parkinson's hallmark protein, α-Synuclein, the central region (approximately residues 30–95) has been identified as the one forming the core of the fibril. Six aggregation-prone regions (residues 24–32, 37–46, 53–67, 75–81, 92–93, and 124–127) were identified for human lysozyme[62].

The entire human proteome was investigated for incidence of APRs, and computer predictions indicate that more than 80% of human proteins contain at least one potential APR and approximately two-thirds (65%) contain two or more APRs. It was also noticed that APRs were generally located close or within proteins binding sites, while they were usually far from post-translational modifications sites[63].

The incidence of Aggregation Prone Regions has been investigated also in proteins used as therapeutics. Commercial antibodies are rich in β-sheet secondary structure, which suggests they may effectively aggregate through mutual β-sheet-like interactions[64]. Using the computational prediction tools described above, a group of commercial antibodies was analysed, revealing that each antibody contained 2–8 aggregation-prone motifs *per* light and heavy chain pair. The APRs in the constant regions were nearly identical among the antibodies studied, due to greater conservation in amino acid composition of these regions. The APRs in variable domains were found primarily located in

the complementarity determining regions, CDRs[64]. By using the same computational approach, APRs were also predicted in other proteins commonly used as therapeutics, such as the fast-acting insulin aspart, the anti-haemophilic Factor VIII, and the growth hormone somatropin. The motifs identified lacked charged residues and were rich in aromatic amino acids. A high incidence of hydroxyl-containing Serine and Threonine was noted, and ascribed to their high tendency to form β-strand and low tendency to form α-helix[64].

In a study published by Buck *et al.* it was observed that within the proteins, catalytic residues frequently establish non-covalent interactions with APRs, with a significantly higher frequency than expected by random chance.[65] APRs were also found to contain more ordered residues than the average, and to be buried further inside the protein core than their hydrophobicity may suggest. From these observations, it was hypothesised that buried APRs can form multiple interactions within the protein structure and hence contribute to stabilize the native conformation. It appears therefore that, despite their aggregation propensity, some of APRs have been highly conserved during protein evolution for their native-conformation stabilising function. On the other side, APR-neutralising mechanisms are often in place within the protein itself to reduce the risk of APRs self-interactions. These mechanisms include the so-called gatekeepers: these are amino acid sequences on the protein backbone that flank the APRs, preventing them from self-assembly. They have repulsive effects, obtained through charged residues (like Arg, Lys, Asp, Glu), large and flexible side-chains, or amino acids whose structure is incompatible

with a β-sheet strand, such as proline. Gatekeeper residues do not contribute to protein native folding in its native conformation, but rather, specifically prevent aggregation from the unfolded state [54, 65]. For example, the TTR 26–57 segment of transthyretin was studied to investigate the protein implication in senile systemic amyloidosis. The segment was found to be rich of potentially amyloid-prone peptides, but further studies highlighted the importance of a lysine residue in position 35, capable of preventing aggregation of the segment through the repulsive effect of its charge. The specific role of $Lys_{35}$ was investigated changing the lysine with one leucine on the TTR 26-57 sequence. The mutated peptide underwent aggregation at two different pHs, 5.0 and 7.5, and at different temperatures between 25 and 50°C, while the wild type remained crystal clear in all the conditions applied[66].

## 1.3.4. Chaperones-mediated folding

Chaperones are a class of endogenous stabilizers that induce folding of freshly expressed proteins. Only a small proportion of freshly expressed proteins are actually able to fold spontaneously and most of them will assume a range of different misfolded or partially folded configurations, before reaching a final stable folded state. The energy barrier between these intermediates delays the folding process, thus increasing the probability for the hydrophobic sequences of the protein to be exposed to the exterior/solvent, inducing protein aggregation. Most of newly synthesised proteins are generally accumulated in the lumen of the endoplasmic reticulum (ER). Here, after post-translational modifications, proteins will fold before they reach their final destination, or, if folding is unsuccessful, they will be subjected to ER associated degradation.

Chaperones can potentially regulate both proteins folding, and degradation of unfolded protein. Chaperones are proteins, usually divided into major classes[67]:

- Heat shock proteins Hsp70s;

- Hsp40s;

- Nucleotide Exchange Factors (NEFs);

- Hsp90s;

- Thiol oxidoreductases;

Hsp70 are the most important class of chaperones. They comprise three domains, a 44 kDa N-terminal ATPase domain, a 15 kDa substrate binding domain, and a 10 kDa C-terminal lid[67]. Binding of unfolded or partially unfolded proteins in the substrate-binding domain is regulated by the energy produced by ATP-hydrolysis, which induces conformational changes in the ATPase domain of Hsp70 that result in the opening of the 10 kDa C-terminal lid, allowing the substrate to interact with the binding domain with high affinity. ADP release from the ATPase domain is followed by ATP re-binding, with subsequent release of the substrate[67-69]. Two different mechanisms of action have been proposed for Hsp70. In the first mechanism Hsp70s are believed to keep the concentration of the free substrate sufficiently low to prevent aggregation by simply binding it, while unbound proteins are free to fold spontaneously to the native state ('kinetic partitioning'). According to this mechanism, chaperones prevent proteins aggregation in a "passive way" (Fig. 1.5).

In the second mechanism, the chaperone can interact with hydrophobic patches that have induced misfolding and aggregation of proteins, favouring their untangling and the release of folded proteins unimers[68, 70, 71].
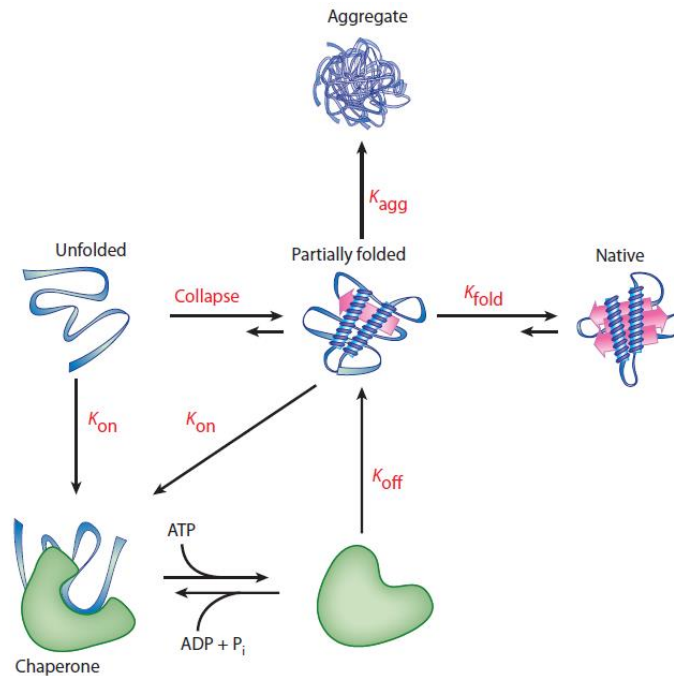


Figure 1.5: Chaperone-mediated protein stabilization. From the unfolded state, the protein collapses to partially folded intermediates, which are prone to aggregation. Chaperones bind these intermediates, preventing their aggregation. If $K_{fold}$ is higher than $K_{on}$ and $K_{agg}$, folding works efficiently. When $K_{on}$ is greater than $K_{fold}$, the chaperones can stabilize partially folded or totally unfolded protein molecules, avoiding their aggregation, but fail in inducing their folding. The presence of co-chaperones may be required to improve the process and ensure correct protein folding. When $K_{agg}$ is greater than both $K_{fold}$ and $K_{on}$ (for example under stress conditions, or when high levels of recombinant therapeutic proteins are expressed in bacteria) protein aggregation occurs. Image taken from reference[70, 72].

Hsp40s can act as co-chaperones modulating complex formation between Hsp70 and polypeptides. Through specific binding domains, they can bind and deliver specific proteins to Hsp70. More importantly, they can induce ATP hydrolysis in Hsp70s, thus stabilising the Hsp70-protein complex[73, 74].

J-domain proteins (JDPs) and Nucleotide Exchange Factors (NEFs) act in a similar way. They both bind Hsp70s in the ATPase domain. JDPs are co-

chaperones, which are able to induce accelerated ATP hydrolysis. NEFs can accelerate ADP-ATP exchange, instead[75].

Hsp90s can a-specifically recognise and bind pre-folded proteins, stabilising the conformation of proteins clefts in the native state, so that hydrophobic residues in these clefts are not allowed to drive protein denaturation. Hsp90s can bind autonomously to these proteins, in the cytoplasm and nucleoplasm, with constant cycles of assembly and disassembly. Alternatively, binding can be promoted by Hsp70s, which bind the protein first. Hsp90s can also cooperate with Hsp70 to form a multichaperone complexes that can identify proteins that have undergone oxidative or other toxic damage and direct them to degradation[76].

Two different lectins, the transmembrane protein Calnexin and the soluble Calreticulin, can bind and stabilise glycoproteins, favouring their release in the fully-folded form[77]. Thiol oxidoreductases are a family of chaperones, usually located in the endoplasmic reticulum, that are involved in disulfide bond formation. They can induce protein folding, and can recognise and target misfolded proteins for ER associated degradation[67].

Chaperones malfunctions can compromise the folding of specific proteins, resulting eventually in aggregates formation. For example, mutations in the Hsp70 co-chaperones family have been correlated with inherited neurodegenerative and cardiac disorders, characterised by deposits of protein aggregates.[78] From a clinical perspective, a better understanding of chaperones mechanism of action and structure might lead to the development of more efficient protein stabilizers.

### 1.3.5. Most frequently used techniques for detection and analysis of protein aggregates

The formation of protein aggregates can be detected *in vitro* by a plethora of different techniques[79, 80 81].

The formation of organized amyloid fibrils can be easily detected by low-molecular weight dyes such as Congo Red and Thioflavin T. These small molecules are known to interact with amyloid plaques, with subsequent significant changes in their fluorescence profile. The binding of Congo Red to fibrils induces a red-shift in CR maximal optical absorbance from 490 nm to 540 nm, while ThT displays a shift of the excitation maximum (from 385 nm to 450 nm) and the emission maximum (from 445 nm to 482 nm) and a dramatic increase of its fluorescence intensity[82, 83].

The presence of protein aggregates can be detected by chromatographic techniques, such as Size Exclusion Chromatography (SEC). Since this technique can separate molecules of different size, the unaggregated protein will be eluted at different retention times of its aggregates. According to the protein investigated, the nature of its aggregation, and the chromatographic column employed, it could be also possible to separate different aggregates of the same protein[84].

The formation of protein aggregates could be further detected by scattering techniques, such as Dynamic Light scattering, which can calculate the size of molecules dispersed in solution in the 0.1-10000 nm range[85].

The increased scattering generated by large aggregates causes also a reduction of transmitted light through the protein solution. The loss of transmittance can be easily recorded with a UV/VIS spectrophotometer in a turbidimetry experiment, working at wavelengths where proteins in solution generally do not adsorb light (e.g. ≥350 nm). This experiment was successfully performed in this thesis to evaluate the aggregation of hen egg lysozyme. Although the measurement does not provide information about the type of the aggregate and its size, the procedure is simple and ideal to quickly assess the formation of aggregates in different protein formulations[79, 86].

Finally, Reverse Phase HPLC chromatography was widely employed through my PhD to indirectly quantify the aggregation of different proteins and peptides, whose large aggregates were easily isolated in solution by centrifugation. RP-HPLC analyses were performed directly on re-solubilised aggregates, allowing to quantify the amount of aggregated protein, or quantifying the amount of protein left in solution in the supernatant after centrifugation. The quantification was calculated using a UV detector and a calibration curve prepared by RP-HPLC analysis of proteins solutions of known concentration.

# 1.4. Aggregation blockers: current strategies

Despite the significant improvements in the manufacturing of biopharmaceuticals in the last 30 years, the stability to aggregation of recombinantly expressed proteins is still a major concern, and substantial investments have been made to address this issue. In parallel, strategies have also been developed to reduce aggregation of endogenous proteins observed aggregates associated with in neurodegenerative diseases.

## 1.4.1. The stabilising effects of low-molecular weight osmolytes

One approach focuses on low-molecular weight osmolytes for the stabilisation of proteins in both liquid and solid formulations. These are naturally occurring molecules, which usually accumulate intracellularly in response to stressful conditions. They counter-balance the intracellular water loss that may result from evaporation into air or osmosis into concentrated aqueous environments. Water loss may lead to cell shrinkage and death[87-89]. The most common osmolytes are polyhydric alcohols, free amino acids and their derivatives, and combinations of urea and methylamines[87]. These small molecules share a similar mechanism of action on proteins, as they are usually excluded from the immediate vicinity of the protein surface. For example, equilibrium dialysis experiments on sucrose highlighted that sucrose concentration was higher in the compartment free of the protein than in the one containing it[90]. This phenomenon is called Preferential Exclusion and results in an increased amount of water surrounding the protein. Repulsion of solute around the protein surface increases protein free energy. However, since, when unfolded, the

protein is less compact and has a higher surface area, it will display an even higher free energy. The protein therefore tries to reduce as much as possible the exposed surface area by adopting a folded conformation, which is energetically favoured. Hence, osmolytes act on unfolded proteins promoting their re-folding[91-93].

Osmolytes are commonly employed in many of the different steps that involve protein expression, purification and formulation. They can be used to increase the amount of soluble folded protein expressed in recombinant *Escherichia coli*. It has been mentioned above that freshly expressed proteins are subjected to aggregation in bacteria. These aggregates, called Inclusion Bodies, are often reversible, and can be re-solubilised. Unfortunately, the solubilising agents normally used in the process, like urea or guanidine hydrochloride, have a destabilising effect on proteins secondary structure, thus leading to re-denaturation of proteins recovered from Inclusion Bodies. The addition of amino acids such as glycine and proline, sugars like trehalose and sucrose, and polyhydric alcohols such as sorbitol can induce the re-folding of solubilised proteins[94, 95].

Osmolytes can also be conveniently used to improve stability of protein liquid and solid formulations, in case of protein exposure to different stress factors, for example high temperature, shaking, agitation, or high concentration, during storage, shipping and handling. For instance, buffers containing the amino acid histidine, lysine and arginine substantially increased the unfolding transition temperature of the three IgG domains, showing stabilising effects[96] when

unfolding transition temperature of ImmunoglobulinG was evaluated by Differential Scanning Calorimetry. Similarly, different amino acids were tested as excipients to avoid the aggregation of Keratinocyte Growth Factor in reconstituting buffers after lyophilisation, with aspartate and glutamate being the most efficient[97].

Arginine has been evaluated for its ability in preventing protein-protein interactions[98]. Its stabilizing properties surpass the Preferential Exclusion effect and have been attributed to its specific molecular structure which promotes the formation of clusters formed by 3-5 arginine molecules. These clusters are characterised by a hydrophobic surface, due to the 3 methylene groups of the amino acid side chain. For this reason, the clusters can bind and mask hydrophobic sequences of the aggregating protein molecules, thus preventing them from interactions and eventual aggregation[99]. However, it has also been shown that arginine in some cases can favour aggregation through interactions of its guanidinium group with several protein residues, resulting in detrimental protein conformational changes[100].

As mentioned above, lyophilisation is a potential trigger of protein aggregation. Typically, sugars are the preferentially employed stabilising agents during the drying process[93]. However, amino acids can be also added, together with other additives, to improve protein stability during the lyophilisation procedure. In a recent work, a panel of 15 amino acids was screened in sucrose-stabilised human serum albumin and α-Chymotrypsin lyophilised formulations; the amino acids were added to the protein-sucrose mixtures before freeze drying

at a 1:1:0.3 (w/w) sucrose-protein-amino acid ratio. Aggregation level of re-dissolved protein formulations was evaluated by SEC. The data show that all the amino acids tested, except glutamic, managed to increase protein stability of tested formulations to various extent[101].

The stabilising action of sugars, like sucrose and trehalose, during the drying process, is not attributed to the Preferential Exclusion effect. Two theories have been formulated to explain their effects on proteins: the vitrification theory suggests the immobilisation of the protein in a rigid, amorphous glassy sugar matrix, resulting in protein physical entrapment which slows down protein unfolding and degradation processes. The vitrification takes place below sugars glass transition temperature, above which sugars are in a rubbery state and the stabilising effect is lost[102, 103]. In agreement with this theory, sugars with higher glass transition temperature, like trehalose, are more effective in their stabilising effects[104, 105].

The second mechanism proposed is the Water Replacement theory, which suggests the presence of H-bond interactions between the hydroxyls groups on the sugar and the protein. These interactions replace H-bonds that the protein normally establishes with water and stabilise the protein in its native conformation[106-108].

## 1.4.2. Covalent PEGylation

The covalent attachment of PEG to therapeutic proteins has been successfully employed in many cases to improve protein stability. PEGylation is believed to stabilise the protein by surrounding the molecule with PEG hydrophilic chain,

thus preventing protein molecules from approaching each other to start the aggregation process. Moreover, PEG protection limits the access of endogenous proteases that may degrade the protein after administration. Protein immunogenicity is also reduced. Finally, PEGylation increases the hydrodynamic volume of PEGylated protein molecules preventing their from renal filtration and secretion, and consequently increasing protein bioavailability and half-life[109]. From Adagen (PEGylated Adenosine Deaminase), first PEGylated protein approved by FDA in 1990[110], more than 10 PEGylated proteins have reached the clinic in the last 25 years[111]. A recent research has highlighted that the global PEGylated proteins market is forecast to reach USD 1,137.8 Million by 2021 from USD 690.6 Million in 2016, with different types of commercialised PEGylated biotherapeutics, including colony stimulating factors, interferons, erythropoietin and mAbs[112]. Different chemistries can be used to covalently attached the PEG chain to the protein. Typically, monofunctional PEG reagents are used to PEGylate proteins, through a functional group attached to one end of the PEG chain, which may react with N-terminal amine, lysine, cysteine, or other amino acids[113, 114].

Unfortunately, PEGylation is associated with certain unavoidable drawbacks: firstly, it has been increasingly reported that PEG itself may be immunogenic and can induce anti-PEG antibodies[115]. Moreover, steric hindrance of the hydrophilic PEG chain may affect the binding of the PEGylated protein to its target receptor or substrate, effecting its activity[116].

In order to overcome the drawbacks of PEGylation, different polymers have been explored as alternatives to PEG to achieve polymer degradability and

reduced immunogenicity. Amongs these are polysaccharides, such as hyaluronic acid, polyaminoacids, like polyglutamic acid, and polymeric materials such as poly-N-vinylpyrrolidone and polyglycerol[5].

A specific strategy aimed at reducing PEG interference on protein-target interaction is to use PEGylation chemistries which result in the release of PEG from protein molecule in specific conditions, developing a "releasable PEGylation". The PEGylated conjugates are stable under storage, and PEG release from the protein occurs upon a trigger following administration. This strategy provides improved protein bioavailability and eliminates PEG influence on the affinity of the protein for its final target. Controlled and gradual release of the PEGylated protein is obtained using a degradable linkage at the attachment site on the protein surface[117].

### 1.4.3. Non-covalent PEGylation

Non-covalent PEGylation is a potential alternative to "classic" PEGylation, and it is somehow similar to 'releasable PEGylation'. The approach is based on non-covalent interactions between the protein and the PEG moiety containing the polymeric chain. Slow release of the protein from the PEG-protein complex ensures increased protein stability, without affecting its affinity for its final target. Without the covalent attachment of PEG, potential material loss and long purification steps resulting from PEG conjugation are also avoided, as it is any type of stress that covalent linking may cause to the protein, with potential unfolding[118].

One approach to non-covalent PEGylation is to promote protein-PEG containing polymer chain interactions through ionic forces. It is the case of polyelectrolyte-based PEG copolymers which electrostatically interact with protein molecules, preventing them from approaching and interacting with each other. For example, Kurinomaru and Shiraki utilised cationic poly(ethylene glycol)-b-poly(N,N-dimethylaminoethyl methacrylate) to reversibly complex the negatively charged protein asparaginase (Fig. 1.6). Results showed that by forming non-covalent complexes the polymer was able to stabilize the protein against mechanical stress (shaking), and against proteolytic degradation by trypsin[119]. The interaction was provided by electrostatic interactions between the protein and the PAMA block, while the PEG increased protein stability to a level comparable to what normally observed in covalent PEGylation.
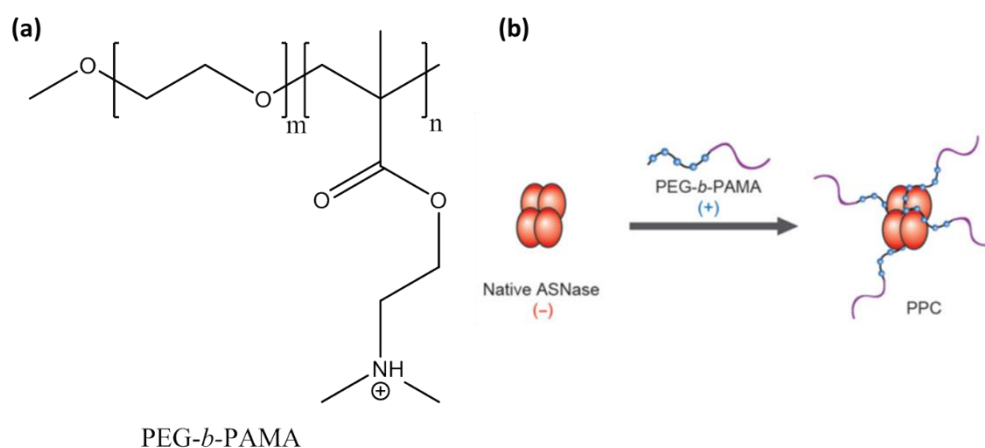


Figure 1. 6: (a) Structure of the positively charged polyelectrolyte that was used to complex asparaginase[119]. (b) The charged copolymers interact electrostatically with the proteins, shielding them and preventing them from interacting. Image taken from reference[119].

The same cationic PEG-b-PAMA was analysed on enzyme α-amylase. Enzyme kinetics studies and molecular dynamic simulations allowed to discover that the

polymer can reversibly inhibit the enzyme activity through random electrostatic interactions[120].

Within our group, mPEG$_{2k}$-poly (glutamic acid) copolymers were utilised to form efficient and reversible complexes with lysozyme through ionic interactions between the protonated amino acid residues on the protein, and the polymer negatively charged glutamic side chains.[121]

Recently, a monocationic PEG was prepared by modification of the PEG chain-end with a positively charged Diethylaminoethyl group. The polymer was employed to electrostatically interact with the protein catalase, and complex formation was confirmed by native PAGE electrophoresis[122]. Another study evaluated poly-amido saccharides, which were thought to stabilize proteins through multiple hydrogen bonds. Tests made on lysozyme showed higher activity for the protein mixed with the polymers after ten lyophilisation cycles, relative to the unmixed control[123].

An alternative approach is based on chelating agents. A multi-arm PEG was conjugated to nitrilotriacetic acid (NTA), a chelating agent which is able to associate with histidine side chain of proteins through reversible coordination bonds mediated by metal ions such as $Ca^{2+}$, $Cu^{2+}$, and $Fe^{3+}$. Interaction between the polymer and the growth hormone G-CSF was observed by Surface Plasmon Resonance, even though the complex failed to prolong G-CSF half-life in vivo[124].

Similarly, PEG was derivatised at its chain-end with sugar Fucose. The resulting Fuc-PEG was used to complex RSL, a hexavalent fucose-binding lectin from Ralstonia solanacearum. The formation of high molecular weight

protein–polymer complexes was shown by size exclusion chromatography (SEC), small-angle X-ray scattering (SAXS), and polyacrylamide and agarose gel electrophoresis experiments[125].

Non-covalent PEGylation based in hydrophobic interactions has also been described. The approach takes advantage of potential hydrophobic pockets that may be present on/close to the proteins surface, or may be exposed to the external solvent upon unfolding. Recently, in Tudor Arvinte's group tryptophan was covalently linked to a 2 kDa PEG. The resulting (PEG-Trp) was successfully employed to significantly reduce the aggregation of salmon calcitonin (sCT), induced in 10 mM pH 6 citrate buffer and measured by turbidity. The interaction between the polymer and the peptide was indeed achieved through the hydrophobic tryptophan group[126]. The same concept was extended, within the same research group, to different hydrophobic moieties, derivatising PEG with cholesterol, dansyl, phenylbutylamino and benzyl groups. The resulting modified PEGs, along with the original tryptophan-PEG, were compared for their ability of preventing the aggregation of salmon calcitonin and hen egg lysozyme. PEG-tryptophan was found to be the most effective to minimise sCT aggregation, while PEG-cholesterol and PEG-phenylbutylamino were the most effective against lysozyme aggregation[127].

Similarly, cholanic acid interaction with proteins has been investigated by the Salmaso and Caliceti group, for reversible non-covalent protein PEGylation through hydrophobic interactions between the cholanic moiety and proteins hydrophobic pockets. Cholanic acid-terminated PEGs of Mn spanning between

5 and 20 kDa were synthesised and tested on two proteins, recombinant human growth hormone (rh-GH) and recombinant human granulocyte colony stimulating factor (rh-G-CSF). The polymers proved to be capable of forming supramolecular nano-complexes with both proteins. The corresponding formulations were tested in rats, where pharmacokinetic studies showed that the complex was able to ensure a slow release of the proteins from the site of injection. As the proteins were slowly released from the polymer-protein nano-complex, the protein half-life was significantly longer, with prolonged effects of the two hormones on rat growth[128, 129].

## 1.4.4.  RAFT polymerization

In this thesis, amphiphilic block copolymers were synthesised and employed to act as non-covalent protein stabilisers, mimicking the effect of non-covalent PEGylation. Instead of using PEG, commercial and synthesised monomers were polymerised using RAFT polymerization. Reversible addition fragmentation chain transfer (RAFT) polymerization belongs to the class of reversible deactivation radical polymerizations (RDRPs), which are characterised by mechanisms that control the rate of chain growth in order to ensure predictable molecular weight and a final molar mass distribution as narrow as possible[130, 131]. In particular, RDRPs rely on the equilibrium of the growing polymer radical chains between active and dormant states. This equilibrium favours the dormant species, ensuring that the concentration of active growing radicals remains low. In this way, the number of irreversible termination events between growing chains, which would broad the final molar mass distribution, is minimised.  In RAFT polymerization this equilibrium is achieved through a

Chain Transfer Agent (CTA or RAFT agent), usually a thiocarbonylthio group (Scheme 1.1)[132].
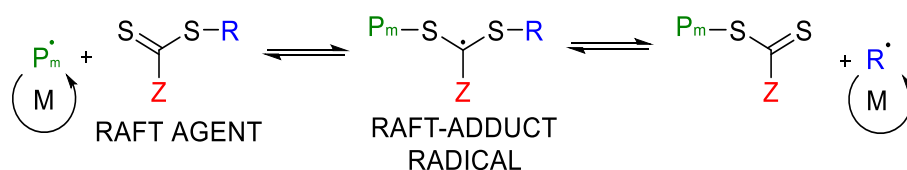


Scheme 1.1: General structure of a chain-transfer RAFT agent and its mechanism of action. The RAFT agent can form stable radical adducts with radical growing polymer chains. Stability of the adduct is essential to slow down the polymerization rate and reduce the number of active species in solution. The Z group is chosen to increase the stability of the adduct. The R group must be stable enough to be released as a radical species, at the same time it must be reactive so that its radical form will react with monomers re-initiating the polymerization process[133].

The RAFT agent can bind and exchange the active, propagating radical chains, thus establishing equilibrium with its dormant species[132], at a higher rate than that of the radical propagation, so that all chains will have a similar degree of polymerization[131]. RAFT polymerization requires a starting radical-generating initiator that produces radicals upon heating, or other stimuli, e.g. light irradiation. These radicals will react with the monomer (M), to give radical propagating, active polymeric chains (P·). The RAFT agent is able to exchange the growing radical chains with its R group, through formation of the RAFT adduct radical, where both P and R are bound to the RAFT agent. P· will therefore be in equilibrium between its active and dormant state (pre-equilibrium), and the generated radical R· will propagate with other monomer restarting the radical propagation process (re-initiation). After the re-initiation has taken place, the propagating chains are constantly exchanged by the RAFT agent (main equilibrium). The general mechanism is shown in Scheme 1.2. At the end of the reaction, the chains will have attached the RAFT agent on one side, and the R group on the other side[132].
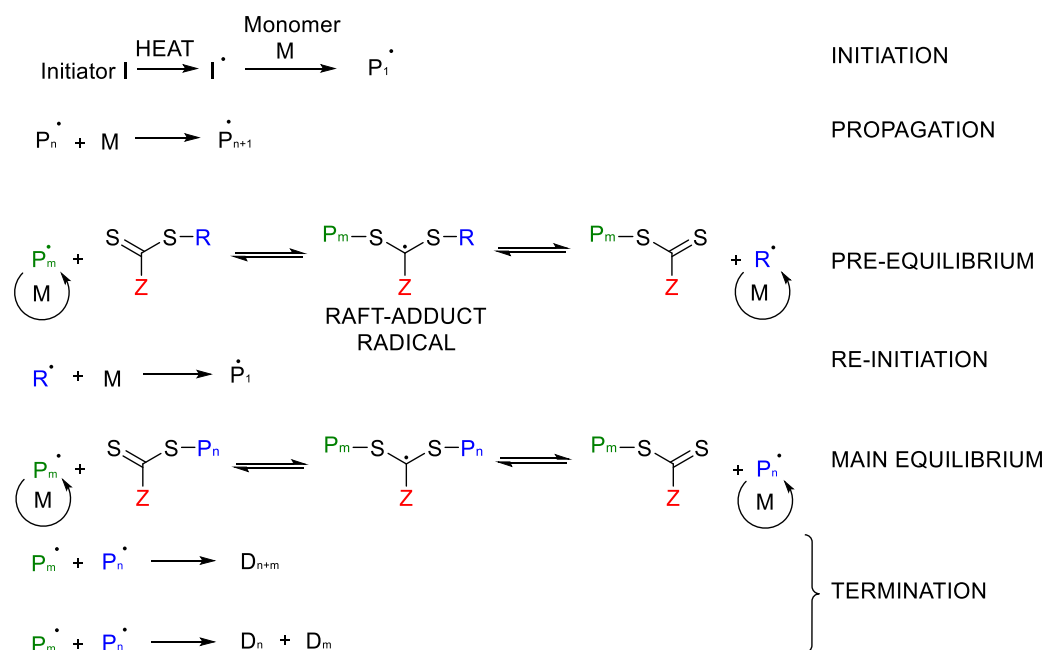
Scheme 1.2: General mechanism of RAFT polymerization[133].

## 1.4.5. Aggregation Prone Regions as target for protein stabilisation

Another strategy of protein stabilisation relies on specific 'neutralization' of APRs. This approach has been used mainly on endogenous proteins, with the aim to prevent the formation of amyloid aggregates that are, as discussed above, observed in several neurodegenerative diseases[26]. Initial studies suggested that synthetic peptides of certain composition, called β-sheet breakers, could be developed, capable of binding the Alzeheimer's amyloid precursor αβ fragment, but unable to self-assemble into a β-sheet structure. Such peptides were typically 11-15 amino acids long and comprised the central aminoacid region of the αβ peptide: LVFFA. Polar amino acids, to improve water solubility, and proline residues, which are highly unfavourable to be incorporated into β-sheet structures[134], were added as well. These peptides

proved to be able to prevent the aggregation of the αβ peptide into amyloid fibrils, and also dissolved preformed fibrils in vitro[135-137]. Interaction between these peptides and the amyloid precursor αβ peptide is attributed to the core LVFFA sequence that both shared. This sequence had been identified as the most important Aggregation Prone Region (APR) of Aβ[138, 139].

Many peptides have been developed since then, designed to bind to APRs, preventing them from self-interacting and therefore blocking the aggregation process. These peptides typically possess the LVFFA core that ensure interaction with Aβ, but are subjected to various chemical modification at the N- and C-Ter that are aimed to block the aggregation process[140].

For example, the central hydrophobic sequence of the Aβ peptide KLVFFA was modified by selectively introducing N-methylgroups in the peptide bonds of hydrophobic amino acids Leu, Val, Phe, and Ala, to generate various monomethylated peptides. The common KLVFFA sequence provided interactions between the Aβ and the peptides, but the N-methylgroup disrupted the hydrogen bonding that usually promotes the formation of β-sheet aggregates. αβ -induced cytotoxicity was evaluated on PC12 cell cultures. Addition of peptides where phenylalanines had been N-methylated resulted in a significant decrease of cytotoxicity[141].

In a different work, the peptidic amyloidogenic sequence LVFFA was chemically conjugated to a poly-hydroxpropylmethacrylate chain, creating a PHPMA-peptide conjugate where the mol % peptide per polymer chain was kept constant at 7% and the polymeric chain length was systematically varied to

explore a range of molecular weights, between 22 and 224 kDa. The polymers were tested on preformed $A\beta_{40}$ fibrils, monitoring their disassembly by DLS, AFM imaging, and ThT fluorescence. Analyses showed that the polymers were able to disassemble the fibrils in a molecular weight-dependant manner, as the biggest polymer was capable of re-solubilise the fibrils into dispersible sub-100 nm structures, with no fibrils remaining after 3 days[142, 143].

In other studies, peptides were linked with sugar moieties. A new peptidomimetic molecule was developed, which was formed by two flanking dipeptides, Ala-Val and Val-Leu, and a central D-glucopyranosyl moiety. The dipeptides were designed to recognise and bind the hydrophobic KLVFF sequence in the central region of $A\beta$ peptide. The sugar was utilised as a potential $\beta$-sheet breaker. Results showed that these peptidomimetics were indeed able to inhibit or increase the lag phase of amyloid formation[144]. However, experiments were conducted in DMSO, while studies in an aqueous, biologically relevant medium were not conducted. Solubility and aggregation issues in aqueous solvents must be considered when these peptidomimetics are designed, because they derive from hydrophobic and aggregation-prone sequences.

The same concept was extended to other neurodegenerative diseases, such as Parkinson's. As mentioned above, the accumulation of amyloid aggregates of pre-sinaptic protein $\alpha$-sinuclein is a hallmark of Parkinson's disease. Hence, it does not surprise that $\beta$-sheet breakers have been developed to target $\alpha$-synuclein fibrilisation. The insurgence of the disease has been correlated to

different α-synuclein mutants with altered fibrillation kinetics, which may pathologically enhance and accelerate the formation of protein aggregates[145]. Research has focused in particular on α-synuclein hydrophobic core, which spans residues 61-95 and comprise a hydrophobic segment, called non-amyloid β component (NAC), whose analogous synthetic peptides have shown to be able to interact with α-synuclein and induce its fibrillisation *in vitro*[146, 147]. A study screened different α-synuclein mutants where amino acids were substituted at specific positions. The study highlighted that six of these mutations did not fibrillate and also inhibited wild type α-synuclein fibrilisation. Importantly, these self-fibrilative defective mutants were also effective on Parkinson's disease related α-synuclein variants[148]. The size of the six mutants was finally reduced to that of around 10 amino acids length peptides, which spanned the fibrillation-suppressing mutation sites. Protein fibrilisation was evaluated, and several peptides reduced the fibrillation of wild type α-synuclein to about half compared to the sample that contained only α-synuclein. The most effective peptide, T72P, proved also to be able to re-dissolve pre-formed fibrils[149].

A similar study focused on mutated α1-Antitrypsin, whose polymerization is correlated with chronic pulmonary diseases. Based on α1-Antitrypsin's hydrophobic reactive loops (RCL), different peptides were synthesised with combinatorial methods, and screened with SDS-PAGE, to assess their ability in binding the mutated protein at the RCL level and consequently blocking protein aggregation. Specific and dose-dependent binding of the selected peptide was confirmed by Surface Plasmon Resonance[150].

### 1.4.6. Solid Phase Peptide Synthesis (SPPS)

Solid Phase Peptide Synthesis (SPPS) is the most commonly used technique for the synthesis of peptides, and it was employed also for the synthesis of the β-sheet breakers discussed above. The major advantage over solution synthesis lies in the significant simplification of the purification steps that take place after each amino acid coupling[151]. Moreover, machines have been developed, which allow the process to be fully automated[152].

The mechanism relies on the covalent attachment of the growing peptide to a solid, polymeric support. The peptide chain is then extended by a series of repetitive steps. Complete coupling is achieved using an excess of reagent, which can be easily washed away by filtration (Fig. 1.7)[153].
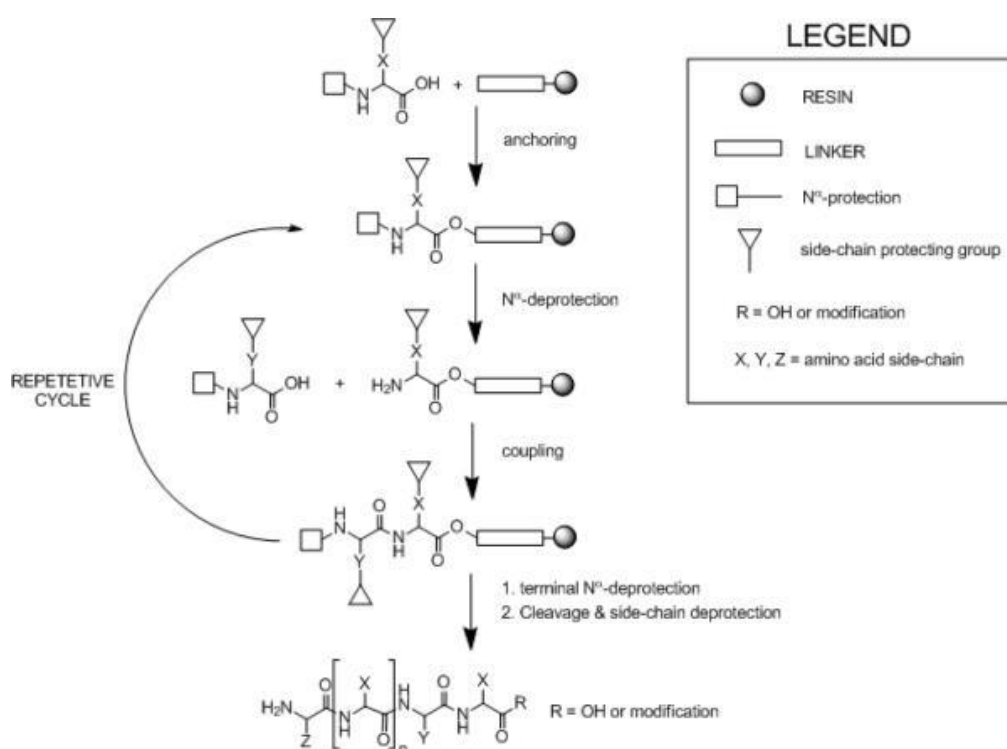


Figure 1.7: SPPS steps. The first amino acid is covalently anchored to a solid, polymeric support. After the removal of the Nα-protecting group, a new amino acid is coupled to the previous one. A cycle of Nα-deprotections and amino acid couplings can be repeated till the sequence is completed. Finally, the side chains-protecting groups are removed and the peptide cleaved from the solid support. Image taken from reference[153].

A plethora of different coupling agents can be used to attach the amino acid to the growing peptide chain. Among them, the most common are carbodiimides such as DIC and DCC, HOBT, HBTU, HATU and Oxyma[151]. For stepwise amino acids coupling, Nα-protection and protected side chains are required. Two different strategies have emerged: in the first case, BOC is used for Nα protection, which can be removed, at the end of each coupling step, with a mild acid such as TFA. Benzyl-based (Cbz) groups are used to protect the amino acids side chains and can be removed at the end of the synthesis with a strong acid such as hydrofluoric acid (HF). Due to the high toxicity of HF, this technique has been mostly replaced by Fmoc SPPS, where Fmoc is used as Nα-protecting group, and removed with piperidine at the end of each coupling step. Different functional groups can be used for side chains protection, including Boc, Pbf, Tbu and Trt, which are easily removed by TFA at the end of the peptide synthesis[151, 153]. Fmoc SPPS was used in this thesis as well.

The choice of the solid support is also very important, as good solvation of the peptide on the support is required for successful coupling. The linker between the peptide and the resin is acid-labile. It is then possible to achieve both peptide deprotection and cleavage by treating the solid support with TFA. Interestingly, trityl derivatised resins are highly acid-sensitive, and can be used to cleave the peptide in milder conditions, e.g. TFE:DCM 2:8 v/v. These conditions do not affect the stability of side chains protecting groups, allowing the cleavage of a fully protected peptide[151]. This strategy was applied also in this thesis.

## 1.5. Hen egg lysozyme Aggregation Prone Region

Hen Egg White lysozyme is a 129-amino acids enzyme, whose main substrate is the peptidoglycan cell wall of Gram-positive bacteria. It can degrade the polysaccharide architecture of many kinds of cell walls, displaying an important role in protection against bacterial infections[154, 155].

The protein comprises a large α-domain containing four α-helices and a smaller β-domain consisting of a triple-stranded anti-parallel β-sheet. Six hydrophobic clusters have been identified, four of which comprise one tryptophan. The protein contains a total of four disulphide bonds[156]. The active site is located on a protein cleft, where two residues, $Glu_{35}$ (glutamic acid) and $Asp_{52}$ (aspartic acid) have an essential role in hydrolysing the β(1-4) glycosidic bond between alternating units of *N*-acetylmuramic acid and *N*-acetylglucosamine, which are the building blocks of peptidoglycan[157].

Interestingly, the aggregation of hen egg lysozyme has been observed in different conditions: when treated at pH 2 and 70 °C, the protein underwent hydrolysis, and the resulting fragments self-assembled into fibrils and finally into amyloid-like aggregates[158]. Protein aggregation was induced in aqueous ethanol solutions and monitored by light scattering[159]. Lysozyme self-assembly was observed also at pH 12, due to the neutralisation of its basic residues and subsequent exposure of its hydrophobic patches[160]. From these studies, some regions on its sequence were identified as highly aggregating. In particular, the sequence 49-64 from wild-type hen egg lysozyme was found to form an extensive network of fibrils following incubation for 24 hours at pH 4.0 and

37°C. The sequence is part of lysozyme β-domain and forms a pair of antiparallel β-strands in its native structure[161]. Hence, lysozyme β-domain was suggested to be responsible for protein fibrillisation observed in acidic conditions. In another study, lysozyme was enzymatically fragmented into different peptides, and the different fragments treated under acidic conditions to detect the formation of fibrils. Fragment 57–107 was found able to generate amyloid fibrils under these conditions, suggesting its role in protein aggregation[162].

In a recent study, the 54-62 sequence was found to be highly amyloidogenic and prone to self-aggregation. The sequence corresponds to the peptide GILQINSRW, which was isolated from lysozyme, and proved to be able not only to self-assemble, but also to induce the aggregation of lysozyme itself at pH 7.5 and 25°C. The sequence was therefore identified as one of hen egg lysozyme aggregation prone regions (APRs)[163] (Fig. 1.7).
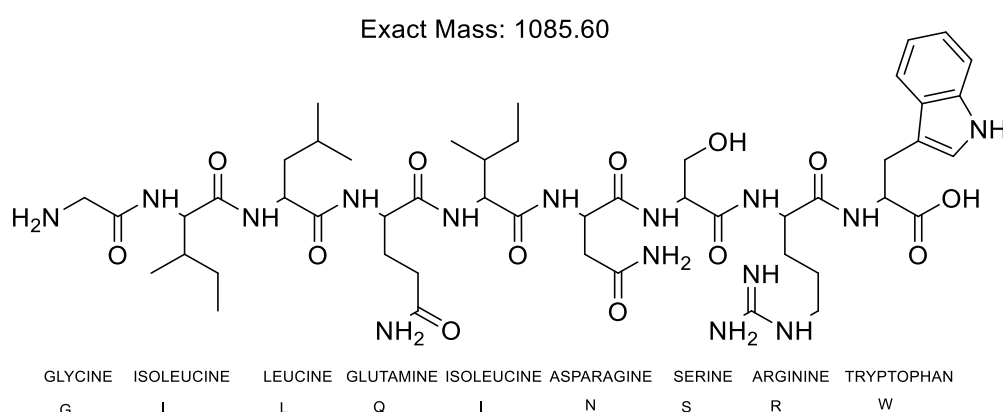


Figure 1.8: structure of Lysozyme APR GILQINSRW.

Another study showed that the sequence is prone to aggregate in the 2-7 pH range, and highlighted the importance of tryptophan in position 62, as its

substitution with a glycine resulted in peptide GILQINSRG, whose self-assembly was completely suppressed[164]. This particular tryptophan had been already studied and had shown to be very important for lysozyme proper folding. Wild type Hen Egg lysozyme was unfolded using guanidine hydrochloride, and subsequently diluted in a denaturant-free aqueous solution. It appeared that $Trp_{62}$, together with $Trp_{63}$, could establish hydrophobic interactions with $Trp_{108}$ and $Trp_1$, allowing lysozyme hydrophobic clusters to interact with each other and form a core nuclei, which stabilised the protein and directed it to proper folding[165]. A single-point mutation (W62G) on lysozyme structure was found to slow down the folding process, increase the chance of random folding and ultimately lead to protein aggregation[166].

By contrast, when both the wild type lysozyme and its W62G mutation were incubated for 15 days at pH 2, the wild type showed fast aggregation into amyloid fibrils, while the mutant remained stable through the whole experiment[167]. It appears then that this residue is very important to direct and accelerate lysozyme proper folding, but it can also drive protein aggregation under stress conditions that induce its prolonged exposure to the external solvent. This behaviour is in line with what, as mentioned above, has been discovered about Aggregation Prone Regions, which are often responsible for proteins aggregation, but in native conformations are buried inside the protein and contribute significantly to the stability of its folded form[65].

## 1.6. Conclusions

Poor stability and potential aggregation are problems that affect the production and application of protein therapeutics. Aggregation may also occur by endogenous proteins and has been correlated to the insurgence of different neurodegenerative diseases. Among the potential factors that may trigger aggregation, the role of Aggregation Prone Regions (APRs) has been highlighted. These are relatively short, hydrophobic amino acid sequences on proteins, usually buried inside the protein core which, if exposed to the external solvent, can self-interact through mutual hydrophobic, β-sheet-like interactions and drive in this way protein aggregation.

Covalent protein modifications, in particular PEGylation, have been successfully employed to improve proteins stability and prevent their aggregation. Unfortunately, they may result in loss of proteins activity and potential enhanced protein immunogenicity. Non-covalent conjugation has been suggested as potential alternative for effective but less invasive protein stabilisation. However, specific groups are required to functionalise the polymer chain-end that allow the non-covalent interaction between the polymeric chain and the protein.

Interestingly, in several studies aggregation of endogenous proteins has been reversed by application of so-called β-sheet breakers peptides, which are short peptide sequences analogues to APRs on endogenous proteins. Thanks to their structural similarity, they can interact with APRs on the protein molecule. However, they cannot propagate the aggregation process, as they have been

chemically modified with β-sheet disruptive moieties. The identification of different APRs on therapeutic proteins, suggests that β-sheet breakers may be developed and used on biotherapeutics as well, to improve their stability in the different stages of their expression, purification and formulation. However, most of β-sheet breakers tested so far derived from specific Aggregation Prone Regions and thus were effective on specific proteins. More generic structures are required that can act on a plethora of different therapeutic proteins. Moreover, substantial engineering of β-sheet breakers structure is generally required to improve their solubility in aqueous media, which is usually very poor, due to their hydrophobic and self-aggregating nature.

## 1.7. Aims and objectives

The work presented in this thesis was aimed at developing a new class of protein excipients, to improve proteins stability and prevent their aggregation. As direct covalent protein modifications may result in loss of proteins activity and potential enhanced protein immunogenicity, we were more focused on protein non-covalent stabilisation.

In particular, we aimed at mediating the stabilising effects of hydrophilic polymer chains through non-covalent interactions between protein hydrophobic patches and β-sheet breakers. Meantime, we aimed at simplifying and minimising the chemical structure of these β-sheet breakers from that of a proper peptide to more generic peptidomimetic hydrophobic sequences, which could interact with a broader range of proteins, and could be more easily synthesised and conjugated to hydrophilic polymeric chains. By incorporating

these hydrophobic moieties into amphiphilic block copolymers, we wanted to greatly increase their aqueous solubility, and ultimately develop different groups of protein stabilisers, whose stabilising effects could be compared to that of a non-covalent PEGylation mediated by hydrophobic interactions. RAFT polymerization was generally employed as polymerization technique to build these amphiphilic block copolymers, using the commercial monomer N-hydroxyethyl acrylamide for the polymerization of the hydrophilic block.

In particular, Chapter 2 focusses on the synthesis and testing of a group of hen egg lysozyme APR analogues. These analogues were applied on lysozyme as β-sheet breakers, to interact with the original APR on lysozyme backbone and stop it from establishing mutual interactions with APRs on other protein molecules (Fig. 1.9).

The APR GILQINSRW peptide fragment was modified by incorporating different hydrophilic molecules, and finally copolymerised with hydrophilic monomer *N*-Hydroxyethylacrylamide, to make it more soluble and potentially able to stop lysozyme aggregation.
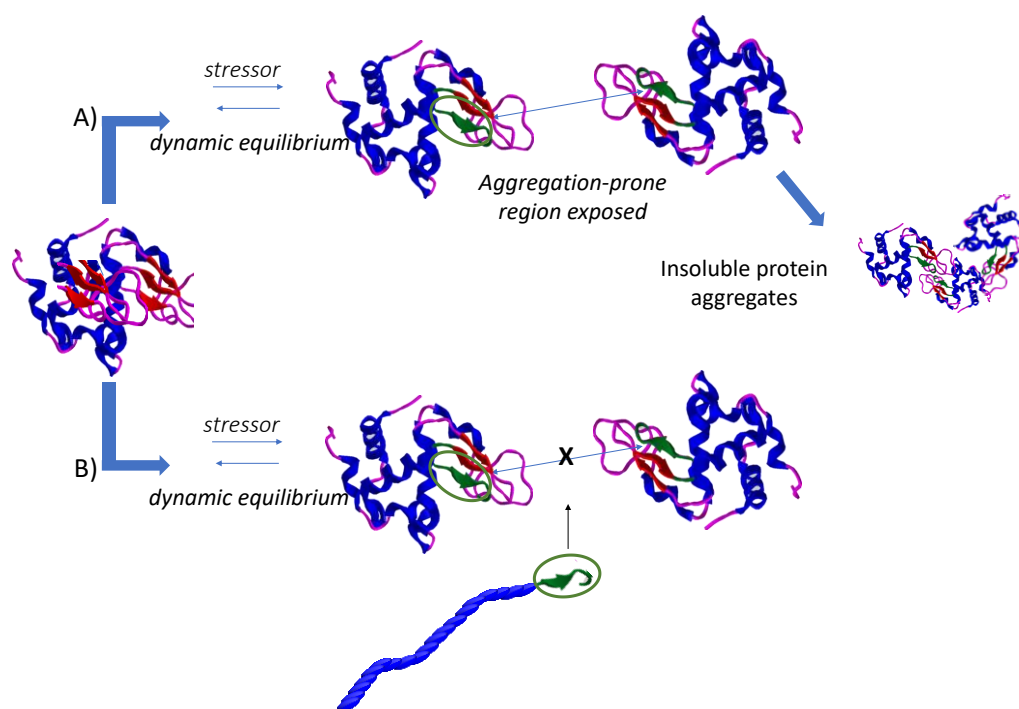
Figure 1.9: Proposed mechanism of action of the APR analogues that were synthesised in the initial part of this work. A) In the absence of APR analogue stabilisers, protein misfolding leads to Aggregation Prone Regions (shown in green) to be exposed to the external solvent. APRs from different protein molecules can start mutual interactions which lead to protein aggregation and ultimately to the formation of large, insoluble protein aggregates. B) Mutual interactions can be established between the synthesised APR peptide analogue and its homologous sequence on lysozyme backbone. We hypothesised that the incorporation of hydrophilic molecules on GILQINSRW backbone could be used to increase its solubility and give it β-sheet disrupting properties.

In Chapter 3, the initial concept was generalised to use, instead of specific APRs, block copolymers comprising a hydrophobic block made of amino acid-like moieties, such as indole 3-acetic acid to mimic tryptophan, potentially able to non-covalently interact with hydrophobic protein domains and prevent protein aggregation. A polyacrylamide chain was used again as hydrophilic block to improve the water solubility of these copolymers and shield target proteins from mutual interactions and final aggregation. The copolymers were tested on lysozyme and other two model polypeptides, bovine pancreatic insulin and antimicrobial peptide IDR 1018.

As some of these amino acid-like moieties showed stabilising effects on the proteins studied, the interaction was further investigated in Chapter 4 to evaluate if it could be used to develop a delivery system for proteins controlled-release. Antimicrobial peptide IDR 1018 was ion-paired to antimicrobial natural molecule usnic acid to develop a hydrophobic complex, which was incorporated into indole-3 acetic acid oligomers-based nanoparticles, for the synergic delivery of two antimicrobial drugs.

Chapter 5 described the synthesis and characterisation of polyacrylamide-cholesterol/cholanic acid conjugates, which were employed for non-covalent protein complexation through the hydrophobic moieties cholanic acid/cholesterol and hydrophobic patches on proteins backbone.

Finally, in Chapter 6 we concentrated on hydrophobic, non-covalent interactions between small hydrophobic probes and a group of linear and 4-arm glycopolymers. This Chapter is a continuation of a previous work started by a former PhD student in our group, Joao Madeira do O. Reversible incorporation of hydrophobic molecule Nile Red into these glycopolymers was confirmed by fluorescence studies. Interestingly, further experiments highlighted that these polymers do not self-assemble into larger aggregates, but are able to incorporate hydrophobic molecules as unimolecular micelles.

# References

1.      Leader, B.; Baca, Q. J.; Golan, D. E., Protein therapeutics: a summary and pharmacological classification. *Nature Reviews Drug Discovery* **2008,** *7*, 21.

2.      Rosenfeld, L., Insulin: Discovery and Controversy. *Clinical Chemistry* **2002,** *48* (12), 2270.

3.      Evans, M.; Schumm-Draeger, P. M.; Vora, J.; King, A. B., A review of modern insulin analogue pharmacokinetic and pharmacodynamic profiles in type 2 diabetes: improvements and limitations. *Diabetes, Obesity and Metabolism* **2011,** *13* (8), 677-684.

4.      Kinch, M. S., An overview of FDA-approved biologics medicines. *Drug Discovery Today* **2015,** *20* (4), 393-398.

5.      AlDeghaither, D.; Smaglo, B. G.; Weiner, L. M., Beyond peptides and mAbs—current status and future perspectives for biotherapeutics with novel constructs. *The Journal of Clinical Pharmacology* **2015,** *55* (S3), S4-S20.

6.      https://www.alliedmarketresearch.com/press-release/protein-therapeutics-market.html.

7.      Wei Wang, C. J. R. Aggregation of Therapeutic Proteins.

8.      Roberts, C. J., Protein aggregation and its impact on product quality. *Current Opinion in Biotechnology* **2014,** *30*, 211-217.

9.      Lee, S.-J.; Lim, H.-S.; Masliah, E.; Lee, H.-J., Protein aggregate spreading in neurodegenerative diseases: Problems and perspectives. *Neuroscience research* **2011,** *70* (4), 339-348.

10.     Sweeney, P.; Park, H.; Baumann, M.; Dunlop, J.; Frydman, J.; Kopito, R.; McCampbell, A.; Leblanc, G.; Venkateswaran, A.; Nurmi, A.; Hodgson, R., Protein misfolding in neurodegenerative diseases: implications and strategies. *Translational Neurodegeneration* **2017,** *6* (1), 6.

11.     https://www.nature.com/subjects/protein-aggregation.

12.     Challener, C. A. Challenges of Protein Aggregation during Purification. http://www.biopharminternational.com/challenges-protein-aggregation-during-purification.

13.     Peternel, Š.; Komel, R., Active Protein Aggregates Produced in Escherichia coli. *International Journal of Molecular Sciences* **2011,** *12* (11).

14.     Natalia G. Bednarska, J. S., Frederic Rousseau, Johan Van Eldere Protein aggregation in bacteria: the thin boundary between functionality and toxicity. *Microbiology* **2013**, *159.*

15.     Lebendiker, M.; Danieli, T., Production of prone-to-aggregate proteins. *FEBS Letters* **2014,** *588* (2), 236-246.

16.     Vázquez-Rey, M.; Lang, D. A., Aggregates in monoclonal antibody manufacturing processes. *Biotechnology and Bioengineering* **2011,** *108* (7), 1494-1508.

17.     Wiesbauer, J.; Prassl, R.; Nidetzky, B., Renewal of the Air–Water Interface as a Critical System Parameter of Protein Stability: Aggregation of the Human Growth Hormone and Its Prevention by Surface-Active Compounds. *Langmuir* **2013,** *29* (49), 15240-15250.

18.     Liu, L.; Qi, W.; Schwartz, D. K.; Randolph, T. W.; Carpenter, J. F., The Effects of Excipients on Protein Aggregation During Agitation: An Interfacial Shear Rheology Study. *Journal of Pharmaceutical Sciences* **2013,** *102* (8), 2460-2470.

19.     Rayfield, W. J.; Kandula, S.; Khan, H.; Tugcu, N., Impact of Freeze/Thaw Process on Drug Substance Storage of Therapeutics. *Journal of Pharmaceutical Sciences* **2017,** *106* (8), 1944-1951.

20.     Goswami, S.; Wang, W.; Arakawa, T.; Ohtake, S., Developments and Challenges for mAb-Based Therapeutics. *Antibodies* **2013,** *2* (3).

21.     Roberts, C. J., Therapeutic protein aggregation: mechanisms, design, and control. *Trends in Biotechnology* **2014,** *32* (7), 372-380.

22.     Moussa, E. M.; Panchal, J. P.; Moorthy, B. S.; Blum, J. S.; Joubert, M. K.; Narhi, L. O.; Topp, E. M., Immunogenicity of Therapeutic Protein Aggregates. *Journal of Pharmaceutical Sciences* **2016,** *105* (2), 417-430.

23.     Vugmeyster Y, X. X., Theil FP, Khawli LA, Leach MW Pharmacokinetics and toxicology of therapeutic proteins: Advances and challenges. *World J Biol Chem* **2012,** *3* (4), 73-92.

24.     Rosenberg, A. S., Effects of protein aggregates: An immunologic perspective. *The AAPS Journal* **2006,** *8* (3), E501-E507.

25.     Ratanji, K. D.; Derrick, J. P.; Dearman, R. J.; Kimber, I., Immunogenicity of therapeutic proteins: Influence of aggregation. *Journal of Immunotoxicology* **2014,** *11* (2), 99-109.

26.     Aguzzi, A.; O'Connor, T., Protein aggregation diseases: pathogenicity and therapeutic perspectives. *Nature Reviews Drug Discovery* **2010,** *9*, 237.

27.     Ross, C. A.; Poirier, M. A., Protein aggregation and neurodegenerative disease. *Nature Medicine* **2004,** *10*, S10.

28.     G Brent Irvine, O. M. E.-A., Ganesh M Shankar, and Dominic M Walsh Protein Aggregation in the Brain: The Molecular Basis for Alzheimer's and Parkinson's Diseases. *Mol Med* **2008,** *14* (7-8), 451-464.

29.     Breydo, L.; Wu, J. W.; Uversky, V. N., α-Synuclein misfolding and Parkinson's disease. *Biochimica et Biophysica Acta (BBA) - Molecular Basis of Disease* **2012,** *1822* (2), 261-285.

30.     Gundersen, V., Protein aggregation in Parkinson's disease. *Acta Neurologica Scandinavica* **2010,** *122* (s190), 82-87.

31.     Carty, N.; Berson, N.; Tillack, K.; Thiede, C.; Scholz, D.; Kottig, K.; Sedaghat, Y.; Gabrysiak, C.; Yohrling, G.; von der Kammer, H.; Ebneth, A.; Mack, V.; Munoz-Sanjuan, I.; Kwak, S., Characterization of HTT Inclusion Size, Location, and Timing in the zQ175 Mouse Model of Huntington´s Disease: An In Vivo High-Content Imaging Study. *PLOS ONE* **2015,** *10* (4), e0123527.

32.     http://www.rsc.org/Education/Teachers/Resources/cfb/proteins.htm.

33.     https://www.khanacademy.org/science/biology/macromolecules/proteins-and-amino-acids/a/orders-of-protein-structure.

34.     Nowick, J. S., Exploring β-Sheet Structure and Interactions with Chemical Model Systems. *Accounts of chemical research* **2008,** *41* (10), 1319-1330.

35.     Lodish H, B. A., Zipursky SL, et al. Molecular Cell Biology. 4th edition. New York: W. H. Freeman; **2000**. Section 3.1, Hierarchical Structure of Proteins.

36.     https://www.particlesciences.com/news/technical-briefs/2009/protein-structure.html.

37.     Dill, K. A.; Ozkan, S. B.; Shell, M. S.; Weikl, T. R., The Protein Folding Problem. *Annual review of biophysics* **2008,** *37*, 289-316.

38.     https://www.creativebiomart.net/native-proteins.htm.

39.     Camilloni, C.; Bonetti, D.; Morrone, A.; Giri, R.; Dobson, C. M.; Brunori, M.; Gianni, S.; Vendruscolo, M., Towards a structural biology of the hydrophobic effect in protein folding. *Scientific Reports* **2016,** *6*, 28285.

40.     Halle, B., Flexibility and packing in proteins. *Proceedings of the National Academy of Sciences of the United States of America* **2002,** *99* (3), 1274-1279.

41.     DuBay, K. H.; Bowman, G. R.; Geissler, P. L., Fluctuations within Folded Proteins: Implications for Thermodynamic and Allosteric Regulation. *Accounts of Chemical Research* **2015,** *48* (4), 1098-1105.

42.     Wang, W.; Nema, S.; Teagarden, D., Protein aggregation—Pathways and influencing factors. *International Journal of Pharmaceutics* **2010,** *390* (2), 89-99.

43.     Xi Wen-Hui, W. G.-H. Amyloid- β peptide aggregation and the influence of carbon nanoparticles. *Chinese Physics B* **2015,** *25.*

44.     Vogtt, K.; Javid, N.; Alvarez, E.; Sefcik, J.; Bellissent-Funel, M.-C., Tracing nucleation pathways in protein aggregation by using small angle scattering methods. *Soft Matter* **2011,** *7* (8), 3906-3914.

45.     Frieden, C., Protein aggregation processes: In search of the mechanism. *Protein Science* **2009,** *16* (11), 2334-2344.

46.     Roberts, C. J., Non-native protein aggregation kinetics. *Biotechnology and Bioengineering* **2007,** *98* (5), 927-938.

47.     Knowles, T. P. J.; Vendruscolo, M.; Dobson, C. M., The amyloid state and its association with protein misfolding diseases. *Nature Reviews Molecular Cell Biology* **2014,** *15*, 384.

48.     Cohen, S. I. A.; Vendruscolo, M.; Dobson, C. M.; Knowles, T. P. J., From Macroscopic Measurements to Microscopic Mechanisms of Protein Aggregation. *Journal of Molecular Biology* **2012,** *421* (2), 160-171.

49.     Narhi, L. O.; Schmit, J.; Bechtold-Peters, K.; Sharma, D., Classification of Protein Aggregates1. *Journal of Pharmaceutical Sciences* **2012,** *101* (2), 493-498.

50.     Gustot, A.; Raussens, V.; Dehousse, M.; Dumoulin, M.; Bryant, C. E.; Ruysschaert, J.-M.; Lonez, C., Activation of innate immunity by lysozyme fibrils is critically dependent on cross-β sheet structure. *Cellular and Molecular Life Sciences* **2013,** *70* (16), 2999-3012.

51.     Singh, S. M.; Panda, A. K., Solubilization and refolding of bacterial inclusion body proteins. *Journal of Bioscience and Bioengineering* **2005,** *99* (4), 303-310.

52.     Biagio, M. D. C. a. D. G. a. P. L. S., Alzheimer's disease: biological aspects, therapeutic perspectives and diagnostic tools. *Journal of Physics: Condensed Matter* **2012,** *24* (24), 244102.

53.     Vetri, V.; Foderà, V., The route to protein aggregate superstructures: Particulates and amyloid-like spherulites. *FEBS Letters* **2015,** *589* (19, Part A), 2448-2463.

54.     Jacinte Beerten, J. S. a. F. R. Aggregation Prone Regions and Gatekeeping Residues in Protein Sequences. *Curr Top Med Chem* **2012,** *12* (22), 2470-2478.

55.     Ivan L. Budyak  Beena Krishnan. Early Folding Events Protect Aggregation-Prone Regions of a β-Rich Protein. *Structure*. **2013** 21(3), 476-85.

56.     Madhusudan Makwana, K.; Mahalakshmi, R., Implications of aromatic–aromatic interactions: From protein structures to peptide models. *Protein Science : A Publication of the Protein Society* **2015,** *24* (12), 1920-1933.

57.     Budyak, I. L.; Zhuravleva, A.; Gierasch, L. M., The role of aromatic-aromatic interactions in strand-strand stabilization of β-sheets. *Journal of molecular biology* **2013,** *425* (18), 3522-3535.

58.     Fujiwara, K.; Toda, H.; Ikeguchi, M., Dependence of α-helical and β-sheet amino acid propensies on the overall protein fold type. *BMC Structural Biology* **2012,** *12*, 18-18.

59.     Chennamsetty, N.; Voynov, V.; Kayser, V.; Helk, B.; Trout, B. L., Prediction of Aggregation Prone Regions of Therapeutic Proteins. *The Journal of Physical Chemistry B* **2010,** *114* (19), 6614-6624.

60.     Smith, C. K.; Withka, J. M.; Regan, L., A Thermodynamic Scale for the .beta.-Sheet Forming Tendencies of the Amino Acids. *Biochemistry* **1994,** *33* (18), 5510-5517.

61.     Pawar, A. P.; DuBay, K. F.; Zurdo, J.; Chiti, F.; Vendruscolo, M.; Dobson, C. M., Prediction of "Aggregation-prone" and "Aggregation-susceptible" Regions in Proteins

Associated with Neurodegenerative Diseases. *Journal of Molecular Biology* **2005,** *350* (2), 379-392.

62.	Tartaglia, G. G.; Pawar, A. P.; Campioni, S.; Dobson, C. M.; Chiti, F.; Vendruscolo, M., Prediction of Aggregation-Prone Regions in Structured Proteins. *Journal of Molecular Biology* **2008,** *380* (2), 425-436.

63.	Prabakaran, R.; Goel, D.; Kumar, S.; Gromiha, M. M., Aggregation prone regions in human proteome: Insights from large-scale data analyses. *Proteins: Structure, Function, and Bioinformatics* **2017,** *85* (6), 1099-1118.

64.	Wang, X.; Das, T. K.; Singh, S. K.; Kumar, S., Potential aggregation prone regions in biotherapeutics: A survey of commercial monoclonal antibodies. *mAbs* **2009,** *1* (3), 254-267.

65.	Buck, P. M.; Kumar, S.; Singh, S. K., On the Role of Aggregation Prone Regions in Protein Evolution, Stability, and Enzymatic Catalysis: Insights from Diverse Analyses. *PLoS Computational Biology* **2013,** *9* (10), e1003291.

66.	Sant'Anna, R.; Braga, C.; Varejão, N.; Pimenta, K. M.; Graña-Montes, R.; Alves, A.; Cortines, J.; Cordeiro, Y.; Ventura, S.; Foguel, D., The Importance of a Gatekeeper Residue on the Aggregation of Transthyretin: IMPLICATIONS FOR TRANSTHYRETIN-RELATED AMYLOIDOSES. *Journal of Biological Chemistry* **2014,** *289* (41), 28324-28337.

67.	Buck, T. M.; Wright, C. M.; Brodsky, J. L., The Activities and Function of Molecular Chaperones in the Endoplasmic Reticulum. *Seminars in cell & developmental biology* **2007,** *18* (6), 751-761.

68.	Mayer, M. P.; Bukau, B., Hsp70 chaperones: Cellular functions and molecular mechanism. *Cellular and Molecular Life Sciences* **2005,** *62* (6), 670-684.

69.	Nollen, E. A. A.; Morimoto, R. I., Chaperoning signaling pathways: molecular chaperones as stress-sensing `heat shock' proteins. *Journal of Cell Science* **2002,** *115* (14), 2809.

70.	Kim, Y. E.; Hipp, M. S.; Bracher, A.; Hayer-Hartl, M.; Ulrich Hartl, F., Molecular Chaperone Functions in Protein Folding and Proteostasis. *Annual Review of Biochemistry* **2013,** *82* (1), 323-355.

71.	Ben-Zvi, A. P.; Goloubinoff, P., Review: Mechanisms of Disaggregation and Refolding of Stable Protein Aggregates by Molecular Chaperones. *Journal of Structural Biology* **2001,** *135* (2), 84-93.

72.	Hartl, F. U.; Hayer-Hartl, M., Converging concepts of protein folding in vitro and in vivo. *Nature Structural &Amp; Molecular Biology* **2009,** *16*, 574.

73.	Martin, J.; Ulrich Hartl, F., Chaperone-assisted protein folding. *Current Opinion in Structural Biology* **1997,** *7* (1), 41-52.

74.	Fan, C.-Y.; Lee, S.; Cyr, D. M., Mechanisms for regulation of Hsp70 function by Hsp40. *Cell Stress & Chaperones* **2003,** *8* (4), 309-316.

75.	Bracher, A.; Verghese, J., The nucleotide exchange factors of Hsp70 molecular chaperones. *Frontiers in Molecular Biosciences* **2015,** *2*, 10.

76.	Pratt, W. B.; Morishima, Y.; Peng, H.-M.; Osawa, Y., Role of the Hsp90/Hsp70-Based Chaperone Machinery in Making Triage Decisions When Proteins Undergo Oxidative and Toxic Damage. *Experimental biology and medicine (Maywood, N.J.)* **2010,** *235* (3), 278-289.

77.	Trombetta, E. S.; Helenius, A., Lectins as chaperones in glycoprotein folding. *Current Opinion in Structural Biology* **1998,** *8* (5), 587-592.

78.	Duncan, E. J.; Cheetham, M. E.; Chapple, J. P.; van der Spuy, J., The Role of HSP70 and Its Co-chaperones in Protein Misfolding, Aggregation and Disease. *The Networking of Chaperones by Co-chaperones: Control of Cellular Protein Homeostasis*, **2015**, 243-273.

79.	den Engelsman, J.; Garidel, P.; Smulders, R.; Koll, H.; Smith, B.; Bassarab, S.; Seidl, A.; Hainzl, O.; Jiskoot, W., Strategies for the assessment of protein aggregates in

pharmaceutical biotech product development. *Pharmaceutical research* **2011,** *28* (4), 920-933.

80. Gregoire, S.; Irwin, J.; Kwon, I., Techniques for Monitoring Protein Misfolding and Aggregation in Vitro and in Living Cells. *Korean J Chem Eng* **2012**, *29*(6), 693–702.

81. http://www.biopharminternational.com/detecting-protein-aggregates-and-evaluating-their-immunogenicity.

82. Frid, P.; Anisimov, S. V.; Popovic, N., Congo red and protein aggregation in neurodegenerative diseases. *Brain Research Reviews* **2007,** *53* (1), 135-160.

83. Biancalana, M.; Koide, S., Molecular mechanism of Thioflavin-T binding to amyloid fibrils. *Biochimica et biophysica acta* **2010,** *1804* (7), 1405-1412.

84. Hong, P.; Koza, S.; Bouvier, E. S. P., Size-Exclusion Chromatography for the Analysis of Protein Biotherapeutics and their Aggregates. *Journal of liquid chromatography & related technologies* **2012,** *35* (20), 2923-2950.

85. Lorber, B.; Fischer, F.; Bailly, M.; Roy, H.; Kern, D., Protein analysis by dynamic light scattering: Methods and techniques for students. *Biochemistry and Molecular Biology Education* **2012,** *40* (6), 372-382.

86. https://www.coriolis-pharma.com/contract-analytical-services/turbidity/.

87. Burg, M. B.; Ferraris, J. D., Intracellular Organic Osmolytes: Function and Regulation. *The Journal of Biological Chemistry* **2008,** *283* (12), 7309-7313.

88. Yancey, P. H., Water Stress, Osmolytes and Proteins1. *American Zoologist* **2001,** *41* (4), 699-709.

89. Zhang, M.; Wang, L.-f.; Zhang, K.; Liu, F.-z.; Wan, Y.-s., Drought-induced responses of organic osmolytes and proline metabolism during pre-flowering stage in leaves of peanut (Arachis hypogaea L.). *Journal of Integrative Agriculture* **2017,** *16* (10), 2197-2205.

90. Lee, J. C.; Timasheff, S. N., The stabilization of proteins by sucrose. *Journal of Biological Chemistry* **1981,** *256* (14), 7193-7201.

91. Khan, S. H.; Ahmad, N.; Ahmad, F.; Kumar, R., Naturally occurring organic osmolytes: From cell physiology to disease prevention. *IUBMB Life* **2010,** *62* (12), 891-895.

92. Bolen, D. W., Protein Stabilization by Naturally Occurring Osmolytes. *Protein Structure, Stability, and Folding*, **2001**, 17-36.

93. Arakawa, T.; Tsumoto, K.; Kita, Y.; Chang, B.; Ejima, D., Biotechnology applications of amino acids in protein purification and formulations. *Amino Acids* **2007,** *33* (4), 587-605.

94. Singh, A.; Upadhyay, V.; Upadhyay, A. K.; Singh, S. M.; Panda, A. K., Protein recovery from inclusion bodies of Escherichia coli using mild solubilization process. *Microbial Cell Factories* **2015,** *14*, 41.

95. Chen, S.; Manabe, Y.; Minamoto, N.; Saiki, N.; Fukase, K., Development of a simple assay system for protein-stabilizing efficiency based on hemoglobin protection against denaturation and measurement of the cooperative effect of mixing protein stabilizers. *Bioscience, Biotechnology, and Biochemistry* **2016,** *80* (10), 1874-1878.

96. Falconer, R. J.; Chan, C.; Hughes, K.; Munro, T. P., Stabilization of a monoclonal antibody during purification and formulation by addition of basic amino acid excipients. *Journal of Chemical Technology & Biotechnology* **2011,** *86* (7), 942-948.

97. Zhang, M. Z.; Wen, J.; Arakawa, T.; Prestrelski, S. J., A New Strategy for Enhancing the Stability of Lyophilized Protein: The Effect of the Reconstitution Medium on Keratinocyte Growth Factor. *Pharmaceutical Research* **1995,** *12* (10), 1447-1452.

98. Baynes, B. M.; Wang, D. I. C.; Trout, B. L., Role of Arginine in the Stabilization of Proteins against Aggregation. *Biochemistry* **2005,** *44* (12), 4919-4925.

99. Das, U.; Hariprasad, G.; Ethayathulla, A. S.; Manral, P.; Das, T. K.; Pasha, S.; Mann, A.; Ganguli, M.; Verma, A. K.; Bhat, R.; Chandrayan, S. K.; Ahmed, S.; Sharma, S.;

Kaur, P.; Singh, T. P.; Srinivasan, A., Inhibition of Protein Aggregation: Supramolecular Assemblies of Arginine Hold the Key. *PLOS ONE* **2007,** *2* (11), e1176.

100.    Eronina, T. B.; Chebotareva, N. A.; Sluchanko, N. N.; Mikhaylova, V. V.; Makeeva, V. F.; Roman, S. G.; Kleymenov, S. Y.; Kurganov, B. I., Dual effect of arginine on aggregation of phosphorylase kinase. *International Journal of Biological Macromolecules* **2014,** *68*, 225-232.

101.    Forney-Stevens, K. M.; Bogner, R. H.; Pikal, M. J., Addition of Amino Acids to Further Stabilize Lyophilized Sucrose-Based Protein Formulations: I. Screening of 15 Amino Acids in Two Model Proteins. *Journal of Pharmaceutical Sciences* **2016,** *105* (2), 697-704.

102.    Corradini, D.; Strekalova, E. G.; Stanley, H. E.; Gallo, P., Microscopic mechanism of protein cryopreservation in an aqueous solution with trehalose. *Scientific Reports* **2013,** *3*, 1218.

103.    Chang, L.; Shepherd, D.; Sun, J.; Ouellette, D.; Grant, K. L.; Tang, X.; Pikal, M. J., Mechanism of protein stabilization by sugars during freeze-drying and storage: Native structure preservation, specific interaction, and/or immobilization in a glassy matrix? *Journal of Pharmaceutical Sciences* **2005,** *94* (7), 1427-1444.

104.    Simperler, A.; Kornherr, A.; Chopra, R.; Bonnet, P. A.; Jones, W.; Motherwell, W. D. S.; Zifferer, G., Glass Transition Temperature of Glucose, Sucrose, and Trehalose: An Experimental and in Silico Study. *The Journal of Physical Chemistry B* **2006,** *110* (39), 19678-19684.

105.    Green, J. L.; Angell, C. A., Phase relations and vitrification in saccharide-water solutions and the trehalose anomaly. *The Journal of Physical Chemistry* **1989,** *93* (8), 2880-2882.

106.    Mensink, M. A.; Frijlink, H. W.; van der Voort Maarschalk, K.; Hinrichs, W. L. J., How sugars protect proteins in the solid state and during drying (review): Mechanisms of stabilization in relation to stress conditions. *European Journal of Pharmaceutics and Biopharmaceutics* **2017,** *114*, 288-295.

107.    Arakawa, T.; Timasheff, S. N., Stabilization of protein structure by sugars. *Biochemistry* **1982,** *21* (25), 6536-6544.

108.    Imamura, K.; Ogawa, T.; Sakiyama, T.; Nakanishi, K., Effects of types of sugar on the stabilization of protein in the dried state. *Journal of Pharmaceutical Sciences* **2002,** *92* (2), 266-274.

109.    Veronese, F. M.; Pasut, G., PEGylation, successful approach to drug delivery. *Drug Discovery Today* **2005,** *10* (21), 1451-1458.

110.    Banerjee, S. S.; Aher, N.; Patil, R.; Khandare, J., Poly(ethylene glycol)-Prodrug Conjugates: Concept, Design, and Applications. *Journal of Drug Delivery* **2012,** *2012*, 103973.

111.    Swierczewska, M.; Lee, K. C.; Lee, S., What is the future of PEGylated therapies? *Expert opinion on emerging drugs* **2015,** *20* (4), 531-536.

112.    https://www.marketsandmarkets.com/PressReleases/pegylated-protein.asp.

113.    Turecek, P. L.; Bossard, M. J.; Schoetens, F.; Ivens, I. A., PEGylation of Biopharmaceuticals: A Review of Chemistry and Nonclinical Safety Information of Approved Drugs. *Journal of Pharmaceutical Sciences* **2016,** *105* (2), 460-475.

114.    Roberts, M. J.; Bentley, M. D.; Harris, J. M., Chemistry for peptide and protein PEGylation. *Advanced Drug Delivery Reviews* **2012,** *64*, 116-127.

115.    Wan, X.; Zhang, J.; Yu, W.; Shen, L.; Ji, S.; Hu, T., Effect of protein immunogenicity and PEG size and branching on the anti-PEG immune response to PEGylated proteins. *Process Biochemistry* **2017,** *52*, 183-191.

116.    Dozier, J. K.; Distefano, M. D., Site-Specific PEGylation of Therapeutic Proteins. *International Journal of Molecular Sciences* **2015,** *16* (10), 25831-25864.

117.    Filpula, D.; Zhao, H., Releasable PEGylation of proteins with customized linkers. *Advanced Drug Delivery Reviews* **2008,** *60* (1), 29-49.

118.    Reichert, C.; Borchard, G., Noncovalent PEGylation, An Innovative Subchapter in the Field of Protein Modification. *Journal of Pharmaceutical Sciences* **2016,** *105* (2), 386-390.

119.    Kurinomaru, T.; Shiraki, K., Noncovalent PEGylation of Asparaginase Using PEGylated Polyelectrolyte. *Journal of Pharmaceutical Sciences* **2015,** *104* (2), 587-592.

120.    Kurinomaru, T.; Kuwada, K.; Tomita, S.; Kameda, T.; Shiraki, K., Noncovalent PEGylation through Protein–Polyelectrolyte Interaction: Kinetic Experiment and Molecular Dynamics Simulation. *The Journal of Physical Chemistry B* **2017,** *121* (28), 6785-6791.

121.    Nieto-Orellana, A.; Di Antonio, M.; Conte, C.; Falcone, F. H.; Bosquillon, C.; Childerhouse, N.; Mantovani, G.; Stolnik, S., Effect of polymer topology on non-covalent polymer–protein complexation: miktoarm versus linear mPEG-poly(glutamic acid) copolymers. *Polymer Chemistry* **2017,** *8* (14), 2210-2220.

122.    Asayama, S.; Nagashima, K.; Kawakami, H., Facile Method of Protein PEGylation by a Mono-Ion Complex. *ACS Omega* **2017,** *2* (5), 2382-2386.

123.    Stidham SE, C. S., Dane EL, Grinstaff MW. Carboxylated Glucuronic Poly-amido-saccharides as Protein Stabilizing Agents. *J. Am. Chem. Soc.* **2017,** *136* (27), 9544-9547.

124.    Mero, A.; Ishino, T.; Chaiken, I.; Veronese, F. M.; Pasut, G., Multivalent and Flexible PEG-Nitrilotriacetic Acid Derivatives for Non-covalent Protein Pegylation. *Pharmaceutical Research* **2011,** *28* (10), 2412.

125.    Antonik, P. M.; Eissa, A. M.; Round, A. R.; Cameron, N. R.; Crowley, P. B., Noncovalent PEGylation via Lectin–Glycopolymer Interactions. *Biomacromolecules* **2016,** *17* (8), 2719-2725.

126.    Mueller, C.; Capelle, M. A. H.; Arvinte, T.; Seyrek, E.; Borchard, G., Tryptophan-mPEGs: Novel excipients that stabilize salmon calcitonin against aggregation by non-covalent PEGylation. *European Journal of Pharmaceutics and Biopharmaceutics* **2011,** *79* (3), 646-657.

127.    Mueller, C.; Capelle, M. A. H.; Seyrek, E.; Martel, S.; Carrupt, P.-A.; Arvinte, T.; Borchard, G., Noncovalent PEGylation: Different Effects of Dansyl-, Tryptophan–, Phenylbutylamino-, Benzyl- and Cholesteryl-PEGs on the Aggregation of Salmon Calcitonin and Lysozyme. *Journal of Pharmaceutical Sciences* **2012,** *101* (6), 1995-2008.

128.    Salmaso, S.; Bersani, S.; Scomparin, A.; Balasso, A.; Brazzale, C.; Barattin, M.; Caliceti, P., A novel soluble supramolecular system for sustained rh-GH delivery. *Journal of Controlled Release* **2014,** *194*, 168-177.

129.    Salmaso, S.; Bersani, S.; Mastrotto, F.; Tonon, G.; Schrepfer, R.; Genovese, S.; Caliceti, P., Self-assembling nanocomposites for protein delivery: Supramolecular interactions between PEG-cholane and rh-G-CSF. *Journal of Controlled Release* **2012,** *162* (1), 176-184.

130.    Shipp, D. A., Reversible-Deactivation Radical Polymerizations. *Polymer Reviews* **2011,** *51* (2), 99-103.

131.    Perrier, S., 50th Anniversary Perspective: RAFT Polymerization—A User Guide. *Macromolecules* **2017,** *50* (19), 7433-7447.

132.    Keddie, D. J.; Moad, G.; Rizzardo, E.; Thang, S. H., RAFT Agent Design and Synthesis. *Macromolecules* **2012,** *45* (13), 5321-5342.

133.    Keddie, D. J., A guide to the synthesis of block copolymers using reversible-addition fragmentation chain transfer (RAFT) polymerization. *Chemical Society Reviews* **2014,** *43* (2), 496-505.

134.    Li, S. C.; Goto, N. K.; Williams, K. A.; Deber, C. M., Alpha-helical, but not beta-sheet, propensity of proline is determined by peptide environment. *Proceedings of the*

*National Academy of Sciences of the United States of America* **1996,** *93* (13), 6676-6681.

135. Soto, C.; Kindy, M. S.; Baumann, M.; Frangione, B., Inhibition of Alzheimer's Amyloidosis by Peptides That Prevent β-Sheet Conformation. *Biochemical and Biophysical Research Communications* **1996,** *226* (3), 672-680.

136. Soto, C.; Sigurdsson, E. M.; Morelli, L.; Asok Kumar, R.; Castaño, E. M.; Frangione, B., β-sheet breaker peptides inhibit fibrillogenesis in a rat brain model of amyloidosis: Implications for Alzheimer's therapy. *Nature Medicine* **1998,** *4*, 822.

137. Adessi, C.; Soto, C., Beta-sheet breaker strategy for the treatment of Alzheimer's disease. *Drug Development Research* **2002,** *56* (2), 184-193.

138. Tjernberg, L. O.; Callaway, D. J. E.; Tjernberg, A.; Hahne, S.; Lilliehöök, C.; Terenius, L.; Thyberg, J.; Nordstedt, C., A Molecular Model of Alzheimer Amyloid β-Peptide Fibril Formation. *Journal of Biological Chemistry* **1999,** *274* (18), 12619-12625.

139. Esler WP, S. E., Ghilardi JR, et al Point substitution in the central hydrophobic cluster of a human beta-amyloid congener disrupts peptide folding and abolishes plaque competence. *Biochemistry*, **1996**, *35* (44), 13914–13921

140. Neddenriep, B.; Calciano, A.; Conti, D.; Sauve, E.; Paterson, M.; Bruno, E.; Moffet, D. A., Short Peptides as Inhibitors of Amyloid Aggregation. *The open biotechnology journal* **2011,** *5*, 39-46.

141. Cruz, M.; Tusell, J. M.; Grillo-Bosch, D.; Albericio, F.; Serratosa, J.; Rabanal, F.; Giralt, E., Inhibition of β-amyloid toxicity by short peptides containing N-methyl amino acids. *The Journal of Peptide Research* **2008,** *63* (3), 324-328.

142. Song, Y.; Cheng, P.-N.; Zhu, L.; Moore, E. G.; Moore, J. S., Multivalent Macromolecules Redirect Nucleation-Dependent Fibrillar Assembly into Discrete Nanostructures. *Journal of the American Chemical Society* **2014,** *136* (14), 5233-5236.

143. Song, Y.; Moore, E. G.; Guo, Y.; Moore, J. S., Polymer–Peptide Conjugates Disassemble Amyloid β Fibrils in a Molecular-Weight Dependent Manner. *Journal of the American Chemical Society* **2017,** *139* (12), 4298-4301.

144. Dorgeret, B.; Khemtémourian, L.; Correia, I.; Soulier, J.-L.; Lequin, O.; Ongeri, S., Sugar-based peptidomimetics inhibit amyloid β-peptide aggregation. *European Journal of Medicinal Chemistry* **2011,** *46* (12), 5959-5969.

145. Hope, A. D.; Myhre, R.; Kachergus, J.; Lincoln, S.; Bisceglio, G.; Hulihan, M.; Farrer, M. J., α-Synuclein missense and multiplication mutations in autosomal dominant Parkinson's disease. *Neuroscience Letters* **2004,** *367* (1), 97-100.

146. Giasson, B. I.; Murray, I. V. J.; Trojanowski, J. Q.; Lee, V. M. Y., A Hydrophobic Stretch of 12 Amino Acid Residues in the Middle of α-Synuclein Is Essential for Filament Assembly. *Journal of Biological Chemistry* **2001,** *276* (4), 2380-2386.

147. Koo, H.-J.; Lee, H.-J.; Im, H., Sequence determinants regulating fibrillation of human α-synuclein. *Biochemical and Biophysical Research Communications* **2008,** *368* (3), 772-778.

148. Koo, H.-J.; Choi, M. Y.; Im, H., Aggregation-defective α-synuclein mutants inhibit the fibrillation of Parkinson's disease-linked α-synuclein variants. *Biochemical and Biophysical Research Communications* **2009,** *386* (1), 165-169.

149. Kim, Y. S.; Lim, D.; Kim, J. Y.; Kang, S. J.; Kim, Y.-H.; Im, H., β-Sheet-breaking peptides inhibit the fibrillation of human α-synuclein. *Biochemical and Biophysical Research Communications* **2009,** *387* (4), 682-687.

150. Chang, Y.-P.; Chu, Y.-H., Blocking formation of large protein aggregates by small peptides. *Chemical Communications* **2013,** *49* (41), 4591-4600.

151. Amblard, M.; Fehrentz, J.-A.; Martinez, J.; Subra, G., Methods and protocols of modern solid phase peptide synthesis. *Molecular Biotechnology* **2006,** *33* (3), 239-254.

152.	Mäde, V.; Els-Heindl, S.; Beck-Sickinger, A. G., Automated solid-phase peptide synthesis to obtain therapeutic peptides. *Beilstein Journal of Organic Chemistry* **2014,** *10*, 1197-1212.

153.	Fields, G. B., Introduction to peptide synthesis. *Current protocols in protein science* **2002,** *Chapter 18*, Unit-18.1.

154.	http://proteopedia.org/wiki/index.php/Hen_Egg-White_(HEW)_Lysozyme.

155.	Vocadlo, D. J.; Davies, G. J.; Laine, R.; Withers, S. G., Catalysis by hen egg-white lysozyme proceeds via a covalent intermediate. *Nature* **2001,** *412*, 835.

156.	M.A.Williams, J. M. T. a. J. M. G. Modelling protein unfolding: hen egg-white lysozyme. *Protein Engineering, Design and Selection*, **1997**, 895–903.

157.	Held, J.; van Smaalen, S., The active site of hen egg-white lysozyme: flexibility and chemical bonding. *Acta Crystallographica Section D: Biological Crystallography* **2014,** *70* (Pt 4), 1136-1146.

158.	Chaari, A.; Fahy, C.; Chevillot-Biraud, A.; Rholam, M., Insights into Kinetics of Agitation-Induced Aggregation of Hen Lysozyme under Heat and Acidic Conditions from Various Spectroscopic Methods. *PLOS ONE* **2015,** *10* (11), e0142095.

159.	Tanaka, S.; Oda, Y.; Ataka, M.; Onuma, K.; Fujiwara, S.; Yonezawa, Y., Denaturation and aggregation of hen egg lysozyme in aqueous ethanol solution studied by dynamic light scattering. *Biopolymers* **2001,** *59* (5), 370-379.

160.	Homchaudhuri, L.; Kumar, S.; Swaminathan, R., Slow aggregation of lysozyme in alkaline pH monitored in real time employing the fluorescence anisotropy of covalently labelled dansyl probe. *FEBS Letters* **2006,** *580* (8), 2097-2101.

161.	Krebs, M. R. H.; Wilkins, D. K.; Chung, E. W.; Pitkeathly, M. C.; Chamberlain, A. K.; Zurdo, J.; Robinson, C. V.; Dobson, C. M., Formation and seeding of amyloid fibrils from wild-type hen lysozyme and a peptide fragment from the β-domain 11Edited by P. E. Wright. *Journal of Molecular Biology* **2000,** *300* (3), 541-549.

162.	Frare, E.; Mossuto, M. F.; Polverino de Laureto, P.; Dumoulin, M.; Dobson, C. M.; Fontana, A., Identification of the Core Structure of Lysozyme Amyloid Fibrils by Proteolysis. *Journal of Molecular Biology* **2006,** *361* (3), 551-561.

163.	Sugimoto, Y.; Kamada, Y.; Tokunaga, Y.; Shinohara, H.; Matsumoto, M.; Kusakabe, T.; Ohkuri, T.; Ueda, T., Aggregates with lysozyme and ovalbumin show features of amyloid-like fibrils. *Biochemistry and Cell Biology* **2011,** *89* (6), 533-544.

164.	Tokunaga Y, S. Y., Kamada Y, Watanabe Ki, Sugimoto Y Analysis of Core Region from Egg White Lysozyme Forming Amyloid Fibrils. *Int J Biol Sci*, **2013,** *9*(2), 219-27.

165.	Klein-Seetharaman, J.; Oikawa, M.; Grimshaw, S. B.; Wirmer, J.; Duchardt, E.; Ueda, T.; Imoto, T.; Smith, L. J.; Dobson, C. M.; Schwalbe, H., Long-Range Interactions Within a Nonnative Protein. *Science* **2002,** *295* (5560), 1719.

166.	Zhou, R.; Eleftheriou, M.; Royyuru, A. K.; Berne, B. J., Destruction of long-range interactions by a single mutation in lysozyme. *Proceedings of the National Academy of Sciences of the United States of America* **2007,** *104* (14), 5824-5829.

167.	Ohkuri, T.; Shioi, S.; Imoto, T.; Ueda, T., Effect of the Structure of the Denatured State of Lysozyme on the Aggregation Reaction at the Early Stages of Folding from the Reduced Form. *Journal of Molecular Biology* **2005,** *347* (1), 159-168.

# Chapter 2

## Synthesis of APRs analogues for Lysozyme stabilisation

_____

## 2.1. Introduction

As discussed in Chapter 1, research and clinical application of therapeutic proteins have dramatically expanded over the last few decades. However, smooth translation of a protein with therapeutic efficacy into a clinically used medicine is often limited by pre- and post-administration stability issues, leading to increased production costs, low pure protein yield, potential immunogenicity, as well as fast renal clearance upon protein administration[1]. To overcome these limitations, non-covalent proteins modifications by potential stabilising molecules have been studied, with the view to improve protein stability and/or delivery, without creating a new therapeutic entity.

Aggregation Prone Regions (APRs) are specific sequences within protein primary structure, which are believed to initiate and mediate protein aggregation. These sequences, usually buried into proteins hydrophobic core or active site, can get exposed to the external environment following protein destabilisation and unfolding. Following solvent exposure, they can initiate self-assembly of protein molecules through mutual beta-sheet interactions, thus leading to protein aggregation[2].

A series of peptides have been developed, called β-sheet breakers, to prevent the aggregation of specific peptides and proteins involved in neurodegenerative diseases. Their structure resembles closely that of the APR sequences responsible for protein/peptide aggregation. The similarity provides them with high hydrophobicity and β-sheet propensity, so that they interact preferentially with the APR through mutual β -sheet interactions. However,

additional amino acids can be incorporated into these peptide sequences to make them charged or more hydrophilic, so that the resulting peptide can still recognise the APR, but will stop its β-sheet-driven self-assembling, thus acting as β-sheet disruptor. These peptides have been successfully used *in vivo*, on animal Alzeihmer models, to prevent the aggregation of the β-amyloid protein (Aβ) into amyloid fibrils, which are specidic hallmarks of Alzehimer's disease[3].

Recently, a specific sequence on hen egg lysozyme backbone, located on the enzyme active site and usually partially buried on its cleft, has been identified as potentially prone to aggregation[4]. The sequence, which correspond to lysozyme 54-62 segment GILQINSRW, was found to be aggregating in the 2 – 7 pH range.

This chapter describes the synthesis of a family of peptides based on the homologous amino acid sequence of hen egg lysozyme's APR, GILQINSRW. The working hypothesis here was that the small 'synthetic APR' could interact with its homologous sequence on lysozyme, and, by occupying this site, prevent its self-aggregation. By using lysozyme as a mode substrate, we aimed at developing a platform technology that by using peptidic β-sheet breakers based on proteins APRs, could potentially be used as excipients to stabilise therapeutic proteins against aggregation. For a graphical represention of our aim, see Figure 1.8 in Chapter 1.

The original GILQINSRW APR sequence was synthesised by solid phase peptide synthesis, and small hydrophilic residues were incorporated in its structure, such as a short PEG and a charged sulfobetaine, to improve peptide solubility

and potentially give it some β-sheet disrupting properties. The resulting derivatives were evaluated, together with the original APR-based peptide, for their potential to interact with lysozyme, by testing their effect on lysozyme's enzymatic activity. The APR homologous peptide was finally conjugated to a hydrophilic polyacrylamide through RAFT-polymerization, in order to make it substantially more hydrophilic and less self-aggregating. The resulting copolymer was investigated for its ability of establishing non-covalent interactions with lysozyme.

## 2.2. Materials and methods

### 2.2.1. Materials

Isopropanol, methanol, dichloromethane (DCM), ethyl acetate, diethyl ether, chloroform, tetrahydrofuran, petroleum ether, *N,N*-dimethylformamide (DMF) and acetone were purchased from Fisher Scientific (Bishop Meadow Rd, Loughborough, UK). Biotech grade DMF, anhydrous dichloromethane, anhydrous MeOH, methoxy PEG 550 Da, bovine serum albumin (BSA) (≥98%), piperidine (99%), PBS buffer, Fmoc-leu-OH (98%), Fmoc-ile-OH (98%), Fmoc-arg(pbf)-OH (≥98%), Fmoc-gly-OH (≥98%), Fmoc-asn-OH (≥96%), Fmoc-trp(boc)-OH (97%), Fmoc-ser(tbu)-OH (≥98%), Fmoc-gln(trt)-OH (98%), DIPEA (≥99%), TEA (≥99%), VA-501 (≥98%), DMTMM (96%), ethylene-dioxy-bis-ethylamine (98%), Di-*tert*-butyl dicarbonate and disuccinimidyl carbonate (≥95%) were obtained from Sigma-Aldrich (St. Louis, Missouri, United States). VA-044 was purchased from Wako Pure Chemical Industries. HATU (98%) was purchased from Fluorochem Ltd, 14 Graphite Way, Hadfield SK13 1QH. 3-[Dimethyl-(2-hydroxyethyl)ammonio]-1-propanesulfonate betaine was purchased from Merck Biosciences Ltd, Padge Rd, Beeston, UK.

### 2.2.2. Synthesis of peptide GILQINSRW (1)
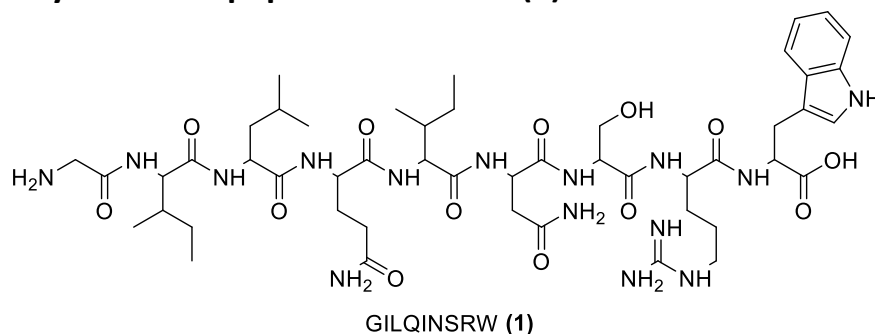


GILQINSRW (1)

Figure 2.1: chemical structure of peptide GILQINSRW **(1)**.

In a glass peptide synthesis vessel, 2-chlorotrytilchloride, polymer bound resin beads (1.6 mmol/g, 1.8 g, 2.9 mmol, 1 eq.) were swelled in biotech grade DMF for 30 min.

After resin swelling, the resin was washed with biotech grade DMF, dry methanol, dry DCM and biotech grade DMF again.

The first amino acid, Fmoc-Trp-OH (2.6 g, 6.0 mmol, 2 eq.) was subsequently added to the suspension, followed by DIPEA (2.1 mL, 15 mmol, 5 eq.), and the resulting mixture stirred for 60 min. After washing, the resin was treated for 15 min with a mixture of anhydrous DCM/ anhydrous MeOH/ DIPEA (80:15:5 in volume) to cap any remaining reactive trityl group. Finally, the protecting Fmoc group was removed from the attached amino acid treating the resin with a 20% v/v piperidine solution in DMF for 30 min. The remaining 8 amino acids were attached following the same procedure: 2 eq. of Fmoc-protected amino acid were previously dissolved in biotech grade DMF, mixed with 1.9 eq of HATU and 3 eq. of DIPEA. The solution was added to the resin and the resulting suspension was stirred for 60 min. The excess of reagents was then removed by filtration and the coupling step repeated using the same procedure. Fmoc deprotection was finally performed with the same procedure described above.

After each amino acid coupling and Fmoc deprotection step, the excess of reagents was removed from the reaction vessel by filtration, and the resin was washed with biotech grade DMF, dry methanol, dry DCM and biotech grade DMF again.

Final peptide cleavage and deprotection were performed using a mixture of TFA /water/triisopropylsilane (95:2.5:2.5 v/v, 10 mL for 200 mg of resin), in which the resin was stirred for 90 min. The supernatant was then collected and dried under vacuum to 1/10 of its volume. The peptide was finally precipitated in diethyl ether and dried overnight in the desiccator. The product was analysed by ESI-MS and RP-HPLC. RP-HPLC was run at a flow rate of 1 mL/min, using a 20-80% acetonitrile gradient in Milli-q water + 0.1% TFA, on a C18 Jupiter Phenomenex column (5μm, 300 Å, 25X4.6 mm). Absorbance was recorded at 280 nm. Yield: 47%.

ESI-MS: expected m/z $[M-H]^+$ 1086.6 and $[M-Na]^+$ 1108.6, found 1086.6 and 1108.6, respectively.

RP-HPLC: retention time 12.7 min. Purity 86%.

### 2.2.3. Synthesis of methoxy PEG-succinimidyl carbonate (2)
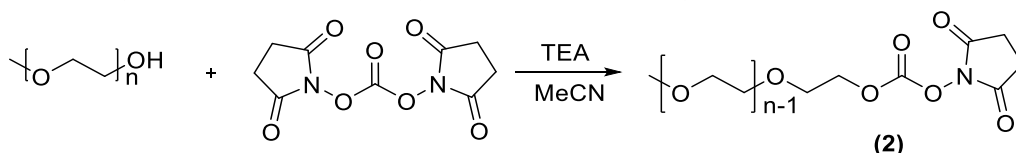


Scheme 2.1: synthesis of methoxy PEG-succinimidyl carbonate **(2)**.

Polyethyleneglycol monomethyl ether 550 (1.00 g, 1.82 mmol, 1 eq.), previously dried by azeotropic distillation in toluene**,** and *N,N'*-disuccinimidyl carbonate (0.70 g, 2.7 mmol, 1.5 eq.) were dissolved in dry acetonitrile (23 mL). Then triethylamine (0.55 g, 0.77 mL, 5.5 mmol, 3 eq.) was added and the reaction stirred overnight at room temperature. The solvent was evaporated under reduced pressure, the residue dissolved in tetrahydrofuran (20 mL) and

the resulting solution further diluted with diethyl ether (40 mL). The resulting precipitate was filtered to remove the unsoluble triethylamine salt, and the solution evaporated to dryness, yielding a clear oily residue. The oil was dissolved in sat. aqueous $NaHCO_3$ (60 mL), extracted with ethyl acetate (2×120 mL), dried with $MgSO_4$, filtered, and the solvent removed under reduced pressure, to give methoxy PEG-succinimidyl carbonate **(2)** as a clear oil. Yield: 42%.

$^1$H NMR (400 MHz, $CDCl_3$, δ, ppm): 4.46 (m, 2H, $CH_2OCO$), 3.64 (m, 42H, PEG $CH_2CH_2O$), 2.84 (s, 4H, succinimide $CH_2CH_2$) (Fig. S2.1).

$^{13}$C NMR (101 MHz, $CDCl_3$, δ, ppm): 168.51 (succinimide CO), 72-69 (PEG $CH_2CH_2O$) (Fig. S2.2).

58.84 ($CH_3O$), 25.45 (succinimide $CH_2$).

FT-IR: 2868 cm$^{-1}$, 1738 cm$^{-1}$ ($\upsilon_{C=O}$), 1089 cm$^{-1}$ ($\upsilon_{CH2-O\ ether}$).

## 2.2.4. Synthesis of PEGylated peptide (4)
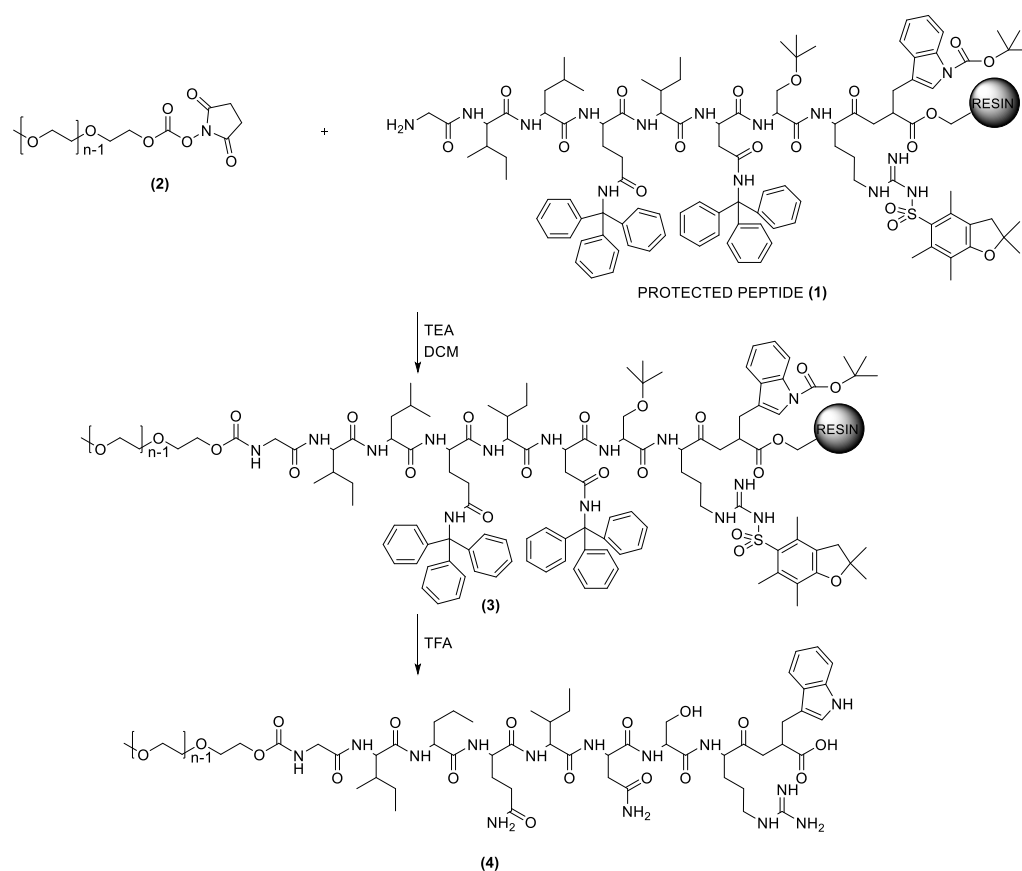


Scheme 2.2: Synthesis of PEGylated peptide **(4)**.

110 mg of resin (containing ca. 69 mg of protected peptide, corresponding to 25 mg, 0.023 mmol of peptide **(1)**, 1 eq.) were swelled in 10 mL of anhydrous DCM for 30 min. PEG-succinimidyl carbonate **(2)** was then added (75 mg, 0.12 mmol, 5 eq.) followed by triethylamine (96 µL, 0.069 mmol, 3 eq.) and the reaction was stirred overnight at room temperature. Cleavage of **(3)** from the resin and subsequent reaction work-up were performed using the same protocol described previously for **(1)**. The mPEG-peptide **(4)** product was analysed by MALDI TOF-MS.

MALDI TOF-MS: m/z [M-H]$^+$ multiple peaks expected, due to commercial PEG polydispersity (ethylene oxide unit $CH_2CH_2O$=44.02 Da). For example, for ethylene oxide units $n$=4, expected m/z [M-H]$^+$ 1320.7, found 1321.3.

## 2.2.5. Synthesis of betaine succinimidyl carbonate (5)
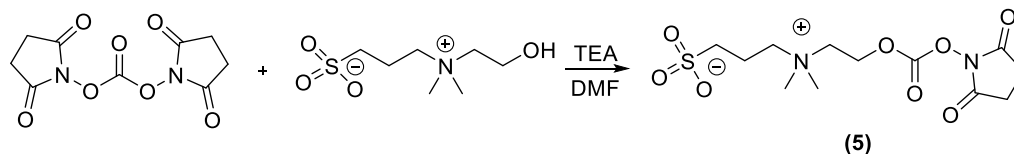


Scheme 2.3: Synthesis of betaine succinimidyl carbonate **(5)**.

3-[Dimethyl-(2-hydroxyethyl)ammonio]-1-propanesulfonate (0.500 g, 2.38 mmol, 1 eq.) and *N,N'*-disuccinimidyl carbonate (1.83 mg, 7.14 mmol, 3 eq.) were suspended in dry DMF (1.5 mL). Then triethylamine (0.995 mL, 7.14 mmol, 3 eq.) was added and the reaction stirred overnight at room temperature. The insoluble precipitate was then washed with acetonitrile 4 times to remove traces of unreacted *N,N'*-disuccinimidyl carbonate. Traces of solvent were removed from the precipitate under reduced pressure. Yield: 70%.

$^1$H NMR (400 MHz, d$_6$-DMSO, δ, ppm): 4.81 (m, 2H, NCH$_2$C*H$_2$*), 3.8 (m, 2H, NC*H$_2$*CH$_2$), 3.51 (m, 2H, CH$_2$C*H$_2$*N), 3.10 (s, 6H, CH$_3$N), 2.83 (s, 4H, succinimide CH$_2$CH$_2$), 2.46 (m, SO$_3$CH$_2$), 2.00 (m, 2H, C*H$_2$*CH$_2$N ) (Fig. S2.3).

## 2.2.6. Synthesis of betaine-modified peptide (7)
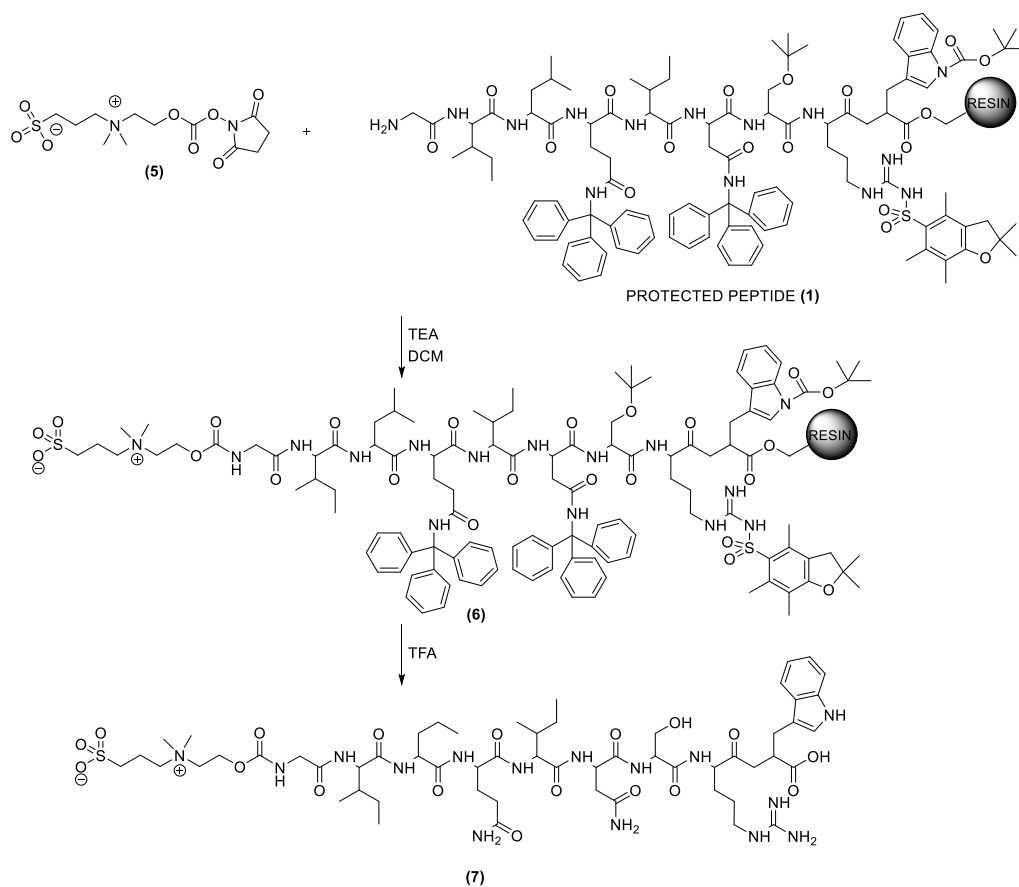


Scheme 2.4: Synthesis of betaine-modified peptide **(7)**.

110 mg of resin (containing ca. 69 mg of protected peptide, corresponding to 25 mg, 0.023 mmol of peptide **(1)**, 1 eq.) were swelled in 6 mL of biotech grade DMF for 30 min. Betaine succinimidyl carbonate **(5)** was then added (258 mg, 0.368 mmol, 32 eq.), together with triethylamine (3.1 µL, 0.023 mmol, 1 eq.) and the suspension was stirred for 7 days at room temperature. The conversion of **(1)** into **(7)** was monitored by ESI-MS every 24h by cleaving from the resin and deprotecting small amounts of peptide. Final cleavage of **(7)** from the resin and subsequent reaction work-up were performed using the same protocol described previously for **(1)**.  Yield: 36%.

ESI-MS: expected m/z [M-H]$^+$ 1323.67 and [M-H-Na]$^{2+}$ 673.3, found 1323.67,

and 673.2, respectively.

## 2.2.7. Synthesis of Chain Transfer Agent (CTA) (10)
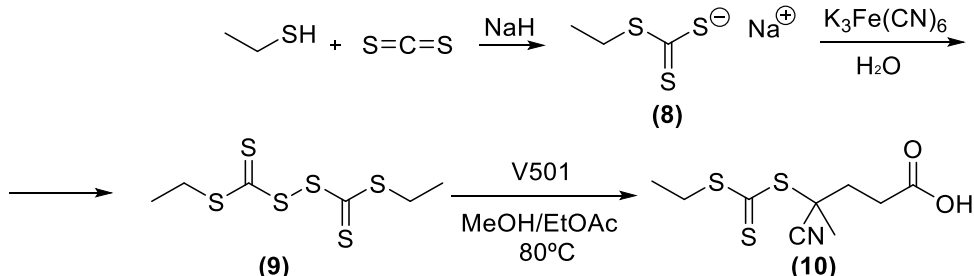


Scheme 2.5: Synthesis of Chain Transfer Agent (CTA) **(10)**[5].

**Sodium ethyl carbonotrithioate (8).** NaH (60 wt % in mineral oil, 2.82 g, 70.4

mmol, 1.06 eq.) was dispersed in diethyl ether (50 mL) and cooled in an ice

bath. Ethanethiol (4.35 g, 70.0 mmol, 1 eq.) was added dropwise under stirring

to the suspension and the mixture was stirred for 10 minutes. CS$_2$ (5.8 mL, 96

mmol, 1.4 eq.) was then added dropwise to the suspension and the reaction

was stirred at room temperature for 1 h. The bright yellow solid was filtered

and washed with diethyl ether and dried under vacuum. Yield: 80 %.

$^1$H NMR (400 MHz, d$_6$-DMSO, δ, ppm): 2.94 (q, J=7.4 Hz, 2H, C*H$_3$*CH$_2$S), 1.13 (t,

J=7.4 Hz, 2H, CH$_3$C*H$_2$*S) (Fig. S2.4).

$^{13}$C NMR (101 MHz, d$_6$-DMSO, δ, ppm): 239.3 (C=S), 33.8 (CH$_3$*C*H$_2$S), 14.01

(*C*H$_3$CH$_2$S) (Fig. S2.5).

**Dithiobis-ethyl carbonotrithioate disulfide (9). (8)** was dissolved in 100 mL of

an aqueous solution of K$_3$Fe (CN)$_6$ (16 g, 49 mmol). The mixture was extracted

with diethyl ether (4 X 500 mL) and the organic fractions, collected, were dried

over MgSO$_4$. Following filtration, the solvent was removed under reduced pressure, yielding product **(9)** as an orange, viscous oil. Yield: 56%.

$^1$H NMR (400 MHz, d$_6$-DMSO, δ, ppm): 3.32 (q, J=7.5 Hz, 2H, CH$_3$C*H$_2$*S), 1.36 (t, J=7.5 Hz, 3H, C*H$_3$*CH$_2$S) (Fig. S2.6).

$^{13}$C NMR (101 MHz, d$_6$-DMSO, δ, ppm): 221.91 (C=S), 33.10 (CH$_3$*C*H$_2$S), 12.98 (*C*H$_3$CH$_2$S) (Fig S2.7).

**CTA (10).** Carbonotrithioate disulfide **(9)** (2.80 g, 13.2 mmol, 1 eq.) and V501 (5.38 g, 19.2 mmol, 1.45 eq.) were dissolved in 1:1 v/v ethyl acetate:methanol (80 mL). The solution was degassed for 30 min by argon bubbling, under stirring. The reaction was then heated to reflux for 17 h. The volatiles were then removed under reduced pressure, and the resulting yellow oily residue was purified by silica gel flash chromatography, using a Pet. Ether:Et$_2$O in gradient, from 9:1 to 7;3 v/v, as the mobile phase. Yield: 30%.

$^1$H NMR (400 MHz, CDCl$_3$, δ, ppm): 3.33 (q, J=7.4 Hz, 2H, CH$_3$C*H$_2$*S), 2.67 (m, 2H, CH$_2$C*H$_2$*COOH), 2.53-2.39 (m, C*H$_2$*CH$_2$COOH), 1.87(s, CH$_3$), 1.09 (t, J=7.4 Hz, 3H, C*H$_3$*CH$_2$S) (Fig S2.8).

$^{13}$C NMR (101 MHz, d$_6$-DMSO, δ, ppm): 218.19 (C=S), 172.72 (COOH), 119.10 (CN), 43.08 (*C*CN), 31.08 (CH$_3$*C*H$_2$S), 29.14 (*C*H$_2$CH$_2$COOH), 23.74 (CH$_3$), 12.63 (*C*H$_3$CH$_2$S) (Fig S2.9).

ESI-TOF mass spectrometry: expected m/z [M-H]$^+$ 264.01, [M-Na]$^+$ 285.99, found 264.02 and 285.99.

FT-IR: 2932 cm$^{-1}$, 2235 cm$^{-1}$ ($\upsilon_{C≡N}$), 1704 cm$^{-1}$ ($\upsilon_{C=O}$).

## 2.2.8. Synthesis of peptide GILQINSRG (11)
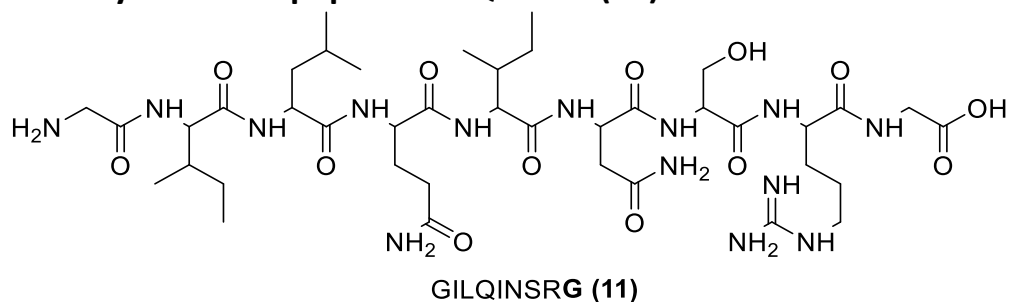


GILQINSR**G (11)**

Figure 2.2: Chemical structure of peptide GILQINSR**G (11)**.

In a glass peptide synthesis vessel, 2-chlorotrytilchloride, polymer bound resin beads (1.6 mmol/g, 1.8 g, 2.9 mmol, 1 eq) were swelled in biotech grade DMF for 30 min.

After swelling, the resin was washed with biotech grade DMF, dry methanol, dry DCM and biotech grade DMF again.

The first amino acid, Fmoc-Gly-OH (1.9 g, 6.0 mmol, 2 eq.) was subsequently added to the suspension, followed by DIPEA (2.1 mL, 15 mmol, 5 eq.), and the resulting mixture stirred for 60 min. After washing, the resin was treated for 15 min with a mixture of anhydrous DCM/ anhydrous MeOH/ DIPEA (80:15:5 in volume) to cap any remaining reactive trityl group. Finally, the protecting Fmoc group was removed from the attached amino acid treating the resin with a 20% v/v piperidine solution in DMF for 30 min. The remaining 8 amino acids were attached following the same procedure: 2 eq. of Fmoc-protected amino acid were previously dissolved in biotech grade DMF, mixed with 1.9 eq of HATU and 3 eq. of DIPEA. The solution was added to the resin and the resulting suspension was stirred for 60 min. The excess of reagents was then removed

by filtration and the coupling step repeated using the same procedure. Fmoc deprotection was finally performed with the same procedure described above.

After each amino acid coupling and Fmoc deprotection step, the excess of reagents was removed from the reaction vessel by filtration, and the resin was washed with biotech grade DMF, dry methanol, dry DCM and biotech grade DMF again.

Final peptide cleavage and deprotection were performed using a mixture of TFA:water:triisopropylsilane (95:2.5:2.5 v/v, 10 mL for 200 mg of resin), in which the resin was stirred for 90 min. The supernatant was then collected and dried under vacuum to 1/10 of its volume. The peptide was finally precipitated in diethyl ether and dried overnight in the desiccator. The product was analysed by ESI-MS and RP-HPLC. RP-HPLC was run at a flow rate of 1 mL/min, using a 20-80% acetonitrile gradient in Milli-q water + 0.1% TFA, on a C18 Zorbax Eclipse Plus C18 column (3.5 μm, 95 Å, 4.6 × 12.5 mm). Absorbance was recorded at 280 nm. Yield: 41%.

ESI-MS: expected m/z [M-H]$^+$ 957.09 and [M+2H]$^{2+}$ 479.05, found 957.55 and 479.28.

RP-HPLC: r.t. 8.5 min. Purity 85%.

### 2.2.9. Synthesis of peptide GILQINSRW-RAFT agent (12) and peptide GILQINSRG-RAFT agent (13)
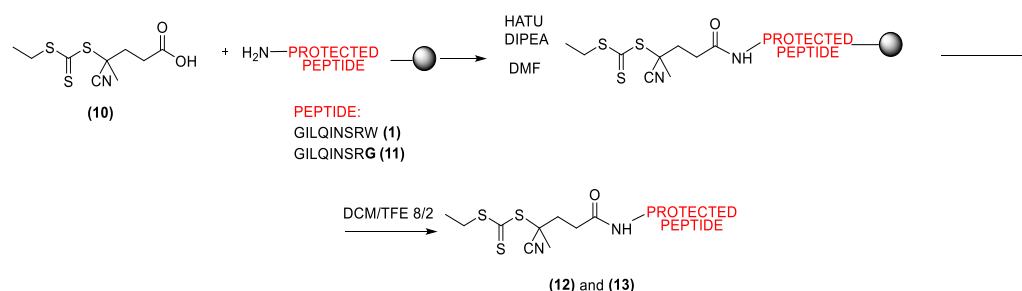


Scheme 2.6: Synthesis of peptide GILQINSRW-RAFT agent **(12)** and peptide GILQINSR**G**-RAFT agent **(13)**.

The same protocol was followed for both protected, resin-bounds peptides **(1)** and **(11)**. 400 mg of resin-bound peptide **(1)** (containing approximately 246 mg of attached, protected peptide (**1**), and 145 mg of starting resin, 1.60 mmol/g, 0.248 mmol, 1 eq.) and 400 mg of resin-bound peptide **(11)** (containing approximately 217 mg of attached, protected peptide (**1**), and 183 mg of starting resin, 1.60 mmol/g, 0.248 mmol, 1 eq.) were swelled for 30 min in DMF. CTA agent (**10**) (196 mg, 0.740 mmol, 3 eq.), DIPEA (173 µL, 0.992 mmol, 4 eq.) and HATU (274 mg, 0.720 mmol, 2.9 eq.) were added to both suspensions, which were left under stirring at room temperature overnight. The resin beads were then repeatedly washed with DCM, and finally treated for 120 min with a DCM:TFE 8:2 v/v solution (10 mL). The suspensions were filtered and concentrated under vacuum. The resulting protected peptidic RAFT agents (**12**) and (**13**) were analysed by $^1$H NMR and ESI-MS.

RAFT agent (**12**) Yield: 68%. $^1$H NMR (400 MHz, d$_6$-DMSO, δ, ppm): 7.40-7.00 (m, 30H, trityl aromatic CH), 1.83 (s, 1H, CTA CH$_3$), 1.59 (s, 9H, Boc CH$_3$), 1.39 (s,

9H, Pbf CH$_3$) 1.28 (t, *J*=14.7Hz, 3H, C*H$_3$*CH$_2$S), 0.91 (s, 9H, tert-butyl CH$_3$), 0.85-0.7 (m, 9H, leucine and isoleucine CH$_3$) (Fig.2.16).

ESI-TOF mass spectrometry: expected m/z [M-H-Na]$^{2+}$ 1124.01 and [M + 2Na]$^{2+}$ 1134.99, found 1124.01 and 1134.99.

RAFT agent **(13)** Yield: 66%. $^1$H NMR (400 MHz, d$_6$-DMSO, δ, ppm): 7.40-7.00 (m, 30H, trityl aromatic CH), 1.83 (s, 1H, CTA CH$_3$), 1.39 (s, 9H, Pbf CH$_3$) 1.28 (t, *J*=14.7Hz, 3H, C*H$_3$*CH$_2$S), 1.06 (s, 9H, tert-butyl CH$_3$), 0.90-0.70 (s, 9H, leucine and isoleucine CH$_3$) (Fig. 2.26).

ESI-TOF mass spectrometry: expected m/z [M]$^-$ 1993.91, found 1993.89.

## 2.2.10. Synthesis of poly(*N*-hydroxyethylacrylamide)-*b*-GILQINSRW (14) and poly(*N*-hydroxyethylacrylamide)-*b*-GILQINSRG (15)



**(12)**

V501
DMF 70 ºC

**(14)** n=90

**(13)**

V501
DMF 70 ºC

**(15)** n=95
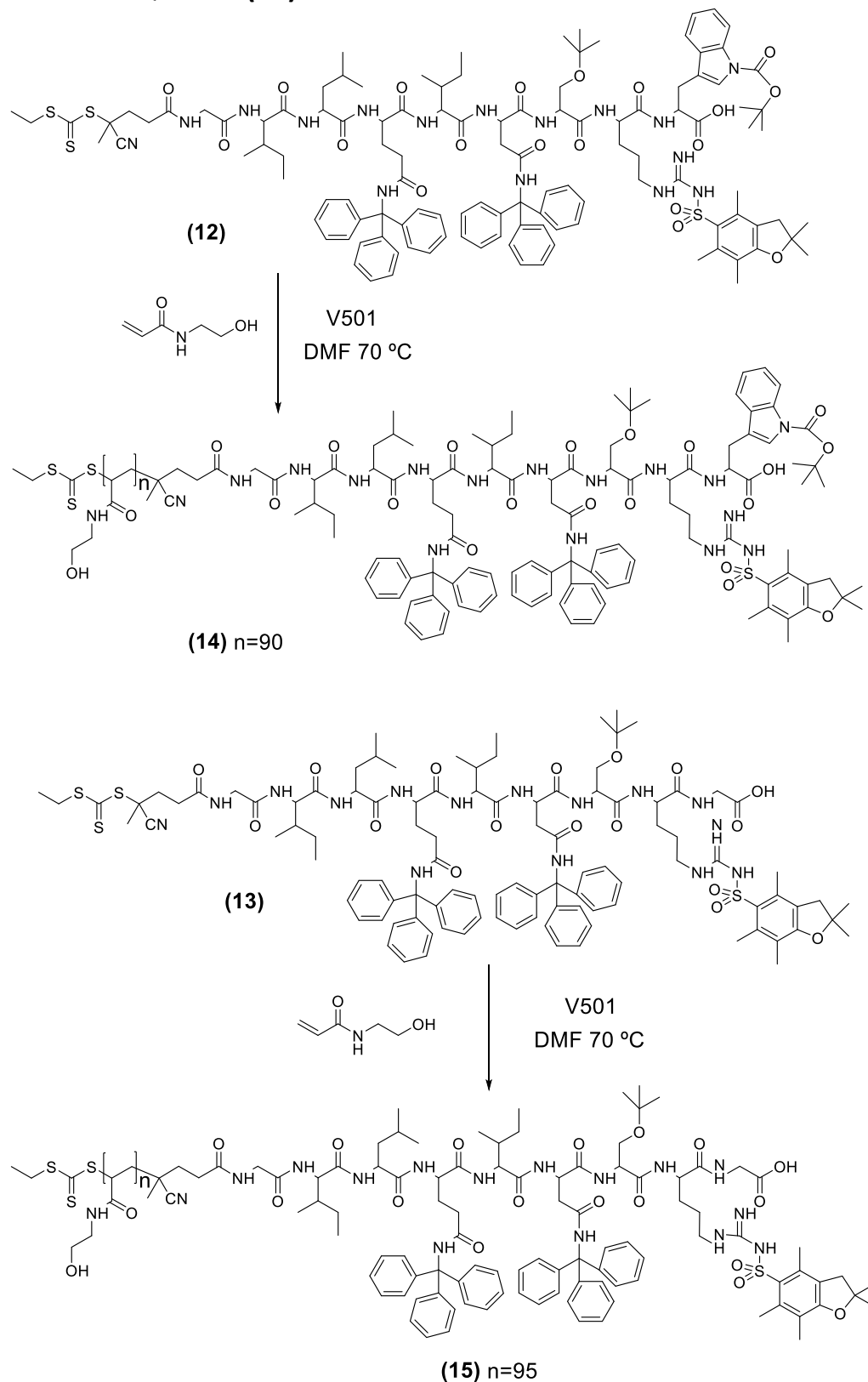
Scheme 2.7: Synthesis of poly(*N*-hydroxyethylacrylamide)-*b*-GILQINSRW **(14)** and poly(N-hydroxyethylacrylamide)-*b*-GILQINSRG **(15)**.

The same synthetic route was used to synthesise copolymers **(14)** and **(15)**.

Copolymer **(14)**: RAFT agent **(12)** (1 eq., 220 mg, 0.096 mmol) was dissolved in DMF (3 mL) and mixed with *N*-hydroxyethylacrilamide (100 eq., 1.12 g, 9.60 mmol). The solution was transferred into a small schlenk tube equipped with a magnetic stirrer, which was put in ice. Initiator V 501 (0.7 mg, 0.002 mmol, 0.1 eq) in DMF (70 µL), was added to the tube. The mixture was degassed for 30 min bubbling argon under stirring at 0°C, and finally put on a paraffin oil bath at 70 ˚C. The reaction was monitored by $^{1}$H NMR, checking the disappearance of acrylamide monomer peaks into the 5-6.5 ppm region, and stopped after 4.5h when 92% conversion was reached. The polymer was then precipitated in THF and dried under high vacuum.

Copolymer **(15)**: RAFT agent **(13)** (1 eq., 200 mg, 0.096 mmol) was dissolved in DMF (3 mL) and mixed with *N*-Hydroxyethylacrilamide (100 eq., 1.12 g, 9.60 mmol). The solution was transferred into a small schlenk tube equipped with a magnetic stirrer, which was put in ice. Initiator V 501 (0.7 mg, 0.002 mmol, 0.1 eq) in DMF (70 µL), was added to the tube. The mixture was degassed for 30 min bubbling argon under stirring at 0°C, and finally put on a paraffin oil bath at 70 ˚C. The reaction was monitored by $^{1}$H NMR, checking the disappearance of acrylamide monomer peaks into the 5-6.5 ppm region, and stopped after 6h when 92% conversion was reached. The polymer was then precipitated in THF and dried under high vacuum.

The products were characterized by $^{1}$H NMR and SEC, performed in DMF with 0.1% LiBr.

Copolymer **(14)** Yield: 44%. $^1$H NMR (400 MHz, $d_6$-DMSO, δ, ppm): 7.8-7.4 (m, 90H, polyacrylamide NH), 7.25-7.10 (m, 30H, trityl groups), 5.10-4.70 (m, 90H, polyacrylamide OH), 2.10-1.70 (m, 90H, polyacrylamide C*H*CH$_2$) 1.60-1.20 (m, 180H, polyacrylamide CHC*H$_2$*), 0.78(m, 12H, leucines and isoleucines CH$_3$) (Fig.2.17). $M_{n,NMR}$: 12.5 kDa, $M_{n,SEC(DMF)}$ 17.0 kDa, Đ 1.09.

Copolymer **(15)** Yield: 47%. $^1$H NMR (400 MHz, $d_6$-DMSO, δ, ppm): 7.8-7.4 (m, 95H, polyacrylamide NH), 7.25-7.10 (m, 30H, trityl groups), 5.10-4.70 (m, 85H, polyacrylamide OH), 2.10-1.70 (m, 95H, polyacrylamide C*H*CH$_2$) 1.60-1.20 (m, 190H, polyacrylamide CHC*H$_2$*), 0.78(m, 12H, leucine and isoleucine CH$_3$) (Fig S2.10). $M_{n,NMR}$: 13.1 kDa, $M_{n,SEC(DMF)}$ 15.0 kDa, Đ 1.16.

## 2.2.11. Removal of trithiocarbonate chain-ends from peptide-*b*-polyHEA copolymers.



**(14)**

DMF 80ºC



**(16)** n=90



**(15**)
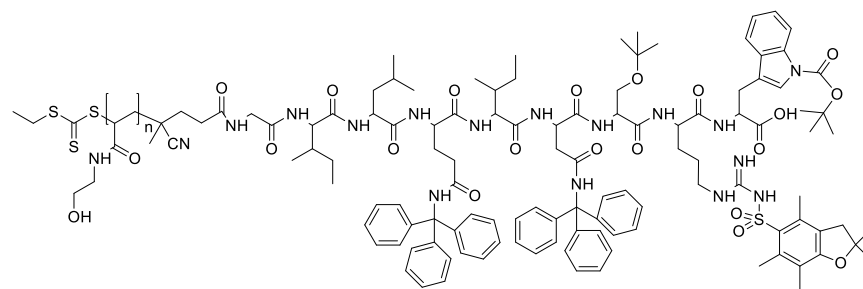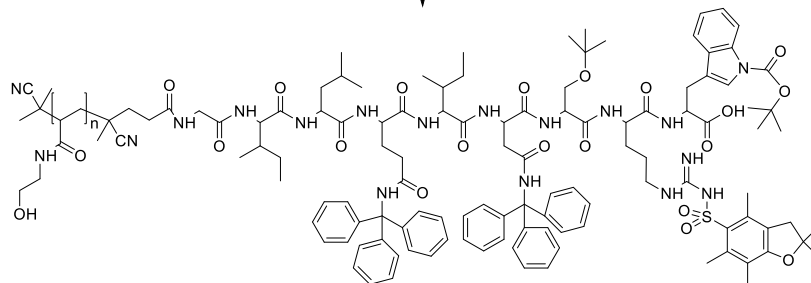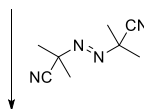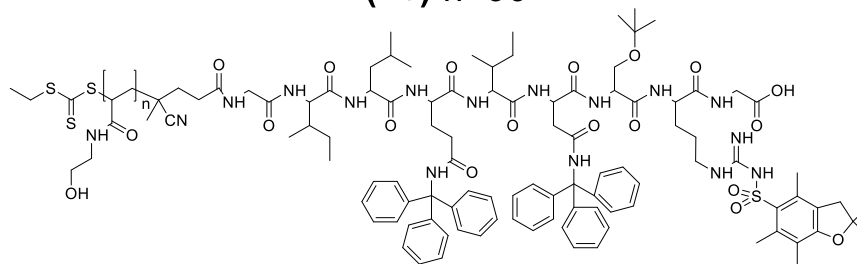
DMF 80ºC
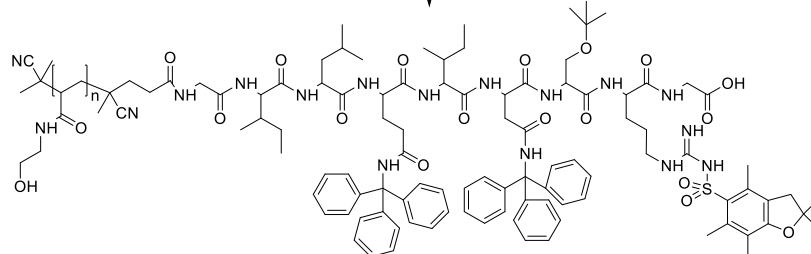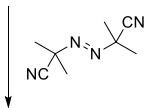


**(17)** n=95

Scheme 2.8: RAFT removal from copolymers **(14)** and **(15)**.

For removal of trithiocarbonate chain-ends from peptide-*b*-polyHEA copolymers, the same procedure was followed for both copolymers **(14)** and **(15)**.

Copolymer **(14)**: the copolymer (350 mg, 0.028 mmol, 1 eq.) was dissolved in DMF (5 mL) together with AIBN (700 mg, 2.4 mmol, 80 eq.). The mixture was degassed in ice for 30 min by bubbling argon under stirring, and then put on an oil bath at 80°C overnight. The solution was then repeatedly precipitated in THF and re-dissolved in MeOH. The precipitate was finally dried under reduced pressure.

Copolymer **(15)**: the copolymer (0.30 g, 0.025 mmol, 1 eq.) was dissolved in DMF (5 mL) together with AIBN (0.56 g, 2.0 mmol, 80 eq.). The mixture was degassed in ice for 30 min by bubbling argon under stirring, and then put on an oil bath at 80°C overnight. The solution was then repeatedly precipitated in THF and re-dissolved in MeOH. The precipitate was finally dried under reduced pressure.

Efficiency of removal of the trithiocarbonate RAFT chain-end from the polymers was estimated by UV spectrophotometry scan on final isolated polymers, measuring absorbance decrease of peak at 300 nm, which is characteristic of the trithiocarbonate group (Fig. S2.11 and S2.12). Copolymers were finally analysed by SEC, using DMF with 0.1% LiBr as solvent.

Copolymer **(16)** Yield: 60%. $M_{n,SEC(DMF)}$ 16.8 kDa, Đ1.08.

Copolymer **(17)** Yield: 64%. $M_{n,SEC(DMF)}$ 15.0 kDa, Đ 1.13.

### 2.2.12. Synthesis of HEA$_{90}$-*b*-GILQINSRW and HEA$_{95}$-*b*-GILQINSRG



**(16)**

0.1 M HCl in HFIP

HEA$_{90}$-*b*-GILQINSRW

**(17)**

0.1 M HCl in HFIP
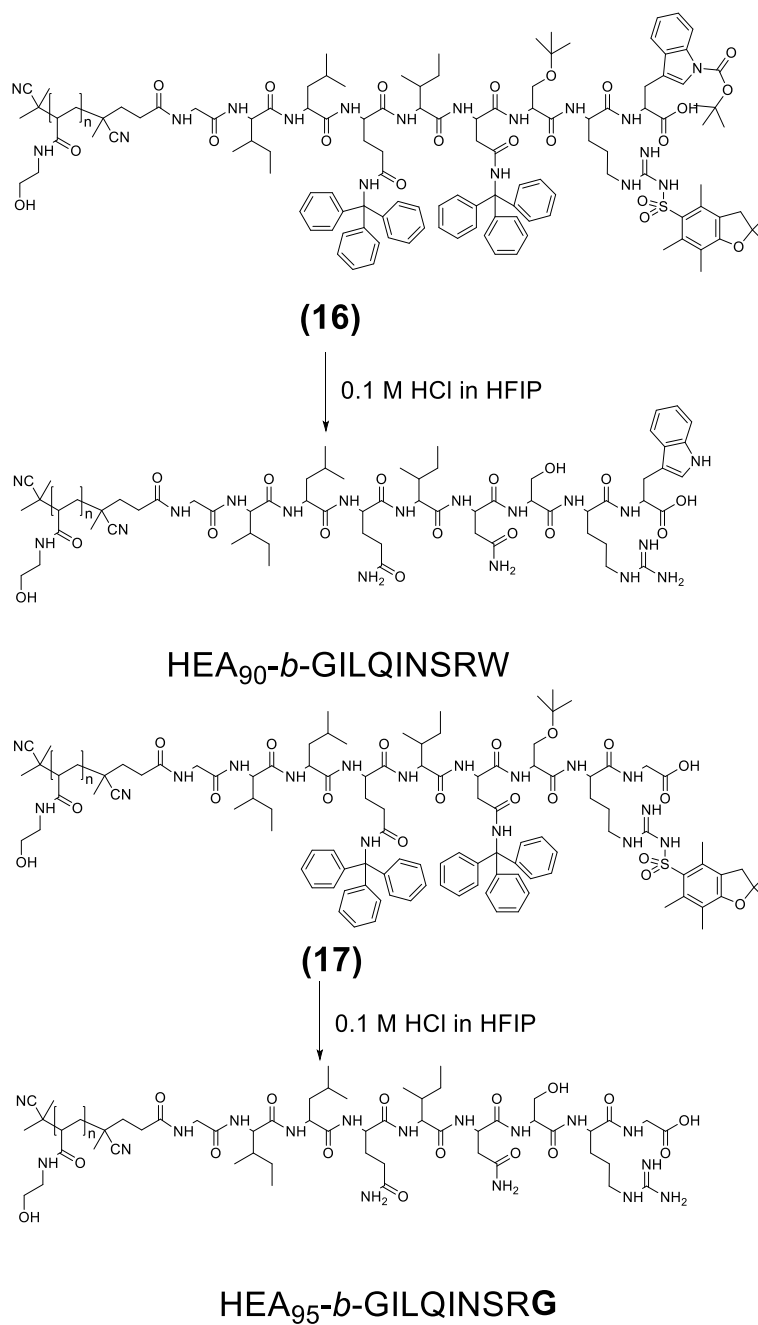
HEA$_{95}$-*b*-GILQINSR**G**

Scheme 2.9: Synthesis of HEA$_{90}$-b-GILQINSRW and HEA$_{95}$-b-GILQINSR**G.**

Protecting groups on amino acid residues were removed from the peptide using the same procedure for both copolymers.

Copolymer **(16)**: the copolymer (200 mg) was dissolved in a solution of 0.1 N

HCl in hexafluoroisopropanol (5 mL). The solution was left stirring for 6 h. The

polymer was then precipitated in diethyl ether, re-dissolved in water, dialysed

against water (5 L, MWCO 3.5 kDa) for 48 h. The solution was finally lyophilised.

Copolymer **(17)**: the copolymer (400 mg) was dissolved in a solution of 0.1 N

HCl in hexafluoroisopropanol (5 mL). The solution was left stirring for 6 h. The

polymer was then precipitated in diethyl ether, re-dissolved in water, dialysed

against water (5 L, MWCO 3.5 kDa) for 48 h. The solution was finally lyophilised.

The final deprotected copolymers were analysed by $^1$H NMR and SEC, using

DMF with 0.1% LiBr.

HEA$_{90}$-*b*-GILQINSRW Yield: 62%. $^1$H NMR (400 MHz, d$_6$-DMSO, δ, ppm): 7.8-7.4

(m, 90H, polyacrylamide NH), 5.10-4.70 (m, 90H, polyacrylamide OH), 2.10-1.70

(m, 90H, polyacrylamide C*H*CH$_2$) 1.60-1.20 (m, 180H, polyacrylamide CHC*H$_2$*),

0.78(m, 12H, leucine and isoleucine CH$_3$) (Fig.2.19). M$_{n,NMR}$: 10.8 kDa, M$_{n,SEC(DMF)}$

17.0 kDa, Đ 1.07.

HEA$_{95}$-*b*-GILQINSR**G** Yield: 58%. $^1$H NMR (400 MHz, d$_6$-DMSO, δ, ppm): 7.8-7.4

(m, 95H, polyacrylamide NH), 5.10-4.70 (m, 95H, polyacrylamide OH), 2.10-1.70

(m, 95H, polyacrylamide C*H*CH$_2$) 1.60-1.20 (m, 190H, polyacrylamide CHC*H$_2$*),

0.78(m, 12H, leucine and isoleucine CH$_3$) (Fig.2.27). M$_{n,NMR}$: 12.1 kDa, M$_{n,SEC(DMF)}$

14.8 kDa, Đ 1.13.

SEC traces are displayed in Fig. S2.13.

## 2.2.13. Synthesis of HEA$_{100}$ control polymer.
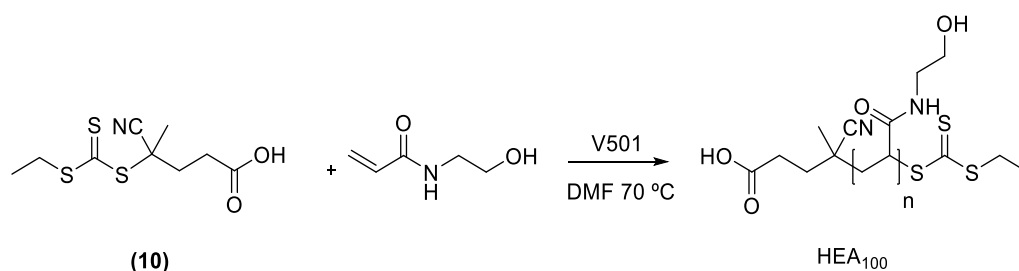


Scheme 2.10: synthesis of HEA$_{100}$ control polymer.

CTA agent (**10**) (0.15 g, 0.53 mmol, 1 eq.) and HEA monomer (5.0 g, 42 mmol, 80 eq.) were dissolved in DMF (8 mL). The mixture was transferred into a glass tube equipped with a magnetic stirrer, which was put in ice. Initiator V 501 (16 mg, 0.050 mmol, 0.1 eq.), in DMF (16 µL), was added to the tube. The mixture was degassed for 30 min bubbling argon under stirring at 0°C, and finally put on a paraffin oil bath at 70 °C. The reaction was monitored by $^1$H NMR, checking the disappearance of acrylamide monomer peaks into the 5-6.5 ppm region, and stopped after 1.5h when 84% conversion was reached. The polymer was then precipitated in THF and dried under high vacuum. The final control polymer HEA$_{110}$ was analysed by $^1$H NMR and SEC, performed in DMF with 0.1% LiBr. Yield: 72%.

HEA$_{100}$: $^1$H NMR (400 MHz, d$_6$-DMSO, δ, ppm): 7.8-7.4 (m, 100H, polyacrylamide NH), 5.10-4.70 (m, 100H, polyacrylamide OH), 2.10-1.70 (m, 100H, polyacrylamide C*H*CH$_2$) 1.60-1.20 (m, 200H, polyacrylamide CHC*H$_2$*) M$_{n,THEO}$: 12.9 kDa, M$_{n,SEC(DMF)}$ 12.1 kDa, Đ 1.14.

### 2.2.14. Lysozyme activity assay

Lysozyme activity assays were carried out measuring the change of absorbance due to light scattering at $\lambda=460$ nm, over time. The first experiment was conducted by mixing 0.90 mL of a 0.044 mg mL$^{-1}$ lysozyme solution in DPBS, with 0.10 mL of three DMSO solutions in which peptides **(1)** (5.3 mg mL$^{-1}$), **(4)** (4 mg mL$^{-1}$) and **(7)** (4 mg mL$^{-1}$), respectively had been previously dissolved.

The second experiment followed a similar procedure, but the samples were in this case put on an oil bath at 90°C and left heating for 1 h, before measurement.

The last experiment was performed by mixing 100 µL of a 0.4 mg mL$^{-1}$ lysozyme solution in DPBS with separate 4.5, 9, 45, 90, 450 and 900 µL of two DMSO solutions in which peptide **(1)** (0.59 mg mL$^{-1}$) and peptide **(4)** (0.44 mg mL$^{-1}$) respectively had been previously dissolved.

For each of the samples described above, 150 µL were added to a Quartz UV cell, and 300 µL of a 10 mg/mL water suspension of substrate *Micrococcus lysodeikticus* cell walls were added immediately prior starting the measurement. The turbidity of the samples was evaluated by measuring absorbance at $\lambda=460$ nm every 1.5 second, for 60 seconds.

### 2.2.15. Lysozyme aggregation assay

A lysozyme stock solution was prepared by dissolving the protein in water at a concentration of 100 mg/mL. 200 µL of this solution were added to 1800 µL of 100 mM phosphate buffer pH 12.3 in which the polymers HEA$_{90}$-*b*- GILQINSRW, HEA$_{95}$-*b*- GILQINSR**G** and HEA$_{100}$ had been previously dissolved, for a final

lysozyme concentration of 10 mg/mL and a polymer: protein molar ratio of 1:1.

From each polymer-protein mixture, 5 aliquots of 300 µL were transferred into

a 96-well plate. The plate was loaded into a TECAN Spark 10M Multi-function

Platereader. Absorbance at λ=500 nm was measured every 30 min for 24 h at

30°C to monitor the increase of turbidity resulting from protein aggregation.

## 2.3. Results and Discussion

The first part of this work focusses on the investigation of potential interactions between proteins and peptides designed to mimic their specific Aggregation Prone Regions. These are typically highly hydrophobic, non-charged protein fragments, usually located in the inner core of the protein. Upon protein unfolding, either reversible or irreversible, they can get exposed to the external environment, and promote self-aggregating processes due to β-sheet mutual associations, which may ultimately lead to formation of proteins amorphous or fibrillary aggregates[2, 6]. Our initial working hypothesis was that peptides with structure homologous or similar to specific APRs, could establish hydrophobic, non-covalent interactions with the protein APR sequence on the protein. We aimed at developing appropriate APR analogues that could have a stabilising effect on therapeutic proteins, preventing self-interactions that could lead to protein aggregation.

Hen egg lysozyme was chosen as model protein to study, as one of its APRs, the GILQINSRW fragment has been identified and characterised[4]. In this chapter, potential interactions between the APR peptide and its homologous intact sequence in native lysozyme, and how chemical modifications of the APR-mimicking peptide could affect these interactions, were investigated.

GILQINSRW APR-mimicking peptide and its chemically modified analogues were found to be prone to self-aggregate under aqueous conditions, hence to increase their solubility, analogues containing a hydrophilic poly-*N*-hydroxyethylacrylamide chain, were synthesised by RAFT polymerisation. The

copolymer was then tested on hen egg lysozyme to evaluate its potential stabilising effects on lysozyme, through the APR incorporated in the copolymer chain.

## 2.3.1. Synthesis of APR-derived peptides

The first part of this work focussed on the synthesis of GILQINSRW peptide APR **(1)**, and its PEGylated **(4)** and sulfobetaine-modified **(7)** derivative (Fig. 2.3), and their ability to interact with lysozyme.
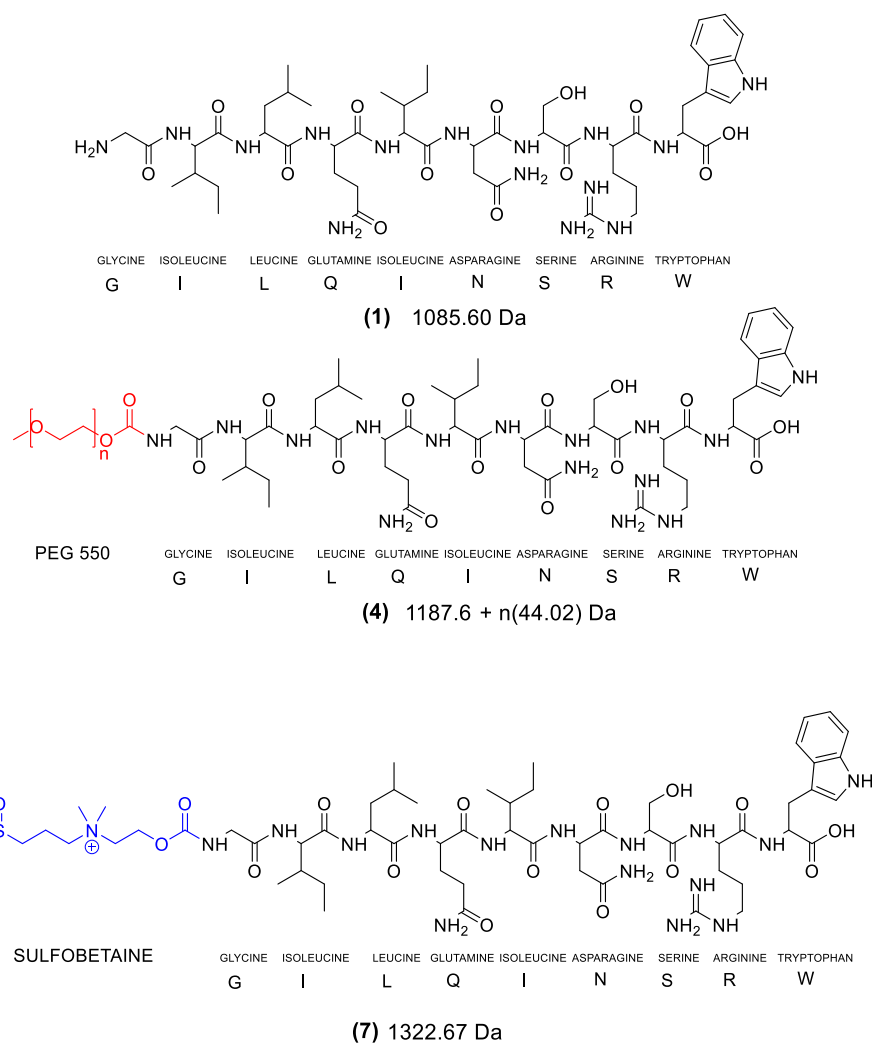


Figure 2.3: Structure of the three peptides synthesised in the initial part of this study: GILQINSRW peptide **(1)**, homologous of one of the APR sequences of hen egg lysozyme[4], and its PEGylated **(4)** and betaine-modified **(7)** derivatives.

Peptide GILQINSRW **(1)** was synthesised by solid phase peptide synthesis in 47% yield, and was found to be analytically pure, as confirmed by ESI-MS. The main peak at 1086.6 m/z corresponds to [M-H]$^+$ (Fig. 2.4). Its purity was further verified by RP-HPLC and was found to be around 85% (Fig. 2.5).
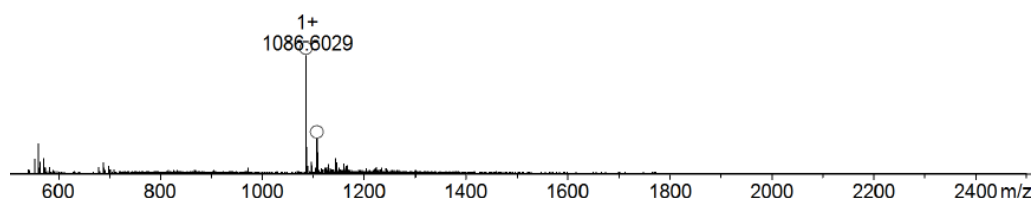


Figure 2.4: ESI-MS analysis of GILQINSRW APR **(1)**. Two peaks are identified: peak at 1086.6 m/z corresponds to [M-H]$^+$, that at 1108.6 to [M-Na]$^+$.
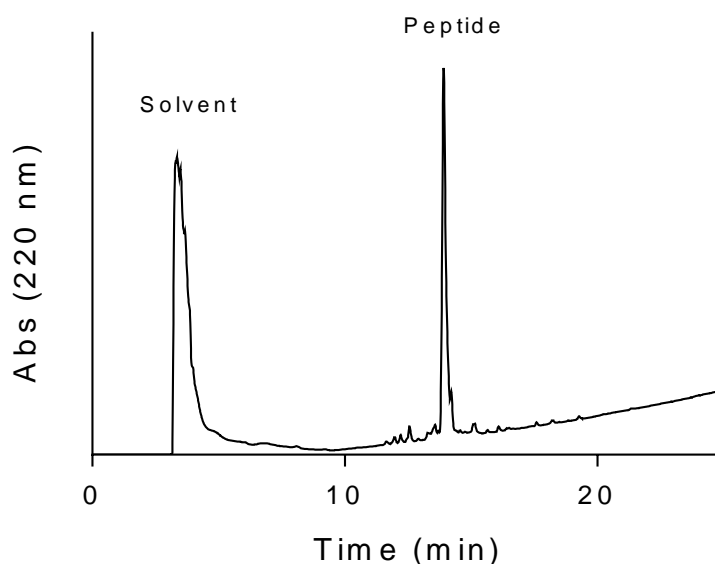


Figure 2.5: RP-HPLC (C$_{18}$) chromatogram of peptide GILQINSRW. The sample was eluted using a 20-90% acetonitrile gradient in water +0.1% TFA. Absorbance was recorded at $\lambda$=220 nm. Purity was estimated by calculating the ratio between the peak area of the peptide and all detected peak areas.

Both mPEG and sulfobetaine peptide derivatives, **(4)** and **(7)** respectively, were synthesised from **(1)**. PEGylated peptide **(4)** was obtained by reacting **(1)** with succinimidyl carbonate of methoxyPEG 550, using a previously established

procedure[7] (Scheme 2.11). An analogous approach was employed with **(7)**,

using 3-[dimethyl-(2-hydroxyethyl)ammonio]-1-propanesulfonate instead of

PEG (Scheme 2.12).
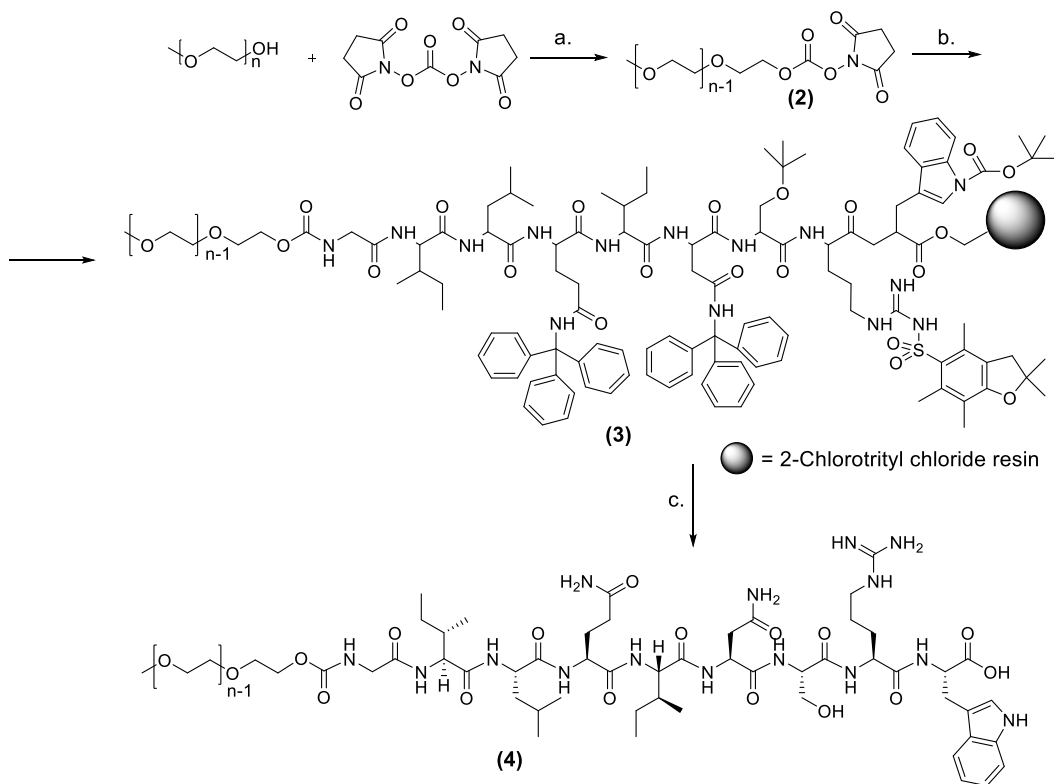


Scheme 2.11: Synthesis of PEGylated GILQINSRW **(4)**. *Reagents and conditions*: (a) TEA, MeCN, room temperature. (b) **(1)**, **(2)**, TEA, DCM, room temperature. (c) **(3)**, TFA :water:triisopropylsilane 95:2.5:2.5 v/v, room temperature.
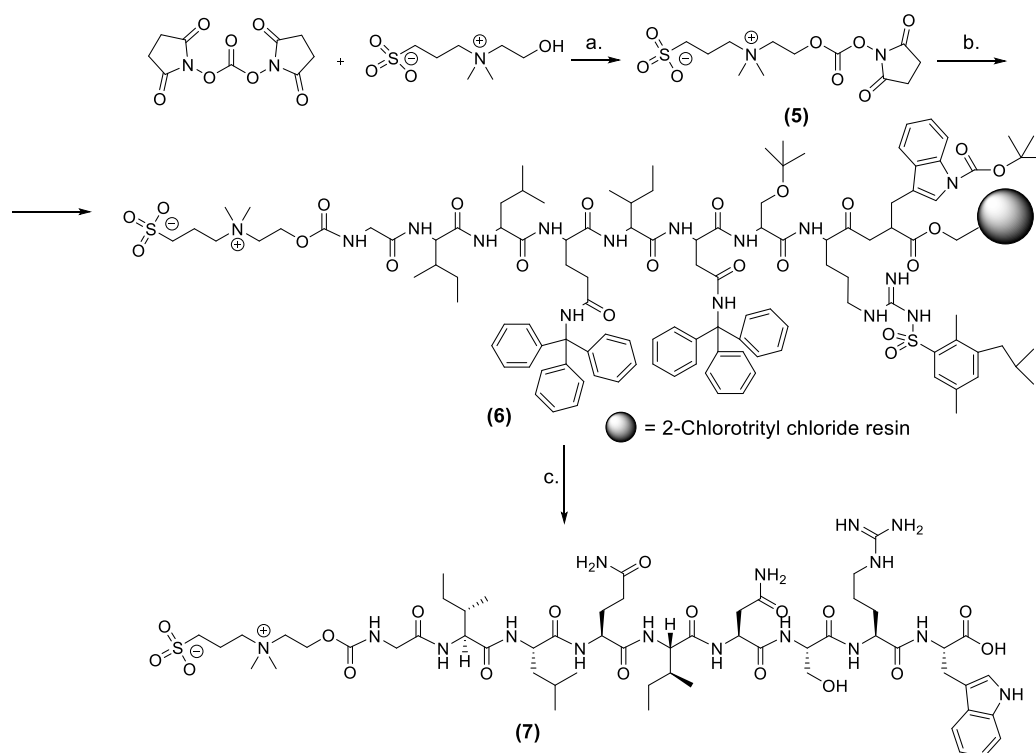
Scheme 2.12: Synthesis of Sulfobetaine GILQINSRW **(7)**. *Reagents and conditions*: (a) TEA, DMF, room temperature. (b) **(1)**, **(5)** TEA, DMF, room temperature. (c) **(6)**, TFA :water:triisopropylsilane 95:2.5:2.5 v/v, room temperature.

Compound **(4)** was characterised by MALDI-MS, compound **(7)** by ESI-MS (Fig.2.6). In both cases MS analysis confirmed successful synthesis and efficient purification of **(4)** and **(7)**. In the mass spectra of both peptide derivatives the peak corresponding to the peptide starting material **(1)** disappeared, confirming quantitative conversion into PEGylated **(4)** and sulfobetaine **(7)** derivatives.

The mass spectrum of **(4)** shows multiple peaks, separated by 44.02 Da (ethylene oxide unit) due to the polydispersity of commercial PEG (Fig. 2.6). In the mass spectrum of **(7)**, peaks at 673.3 m/z for $[M-H-Na]^{2+}$ and at 1323.7 for $[M-H]^{+}$ were clearly identified (Fig. 2.7).
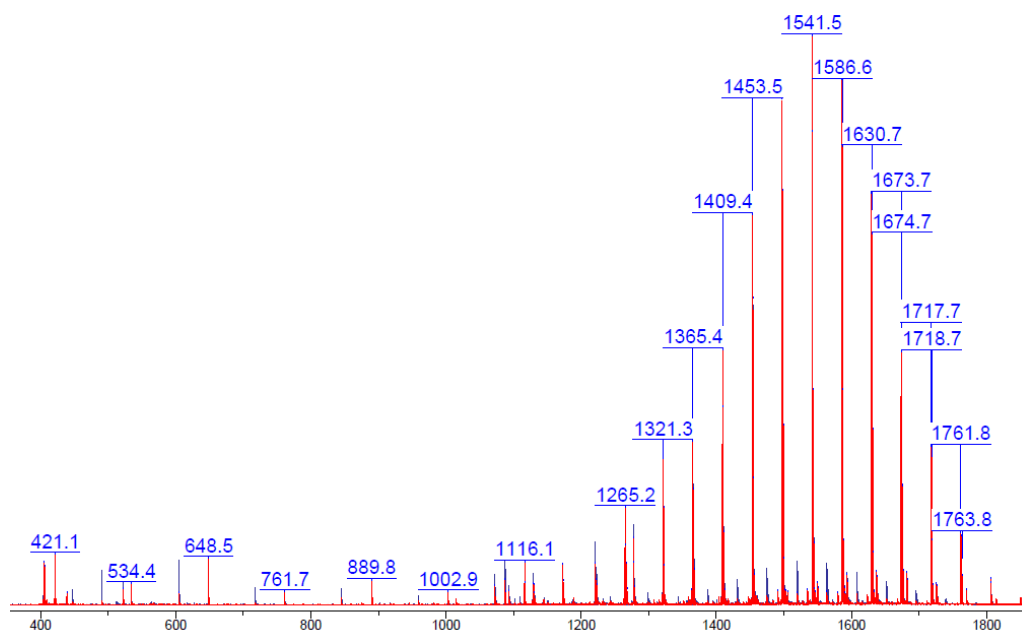
Figure 2.6: MALDI TOF-MS analysis of PEGylated peptide **(4)**, showing the complete disappearance of APR peptide **(1)** starting material.
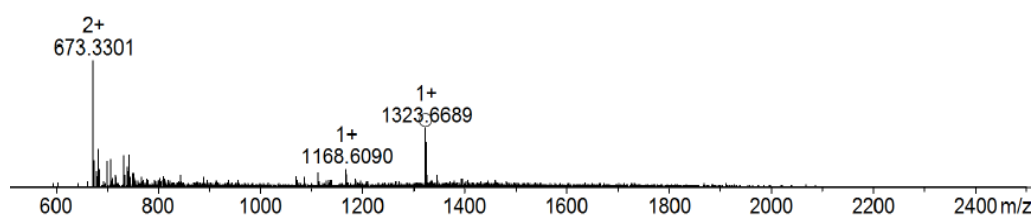


Figure 2.7: ESI-MS analysis of product of sulfobetaine peptide **(7)**. The main peak at 673.3 m/z corresponds to $[M-H-Na]^{2+}$, the smaller peak at 1323.7 to $[M-H]^{+}$.

Solubility of the three compounds was investigated in different solvents, such as DCM, MeOH, DMSO, 2-propanol, acetonitrile, chloroform, acetone, tetrahydrofuran, ethyl acetate, hexane, water and petroleum ether. The compounds were found to be insoluble in all these solvents, with the exception of DMSO. This behaviour was ascribed to the physico-chemical nature of the APR GILQINSRW, which is intrinsically prone to form insoluble aggregates. Its self-assembly is driven by different hydrophobic amino acids, like the aliphatic

leucine, isoleucine and glycine, and the aromatic tryptophan[4]. Chemical modification with mPEG or sulfobetaine was found not to be sufficient to significantly modulate this behaviour, and no increase in solubility for these derivatives, compared to their GILQINSRW peptide precursor, were observed. In an initial aggregation test, lysozyme APR derivatives **(1)**, **(4)** and **(7)** were solubilised in 100 µL of DMSO at a concentration of 10 mg/mL, and when 300 µL of water were added, these species re-precipitated, forming visible aggregates that could be easily seen with an optical microscope (Fig. 2.8).



**1**           **4**           **7**
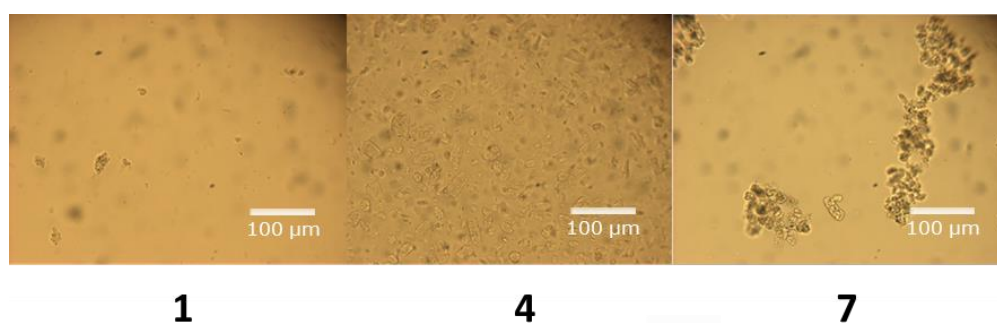
Figure 2.8: Optical microscopy images of compounds **(1)**, **(4)** and **(7)** aggregates formed by initial solubilisation of the three compounds in DMSO (100 µL) at 10 mg/mL concentration, followed by addition of 300 µL of water.

## 2.3.2. Interactions of APR-derived peptides with lysozyme: enzymatic assay

Potential non-covalent physical association between the peptides **(1)**, **(4)** and **(7)** and hen egg lysozyme was evaluated by enzymatic activity assay. The working hypothesis was that the APR sequence on the hydrophobic core of lysozyme could recognise its homologous peptide on the 3 compounds, developing non-covalent, hydrophobic interactions, similarly to the beta sheet interactions between APRs that lead to protein aggregation. The modulation of lysozyme enzymatic activity was used to assess the ability of the APR-mimicking

peptides to non-covalently interact with the enzyme, as these interactions could alter protein folding and/or its interaction with the substrate, thus reducing its enzymatic activity.

Lysozyme activity was determined using a *Micrococcus lysodeikticus*–based turbidimetric assay, which measures the decrease in turbidity of a lyophilised *Micrococcus lysodeikticus* cells walls suspension in the presence of this enzyme. These cells walls are made of polysaccharides containing 1,4-β-linkages between *N*-acetylmuramic acid and *N*-acetyl-D-glucosamine which can be hydrolysed in the presence of lysozyme[8], resulting in a progressive decrease of turbidity which is monitored by visible spectrophotometry (λ=460 nm).

In the first experiment, compounds **(1)**, **(4)** and **(7)** were separately solubilised in 100 μL of DMSO and each solution diluted 10 times in a DPBS solution in which lysozyme had been previously dissolved. The final w/w ratio between the compounds and the protein was 10:1 for compounds **(4)** and **(7)**, and 13:1 for peptide **(1)**. A relatively low concentration for these species - between 0.4 and 0.53 mg mL$^{-1}$ depending on the experiment - was chosen to avoid their aggregation/precipitation when the DMSO was diluted with PBS. 300 μL of a 10 mg/mL water suspension of *Micrococcus lysodeikticus* cells walls were then added to 150 μL of each protein-peptide mixture, recording absorbance at 460 nm (Fig. 2.9).
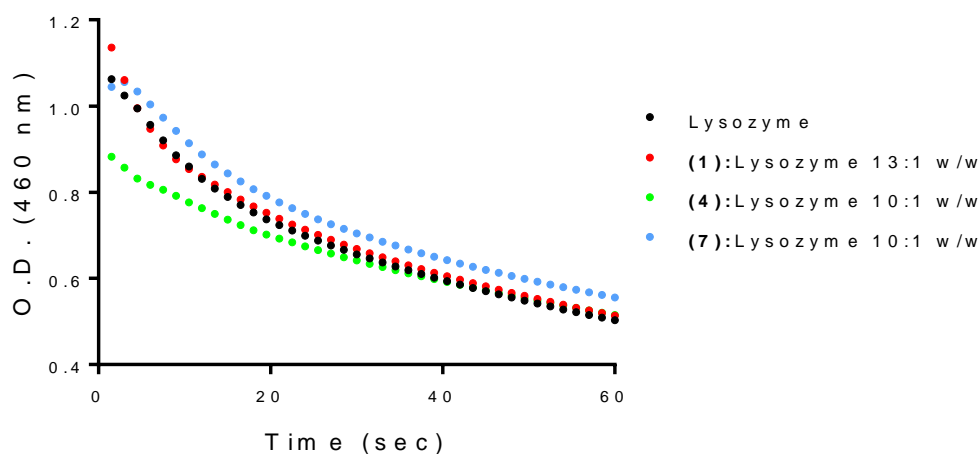
Figure 2.9: Lysozyme activity assay. Activity was measured for native lysozyme, and mixtures between lysozyme and compounds **(1)**, **(4)** and **(7)**, at 13:1 **(1)**:lysozyme, 10:1 **(4)**:lysozyme and **(7)**:lysozyme w/w ratio.
Final concentrations were of 0.04 mg/mL for lysozyme, 0.53 mg/mL for peptide **(1)**, and 0.4 mg/mL for peptide **(4)** and **(7)**. After mixing lysozyme:(APR peptide) mixtures with Micrococcus lysodeikticus cells walls, the decrease in light scattering (λ=460 nm) was monitored over time.

No difference in substrate degradation rate was observed between lysozyme alone (positive control) and its mixture with the peptides **(1), (4)** and **(7)** indicating that these compounds did not affect protein activity, as a clear decrease in turbidity over time was observed, and this was not affected by the addition of the APR-derived compounds.

The potential of compounds **(1)**, **(4**) and **(7)** to stabilise lysozyme against thermal-induced aggregation was then tested in an analogous set of experiments which were carried out at the same experimental conditions as the previous ones, except that initially solutions of lysozyme, alone or in the presence of each of the three APR peptide derivatives, at 90˚C for 1 h (Fig. 2.10). In the absence of stabilisers, at this temperature the lysozymes permanently denatures[9], hence no activity is observed. The initial hypothesis was that

protein-peptide interactions could stabilize lysozyme at least in part, thus with retention of part of its enzymatic activity after thermal treatment.
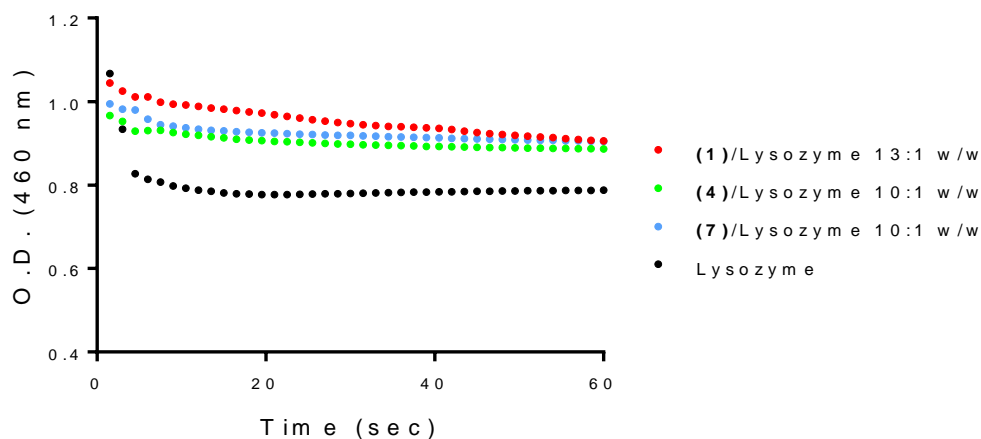


Figure 2.10: lysozyme activity after application of a thermal stress - 90 °C for 1 hour. Lysozyme was mixed with the three peptides **(1)**, **(4)** and **(7)** before heating at 13:1 **(1)**:lysozyme and 10:1 **(4)**:lysozyme and **(7)**:lysozyme w/w ratios. Final concentrations were of 0.04 mg/mL for lysozyme, 0.53 mg/mL for peptide **(1)**, and 0.4 mg/mL for peptide **(4)** and **(7)**.

The experiment confirmed the loss of protein activity upon heating-caused denaturation. Again, the presence of APR-derived peptides **(1)**, **(4)**, and **(7)** did not influence the protein behaviour.

Considering the poor solubility of the compounds, it was hypothesised that the high ionic strength of the DPBS-containing medium in the samples could have caused their aggregation, even if during the experiment their precipitation was not visually observed, likely because of their low final concentration. Therefore, the experiment was repeated increasing the amount of DMSO and reducing DPBS to the minimum amount necessary to solubilise lysozyme. Indeed in our study the protein alone was able to show activity in DMSO, despite previous works have shown its complete denaturation when solubilised in more than

70% DMSO[10]. We hypothesised that addition of water may cause instantaneous refolding of lysozyme, thus restoring its enzymatic activity.

Samples were made by preparing lysozyme solutions in 100 μL of DPBS at 0.4 mg/mL, and then diluting them 10 times with DMSO solutions in which different amounts of compounds **(1)** and **(4)** had been previously separately dissolved. Different w/w ratios between the compounds and the enzyme were tested, ranging from 0.13:1 to 13:1 peptides **(1)**/lysozyme w/w ratio and from 0.01:1 to 10:1 peptide **(4)**/lysozyme w/w ratio (Fig.2.11 and 2.12).
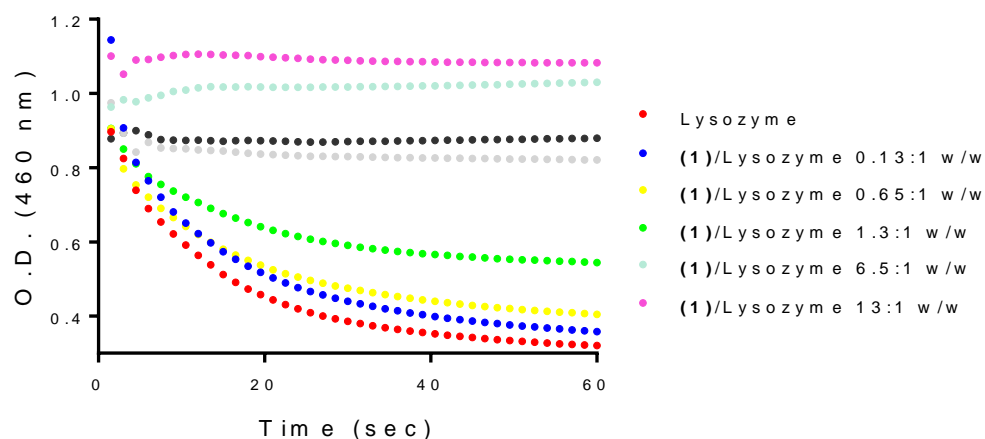


Figure 2.11: Enzymatic activity assay of lysozyme mixed with increasing quantities of peptide **(1)**. Samples were prepared at lysozyme final concentration of 0.04 mg mL$^{-1}$. Concentration of peptide **(1)** ranged from 0.0053 mg mL$^{-1}$ to 0.53 mg mL$^{-1}$, for **(1)**:lysozyme w/w ratios of 0.13:1, 0.65:1, 1.3:1, 6.5:1 and 13:1.
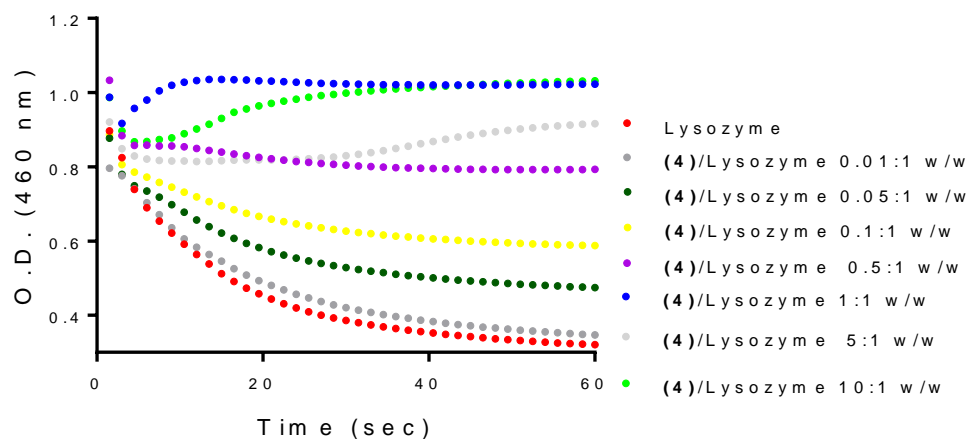
Figure 2.12: Enzymatic activity assay of lysozyme mixed with increasing quantities of compound **(4)**. Samples were prepared at lysozyme final concentration of 0.04 mg mL$^{-1}$. Concentration of of peptide **(4)** ranged from 0.004 to 0.4 mg mL$^{-1}$, for **(4)**:lysozyme w/w ratios of 0.01:1, 0.05:1, 0.1:1, 0.5:1, 1:1, 5:1 and 10:1.

Results showed a concentration-dependent inhibition of lysozyme activity when APR peptides **(1)** and **(4)** where mixed with the protein above peptide **(1)**:lysozyme 6.5:1 w/w ratio, and above peptide **(4)**:lysozyme 5:1 w/w ratio. The inhibition suggested a potential non-covalent interaction of peptides **(1)** and **(4)** with their homologous intact Aggregation Prone Region on lysozyme backbone, thus interfering with its enzymatic activity. At the highest **(1)**:lysozyme and **(4)**:lysozyme molar ratios, the scattering appeared to increase over time. The increase was ascribed to the mixing of the added *Micrococcus lysodeikticus* suspension with lysozyme water solution inside the UV cuvette, leading to a more homogeneous mixture. Some differences in scattering intensity between the samples could also be noticed at the starting point of the measurements. These differences were ascribed to the manual procedure employed to analyse the samples: for each sample, the *Micrococcus lysodeikticus* suspension was manually added to the cuvette, and the

measurement started immediately after the addition. Small changes in the way the suspension was added or in the time elapsed between the addition and the experiment start are presumably responsible for the differences observed.

However, subsequent studies carried out using DPBS to suspend the substrate (*Micrococcus lysodeikticus* cell walls) instead of water led to complete recovery of lysozyme activity.

We therefore hypothesised that the inhibition of lysozyme activity seen in the previous experiments had been caused by contaminants in our peptides. The activity of hen egg lysozyme has been previously reported to be pH-dependent, and sharply decreasing as pH decreases from to 7.4, until no activity is recorded at pH 5[11]. TFA was used in the final step of the synthesis of the peptides, to remove the protecting groups from aminoacid residues and cleave the peptide from the solid phase support. To assess whether residual TFA on the peptides could indeed affect the enzymatic assay, lysozyme was dissolved in 100 µL of PBS and then diluted 10 times with DMSO. TFA was added to the final solution, at 0.1% v/v. The enzymatic assay was performed on the sample and showed no activity from lysozyme, proving that TFA did indeed inhibit its enzymatic activity (Fig. 2. 13). This result suggested that it was the residual TFA in the peptides rather than APR peptide which inhibited the enzyme. Again, some differences in scattering between the samples could be noticed at the starting point of the measurements, and were ascribed to the manual procedure employed to perform the measurement.
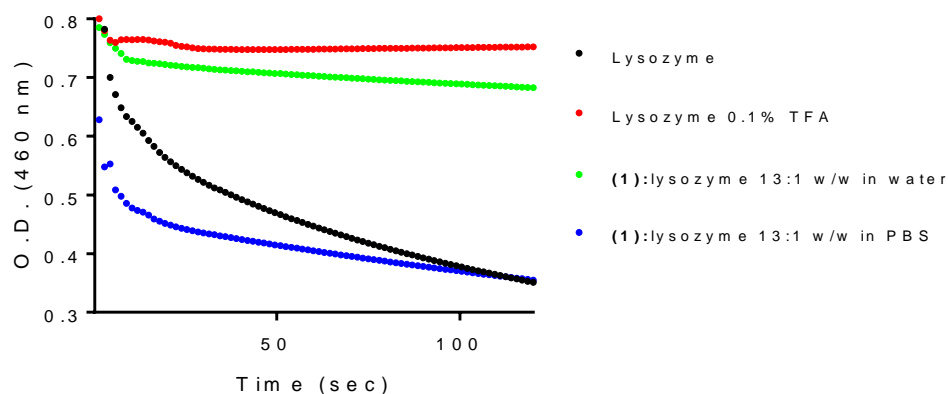
Figure 2.13: lysozyme enzymatic activity studies performed at different conditions to assess the influence of TFA on lysozyme.

Thus, from these initial experiments no influence of compounds **(1)**, **(4)** and **(7)** on lysozyme activity was observed, which may be suggestive of no significant interaction between APR GILQINSRW peptide and lysozyme.

However, it has been previously shown by Tokunaga *et Al* that the target intact APR sequence, the segment 54-62 GILQINSRW, is located on lysozyme active site, and it is partially buried in its cleft (Fig.2.14)[4].
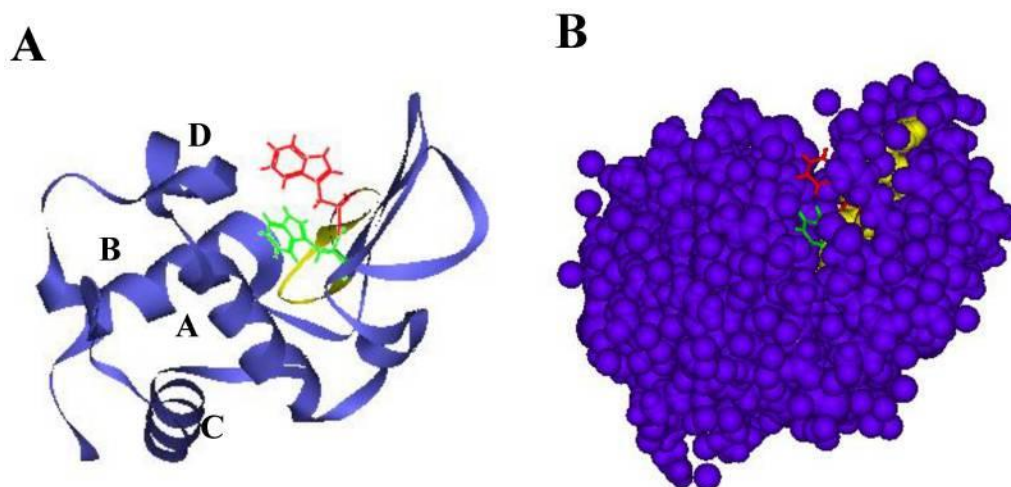


Figure 2.14: Figure taken from Tokunaga *et Al*[4]. Structure of HEWL and location of the APR region. A. Illustration by ribbon representation. In red the APR with the side chain of tryptophan

62. B. Illustration by space-filling model. Red and yellow show tryptophan 62 and other amino acids of the APR, respectively. Amino acids in the APR are largely buried inside lysozyme.

From previous studies and from the experiments we have conducted, lysozyme has shown to be a very stable protein, whose denaturation can be obtained only in extreme conditions, e.g. using high percentages of a denaturating solvent[12] or really high temperatures[13]. When heating was applied, the enzyme was able to keep its folded state until up to 70 °C. In its native form, lysozyme Aggregation Prone Region, partially buried inside lysozyme active site cleft, may be not accessible to compounds **(1)**, **(4)** and **(7)**.

Moreover, the high insolubility of these initial GILQINSRW APR derivatives made it very difficult to conduct any type of experiment together with the protein unless a very high proportion of DMSO was used. These APR derivatives were very poorly soluble in aqueous conditions, and when water was slowly added to their solutions in DMSO they rapidly precipitated, forming aggregates. Introducing relatively small hydrophilic residues, like betaine or a short PEG, did not improve significantly the physico-chemical characteristics of the peptide.

### 2.3.3. Synthesis of HEA$_{90}$-*b*-GILQINSRW

To circumvent the solubility issues of compounds **(1)**, **(4)** and **(7)**, a larger hydrophilic polymer block was introduced into the GILQINSRW peptide **(1)** in the form of a polymeric chain. *N*-hydroxyethylacrylamide was selected as starting monomer, to generate an amphipathic copolymer with better water solubility than the original peptide. The copolymer was synthesised via RAFT polymerization with a poly(*N*-hydroxyethylacrylamide) block of 10 kDa (Scheme

2.13). $^1$H NMR and $^{13}$C NMR spectra of the different steps of this synthesis are included in the Supporting Information.
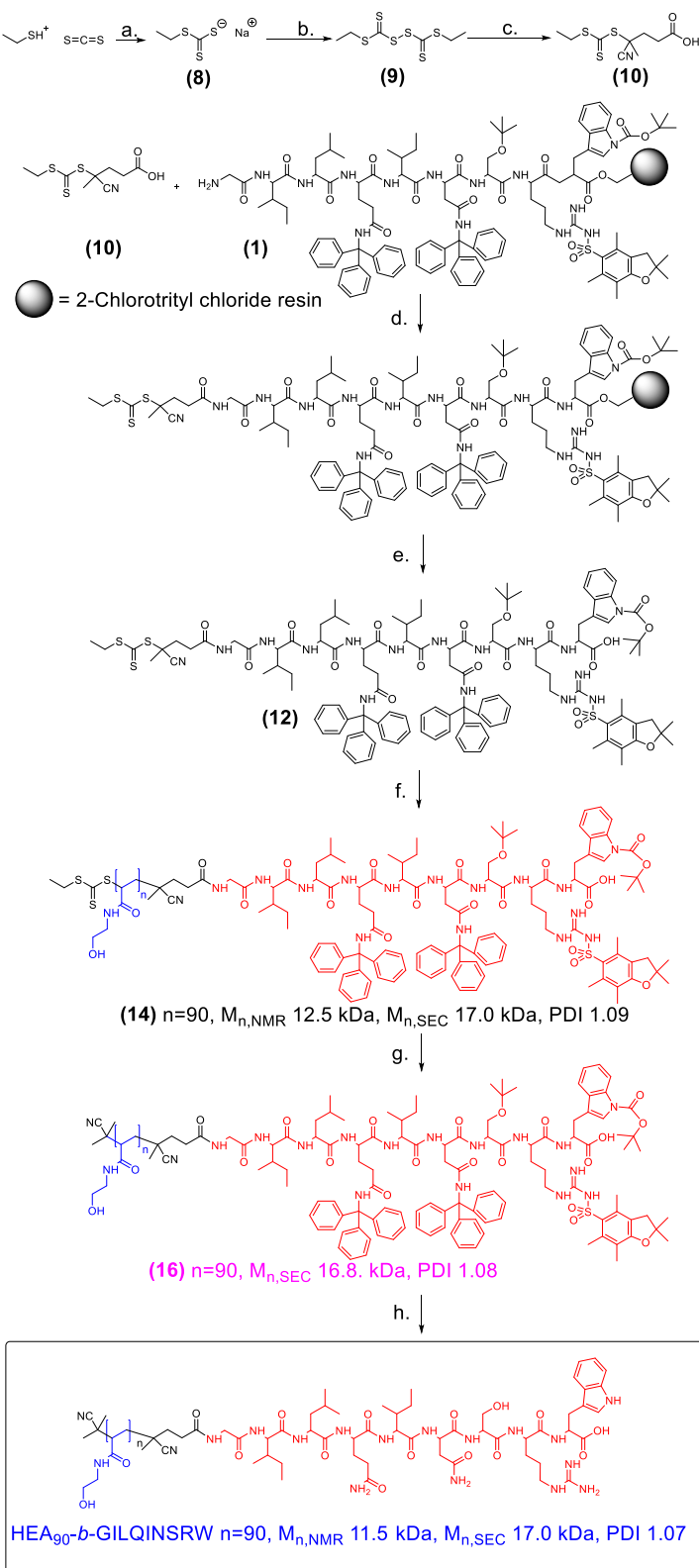
Scheme 2.13: Synthesis of HEA$_{90}$-b-GILQINSRW copolymer. *Reagents and conditions*: (a) Et$_2$O, room temperature. (b) K$_3$Fe(CN)$_6$, H$_2$O, room temperature. (c) V501, MeOH, ethyl acetate, 80°C. (d) HATU, TEA, DMF, room temperature. (e) DCM/TFE 8:2 v/v, room temperature. (f) N-Hydroxyethylacrylamide, V501, DMF, 70 °C. (g) AIBN, DMF, 80 °C. (h) 0.1 N HCl in HFIP at room temperature. SEC analyses were conducted using DMF + 0.1% LiBr as the mobile phase.

**2.3.3.1.Synthesis of peptide GILQINSRW -RAFT agent (12)**

The trithiocarbonate CTA **(10)** was synthesised in 3 steps, following a modified version of a reported protocol[5]. The protocol started with the reaction of carbon disulfide with ethanethiol in presence of sodium hydride, affording sodium ethyl carbonotrithioate **(8)**. Compound **(8)** was then oxidised with $K_3Fe(CN)_6$ giving dithiobis ethyl carbonotrithioate disulfide **(9)**, which was finally converted into CTA **(10)** by reacting with V501 radical initiator. CTA **(10)** was then coupled to the APR **(1)** GILQINSRW through its carboxyl group. The coupling was performed in solid phase, using a modified version of a previous established procedure[18], and gave the peptidic, resin-bound GILQINSRW-RAFT agent intermediate. The peptide was then cleaved from the resin using mild conditions (a 8:2 mixture of DCM and TFE), which did not remove the protecting groups on the amino acids side chains, finally affording the GILQINSRW-RAFT agent **(12)**. In order to avoid any side reactions between the side chains of the peptide and the trithiocarbonate of the RAFT agent, peptide deprotection was carried out as the last step, after the synthesis of the poly(hydroxyethyl acrylamide)-*b*-peptide. The purity of GILQINSRW-RAFT agent **(12)** was verified by $^1$H NMR and ESI-MS (Fig. 2.15 and 2.16).
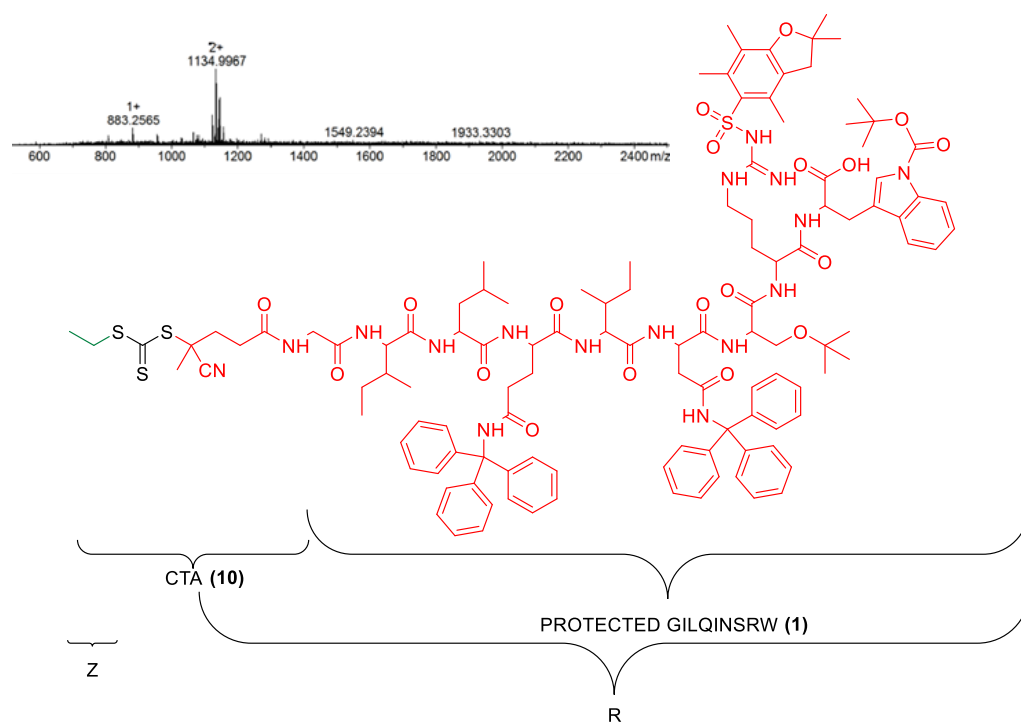
Figure 2.15: Structure of peptidic GILQINSRW-RAFT agent **(12)** and its ESI MS spectrum. Peak at 1135 corresponds to [M + 2Na]$^{2+}$.

$^1$H NMR analysis allowed the identification of some of the methyl peaks belonging to GILQINSRW protecting groups, such as the aromatic trityl-protecting groups at around 7.5 ppm, alongside with the methyl peaks belonging to leucines and isoleucines residues on the APR backbone. These peaks were later used to calculate the *N*-Hydroxyethylacrylamide DP of the final copolymer.
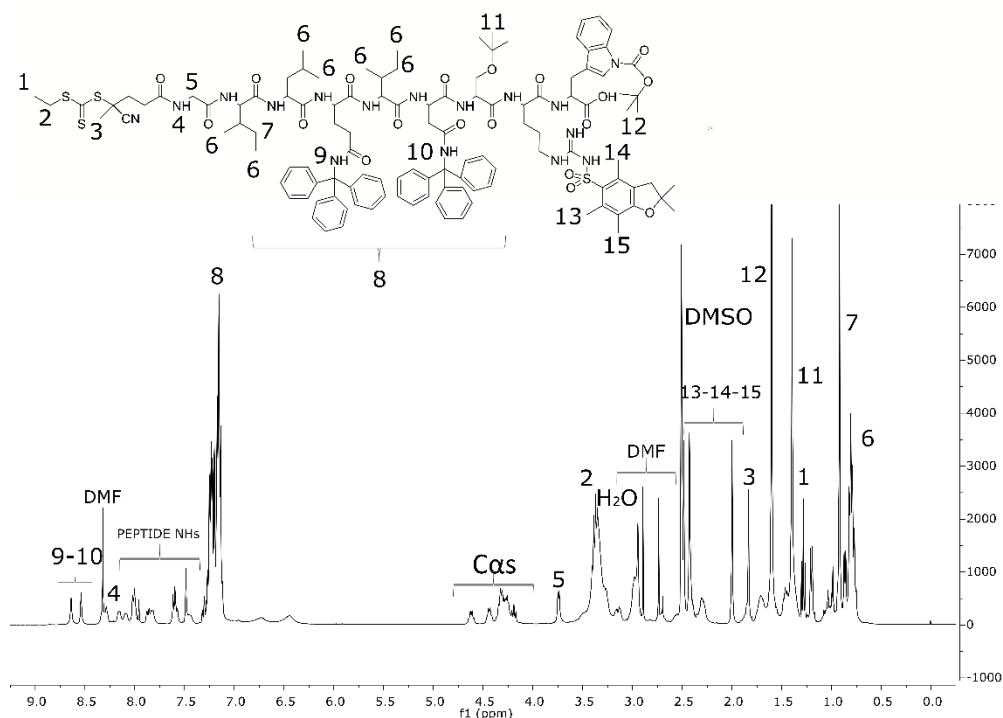
Figure 2.16: $^1$H NMR spectrum of RAFT-GILQINSRW **(11)** in d$_6$-DMSO.

.

## 2.3.3.2.Synthesis of HEA$_{90}$-*b*- GILQINSRW

The RAFT agent was then used to mediate the RAFT polymerization of monomer *N*-hydroxyethylacrylamide, α affording poly(*N*-hydroxyethylacrylamide)-*b*-GILQINSRW **(14)**. Its M$_{n,NMR}$ was estimated by $^1$H NMR spectroscopy by comparing the integrals of peaks characteristic for the protected peptide moiety (e.g. the trityl protecting groups) with those of the poly(HEA) block (Fig. 2.17), obtaining a final M$_{n,NMR}$ of 12.5 kDa. The polymerization was found to be controlled, as confirmed by SEC analysis in DMF (PMMA standards), with final narrow molecular weight distributions observed (Đ = 1.09 with M$_{n,SEC=}$ 17 kDa).
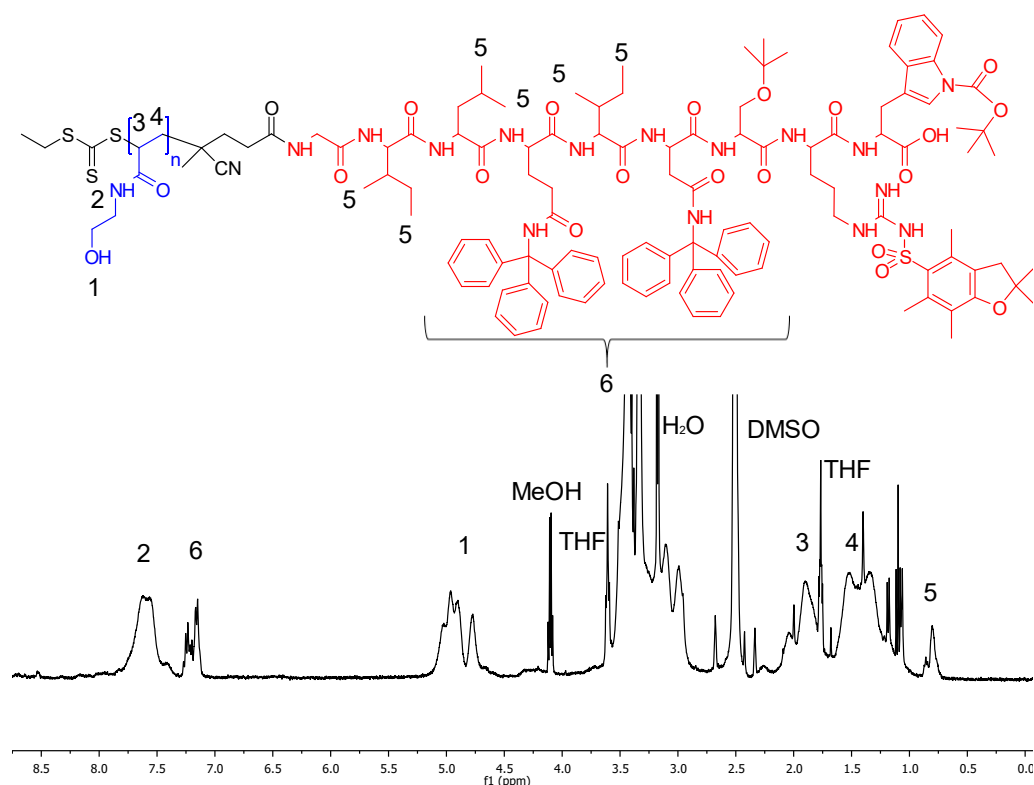
Figure 2. 17: ^{1}H NMR spectrum of poly(N-hydroxyethylacrylamide)-*b*-GILQINSRW **(14)** in d$_6$-DMSO. Peaks of peptide protecting groups are compared to that of the polyHEA block, confirming copolymer synthesis, and a chain length of 90 HEA monomer units, giving a $M_{n,NMR}$ = 12.5 kDa.

The acidic conditions required for peptide deprotection may cause hydrolysis of the polymer, generating thiol-terminated polymer chains which in the presence of oxygen could dimerize. Therefore, the trithiocarbonate end-group was removed from the copolymers before peptide deprotection, using an excess of radical initiator AIBN, as described by Perrier and co-workers[19]. The reaction afforded poly(*N*-hydroxyethylacrylamide)-*b*-GILQINSRW **(16)**. A UV/Vis analysis was carried out before and after this reaction, showing the disappearance of the broad band between 290 and 320 nm, which is due to the trithiocarbonate group chain-end (Fig. 2.18).
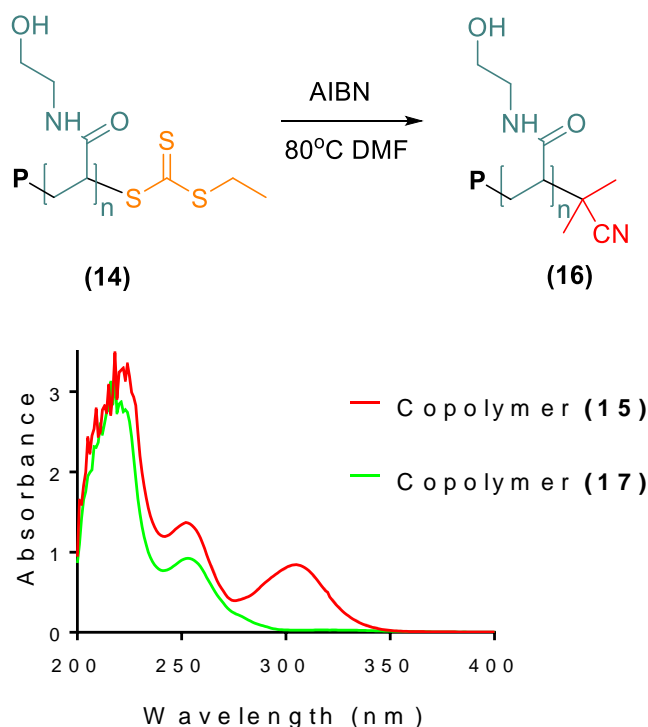
Figure 2.18: Removal of trithiocarbonate polymer chain-ends. UV spectra of poly(N-hydroxyethylacrylamide)-b-GILQINSRW **(14)** (before removal of the trithiocarbonate moiety), and poly(N-hydroxyethylacrylamide)-b-GILQINSRW **(16)** (after removal). The progress of the reaction was followed by monitoring the disappearance of the band at $\lambda_{max} \sim 310$ nm.

After removal of the trithiocarbonate end-group, poly(*N*-hydroxyethylacrylamide)-*b*-GILQINSRW **(16)** was finally converted into HEA$_{90}$-*b*-GILQINSRW by removal of amino acid protecting groups from the GILQINSRW block. $^1$H NMR analysis of the final copolymer showed the characteristic peaks of poly(*N*-hydroxyethylacrylamide), while the signals of the protecting groups were no longer present, confirming quantitative deprotection of the peptide block (Fig. 2.19). A final $M_{n,NMR}$ of 11.5 kDa was calculated by comparing the

signal of the methyl group of leucine and isoleucine residues of the GILQINSRW peptide block to the peaks of the polyacrylamide block.

SEC analysis in DMF (PMMA standards) confirmed the narrow distribution observed before RAFT removal with a PDI of 1.07 and $M_{n,SEC}$= 17 kDa.
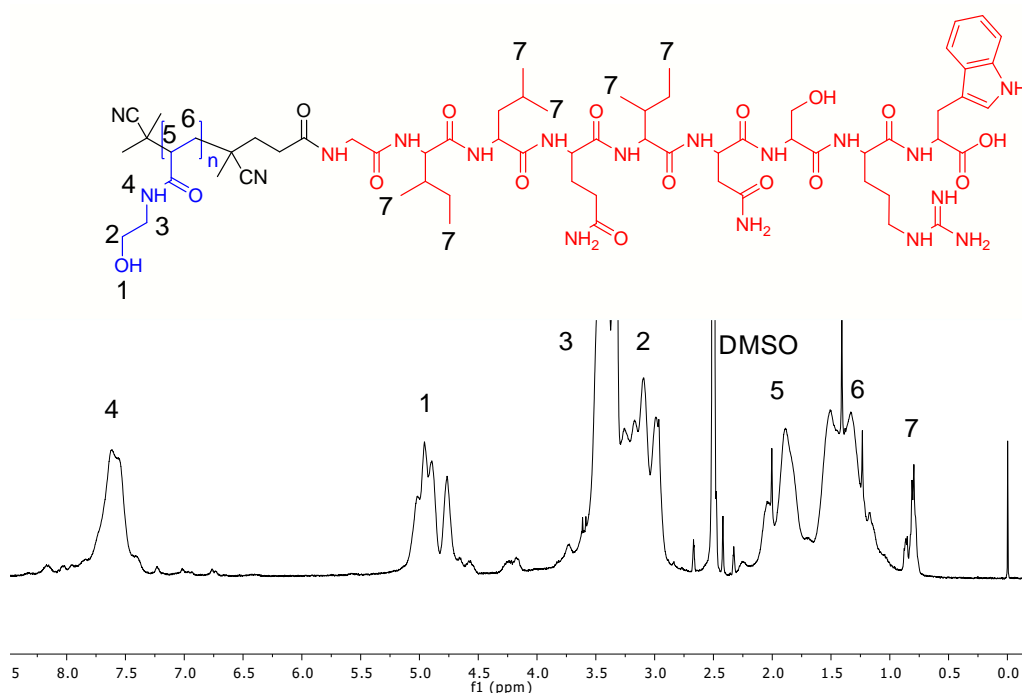


Figure 2.19: $^1$H NMR spectrum of HEA$_{90}$-*b*-GILQINSRW in d6-DMSO. The area of the signal of the methyl group of leucine and isoleucines of GILQINSRW peptide at 0.81 ppm was compared to peaks of OH and NH of polyacrylamide, to estimate a polymer chain length of around 90 monomer units, and a $M_{n,NMR}$ of 11.5 kDa.

### 2.3.4. Potential interactions of HEA$_{90}$-*b*- GILQINSRW with lysozyme: enzymatic assay

Potential interaction between HEA$_{90}$-*b*- GILQINSRW and lysozyme in PBS was assessed by performing a lysozyme activity assay. The protein and the copolymer were mixed at 1:1 molar ratio. The copolymer was found to be fully soluble in DPBS at the concentration tested (0.035 mg/mL), allowing to

overcome the solubility problems experienced with original APR-mimicking peptide **(1)**.

Results showed that addition of HEA$_{90}$-*b*-GILQINSRW did not have any relevant effect on lysozyme activity (Fig. 2.20), as it was previously observed for peptide GILQINSRW **(1)**. Despite copolymer full solubility in DPBS, no interaction could be observed between the copolymer and the protein.
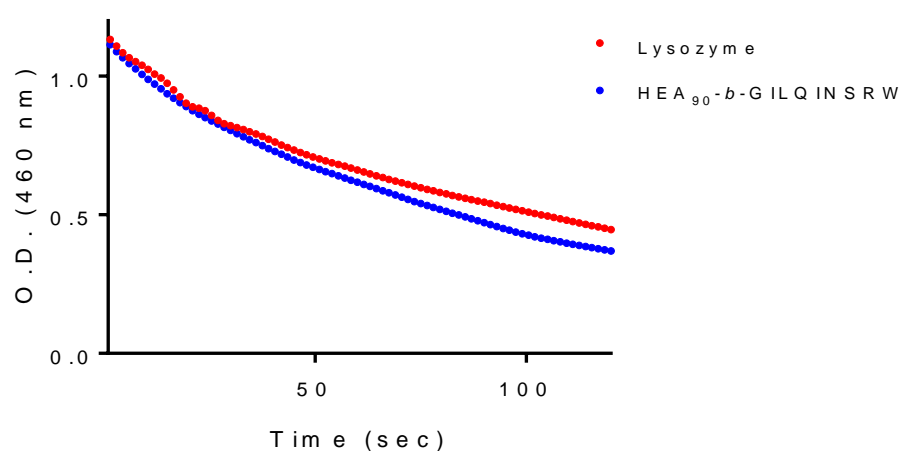


Figure 2.20: activity assay of lysozyme mixed with HEA$_{90}$-*b*-GILQINSRW at 1:1 molar ratio. Samples were prepared at lysozyme final concentration of 0.04 mg/mL in PBS.

## 2.3.5. Potential interactions of HEA$_{90}$-*b*- GILQINSRW with lysozyme: lysozyme aggregation assay

Despite the synthesis of a fully water-soluble APR-incorporating copolymer, it was not observed any difference in lysozyme activity upon copolymer addition, suggesting that there was no interaction occurring between the two macromolecules. The lack of interaction may be ascribed to potential low accessibility of lysozyme homologous intact APR sequence, which is, when the protein is in folded state, partially buried in the active site cleft.

For this reason, potential interaction between the copolymer and the protein was investigated in denaturant conditions, which could force the protein to unfold, increasing the solvent exposure and the accessibility of its APR.

Lysozyme aggregation has been observed at alkaline pH by Homchaudhuri *et al*. Protein incubation at pH 12 in phosphate buffer led to the formation of visible aggregates. Aggregation rate was found to be concentration dependent, and irreversible under these strongly basic conditions[20]. Another study highlighted that the protein, polycationic at neutral pH, above its isoelectric point of 11.8 has an overall net charge close to zero, which triggers protein unfolding and exposure of hydrophobic patches with subsequent protein aggregation[21].

The exposure of these hydrophobic patches, usually hidden inside lysozyme core, in denaturing conditions, was conveniently used to improve lysozyme stability by Muller *et al*., who covalently linked different hydrophobic groups, such as tryptophan, cholesterol and dansyl, to PEGs of different molecular weight (2 and 5 kDa). The resulting PEG-conjugates were tested on hen egg lysozyme, whose aggregation onset, induced in pH 12 phosphate buffer, was significantly delayed in the presence of the polymers. The interaction between the polymers and the protein was achieved through the hydrophobic group at the polymer chain-end, developing a non-covalent PEGylation system based on hydrophobic interactions[22].

It was reasonable to hypothesise that, due to GILQINSRW aggregation-prone, self-interacting nature, the HEA$_{90}$-*b*-GILQINSRW copolymer could establish

non-covalent hydrophobic interactions with the intact APR homologous on lysozyme sequence, or with other hydrophobic, potentially self-assembling pockets on the protein backbone.

Lysozyme was therefore dissolved at a final concentration of 10 mg/mL, and mixed with the block copolymer for a final lysozyme:copolymer 1:1 molar ratio. Aggregation was followed by turbidimetry, recording absorbance at 500 nm on a 96-well plate over 24 h (Fig. 2.21).
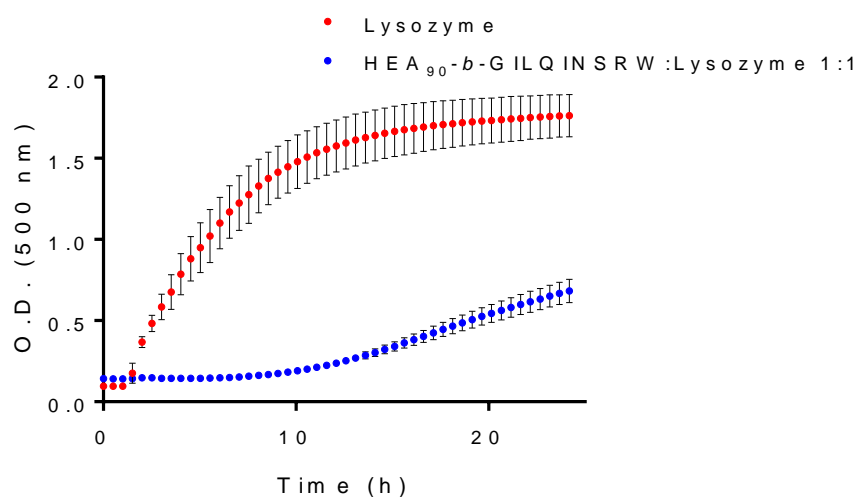


Figure 2.21: aggregation assay of Lysozyme and a mixture between HEA$_{90}$-*b*-GILQINSRW and lysozyme at 1:1 HEA$_{90}$-*b*-GILQINSRW:lysozyme molar ratio. [Lysozyme]= 10 mg/mL in 100 mM pH 12.3 phosphate buffer. Lysozyme aggregation was assessed by turbidimetry, recording Abs $\lambda$=500 nm every 30 min for 24 h.

Results confirmed the formation of large aggregates from pure lysozyme samples. Aggregation onset started after ca. 1 h of incubation in the plate reader and reached its maximum after around 20 h. HEA$_{90}$-*b*-GILQINSRW delayed significantly the onset of the aggregation process. In the HEA$_{90}$-*b*-

GILQINSRW:Lysozyme sample, aggregation only started after 10 h, and by the end of the experiment the amount of scattering due to the presence of aggregates was still significantly lower compared to that of the free protein.

The experiment suggested that a non-covalent interaction may have occurred between the APR fragment on the copolymer chain and hydrophobic, self-aggregating patches on lysozyme sequence. The interaction could successfully delay the onset of lysozyme aggregation and the amount of final aggregate. This stabilising effect may have been favoured by the copolymer polyacrylamide hydrophilic chain that shielded the protein, preventing multiple proteins to come in contact and aggregate. The stabilising mechanism of action may be then analogous to that of hydrophobic non-covalent PEGylation, where a transient stabilising interaction between proteins and PEG is developed through functional groups linked to the PEG chain, able to establish non-covalent interactions with specific areas on the protein backbone[23].

## 2.3.6. APR modification: assessing the importance of Tryptophan for APR-lysozyme interaction

The previous experiment showed that copolymer HEA$_{90}$-*b*-GILQINSRW had stabilising effects on lysozyme. Due to the hydrophobic nature of peptide GILQINSRW, it was reasonable to hypothesise that these effects had been mediated by non-covalent hydrophobic interactions between the peptide and hydrophobic patches on lysozyme backbone. However, more studies were needed to understand the exact nature of this interaction. In particular, since it has been verified by Tokunaga *et al*. that APR GILQINSRW fragment can self-assembly through mutual β-sheet interactions[4], if an analogous interaction was

established with the homologous intact APR of lysozyme, a change in the amino acidic composition of the APR-mimicking fragment, capable of suppressing its self-aggregation, could potentially also suppress its interaction with the protein.

Interestingly, in the same work that identified GILQINSRW as one of lysozyme's APRs, Tokunaga *et al*. highlighted that a single amino acid change, the substitution of tryptophan with a glycine, completely suppressed GILQINSRW aggregation (Table 2.1)[4].

Table 2.1: aggregation-propensity of peptide GILQINSRW is completely suppressed by the susbstitution of tryptophan with glycine (terminal glycine (G) residue in bold to highlight the amino acid that was introduced compared to the original GILQINSRW sequence). Table rearranged from Tokunaga *et Al*[4]. pI=isoelectric point, ++ high propensity, + propensity, - no propensity.

| Peptide | pI | pH 2 | pH 4 | pH 7 | pH 9 |
| --- | --- | --- | --- | --- | --- |
| GILQINSRW | 9.75 | + | ++ | + | - |
| GILQINSR**G** | 9.75 | - | - | - | - |

This is of no surprise if we consider the importance that tryptophan has in protein aggregation[24]. Together with the other aromatic amino acids, tryptophan is believed to form β-sheet-directed aggregates through the π-stacking interactions that multiple tryptophan side chains can mutually establish. Studies have used specific algorithms to predict the propensity to

aggregate of each amino acid, and tryptophan was found to be the one with the highest aggregation propensity[25].

In analogy with Tokunaga's work[4], to gain further insight into the mechanisms by which HEA$_{90}$-*b*-GILQINSRW delayed and minimised aggregation of lysozyme, an analogous of GILQINSRW **(1)**, where tryptophan was replaced by a glycine residue, was synthesised.

The newly synthesised peptide GILQINSR**G** was thus coupled to CTA **(10)** and used to mediate the RAFT polymerization of *N*-Hydroxyethylacrylamide monomer as it was done with the original APR GILQINSRW. The resulting copolymer was then tested to assess its ability to prevent lysozyme aggregation, compared to the original HEA$_{90}$-*b*-GILQINSRW.

### 2.3.6.1.Synthesis of GILQINSRG peptide (11)

Synthesis of GILQINSR**G** peptide **(11)** (Fig. 2.22) was accomplished through solid phase synthesis, following the same procedure used for GILQINSRW **(1)**. Chemical identity and purity of GILQINSR**G** **(11)** were confirmed by ESI-MS and RP-HPLC (Fig. 2.23 and 2.24).

Exact Mass: 956.54
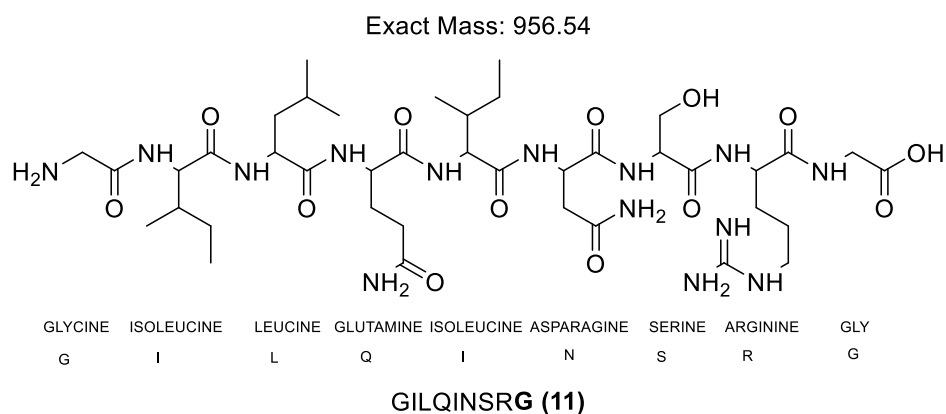


GILQINSR**G (11)**

Figure 2.22: Structure of GILQINSR**G (11)**, which was synthesised as a modified version of APR GILQINSRW **(1)** to verify the importance of tryptophan in APR sequence for its interaction with lysozyme. (terminal glycine (G) residue in bold to highlight the amino acid that was introduced compared to the original GILQINSRW sequence).
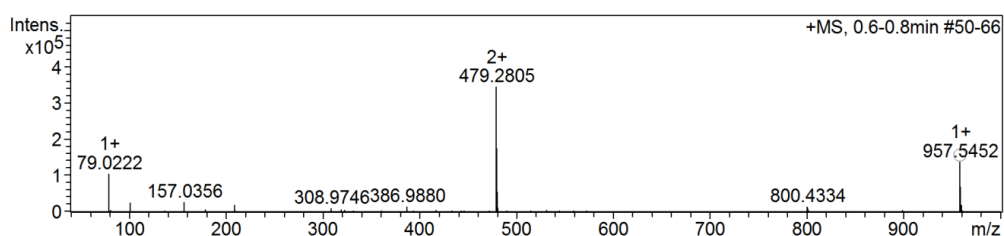


Figure 2.23: ESI MS analysis of GILQINSR**G (11)** (terminal glycine (G) residue in bold to highlight the amino acid that was introduced compared to the original GILQINSRW sequence)**.** Two peaks are identified: peak at 957.5 m/z corresponds to [M-H]$^+$, that at 479.3 to [M+2H]$^{2+}$.
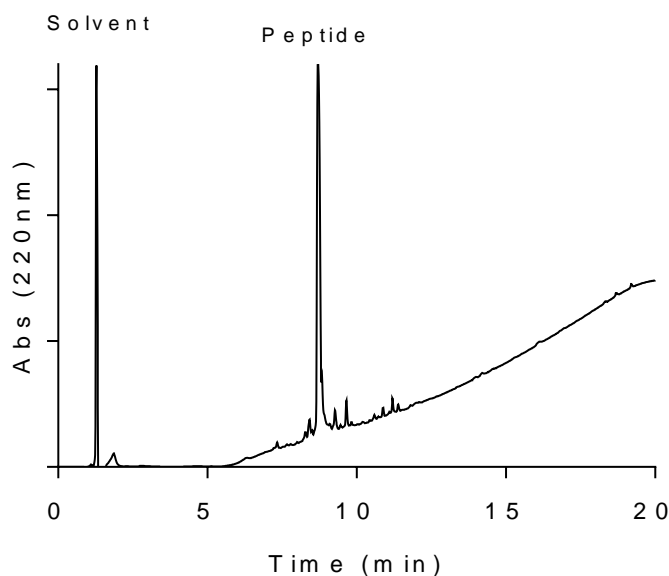


Figure 2.24: RP-HPLC chromatogram of GILQINSR**G** peptide (terminal glycine (G) residue in bold to highlight the amino acid that was introduced compared to the original GILQINSRW sequence). The sample was eluted using a 20-90% acetonitrile gradient in water +0.1% TFA. Absorbance was recorded at λ=220 nm. Purity was estimated by calculating the ratio between the peak area of the peptide and all detected peak areas.

116

By RP-HPLC chromatography it was possible to estimate a purity of ~85%. The peptide was used directly to react with CTA **(10)** without further purification.

### 2.3.6.2.Synthesis of HEA$_{95}$-*b*-GILQINSRG

The synthesis of HEA$_{95}$-*b*- GILQINSR**G** followed the same steps taken for HEA$_{90}$-*b*- GILQINSRW (Scheme 2.16).
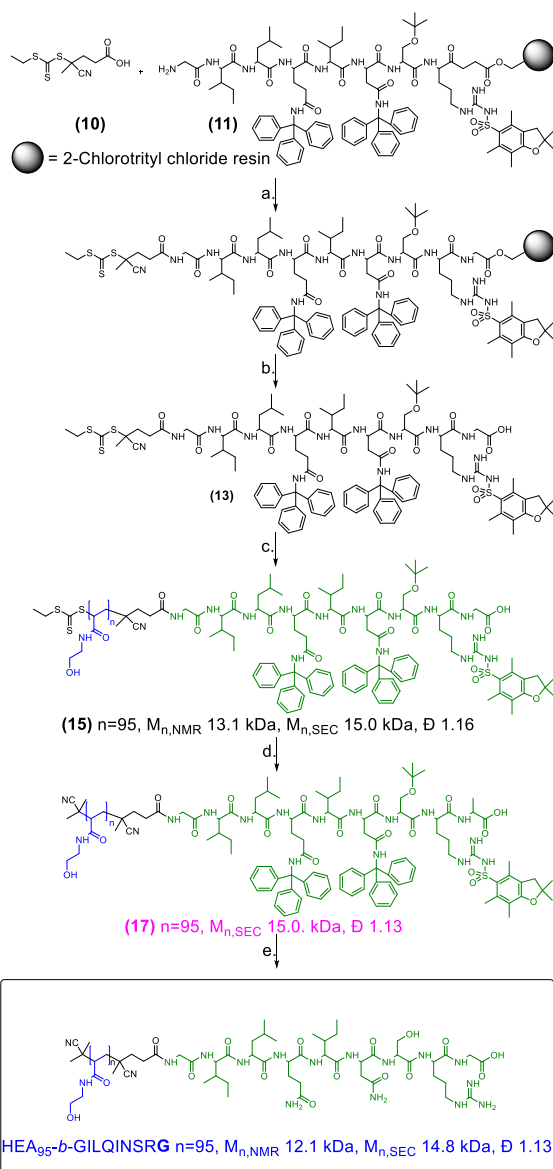


Scheme 2.14: synthesis of HEA$_{95}$-*b*-GILQINSR**G** copolymer (terminal glycine (G) residue in bold to highlight the amino acid that was introduced compared to the original GILQINSRW sequence). *Reagents and conditions*: (a) Et$_2$O, room temperature. (b) K$_3$Fe(CN)$_6$, H$_2$O, room temperature. (c) V501, MeOH, ethyl acetate, 80ºC. (d) HATU, TEA, DMF, room temperature. (e) DCM:TFE 8/2 v/v, room temperature. (f) *N*-Hydroxyethylacrylamide, V501, DMF, 70 ºC. (g) AIBN, DMF, 80 °C. (h) 0.1 N HCl in HFIP at room temperature.

As first step, CTA **(10)** was coupled to GILQINSR**G** through solid-phase, HATU-mediated coupling. The resulting resin-bound, RAFT- GILQINSR**G** **(13)** was cleaved from the resin using a 8:2 DCM:TFE v/v mixture to avoid the removal of the protecting groups. Cleaved **(13)** was then analysed by ESI-MS and $^1$H NMR (Fig. 2.25 and 2.26).
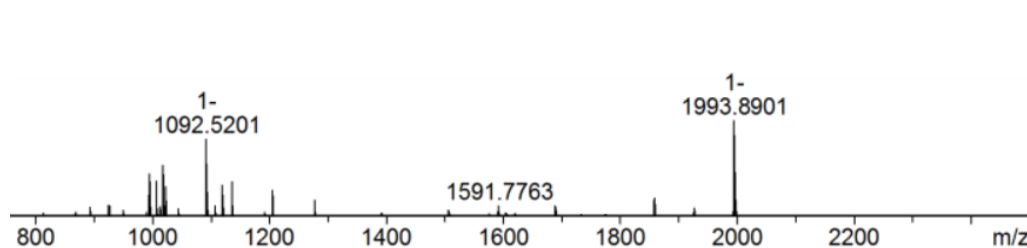


Figure 2.25: ESI MS analysis of RAFT- GILQINSR**G** **(13)** (terminal glycine (G) residue in bold to highlight the amino acid that was introduced compared to the original GILQINSRW sequence). Peak at 1993.9 m/z corresponds to [M]$^-$.
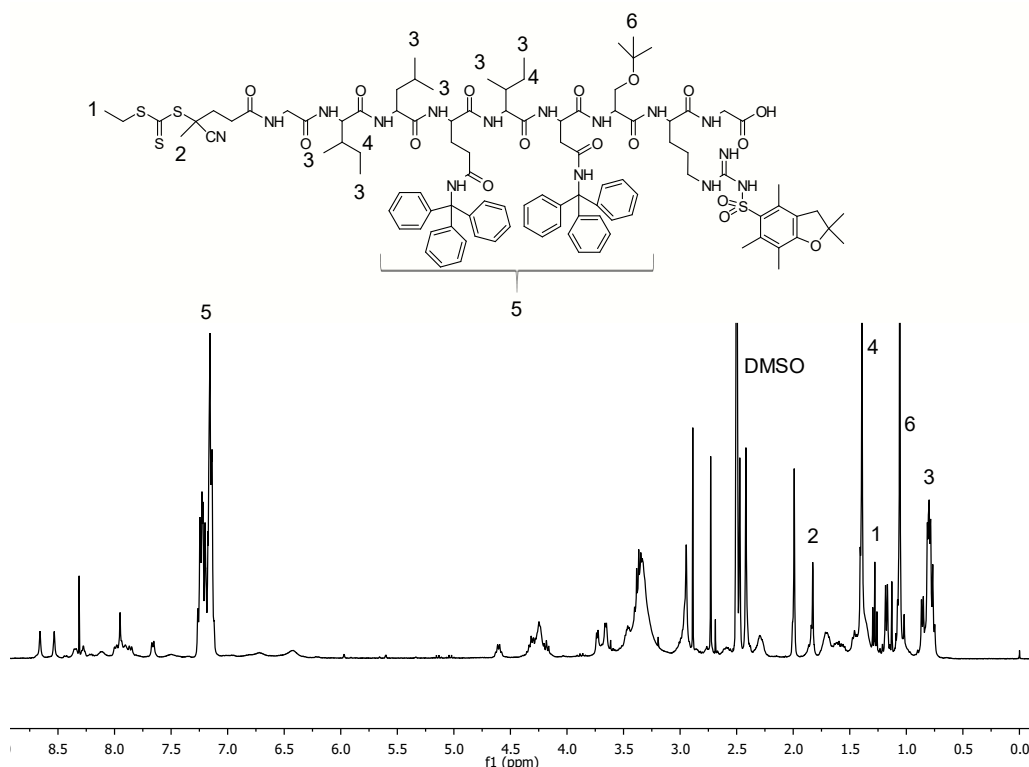


Figure 2.26: $^1$H NMR spectrum of RAFT-GILQINSR**G** **(11)** (terminal glycine (G) residue in bold to highlight the amino acid that was introduced compared to the original GILQINSRW sequence) in d6-DMSO.

The RAFT agent was then used to mediate the RAFT polymerization of *N*-hydroxyethylacrylamide, affording poly(N-hydroxyethylacrylamide)-*b*-GILQINSR**G** **(15)**. Its chemical identity was confirmed by $^1$H NMR, as done previously for poly(*N*-hydroxyethylacrylamide)-*b*-GILQINSRW **(14)**, obtaining a final $M_{n,NMR}$ of 13.1 kDa and a DP of 95 (see Appendix). The polymerization was found to be controlled, as confirmed by SEC analysis, with final narrow molecular weight distributions observed (Đ= 1.26 and $M_{n,SEC}$ 16.4 kDa).

Similarly to what done before for copolymer **(14)**, the trithiocarbonate end-group was removed from the copolymer before peptide deprotection, using an excess of the radical initiator AIBN, as described by Perrier and co-workers[19]. The reaction afforded poly(N-hydroxyethylacrylamide)-*b*-GILQINSR**G** **(17)**. A UV-Vis analysis was performed before and after this reaction, showing the disappearance of the broad band between 290 and 320 nm, which is due to the trithiocarbonate group chain-end (see Supporting Information).

Finally, protected poly(N-hydroxyethylacrylamide)-*b*-GILQINSR**G** **(17)** was converted into final HEA$_{95}$-*b*-GILQINSR**G** by removal of amino acid protecting groups of the peptide GILQINSR**G**. The final copolymer was analysed by $^1$H NMR (Fig.2.27). A final $M_{n,NMR}$ of 12.1 kDa was calculated by comparing the signal from leucine and isoleucines CH$_3$ of the GILQINSR**G** peptide block to peaks of polyacrylamide. SEC analysis confirmed the narrow distribution observed immediately after polymerization, with a Đ of 1.13.
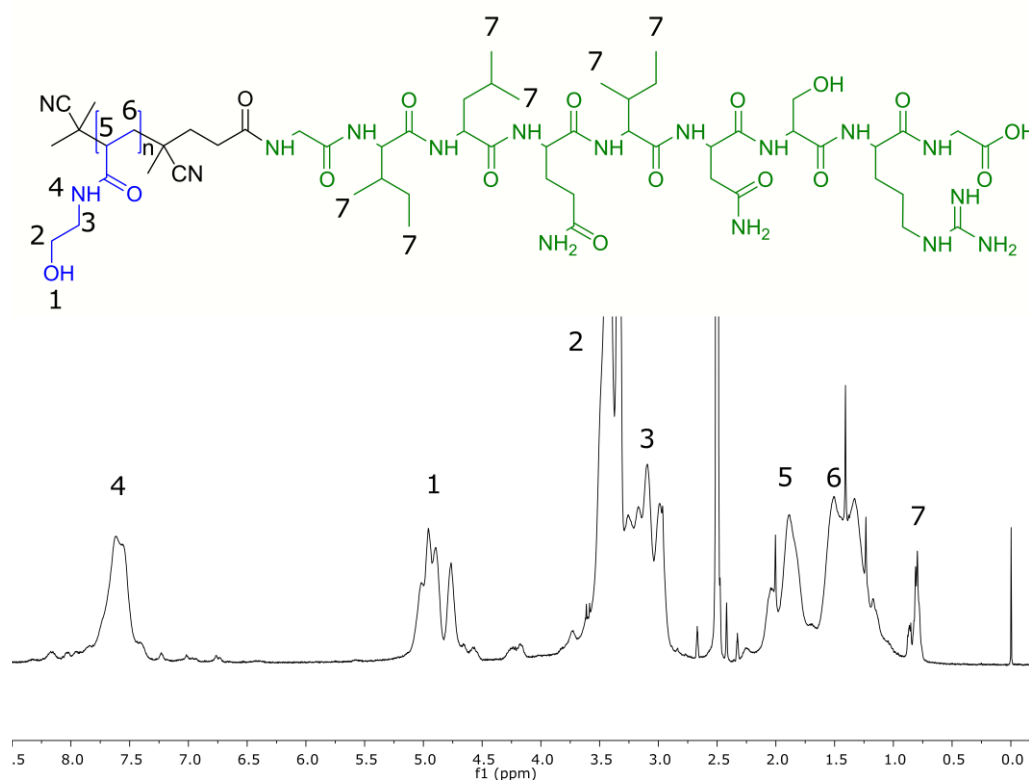
Figure 2.27: ¹H NMR spectrum of HEA$_{95}$-*b*-GILQINSR**G** in d$_6$-DMSO. The area of the signal of the methyl groups of leucine and isoleucine of GILQINSR**G** peptide at 0.81 ppm was compared to characteristic peaks of polyacrylamide (1 and 4), to estimate a polymer chain length of around 85 monomer units, and a M$_{n,NMR}$ of 12.1 kDa.

### 2.3.6.3. Synthesis of control polymer HEA$_{100}$

A polymer lacking the APR GILQINSRW peptide at its chain-end was synthesised using CTA **(10)** as RAFT agent and *N*-hydroxyethylacrylamide as monomer (Scheme 2.17). The resulting HEA$_{100}$ was used as a control polymer in the subsequent protein-polymers association experiment, as it had a similar N-hydroxyethylacrylamide DP of synthesised copolymers.
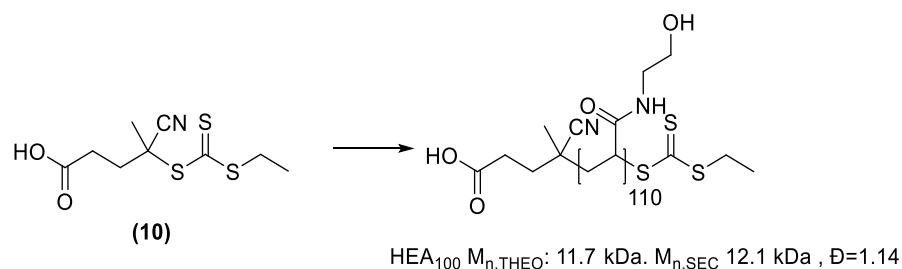
Scheme 2.15: synthesis of HEA$_{100}$. *Reagents and conditions*: *N*-hydroxyethylacrylamide, V501, DMF at 70 °C.

### 2.3.6.4. Comparison between HEA$_{90}$-*b*- GILQINSRG and HEA$_{95}$-*b*- GILQINSRG: lysozyme aggregation assay

The two copolymers and the control HEA$_{100}$ were tested on lysozyme aggregation assay, to compare their anti-aggregation behaviour (Fig.2.28).
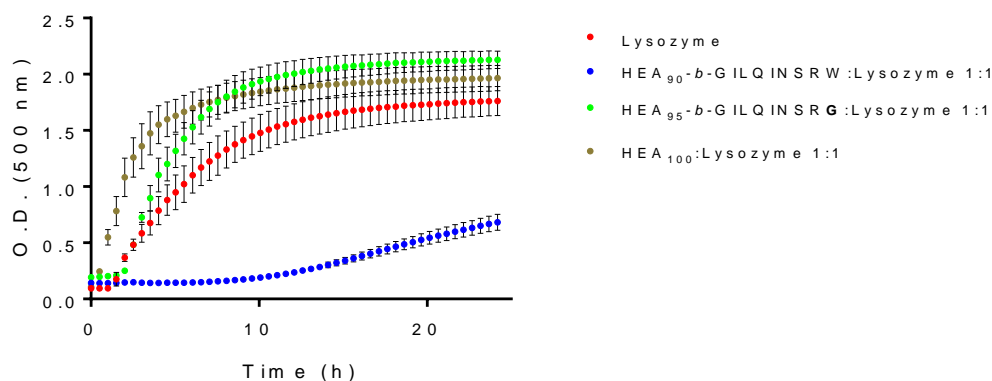


Figure 2.28: aggregation assay of lysozyme and a mixture between the polymers and lysozyme at 1:1 polymers:lysozyme molar ratio. [Lysozyme]= 10 mg/mL in 100 mM pH 12.3 phosphate buffer. Lysozyme aggregation was assessed by turbidimetry, recording Abs λ=500 nm every 30 min for 24 h.

It is clear from Fig. 2.28 that HEA$_{95}$-*b*-GILQINSR**G** does not have any ability to modulate lysozyme aggregation, as its turbidimetry curve is almost overlapping that of pure lysozyme. From the absorbance (due to light scattering) values it appears that the copolymer is increasing the amount of final aggregated lysozyme. A very similar behaviour was observed from the control polymer

HEA$_{100}$, which confirms that the polyacrylamide chain on its own is not able to establish any stabilising interaction with lysozyme in these conditions.

Results appear to confirm the initial hypothesis: the modification of the APR sequence has been reported to suppress its self-aggregating properties, and we have experimentally proven that it has also suppressed the interaction of the corresponding copolymer with lysozyme. This may suggest that this interaction was established between the APR GILQINSRW fragment that we synthesised, and its homologous APR on lysozyme, based on the ability of APRs to self-assemble through mutual interactions.

Results have also highlighted the importance of tryptophan as a key amino acid to maintain the lysozyme anti-aggregation properties of the APR sequence. A single change caused a drastic difference, which may be ascribed to tryptophan important role in APRs for the development of β-sheet-like supramolecular aggregates.

## 2.4. Final considerations

In this chapter, hen egg lysozyme's Aggregation Prone Region (APR) was chosen as target to improve lysozyme stability and prevent its aggregation[4]. APRs can drive protein self-aggregation through β-sheet mutual interactions. Our working hypothesis was that a synthetic peptide, identical or very similar to Lysozyme APR, could interact with its homologous sequence on the protein with mutual, non-covalent, hydrophobic interactions. These interactions could be used to prevent Lysozyme APRs from self-interacting, thus preventing protein aggregation. A small library of APR GILQINSRW peptides analogues was synthesised. Small hydrophilic molecules were incorporated into the APR structure, to improve peptide solubility and potentially give it some β-sheet disrupting properties, so that it could interact with lysozyme, and minimise its aggregation.

However, initial experiments failed to detect significant interaction between lysozyme and APR peptide GILQINSRW, under the conditions investigated, as assessed by lysozyme activity assay. This could be ascribed to a number of contributing factors. The APR within the lysozyme structure is partially buried in the cleft that comprises lysozyme active site, thus it may be difficult to access. Moreover, the synthesised APR GILQINSRW fragment was found to be very insoluble, and its self-aggregating behaviour may prevent it to interact with the protein. APR GILQINSRW analogues that were synthesised to improve its solubility displayed the same behaviour.

Thus, a different approach was followed, where the APR peptide GILQINSRW was converted into a RAFT agent and this used to mediate the polymerisation of *N*-hydroxyethylacrylamide, to provide the hydrophobic peptide with a long hydrophilic polymer block that could improve its solubility in water. The interaction between the resulting copolymer HEA$_{90}$-*b*-GILQINSRW and lysozyme was evaluated using again the lysozyme enzymatic activity assay. As no difference in lysozyme activity was observed upon copolymer addition, we enhanced the solvent exposure of lysozyme APR by inducing lysozyme denaturation and aggregation at pH 12. This time an interaction between the HEA$_{90}$-*b*-GILQINSRW and the protein was observed, as lysozyme aggregation onset was significantly delayed in the presence of HEA$_{90}$-*b*-GILQINSRW.

The stabilising effects of HEA$_{90}$-*b*-GILQINSRW was ascribed to non-covalent hydrophobic interactions between the GILQINSRW peptide fragment on the copolymer and hydrophobic patches on lysozyme backbone.

To further investigate if the self-assembly, β-sheet-forming nature of GILQINSRW was a key factor to develop this interaction, tryptophan on GILQINSRW was substituted with a glycine. This substitution was based on a previous study, where it was shown that without tryptophan the self-aggregating behaviour of the APR GILQINSRW peptide was completely suppressed. Interestingly, the newly synthesised copolymer HEA$_{85}$-*b*-GILQINSR**G** lost completely its ability to interact with lysozyme and prevent its aggregation.

Results indicate that peptide GILQINSRW can be used to interact with hydrophobic patches on lysozyme to prevent or delay its aggregation. They also suggest that if GILQINSRW self-assembling nature is supressed, its interaction with the protein is greatly reduced. It may then be hypothesised that GILQINSRW is stabilising lysozyme by interacting with its homologous APR sequence on the protein, with the same type of mutual interactions that usually lead to protein aggregation. The polyacrylamide block may surround and shield the protein, in this way preventing proteins from coming together and aggregate. If confirmed, the hypothesis suggests a potentially new approach to address aggregation of therapeutic proteins, by targeting their aggregation prone regions through homologous APR-copolymers that act as non-covalent stabilisers.

However, more studies are required to elucidate the specificity of GILQINSRW for its homologous APR on lysozyme backbone. Other hydrophobic patches on the protein could be capable of interacting with GILQINSRW. A proper technique, like for example Isothermal Titration Calorimetry, could help to estimate the number of $HEA_{90}$-*b*-GILQINSRW chains that are interacting per protein molecule. More investigations are also required to understand if the protein retains its enzymatic activity after being treated with the copolymer. Even though after 24h at pH 12 almost no visible aggregate was observed, the protein may still be partially or completed unfolded. The non-covalent interactions that undergo between the two macromolecules may induce conformational changes in the protein structure, with partial unfolding and subsequent loss of protein functionality.

Finally, further studies conducted on GILQINSRW revealed that its poor solubility in water and also many organic solvents was at least partially due to the procedure that was used to purify the peptide after cleavage from the resin. The cleaved GILQINSRW was precipitated in diethyl ether and used directly without any further purification, as HPLC analysis revealed a purity of around 85%.

However, its purification was later attempted, using a semi-preparative HPLC column. The collected fractions afforded a ≥95% purity peptide, which, once dissolved in DMSO, surprisingly did not precipitate anymore upon water addition.

The low degree of solubility observed on un-purified GILQINSRW could be ascribed to its precipitation in diethyl ether, which may have induced its self-assembly into very insoluble aggregates. Further studies would therefore be necessary to understand if the APR GILQINSRW fragment is now potentially able to interact with its homologous on lysozyme backbone, without the need for its copolymerization with a long hydrophilic chain to make it more soluble.

# References

1.      Roberts, C. J., Protein aggregation and its impact on product quality. *Current Opinion in Biotechnology* **2014,** *30*, 211-217.

2.      Jacinte Beerten, J. S. a. F. R. Aggregation Prone Regions and Gatekeeping Residues in Protein Sequences. *Curr Top Med Chem* **2012**, 12(22), 2470-8.

3.      Lin, L.-x.; Bo, X.-y.; Tan, Y.-z.; Sun, F.-x.; Song, M.; Zhao, J.; Ma, Z.-h.; Li, M.; Zheng, K.-j.; Xu, S.-m., Feasibility of β-Sheet Breaker Peptide-H102 Treatment for Alzheimer's Disease Based on β-Amyloid Hypothesis. *PLOS ONE* **2014,** *9* (11), e112052.

4.      Tokunaga Y, S. Y., Kamada Y, Watanabe Ki, Sugimoto Y., Analysis of Core Region from Egg White Lysozyme Forming Amyloid Fibrils. *Int J Biol Sci* **2013**; 9(2):219-227.

5.      Mastrotto, F.; Salmaso, S.; Lee, Y. L.; Alexander, C.; Caliceti, P.; Mantovani, G., pH-responsive poly(4-hydroxybenzoyl methacrylates) – design and engineering of intelligent drug delivery nanovectors. *Polymer Chemistry* **2013,** *4* (16), 4375-4385.

6.      Wei Wang, C. J. R. Aggregation of Therapeutic Proteins. **2010**.

7.      Miron, T.; Wilchek, M., A simplified method for the preparation of succinimidyl carbonate polyethylene glycol for coupling to proteins. *Bioconjugate Chemistry* **1993,** *4* (6), 568-569.

8.      Held, J.; van Smaalen, S., The active site of hen egg-white lysozyme: flexibility and chemical bonding. *Acta Crystallographica Section D: Biological Crystallography* **2014,** *70* (Pt 4), 1136-1146.

9.      Nohara, D.; Mizutani, A.; Sakai, T., Kinetic study on thermal denaturation of hen egg-white lysozyme involving precipitation. *Journal of Bioscience and Bioengineering* **1999,** *87* (2), 199-205.

10.     Voets, I. K.; Cruz, W. A.; Moitzi, C.; Lindner, P.; Arêas, E. P. G.; Schurtenberger, P., DMSO-Induced Denaturation of Hen Egg White Lysozyme. *The Journal of Physical Chemistry B* **2010,** *114* (36), 11875-11883.

11.     Jensen, H. B.; Kleppe, K., Effect of Ionic Strength, pH, Amines and Divalent Cations on the Lytic Activity of T4 Lysozyme. *European Journal of Biochemistry* **1972,** *28* (1), 116-122.

12.     Meersman, F.; Atilgan, C.; Miles, A. J.; Bader, R.; Shang, W.; Matagne, A.; Wallace, B. A.; Koch, M. H. J., Consistent Picture of the Reversible Thermal Unfolding of Hen Egg-White Lysozyme from Experiment and Molecular Dynamics. *Biophysical Journal* **2010,** *99* (7), 2255-2263.

13.     Holley, M.; Eginton, C.; Schaefer, D.; Brown, L. R., Characterization of amyloidogenesis of hen egg lysozyme in concentrated ethanol solution. *Biochemical and Biophysical Research Communications* **2008,** *373* (1), 164-168.

14.     Shipp, D. A., Reversible-Deactivation Radical Polymerizations. *Polymer Reviews* **2011,** *51* (2), 99-103.

15.     Perrier, S., 50th Anniversary Perspective: RAFT Polymerization—A User Guide. *Macromolecules* **2017,** *50* (19), 7433-7447.

16.     Keddie, D. J.; Moad, G.; Rizzardo, E.; Thang, S. H., RAFT Agent Design and Synthesis. *Macromolecules* **2012,** *45* (13), 5321-5342.

17.     Keddie, D. J., A guide to the synthesis of block copolymers using reversible-addition fragmentation chain transfer (RAFT) polymerization. *Chemical Society Reviews* **2014,** *43* (2), 496-505.

18.     Hentschel, J.; Bleek, K.; Ernst, O.; Lutz, J.-F.; Börner, H. G., Easy Access to Bioactive Peptide–Polymer Conjugates via RAFT. *Macromolecules* **2008,** *41* (4), 1073-1075.

19.     Perrier, S.; Takolpuckdee, P.; Mars, C. A., Reversible Addition–Fragmentation Chain Transfer Polymerization: End Group Modification for Functionalized Polymers and Chain Transfer Agent Recovery. *Macromolecules* **2005,** *38* (6), 2033-2036.
20.     Homchaudhuri, L.; Kumar, S.; Swaminathan, R., Slow aggregation of lysozyme in alkaline pH monitored in real time employing the fluorescence anisotropy of covalently labelled dansyl probe. *FEBS Letters* **2006,** *580* (8), 2097-2101.
21.     Ravi, V. K.; Swain, T.; Chandra, N.; Swaminathan, R., On the Characterization of Intermediates in the Isodesmic Aggregation Pathway of Hen Lysozyme at Alkaline pH. *PLOS ONE* **2014,** *9* (1), e87256.
22.     Mueller, C.; Capelle, M. A. H.; Seyrek, E.; Martel, S.; Carrupt, P.-A.; Arvinte, T.; Borchard, G., Noncovalent PEGylation: Different Effects of Dansyl-, Tryptophan–, Phenylbutylamino-, Benzyl- and Cholesteryl-PEGs on the Aggregation of Salmon Calcitonin and Lysozyme. *Journal of Pharmaceutical Sciences* **2012,** *101* (6), 1995-2008.
23.     Reichert, C.; Borchard, G., Noncovalent PEGylation, An Innovative Subchapter in the Field of Protein Modification. *Journal of Pharmaceutical Sciences* **2016,** *105* (2), 386-390.
24.     Xiaoling Wang, T. K. D., Satish K Singh, and Sandeep Kuma Potential aggregation prone regions in biotherapeutics, *MAbs*, **2009**, 1(3), 254-67.
25.     Pawar, A. P.; DuBay, K. F.; Zurdo, J.; Chiti, F.; Vendruscolo, M.; Dobson, C. M., Prediction of "Aggregation-prone" and "Aggregation-susceptible" Regions in Proteins Associated with Neurodegenerative Diseases. *Journal of Molecular Biology* **2005,** *350* (2), 379-392.

# Supporting Information Chapter 2

$^1$H and $^{13}$C NMR spectra were recorded on a Bruker DPX400 UltraShield™ Spectrometer and processed with MestReNova 12.0© 2017 Mestrelab Research S.L. All chemical shifts are reported in ppm (δ) relative to tetramethylsilane or referenced to the chemical shifts of residual solvent resonances.

ESI TOF Mass spectrometry analyses were conducted on a Bruker microTOF II. MALDI TOF analyses were performed on a Bruker Ultraflex III analyser.

FT-IR spectra were recorded using an Agilent Cary630.

Polymer SEC analyses were performed on a Polymer Laboratories GPC 50 system equipped with a refractive index detector, using a system made of two PLgel Mixed-D (5 µm bead, 7.8 × 300 mm) columns and a matching guard (7.8 × 50 mm). Analyses were performed in DMF at a flow rate of 1 mg/mL with 0.1% w/v LiBR. Narrow PMMA standards were used for calibration.

HPLC experiments were performed on a Shimadzu HPLC (LC-20AD pump) equipped with a SPD-M20A UV detector and SIL-20A autosampler. Reverse phase analyses were completed using a C18 Zorbax Eclipse Plus C18 column (3.5 µm, 95 Å, 4.6 × 12.5 mm).

Lysozyme activity assays were performed using a using a DU-800 UV/Vis Spectrophotometer from Beckman Coulter, US.

Lysozyme aggregation assays were performed using a TECAN Spark 10M Multi-function Platereader, measuring Absorbance at λ=500 nm every 30 min for 24 h at 30°C.
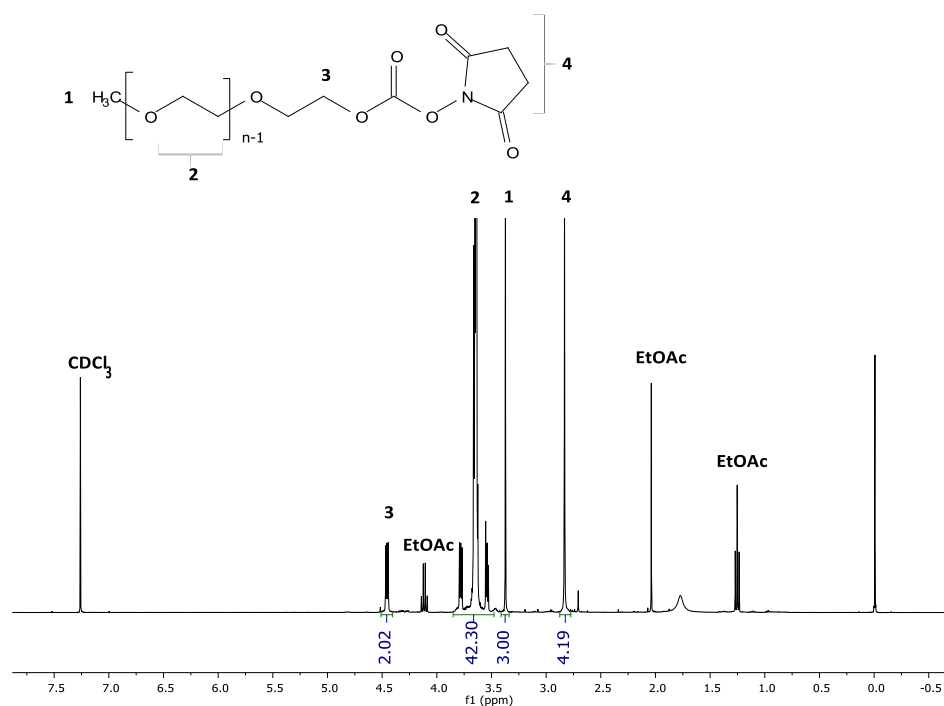


Figure S2.1: $^1$H NMR spectrum of PEG Succinimidyl Carbonate **(3)** in CDCl$_3$.
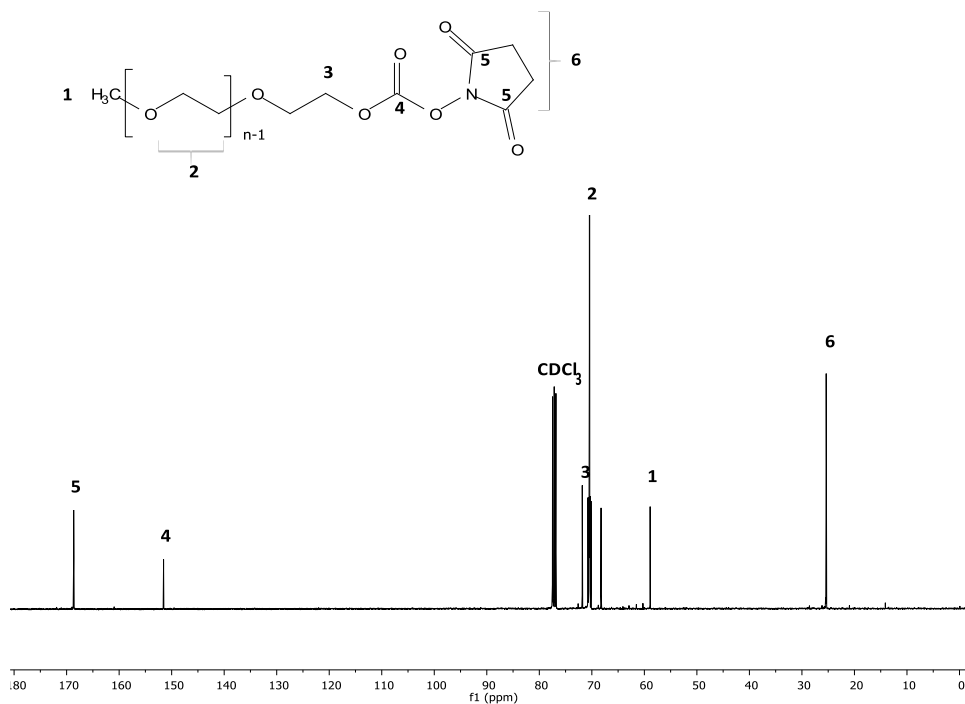
Figure S2.2: $^{13}$C NMR spectrum of PEG Succinimi$^d$yl Carbonate **(3)** in CDCl$_3$.
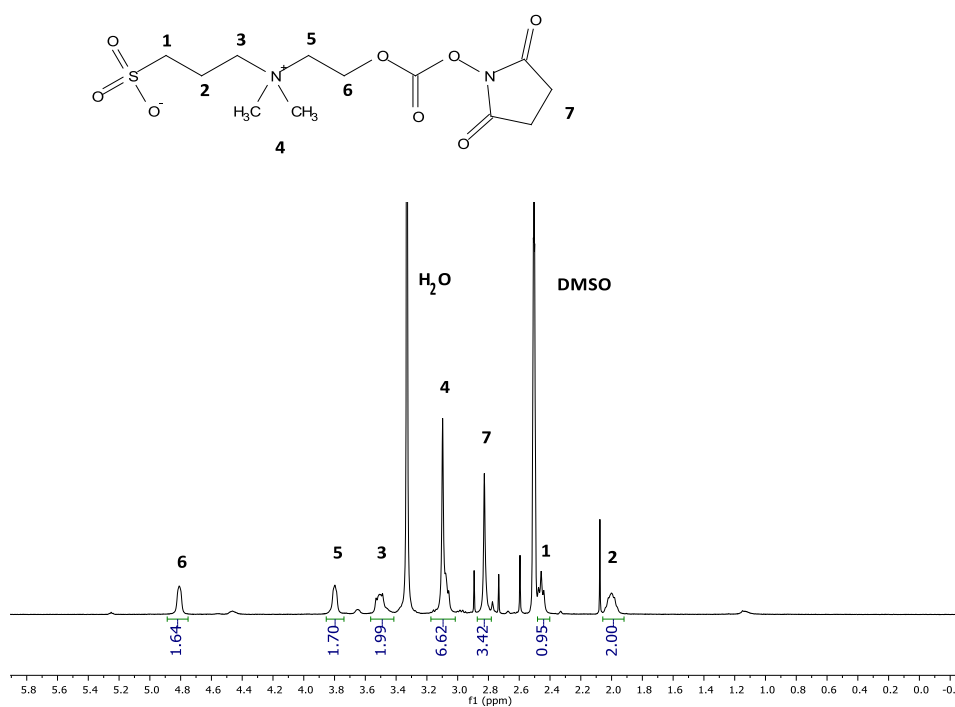


Figure S2.3: $^1$H NMR spectrum of sulfobetaine succinimidyl carbonate **(6)** in d$_6$-DMSO.
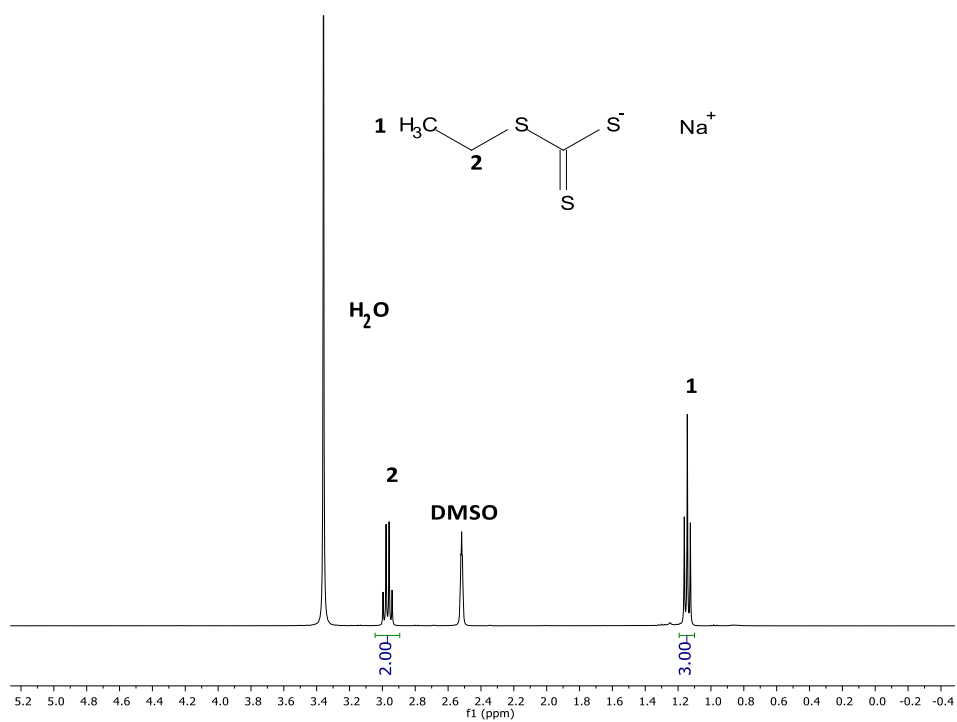
Figure S2.4: $^1$H NMR spectrum of Sodium ethyl carbonotrithioate **(8)** in d$_6$-DMSO.
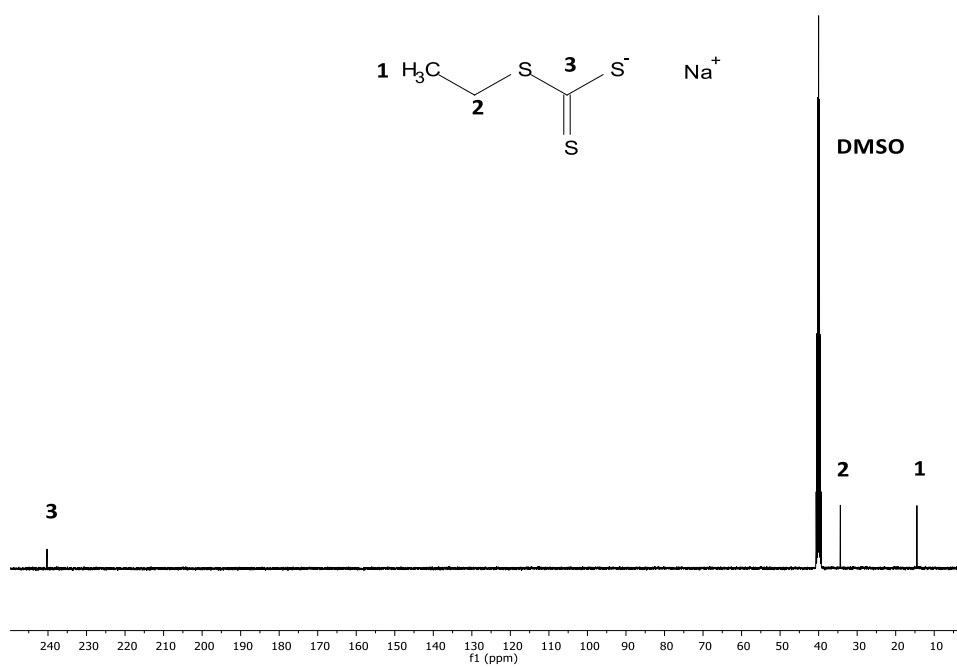


Figure S2.5: $^{13}$C NMR spectrum of Sodium ethyl carbonotrithioate **(8)** in d$_6$-DMSO.

Figure S2.6: $^1$H NMR spectrum of dithyiobis ethyl carbonotrithioate disulfide **(9)** in CDCl$_3$.
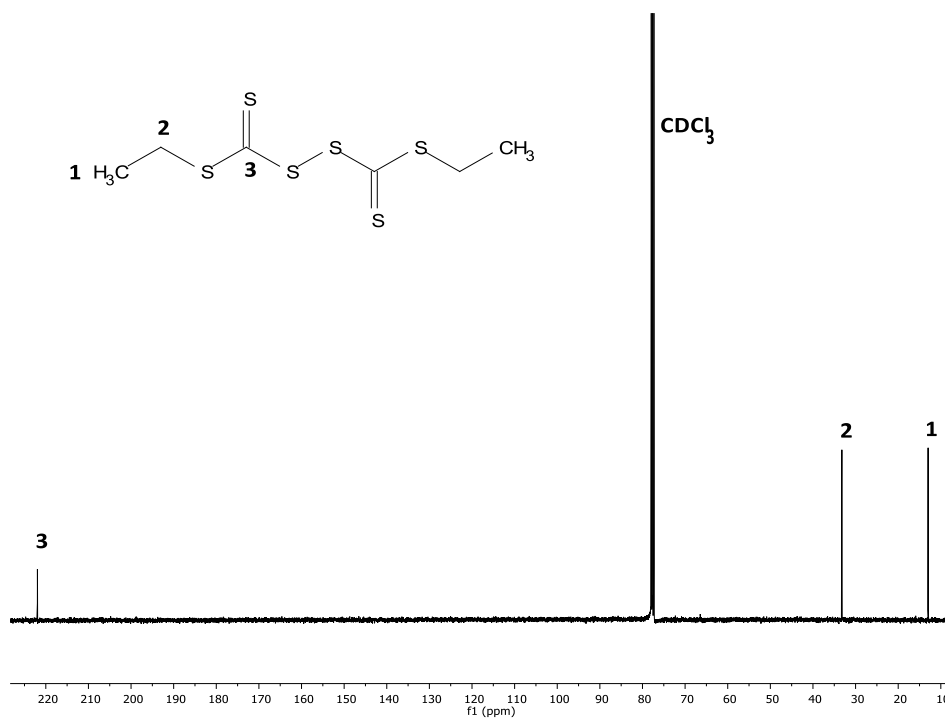


Figure S2.7: $^{13}$C NMR spectrum of dithyiobis ethyl carbonotrithioate disulfide **(9)** in CDCl$_3$.
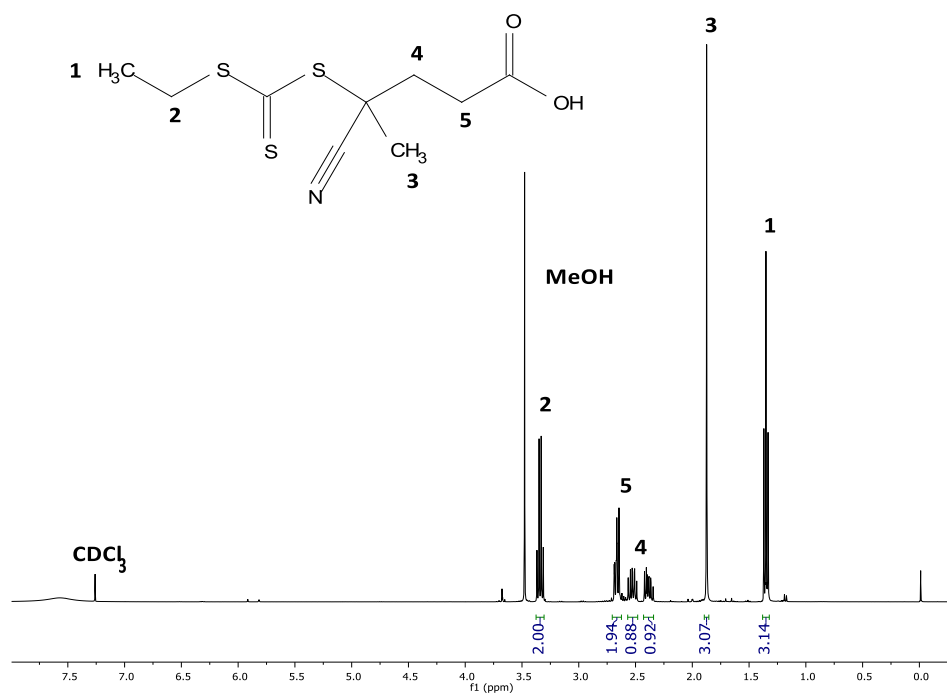
Figure S2.8: $^1$H NMR spectrum of CTA **(10)** in CDCl$_3$.
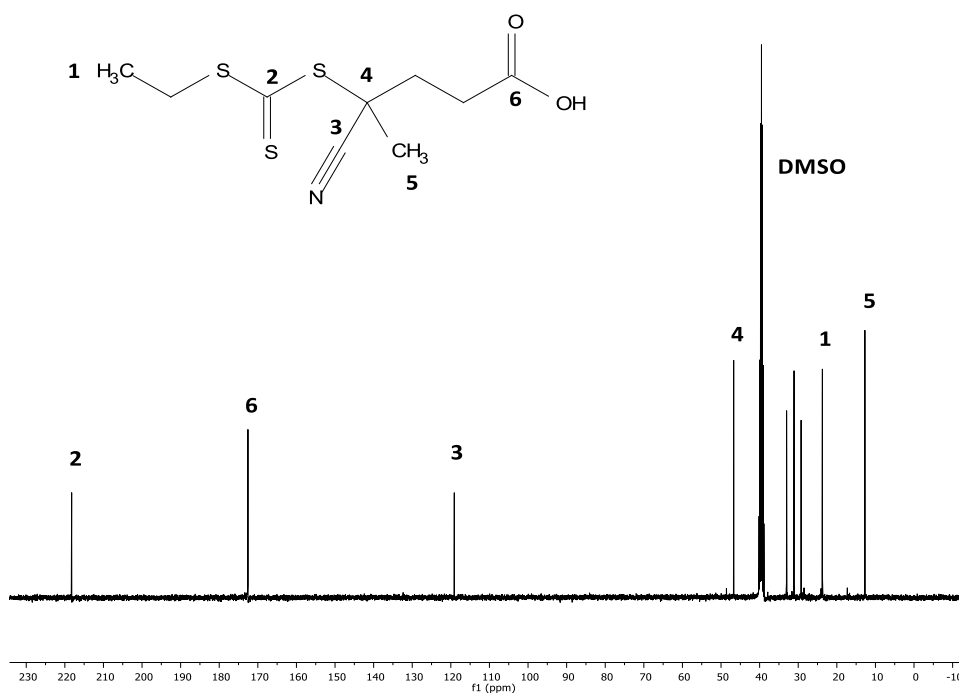


Figure S2.9: $^{13}$C NMR spectrum of CTA **(10)** in d$_6$-DMSO.
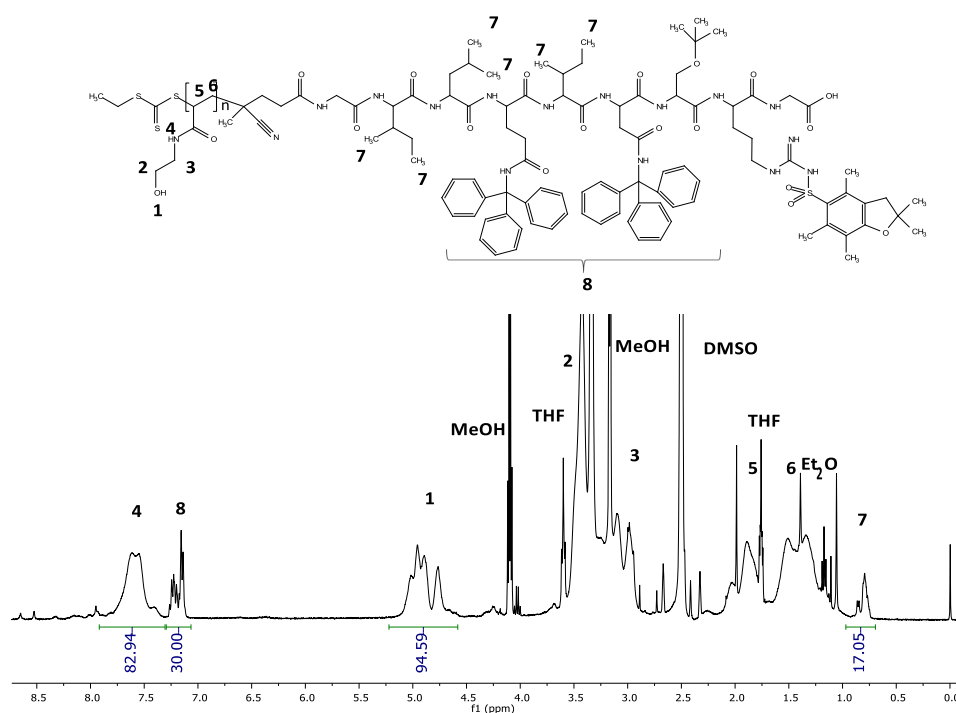
Figure S2.10: $^{1}$H NMR spectrum of poly(*N*-hydroxyethylacrylamide)-*b*-GILQINSR**G (15)** in d$_6$-DMSO.
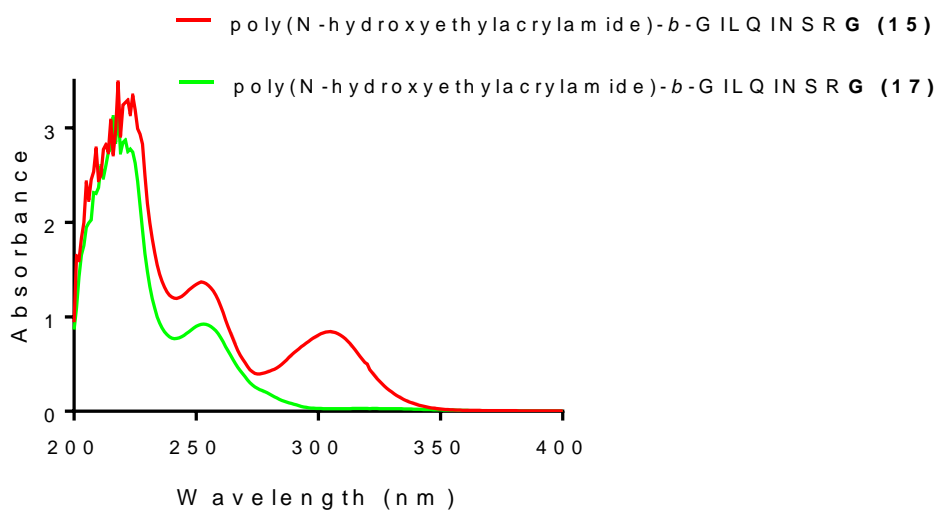


Figure S2.11: Removal of trithiocarbonate polymer chain-ends. UV spectra of poly(N-hydroxyethylacrylamide)-b-GILQINSR**G (15)** (before removal of the trithiocarbonate moiety), and poly(*N*-hydroxyethylacrylamide)-*b*-GILQINSR**G (17)** (after removal). The progress of the reaction was followed by monitoring the disappearance of the band at λ$_{max}$ ~ 310 nm.
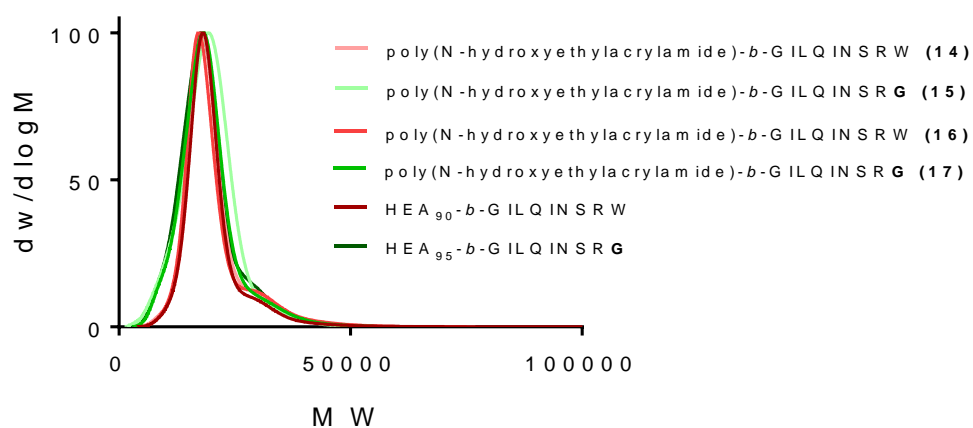
Figure S2.12: normalised SEC traces of HEA$_{90}$-b-GILQINSRW, HEA$_{95}$-b-GILQINSR**G** and their polymeric precursors. SEC analyses were performed in DMF + 0.1 % LiBr (PMMA standards).

# Chapter 3

**Hydrophobic amino acids-like moieties for protein stabilisation**

_____

## 3.1. Introduction

In the previous chapter, we hypothesised that a peptide derived from one of lysozyme's aggregation prone regions was able to non-covalently interact with its homologous sequence on lysozyme itself. A copolymer incorporating such peptide was able to significantly delay lysozyme aggregation in strong basic conditions.

These results suggested that peptides with amino acid sequences analogous to that of protein aggregation prone regions, as naturally self-aggregating sequences, could be used to interact through the same mechanism with similar, hydrophobic and self-aggregating sequences on proteins backbone. These materials may potentially be used to prevent or delay protein aggregation, improve protein solubility or, when included in protein delivery carriers, promote controlled-release or targeted delivery of therapeutic proteins.

Interestingly, in our initial work we observed that a single change in the amino acids sequence, the replacement of tryptophan with glycine, completely suppressed any interaction between this peptide and lysozyme, thus highlighting an important role that tryptophan may have on protein aggregation.

Tryptophan is one of the four aromatic amino acids, together with histidine, phenylalanine and tyrosine: its side chain is characterised by an aromatic indole functional group, which can interact with other aromatic groups on the protein sequence through the π-electron cloud over the indole ring. There are 3 types

of interactions that aromatic rings may establish: edge-to-face or T-shaped, face-to face and parallel displaced or offset stacked (Fig. 3.1)[1].

Edge-to-face     Face-to-face     Parallel displace
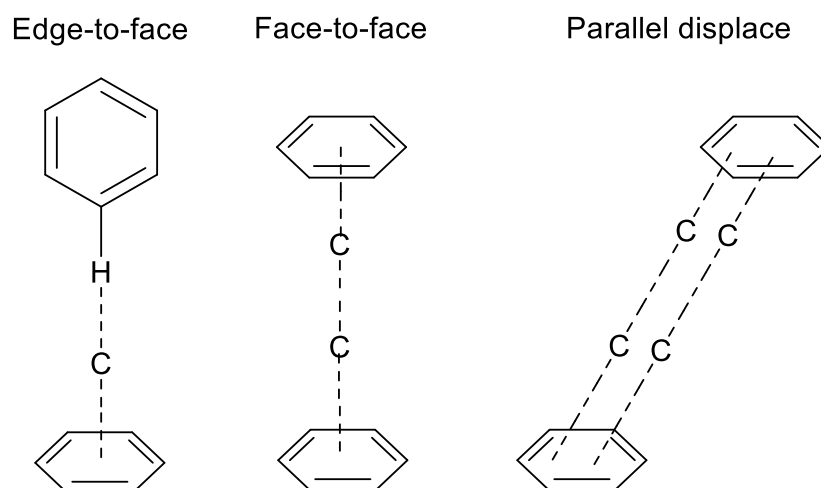
Figure 3.1: different types of π-interactions established by aromatic rings.

Through its indole N-H, tryptophan is also able to establish H-bonds with carbonyl groups of phospholipids in cell membranes, improving the stability of transmembrane proteins[2].

The role of tryptophan in mediating protein aggregation has been previously investigated. A specific algorithm was developed to calculate the propensity of each amino acid to promote the conversion of a polypeptide chain into amyloid aggregates and tryptophan has been identified as the amino acid with the highest intrinsic aggregation propensity at neutral pH[3]. Cecchini *et. al* investigated the importance of tryptophan in the amyloidogenic fibrillation of myoglobin, by substituting $Trp_7$ and $Trp_{14}$ from myoglobin aggregation prone regions with two alanines. The resulting peptides were dissolved in 10 mM HCl,

pH 2.0 and while the original peptide readily self-assembled into a β-sheet structure, under the same conditions its modified analogues retained a completely unfolded structure[4]. The role of tryptophan-tryptophan interactions in stabilizing the protein motif β-hairpin (two anti-parallel β-strands that resemble a hairpin) was had been previously elucidated by Cochran and co-workers [5].

Within the context of protein formulation, the propensity of tryptophan for hydrophobic interactions and β-sheet structure has made it a good candidate for the development of proteins stabilizers.

Its potential use as component of protein excipient was explored by Tudor Arvinte's group, where tryptophan was covalently linked to PEGs of different molecular weight (2 and 5 kDa). The resulting (PEG-Trp)s were tested on salmon calcitonin (sCT), a 3.4 kDa peptide whose aggregation, induced in 10 mM pH 6 citrate buffer and measured by turbidimetry, was significantly reduced in the presence of the 2 kDa polymer. The interaction between the polymer and the peptide was achieved through the tryptophan group, developing a non-covalent PEGylation system based on hydrophobic interactions[6]. The same concept was extended, within the same group, to different hydrophobic groups, derivatising PEG with cholesterol, dansyl, phenylbutylamino and benzyl groups. The resulting modified PEGs, along with the original tryptophan-PEG, were compared for their ability of preventing the aggregation of salmon calcitonin and hen egg lysozyme. PEG-tryptophan was found to be the most

effective to minimise sCT aggregation, while PEG-cholesterol, PEG-phenylbutylamino and PEG-dansyl gave the best results with lysozyme[7].

In the present part of this thesis work, we aimed at further exploring the efficacy of tryptophan as excipient for protein formulation to develop a family of protein stabilisers. We wanted to develop a library of amphiphilic block copolymers, comprising amino acid-like moieties, potentially able to non-covalently interact with hydrophobic, self-aggregating protein domains, and prevent protein aggregation/denaturation.

As most of the non-covalent interactions discussed thus far can be ascribed to tryptophan's side group indole, we decided to incorporate one or more indoles into these potential protein stabilisers. Accordingly, we first created an indole-bearing monomer starting from the molecule indole 3-acetic acid. The monomer was then oligomerised by RAFT polymerization to obtain a series of oligomeric CTAs with DP between 1 and 10. For comparative purposes, a range of hydrophobic oligomeric CTAs incorporating phenyl and methylisobutyric moieties were also made, to mimic the side groups of phenylalanine and isoleucine (Fig. 3.2).

As these oligomers were highly hydrophobic, they were thus copolymerized with *N*-hydroxyethylacrylamide, obtaining final water-soluble copolymers. The copolymers were tested as stabilizers and solubilisers for three different proteins: hen egg lysozyme, bovine pancreatic insulin and the antimicrobial peptide IDR1018. The efficacy of the copolymers was assessed by turbidimetry and solubility studies.
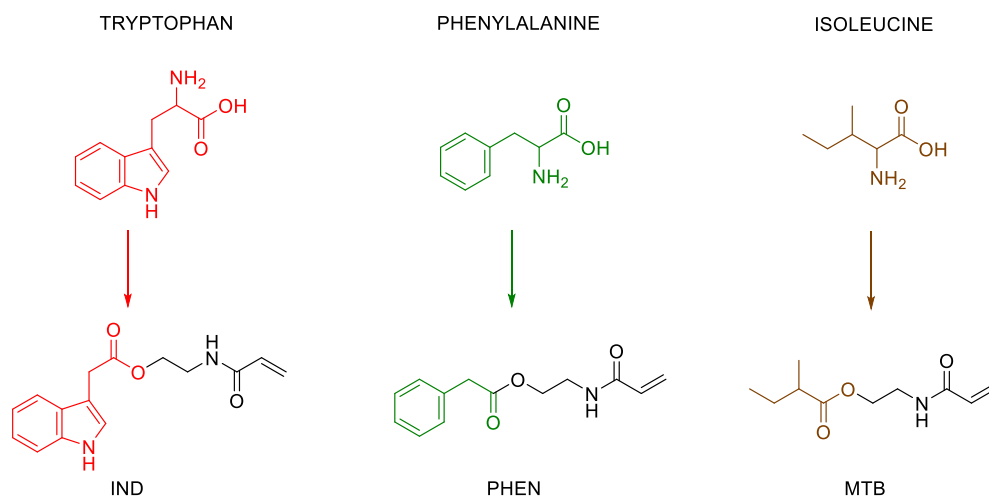
Figure 3.2: chemical structure of the three monomers that were used to mimic the side chains of Trp, Phen and Ile: the indole-bearing IND monomer, PHEN monomer which incorporates phenylacetic acid and MTB which comprises a methylbutyric acid functionality.

## 3.2. Materials and methods

### 3.2.1. Materials

Methanol, dichloromethane (DCM), ethyl acetate, diethyl ether, chloroform, tetrahydrofuran, petroleum ether, *N,N*-dimethylformamide (DMF) and acetone were purchased from Fisher Scientific (Bishop Meadow Rd, Loughborough, UK). *N*-hydroxyethylacrylamide (97%), indole 3-acetic acid (≥98%), phenylacetic acid (99%), methylbutyric acid (98%), 1-ethyl-3-(3-dimethylaminopropyl)carbodiimide-HCl (≥97%), dimethylamino pyridine (≥99%), bovine pancreatic insulin , hen egg lysozyme (≥95%), DPBS buffer, DIPEA (≥99%), TEA (≥99%),and VA-501 (≥98%) were obtained from Sigma-Aldrich (St. Louis, Missouri, United States). Azobisisobutyronitrile (AIBN) was purchased from FUJIFILM Wako Pure Chemical, Ltd.

### 3.2.2. Synthesis of monomers IND, PHEN and MTB
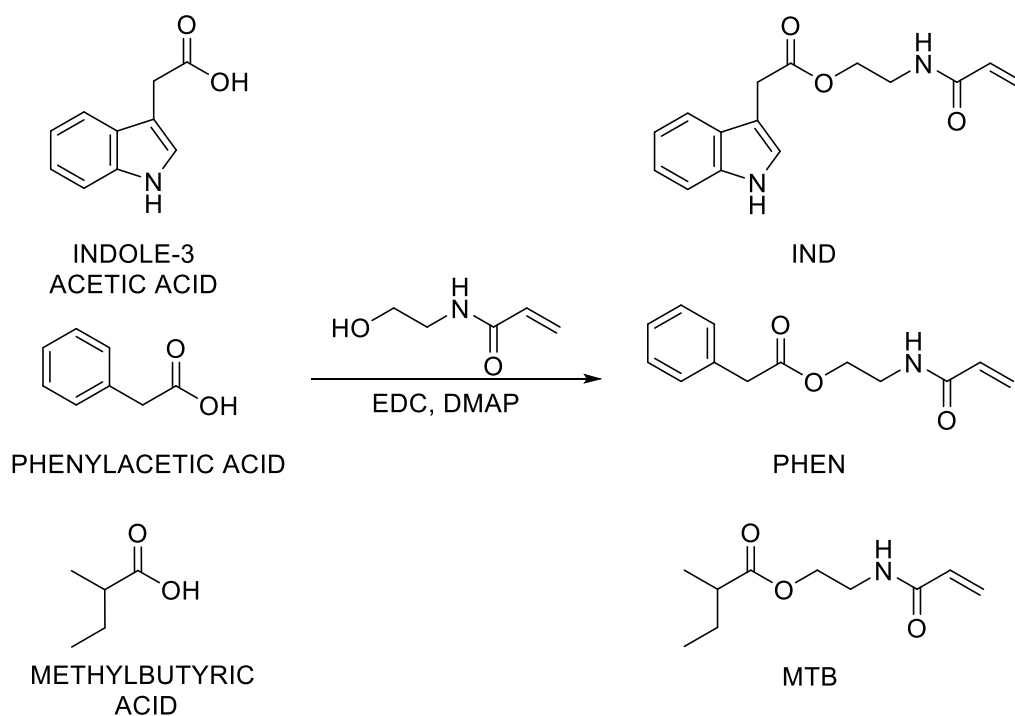


Scheme 3. 1: Synthesis of IND, PHEN and MTB monomers.

The synthesis of the acrylamide monomers IND, PHEN and MTB was carried out by reaction of 2-hydroxyethyl acrylamide (HEA) with 3-indole-acetic acid, phenyl-acetic acid and methylbutyric acid, respectively. A solution of EDC-HCl (1.2 g, 6.3 mmol, 1.1 eq.) in anhydrous DCM (20 mL) was added dropwise under stirring over 1 h to a solution of one of the three acid derivatives (5.7 mmol, 1 eq.), DMAP (0.07 g, 0.6 mmol, 0.1 eq.) and HEA (0.89 mL, 8.6 mmol, 1.5 eq) in DCM (50 mL), kept at 0°C with an ice bath. The reaction was then left stirring for 16 hours at room temperature. The solution was concentrated under reduced pressure and washed twice with brine and twice with HCl 2M. The organic phase was then dried over $MgSO_4$, filtered, and the solvent was removed under reduced pressure. The resulting oil was used for the polymerisation experiments without further purification.

IND Yield: 60%. $^1$H NMR (400 MHz, $CDCl_3$, δ, ppm), 8.68 (s, 1H, indole NH), 7.6 (d, *J*=6.5 Hz, 1H, aromatic CH), 7.34 (d, *J*=8.1 Hz, 1H, CH aromatic), 7.20 (t, *J*=8.2 Hz, 1H, CH aromatic), 7.13 (m, 1H, CH aromatic), 7.07 (d, *J*=2.4 Hz, 1H, CH aromatic), 6.13 (dd, *J*=17.0, 1.4 Hz, 1H, *CH*=CH$_2$), 5.74 (dd, *J*=17.0, 10.3 Hz, 1H, CH=C*H*H), 5.53 (dd, *J*=10.4, 1.4 Hz, 1H, CH=CH*H*), 4.16 (t, *J*=5.3 Hz, 2H, *CH$_2$*CH$_2$NH), 3.77 (s, 2H, CH$_2$COO) 3.49 (q, *J*=5.5 Hz, 2H, CH$_2$*CH$_2$*NH) (Fig.3.3).

$^{13}$C NMR (101 MHz, $CDCl_3$, δ, ppm): 172.31 (CONH), 166.05 (C(O)O), 136.24, 130.38, 126.61, 123.66, 121.95, 119.48, 118.42, 111.65, 107.50, 63.11 (COO*CH$_2$*CH$_2$), 38.41, 31.31 (Fig. S3.1).

FT-IR: 3346 cm$^{-1}$ (υ$_{N-H}$), 1721 cm$^{-1}$ (υ$_{C=O\ ester}$), 1660.4 cm$^{-1}$ (υ$_{C=Oamide}$), 1545.5 cm$^{-1}$ (υ$_{C-Namide}$).

ESI-TOF mass spectrometry: expected m/z [M-H]$^+$ 273.12 and [M-Na]$^+$ 295.11, found 273.12, and 295.10, respectively .

PHEN Yield: 67%. $^1$H NMR (400 MHz, $CDCl_3$, δ, ppm), 7.4-7.2 (m, 5H, aromatic), 6.23 (dd, *J*=17.0, 1.3 Hz, 1H, *CH*=CH$_2$), 5.99 (dd, *J*=17.0, 10.3 Hz, 1H, CH=C*H*H),

5.64 (dd, *J*=10.3, 1.3 Hz, 1H, CH=CH*H*), 4.22 (m 2H, *CH₂*CH₂NH), 3.65 (s, 2H, CH₂C(O)O) 3.58 (q, *J*=5.6 Hz, 2H, CH₂*CH₂*NH) (Fig.S3.2).

$^{13}$C NMR (101 MHz, CDCl₃, δ, ppm): 171.69 (CONH), 165.74 (C(O)O), 133.84, 130.56, 129.22, 128.7, 127.28, 127.27, 126.62, 63.41 (CO*CH₂*CH₂), 41.29, 38.67 (Fig. S3.3).

FT-IR: 1731 cm$^{-1}$ (υ$_{C=Oester}$), 1654.5 cm$^{-1}$ (υ$_{C=Oamide}$), 1560.3 cm$^{-1}$(υ$_{C-Namide}$).

ESI-TOF mass spectrometry: expected m/z [M-H]$^+$ 234.11 and M-Na]$^+$ 256.10, found 234.11 and 256.10.


MTB Yield: 70%. $^1$H NMR (400 MHz, CDCl₃, δ, ppm), 6.28 (dd, *J*=17.0, 1.3 Hz, 1H, *CH*=CH₂), 6.09 (dd, *J*=17.0, 10.3 Hz, 1H, CH=C*H*H), 5.66 (dd, *J*=10.3, 1.3 Hz, 1H, CH=CH*H*), 4.23 (t, *J*=5.4Hz, 2H, *CH₂*CH₂NH), 3.62 (q, *J*=5.6 Hz, 2H, CH₂*CH₂*NH), 2.4 (h, *J*=7 Hz  1H, *CH*CH₃), 1.15 (d, *J*=7Hz, 3H, CH*CH₃*), 0.90 (t, *J*=7.4Hz, 3H, CH₂*CH₃*) (Fig. S3.4).

$^{13}$C NMR (101 MHz, CDCl₃, δ, ppm): 177.08 (COO), 165.87 (CONH), 130.70 (CH), 126.75 (CH), 62.76 (CO*CH₂*CH₂), 41.00, 39.05, 26.78, 16.62 (CH*CH₃*), 11.64(CH₂*CH₃*) (Fig. S3.5).

FT-IR: 1732.6 cm$^{-1}$ (υ$_{C=Oester}$), 1655.8 cm$^{-1}$ (υ$_{C=Oamide}$), 1541.8 cm$^{-1}$(υ$_{C-Namide}$).

ESI-TOF mass spectrometry: expected m/z [M-H]$^+$ 200.12 and M-Na]$^+$ 222.11, found 200.13 and 222.11.

### 3.2.3. Synthesis of oligomeric CTAs IND$_1$, PHEN$_1$, MTB$_1$, IND$_3$, PHEN$_3$, MTB$_3$, IND$_{10}$, PHEN$_{10}$ and MTB$_{10}$
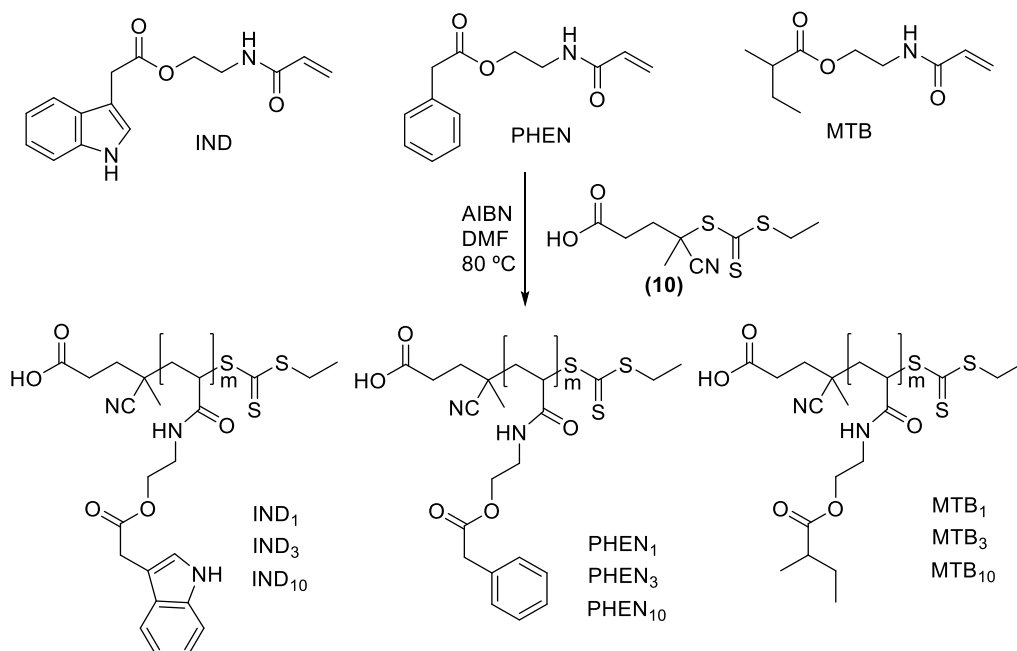


Scheme 3. 2: Synthesis of oligomeric chain transfer agents IND$_1$, IND$_3$, IND$_{10}$, PHEN$_1$, PHEN$_3$, PHEN$_{10}$, MTB$_1$, MTB$_3$ and MTB$_{10}$.

The synthesis of the hydrophobic oligomeric CTAs was carried out by RAFT polymerization, using different [monomer]:[CTA **(10)**] molar ratios in combination with IND, PHEN and MTB.

Typically, IND, PHEN and MTB (3.68 mmol) and CTA **(10)** (1 eq., 0.78 g, 2.94 mmol for IND$_1$, PHEN$_1$ and MTB$_1$, 0.24 g, 0.92 mmol for IND$_3$, PHEN$_3$ and MTB$_3$, 0.08g, 0.3 mmol for IND$_{10}$, PHEN$_{10}$ and MTB$_{10}$) were mixed together in 1 mL of DMF. The solutions were transferred into a small Schlenk tube equipped with a magnetic stirrer, which was put on ice. Radical initiator AIBN (0.1 eq., 0.08 g, 0.29 mmol for IND$_1$, PHEN$_1$ and MTB$_1$, 0.026 g, 0.09 mmol for IND$_3$, PHEN$_3$ and MTB$_3$, 0.008 g, 0.03 mmol for IND$_{10}$, PHEN$_{10}$ and MTB$_{10}$), previously dissolved in DMF (80 μL for IND$_1$, 26 μL for PHEN$_1$ and 8 μL for MTB$_1$) was added to the

tubes. The mixtures were degassed for 30 min bubbling argon under stirring at

0°C and finally put on a paraffin oil bath at 80 ˚C. The reactions were monitored

by $^1$H NMR, checking the disappearance of acrylamide monomer peaks into the

5-6.5 ppm region, until ~ 80% conversion was reached. See Table below for

reaction times and conversions.

Table 3. 1: reaction times and conversions of short IND-, PHEN- and MTB-based copolymers.

| POLYMER | REACTION TIME (h) | CONVERSION (%) |
|---------|-------------------|----------------|
| $IND_1$ | 7 | 74 |
| $PHEN_1$ | 7 | 70 |
| $MTB_1$ | 7 | 67 |
| $IND_3$ | 9 | 71 |
| $PHEN_3$ | 8 | 83 |
| $MTB_3$ | 9 | 87 |
| $IND_{10}$ | 23 | 70 |
| $PHEN_{10}$ | 8 | 84 |
| $MTB_{10}$ | 8 | 79 |

The reaction solutions were then transferred into a 25 mL round bottom flask,

and DMF was removed under reduced pressure to give a residue that was

purified as follows:

$IND_1$, $PHEN_1$ and $MTB_1$ were purified by flash chromatography using Pet.

Ether:EtOAc 2:8 v/v as the eluent. Purification of $IND_3$, $PHEN_3$ and $MTB_3$ was

performed by reversed phase chromatography on an Agilent 971-FP automated

flash purification system using a BIOTAGE KP-C18-HS 12 g column. Elution was

performed using a linear gradient from 20% to 80% MeCN in water over 250

min at a flow rate of 8 mL min$^{-1}$. $IND_{10}$, $PHEN_{10}$ and $MTB_{10}$ were re-dissolved in

acetone and purified by multiple precipitations in $Et_2O$. The final precipitates

were dried under vacuum and used without any further purification. $IND_1$, $PHEN_1$ and $MTB_1$ were analysed by ^{1}H NMR, ^{13}C NMR and ESI-TOF. $IND_3$, $PHEN_3$ and $MTB_3$ were analysed by ^{1}H NMR and ESI-TOF. $IND_{10}$, $PHEN_{10}$ and $MTB_{10}$ were analysed by ^{1}H NMR and SEC in THF.

$IND_1$ Yield: 32%. ^{1}H NMR (400 MHz, d6-DMSO, δ, ppm), 10.93 (s, 1H, indole NH), 8.84 (s, 1H, acrylamide NH), 7.48 (d, *J*= 7.8Hz, 1H, CH aromatic), 7.34 (d, *J*= 8.1Hz, 1H, CH aromatic), 7.24 (d, *J*= 2.0Hz, 1H, CH aromatic), 7.07 (m, 1H, CH aromatic), 6.98 (t, *J*= 7.3Hz, 1H, CH aromatic), 4.85 (m, 1H, CH), 4.06 (m, 2H, $CH_2$), 3.73 (d, *J*= 2.3Hz, 2H, $CH_2$), 1.26 (m, 3H, $CH_3$) (Fig.3.5).

^{13}C NMR (101 MHz, $d_6$-DMSO, δ, ppm): 222.64 (C=S), 176.20 (COOH), 172.03 (CONH), 169.28 (COO), 136.14 (CH, C aromatic), 127.17 (CH, C aromatic), 123.32 (CH, C aromatic), 127.17 (CH, C aromatic), 122.31 (CH, C aromatic), 119.78 (CN), 118.69 (CH, C aromatic), 111.56 (CH, C aromatic), 108.11 (CH, C aromatic), 62.83 (COO$CH_2CH_2$), 49.03 ($CH_2CH$), 39.16, 36.9, 30.95, 24.34, 23.41, 20.85, 18.44, 12.83 (Fig S3.6).

ESI-TOF mass spectrometry: expected m/z [M]⁻ 534.13, found 534.12.

$IND_3$ Yield: 8%. ^{1}H NMR (400 MHz, d6-DMSO, δ, ppm), 7.49 (m 2.52H, CH), 7.35 (d, *J*= 8.2Hz, 2.52H, CH, CH aromatic), 7.23 (m, 2.52H, CH, CH aromatic), 7.07 (m, 2.52H, CH, CH aromatic), 6.97 (m, 2.52H, CH, CH aromatic), 4.03 (m, 5.04H, $CH_2$), 3.72 (m, 5.04H, $CH_2$) (Fig.3.5).

ESI-TOF mass spectrometry: expected m/z [M]⁻ 1078.35, found 1078.35 (*n*=3, 52%) and 806.24 (*n*=2, 48%).

$IND_{10}$ Yield: 58%. ^{1}H NMR (400 MHz, d6-DMSO, δ, ppm), 10.90 (s, 10H, indole NH), 7.46 (m, 10H, CH, CH aromatic), 7.34 (m, 10H, CH, CH aromatic), 7.21 (m, 10H, CH, CH aromatic), 7.05 (m, 10H, CH, CH aromatic), 6.95 (m, 10H, CH, CH aromatic), 4.04 (m, 20H, $CH_2$), 3.7 (m, 20H, $CH_2$), 2.38-1.88 (m, 10H $CH_2CH$), 1.8-1 (m, 20H $CH_2$CH) (Fig.3.9). $M_{n,THEO}$: 3 kDa. $M_{n,SEC(THF)}$ 1.56 kDa, Đ=1.12.

$PHEN_1$ Yield: 38%. ^{1}H NMR (400 MHz, CDCl$_3$, δ, ppm), 7.23-7.27 (m, 5H, aromatic), 6.60-6.55 (m, 1H, acrylamide NH), 4.85 (dd, *J*=8.1, 4.8Hz, 1H, CH), 4.09 (d, *J*= 5.3Hz, 2H, $CH_2CH_2$NH), 3.57 (m, 2H, $CH_2$), 3.42 (m, 2H, $CH_2CH_2$NH), 3.32 (q, *J*= 7.3Hz, 2H, $CH_2CH_3$) (Fig S3.7).

^{13}C NMR (101 MHz, CDCl$_3$, δ, ppm): 223.01 (C=S), 176.55 (COOH), 171.58 (CONH), 169.28 (COO), 133.68 (CH, C aromatic), 129.33 (CH, C aromatic), 128.7 (CH, C aromatic), 127.28 (CH, C aromatic), 122.26 (CN), 63.08 (COO$CH_2CH_2$),

48.69 (CH$_2$*C*H), 41.18, 39.09, 34.42, 33.55, 32.23, 29.47, 24.48, 23.68, 12.84 (Fig S3.8).

ESI-TOF mass spectrometry: expected m/z [M]$^-$ 495.12, found 495.10.

PHEN$_3$ Yield: 12%. $^1$H NMR (400 MHz, CDCl$_3$, δ, ppm), 7.5-7.2 (m, 15H, aromatic), 7.2-6.5 (m, 3H, acrylamide NH), 4.9-4.5 (m, 3H, CH), 4.18 (m, 6H, *CH$_2$*CH$_2$NH), 3.63 (m, 6H, CH$_2$CO), 3.55-3.25 (m, 6H, CH$_2$*CH$_2$*NH, and m, 2H, *CH$_2$*CH$_3$) (Fig S3.9).

ESI-TOF mass spectrometry: expected m/z [M]$^-$ 961.33, found 961.32.

PHEN$_{10}$ Yield: 64%. $^1$H NMR (400 MHz, d$_6$-DMSO, δ, ppm), 8.4-7.4 (m, 10H, acrylamide NH), 7.35-7.15 (m, 50H, aromatic), 7.2-6.5 (m, 10H, acrylamide NH), 4.03 (m, 20H, *CH$_2$*CH$_2$NH), 3.83 (m, 20H, CH$_2$CO), 2.4-1.85 (m, 10H CH$_2$*C*H), 1.8-1 (m, 20H *CH$_2$*CH) (Fig.S3.10). M$_{n,THEO}$: 2.6 kDa. M$_{n,SEC(THF)}$ 1.6 kDa, Đ=1.09.

MTB$_1$ Yield: 41%. $^1$H NMR (400 MHz, CDCl$_3$, δ, ppm), 6.83-6.79 (m, 1H, acrylamide NH), 4.93 (dd, *J*= 8.0, 4.9Hz, 1H, CH$_2$*C*H), 4.12 (t, *J*= 5.2Hz, 2H, *CH$_2$*CH$_2$NH), 3.50 (m, 2H, CH$_2$*CH$_2$*NH), 3.37 (q, *J*= 7.4Hz, 2H, *CH$_2$*CH$_3$), 2.53 (m, 2H, *CH$_2$*CH$_2$) 2.35 (h, *J* =6.9 Hz, 1H, *C*HCH$_3$), 2.15-1.8 (m, 2H, CH$_2$*CH$_2$*),1.7-1.4 (m, 2H, *CH$_2$*CH$_3$), 1.33 (m, 3H, CH$_2$*CH$_3$*), 1.13 (m 3H, CH*CH$_3$*), 0.88 (td, *J*= 7.4, 2.5Hz, 3H, CH$_2$*CH$_3$*) (Fig S3.11).

$^{13}$C NMR (101 MHz, d$_3$- CDCl$_3$, δ, ppm): 223.25 (C=S), 177.17 (COOH), 169.88 (CONH), 122.65 (CN), 62.27 (COO*C*H$_2$CH$_2$), 49.21 (CH$_2$*C*H), 41.3, 39.59, 36.29, 34.86, 30.00, 24.02, 19.66, 16.86, 13.21, 12.02 (Fig S3.12).

ESI-TOF mass spectrometry: expected m/z [M]$^-$ 461.13, found 461.13.

MTB$_3$ Yield: 10%. $^1$H NMR (400 MHz, CDCl$_3$, δ, ppm), 7.2-6.8 (m, 3H, acrylamide NH), 4.4-4.0 (m, 6H, *CH$_2$*CH$_2$NH), 3.55-3.25 (m, 6H, CH$_2$*CH$_2$*NH, and m, 2H, *CH$_2$*CH$_3$), 1.14 (m, 9H, CH*CH$_3$*), 0.9 (m, 9H, CH$_2$*CH$_3$*) (Fig S3.13).

ESI-TOF mass spectrometry: expected m/z [M]$^-$ 859.37, found 859.37.

MTB$_{10}$ Yield: 57%. $^1$H NMR (400 MHz, d$_6$-DMSO, δ, ppm), 8.4-7.1 (m, 10H, acrylamide NH), 4.01 (m, 20H, *CH$_2$*CH$_2$NH), 2.33 (m, 1H, *C*HCH$_3$), 1.06 (m, 30H, CH*CH$_3$*), 0.83 (m, 30H, CH$_2$*CH$_3$*). (Fig S3.14). M$_{n,THEO}$: 2.3 kDa. M$_{n,SEC(THF)}$ 1.47 kDa, Đ=1.10.

SEC traces of IND$_{10}$, PHEN$_{10}$ and MTB$_{10}$ can be found in Fig. S3.35.

### 3.2.4. Synthesis of IND$_1$-, PHEN$_1$-, MTB$_1$-, IND$_3$-, PHEN$_3$-, MTB$_3$-, IND$_{10}$-, PHEN$_{10}$- and MTB$_{10}$-copolymers



IND$_1$
IND$_3$
IND$_{10}$

HEA, V501
DMF, 80°C

IND$_1$-*b*-HEA$_{37}$    IND$_1$-*b*-HEA$_{100}$
IND$_3$-*b*-HEA$_{53}$    IND$_3$-*b*-HEA$_{98}$
IND$_{10}$-*b*-HEA$_{46}$   IND$_{10}$-*b*-HEA$_{95}$

PHEN$_1$
PHEN$_3$
PHEN$_{10}$

HEA, V501
DMF, 80°C

PHEN$_1$-*b*-HEA$_{37}$    PHEN$_1$-*b*-HEA$_{100}$
PHEN$_3$-*b*-HEA$_{45}$    PHEN$_3$-*b*-HEA$_{99}$
PHEN$_{10}$-*b*-HEA$_{38}$   PHEN$_{10}$-*b*-HEA$_{88}$

MTB$_1$
MTB$_3$
MTB$_{10}$

HEA, V501
DMF, 80°C

MTB$_1$-*b*-HEA$_{37}$    MTB$_1$-*b*-HEA$_{111}$
MTB$_3$-*b*-HEA$_{42}$    MTB$_3$-*b*-HEA$_{82}$
MTB$_{10}$-*b*-HEA$_{43}$   MTB$_{10}$-*b*-HEA$_{105}$
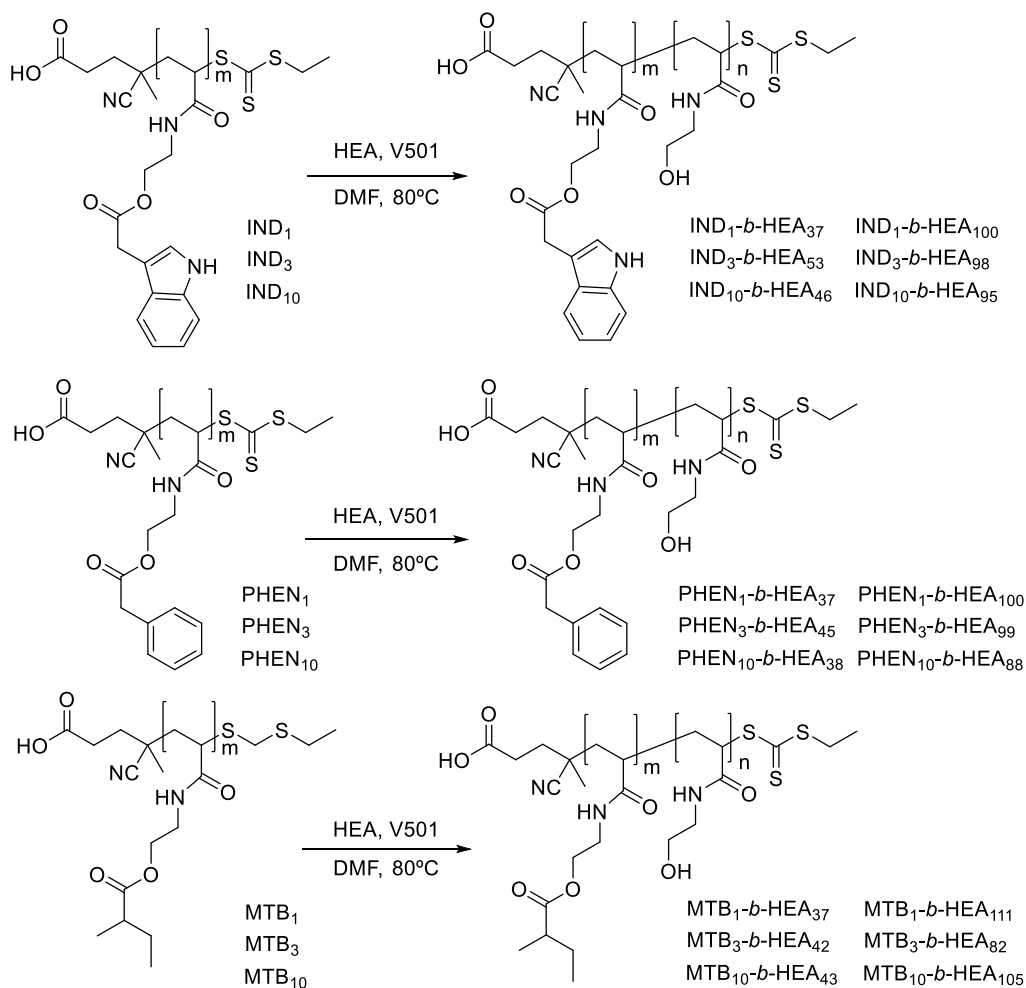
Scheme 3. 3: synthesis of IND$_1$-, IND$_3$-, IND$_{10}$-, PHEN$_1$-, PHEN$_3$-, PHEN$_{10}$-, MTB$_1$-, MTB$_3$- and MTB$_{10}$-*b*-HEA$_n$ block copolymers.

Synthesis of amphiphilic block copolymers was then carried out by RAFT polymerization of commercial monomer N-hydroxyethylacrylamide (HEA) using the previously synthesised oligomeric CTAs macro RAFT agents. Typically, the CTAs (0.10 mmol for IND$_1$, PHEN$_1$, MTB$_1$, 0.050 mmol for IND$_3$, PHEN$_3$, MTB$_3$ and 0.050 mmol for IND$_{10}$, PHEN$_{10}$, MTB$_{10}$), where dissolved in DMF along with HEA (50 eq. for final target DP =40 (aiming to stop the reaction at ~ 80% monomer

conversion), 100 eq. for final target DP *n*=100). See Tables below for reaction times and conversions.

Table 3. 2: Reaction times and conversions of short IND-, PHEN- and MTB-based copolymers.

| POLYMER | REACTION TIME (h) | CONVERSION (%) |
|---|---|---|
| IND$_1$-*b*-HEA$_{37}$ | 1.5 | 54 |
| PHEN$_1$-*b*-HEA$_{37}$ | 1.5 | 76 |
| MTB$_1$-*b*-HEA$_{37}$ | 1.5 | 81 |
| IND$_3$-*b*-HEA$_{53}$ | 2 | 81 |
| PHEN$_3$-*b*-HEA$_{45}$ | 1.5 | 85 |
| MTB$_3$-*b*-HEA$_{42}$ | 1.5 | 78 |
| IND$_{10}$-*b*-HEA$_{40}$ | 4 | 52 |
| PHEN$_{10}$-*b*-HEA$_{38}$ | 1.5 | 78 |
| MTB$_{10}$- *b*-HEA$_{43}$ | 1.5 | 87 |

Table 3. 3: Reaction times and conversions of short IND-, PHEN- and MTB-based copolymers.

| POLYMER | REACTION TIME (h) | CONVERSION (%) |
|---|---|---|
| IND$_1$-*b*-HEA$_{100}$ | 1.5 | 74 |
| PHEN$_1$-*b*-HEA$_{100}$ | 1.5 | 81 |
| MTB$_1$-*b*-HEA$_{111}$ | 1.5 | 91 |
| IND$_3$-*b*-HEA$_{98}$ | 1.25 | 82 |
| PHEN$_3$-*b*-HEA$_{99}$ | 1.25 | 78 |
| MTB$_3$-*b*-HEA$_{82}$ | 1.25 | 73 |
| IND$_{10}$-*b*-HEA$_{95}$ | 1.5 | 50 |
| PHEN$_{10}$-*b*-HEA$_{88}$ | 1.5 | 56 |
| MTB$_{10}$-*b*-HEA$_{105}$ | 1.5 | 81 |

The initial monomer concentration in the reaction solution was 3.0 M. The mixtures were transferred into small schlenk tubes equipped with a magnetic stirrer, which were put in ice. Initiator V 501 (0.1 eq.), previously dissolved in DMF, was added to each tube. The mixtures were degassed for 30 min bubbling argon under stirring at 0°C, and finally put on a paraffin oil bath at 70 ˚C. The reactions were monitored by $^1$H NMR, checking the disappearance of acrylamide monomer peaks into the 5-6.5 ppm region until ~ 80% conversion

was reached. The polymers were then repeadetly precipitated in a 8:2 v/v THF:Et$_2$O mixture and re-dissolved in MeOH. After three precipitation cycles they were dried under high vacuum. The polymers were analysed by $^1$H NMR and SEC in DMF with 0.1% LiBr.

IND$_1$-*b*-HEA$_{37}$ Yield: 75%. $^1$H NMR (400 MHz, d6-DMSO, δ, ppm), 7.80-7.40 (m, 37H, polyacrylamide NH), 7.34 (d, 1H, CH, CH aromatic), 7.24 (m, 1H, CH, CH aromatic), 7.08 (t, 1H, CH, CH aromatic), 6.99 (t, 1H, CH, CH aromatic), 5.50-4.30 (m, 37H, polyacrylamide OH), 4.04 (m, 2H, CH$_2$), 3.78 (m, 2H, CH$_2$), 2.10-1.70 (m, 37H, polyacrylamide *CH*CH$_2$) 1.60-1.20 (m, 74H, polyacrylamide CH*CH$_2$*) (Fig.S3.15). M$_{n,NMR}$: 5 kDa. Mn,$_{SEC(DMF)}$ 8.7 kDa, Đ=1.07.

PHEN$_1$-*b*-HEA$_{37}$ Yield: 78%. $^1$H NMR (400 MHz, d6-DMSO, δ, ppm): 7.80-7.40 (m, 37H, polyacrylamide NH), 7.35-7.22 (m, 5H, aromatic), 5.50-4.30 (m, 37H, polyacrylamide OH), 4.04 (m, 2H, CH$_2$), 2.10-1.70 (m, 37H, polyacrylamide *CH*CH$_2$) 1.60-1.20 (m, 74H, polyacrylamide CH*CH$_2$*) (Fig.S3.16). M$_{n,NMR}$: 4.8 kDa. Mn,$_{SEC(DMF)}$ 9 kDa, Đ=1.07.

MTB$_1$-*b*-HEA$_{37}$ Yield: 82%. $^1$H NMR (400 MHz, d6-DMSO, δ, ppm): 7.80-7.40 (m, 37H, polyacrylamide NH), 5.50-4.30 (m, 38H, polyacrylamide OH), 4.02 (m, 2H, CH$_2$), 2.10-1.70 (m, 38H, polyacrylamide *CH*CH$_2$) 1.60-1.20 (m, 76H, polyacrylamide CH*CH$_2$*), 1.07 (d, 3H, CH$_3$), 0.84 (t, 3H, CH$_3$) (Fig.S3.17). M$_{n,NMR}$: 4.8 kDa. M$_{n,SEC(DMF)}$ 10.4 kDa, Đ=1.05.

IND$_3$-*b*-HEA$_{53}$ Yield: 46%. $^1$H NMR (400 MHz, d6-DMSO, δ, ppm), 7.80-7.40 (m, 53H, polyacrylamide NH), 7.34 (d, 2.52H, CH, CH aromatic), 7.24 (m, 2.52H, CH, CH aromatic), 7.08 (t, 2.52H, CH, CH aromatic), 6.99 (t, 2.52H, CH, CH aromatic), 5.50-4.30 (m, 53H, polyacrylamide OH), 4.03 (m, 5.04H, CH$_2$), 3.74 (m, 5.04H, CH$_2$), 2.10-1.70 (m, 53H, polyacrylamide *CH*CH$_2$) 1.60-1.20 (m, 106H, polyacrylamide CH*CH$_2$*) (Fig.S3.18). M$_{n,NMR}$: 7.2 kDa. Mn,$_{SEC(DMF)}$ 11.7 kDa, Đ=1.09.

PHEN$_3$-*b*-HEA$_{45}$ Yield: 70%. $^1$H NMR (400 MHz, d6-DMSO, δ, ppm): 7.80-7.40 (m, 45H, polyacrylamide NH), 7.35-7.22 (m, 15H, aromatic), 5.50-4.30 (m, 45H, polyacrylamide OH), 4.05 (m, 6H, CH$_2$), 2.10-1.70 (m, 45H, polyacrylamide *CH*CH$_2$) 1.60-1.20 (m, 90H, polyacrylamide CH*CH$_2$*) (Fig.S3.19). M$_{n,NMR}$: 6.2 kDa. Mn,$_{SEC(DMF)}$ 9.6 kDa, Đ=1.07.

MTB$_3$-*b*-HEA$_{42}$ Yield: 80%. $^1$H NMR (400 MHz, d6-DMSO, δ, ppm): 7.80-7.40 (m, 42H, polyacrylamide NH), 5.50-4.30 (m, 42H, polyacrylamide OH), 4.02 (m, 6H, CH$_2$), 2.10-1.70 (m, 42H, polyacrylamide *CH*CH$_2$) 1.60-1.20 (m, 84H, polyacrylamide CH*CH$_2$*), 1.07 (d, 9H, CH$_3$), 0.84 (t, 9H, CH$_3$) (Fig.S3.20). M$_{n,NMR}$: 5.8 kDa. M$_{n,SEC(DMF)}$ 10.9 kDa, Đ=1.05.

$IND_{10}$-*b*-$HEA_{40}$ Yield: 46%. $^1$H NMR (400 MHz, d6-DMSO, δ, ppm), 7.80-7.40 (m, 40H, polyacrylamide NH), 7.34 (d, 10H, CH, CH aromatic), 7.24 (m, 10H, CH, CH aromatic), 7.08 (t, 10H, CH, CH aromatic), 6.99 (t, 10H, CH, CH aromatic), 5.50-4.30 (m, 40H, polyacrylamide OH), 4.03 (m, 20H, $CH_2$), 3.74 (m, 20H, $CH_2$), 2.10-1.70 (m, 40H, polyacrylamide *CH*$CH_2$) 1.60-1.20 (m, 80H, polyacrylamide CH*CH$_2$*) (Fig.S3.21). $M_{n,NMR}$: 7.7 kDa. $Mn_{,SEC(DMF)}$ 8.9 kDa, Đ=1.07.

$PHEN_{10}$-*b*-$HEA_{38}$ Yield: 70%. $^1$H NMR (400 MHz, d6-DMSO, δ, ppm): 7.80-7.40 (m, 38H, polyacrylamide NH), 7.35-7.22 (m, 50H, aromatic), 5.50-4.30 (m, 38H, polyacrylamide OH), 4.03 (m, 20H, $CH_2$), 2.10-1.70 (m, 38H, polyacrylamide *CH*$CH_2$) 1.60-1.20 (m, 76H, polyacrylamide CH*CH$_2$*) (Fig.S3.22). $M_{n,NMR}$: 7 kDa. $Mn_{,SEC(DMF)}$ 10.7 kDa, Đ=1.08.

$MTB_{10}$-*b*-$HEA_{43}$ Yield: 68%. $^1$H NMR (400 MHz, d6-DMSO, δ, ppm): 7.80-7.40 (m, 43H, polyacrylamide NH), 5.50-4.30 (m, 43H, polyacrylamide OH), 4.02 (m, 20H, $CH_2$), 2.10-1.70 (m, 43H, polyacrylamide *CH*$CH_2$) 1.60-1.20 (m, 86H, polyacrylamide CH*CH$_2$*), 1.07 (d, 30H, $CH_3$), 0.84 (t, 30H, $CH_3$) (Fig.S3.23). $M_{n,NMR}$: 7.7 kDa. $M_{n,SEC(DMF)}$ 10 kDa, Đ=1.07.

$IND_1$-*b*-$HEA_{100}$ Yield: 67%. $^1$H NMR (400 MHz, d6-DMSO, δ, ppm), 7.80-7.40 (m, 100H, polyacrylamide NH), 7.34 (d, 1H, CH, CH aromatic), 7.24 (m, 1H, CH, CH aromatic), 7.08 (t, 1H, CH, CH aromatic), 6.99 (t, 1H, CH, CH aromatic), 5.50-4.30 (m, 100H, polyacrylamide OH), 4.04 (m, 2H, $CH_2$), 3.78 (m, 2H, $CH_2$), 2.10-1.70 (m, 100H, polyacrylamide *CH*$CH_2$) 1.60-1.20 (m, 200H, polyacrylamide CH*CH$_2$*) (Fig.S3.24). $M_{n,NMR}$: 8.7 kDa. $M_{n,SEC(DMF)}$ 13.8 kDa, Đ=1.07.

$PHEN_1$-*b*-$HEA_{100}$ Yield: 81%. $^1$H NMR (400 MHz, d6-DMSO, δ, ppm): 7.80-7.40 (m, 100H, polyacrylamide NH), 7.35-7.22 (m, 5H, aromatic), 5.50-4.30 (m, 100H, polyacrylamide OH), 4.04 (m, 2H, $CH_2$), 2.10-1.70 (m, 100H, polyacrylamide *CH*$CH_2$) 1.60-1.20 (m, 200H, polyacrylamide CH*CH$_2$*) (Fig.S3.25). $M_n$,NMR: 12.2 kDa. $Mn,SEC_{(DMF)}$ 18.6 kDa, Đ=1.08.

$MTB_1$-*b*-$HEA_{111}$ Yield: 72%. $^1$H NMR (400 MHz, d6-DMSO, δ, ppm): 7.80-7.40 (m, 111H, polyacrylamide NH), 5.50-4.30 (m, 111H, polyacrylamide OH), 4.02 (m, 2H, $CH_2$), 2.10-1.70 (m, 111H, polyacrylamide *CH*$CH_2$) 1.60-1.20 (m, 222H, polyacrylamide CH*CH$_2$*), 1.07 (d, 3H, $CH_3$), 0.84 (t, 3H, $CH_3$) (Fig.S3.26). $M_{n,NMR}$: 13.2 kDa. $M_{n,SEC(DMF)}$ 19.8 kDa, Đ=1.09.

$IND_3$-*b*-$HEA_{98}$ Yield: 57%. $^1$H NMR (400 MHz, d6-DMSO, δ, ppm), 7.80-7.40 (m, 98H, polyacrylamide NH), 7.34 (d, 2.6H, CH, CH aromatic), 7.24 (m, 2.52H, CH, CH aromatic), 7.08 (t, 2.52H, CH, CH aromatic), 6.99 (t, 2.52H, CH, CH aromatic), 5.50-4.30 (m, 98H, polyacrylamide OH), 4.05 (m, 5.04H, $CH_2$), 3.74 (m, 5.04H, $CH_2$), 2.10-1.70 (m, 98H, polyacrylamide *CH*$CH_2$) 1.60-1.20 (m, 196H, polyacrylamide CH*CH$_2$*) (Fig.S3.27). $M_{n,NMR}$: 12 kDa. $M_{n,SEC(DMF)}$ 17 kDa, Đ=1.11.

$PHEN_3$-*b*-$HEA_{99}$ Yield: 66%. $^1$H NMR (400 MHz, d6-DMSO, δ, ppm): 7.80-7.40 (m, 99H, polyacrylamide NH), 7.35-7.22 (m, 15H, aromatic), 5.50-4.30 (m, 99H,

polyacrylamide OH), 4.04 (m, 6H, CH$_2$), 2.10-1.70 (m, 99H, polyacrylamide *CH*CH$_2$) 1.60-1.20 (m, 198H, polyacrylamide CH*CH$_2$*) (Fig.S3.28). M$_{n,NMR}$: 12.5 kDa. M$_{n,SEC(DMF)}$ 17.25 kDa, Đ=1.06.

MTB$_3$-*b*-HEA$_{82}$ Yield: 80%. $^1$H NMR (400 MHz, d6-DMSO, δ, ppm): 7.80-7.40 (m, 82H, polyacrylamide NH), 5.50-4.30 (m, 82H, polyacrylamide OH), 4.01 (m, 6H, CH$_2$), 2.10-1.70 (m, 82H, polyacrylamide *CH*CH$_2$) 1.60-1.20 (m, 164H, polyacrylamide CH*CH$_2$*), 1.07 (d, 9H, CH$_3$), 0.84 (t, 9H, CH$_3$) (Fig.S3.29). M$_{n,NMR}$: 10.5 kDa. M$_{n,SEC(DMF)}$ 16.8 kDa, Đ=1.07.

IND$_{10}$-*b*-HEA$_{95}$ Yield: 57%. $^1$H NMR (400 MHz, d6-DMSO, δ, ppm), 7.80-7.40 (m, 95H, polyacrylamide NH), 7.34 (d, 10H, CH, CH aromatic), 7.24 (m, 10H, CH, CH aromatic), 7.08 (t, 10H, CH, CH aromatic), 6.99 (t, 10H, CH, CH aromatic), 5.50-4.30 (m, 95H, polyacrylamide OH), 4.03 (m, 20H, CH$_2$), 3.74 (m, 2H, CH$_2$), 2.10-1.70 (m, 95H, polyacrylamide *CH*CH$_2$) 1.60-1.20 (m, 190H, polyacrylamide CH*CH$_2$*) (Fig.S3.30). M$_{n,NMR}$: 12 kDa. M$_{n,SEC(DMF)}$ 18.4 kDa, Đ=1.11.

PHEN$_{10}$-*b*-HEA$_{88}$ Yield: 60%. $^1$H NMR (400 MHz, d6-DMSO, δ, ppm): 7.80-7.40 (m, 88H, polyacrylamide NH), 7.35-7.22 (m, 50H, aromatic), 5.50-4.30 (m, 88H, polyacrylamide OH), 4.02 (m, 20H, CH$_2$), 2.10-1.70 (m, 88H, polyacrylamide *CH*CH$_2$) 1.60-1.20 (m, 176H, polyacrylamide CH*CH$_2$*) (Fig.S3.31). M$_{n,NMR}$: 12.9 kDa. M$_{n,SEC(DMF)}$ 17.4 kDa, Đ=1.07.

MTB$_{10}$-*b*-HEA$_{105}$ Yield: 80%. $^1$H NMR (400 MHz, d6-DMSO, δ, ppm): 7.80-7.40 (m, 105H, polyacrylamide NH), 5.50-4.30 (m, 105H, polyacrylamide OH), 4.02 (m, 20H, CH$_2$), 2.10-1.70 (m, 105H, polyacrylamide *CH*CH$_2$) 1.60-1.20 (m, 210H, polyacrylamide CH*CH$_2$*), 1.07 (d, 30H, CH$_3$), 0.84 (t, 30H, CH$_3$) (Fig.S3.32). M$_{n,NMR}$: 12.5 kDa. M$_{n,SEC(DMF)}$ 18.7 kDa, Đ=1.07.

SEC traces can be found in Fig. S3.36 and S3.37.

### 3.2.5. Synthesis of control polymer HEA$_{36}$

CTA agent (**10**) (150 mg, 0.53 mmol, 1 eq.), was dissolved with monomer HEA (2.48 g, 21.2 mmol, 40 eq.) in 3 mL of DMF. The mixture was transferred into a small schlenk tube equipped with a magnetic stirrer, which was put in ice. Initiator V 501 (17 mg, 0.053 mmol, 0.1 eq.), previously dissolved in DMF (170 μL), was added to the tube. The mixture was degassed for 30 min bubbling argon under stirring at 0°C, and finally put on a paraffin oil bath at 70 ˚C. The reaction was monitored by $^1$H NMR, checking the disappearance of acrylamide monomer peaks into the 5-6.5 ppm region, for 90 minutes until 80% conversion

was reached and the reaction was stopped. The polymer was then precipitated in THF and dried under high vacuum. The polymer was characterised by $^1$H NMR and SEC in DMF with 0.1% LiBr.

Yield: 80%. $^1$H NMR (400 MHz, d6-DMSO, δ, ppm): 7.80-7.40 (m, 36H, polyacrylamide NH), 5.50-4.30 (m, 36H, polyacrylamide OH), 2.10-1.70 (m, 36H, polyacrylamide *CH*CH$_2$) 1.60-1.20 (m, 72H, polyacrylamide CH*CH$_2$*) (Fig.S3.33).

$M_{n,THEO}$: 4.5 kDa. $M_{n,SEC(DMF)}$ 8.5 kDa, Đ=1.04.

## 3.2.6. Lysozyme aggregation assay

A lysozyme stock solution was prepared by dissolving the protein in water at a concentration of 100 mg/mL. 200 μL of this solution were added to 1800 μL of 100 mM phosphate buffer pH 12.3 in which the polymers had been previously dissolved, for a final lysozyme concentration of 10 mg/mL and a polymer: protein molar ratio of 1:1. From each polymer-protein mixture, 5 aliquots of 300 μL were transferred into a 96-well plate. The plate was loaded into a TECAN Spark 10M Multi-function Platereader. Absorbance at λ=500 nm was measured every 30 min for 24h at 30°C to monitor the increase of turbidity resulting from protein aggregation.

## 3.2.7. Binding of copolymers to insulin: solubility studies

An insulin stock solution was prepared by dissolving the protein in 10 mM phosphate buffer pH 2 at a concentration of 4 mg/mL. Polymers stock solutions were prepared by dissolving various amounts of polymers in the same buffer. Different amounts of insulin and polymers stock solutions were mixed to have a final protein concentration of 2 mg/mL and polymer:protein molar ratio of 5:1 and 10:1 in a final volume of 485 μL. After mixing, polymer/protein solutions were let under gentle stirring for 2 h. The pH was then raised to 5.3 by adding

15 µL of NaOH 0.5 M solution to each of the polymers:protein mixtures, which were left overnight at ambient temperature. The mixtures were then centrifuged, the supernatants discarded, and the precipitates re-dissolved in 10 mM pH2 phosphate buffer to be analysed by RP-HPLC, using a Zorbax Eclipse Plus C18 column (3.5 µm, 95 Å, 4.6 × 12.5 mm), with a linear gradient of 20-90% acetonitrile in Milli-q water with 0.1% TFA.

### 3.2.8. Binding of copolymers to insulin: Circular Dichroism analysis

Circular Dichroism (CD) analyses were conducted at Universtiy of Cambridge by Dr. Marco di Antonio. Spectra were recorded on an Applied Photo-physics Chirascan circular dichroism spectropolarimeter using a 1 mm path length quartz cuvette. CD measurements were performed at 25°C over a 180-280 nm wavelength range, using a response time of 1 s, 1 nm pitch and 0.5 nm bandwidth. The recorded spectra represent a smoothed of the original scan. An insulin stock solution was prepared by dissolving the protein in 10 mM pH 2 phosphate buffer at a concentration of 4 mg/mL. $IND_{10}$-*b*-$HEA_{95}$ stock solution was prepared by dissolving the polymer in the same buffer at 98.4 mg/mL. Different amounts of insulin and polymers stock solutions were mixed to have a final protein concentration of 2 mg/mL and polymer:protein molar ratio of 5:1 and 10:1 in a final volume of 990 µL. After mixing, polymer/protein solutions were let under gentle stirring for 2 h. The pH was then raised to 5.3 by adding 10 µL of NaOH 1 M solution to each of the polymers/protein mixtures. The mixtures were then purified by semi-preparative HPLC, using a Phenomenex Jupiter C18 column (10 µm, 300 Å, 10 × 250 mm), with a linear gradient of 30-

60% acetonitrile. Purified protein samples were lyophilised and re-dissolved in 10 mM pH 2 phosphate buffer at a concentration of 0.2 mg/mL. pH was raised again to 7.4 before the analysis.

### 3.2.9. Binding of copolymers to peptide IDR1018: solubility studies

A 1.0 mM peptide stock solution was prepared in water. 0.11 mM polymers stock solutions were prepared by dissolving the polymers in 100 mM phosphate buffer, pH 7.2. 50 μL of peptide were diluted in 450 μL of each polymer solution, for a final volume of 500 μL and a concentration of 0.10 mM for both peptide and the polymers. The solutions were let under stirring for 5 h and finally centrifuged. The supernatant was analysed by RP-HPLC to detect the amount of peptide left in solution, using a Zorbax Eclipse Plus C18 column (3.5 μm, 95 Å, 4.6 × 12.5 mm), with a linear gradient of 25-90% acetonitrile in Milli-q water with 0.1% TFA. Absorbance was recorded at $\lambda$= 280 nm.

### 3.2.10. Analysis of potential polymers self-assembly

The polymers were dissolved in Milli-Q water at a concentration of 1 mg/mL. The solutions were left mixing for 2 h, and then analysed using a Malvern Zetasizer Nano. 3 repetitions were made for each sample.

### 3.2.11. Critical Micelle Concentration measurements of IND$_3$-*b*-HEA$_{98}$ and IND$_{10}$-*b*-HEA$_{95}$

IND$_3$-*b*-HEA$_{98}$ and IND$_{10}$-*b*-HEA$_{95}$ were dissolved in Milli-Q water at concentrations ranging from 0.05 to 15 mg/mL. The surface tension of each copolymer dilution was measured on a Kruss DSA 100 using the "pendant drop"

method. Two droplets were analysed per sample, taking multiple measurement

from each droplet.

## 3.3. Results and discussion

This chapter was dedicated to the synthesis of a library of amphiphilic block copolymers, incorporating amino acid-like chemical structure, capable of hydrophobic, non-covalent interactions with hydrophobic pockets on proteins, as a class of new potential proteins stabilizers/solubilizers.

Since tryptophan is the amino acid that we chose to use to establish these interactions, we mimicked its structure by synthesising an indole-containing monomer, as indole is tryptophan side-chain and it is the part of tryptophan which is ultimately responsible for its properties[8]. The minimization approach provided us with a monomer that could be oligomerised *via* RAFT polymerization to yield short oligomers bearing varying indole units. These oligomers were used as macro CTA RAFT agents to mediate the copolymerisation of *N*-hydroxyethylacrylamide. As in the previous chapter, the monomer was chosen for its high hydrophilicity, to develop a hydrophilic chain that could ensure good water solubility of final copolymers. To compare the effects of one or more indoles with that of different amino acids side chains, two more monomers were synthesised, oligomerised and copolymerised. The first was built from phenylacetic acid, and was effectively a minimised version of phenylalanine[9], the second resulted from methylbutyric acid, and its structure resembled that of isoleucine. The oligomerization and copolymerization of the 3 monomers resulted in the development of a copolymers library (Scheme 3.4), whose properties where screened, to assess potential protein anti-aggregation and solubilisation activity, on three different

model proteins: hen egg lysozyme, bovine pancreatic insulin and the antimicrobial peptide IDR 1018.
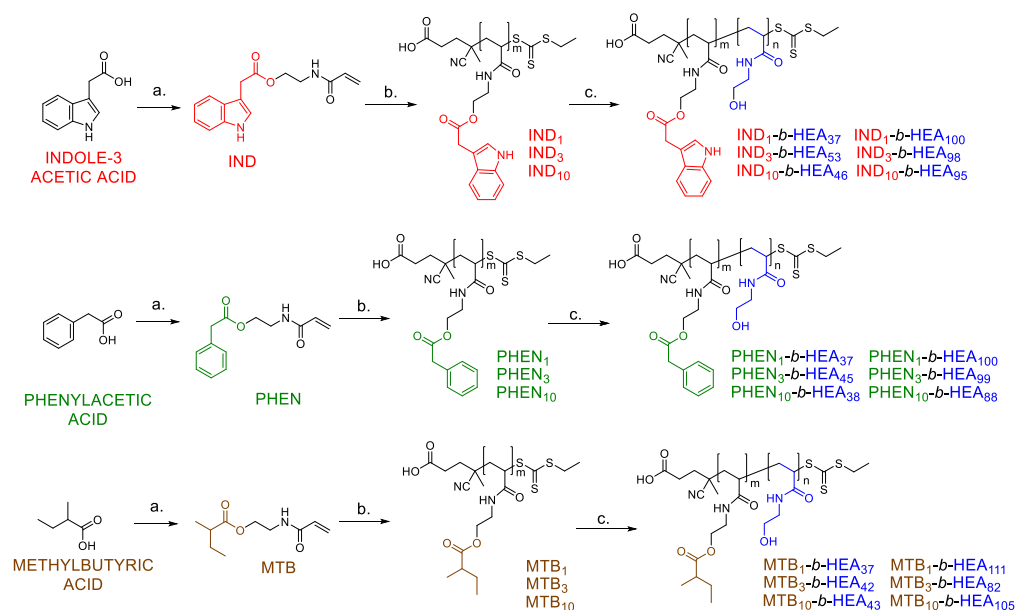


Scheme 3.4: Synthesis of $IND_m$-, $MTB_m$- and $PHEN_m$-b-$HEA_n$ amphiphilic block copolymers. *Reagents and conditions*: (a) EDC-HCl, DMAP, *N*-hydroxyethylacrylamide, room temperature. (b) AIBN, CTA (**10**), DMF at 80ºC. (c) *N*-hydroxyethylacrylamide, V501, DMF at 70 ˚C.

### 3.3.1. Synthesis of IND, (PHEN) and (MTB) monomers

The synthesis of IND, PHEN, and MTB monomers was accomplished by esterification of *N*-hydroxyethylacrylamide with three different acid precursors: Indole-3 acetic acid, phenylacetic acid and methylbutyric acid using EDC-HCl[10] as coupling agent. Chemical identity of the three monomers was confirmed by using a range of characterization techniques (see Supporting Information). The ^{1}H NMR and mass spectra of monomer IND are shown in Figure 3.3 and 3.4, respectively.
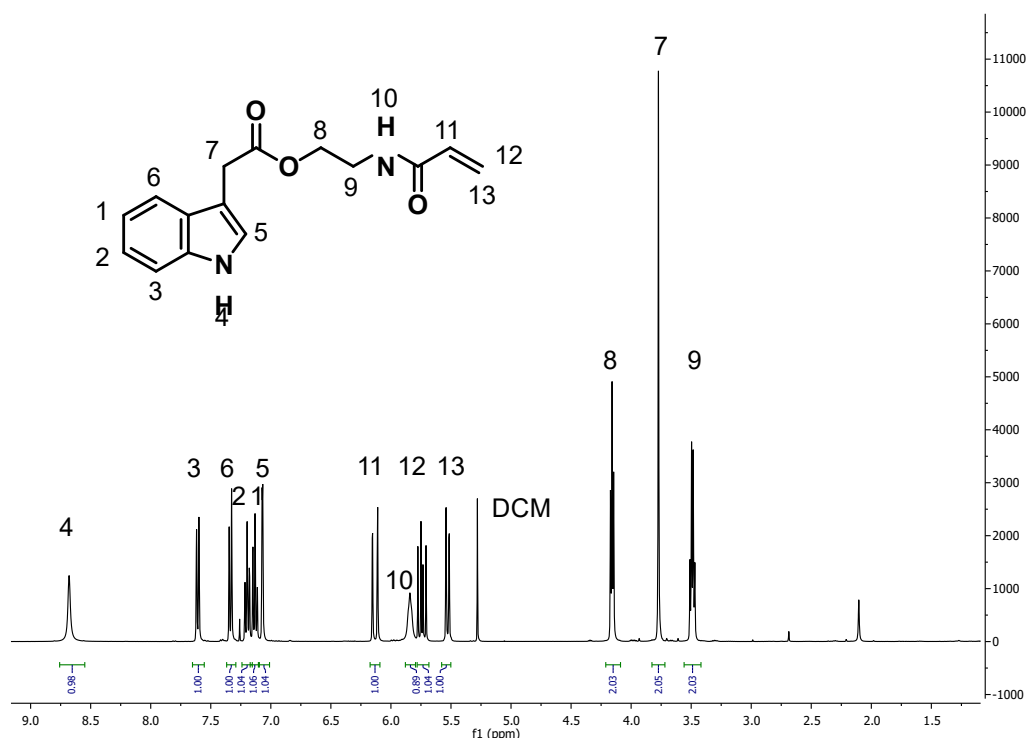
Figure 3.3: $^1$H NMR spectrum of monomer IND in CDCl$_3$.
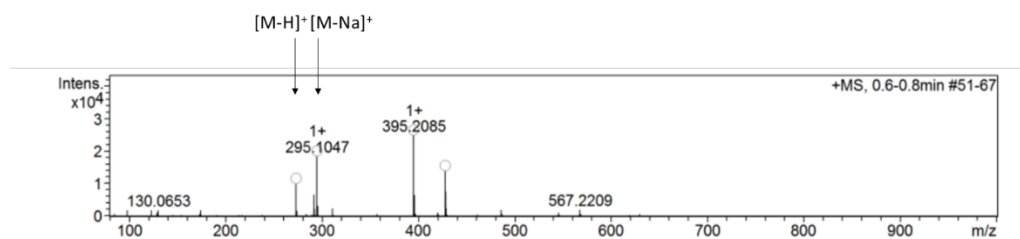


Figure 3.4: ESI-MS analysis of monomer IND. Two peaks are identified: peak at 273.1 m/z corresponds to [M-H]$^+$, that at 295.1 to [M-Na]$^+$.

## 3.3.2. Synthesis of oligomeric CTAs IND$_1$, PHEN$_1$, MTB$_1$, IND$_3$, PHEN$_3$, MTB$_3$, IND$_{10}$, PHEN$_{10}$ and MTB$_{10}$

In this part of this thesis work, three small libraries of oligomeric hydrophobic RAFT chain transfer agents with DP in the 1-10 range were synthesised. Accordingly, CTA **(10),** synthesised as described in Chapter 2, was used to mediate the RAFT polymerization of the three monomers IND, PHEN and MTB. DP of 1, 3 and 10 were targeted. The [CTA **(10)**]$_0$:[monomer]$_0$ molar ratios were chosen accordingly.  Oligomeric CTAs with an average DP of 10, IND$_{10}$, PHEN$_{10}$

and MTB$_{10}$, were synthesised using a CTA:monomer molar ratio of 1:12.5. The reactions were stopped at a monomer conversion of around 80%, which was typically reached within a few hours. Interestingly, the synthesis of IND$_{10}$ was found more difficult, as polymerisation was slower than for the other monomers, requiring 1-2 further additions of AIBN initiator over 24 h to reach 80% conversion. Whilst this result was quite difficult to rationalise at this stage and was not specifically investigated, it is possible that partial indole-driven aggregation of the growing chain in DMF could have been responsible for this behaviour. The IND$_{10}$, PHEN$_{10}$ and MTB$_{10}$ oligomers were isolated by precipitation and used without any further purification. Their chemical identity was confirmed by $^1$H NMR and SEC (Table 3.1). The discrepancy between M$_{n,SEC}$ and the expected ones may be ascribed to differences between the hydrodynamic volumes of the oligomeric CTAs and those of the narrow PMMA standards used to calibrate the SEC (see Fig S.3.43 for SEC traces).

Table 3.4: Composition, M$_n$, and dispersity of the short hydrophobic-oligomers prepared in this study.

| Name | Hydrophobic monomer | Average hydrophobic monomer units, m | M$_{n,THEO}$[a] (kDa) | M$_{n,SEC}$ (kDa)[b] | Đ[b] |
|---|---|---|---|---|---|
| IND$_{10}$ | IND | 10 | 3.0 kDa | 1.56 | 1.12 |
| PHEN$_{10}$ | PHEN | 11 | 2.6 kDa | 1.60 | 1.09 |
| MTB$_{10}$ | MTB | 10 | 2.2 kDa | 1.47 | 1.10 |

[a]Calculated from initial [HEA]$_0$:[CTA]$_0$ and final monomer conversion [b]Obtained from SEC analysis in THF (PMMA standard).

Aiming at obtaining fully monodisperse RAFT agents, chromatographic purification of CTAs with targeted DP of 1 and 3 were attempted. Isolation of individual n-mers from oligomeric mixtures is a challenging task, for which Size Exclusion Chromatography is a potentially useful technique. It allows the

elution of molecules at different retention times according to their size. It is then successfully employed to separate proteins with considerable differences in MW, or protein aggregates that have generated a multimeric population[11]. Oligomers separation is more difficult due to the small size difference between the species in solution, but it has proven successful for specific oligomers mixture of low molecular weight[12]. As the Mn increases, separation of a polymer of *n* units from one of *n+1* units becomes more difficult[12]. Poly(ethylene Terephthalate) cyclic oligomers were successfully separated by SEC, affording pure dimer, trimer, tetramer and pentamer[13].

Monomer, dimer and trimer of different fatty acids were successfully separated using a High Performance SEC system made of two connected columns packed with styrene/divinylbenzene copolymer as stationary phase and toluene as the eluent[14].

In another work, RAFT polymerization was used for the sequential insertion of up to four monomers. The oligomerization was organised in steps, where 10 equivalents of monomer were added each time, followed by ten minutes polymerization and *n+1* oligomer purification by SEC[15].

Recently, a group of tert-butyl acrylate oligomers was synthesised and separated by Hawker et al[16]. In this case, an automated chromatographic system was used, running a hexane/ethyl acetate solvent gradient on a silica gel-filled column. Shorter oligomers were eluted first, suggesting that separation was based on oligomer-silica interactions rather than size exclusion. Discrete oligomers from trimer to decamer were successfully purified.

In our case, two different chromatographic techniques were employed to attempt discrete separation of pure oligomers. CTAs incorporating only one monomer units were purified by standard silica gel column chromatography, using a Pet.Et./Ethyl acetate gradient as the mobile phase. The RAFT oligomerisations were performed using a starting 1:1.25 [CTA **(10)**]$_0$:[monomer]$_0$ molar ratio. After flash chromatography IND$_1$, PHEN$_1$ and MTB$_1$, were isolated and characterised by $^1$H NMR, $^{13}$C NMR and COSY. A representative example, IND$_1$, is shown in Fig. 3.5.
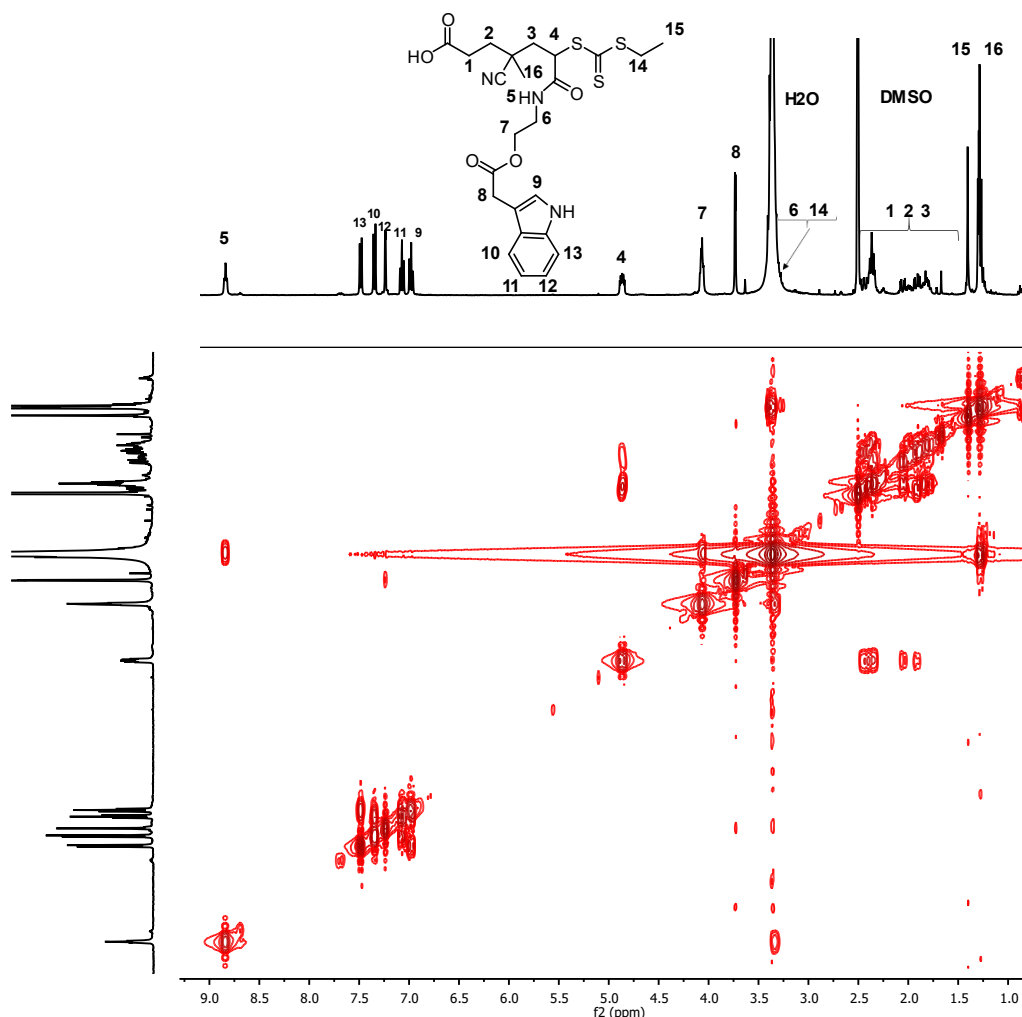


Figure 3.5: 2D COSY-NMR spectrum of IND$_1$ in d$_6$-DMSO. Peaks of protons 6 and 14 are hidden by water peak.

A 1:4 [CTA **(10)**]$_0$:[monomer]$_0$ molar ratio was used to target a DP of 3. In this case, initial purification attempts by silica gel chromatography proved to be unsuccessful. Mixtures of two or more oligomers were collected from the elution of oligomers with DP higher than 1, indicating that the similarity between them was a serious limitation to their separation. Different eluting solvents were tested without any improvement.

Thus, reverse phase chromatography was utilised. In this case, due to the hydrophobic nature of the stationary phase, a solvent gradient of increased hydrophobicity is employed and more hydrophilic compounds are eluted first. Reverse phase chromatography has been used in the past to obtain discrete oligomers purification. Cramers and co-workers utilised a range of different columns and mobile phases to separate 3-hexylthiophene oligomers with 3-30 repeating units[17]. Rissler *et al* compared C18 reversed-phase and Si80 polar stationary phases to optimise the separation of low molecular weight PEG oligomers, and found better peak resolution on reversed phase for PEG200 and PEG300 chain[18].

Given the hydrophobic nature of the IND, PHEN, and MTB monomers used for the synthesis of the oligomeric CTAs, we expected that the hydrophobicity of the latter would increase with their molecular weight, and thus that larger CTAs would be eluted later in a reversed-phase chromatographic separation. A pre-filled C18 silica-bonded cartridge was employed, using a 20-80% acetonitrile gradient in water as the mobile phase. The purification of PHEN and MTB oligomers gave good results, leading to the successful separation of dimer,

trimer, tetramer, pentamer and hexamer CTAs resulting from PHEN oligomerization, and dimer, trimer, tetramer and pentamer from MTB oligomerization. As expected, compounds with lower DP were eluted first, whilst larger oligomers were eluted last, at higher concentrations of acetonitrile and came out in larger peaks, confirming a stronger affinity to the hydrophobic stationary phase. Purification of indole oligomers was partially successful, providing the elution of pure dimer and a mixture of dimer and trimer. The other fractions that were collected were found to be a mixture of dimer, trimer, tetramer and pentamer. The poor resolution may be attributed to a stronger interaction of the indole side chain with the stationary phase, which caused the oligomers to be eluted slowly over time, with subsequent poor resolution and peaks overlapping. Moreover, self-interactions between indole aromatic rings may have induce the formation of large aggregates, containing a mixture of different oligomers that were eluted together. The purified oligomers were characterised by ^{1}H NMR and ESI-MS (Figs. 3.6, 3.7 and 3.8).
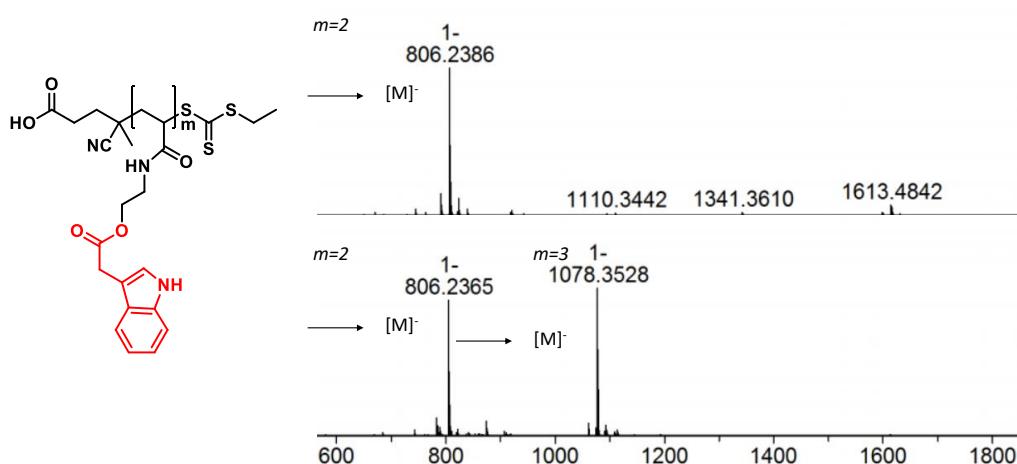


Figure 3.6: ESI-MS spectra of purified IND$_2$ and a partially purified mixture of IND$_2$ and IND$_3$ RAFT agents (m= 2 and 3) isolated after reversed-phase chromatographic separation of an average DP ≈ 3 oligomers mixture.
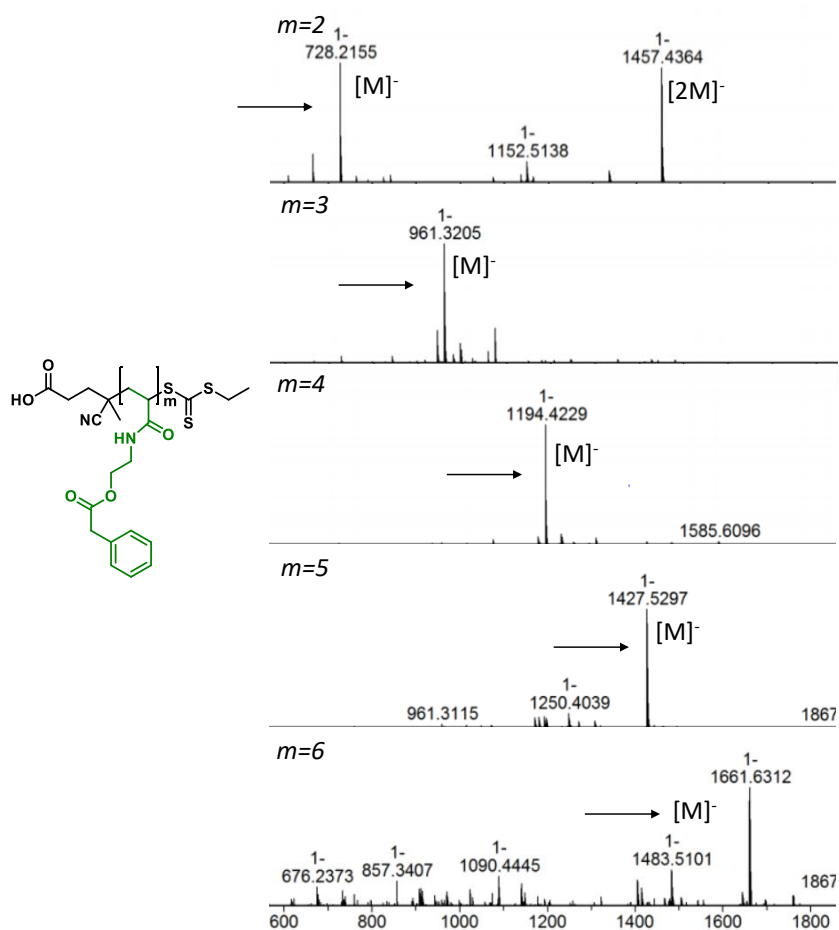
Figure 3.7: ESI-MS spectra of purified PHEN$_m$ RAFT agents (m= 2, 3, 4, 5 and 6) isolated after reversed-phase chromatographic separation of an average DP ≈ 3 oligomers mixture. Peak at 1457.4 in the m= 2 spectrum can be attributed to non-covalent dimerization between two PHEN$_2$ molecules.
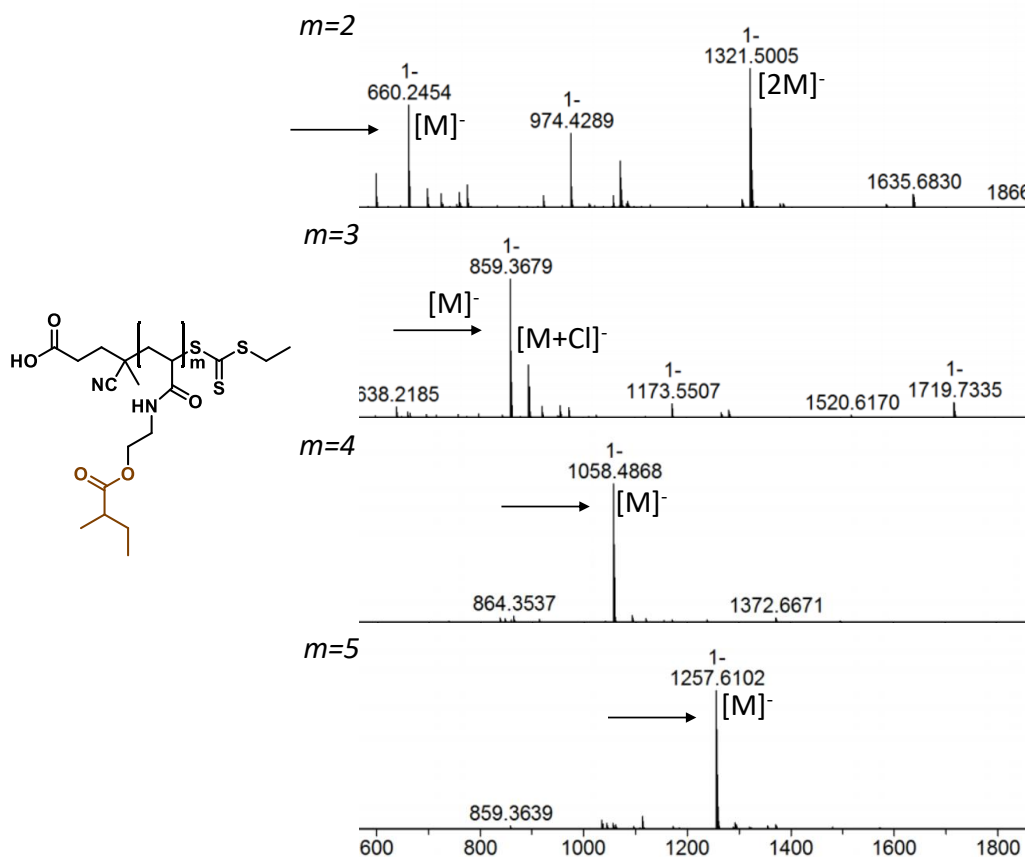
Figure 3.8: ESI-MS spectra of purified MTB$_m$ RAFT agents (m= 2, 3, 4, and 5) isolated after reversed-phase chromatographic separation of an average DP ≈ 3 oligomers mixture. Peak at 1321.5 in the n= 2 spectrum can be attributed to non-covalent dimerization between two MTB$_2$ molecules.

A comparison between the $^1$H NMR spectra of IND$_1$, IND$_3$ and IND$_{10}$ showed that the signals become broader and less defined as the DP increases (Fig 3.9). Polymer peaks are usually broad, due to magnetic dipolar interactions between the protons on the polymer backbone[19], slow nuclei longitundinal relaxation time[20] and polymer chain microtacticity[21].
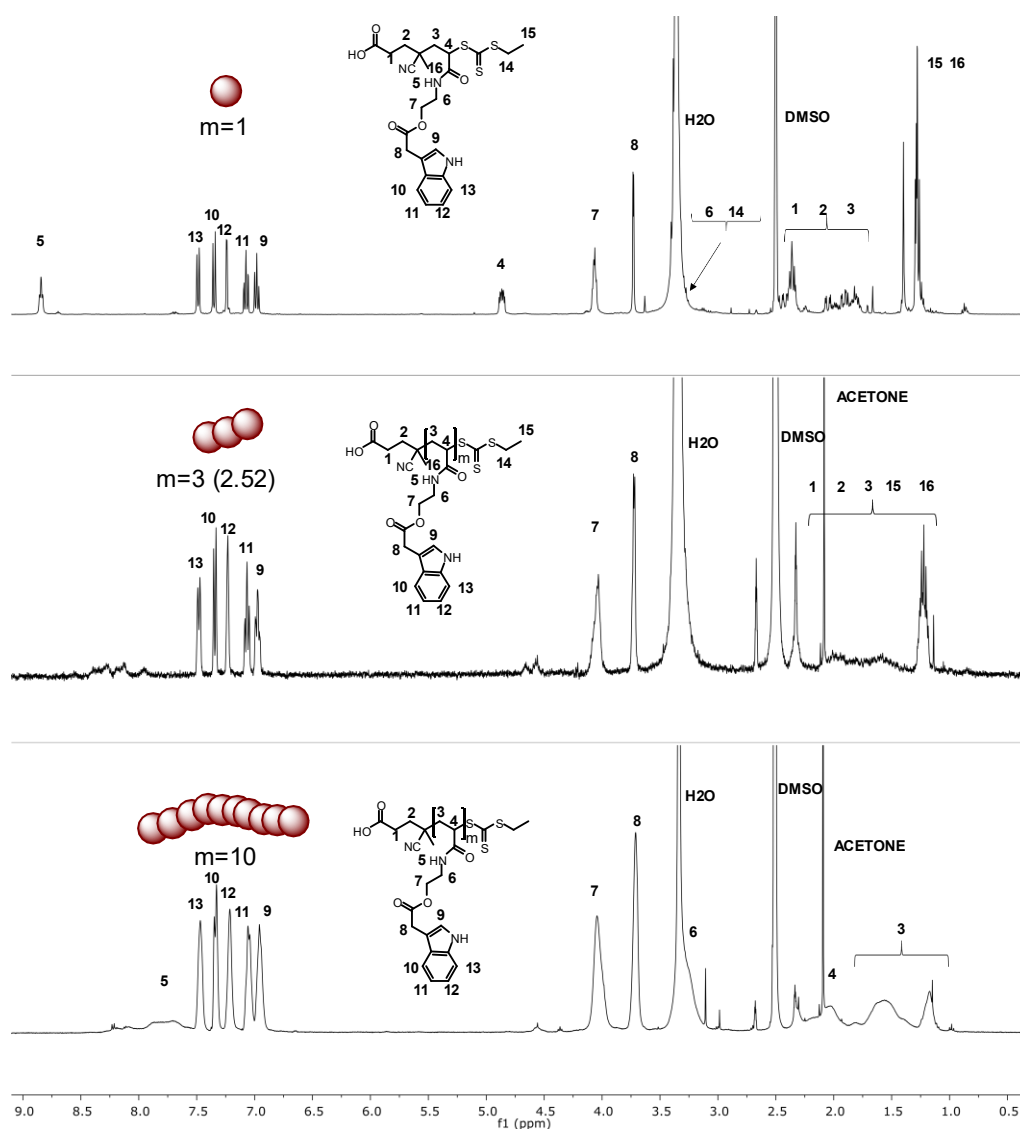
Figure 3.9: $^1$H NMR spectra of oligomeric CTA RAFT agents $IND_1$, $IND_3$ and $IND_{10}$ in $d_6$-DMSO.

### 3.3.3. Synthesis of $IND_1$-, $PHEN_1$-, $MTB_1$-, $IND_3$-, $PHEN_3$-, $MTB_3$-, $IND_{10}$-, $PHEN_{10}$- and $MTB_{10}$-copolymers

The trimers obtained from PHEN and MTB oligomerizations, $PHEN_3$ and $MTB_3$, and the dimer/trimer mixture from IND oligomerization, called here $IND_3$ for simplicity, were then utilised as macro-CTA RAFT agents to mediate the RAFT polymerisation of *N*-hydroxyethylacrylamide, together with $IND_1$, $PHEN_1$, $MTB_1$, $IND_{10}$, $PHEN_{10}$ AND $MTB_{10}$.

RAFT polymerization is widely used for the synthesis of block-copolymers, ensuring good polymerization control and narrow polymer molecular weight dispersity[22-24].

Two different chain lengths, with DP 40 and 100, were targeted, to investigate the influence of the size of the polyHEA block on protein-copolymer interaction. The combination of nine oligomeric RAFT agents and two different p(HEA) chains length resulted in the synthesis of a library of eighteen amphiphilic $IND_m$-$b$-$HEA_n$, $PHEN_m$-$b$-$HEA_n$, and $MTB_m$-$b$-$HEA_n$ block co-polymers. A control polymer lacking the hydrophobic block was synthesised using CTA (**10**) as RAFT agent and *N*-hydroxyethylacrylamide (Scheme 3.5). The resulting $HEA_{36}$ together with $HEA_{100}$ synthesised in the previous chapter, were used as negative control polymers in the subsequent protein-polymers association experiments, as they had similar *N*-hydroxyethylacrylamide DP of the block copolymers.



$HEA_{36}$ $M_{n,THEO}$: 4.5 kDa. $M_{n,SEC}$ 8.5 kDa , PDI=1.04
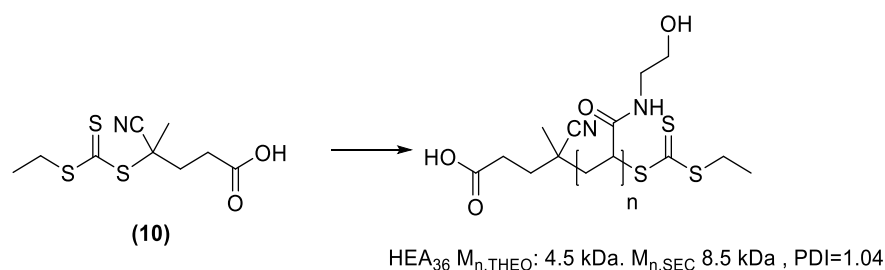
Scheme 3.5: synthesis of $HEA_{36}$. *Reagents and conditions*: *N*-hydroxyethylacrylamide, V501, DMF at 70 °C.

A representative example of ^{1}H NMR of these amphiphilc bock copolymers, $IND_{10}$-$b$-$HEA_{95,}$ is shown in Figure 3.10. For $IND_m$-$b$-$HEA_n$ copolymers, $M_{n,NMR}$ were calculated by comparing the integrals of the indole aromatic signals in the

6-8 ppm region, with those of the NH and OH groups of the pHEA block. For PHEN$_m$-*b*-HEA$_n$ copolymers, the two protons of the methylene CH$_2$ at around 4 ppm were used instead. Finally, for PHEN$_m$-*b*-HEA$_n$ copolymers, the triplets from the MTB methyl groups at around 0.8 ppm were used (all spectra can be found in the Supp. Info section at the end of this thesis). Degrees of polymerisation estimated by $^1$H NMR were generally found to be close to the theoretical ones, calculated from the initial [monomer]$_0$:[Oligo CTA]$_0$ ratios and final monomer conversion. However, it was noticed that calculated values became increasingly higher than theoretical ones as the size of the hydrophobic block increased. In particular, for IND$_{10}$-*b*-HEA$_n$ copolymers the final HEA$_n$ chain length was found to be approximately 25% longer than expected from theoretical values, suggesting that part of IND$_{10}$ CTA was unable to efficiently mediate RAFT polymerisation of HEA. The difference may be attributed to the high hydrophobicity of IND$_{10}$, which may have reduced their solubility in DMF, or caused their partial aggregation. Moreover, as IND$_{10}$ oligomerisation was slower than the others and required more than one addition of initiator, the lack of reactivity of the final product may be explained with partial chain termination that the excess of initiator caused during the oligomerization[25, 26]. Loss of the trithiocarbonate functionality could not be verified by $^1$H NMR, as the peaks belonging to the RAFT agent are covered by the oligomer backbone peaks. If a fraction of trithiocarbonate RAFT agent functionalities had been lost, that could be maybe verified by UV-analysis, as the trithiocarbonate functional group has a distinctive peak at ca. 350 nm. Potential aggregation in DMF could

be instead verified by Dynamic Light Scattering. This point was not addressed

at this stage, but it is part of ongoing research within our group.
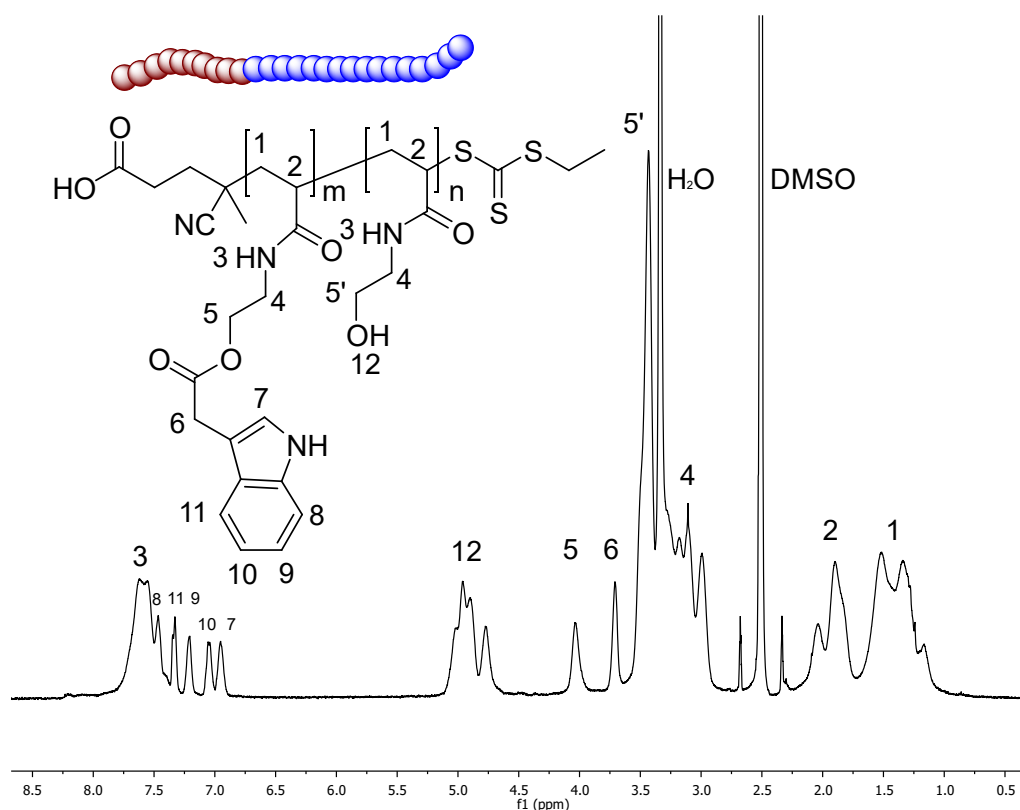


Figure 3.10: $^1$H NMR spectrum of IND$_{10}$-*b*-HEA$_{95}$ in d$_6$-DMSO. M$_{n,NMR}$ was determined by comparing the integrals of indole aromatic protons between 6.8 and 7.3 ppm, with those of NH and OH groups of the pHEA at 7.5-7.8 and 4.6-5.2 ppm, respectively and those of the polymer backbone between 1 and 2 ppm.

Characterisation of final copolymers is shown in Tables 3.1 and 3.2. As for the

oligomeric CTA RAFT agents, The discrepancy between M$_{n,SEC}$ and the expected

ones may be ascribed to differences between the hydrodynamic volumes of the

oligomeric CTAs and those of the narrow PMMA standards used to calibrate the

SEC. however, they all showed a narrow molar mass distribution, with Đ < 1.2

for all copolymers (See Fig S.3.44 and S3.45 for SEC traces).

Table 3.5: Composition, $M_n$, and dispersity of 40 HEA-DP copolymers prepared in this study.

| NAME | Hydrophobic monomer | Hydrophobic monomer units, m | Hydrophilic HEA monomer units, n | $M_{n,THEO}$[a] (kDa) | $M_{n,NMR}$ (kDa) | $M_{n,SEC}$[e] (kDa) | Đ |
|---|---|---|---|---|---|---|---|
| $IND_1$-*b*-$HEA_{37}$ | IND | 1 | 37 | 5.5 | 5.0[b] | 8.7 | 1.07 |
| $PHEN_1$-*b*-$HEA_{37}$ | PHEN | 1 | 37 | 5.1 | 4.8[c] | 9 | 1.07 |
| $MTB_1$-*b*-$HEA_{37}$ | MTB | 1 | 37 | 5.9 | 4.8[d] | 10.4 | 1.05 |
| $IND_3$-*b*-$HEA_{53}$ | IND | 2.52 | 53 | 5.4 | 6.7[b] | 11.7 | 1.09 |
| $PHEN_3$-*b*-$HEA_{45}$ | PHEN | 3 | 45 | 5.4 | 6.2[c] | 9.6 | 1.07 |
| $MTB_3$-*b*-$HEA_{42}$ | MTB | 3 | 42 | 6.4 | 7.3[d] | 10.9 | 1.05 |
| $IND_{10}$-*b*-$HEA_{40}$ | IND | 10 | 40 | 6.1 | 7.7[b] | 10.5 | 1.15 |
| $PHEN_{10}$-*b*-$HEA_{38}$ | PHEN | 10 | 38 | 6.8 | 7.0[c] | 10.7 | 1.08 |
| $MTB_{10}$- *b*-$HEA_{43}$ | MTB | 10 | 43 | 6.7 | 7.2[d] | 10 | 1.07 |
| $HEA_{36}$ | - | 0 | 36 | 4.5 | | 8.5 | 1.04 |

[a]Calculated from initial [HEA]$_0$:[CTA]$_0$ and final monomer conversion.[b-d]Number of repeating unit of NHEA monomers, were calculated by $^1H$ NMR by comparing the integral of [b]indole aromatic proton peak, [c]methylene protons at 4 ppm and [d]methylbutyril $CH_3$ peak with the hydroxyl peak of HEA repeating units. [e]Obtained from SEC analysis in DMF + 0.1% LiBr (PMMA standards).

Table 3.6: Composition, Mn, and dispersity of 100 HEA-DP copolymers prepared in this study.

| NAME | Hydrophobic Monomer | Hydrophobic monomer units, m | Hydrophilic monomer HEA units, n | $M_{n,THEO}$[a] (kDa) | $M_{n,NMR}$ (kDa) | $M_{n,SEC}$[e] (kDa) | Đ |
|---|---|---|---|---|---|---|---|
| $IND_1$-*b*-$HEA_{100}$ | IND | 1 | 100 | 9 | 8.7[b] | 13 | 1.08 |
| $PHEN_1$-*b*-$HEA_{100}$ | PHEN | 1 | 100 | 12 | 12.2[c] | 18.6 | 1.08 |
| $MTB_1$-*b*-$HEA_{111}$ | MTB | 1 | 111 | 13.1 | 13.2[d] | 19.8 | 1.09 |
| $IND_3$-*b*-$HEA_{98}$ | IND | 2.52 | 98 | 11.5 | 12 [b] | 17 | 1.11 |
| $PHEN_3$-*b*-$HEA_{99}$ | PHEN | 3 | 99 | 11.7 | 12.5[c] | 17.5 | 1.06 |
| $MTB_3$-*b*-$HEA_{82}$ | MTB | 3 | 82 | 10.2 | 10.5[d] | 16.8 | 1.07 |
| $IND_{10}$-*b*-$HEA_{95}$ | IND | 10 | 95 | 10.7 | 14.1[b] | 18.4 | 1.11 |
| $PHEN_{10}$-*b*-$HEA_{88}$ | PHEN | 10 | 88 | 12.6 | 12.9[c] | 17.4 | 1.07 |
| $MTB_{10}$-*b*-$HEA_{105}$ | MTB | 10 | 105 | 12.5 | 15[d] | 18.7 | 1.07 |
| $HEA_{100}$ | - | 0 | 100 | 13 | | 12.1 | 1.14 |

[a]Calculated from initial [HEA]$_0$:[CTA]$_0$ and final monomer conversion. [b-d]Number of repeating unit of NHEA monomers, were calculated by $^1H$ NMR by comparing the integral of [a]indole aromatic proton peak, [b]methylene $CH_2$ protons at 4 ppm and [c]methylbutyril $CH_3$ with the hydroxyl peak of HEA repeating units. [e]Obtained from SEC analysis in DMF + 0.1% LiBr (PMMA standards).

## 3.3.4. Prevention of lysozyme aggregation

The polymers were tested on hen egg lysozyme to evaluate their potential as anti-aggregation agents. The experiments were carried out under the same conditions used in Chapter 2. Briefly, the copolymers and the protein were mixed at 1:1 molar ratio in 100 mM phosphate buffer pH 12.33, and left under shaking for 24 h. Lysozyme aggregation was estimated by turbidimetry (Figs 3.11 and 3.12).
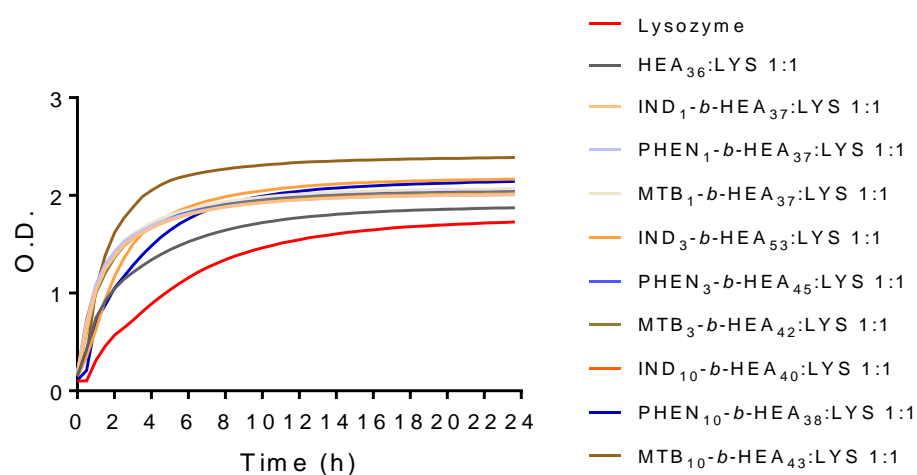


Figure 3.11: aggregation assay of Lysozyme and a mixture between 40 HEA-DP copolymers and lysozyme at 1:1 copolymers:lysozyme molar ratio. [Lysozyme]= 10 mg/mL in 100 mM pH 12.3 phosphate buffer. Lysozyme aggregation was assessed by turbidimetry, recording Abs λ=500 nm every 30 min for 24.

Interestingly, the copolymers did not delay the onset of lysozyme aggregation, and from the final turbidity values it can be observed that when the copolymers are mixed with the protein, the final amount of aggregated lysozyme is higher than the one resulting from the control sample with lysozyme alone. In the presence of the block copolymers, the aggregation rate in the first few hours was also found to be faster, suggesting that all copolymers induced lysozyme

aggregation. The negative control HEA$_{36}$ also accelerated protein aggregation, as already observed in the experiments described in the previous chapter, even though its overall turbidity at the end of the experiment is similar to that of the lysozyme alone control sample.
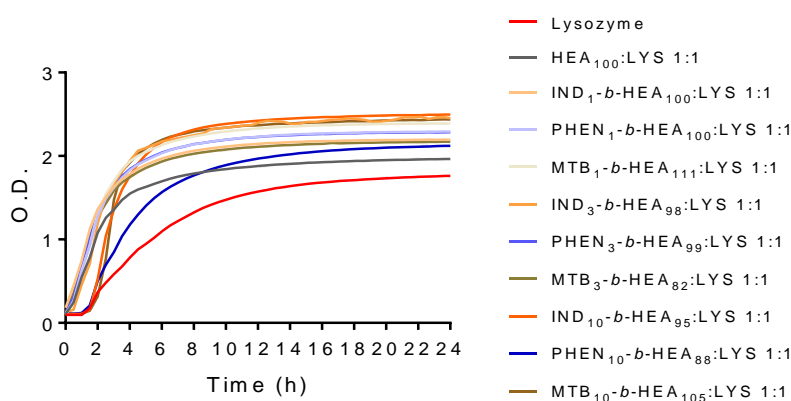


Figure 3.12: aggregation assay of Lysozyme and a mixture between 100 HEA-DP copolymers and lysozyme at 1:1 copolymers:lysozyme molar ratio. [Lysozyme]= 10 mg/mL in 100 mM pH 12.3 phosphate buffer. Lysozyme aggregation was assessed by turbidimetry, recording Abs at 500 nm every 30 min for 24.

The second sub-family of copolymers, with a HEA$_{82-111}$, were also found to induce aggregation and to increase the final amount of aggregated lysozyme. Again, the extent of protein aggregation was found to be independent from the composition and length of copolymers' hydrophobic blocks. The negative control polymer HEA$_{100}$ induces protein aggregation, while its final turbidity levels are lower than the ones observed with copolymers.

As mentioned in this chapter's introduction, a similar experiment was performed by Tudor Arvinte's group, where lysozyme aggregation was induced in the presence of different polymers, and PEG-tryptophan showed a moderate, one hour-delay of lysozyme aggregation onset[7]. A similar behaviour

could be expected from our IND-terminating copolymers, in particular $IND_1$-*b*-$HEA_{37}$ and $IND_1$-*b*-$HEA_{70}$ which present only one indole and therefore resemble more closely the structure of the original PEG-trp. The main differences lie in the nature of the hydrophilic chain, which in our case consists of repeating hydroxyacrylamide units, whereas in Arvinte's work is a PEG chain. The polymers size is also different, as it spans between 5 and 14 kDa between the two copolymers sub-families, compared to the 2.0 kDa PEG used by Arvinte's group, who also found that longer PEG 5.0 induced lysozyme aggregation.

In Arvinte's work a tryptophan moiety was conjugated to the PEG chain through a carbamate bond, while in our case indole side groups are connected to the copolymer backbone through an ester bond, which may be less hydrolytically stable at the basic pH buffer employed for the experiment. The hydrolysis of the indole group would convert the copolymers into a simple polyacrylamide with carboxylic side chains, which has already shown in this experiment and also in the previous chapter to be able to induce lysozyme aggregation. Moreover, the hydrolysis would release the original hydrophobic molecules that were used to synthesise the hydrophobic monomers: indole 3-acetic acid, phenylacetic acid and methylbutyric acid. These molecules suspended in the polymer/protein mixture could further increase the final overall turbidity, thus explaining the very high optical density levels observed at the end of the experiments.

The aggregation-prone effect that we experience with polyacrylamide could be related to the macromolecular crowding induced by the simultaneous presence

in solution of two macromolecules, the protein and the polymer, at relatively high concentration (10 mg/mL lysozyme, 9 mg/mL $HEA_{100}$). The polymer occupies a specific volume, which becomes unavailable to the protein, and is for this reason called "excluded volume". The consequence of this phenomenon is a general decrease of the entropy solution, because the volume occupied by one macromolecule is unavailable to the other one. Hence, different protein properties are affected: for example, as the protein is forced to occupy a reduced volume in solution, its concentration will locally increase, with reduced solubility and higher chances of precipitation[27, 28]. Interestingly, different proteins have shown an accelerated aggregation in the presence of a crowding agent: K-synuclein fibrillation in vitro was dramatically accelerated by the addition of different macromolecules, such as proteins, polysaccharides and polyethylene glycols[29]. Influence of Dextran 70 and different PEGs on β-lactoglobulin fibrillisation was investigated, highlighting shorter lag time and faster growth of fibrils [29, 30].

To verify whether under these conditions hydrolysis of the polymer ester bonds could occur, $IND_{10}$-*b*-$HEA_{95}$ was incubated for 24 h in the same, highly basic buffer used for lysozyme aggregation experiment. The polymer was re-precipitated in THF and analysed by $^1H$ NMR. The spectrum showed the completely disappearance of indole aromatic protons peaks, confirming the complete hydrolysis of indole 3-acetic acid from the polymer backbone (Fig. 3.13).
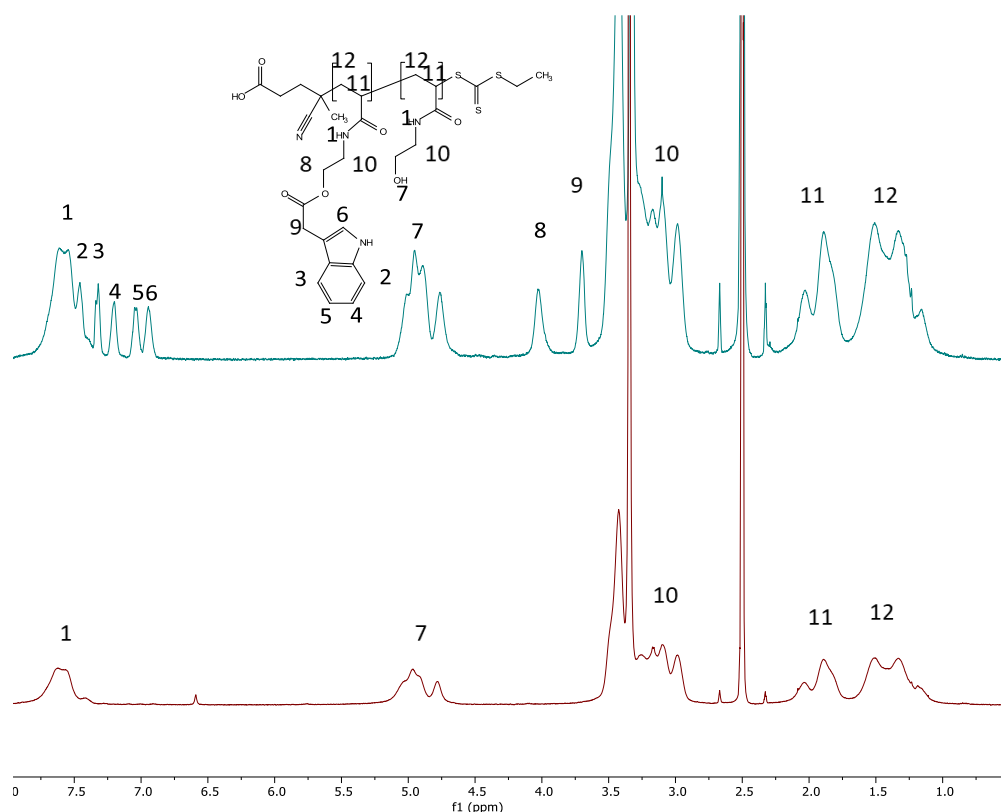
Figure 3.13: $^1$H NMR spectra of IND$_{10}$-*b*-HEA$_{95}$ (a) before and (b) after 24 h treatment in 100 mM pH 12 phosphate buffer. The two peaks belonging to acrylamide NH and OH are visible in both spectra, while indole aromatic peaks in the 7.0-7.5 ppm region have completely disappeared, thus confirming the complete hydrolysis of indole 3-acetic acid from the polymer backbone.

## 3.3.5. Binding of copolymers to insulin: solubility studies

The second model protein was bovine pancreatic insulin, a 51-amino acids, 5733 Da protein. The protein consists of one α-chain and one β-chain, connected together by two disulphide bridges. Another intrachain disulphide bridge is present on the α-chain[31]. Insulin was chosen for its pH-dependent solubility profile. It is only slightly soluble at physiological pH, and it is usually dissolved at acidic pH, where it is fully soluble. Solubility drastically decreases as the pH is brought to its isoelectric point at 5.3. At this pH the protein forms large and visible aggregates that precipitate over time[32]. Our copolymers where

therefore mixed with the protein at this pH to investigate any stabilising effect, able to prevent protein aggregation and precipitation (Fig. 3.15).

Several approaches have been undertaken to improve insulin solubility in the 5-7.5 pH range. Intranasal absorption of porcine insulin was increased by improving its solubility with a mixture of bile salts. The protein and the salts were mixed together at acidic pH, which was then raised to physiological values, generating micelles that were applied on the nasal mucosa[33]. The solubility at pH 4-7 of human and many other commercial insulins was greatly improved by the addition of protamine, an arginine-rich nuclear protein, resulting in long-term stable formulations at mildly acidic pH[34].

In another work, linkers bearing 1-2 aminic basic groups were attached to insulin through diazo modification of insulin carboxyl groups, generating a photocleavable bond. The modification resulted in a shift of insulin isoelectric point, from 5.3 to 7.2: the protein was fully soluble in mildly acidic pH, while underwent aggregation at physiological levels. The photocleavable bond was broken by irradiation, releasing native and fully insulin. This approach was proposed  for the development of photoactivated depot materials[35].

In this chapter, the ability of our amphiphilic block copolymers to develop hydrophobic non-covalent interactions with insulin was assessed by solubility studies. Accordingly, the protein was dissolved at a concentration of 4 mg/mL in 10 mM pH 2.0 phosphate buffer and mixed with 5 and 10 molar excess of polymers in the same buffer for a final insulin concentration of 2 mg/mL. When the pH was raised to 5.3, the mixtures were left stirring for 2h and then

centrifuged to precipitate the aggregated insulin. The precipitate was then re-dissolved in acidic buffer and analysed by RP-HPLC. The concentration of precipitated insulin was calculated integrating the area under insulin peak in the HPLC chromatogram for every insulin:copolymer blend, referring to a calibration curve previously prepared analysing different dilutions of insulin in the 0.1-2 mg/mL range (see Supporting Information Fig S3.38).

The concentration of residual insulin in solution was then calculated by difference between starting insulin concentration and concentration of precipitated insulin.
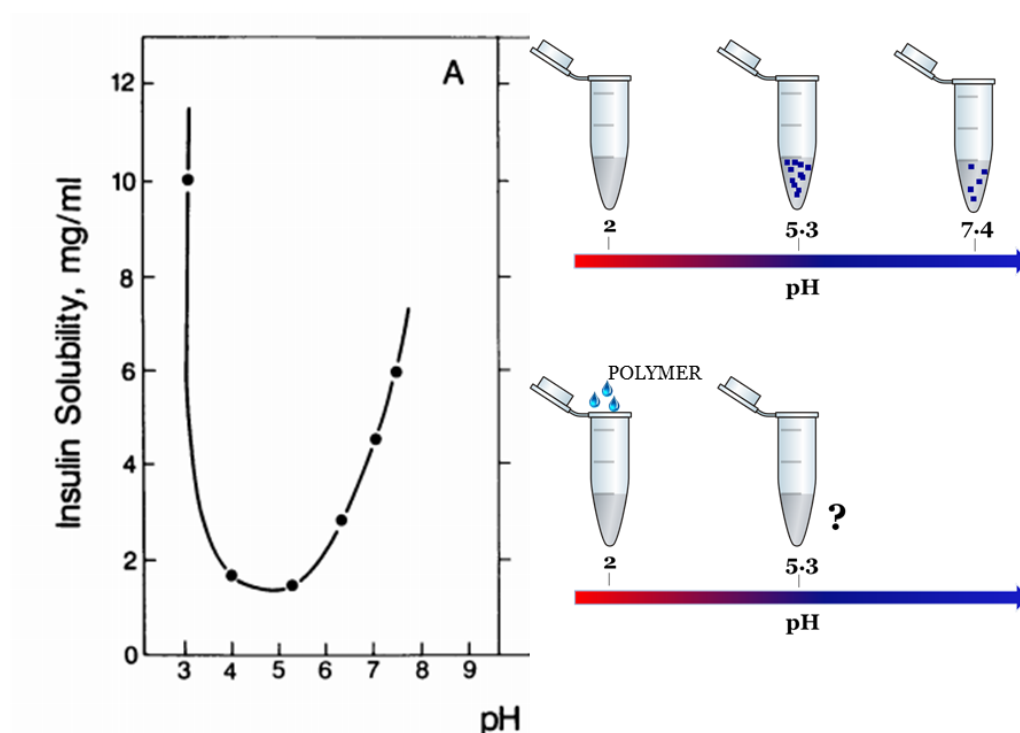


Figure 3.14: Schematic description of insulin solubility assay. Bovine pancreatic insulin possesses a pH-dependent solubility profile[32]. In particular, it is almost unsoluble in the 4-6 pH range, and slightly more soluble at pH 7. It can be solubilised at pH 2, but if the pH is raised at a value close to its isoelectric point 5.3, it will aggregate and precipitate. Here polymers were added to an insulin solution at pH 2.0, and following the increase of pH to 5.3, potential suppression of protein precipitation was assessed.

The polymers were again split in 2 groups, where 40 HEA-DP copolymers were analysed first (Fig. 3.15).
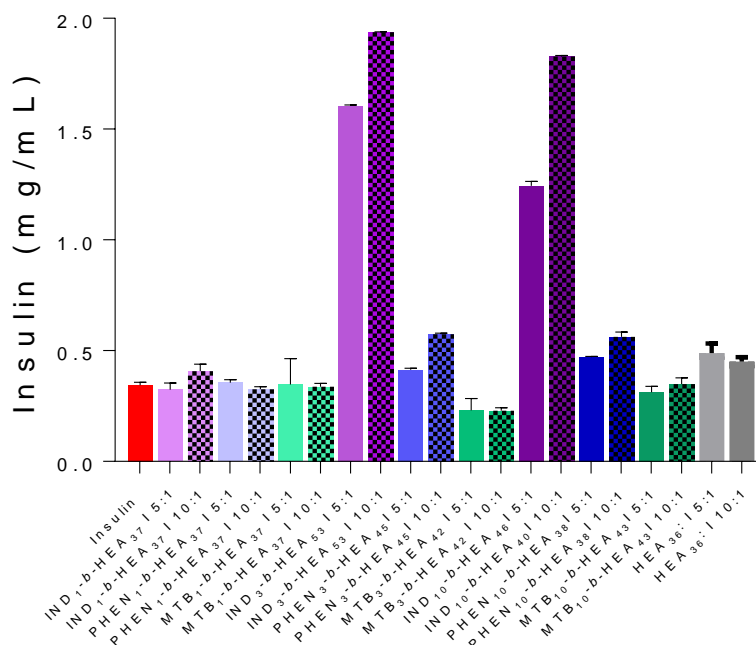


Figure 3.15: Insulin solubility studies. The concentration of soluble insulin at pH 5.3 is reported for native insulin and insulin mixed with 40-HEA DP copolymers. Samples were prepared in 10 mM phosphate buffer pH 2 at a final insulin concentration of 2 mg/mL and copolymers:insulin molar ratios of 5:1 and 10:1. After the pH was raised to 5.3, precipitated insulin was isolated by centrifugation and re-dissolved in 1 mL of 10 mM phosphate buffer pH 2. The concentration of precipitated insulin, expressed in mg/mL, was calculated by C18 RP-HPLC. HPLC measurements were performed with a linear gradient of 20–90% MeCN in water containing 0.1% TFA over 18 min at a flow rate of 1 mL/ min. Absorbance was recorded at λ=280 nm. For each sample, the precipitated insulin was quantified via integration of the peak area of insulin in the HPLC chromatograms, referring to a calibration curve previously prepared analysing different dilutions of insulin in the 0.1-2 mg/mL range (Fig. S3.46). Concentration of solubilised insulin was calculated by subtracting the concentration of the precipitated insulin from the starting concentration.

In the absence of block copolymers, following incubation at pH 5.3 only a small amount, around 0.3 mg/mL, of insulin remained in solution. Most of the copolymers had only a marginal impact on protein solubility, with values ranging from 0.3 to 0.5 mg/mL.

By contrast, $IND_3$-*b*-$HEA_{53}$ and $IND_{10}$-*b*-$HEA_{40}$ copolymers increased insulin solubility of around three times, suggesting an association between the polymers and insulin. The effect was also concentration dependent, as at 10:1 [polymer]:[insulin] molar ratio the copolymers were more effective, keeping almost 100% of the protein fully solubilised. Interestingly, $IND_1$-*b*-$HEA_{37}$, possessing only one indole at its chain-end, had only a weak impact on protein solubility.

Similar results were obtained with 100 HEA-DP copolymers (Figure 3.16). Again, copolymers possessing 3 and 10 indole repeating units $IND_3$-*b*-$HEA_{98}$ and $IND_{10}$-*b*-$HEA_{95}$ were found to be the most effective in increasing insulin solubility. In particular, $IND_3$-*b*-$HEA_{98}$ displayed a concentration-dependent solubilising effect, with 30% to almost 100% protein kept in solution, for 5:1 and 10:1 polymer:protein molar ratios, respectively. $IND_{10}$-*b*-$HEA_{95}$ was more effective, as almost 100% of the protein was kept in solution already at 5:1 polymer:protein molar ratio. Results confirmed the efficacy of the indole as complexing agent, but also that one indole are completely ineffective in solubilising insulin at pH 5.3. Among the other polymers, PHEN-containing copolymers showed the best results, with $PHEN_{10}$-*b*-$HEA_{88}$ which is able to stabilise between 35% and 50% of insulin.
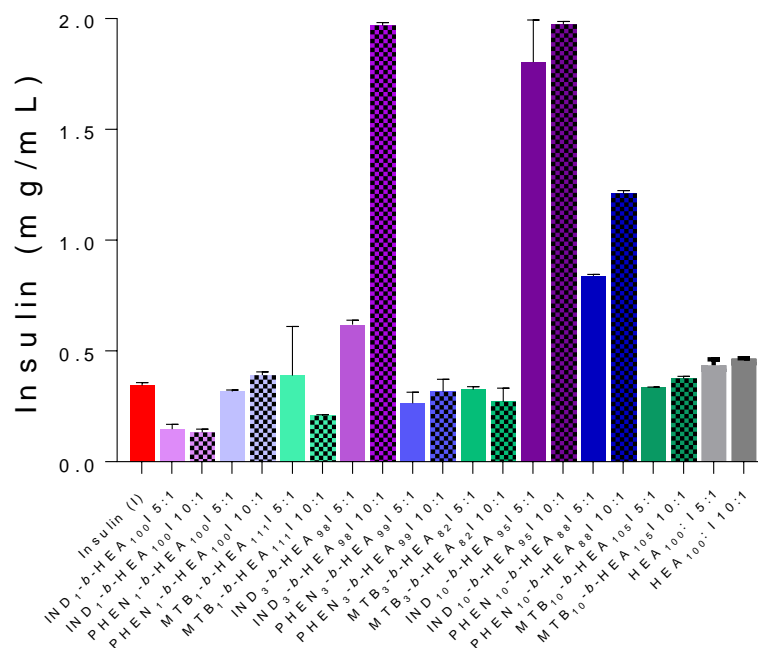
Figure 3.16: Insulin solubility studies. The concentration of soluble insulin at pH 5.3 is reported for native insulin and insulin mixed with 100-HEA DP copolymers. Samples were prepared in 10 mM phosphate buffer pH 2 at a final insulin concentration of 2 mg/mL and copolymers:insulin molar ratios of 5:1 and 10:1. After the pH was raised to 5.3, precipitated insulin was isolated by centrifugation and re-dissolved in 1 mL of 10 mM phosphate buffer pH 2. The concentration of precipitated insulin, expressed in mg/mL, was calculated by C18 RP-HPLC. HPLC measurements were performed with a linear gradient of 20–90% MeCN in water containing 0.1% TFA over 18 min at a flow rate of 1 mL/ min. Absorbance was recorded at λ=280 nm. For each sample, the precipitated insulin was quantified via integration of the peak area of insulin in the HPLC chromatograms, referring to a calibration curve previously prepared analysing different dilutions of insulin in the 0.1-2 mg/mL range (Fig. S3.45). Concentration of solubilised insulin was calculated by subtracting the concentration of the precipitated insulin from the starting concentration.

The low solubility that insulin displays at pHs between 5 and 7 can be explained

from its amino acidic composition[36] (Fig. 3.17).
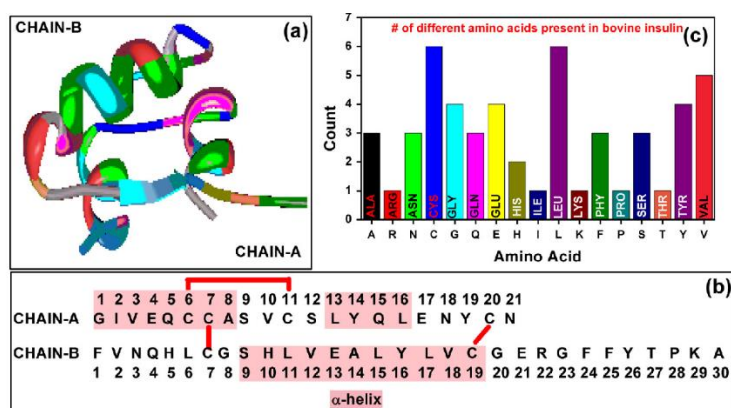
Figure 3.17: Insulin primary and secondary structure.[36].

There are 6 basic residues on the protein primary structure: two N-terminal amino groups (pKa 7-9), two histidine (pKa ~ 6), one lysine (pKa ~ 11) and one arginine(pKa ~ 12.5). There are then 6 acidic ones: two C-terminal carboxylates (pKa ~ 3.8) and four glutamates (pKa ~ 4.2)[37, 38]. At pH values between 5 and 6.5 the charges of the basic residues are counterbalanced by that of the acidic ones, so that the final net charge is zero[37]. Most of the other residues are either aliphatic hydrophobic (leucines, glycines, valines and alanines) or aromatic (3 phenylalanines and 4 tyrosines). These residues, which are responsible for the hydrophobic nature of the protein when its net charge is close to zero, may be involved in the interactions established with the amphiphilic copolymers utilised in this work. In particular, the aromatic amino acids may be involved in π-π interactions with the indole and phenyl moieties on the hydrophobic blocks of the copolymers.

## 3.3.6. Binding of copolymers to insulin: circular dichroism studies

The interaction between the polymers and insulin was further investigated by circular dichroism analysis, to assess the potential effects of this interaction on

insulin secondary structure, and to understand if any of these alterations would be permanent or not.

Circular dichroism (CD) is a useful tool which can be employed to characterise protein folding and secondary structure. The technique is based on the unequal absorption of right- and left- handed circularly polarized lights $E_r$ and $E_l$ by chiral, asymmetric molecules such as proteins. As a result, the light which passes through a solution of the chiral species becomes elliptically polarized, and the instrument can record the degree of ellipticity [θ], which is defined as the tangent of the ratio of the minor to major elliptical axis[39]. The degree of ellipticity [θ], will change according to the difference between $E_r$ and $E_l$ absorption, which will be then related to the specific conformation that the protein takes in solution. α-helix, β-sheet or random coil give characteristic [θ] *vs.* wavelength CD profiles, which makes this technique particularly suited to investigate protein secondary structure (Fig. 3.18)[39].
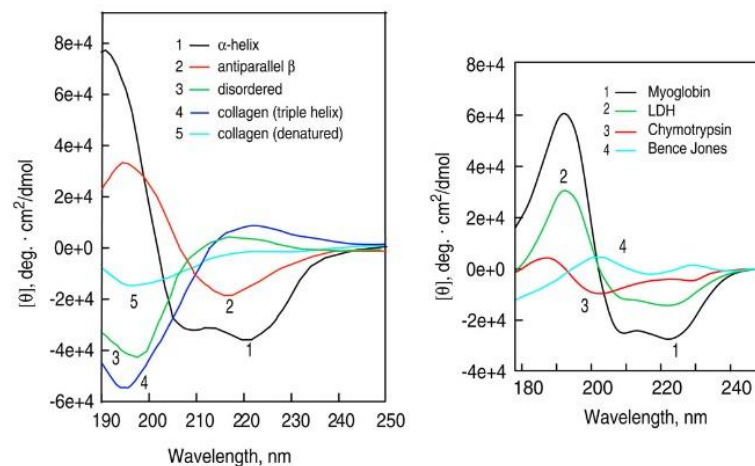


Figure 3.18: examples of circular dichroism profiles of different proteins[39].

One of the drawbacks of CD is potential poor signal-to noise ratio when highly UV-active excipients are present in protein formulations. Even though these molecules are not chiral, their high absorptivity can ultimately compromise the signal, making impossible to discern the protein secondary structure.

For our CD study, we utilised $IND_{10}$-*b*-$HEA_{95}$, as this was one of the most effective in preventing insulin aggregation at pH 5.3. Accordingly, the copolymer was mixed with insulin at 5:1 and 10:1 ratio in 10 mM pH 2 phosphate buffer. The pH was then raised to 5.3 and the solutions centrifuged to separate any traces of precipitated protein. The supernatant was then analysed by CD spectrophotometry, but unfortunately the signal quality was found to be too poor due to the high absorptivity of the polymers. Thus, to allow a meaningful measurement, it was decided to separate the two macromolecules and measure the protein CD profile after separation. Whilst this experiment cannot provide any information on the secondary structure alterations that occur when insulin is complexed with $IND_{10}$-*b*-$HEA_{95}$, it can still give important insight on the reversibility of the interaction and whether polymer complexation can induce irreversible changes of the protein secondary structure. The polymer-protein blends at pH 5.3 were then purified using a semi-prep HPLC column, using a 30-90% acetonitrile gradient in water. Insulin peak was collected and the protein lyophilised, re-dissolved in 10 mM pH 2 phosphate buffer, the pH shifted to 7.4 and the samples finally analysed (Fig. 3.19).
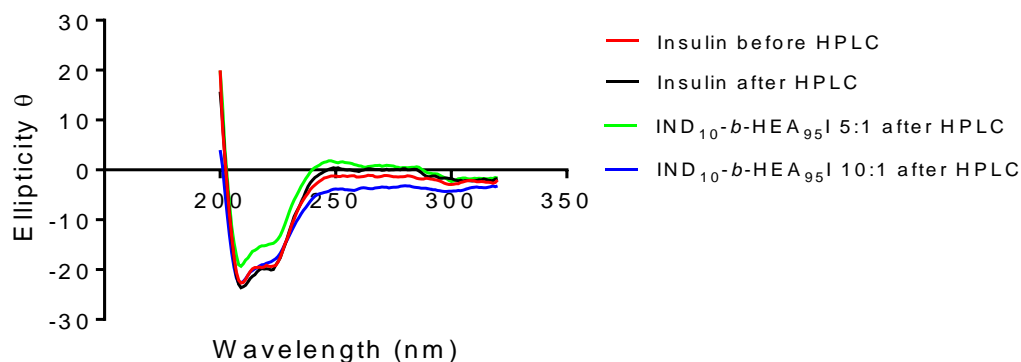
Figure 3.19: CD profiles of insulin, insulin after RP-HPLC elution (control sample used to assess whether HPLC purification can affect insulin secondary structure) and insulin:$IND_{10}$-b-$HEA_{95}$ mixtures at 5:1 and 10:1 polymer:insulin molar ratio, purified by RP HPLC. RP HPLC runs were performed with a linear gradient from 30–90% MeCN in water containing 0.1% TFA over 18 min at a flow rate of 5 mL/ min. After purification the protein samples were freeze dried and re-dissolved in 10 mM pH 2.0 phosphate buffer, at a concentration of 0.2 mg/mL.  For each sample, pH was raised to 7.4 prior to analysis.

The profile obtained from the protein before HPLC purification shows two negative peaks, one at 208 nm and the other at 222 nm, which have been previously described for bovine insulin, and are typical of a α-helix secondary structure[40]. A very similar profile was obtained from the control sample used to assess whether HPLC purification can affect insulin secondary structure. The two samples pre-treated with $IND_{10}$-*b*-$HEA_{95}$ at 10:1 and 5:1 polymer:insulin molar ratios also showed [θ] *vs.* wavelength CD profiles very similar to that of native insulin. The 5:1 polymer:protein sample appeared to have a slightly weaker intensity signal,  but that could be due to a slightly lower concentration in solution of recovered insulin. From this part of the study it can be concluded that neither the formation of a complex with the copolymer, nor the subsequent RP HPLC purification process have caused any major and permanent alteration of insulin secondary structure.

### 3.3.7. Binding of copolymers to peptide IDR 1018: solubility studies

Host defence peptides are a class of short and cationic amphiphilic peptides, which display a wide variety of direct antimicrobial[41] and immunomodulatory[42] activity. The direct antimicrobial activity is correlated with their amphiphilic nature. The presence of hydrophobic residues allows them to interact with bacterial membranes leading to their disfunction with subsequent bacterial death, or their translocation into the cytoplasm where they may act at different cytosolic targets[43].

Among these peptides, synthetic peptide IDR 1018 was identified for its dual antimicrobial and immunomodulatory activity. Its moderate direct bactericidal properties were tested *in vitro* on different bacterial strains, including *P. aeruginosa* (MIC 19 µg/mL) and *S. aureus* (MIC 4 µg/mL)[44]. The peptide is able to disrupt and prevent the formation of biofilms and can decrease bacterial infections on orthopaedic implants[45]. Studies have highlighted that the peptide does not significantly perturb model membranes, suggesting an intracellular target, that has yet to be fully understood[46, 47]. As an immunomodulatory agent, the peptide can stimulate differentiation of macrophages and neutrophils [48].

Unfortunately, like other antimicrobial immunomodulatory peptides, IDR 1018 has shown to aggregate in aqueous solution, under different conditions, from several buffers to tissue culture media. Various buffers have been tested to evaluate the influence of different salts on its aggregation. Sodium salt buffers caused significant peptide aggregation, dependent on peptide and salt concentration. Aggregation seems to be favoured by the presence of numerous

hydrophobic amino acids on the peptide backbone. In particular, the 5 consecutive hydrophobic residues between Leu-3 and Val-7 are believed to form an aggregation-prone hydrophobic patch (Fig. 3.20). Modifications of this sequence in peptides derivatives of IDR 1018 significantly reduced the likelihood of aggregation[49]. Interestingly, one tryptophan residue is also present in IDR 1018 sequence.

Aggregation unavoidably reduces peptide efficacy, altering the amount which is effectively delivered to the site of infection. Moreover, the immunomodulatory activity of the peptide was also altered as consequence of aggregates formation[47].



Val   Arg   Leu   Ile   Val   Ala   Val   Arg   Ile   Trp   Arg   Arg
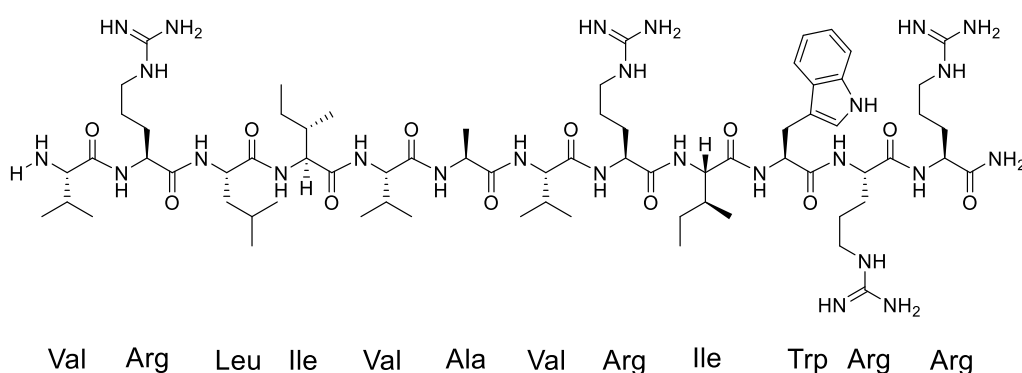
Figure 3.20: Amino acids sequence and chemical structure of peptide IDR 1018.

The potential interaction between amphiphilic $IND_m$-*b*-$HEA_n$, $PHEN_m$-*b*-$HEA_n$, and $MTB_m$-*b*-$HEA_n$ block co-polymers and IDR 1018 peptide was investigated in concentrated phosphate buffer, simulating conditions in which the peptide aggregates, to evaluate if polymer-peptide nanocomplexes are able to prevent peptide aggregation. The addition of salts to a biomacromolecule aqueous solution can have opposite effect according to the specific salt employed. The precipitation of peptides/proteins and other biomacromolecules in high ionic

strength solutions is called "salting out" and it is also employed, for example, to purify newly expressed protein therapeutics by selectively precipitating them[50]. In aqueous solutions of low ionic strength, hydrophobic residues of proteins are usually buried within the protein core, while charged and polar residues on the protein surface interact with water molecules through H-bonds. These interactions form a water solvation layer around the protein which improves protein stability and solubility[51]. The addition of salts into the solution is followed by the dissociation of the salt molecules into ionic species, which interact with water molecules. As more salt is added, less water molecules are available to interact with charged residues on the protein surface. The protein starts unfolding and the solvent exposure of protein hydrophobic residues finally leads to protein aggregation and precipitation[51, 52]. A variety of cations and anions are known to induce macromolecules salting out, where the most effective, called kosmotropes, display strong association with water molecules[49]. Both cations and anions have been ranked for their ability in inducing protein aggregation and precipitation, with anions order being $CO_3^{2-}$ > $SO_4^{2-}$ > $S_2O_3^{2-}$ > $H_2PO_4^-$ > $F^-$ > $Cl^-$ > $Br^-$ ≈ $NO_3^-$ > $I^-$ > $ClO_4^-$ > SCN and cations order being $(CH_3)_4N^+$ > $Cs^+$ > $Rb^+$ > $NH_4^+$ > $K^+$ > $Na^+$ > $Li^+$ > $Mg^{2+}$ > $Ca^{2+}$ from the most to the least precipitating, respectively[53]. A similar behaviour could be expected from IDR 1018. At high ionic strength, its hydrophobic amino acid residues could drive its self-interaction and final aggregation. At the same time, these residues may potentially establish hydrophobic interactions with our amphiphilic copolymers.

Firstly, each copolymer was first solubilised in 100 mM pH 7.2 phosphate buffer. A solution of IDR 1018 peptide in water was then added to the copolymer solutions, to give a final peptide concentration of 0.10 mM, and a 1:1 copolymer:peptide molar ratio. The resulting peptide aggregates were removed by centrifugation and the supernatant was analysed via HPLC to quantify the amount of residual IDR 1018 (Fig. 3.21). Concentration of IDR 1018 in solution was calculated referring to a calibration curve previously prepared analysing different dilutions of IDR 1018 in the 0.0005-0.2 mM range (see Supporting Information Fig. S3.39).
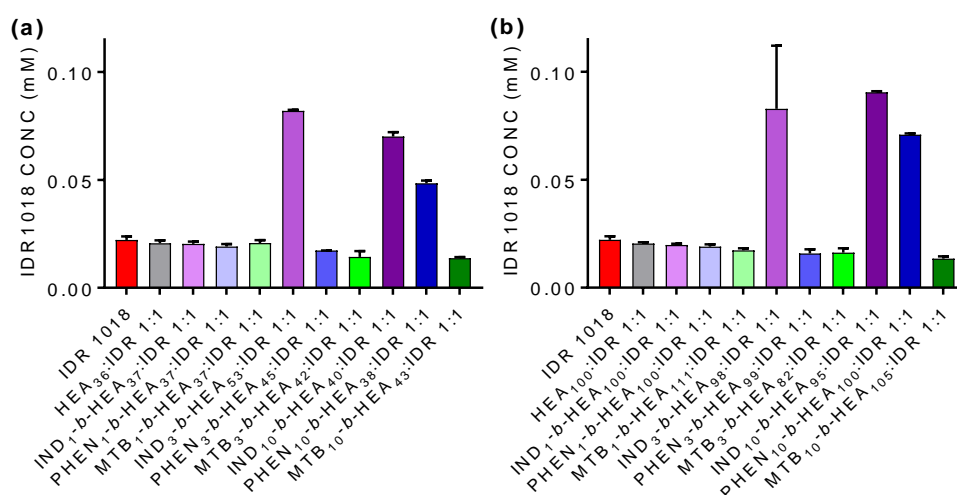


Figure 3.21: Peptide IDR 1018 solubility study. The concentration of soluble IDR 1018 in 100 mM pH 7.2 phosphate buffer is reported for native peptide and peptide mixed with (a) 40-HEA and (b) 100-HEA DP copolymers. A 1 mM IDR 1018 stock solution in deionised water was prepared. The copolymers were separately dissolved in 450 µL of 100 mM phosphate buffer pH 7.2. To these solutions, 50 µL of IDR 1018 stock solution were added, for a final IDR 1018 concentration of 0.1 mM and a 1:1 copolymers: IDR 1018 molar ratio. After 5h stirring, the solutions were centrifuged, and the supernatant analysed by C18 RP-HPLC. HPLC measurements were performed using a 25−90% MeCN gradient in water containing 0.1% TFA over 18 min at a flow rate of 1 mL/ min. Absorbance was recorded at $\lambda$=280 nm. For each sample, the concentration of residual IDR 1018, expressed in mM, was quantified via integration of the peak area of IDR 1018 in the HPLC chromatograms.

As shown in Fig. 3.21, in the absence of amphiphilic copolymers the concentration of residual unprecipitated IDR 1018 peptide was quantified by RP-HPLC to be around 0.025 mM, and, similarly to what observed with insulin, most of the copolymers did not induce a significant prevention of aggregation. Again, $IND_3$- and $IND_{10}$-copolymers, regardless of the length of the HEA hydrophilic block, decreased significantly peptide aggregation, resulting in the highest peptide concentrations left in solution. In particular, $IND_3$-*b*-$HEA_{53}$, $IND_{10}$-*b*-$HEA_{40}$, $IND_3$-*b*-$HEA_{98}$ and $IND_{10}$-*b*-$HEA_{95}$ kept almost 100% of the peptide in solution. Similar effects were obtained with $PHEN_{10}$-copolymers, in particular $PHEN_{10}$-*b*-$HEA_{88}$, whose effects are comparable to indole containing copolymers.

Results obtained with peptide IDR 1018 confirm that indole-terminating copolymers have the ability to complex and solubilise different proteins and peptides. Again, this study also confirmed that one indole is not enough to establish a successful interaction.

### 3.3.8. Potential self-association of copolymers

The results obtained thus far indicated that only copolymers containing a sufficient number of indole repeating units (three or ten in this case), and in part those with with ten phenylalanine residues, were able to interact with insulin and IDR 1018 peptide, and minimise their aggregation in solution.

It could be that a minimum number of indoles is necessary to establish interactions with proteins hydrophobic regions. However, it is also possible that the hydrophobic block, above a sufficient length, can trigger polymers self-

assembling, and the resulting nanoparticles can complex the proteins. Proteins-copolymers interactions that we have experienced so far, could be due proteins complexation more than a single chain-protein interaction.

Since the amphiphilic $IND_m$-$b$-$HEA_n$, $PHEN_m$-$b$-$HEA_n$, and $MTB_m$-$b$-$HEA_n$ block copolymers consist of one hydrophobic and one hydrophilic block, thus under aqueous conditions it is reasonable to hypothesise that they could self-assemble into supramolecular aggregates, where contact between water and the hydrophobic block is minimised. Block copolymers can potentially self-assemble into a range of different supramolecular aggregates in aqueous environment. Among them, we can remember micelles, worm-like micelles and polymersomes[54]. The nature of the aggregate depends on the chemical structure of both the hydrophilic and the hydrophobic blocks, and on the ratio between the two. For example, there is experimental evidence that for PEG-based block copolymers, micelles are the most likely form of supramolecular aggregate when PEG volume fraction (*f*) is above 50%[55]. In case of our block copolymers, the ratio between the hydrophilic and the hydrophobic blocks span from 4:1 of $IND_{10}$-$b$-$HEA_{40}$ to 111:1 of $MTB_1$-$b$-$HEA_{111}$. With such a high hydrophilic/hydrophobic ratio, micelles are the most likely type of supramolecular aggregates that the copolymers may be forming in aqueous solutions, even if further experiments, such as for example TEM or comparative incorporation of hydrophilic and hydrophobic probes, would be required to confirm the exact nature of these nanoparticles. Micelles are nanoparticles of spherical shape and size generally between 10 and 100 nm, where the hydrophobic blocks are inside the sphere and the hydrophilic, polar ones, are

facing water, forming the outside surface of the micelle. Micelles are always in a dynamic equilibrium with their unimeric form (Fig. 3.22)[56].



NANOPARTICLES                    UNIMER
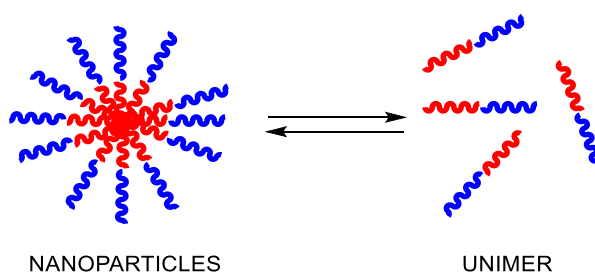
Figure 3.22: Illustration of the equilibrium between micelles and unimeric polymer chains in aqueous enviroment. The hydrophobic block is coloured in red.

Polymeric micelles are widely used in drug delivery as valid excipients for the encapsulation of poorly water-soluble drugs[57]. The nature and stability of a micelle is highly dependent on the length and properties of the hydrophobic and hydrophilic blocks[58]. In our case, the hydrophobic block on $IND_1$-terminating copolymers may be too short to induce micellization, thus explaining their lack of activity.

The potential self-assembly of the copolymers was then analysed by Dynamic Light Scattering (DLS). DLS is used to evaluate size and size distribution of macromolecules and small particles, like protein, polymers, and supramolecular complexes with size between 1 and 1000 nm.

The co-polymers were dissolved in water at a concentration of 1.0 mg/mL. The copolymers hydrodynamic diameter, calculated by volume distribution, is reported in the table below. The volume distribution is displayed in Figure 3.23.

Table 3.7: Copolymers hydrodynamic diameter, calculated in volume by Dynamic Light Scattering. Copolymers were analysed in water at 1 mg/mL.

| POLYMER | IND$_1$-$b$-HEA$_{37}$ | PHEN$_1$-$b$-HEA$_{37}$ | MTB$_1$-$b$-HEA$_{37}$ | IND$_3$-$b$-HEA$_{53}$ | PHEN$_3$-$b$-HEA$_{45}$ | MTB$_3$-$b$-HEA$_{42}$ | IND$_{10}$-HEA$_{40}$ | PHEN$_{10}$-$b$-HEA$_{38}$ | MTB$_{10}$-$b$-HEA$_{43}$ |
|---|---|---|---|---|---|---|---|---|---|
| SIZE (nm) | 2.93 | 2.99 | 3.23 | 5.23 | 3.19 | 3.69 | 9.72 | 9.7 | 6.54 |
| PDI | 0.15 | 0.56 | 0.08 | 0.18 | 0.05 | 0.1 | 0.16 | 0.19 | 0.2 |
| POLYMER | IND$_1$-$b$-HEA$_{100}$ | PHEN$_1$-$b$-HEA$_{100}$ | MTB$_1$-$b$-HEA$_{111}$ | IND$_3$-$b$-HEA$_{98}$ | PHEN$_3$-$b$-HEA$_{99}$ | MTB$_3$-$b$-HEA$_{82}$ | IND$_{10}$-$b$-HEA$_{95}$ | PHEN$_{10}$-$b$-HEA$_{88}$ | MTB$_{10}$-$b$-HEA$_{105}$ |
| SIZE (nm) | 5.97 | 5.4 | 6.02 | 5.21 | 5.13 | 4.64 | 14.28 | 12 | 5.38 |
| PDI | 0.13 | 0.15 | 0.06 | 0.27 | 0.1 | 0.25 | 0.15 | 0.16 | 0.33 |
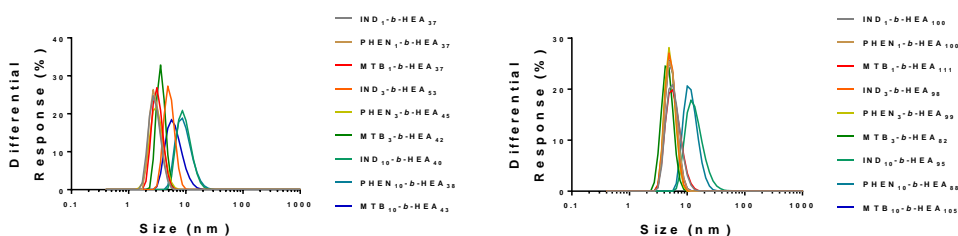


Figure 3. 23: Copolymers size volume distribution, calculated in volume by DLS. Copolymers were analysed in water at 1 mg/mL.

Most of the copolymers display size between 3 and 6 nm. Such small values suggest that there is no self-assembly taking place, and the only species detected are individual polymeric chains. For example, similar hydrodynamic diameters have been assessed for DLS and small angle neutron scattering analyses of PEG 2000[59]. By contrast, higher values, between 10 and 15 nm, were observed for IND$_{10}$ and PHEN$_{10}$ containing copolymers. These values suggest that these polymers could self-assemble under aqueous solutions and support the idea that insulin and IDR 1018 peptide were surrounded by polymer chains in a micellar interaction.

However, IND$_3$-terminating copolymers IND$_3$-$b$-HEA$_{53}$ and IND$_3$-$b$-HEA$_{98}$ display a smaller size, of around 5 nm, which indicates that these polymers may not be

self-assembling. Hence, their stabilising and solubilising effects may be more likely due to a single protein-single polymer chain stabilizing interaction, accomplished through the short indole block at the end of the chain.

Further studies were performed on the two copolymers $IND_3$-*b*-$HEA_{98}$ and $IND_{10}$-*b*-$HEA_{95}$. The two copolymers were chosen as they both displayed stabilising interactions with insulin and the antimicrobial peptide IDR 1018, yet from DLS analysis it appears that only $IND_{10}$-*b*-$HEA_{95}$ may be self-assembling. The potential self-assembling characteristics of these materials was investigated by assessing their potential Critical Micelle Concentration. The CMC is the concentration of surfactants above which micelles form. Below this concentration, surfactant exists in solution as un-associated monomers. The identification of the CMC can be achieved using a range of different techniques. In this study, the CMC of $IND_3$-*b*-$HEA_{98}$ and $IND_{10}$-*b*-$HEA_{95}$ was estimated by water surface tension measurements at different polymer concentrations.

Changes on water's surface tension upon addition of a surfactant are due to the surfactant ability to partition at the interface between water and air, with its hydrophilic block that remains in water and the hydrophobic one in contact with air, emerging from the water surface[60]. The presence of the surfactant at the interface will reduce the surface free energy (surface tension) of water, with a direct correlation between the surfactant concentration and the surface tension: as the first increases, the latter decreases. Above the CMC the surfactant molecules start to self-assemble into micelles, and any further surfactant added in solution will form more micelles. As a result, there will be

no additional surfactant molecules at the interface, and as a result the surface tension will stabilise as well. The CMC can then be identified as the concentration above which increasing amounts of surfactant have no more significant influence on water surface tension[61].

Firstly, $IND_3$-*b*-$HEA_{98}$ and $IND_{10}$-*b*-$HEA_{95}$ were dissolved in water at various concentrations, and the surface tension of the resulting solutions was measured with the "pendant drop" method[62]. The calculated surface tensions of the various polymer solutions were plotted against polymers concentration (Fig. 3.23).
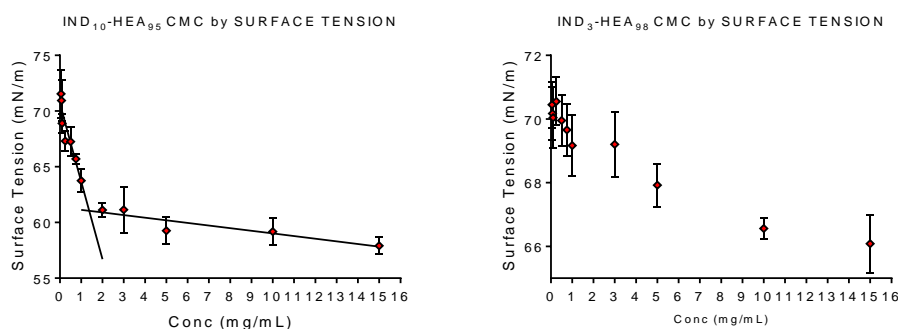


Figure 3.24: CMC measurement for copolymers $IND_{10}$-*b*-$HEA_{95}$ and $IND_3$-*b*-$HEA_{98}$, assessed by Surface Tension analysis.

$IND_{10}$-*b*-$HEA_{95}$ induced a surface tension decrease from 72 mN/m to 59 mN/m. However, the surface tension declined steeply in the 0.01-2 mg/mL concentration range, but much less at higher concentrations. The graph can be therefore divided into two different sections, and the intersection of the fitting lines interpolating data points in these two regions, at a concentration of 1.5 mg/mL, defines the CMC of $IND_{10}$-*b*-$HEA_{95}$.

In case of $IND_3$-*b*-$HEA_{98}$, the surface tension appears to decrease more gradually, from 71 to 66 mN/m, as the copolymer concentration increased, with

no clear discontinuity in the surface tension *vs.* polymer concentration plot, suggesting that $IND_3$-*b*-$HEA_{98}$ may not form micelles in this range of concentrations. The result would be in good agreement with DLS values that highlighted the absence of self-assembled nanoparticles for $IND_3$-*b*-$HEA_{98}$. The main difference between the two copolymers lies in the length of the hydrophobic block, which is shorter in $IND_3$-*b*-$HEA_{98}$, with an average of 2.52 indoles per polymer chain. A very low ratio between the hydrophobic and the hydrophilic part generally results in increased CMC values and reduced micelle stability, since the self-assembly is driven by the attraction between the hydrophobic segments[58]. As both $IND_3$-*b*-$HEA_{98}$ and $IND_{10}$-*b*-$HEA_{95}$ could prevent insulin and IDR 1018 peptide aggregation this study may suggest that the interaction established by the polymer with insulin and IDR 1018 are not necessarily or not completely of micellar type. The insulin solubility experiment was performed at $IND_3$-*b*-$HEA_{98}$ concentrations between 20 and 40 mg/mL. These concentrations are higher than the range explored for CMC determination. However, in IDR 1018 peptide solubility study the polymer concentration was much lower, ca. 1.5 mg/mL, in a range that was covered by the DLS and Surface Tension measurements and where $IND_3$-*b*-$HEA_{98}$ did not show any significant self-assembly. Another possible explanation is that the presence of insulin and IDR 1018 peptide may promote a guest molecule-induced self-assembly.

## 3.4. Final considerations

In this chapter, we wanted to develop a family of copolymers of different composition and length that could act as protein stabilisers. These copolymers incorporated a variable number of hydrophobic amino acid-like functional group, to interact with different proteins through non-covalent hydrophobic interactions, preventing their aggregation/precipitation. The copolymers were then characterised by short hydrophobic blocks of DP 1, 3 and 10, and a hydrophilic poly(N-hydroxyethyl acrylamide) block of variable length. Synthesis was accomplished through RAFT polymerization, which ensured narrow molecular weight dispersity and $M_n$ close to the expected theoretical ones. The ability of these materials to modulate protein aggregation was investigated on three different model proteins and peptides, hen egg lysozyme, bovine pancreatic insulin and the antimicrobial peptide IDR 1018. Turbidity tests were performed to evaluate the aggregation of hen egg lysozyme. Results showed that none of the copolymers was able to delay the aggregation onset. On the contrary, the aggregation rate was accelerated. An investigation on the stability of the copolymers used in these experiments showed significant hydrolysis of the hydrophobic side chains, thus providing an explanation for the unexpected results obtained in the lysozyme stabilisation experiments.

Tests on a different protein, bovine pancreatic insulin, showed that amphiphilic copolymers containing $IND_3$- and $IND_{10}$-blocks greatly decrease protein precipitation. However, copolymers bearing only one indole at the polymer chain-end were completely ineffective, suggesting that one indole is not

enough to establish a sufficiently strong interaction between the polymer and the protein backbone. PHEN$_{10}$-containing copolymers induced partial insulin solubilisation.

A similar experiment was performed on antimicrobial peptide IDR1018, which is known to aggregate and precipitate in a wide range of buffers and media. Again, IND$_{3-}$ and IND$_{10}$-containing copolymers were able to significantly reduce the aggregation and prevent the precipitation of the peptide. By contrast, the other copolymers failed to improve peptide solubility, with the relevant exception of PHEN$_{10-}$ containing copolymers, which again partially prevented peptide aggregation.

Experiments on these last two proteins highlight the efficacy of indole-, and partially phenyl-bearing polymers, compared to the completely aliphatic monomer MTB, which proved to be completely ineffective. They suggest that tryptophan and phenylalanine aromatic side chains can be used to interact with hydrophobic residues and pockets on the protein backbone. Furthermore, copolymers efficacy was found to be independent on the size of the hydrophilic poly(*N*-hydroxyethyl acrylamide) block, within the range of poly(HEA) investigated, HEA$_{\sim 50}$ and HEA$_{\sim 100}$. As it was hypothesised in Chapter 2, also in this case the HEA-hydrophilic chain may contribute to proteins stabilisation by surrounding and shielding the proteins molecules, protecting them from self-interactions that lead to aggregation.

In these experiments, polymers containing one indole moiety were found to be ineffective in preventing protein aggregation/precipitation. Thus, we

hypothesised that longer hydrophobic blocks could induce copolymers self-assembly and that the interaction we observed was more similar to that of a micelle encapsulating a hydrophobic guest molecule.

Thus, self-assembly of copolymers was investigated by Dynamic Light Scattering. The presence of particles was detected only for $IND_{10}$-containing copolymers, while $IND_3$-copolymers had ≤5 nm size, which suggested that only indiviual polymer chains existed in solution. Potential self-association into micelles was further investigated by surface tension measurements on copolymers $IND_{10}$-*b*-$HEA_{95}$ and $IND_3$-*b*-$HEA_{98}$. A CMC could be identified only for the $IND_{10}$-*b*-$HEA_{95}$ copolymer, suggesting that $IND_3$-*b*-$HEA_{98}$, due to its short poly(IND) block, may form unstable micelles, or its CMC may be at higher copolymer concentrations than those investigated here. It is also possible that copolymers can improve protein/peptide stability in both ways, by surrounding the protein in a micelle-like fashion but also establishing specific interactions on the protein sequence through their indole block.

Micelles formation and/or stabilisation could also be induced by interactions between the aggregating/precipitating protein/peptide and the copolymer. More insights on this mechanism of interaction could be obtained by analysing copolymer-proteins mixtures, for example by DLS or a microscopy technique such as TEM, to detect and characterise particles potentially resulting from protein-polymer complexation.

# References

1.      Anjana, R.; Vaishnavi, M. K.; Sherlin, D.; Kumar, S. P.; Naveen, K.; Kanth, P. S.; Sekar, K., Aromatic-aromatic interactions in structures of proteins and protein-DNA complexes: a study based on orientation and distance. *Bioinformation* **2012,** *8* (24), 1220-1224.

2.      de Jesus, A. J.; Allen, T. W., The role of tryptophan side chains in membrane protein anchoring and hydrophobic mismatch. *Biochimica et Biophysica Acta (BBA) - Biomembranes* **2013,** *1828* (2), 864-876.

3.      Pawar, A. P.; DuBay, K. F.; Zurdo, J.; Chiti, F.; Vendruscolo, M.; Dobson, C. M., Prediction of "Aggregation-prone" and "Aggregation-susceptible" Regions in Proteins Associated with Neurodegenerative Diseases. *Journal of Molecular Biology* **2005,** *350* (2), 379-392.

4.      Cecchini, P.; De Franceschi, G.; Frare, E.; Fontana, A.; Polverino de Laureto, P., The role of tryptophan in protein fibrillogenesis: relevance of Trp7 and Trp14 to the amyloidogenic properties of myoglobin. *Protein Engineering, Design and Selection* **2012,** *25* (4), 199-203.

5.      Cochran, A. G.; Skelton, N. J.; Starovasnik, M. A., Tryptophan zippers: Stable, monomeric β-hairpins. *Proceedings of the National Academy of Sciences* **2001,** *98* (10), 5578.

6.      Mueller, C.; Capelle, M. A. H.; Arvinte, T.; Seyrek, E.; Borchard, G., Tryptophan-mPEGs: Novel excipients that stabilize salmon calcitonin against aggregation by non-covalent PEGylation. *European Journal of Pharmaceutics and Biopharmaceutics* **2011,** *79* (3), 646-657.

7.      Mueller, C.; Capelle, M. A. H.; Seyrek, E.; Martel, S.; Carrupt, P.-A.; Arvinte, T.; Borchard, G., Noncovalent PEGylation: Different Effects of Dansyl-, Tryptophan–, Phenylbutylamino-, Benzyl- and Cholesteryl-PEGs on the Aggregation of Salmon Calcitonin and Lysozyme. *Journal of Pharmaceutical Sciences* **2012,** *101* (6), 1995-2008.

8.      Bar, T.; Okon, Y., Tryptophan conversion to indole-3-acetic acid via indole-3-acetamide in Azospirillum brasilense Sp7. *Canadian Journal of Microbiology* **1993,** *39* (1), 81-86.

9.      Allison, M. J., Phenylalanine biosynthesis from phenylacetic acid by anaerobic bacteria from the rumen. *Biochemical and Biophysical Research Communications* **1965,** *18* (1), 30-35.

10.     Tsakos, M.; Schaffert, E. S.; Clement, L. L.; Villadsen, N. L.; Poulsen, T. B., Ester coupling reactions – an enduring challenge in the chemical synthesis of bioactive natural products. *Natural Product Reports* **2015,** *32* (4), 605-632.

11.     Cutler, P., Size-Exclusion Chromatography. In *Protein Purification Protocols*, Humana Press: Totowa, NJ, **2004**; pp 239-252.

12.     Bouvier, E. S. P.; Koza, S. M., Advances in size-exclusion separations of proteins and polymers by UHPLC. *TrAC Trends in Analytical Chemistry* **2014,** *63*, 85-94.

13.     Shiono, S., Separation and identification of poly(ethylene terephthalate) oligomers by gel permeation chromatography. *Journal of Polymer Science: Polymer Chemistry Edition* **1979,** *17* (12), 4123-4127.

14.     Christopoulou, C. N.; Perkins, E. G., High performance size exclusion chromatography of monomer, dimer and trimer mixtures. *Journal of the American Oil Chemists' Society* **1989,** *66* (9), 1338-1343.

15.     Vandenbergh, J.; Reekmans, G.; Adriaensens, P.; Junkers, T., Synthesis of sequence controlled acrylate oligomers via consecutive RAFT monomer additions. *Chemical Communications* **2013,** *49* (88), 10358-10360.

16.     Lawrence, J.; Lee, S.-H.; Abdilla, A.; Nothling, M. D.; Ren, J. M.; Knight, A. S.; Fleischmann, C.; Li, Y.; Abrams, A. S.; Schmidt, B. V. K. J.; Hawker, M. C.; Connal, L. A.; McGrath, A. J.; Clark, P. G.; Gutekunst, W. R.; Hawker, C. J., A Versatile and Scalable Strategy to Discrete Oligomers. *Journal of the American Chemical Society* **2016,** *138* (19), 6306-6310.

17.     Vonk, E. C.; Langeveld-Voss, B. M. W.; van Dongen, J. L. J.; Janssen, R. A. J.; Claessens, H. A.; Cramers, C. A., Separation and characterization of oligomers by reversed-phase high-performance liquid chromatography; a study on well-defined oligothiophenes. *Journal of Chromatography A* **2001,** *911* (1), 13-26.

18.     Rissler, K.; Fuchslueger, U.; Grether, H. J., Separation of Polyethylene Glycol Oligomers on Normal-Phase and Reversed-Phase Materials by Gradient High Performance Liquid Chromatography and Detection by Evaporative Light Scattering. A Comparative Study. *Journal of Liquid Chromatography* **1994,** *17* (14-15), 3109-3132.

19.     Miller, J. B.; McGrath, K. J.; Roland, C. M.; Trask, C. A.; Garroway, A. N., Nuclear magnetic resonance study of polyisoprene/poly(vinylethylene) miscible blends. *Macromolecules* **1990,** *23* (21), 4543-4547.

20.     James, T. L. Fundamentals of NMR, San Francisco: Department of Pharmaceutical Chemistry, University of California, **1998** (pp. 1–31).

21.     Chûjô, R., Microtacticity and Mean Length of Sequences of the Stereospecific Polymers Obtained by the Control of both Symmetric and Asymmetric Sites. *Polymer Journal* **1975,** *7*, 409.

22.     Kurtulus, I.; Yilmaz, G.; Ucuncu, M.; Emrullahoglu, M.; Becer, C. R.; Bulmus, V., A new proton sponge polymer synthesized by RAFT polymerization for intracellular delivery of biotherapeutics. *Polymer Chemistry* **2014,** *5* (5), 1593-1604.

23.     Mastrotto, F.; Breen, A. F.; Sicilia, G.; Murdan, S.; Johnstone, A. D.; Marsh, G. E.; Grainger-Boultby, C.; Russell, N. A.; Alexander, C.; Mantovani, G., One-pot RAFT and fast polymersomes assembly: a 'beeline' from monomers to drug-loaded nanovectors. *Polymer Chemistry* **2016,** *7* (44), 6714-6724.

24.     Pal, S.; Ghosh Roy, S.; De, P., Synthesis via RAFT polymerization of thermo- and pH-responsive random copolymers containing cholic acid moieties and their self-assembly in water. *Polymer Chemistry* **2014,** *5* (4), 1275-1284.

25.     Moad, G.; Rizzardo, E.; Thang, S. H., Radical addition–fragmentation chemistry in polymer synthesis. *Polymer* **2008,** *49* (5), 1079-1131.

26.     Hill, M. R.; Carmean, R. N.; Sumerlin, B. S., Expanding the Scope of RAFT Polymerization: Recent Advances and New Horizons. *Macromolecules* **2015,** *48* (16), 5459-5469.

27.     Kuznetsova, M. I.; Zaslavsky, Y. B.; Breydo, L.; Turoverov, K. K.; Uversky, N. V., Beyond the Excluded Volume Effects: Mechanistic Complexity of the Crowded Milieu. *Molecules* **2015,** *20* (1).

28.     Kuznetsova, M. I.; Turoverov, K. K.; Uversky, N. V., What Macromolecular Crowding Can Do to a Protein. *International Journal of Molecular Sciences* **2014,** *15* (12).

29.     Uversky, V. N.; M. Cooper, E.; Bower, K. S.; Li, J.; Fink, A. L., Accelerated α-synuclein fibrillation in crowded milieu. *FEBS Letters* **2002,** *515* (1-3), 99-103.

30.     Ma, B.; Xie, J.; Wei, L.; Li, W., Macromolecular crowding modulates the kinetics and morphology of amyloid self-assembly by β-lactoglobulin. *International Journal of Biological Macromolecules* **2013,** *53*, 82-87.

31.     Stretton, A. O. W., The first sequence. Fred Sanger and insulin. *Genetics* **2002,** *162* (2), 527-532.

32.     Fischel-Ghodsian F, B. L., Mathiowitz E, Brandenburg D, Langer R., Enzymatically controlled drug delivery. *Proceedings of the National Academy of Sciences of the United States of America* **1988**

33.     Gordon, G. S.; Moses, A. C.; Silver, R. D.; Flier, J. S.; Carey, M. C., Nasal absorption of insulin: enhancement by hydrophobic bile salts. *Proceedings of the National Academy of Sciences of the United States of America* **1985,** *82* (21), 7419-7423.

34.     Helle Birk, OlsenNiels, Christian Kaarsholm, Per Balschmidt, Soluble, stable insulin-containing formulations with a protamine salt. Patent US8263551B2, **2005**.

35.     Nadendla, K.; Friedman, S. H., Light Control of Protein Solubility Through Isoelectric Point Modulation. *Journal of the American Chemical Society* **2017,** *139* (49), 17861-17869.

36.     Tah, B.; Pal, P.; Roy, S.; Dutta, D.; Mishra, S.; Ghosh, M.; Talapatra, G. B., Quantum-mechanical DFT calculation supported Raman spectroscopic study of some amino acids in bovine insulin. *Spectrochimica Acta Part A: Molecular and Biomolecular Spectroscopy* **2014,** *129*, 345-351.

37.     Iyire, A.; Alaayedi, M.; Mohammed, A. R., Pre-formulation and systematic evaluation of amino acid assisted permeability of insulin across in vitro buccal cell layers. *Scientific Reports* **2016,** *6*, 32498.

38.     https://www.thermofisher.com/uk/en/home/life-science/protein-biology/protein-biology-learning-center/protein-biology-resource-library/pierce-protein-methods/amino-acid-physical-properties.html.

39.     Greenfield, N. J., Using circular dichroism spectra to estimate protein secondary structure. *Nature protocols* **2006,** *1* (6), 2876-2890.

40.     Goldman, J.; Carpenter, F. H., Zinc binding, circular dichroism, and equilibrium sedimentation studies on insulin (bovine) and several of its derivatives. *Biochemistry* **1974,** *13* (22), 4566-4574.

41.     Lange, J. C. Y. L. a. D., Current and Potential Applications of Host-Defense Peptides and Proteins in Urology. *BioMed Research International* **2015**.

42.     Mansour, S. C.; Pena, O. M.; Hancock, R. E. W., Host defense peptides: front-line immunomodulators. *Trends in Immunology* **2014,** *35* (9), 443-450.

43.     Nijnik, A.; Hancock, R. E. W., Host defence peptides: antimicrobial and immunomodulatory activity and potential applications for tackling antibiotic-resistant infections. *Emerging Health Threats Journal* **2009,** *2*, e1.

44.     Wieczorek, M.; Jenssen, H.; Kindrachuk, J.; Scott, W. R. P.; Elliott, M.; Hilpert, K.; Cheng, J. T. J.; Hancock, R. E. W.; Straus, S. K., Structural Studies of a Peptide with Immune Modulating and Direct Antimicrobial Activity. *Chemistry & Biology* **2010,** *17* (9), 970-980.

45.     Choe, H.; Narayanan, A. S.; Gandhi, D. A.; Weinberg, A.; Marcus, R. E.; Lee, Z.; Bonomo, R. A.; Greenfield, E. M., Immunomodulatory Peptide IDR-1018 Decreases Implant Infection and Preserves Osseointegration. *Clinical Orthopaedics and Related Research* **2015,** *473* (9), 2898-2907.

46.     de la Fuente-Núñez, C.; Reffuveille, F.; Haney, E. F.; Straus, S. K.; Hancock, R. E. W., Broad-Spectrum Anti-biofilm Peptide That Targets a Cellular Stress Response. *PLOS Pathogens* **2014,** *10* (5), e1004152.

47.     Andresen, L.; Tenson, T.; Hauryliuk, V., Cationic bactericidal peptide 1018 does not specifically target the stringent response alarmone (p)ppGpp. *Scientific Reports* **2016,** *6*, 36549.

48.     Pena, O. M.; Afacan, N.; Pistolic, J.; Chen, C.; Madera, L.; Falsafi, R.; Fjell, C. D.; Hancock, R. E. W., Synthetic Cationic Peptide IDR-1018 Modulates Human Macrophage Differentiation. *PLOS ONE* **2013,** *8* (1), e52449.

49.     Haney, E. F.; Wu, B.; Lee, K.; Hilchie, A. L.; Hancock, R. E. W., Aggregation and Its Influence on the Immunomodulatory Activity of Synthetic Innate Defense Regulator Peptides. *Cell Chemical Biology* **2017,** *24* (8), 969-980.e4.

50.     Duong-Ly, K. C.; Gabelli, S. B., Chapter Seven - Salting out of Proteins Using Ammonium Sulfate Precipitation. *Methods in Enzymology*, Lorsch, J., Ed. Academic Press **2014**; Vol. 541, pp 85-94.

51.     Hyde, A. M.; Zultanski, S. L.; Waldman, J. H.; Zhong, Y.-L.; Shevlin, M.; Peng, F., General Principles and Strategies for Salting-Out Informed by the Hofmeister Series. *Organic Process Research & Development* **2017,** *21* (9), 1355-1370.

52.     Arakawa, T.; Timasheff, S. N., Mechanism of protein salting in and salting out by divalent cation salts: balance between hydration and salt binding. *Biochemistry* **1984,** *23* (25), 5912-5923.

53.     Release of proteins from the inner surface of squid axon membrane labeled with tritiated N-ethylmaleimide. *The Journal of General Physiology* **1976,** *68* (4), 385-395.

54.     Marina Gallarate, L. B., E. Peira, and Michele Trotta., Peptide-Loaded Solid Lipid Nanoparticles Prepared through Coacervation Technique. *International Journal of Chemical Engineering,* **2011**.

55.     Guan, L.; Rizzello, L.; Battaglia, G., Polymersomes and their applications in cancer delivery and therapy. *Nanomedicine* **2015,** *10* (17), 2757-2780.

56.     Letchford, K.; Burt, H., A review of the formation and classification of amphiphilic block copolymer nanoparticulate structures: micelles, nanospheres, nanocapsules and polymersomes. *European Journal of Pharmaceutics and Biopharmaceutics* **2007,** *65* (3), 259-269.

57.     Kulthe, S. S.; Choudhari, Y. M.; Inamdar, N. N.; Mourya, V., Polymeric micelles: authoritative aspects for drug delivery. *Designed Monomers and Polymers* **2012,** *15* (5), 465-521.

58.     Uchegbu, I. F., Polymers in Drug Delivery. *Journal of Drug Targeting* **2004,** *12* (8), 475-475.

59.     Linegar, K. L.; Adeniran, A. E.; Kostko, A. F.; Anisimov, M. A., Hydrodynamic radius of polyethylene glycol in solution obtained by dynamic light scattering. *Colloid Journal* **2010,** *72* (2), 279-281.

60.     Inoue, T.; Nakashima, K.; Suzuki, M., Surface Tension Study on Aqueous Solution of Nonionic Surfactant with Unsaturated Hydrocarbon Chain. *Journal of Oleo Science* **2002,** *51* (12), 753-760.

61.     Chakraborty, T.; Chakraborty, I.; Ghosh, S., The methods of determination of critical micellar concentrations of the amphiphilic systems in aqueous medium. *Arabian Journal of Chemistry* **2011,** *4* (3), 265-270.

62.     Stauffer, C. E., The Measurement of Surface Tension by the Pendant Drop Technique. *The Journal of Physical Chemistry* **1965,** *69* (6), 1933-1938.

# Supporting Information Chapter 3

$^1$H and $^{13}$C NMR spectra were recorded on a Bruker DPX400 UltraShield™ Spectrometer and processed with MestReNova 12.0© 2017 Mestrelab Research S.L. All chemical shifts are reported in ppm ($\delta$) relative to tetramethylsilane or referenced to the chemical shifts of residual solvent resonances.

ESI TOF Mass spectrometry analyses were conducted on a Bruker microTOF II.

FT-IR spectra were recorded using an Agilent Cary630.

Purification of IND$_m$, PHEN$_m$ and MTB$_m$ oligomers (from m=2 to m=6) was performed on an Agilent 971-FP Flash Purification System using a BIOTAGE KP-C18-HS 12 g column.

Polymer SEC analyses were performed on a Polymer Laboratories GPC 50 system equipped with a refractive index detector, using a system made of two PLgel Mixed-D (5 µm bead, 7.8 × 300 mm) columns and a matching guard (7.8 × 50 mm). Analyses were performed in DMF at a flow rate of 1 mg/mL with 0.1% w/v LiBR. Narrow PMMA standards were used for calibration.

HPLC experiments were performed on a Shimadzu HPLC (LC-20AD pump) equipped with a SPD-M20A UV detector and SIL-20A autosampler. Reverse phase analyses were completed using a C18 Zorbax Eclipse Plus C18 column (3.5 µm, 95 Å, 4.6 × 12.5 mm).

Dynamic light scattering was performed using a Nano-Zs from Malvern Instruments, UK. The size was measured at 25 ˚C. Analyses were repeated 3

times for each sample, and a minimum of 10 measurements was performed

for each analysis.

Surface Tension Measurements were performed on a Kruss DSA 100 using the

"pendant drop" method.
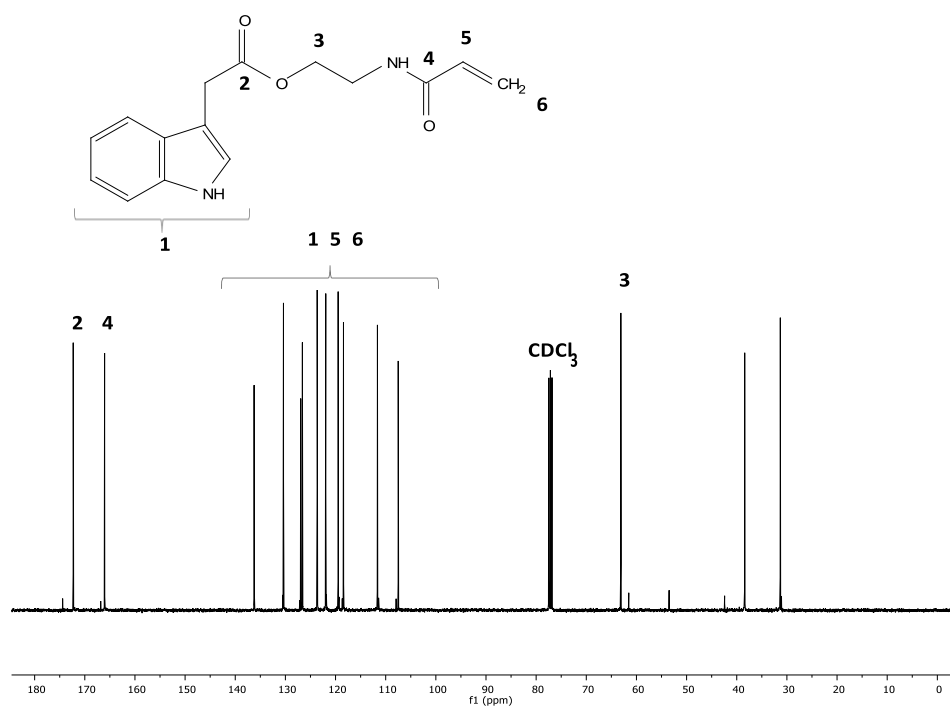


Figure S3.1: $^{13}$C NMR spectrum of monomer IND in CDCl$_3$.
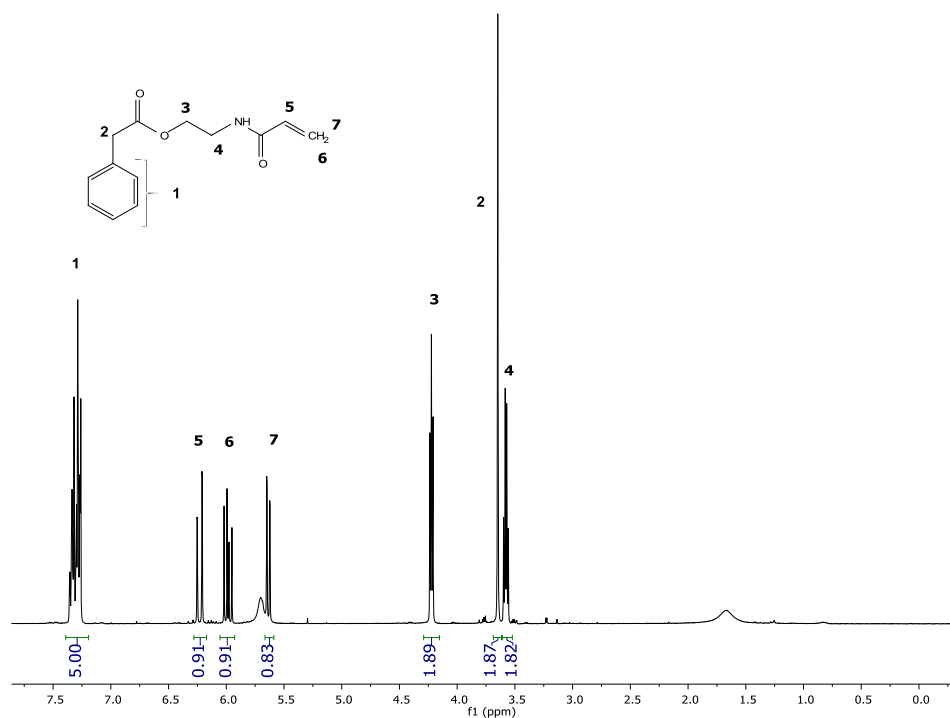
Figure S3. 2: $^1$H NMR spectrum of monomer PHEN in CDCl$_3$.
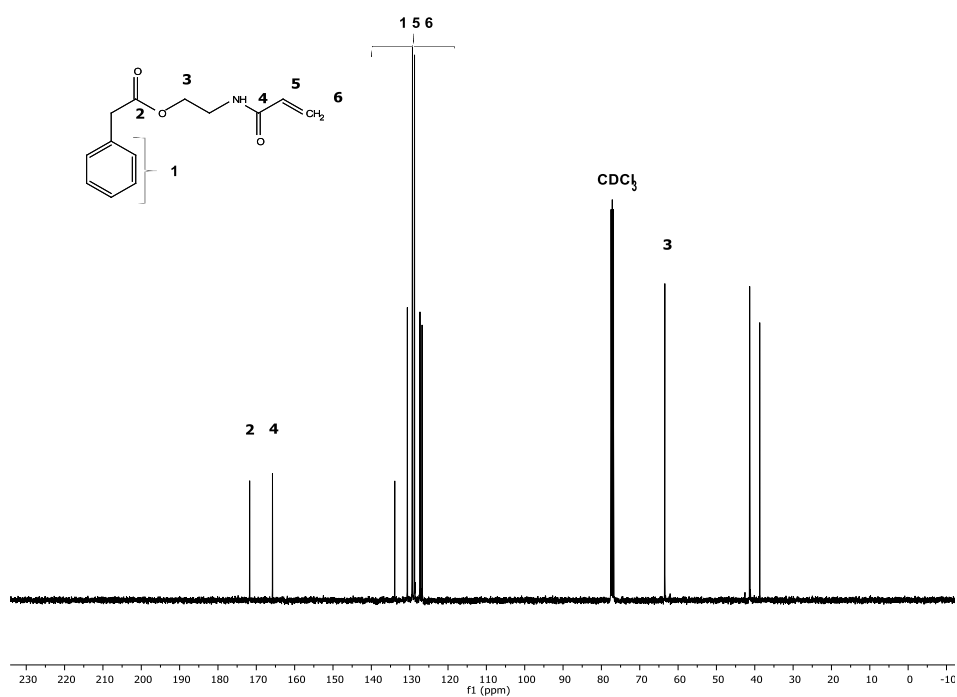


Figure S3.3: $^{13}$C NMR spectrum of monomer PHEN in CDCl$_3$.
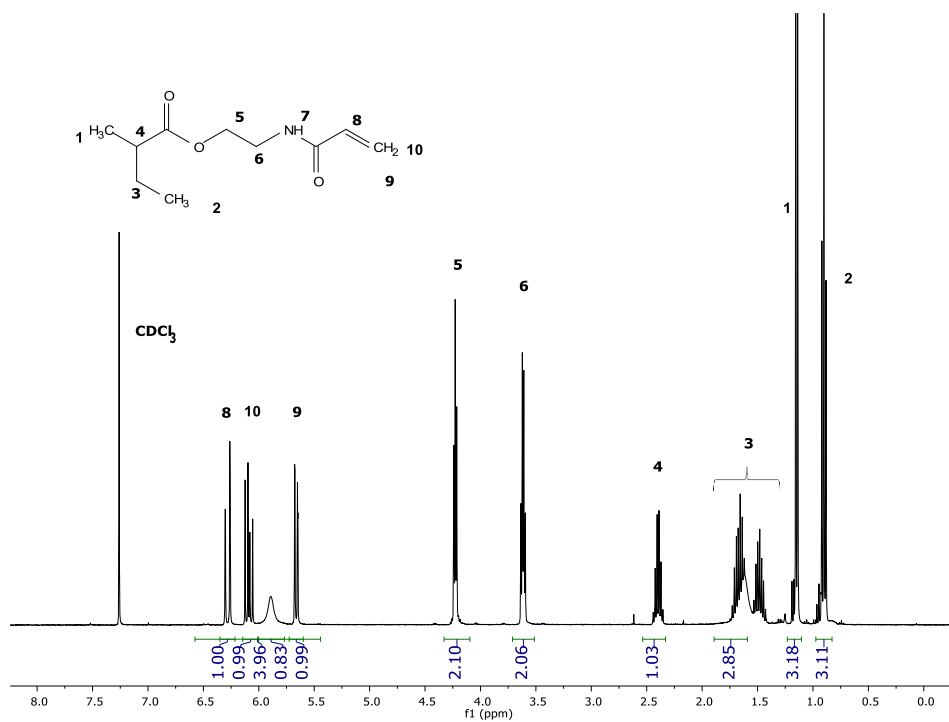
Figure S3. 4: $^1$H NMR spectrum of monomer MTB in CDCl$_3$.
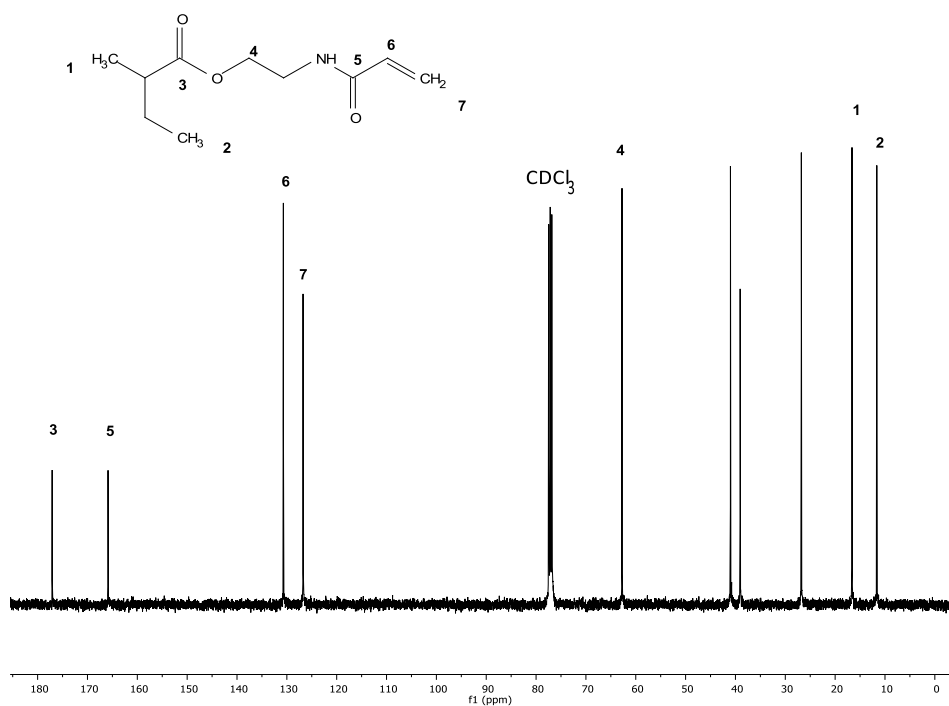


Figure S3.5: $^{13}$C NMR spectrum of monomer MTB in CDCl$_3$.
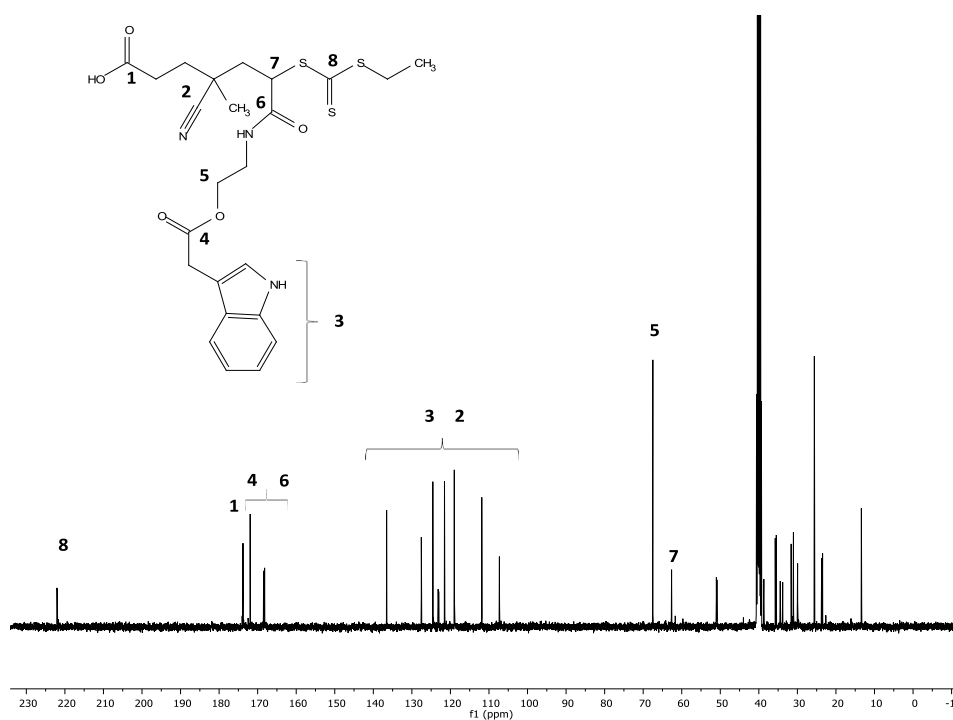
Figure S3. 6:$^{13}$C NMR spectrum of oligomer IND$_1$ in d$_6$-DMSO.
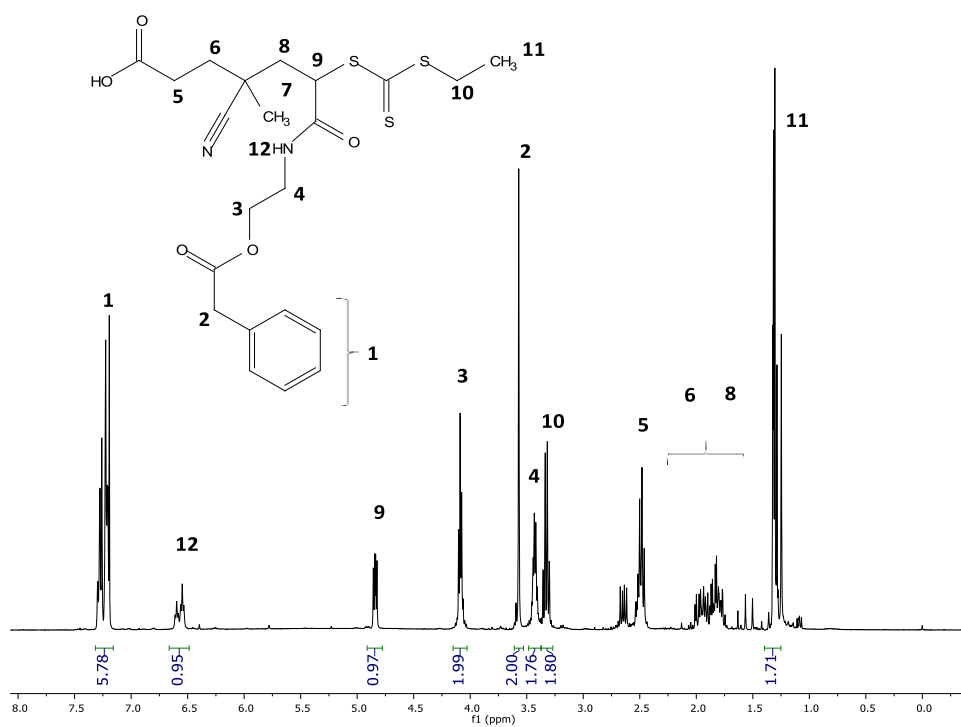


Figure S3.7: $^1$H NMR spectrum of oligomer PHEN$_1$ in CDCl$_3$.
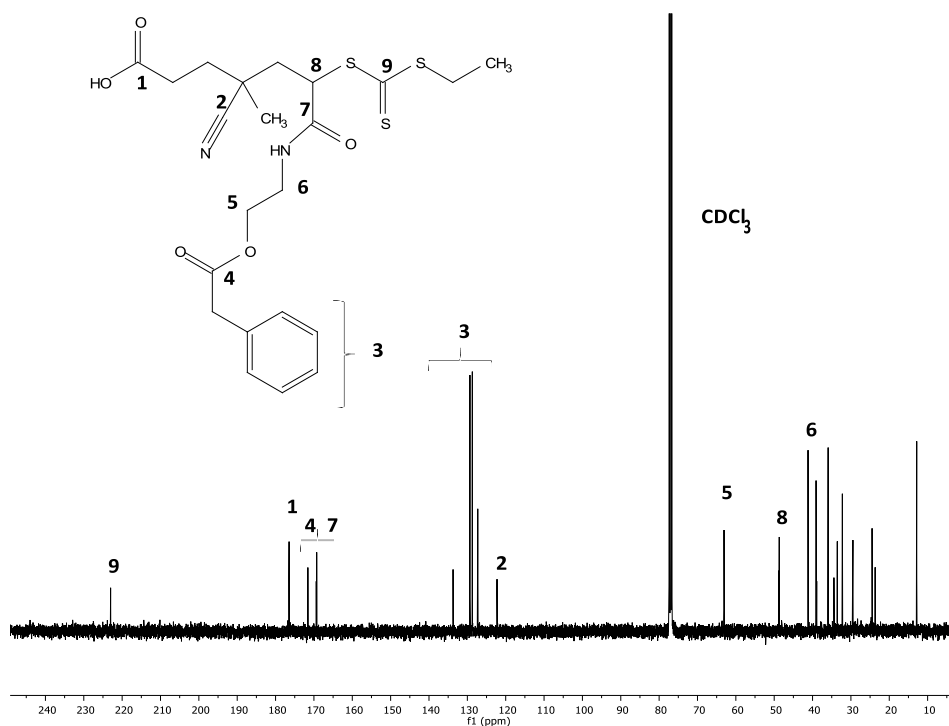
Figure S3.8: $^{13}$C NMR spectrum of oligomer PHEN$_1$ in CDCl$_3$.
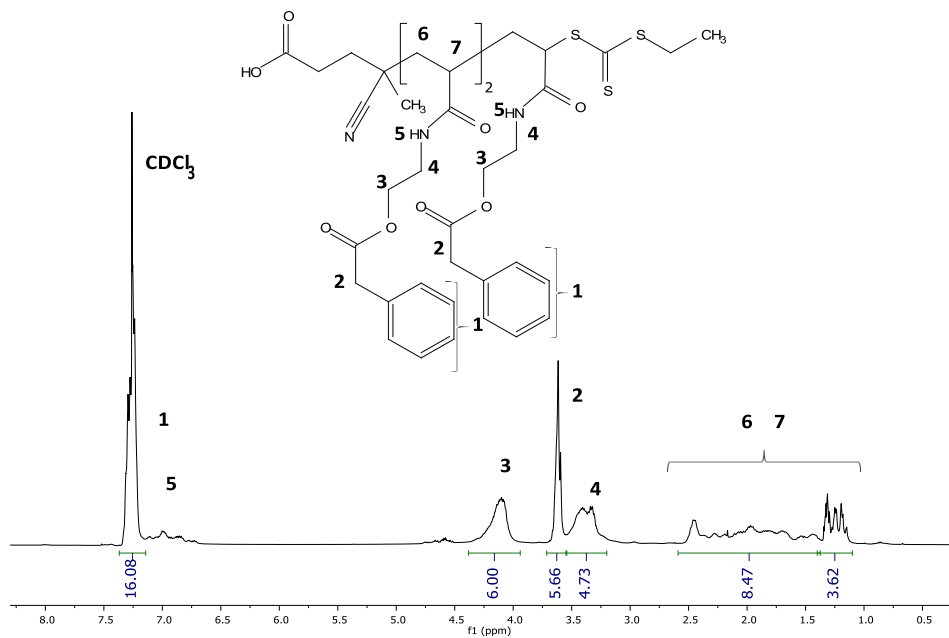


Figure S3.9: $^1$H NMR spectrum of oligomer PHEN$_3$ in CDCl$_3$.
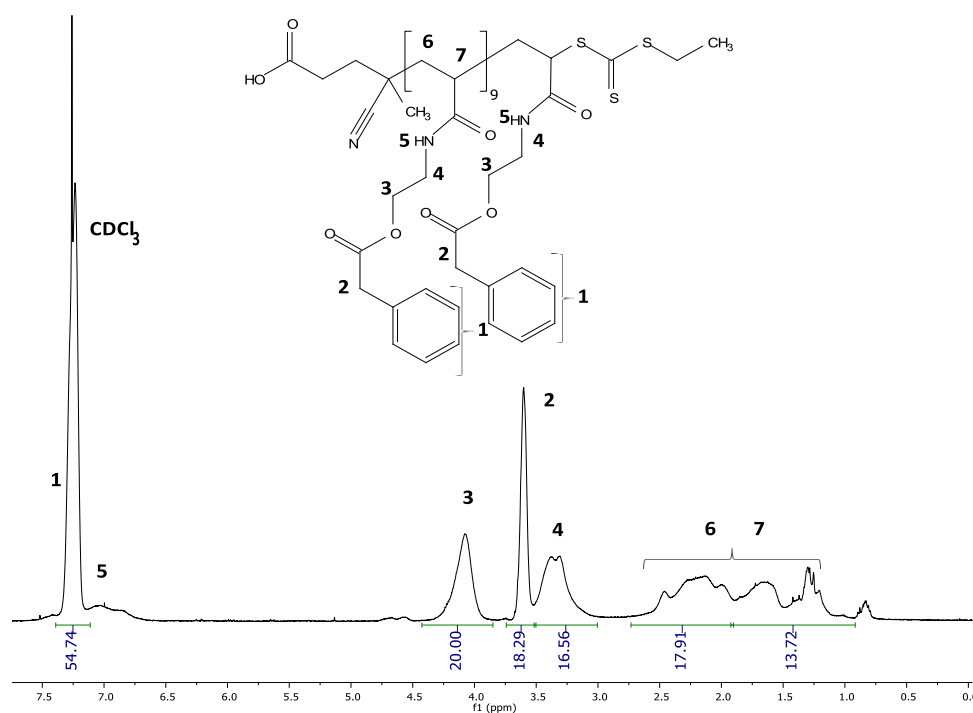
Figure S3.10: $^1$H NMR spectrum of oligomer PHEN$_{10}$ in CDCl$_3$.
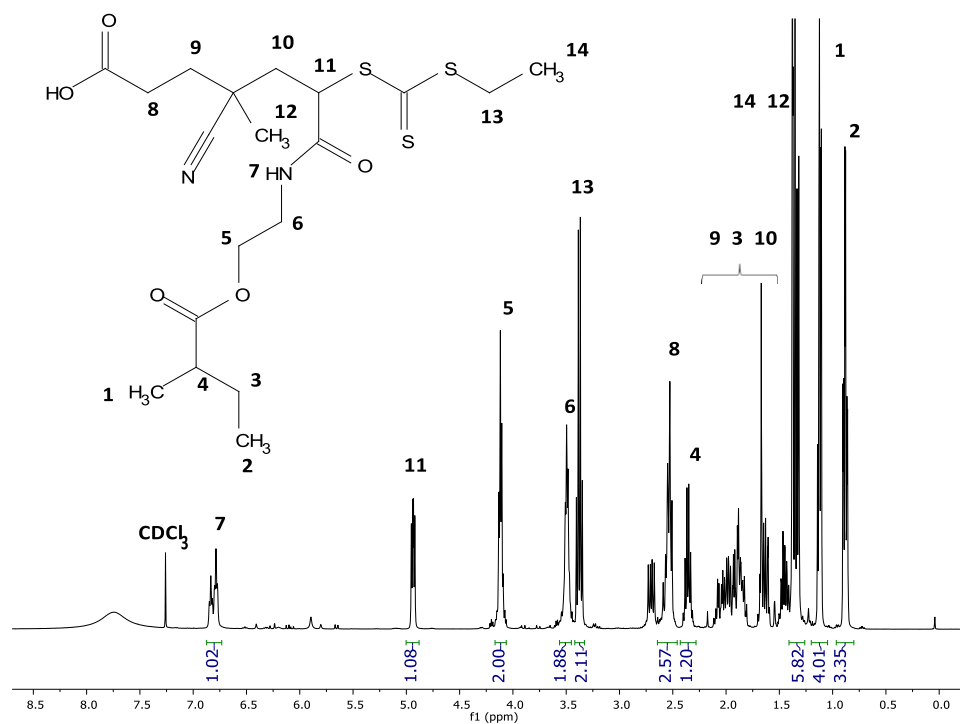


Figure S3.11: $^1$H NMR spectrum of oligomer MTB$_1$ in CDCl$_3$.
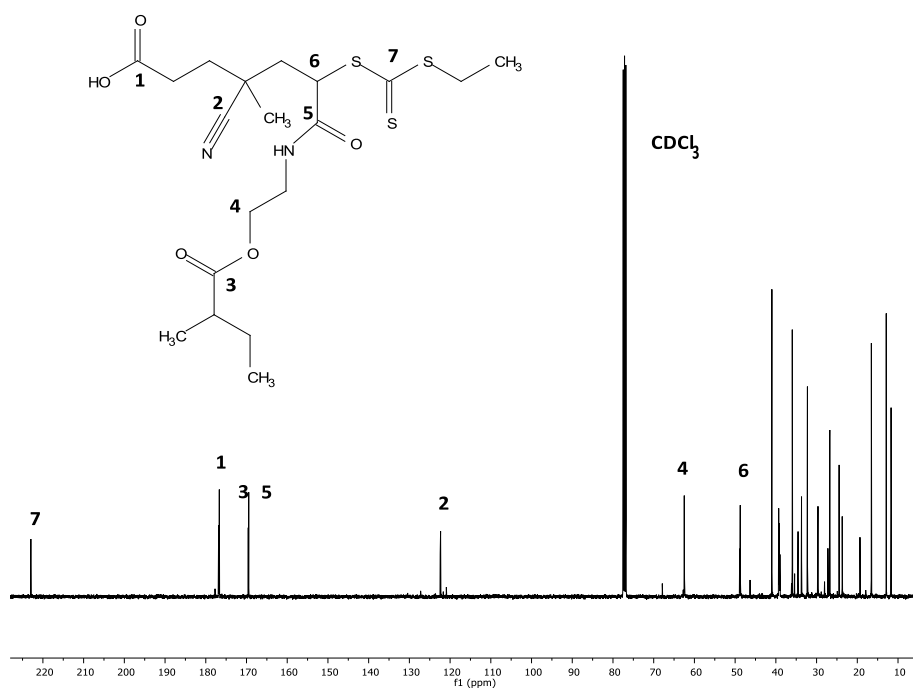
Figure S3.12: $^{13}$C NMR spectrum of oligomer MTB$_1$ in CDCl$_3$.
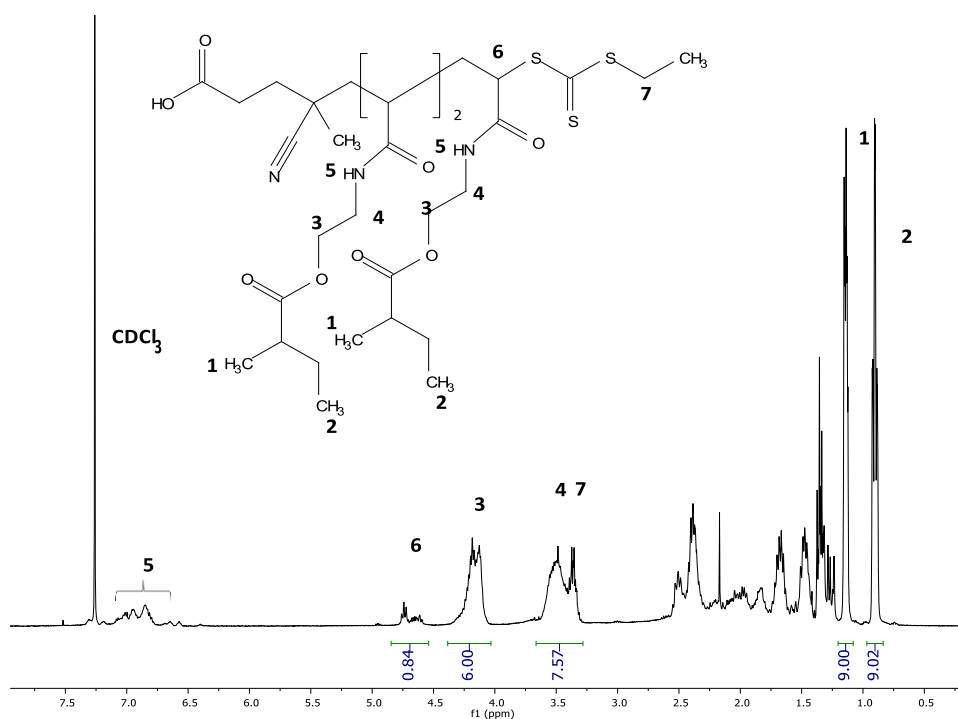


Figure S3.13: $^1$H NMR spectrum of oligomer MTB$_3$ in CDCl$_3$.
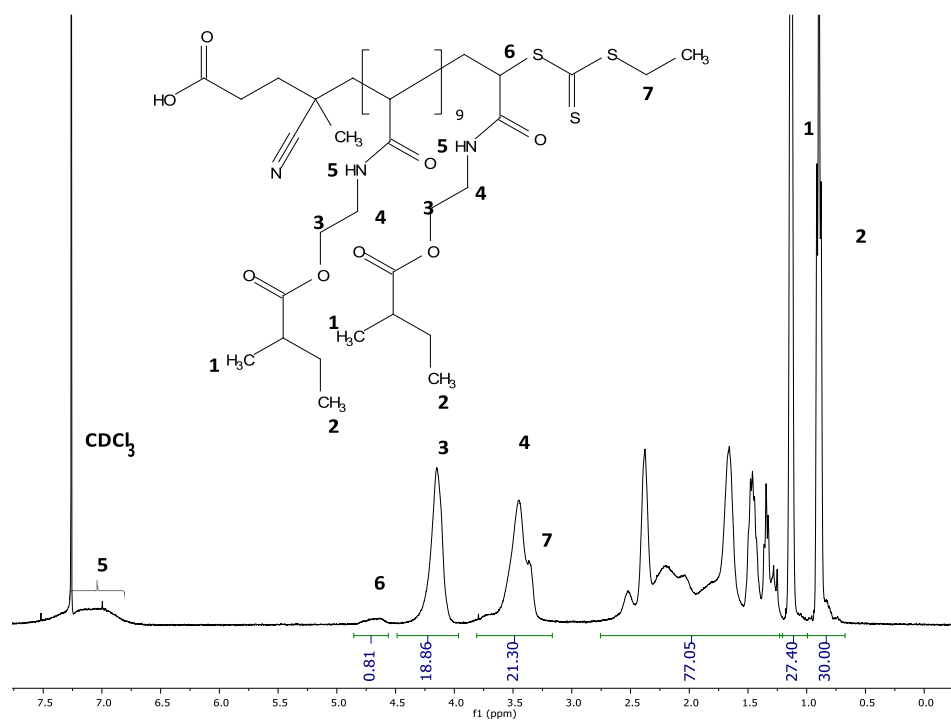
Figure S3.14: $^1$H NMR spectrum of oligomer MTB$_{10}$ in CDCl$_3$.
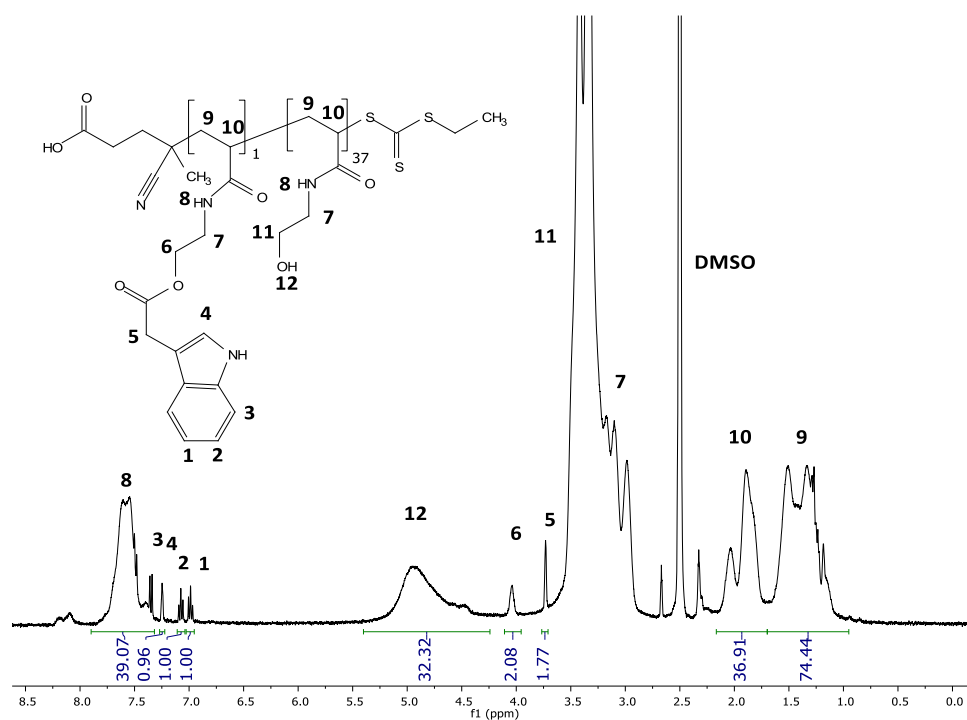


Figure S3.15: $^1$H NMR spectrum of copolymer IND$_1$-*b*-HEA$_{37}$ in d$_6$-DMSO.
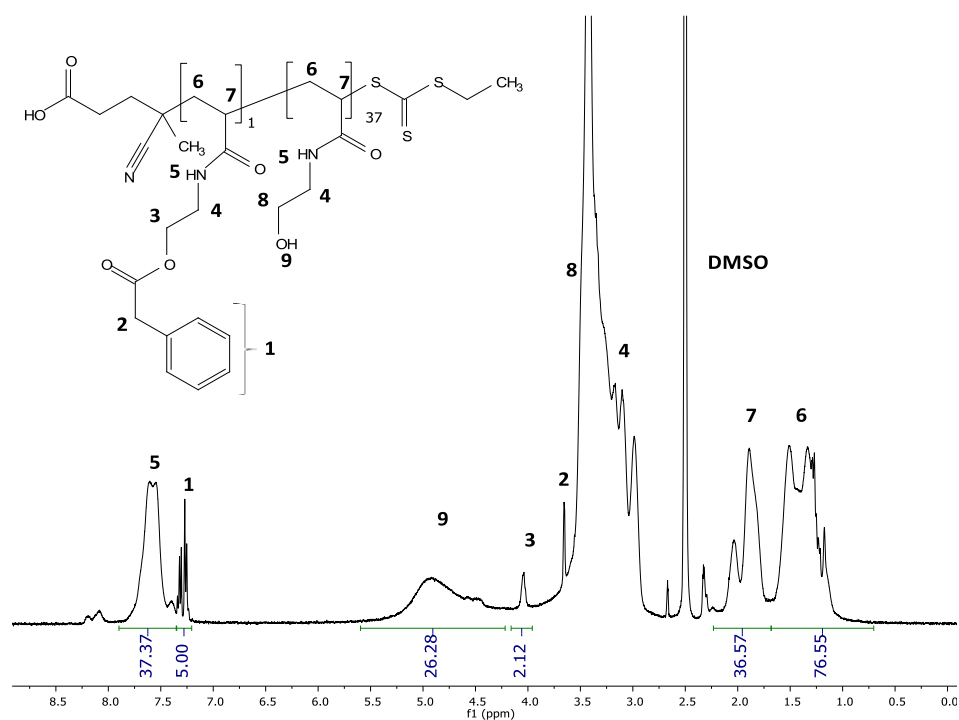
Figure S3.16: $^1$H NMR spectrum of copolymer PHEN$_1$-*b*-HEA$_{37}$ in d$_6$-DMSO.
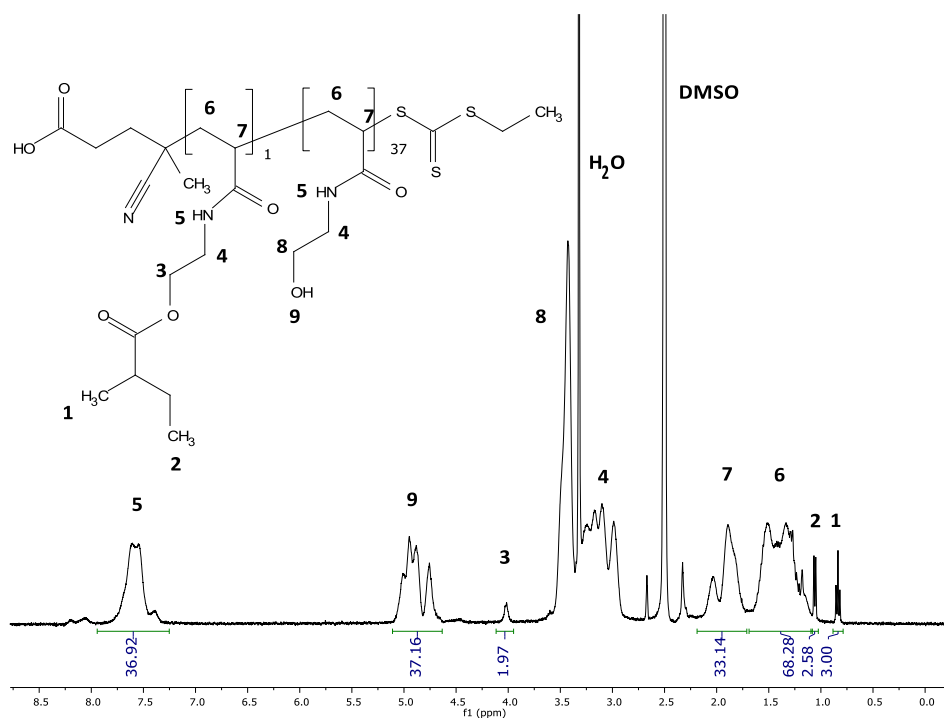


Figure S3.17: $^1$H NMR spectrum of copolymer MTB$_1$-*b*-HEA$_{37}$ in d$_6$-DMSO.
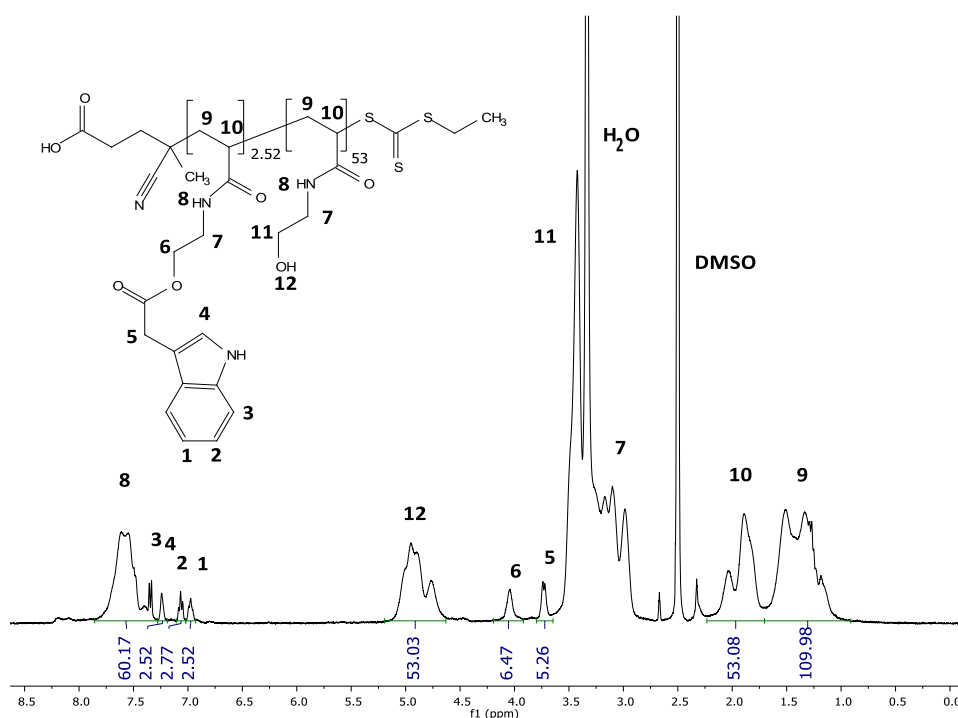
Figure S3.18: $^1$H NMR spectrum of copolymer IND$_3$-*b*-HEA$_{53}$ in d$_6$-DMSO.
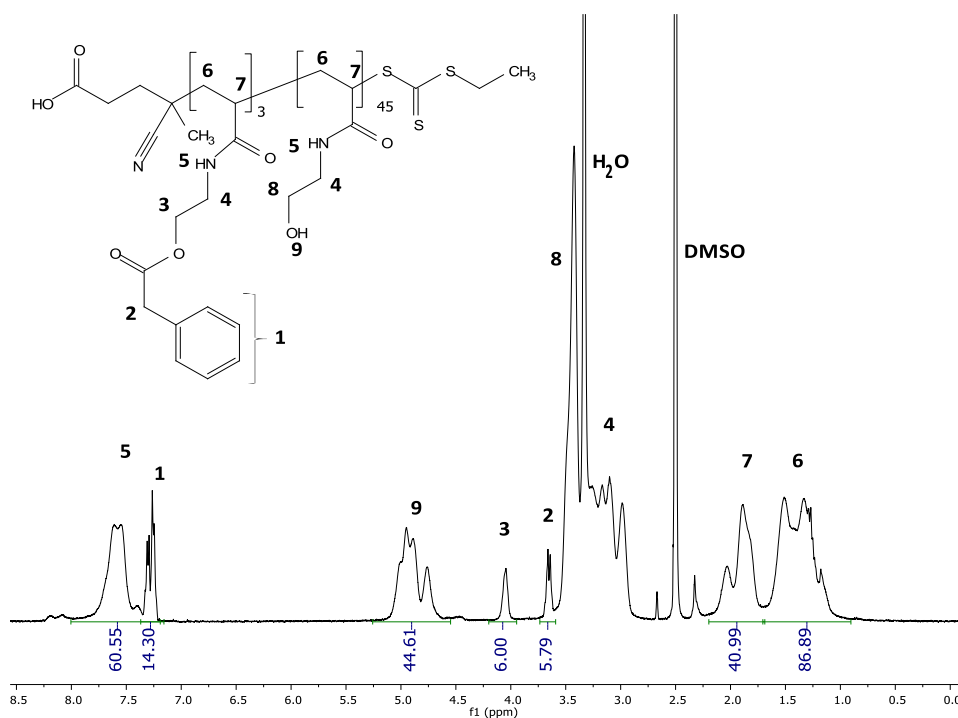


Figure S3.19: $^1$H NMR spectrum of copolymer PHEN$_3$-*b*-HEA$_{45}$ in d$_6$-DMSO.
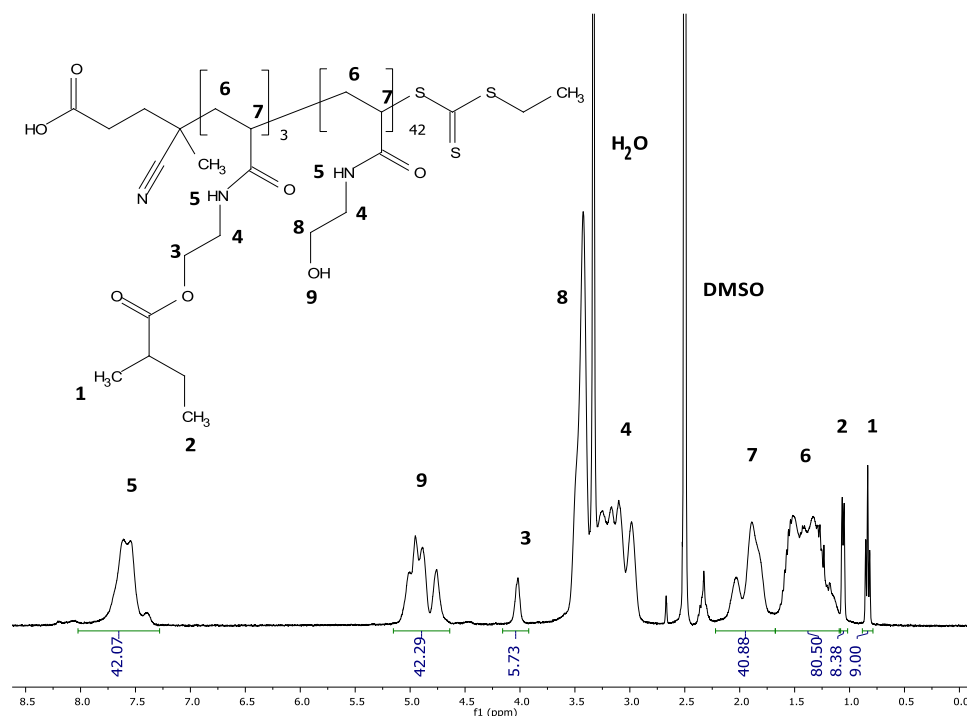
Figure S3.20: $^1$H NMR spectrum of copolymer MTB$_3$-*b*-HEA$_{42}$ in d$_6$-DMSO.
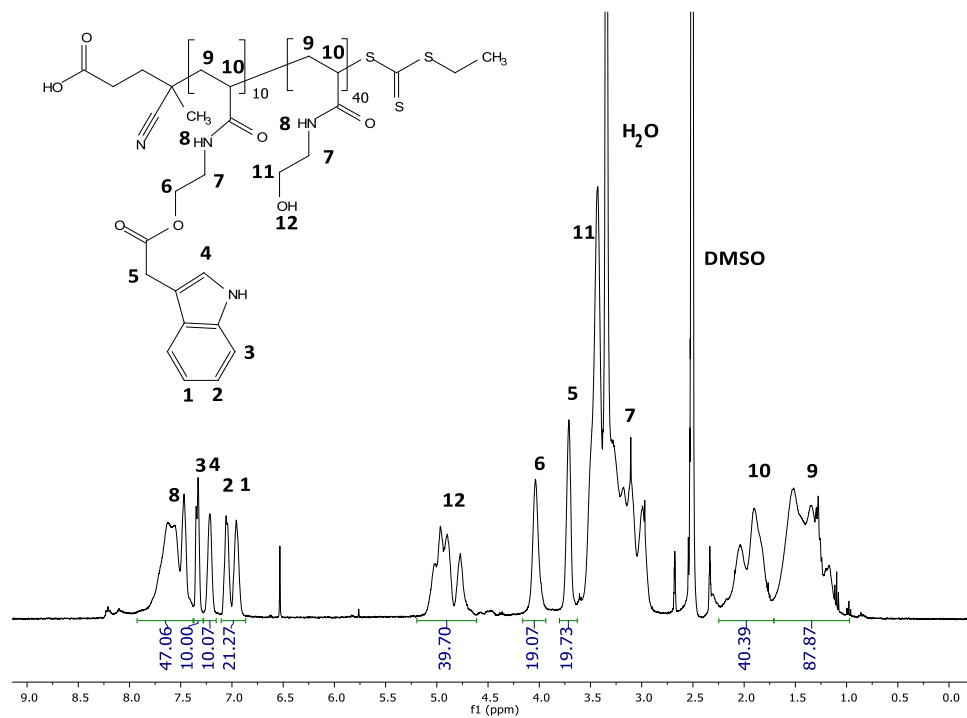


Figure S3.21: $^1$H NMR spectrum of copolymer IND$_{10}$-b-HEA$_{40}$ in d$_6$-DMSO.
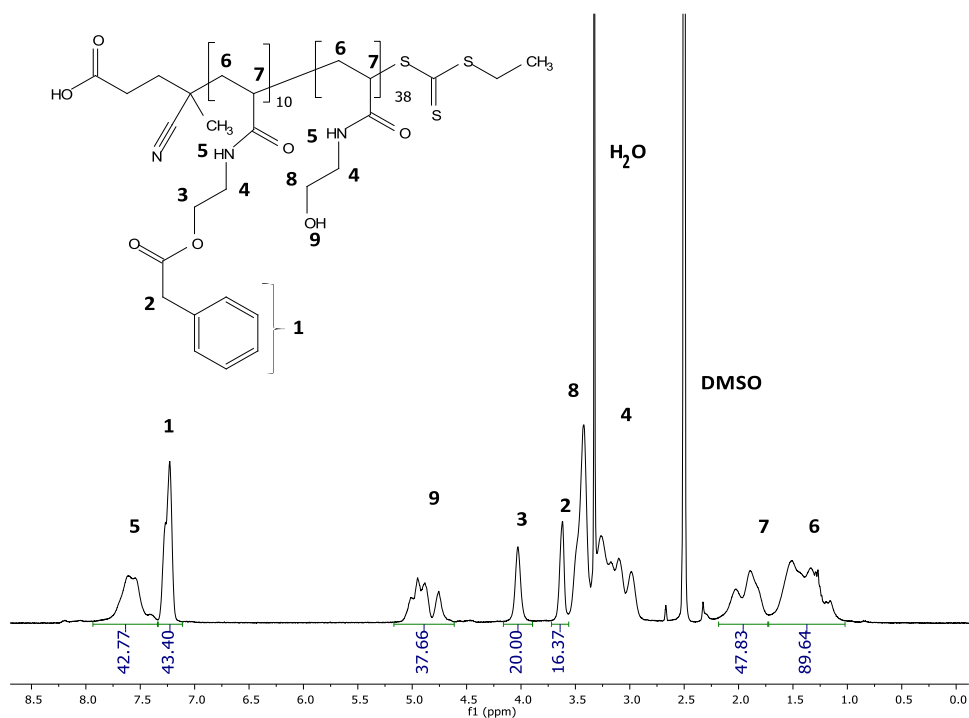
Figure S3.22: ¹H NMR spectrum of copolymer PHEN₁₀-*b*-HEA₃₈ in d₆-DMSO.
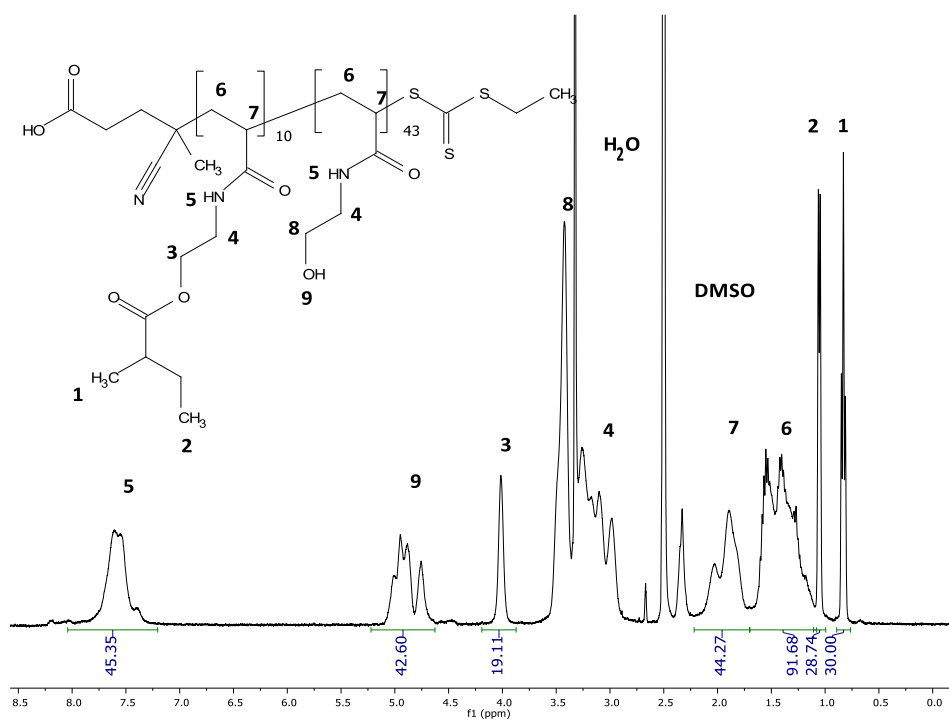


Figure S3.23: ¹H NMR spectrum of copolymer MTB₁₀-*b*-HEA₄₃ in d₆-DMSO.
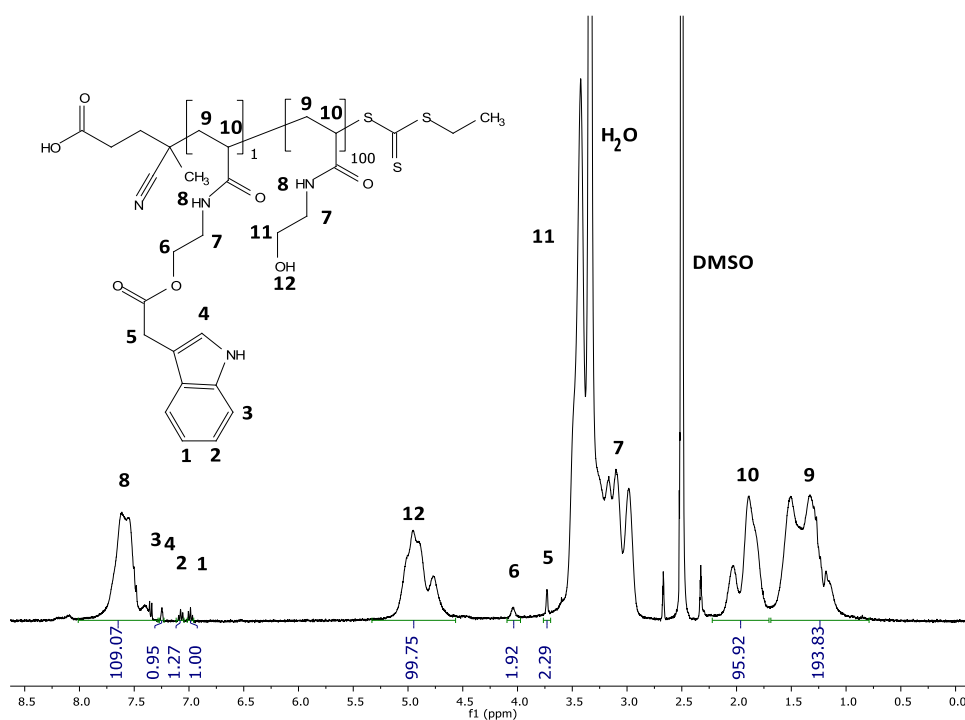
Figure S3.24: $^1$H NMR spectrum of copolymer IND$_1$-*b*-HEA$_{100}$ in d$_6$-DMSO.
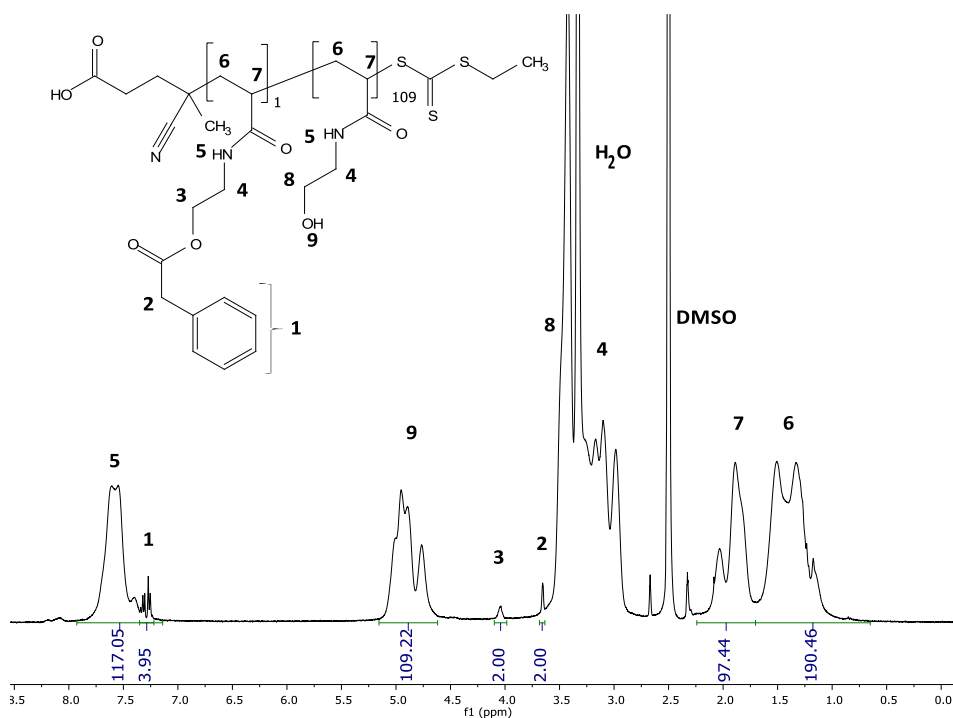


Figure S3.25: $^1$H NMR spectrum of copolymer PHEN$_1$-*b*-HEA$_{109}$ in d$_6$-DMSO.
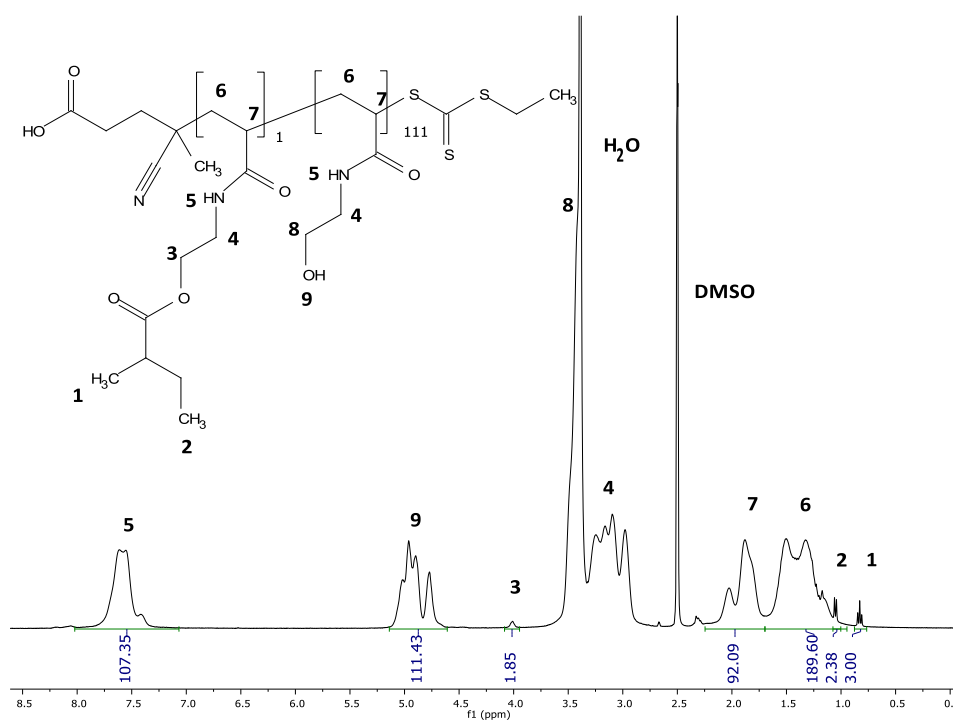
Figure S3.26: $^1$H NMR spectrum of copolymer MTB$_1$-*b*-HEA$_{111}$ in d$_6$-DMSO.
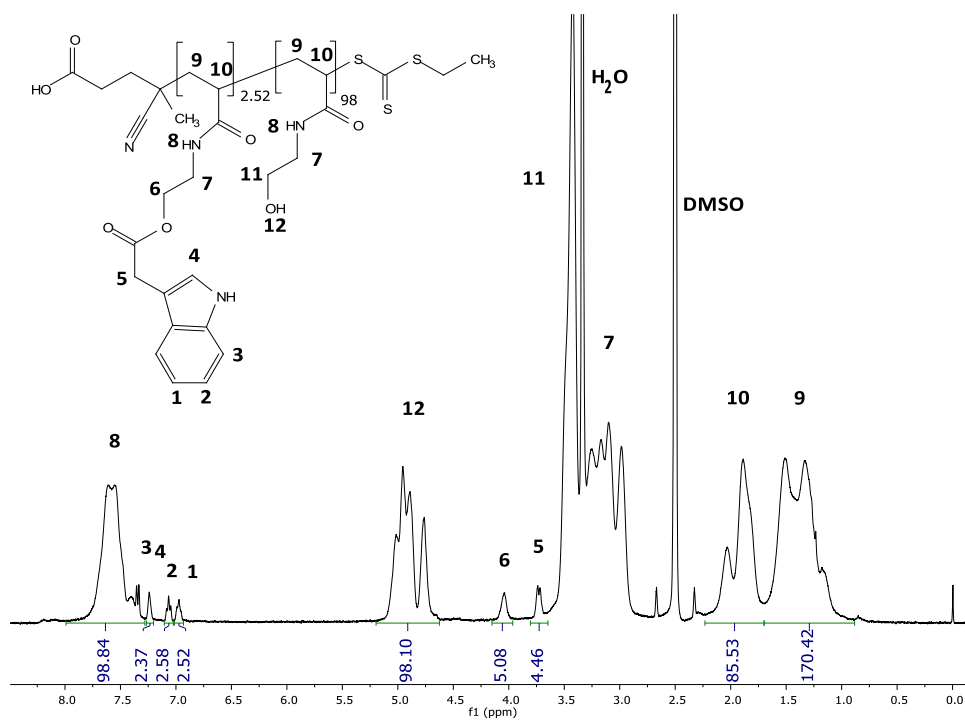


Figure S3.27: $^1$H NMR spectrum of copolymer IND$_3$-*b*-HEA$_{98}$ in d$_6$-DMSO.
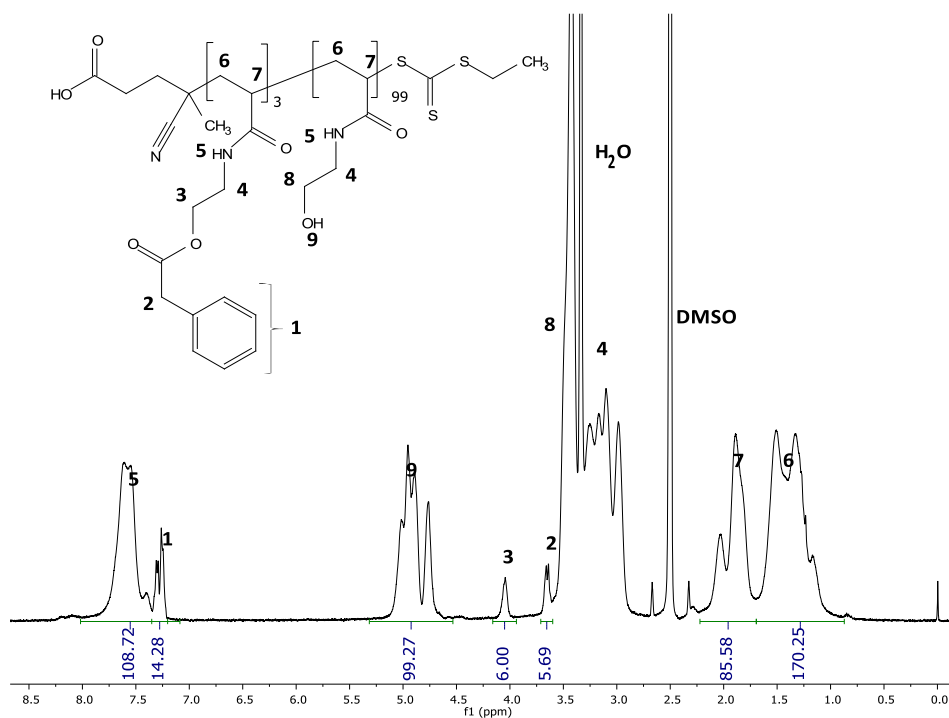
Figure S3.28: $^1$H NMR spectrum of copolymer PHEN$_3$-*b*-HEA$_{99}$ in d$_6$-DMSO.
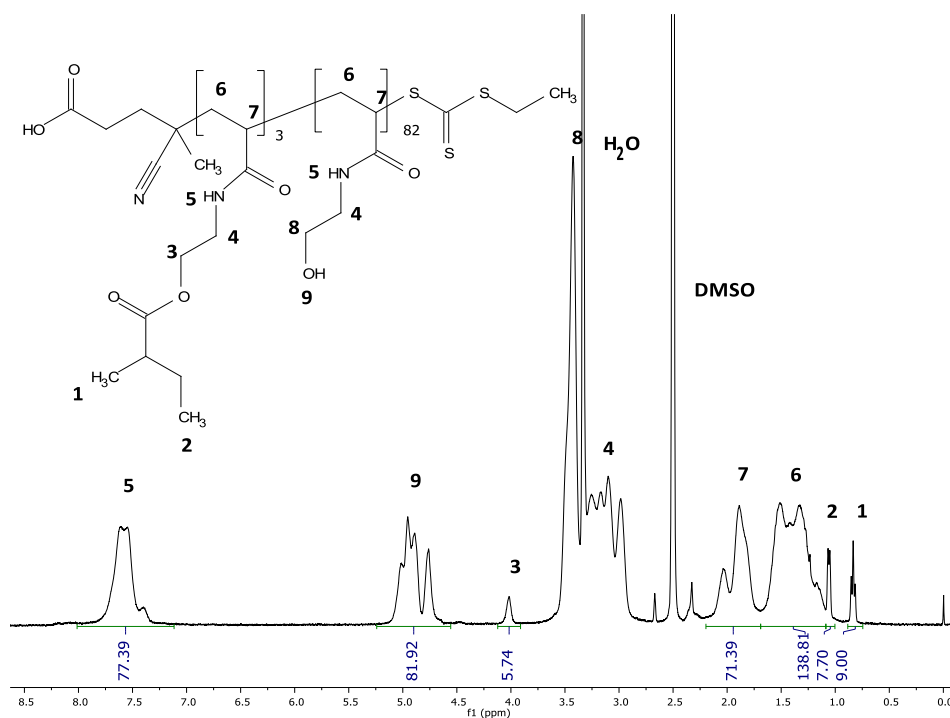


Figure S3.29: $^1$H NMR spectrum of copolymer MTB$_3$-*b*-HEA$_{82}$ in d$_6$-DMSO.
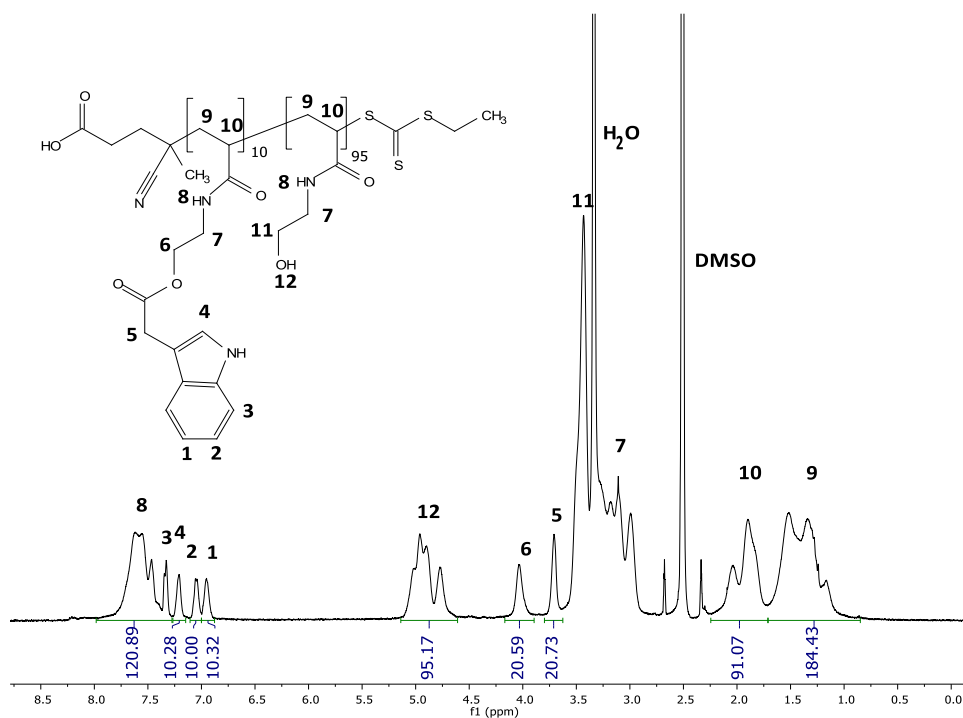
Figure S3.30: $^1$H NMR spectrum of copolymer IND$_{10}$-*b*-HEA$_{95}$ in d$_6$-DMSO.
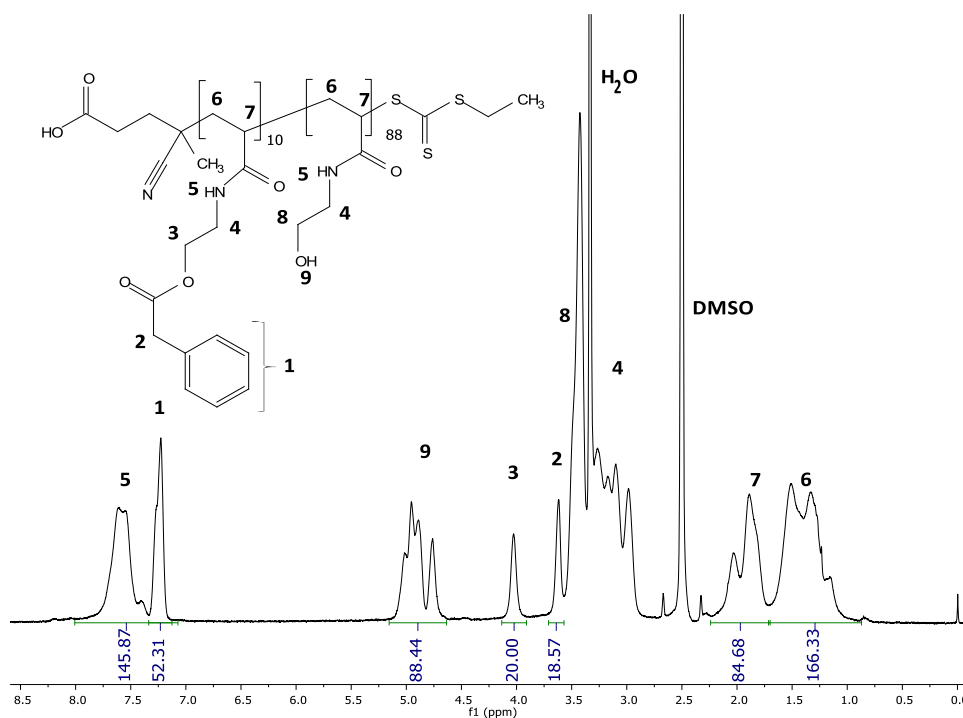


Figure S3.31: $^1$H NMR spectrum of copolymer PHEN$_{10}$-*b*-HEA$_{88}$ in d$_6$-DMSO.

223
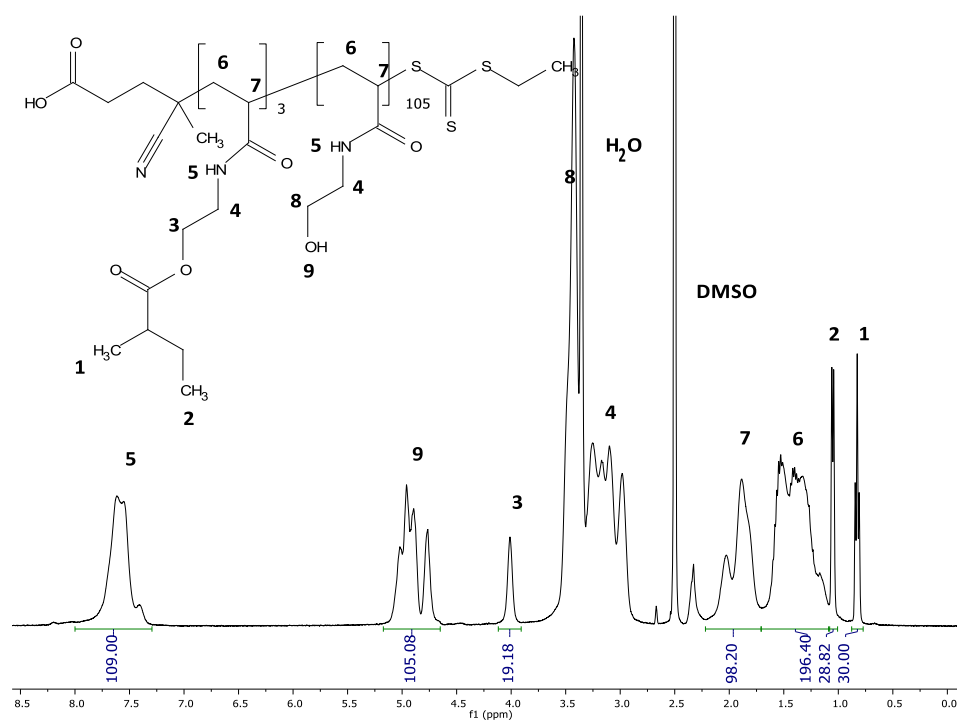
Figure S3.32: $^1$H NMR spectrum of copolymer MTB$_3$-*b*-HEA$_{105}$ in d$_6$-DMSO.
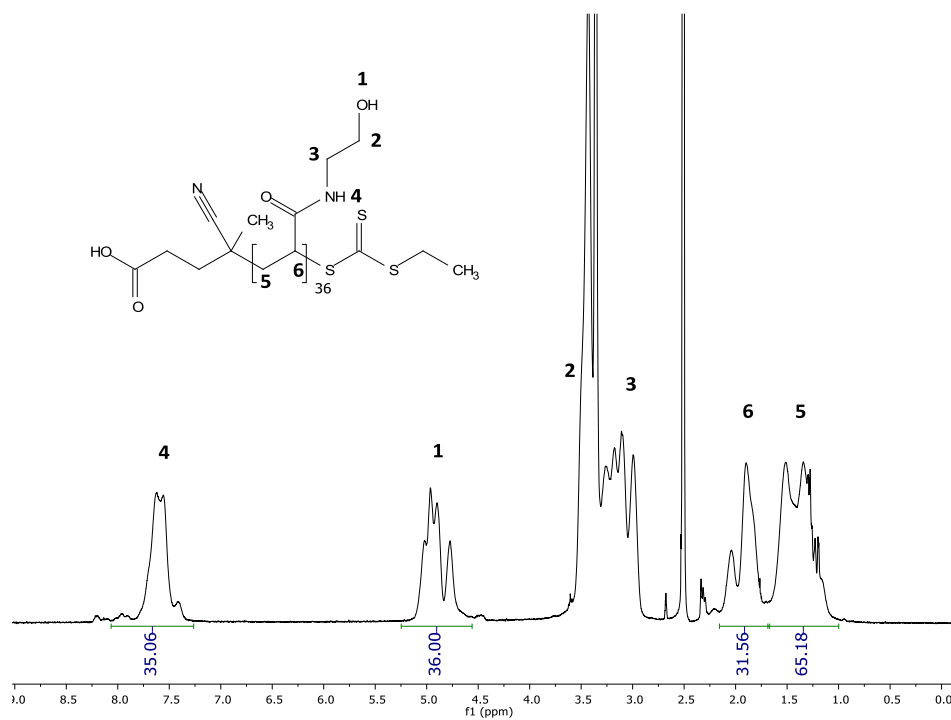


Figure S3.33: $^1$H NMR spectrum of polymer HEA$_{36}$ in d$_6$-DMSO.
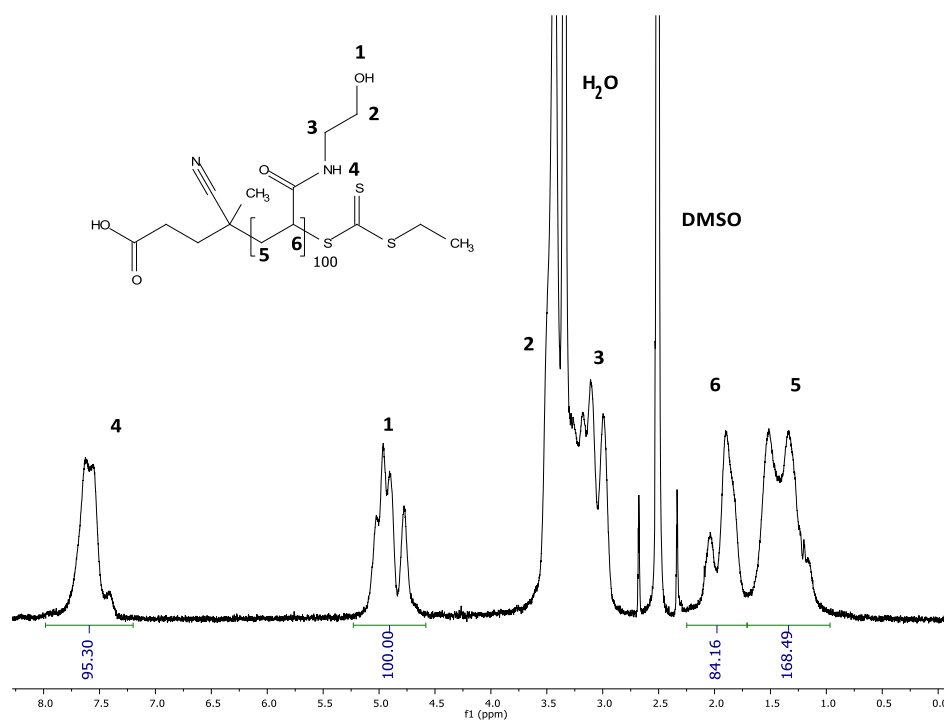
Figure S3.34: $^1$H NMR spectrum of polymer HEA$_{100}$ in d$_6$-DMSO.
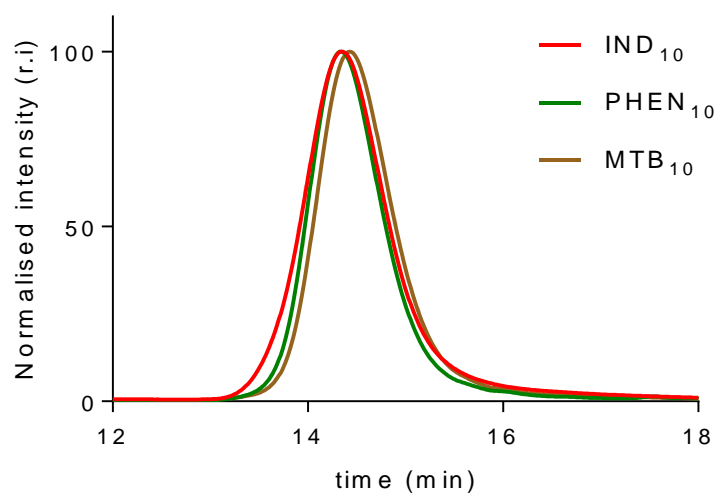


Figure S3.35: normalised SEC traces of IND$_{10}$, PHEN$_{10}$ and MTB$_{10}$. SEC analyses were performed in THF (PMMA standards).
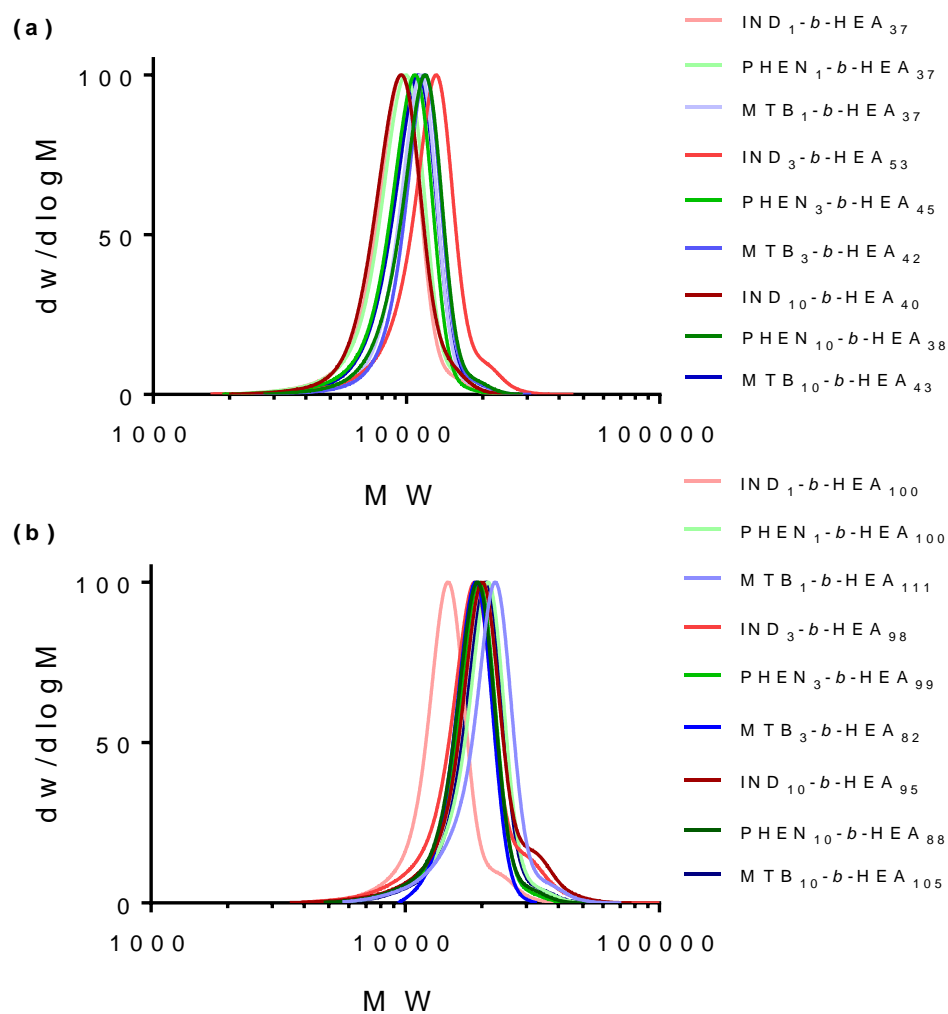
Figure S3.36: normalised SEC traces of (a) HEA 40 DP and (b) HEA 100 DP $IND_m$-*b*-$HEA_n$ copolymers. SEC analyses were performed in DMF + 0.1 % LiBr (PMMA standards).
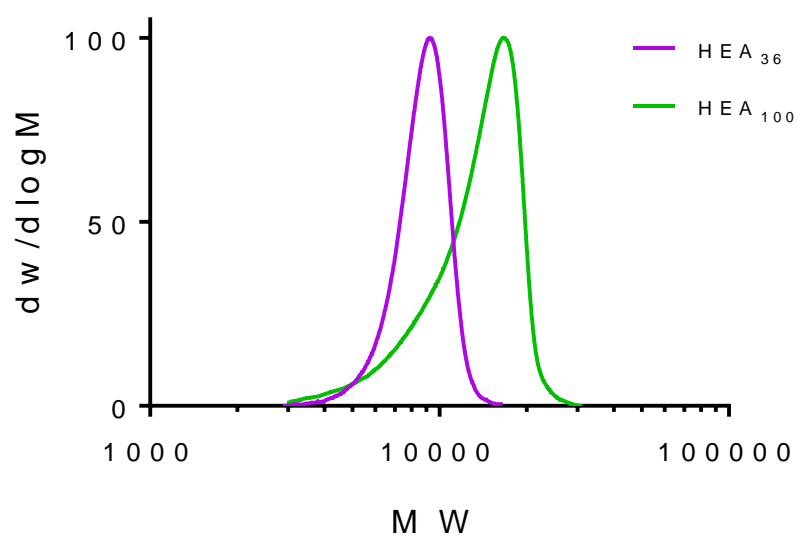
Figure S3.37: normalised SEC traces of control polymers HEA$_{36}$ and HEA$_{100}$. SEC analyses were performed in DMF + 0.1 % LiBr (PMMA standards).
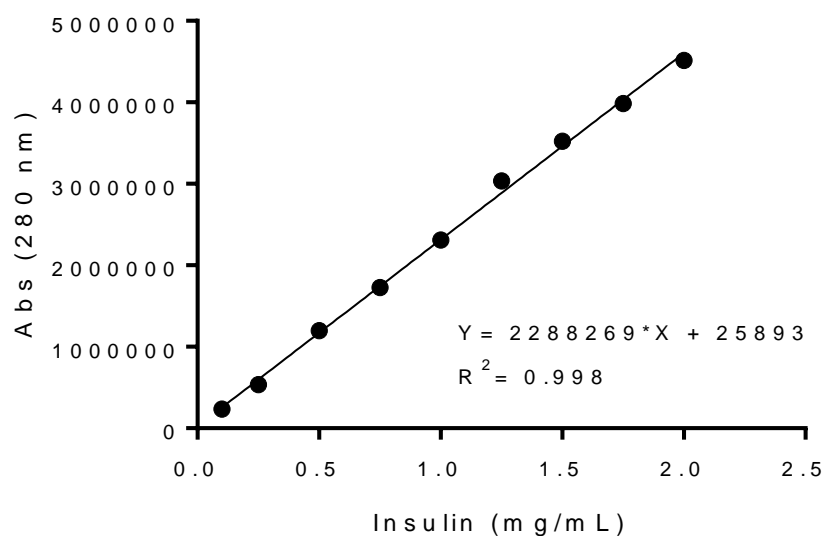
Figure S3.38: insulin calibration curve. Insulin was dissolved in 10 mM pH2 phosphate buffer at different concentrations in the 0.1-2 mg/mL range. The samples were analysed in triplicates by RP-HPLC, using a 20-80% MeCN gradient in Milli-q water + 0.1 % TFA. Absorbance was recorded at 280 nm. The area under insulin peak was calculated for each concentration.
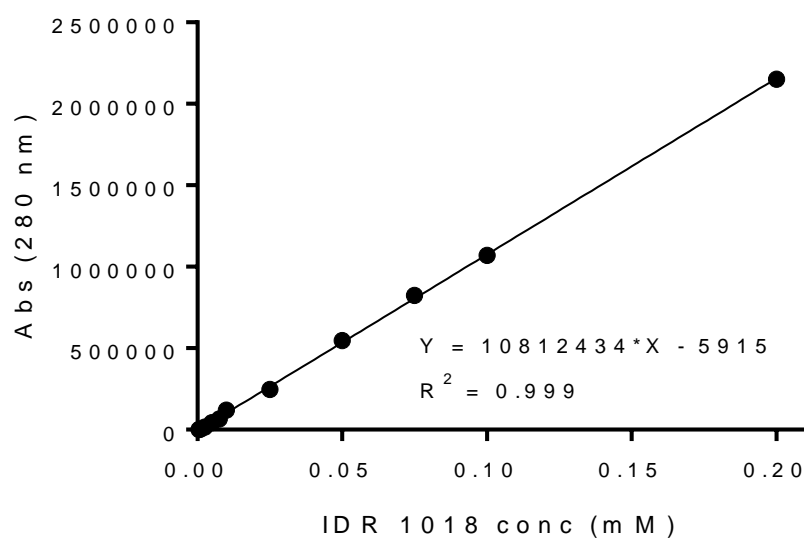


Figure S3.39: IDR 1018 calibration curve. IDR 1018 was dissolved in deionised water at different concentrations in the 0.0005-0.2 mM range. The samples were analysed in triplicates by RP-HPLC, using a 25-80% MeCN gradient in Milli-q water + 0.1 % TFA. Absorbance was recorded at 280 nm. The area under IDR 1018 peak was calculated for each concentration.

# Chapter 4

**Hydrophobic ion paired-complexes for the co-delivery of two antimicrobial drugs**

_____

## 4.1. Introduction

Antimicrobial resistance has become an increasingly concerning threat. The diffusion of new resistance mechanisms (e.g. chemical modification of the antibiotic molecule by bacterial enzymes, decreased antibiotic penetration and increased efflux, changes in the target sites[1]) may eventually hamper the efficacy of current treatments for common infectious diseases, leading to longer recovery times, increased number of deaths and higher healthcare costs[2]. A recent review commissioned by the UK government estimates the number of deaths caused by antimicrobial resistance to increase worldwide from approximately 700,000 to 10 million per year by 2050[3].

Considerable efforts have been made to identify new potential therapies that could overcome antimicrobial resistance. Among these, antimicrobial peptides (AMPs) have emerged as a potential alternative to treat various infections. AMPs often combine antibacterial activity with anti-inflammatory and immunomodulatory properties[4]. In Nature, AMPs can be found in both prokaryotes and eukaryotes: in evolved organisms they actively protect the host against infections; in bacteria, they are produced to kill other bacteria competing for the same ecological niche[5]. AMPs are characterised by a wide range of potential therapeutic applications, as they can display antimicrobial activity on both Gram-positive and Gram-negative bacteria, together with immunostimulant properties[5].

These peptides are usually characterised by less than 50 amino acid residues with an overall positive charge, due to multiple lysine and arginine residues,

and a proportion of hydrophobic residues that confer AMPs an amphipathic character. Based on their secondary structure, they are generally divided on four classes: β-sheet, α-helical, loop, and extended peptides[6]. They can also be classified based on their mechanism of action: most of antimicrobial peptides exert their activity through membrane permeabilization, which induce membrane rupture and cell death. Bacterial membranes of both Gram-positive and Gram-negative bacteria are rich in phosphatidylglycerol, cardiolipin, and phosphatidylserine phospholipids, whose negatively charged head groups can attract the positive residues on peptides sequence. Once the peptide is in contact with the membrane, its hydrophobic residues allow peptide insertion in the membrane, causing leakage of ions and nutrients, and eventually membrane depolarization and disruption[5].

Recently, there has been increased evidence on the existence also of intracellular targeting AMPs. These peptides can cross bacterial cytoplasmic membrane through endocytosis, and act as inhibitors at specific targets on bacterial cytoplasm. For example, they can hamper nucleic acid or protein biosynthesis, protein folding, protease activity, and cell wall or cell membrane biosynthesis[7]. A number of AMPs can act at more than one intracellular target, and even combine intracellular activity with membrane disruption. As mentioned above, often bactericidal activity is accompanied by immunomodulatory properties (e.g. modulation of immune cell differentiation and initiation of adaptive immunity, suppression of proinflammatory cytokines and anti-endotoxin activity[5]), so it is no surprise that these molecules can act

over a range of different bacteria, and the insurgence of mechanisms of bacterial resistance is more unlikely[5].

### 4.1.1. Nanoparticles as delivery systems for antimicrobial peptides

However, different challenges can be identified which significantly hamper the development of antimicrobial peptides for clinical applications. Antimicrobial Peptides can be degraded by both human and bacterial proteases, which are often present in high concentrations in infected tissues. Rapid degradation is therefore to be expected after peptide local or systemic administration. Moreover, peptides are likely to undergo a very fast renal clearance due to their small size[8]. In some infections, like for example tuberculosis, bacteria are usually localised inside macrophages, requiring suitable targeted delivery systems which can increase the specific internalisation of antimicrobial peptides in this cell line[9].

Controlled-release of AMPs has been achieved using different inorganic nanoparticles. Antimicrobial peptide LL-37 was successfully incorporated into anionic mesoporous silica nanoparticles, through electrostatic interactions. Nanoparticles were found to protect *in vitro* the incorporated peptide from infection-related proteases [10]. Cyclic peptide *N*-halamine was immobilised on polystyrene-coated silica nanoparticles, which then displayed 2–8 times higher antimicrobial activity against *S. aureus* and *E. coli* than the corresponding unloaded nanoparticles[11].

Polymeric nanoparticles have also been explored as carriers for antimicrobial peptides: the peptide colistin was loaded into chitosan-decorated PLGA nanoparticles. Loaded particles showed prolonged eradication efficacy, compared to free colistin, against *P. aeruginosa* biofilm, ascribed to particles penetration inside the biofilm[12]. Antibacterial peptide nisin was encapsulated into chitosan-decorated polyglutamic nanoparticles, and loaded nanoparticles were more effective than nisin alone in inhibiting the growth of *E.coli*[13].

## 4.1.2. Antimicrobial peptides ion pairing and the role of ion pairs in drug delivery

In a recent study, Prud'homme and co-workers presented an innovative approach where cationic AMPs were electrostatically ion paired to form hydrophobic complexes of sub-micron size.[14] In this work, two peptides, gentamicin and polymyxin B, were mixed in water together with a wide range of amphiphilic molecules, such as fatty acids and surfactant. Basic residues on the peptides sequence established an electrostatic interaction with acidic, negatively charged functional groups on these amphiphilic molecules. As a result of these ionic interactions, charges on both molecules were neutralised, and the hydrophobic residues on the peptides and the surfactants caused the precipitation in water of both the peptides and their ionic counterparts. The addition of polymeric PEG-*b*-PCL stabilisers allowed to control the precipitation process and generate colloidally stable, neutral ion pair nanoparticles[14].

Ion pairing is defined as the association of oppositely charged ions in electrolyte solutions to form distinct chemical species called ion pairs[15]. Ion pairing is a convenient technique to increase lipophilicity of water soluble drugs, to

enhance their encapsulation in nanoparticles systems[16]. For example, minocycline, an antibiotic with anti-inflammatory and neuroprotective properties, was ion paired with sodium bis(2-ethylhexyl) sulfosuccinate surfactant, wich allowed to enhance its encapsulation in PLGA nanoparticles from 1 % to over 40 %[17]. Insulin encapsulation into Solid Lipid Nanoparticles (SLN) was accomplished by ion-pairing the protein with SDS in an aqueous pH 2.5 HCl solution. Ion pair incorporation resulted in 89% insulin encapsulation.[18].

## 4.1.3. Aims and objectives

In the previous chapter, we synthesised the hydrophobic oligomer $IND_{10}$ as a macro-CTA RAFT agent to mediate the copolymerisation of monomer *N*-Hydroxyethylacrylamide. In preliminary experiments, we observed that in water $IND_{10}$ forms homogenous milky-like mixtures, suggestive of the formation of sub-micron nanoparticles (Fig. 4.1).

In this part of our work, we decided to induce the controlled self-assembly of $IND_{10}$ into nicely shaped and narrowly disperse nanoparticles with a nanoprecipitation method, to investigate the loading of antimicrobial peptide IDR 1018 into these nanoparticles.
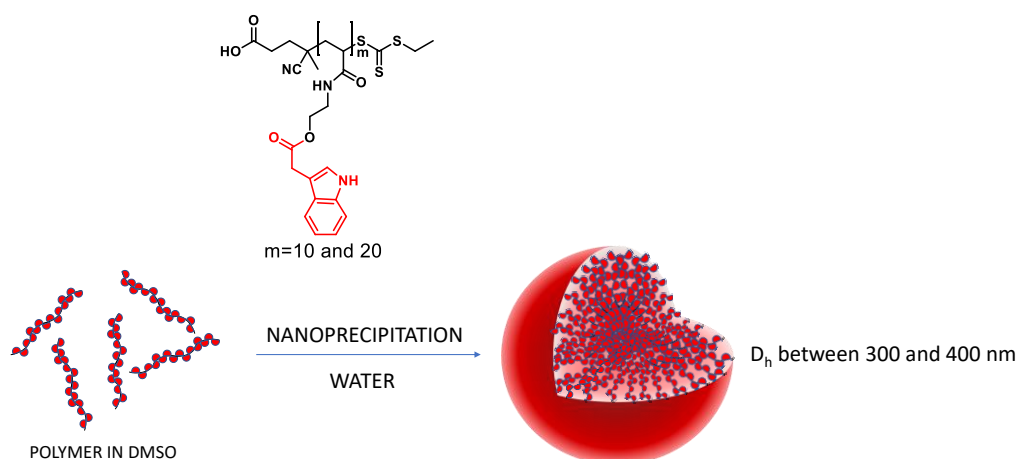
Figure 4.1: self-assembly of IND-oligomers was investigated in this chapter. Nanoparticles formation was induced by nanoprecipitation, by addition of water to solutions of oligomers in DMSO.

As discussed in the previous chapter, IDR 1018 is a synthetic peptide known for its dual antimicrobial and immunomodulatory activity. Its moderate direct bactericidal properties were tested *in vitro* on different bacterial strains, including *P. aeruginosa* (MIC 19 μg/mL) and *S. aureus* (MIC 4 μg/mL)[19]. Like many AMPs, this amphipathic peptide structure comprises basic and hydrophobic residues (Fig. 4.2). Although its mechanism of action has not been completely elucidated, its lack of interaction with bacterial membranes suggests an intracellular target[19].
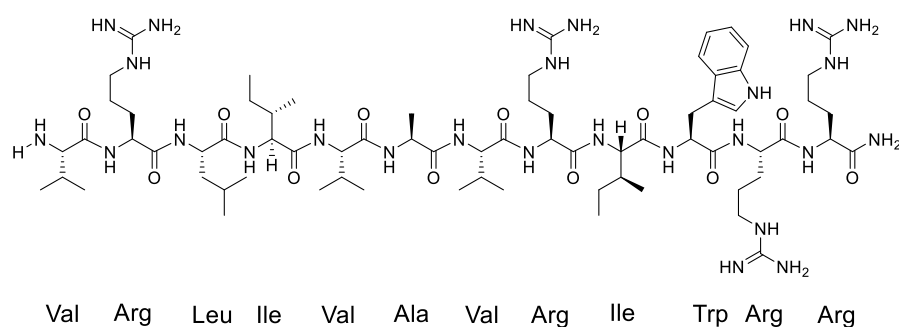


Figure 4.2: chemical structure of peptide IDR 1018.

Previous research within our group by Dr Vincenzo Taresco, focussed on lichen metabolite usnic acid[20](Fig. 4.3). Usnic acid possesses weak antimicrobial properties with a MIC of 32 µg/ml against *S. aureus* and 256 µg/ml for *P. aeruginosa*. Again, its mechanism of action has not been completely elucidated, but experimental evidence suggests intracellular targets, with inhibition of RNA transcription[21]. Relevant with our work, in a recent study by Taresco *et Al*, manganese iron oxide magnetic nanoparticles were coated with a hydrophilic cationic poly-dibutylaminoethylacrylamide, whose tertiary amino groups were employed to electrostatically entrap usnic acid through its acidic hydroxyl groups. The specific ionic interaction ensured high loading (0.48 ± 0.05 mg UA/mg NPs), and nanoparticles displayed good antimicrobial activity on *Staphylococcus epidermidis* (MIC = 0.1 mg/mL)[22].
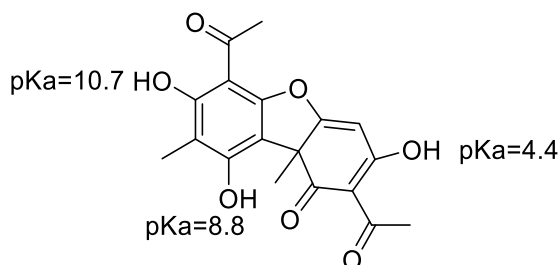


Figure 4.3: chemical structure of usnic acid.

Due to its antimicrobial activity and its ability to form electrostatic interactions with basic groups, we decided to use usnic acid as potential IDR 1018 counter ion for ion pairing. We anticipated that the electrostatic complex would have increased hydrophobic character compared to uncomplexed, positively charged IDR 1018, enhancing IDR 1018 incorporation into nanoparticles and allowing the co-delivery of two antimicrobial drugs, IDR 1018 and usnic acid.

Hence, in this chapter we aimed at developing a family of different IND-based nanoparticles, characterised by narrow polydispersity, to be used for the controlled release of two different antimicrobial drugs, encapsulated as a hydrophobic complex, and evaluate potential for antimicrobial synergistic effect (Fig. 4.4).
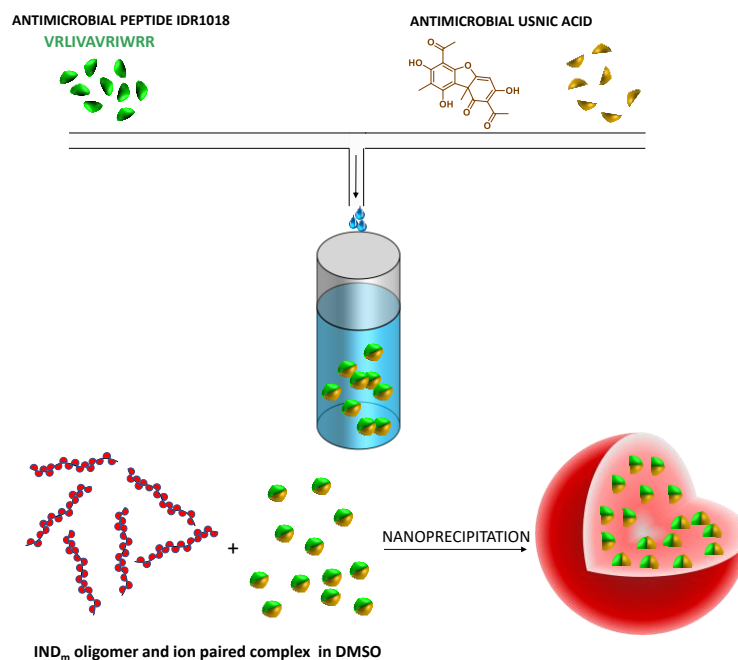


Figure 4.4: Assembly of ion-paired $IND_m$-based-nanoparticles: general strategy. Aqueous solutions of IDR 1018 peptide and usnic acid sodium salt were mixed together, to generate hydrophobic, water-insoluble ion paired complexes through electrostatic interactions. These were then incorporated within $IND_m$-based-nanoparticles by nanoprecipitation.

A suitable method for IND-oligomers self-assembly into nanoparticles was therefore developed. Complexes resulting from different ratios of IDR 1018 and usnic acid were evaluated to find the best conditions for IDR 1018-usnic acid complex encapsulation. Loading and encapsulation were evaluated by RP-HPLC, while the size and shape of free and loaded nanoparticles were evaluated by DLS and TEM.

Finally, antimicrobial activity of complex-loaded nanoparticles was evaluated

on *salmonella*-infected macrophages in a preliminary study (Fig. 4.5).
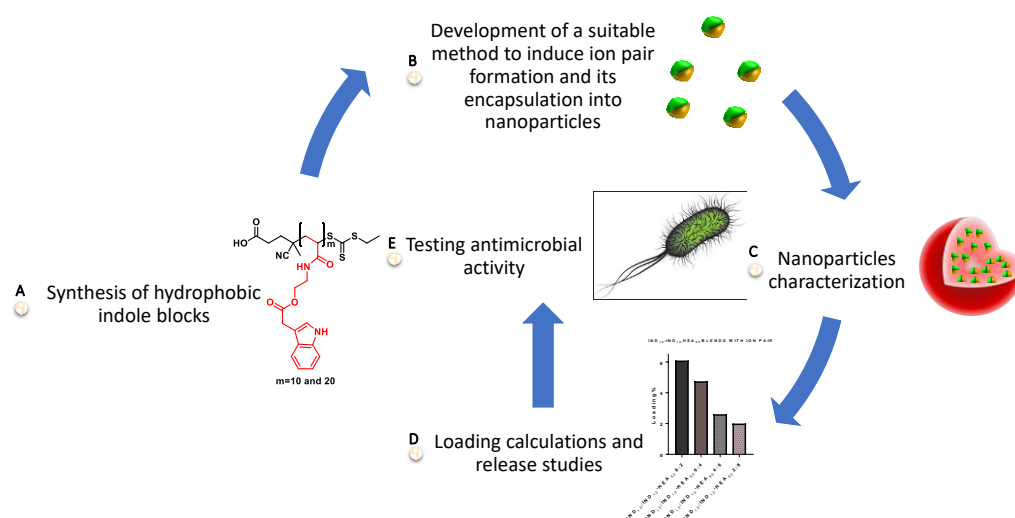


Figure 4.5: experimental plan for this chapter: (A) Synthesis of hydrophobic $IND_m$ oligomers ($IND_{10}$ and $IND_{20}$), to be self-assembled into nanoparticles. (B) Ion pairing between usnic acid and peptide IDR 1018 for IDR 1018-usnic acid complex precipitation. (C) Formulation of unloaded, and complex-loaded nanoparticles. (D) Quantification of complex loading capacity and encapsulation efficiency for each nanoparticle formulation. (E) Investigations on antimicrobial activity of complex-loaded nanoparticles.

# 4.2. Materials and methods

## 4.2.1. Materials

Peptide IDR 1018 was a kind gift from MedImmune LTD (Cambridge, United Kingdom). Methanol, acetonitrile, diethyl ether, tetrahydrofuran, *N,N*-dimethylformamide (DMF) and acetone were purchased from Fisher Scientific (Bishop Meadow Rd, Loughborough, UK). *N*-hydroxyethylacrylamide (97%), indole 3-acetic acid (≥98%), sodium hydroxide, usnic acid (98%) and VA-501 (≥98%),were obtained from Sigma-Aldrich (St. Louis, Missouri, United States). Azobisisobutyronitrile (AIBN) was purchased from FUJIFILM Wako Pure Chemical, Ltd.

## 4.2.2. Synthesis of homo-oligomer IND$_{20}$



IND$_{20}$ m=20 $M_{n,THEO}$: 5.40 kDa; $M_{n,SEC}$:8.60 kDa. PDI 1.13
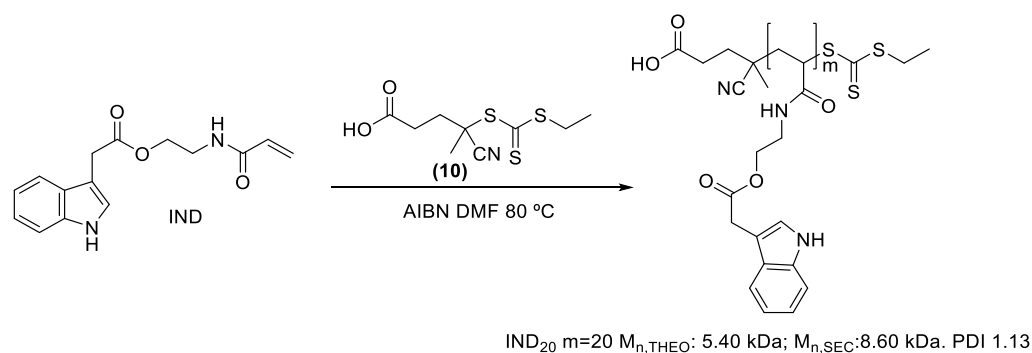
Scheme 4.1: synthesis of oligomer IND$_{20}$.

The synthesis of the hydrophobic homo-oligomer IND$_{20}$ was achieved through RAFT polymerization, using CTA (**10**) as RAFT agent (synthesised in Chapter 2) in combination with monomer IND (synthesised in Chapter 3). CTA (**10**) (1 eq., 0.050 g, 0.19 mmol) and monomer IND (25 eq., 1.29 g, 4.75 mmol) were mixed together in 2 mL of DMF. The solution was transferred into a small Schlenk tube equipped with a magnetic stirrer, which was put on ice. Initiator AIBN (0.1 eq.,

5 mg, 0.02 mmol), previously dissolved in DMF (50 µL), was added to the tube.

The mixture was degassed for 30 min under argon at 0˚C, and finally put on a

paraffin oil bath at 80˚C. The reaction was monitored by $^1$H NMR, checking the

disappearance of acrylamide monomer peaks into the 5-6.5 ppm region, until

~ 80% conversion was reached. The solution was then diluted with acetone and

purified by multiple precipitations in Et$_2$O. The final precipitate was dried under

reduced pressure. IND$_{20}$ was characterised by $^1$H NMR and SEC, using DMF with

0.1 % LiBr as the mobile phase.

IND$_{20}$ Yield: 67%. $^1$H NMR (400 MHz, d6-DMSO, δ, ppm), 10.89 (s, 20H, indole NH), 7.45 (m, 20H, CH, CH aromatic), 7.32 (m, 20H, CH, CH aromatic, 7.20 (m, 20H, CH, CH aromatic), 7.03 (m, 20H, CH, CH aromatic), 6.93 (m, 20H, CH, CH aromatic), 4.03 (m, 40H, C$H_2$CH$_2$NH), 3.69 (m, 40H, CH$_2$CO), 2.4-1.9 (m, 20H CH$_2$C$H$), 1.9-1 (m, 40H C$H_2$CH) (Fig. S4.1). M$_{n,THEO}$: 5.70 kDa. M$_{n,SEC(DMF)}$ 8.40 kDa, Đ=1.13 (Fig. S4.9).

IND$_{10}$ characterisation is reported in Chapter 3.

### 4.2.3. Synthesis of IND$_{10}$-*b*-HEA$_{268}$, IND$_{20}$-*b*-HEA$_{74}$ and IND$_{20}$-*b*-HEA$_{240}$ copolymers
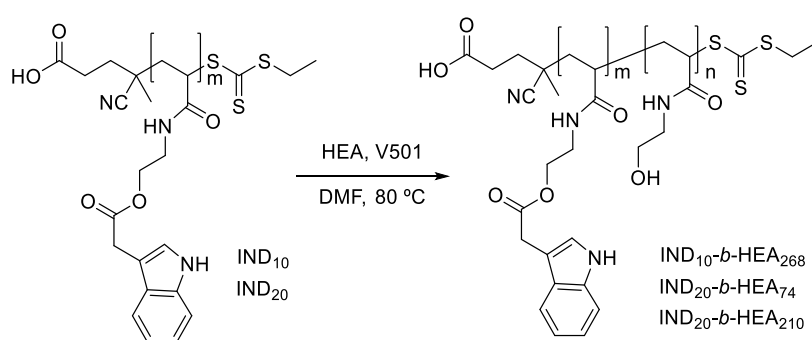


Scheme 4.2: synthesis of copolymers IND$_{10}$-*b*-HEA$_{268}$, IND$_{20}$-*b*-HEA$_{74}$, IND$_{20}$-*b*-HEA$_{240}$.

Copolymers were prepared by polymerization of commercial monomer *N*-

hydroxyethylacrylamide (HEA), using the oligomers IND$_{10}$ (synthesised in the

previous chapter) and $IND_{20}$ as macro RAFT agents. Typically, the oligomers (1 eq.; 0.10 g, 0.033 mmol of $IND_{10}$; or 0.20 g, 0.035 mmol of $IND_{20}$), were dissolved in DMF along with HEA (250 eq., 0.980 g, 8.25 mmol for $IND_{10}$-*b*-$HEA_{268}$, 100 eq., 0.421 g, 3.50 mmol for $IND_{20}$-*b*-$HEA_{74}$, 250 eq., 1.02 g, 8,75 mmol for $IND_{20}$-*b*-$HEA_{240}$) in DMF (2 mL for $IND_{10}$-*b*-$HEA_{230}$ and $IND_{20}$-*b*-$HEA_{240}$, 1 mL for $IND_{20}$-*b*-$HEA_{74}$). The mixtures were transferred into small schlenk tubes equipped with a magnetic stirrer, which were put in ice. Initiator V 501 (0.1 eq.), previously dissolved in DMF, was added to each tube. The mixtures were degassed for 30 min by Argon bubbling at 0˚C, and finally put on a paraffin oil bath at 70˚C. The reactions were monitored by ^{1}H NMR, checking the disappearance of acrylamide monomer peaks into the 5-6.5 ppm region, until ~ 80 % conversion was reached.

See Table below for reaction times and conversions.

Table 4. 1: Reaction times and conversions of copolymers.

| POLYMER | REACTION TIME (h) | CONVERSION (%) |
|---|---|---|
| $IND_{10}$-*b*-$HEA_{268}$ | 2 | 55 |
| $IND_{20}$-*b*-$HEA_{74}$ | 3 | 69 |
| $IND_{20}$-*b*-$HEA_{240}$ | 3 | 77 |

The copolymers were then precipitated in a 8:2 v/v $THF:Et_2O$ mixture, dried under reduced pressure and finally characterised by ^{1}H NMR and SEC in DMF using DMF with 0.1 % LiBr as the mobile phase.

$IND_{10}$-*b*-$HEA_{268}$ Yield: 47%. ^{1}H NMR (400 MHz, d6-DMSO, δ, ppm), 7.85-7.30 (m, 268H, polyacrylamide NH), 7.32 (m, 10H, CH, CH aromatic), 7.19 (m, 10H, CH, CH aromatic), 7.04 (m, 10H, CH, CH aromatic), 6.95 (m, 10H, CH, CH aromatic), 5.21-4.70 (m, 268H, polyacrylamide OH), 4.03 (m, 20H, $CH_2$), 2.25-1.70 (m, 268H, polyacrylamide C*H*$CH_2$) 1.70-0.90 (m, 536H, polyacrylamide CHC*H*$_2$). $M_{n,NMR}$: 34.4 kDa (Fig. S4.2). $M_{n,SEC(DMF)}$ 32.2 kDa, Đ=1.19.

$IND_{20}$-*b*-$HEA_{74}$ Yield: 32%. $^1$H NMR (400 MHz, d6-DMSO, δ, ppm), 7.95-7.20 (m, 74H, polyacrylamide NH), 7.32 (m, 20H, CH, CH aromatic), 7.20 (m, 20H, CH, CH aromatic), 7.03 (m, 20H, CH, CH aromatic), 6.94 (m, 20H, CH, CH aromatic), 5.20-4.60 (m, 74H, polyacrylamide OH), 4.03 (m, 40H, $CH_2$), 2.25-1.75 (m, 74H, polyacrylamide C*H*$CH_2$) 1.75-0.90 (m, 148H, polyacrylamide CHC*H$_2$*). $M_{n,NMR}$: 14.3 kDa (Fig S4.3). $M_{n,SEC(DMF)}$ 12.3 kDa, Đ=1.17.

$IND_{20}$-*b*-$HEA_{240}$ Yield: 61%. $^1$H NMR (400 MHz, d6-DMSO, δ, ppm), 8.00-7.20 (m, 240H, polyacrylamide NH), 7.31 (d, 20H, CH, CH aromatic), 7.18 (m, 20H, CH, CH aromatic), 7.03 (t, 20H, CH, CH aromatic), 6.93 (t, 20H, CH, CH aromatic), 5.20-4.70 (m, 240H, polyacrylamide OH), 4.03 (m, 40H, $CH_2$), 2.20-1.70 (m, 240H, polyacrylamide C*H*$CH_2$) 1.70-0.80 (m, 480H, polyacrylamide CHC*H$_2$*) (Fig S4.4). $M_{n,NMR}$: 33.8 kDa. $M_{n,SEC(DMF)}$ 27.1 kDa, Đ=1.23.

SEC traces reported in Figure S4.10.

## 4.2.4. Preparation of Sodium Usnate

Usnic acid (1 eq., 0.050 g, 0.15 mmol) was suspended in 2 mL of deionised water. 300 µL of a 1M NaOH solution (0.30 mmol) were added to the suspension, for a final 1:2 usnic acid:NaOH molar ratio. The mixture was let under stirring for 2 h. Non-solubilised usnic acid was then removed by filtration using a 0.22 µm PVDF filter. The filtered solution was lyophilised, and the resulting light yellow powder used without any further purification step.

## 4.2.5. Assembly of IDR 1018-sodium usnate complexes

IDR 1018 peptide and sodium usnate were mixed at different molar ratios, to determine the amount of sodium usnate that could induce complete IDR 1018 precipitation. A 0.50 mM solution of IDR 1018 in water was prepared, and mixed with varying amounts of a 4.0 mM sodium usnate water solution, to reach a final volume of 500 µL and sodium usnate:IDR 1018 molar ratios of 4:1, 2:1, 1:1 and 0.5:1. The solutions were let stirring for 2 h. The precipitated complex was then removed by centrifugation and the supernatant analysed by RP-HPLC to determine the amount of residual IDR 1018 in solution. RP-HPLC

analyses were performed using a Zorbax Eclipse Plus C18 column (3.5 μm, 95 Å, 4.6 × 12.5 mm), with a linear gradient of 25-90% acetonitrile in milli-Q water + 0.1% TFA.

A 4:1 sodium usnate:IDR 1018 was found to induce complete IDR 1018 precipitation. Based on these results, IDR 1018 (1 eq., 15 mg, 0.01 mmol) and sodium usnate (4 eq., 15 mg, 0.04 mmol) were separately dissolved in 2 mL of water and finally mixed together. The suspension was centrifuged at 5000 rpm for 5 minutes. The precipitated IDR 1018-sodium usnate complex was resuspended and recentrifuged in water for three times, to remove any residual soluble IDR1018 or sodium usnate.

## 4.2.6. Preparation of non-loaded $IND_m$-based nanoparticles.

Nanoparticles were prepared from $IND_m$ and their corresponding $IND_m$-*b*-$HEA_n$ block copolymers, mixed at different molar ratios. More specifically, mixtures were prepared from oligomer $IND_{10}$ and its corresponding copolymers $IND_{10}$-*b*-$HEA_{95}$ and $IND_{10}$-*b*-$HEA_{268}$, and from oligomer $IND_{20}$ and its corresponding copolymers $IND_{20}$-*b*-$HEA_{74}$ and, $IND_{20}$-*b*-$HEA_{240}$ (Tables 4.1-4.4). Separate oligomer and copolymer solutions were prepared in DMSO, each at a concentration of 11.1 mg/mL. These solutions were mixed to obtain the desired different molar ratios between each oligomer and its copolymers, and the final volume was adjusted to 500 μL.

Table 4.2: $IND_{10}$ (OLI) and $IND_{10}$-b-$HEA_{95}$ (COP) blends used in this work.

| 11.1 mg/mL in DMSO | OLI 100% | OLI:COP 8:2 | OLI:COP 6:4 | OLI:COP 4:6 | OLI:COP 2:8 | COP 100% |
|---|---|---|---|---|---|---|
| $IND_{10}$ (µL) | 450 | 207 | 112.5 | 54 | 23 | 0 |
| $IND_{10}$-*b*-$HEA_{95}$ (µL) | 0 | 243 | 337.5 | 396 | 427 | 450 |

Table 4.3: $IND_{10}$ (OLI) and $IND_{10}$-*b*-$HEA_{268}$ (COP) blends used in this work.

| 11.1 mg/mL in DMSO | OLI 100% | OLI:COP 8:2 | OLI:COP 6:4 | OLI:COP 4:6 | OLI:COP 2:8 | COP 100% |
|---|---|---|---|---|---|---|
| $IND_{10}$ (µL) | 450 | 111 | 61 | 28 | 11 | 0 |
| $IND_{10}$-*b*-$HEA_{268}$ (µL) | 0 | 339 | 389 | 422 | 439 | 450 |

Table 4.4: $IND_{20}$ (OLI) and $IND_{20}$-*b*-$HEA_{74}$ (COP) blends used in this work.

| 11.1 mg/mL in DMSO | OLI 100% | OLI:COP 8:2 | OLI:COP 6:4 | OLI:COP 4:6 | OLI:COP 2:8 | COP 100% |
|---|---|---|---|---|---|---|
| $IND_{20}$ (µL) | 450 | 212 | 112.5 | 54 | 45 | 0 |
| $IND_{20}$-*b*-$HEA_{74}$ (µL) | 0 | 238 | 337.5 | 396 | 405 | 450 |

Table 4.5: $IND_{20}$ (OLI) and $IND_{20}$-*b*-$HEA_{240}$ (COP) blends used in this work.

| 11.1 mg/mL in DMSO | OLI 100% | OLI:COP 8:2 | OLI:COP 6:4 | OLI:COP 4:6 | OLI:COP 2:8 | COP 100% |
|---|---|---|---|---|---|---|
| $IND_{20}$ (µL) | 450 | 194 | 100 | 51 | 20 | 0 |
| $IND_{20}$-*b*-$HEA_{240}$ (µL) | 0 | 256 | 350 | 399 | 430 | 450 |

Nanoparticles formation was induced by nanoprecipitation, by diluting each polymer mixture with 500 µL of water slowly added with a syringe driven by a Cole-Palmer 789210C syringe pump, at a flow rate of 0.50 mL/min, under vigorous stirring. To remove the DMSO, the nanoparticles suspensions were

transferred into a dialysis bag (1 kDa MWCO) and dialyzed against 5 L of de-ionised water for 24 hours at room temperature with at least 3 solvent exchanges.

### 4.2.7 Preparation of IDR 1018-sodium usnate complexes -loaded $IND_m$-based nanoparticles

IDR 1018-sodium usnate complex-loaded nanoparticles were prepared using the same procedure described above for the preparation of empty nanoparticles. After $IND_m$:$IND_m$-*b*-$HEA_n$ blends preparation, 50 μL of a 10 mg/mL IDR 1018-sodium usnate complexes solution in DMSO were added to each 450 μL blend, to a final volume of 500 μL, for final $IND_m$:$IND_m$-*b*-$HEA_n$ blend concentration of 10 mg/mL and final IDR 1018-sodium usnate complexes concentration of 1 mg/mL (10% w/w complexes/polymers). After nanoprecipitation, excess of DMSO was removed by dialysis, as it was done for unloaded blank nanoparticles. To remove potentially unencapsulated IDR 1018-sodium usnate complexes, after dialysis the nanoparticle suspensions were purified through a Sephadex G-25 PD-10 Desalting Column. The ion-pair loaded nanoparticles were collected from the first 3.5 mL eluted from the column and analysed by DLS and TEM.

### 4.2.8. Nanoparticle size analysis

Empty and complexes-loaded nanoparticle suspensions were diluted with de-ionised water to a polymer concentration of 1.0 mg/mL and then analysed by Dynamic Light Scattering (DLS) using a Zetasizer Nano spectrometer (Malvern Instruments Ltd) equipped with a 633 nm laser at a fixed angle of 173°.

### 4.2.9. Nanoparticles TEM analysis

Transmission Electron Microscopy (TEM) was conductd on a FEI TecnaiTM 12 Biotwin transmission electron microscope. 10 μL of 0.5 mg/mL nanoparticles suspension in water were placed on a Formvar® coated 3 mm 75 mesh copper grid. After 5 minutes the excess of volume was removed with filter paper, the samples were negatively stained with 3% uranyl acetate in deionised water and analysed.

### 4.2.10. Quantification of IDR 1018-sodium usnate complexes loading and encapsulation

Complexes loaded-nanoparticles were lyophilised after PD-10 column purification. The samples were re-dissolved in DMSO at a concentration of 1 mg/mL. The amount of IDR 1018 and usnic acid loaded into each nanoparticle sample was calculated by RP-HPLC, using a C18 column (Zorbax, 5 μm, 12.5 x 46 mm, Agilent), with a linear gradient of 25-90% acetonitrile in milli-Q water + 0.1% TFA. Absorbance was recorded at λ=280 nm. The amount of loaded IDR 1018 and sodium usnate were separately calculated referring to calibration curves previously prepared analysing different dilutions of both IDR 1018 and sodium usnate in the 0.0005-0.2 mM range (see Supporting Information).

Loading Capacity (LC) and Encapsulation Efficiency (EE) were calculated as:

$$LC = \frac{\text{Loaded IDR 1018/ Sodium usnate} \ \ (mg) * 100}{\text{Amount of polymer + ion pair (mg)}}$$

$$EE = \frac{\text{Loaded IDR 1018/ Sodium usnate (mg)} * 100}{\text{Initial amount of ion pair (mg)}}$$

### 4.2.11. Complexes release studies

3 samples of ion complexes-loaded freeze-dried $IND_{20}:IND_{20}$-*b*-$HEA_{240}$ 8:2 nanoparticles were suspended at a concentration of 4 mg/mL in PBS, 15.4 mM NaCl, and 100 mM NaAc buffer pH 4.0. 0.50 mL from each suspension were placed in a dialysis device (Slide-A-Lyzer mini dialysis device, 3.5 KDa MWCO, Thermo Scientific). The suspensions were dialyzed against 1.5 mL of the same buffer employed to suspend the nanoparticles, under agitation, at 37 °C. Release buffer was taken at appropriate time points and replaced with 1.5 mL of fresh buffer. From each time point, IDR 1018 and usnic acid release was quantified by RP-HPLC using a C18 column (Zorbax, 5 µm, 12.5 x 46 mm, Agilent), with a linear gradient of 25-90% acetonitrile in milli-Q water + 0.1% TFA. Absorbance was recorded at $\lambda$=280 nm.

### 4.2.12. RAW 264.7 Cell cultures

Dulbecco's Modified Eagle's medium (DMEM) for sub-culturing was supplemented with FBS, HEPES and Amphotericin B/penicillin/streptomycin solution at final concentrations of 10% v/v, 2.4% v/v and 1% v/v respectively. RAW 264.7 cells were cultured in 58 $cm^2$ dishes at 5% $CO_2$, 95% relative humidity and 37°C until near-confluence (approximately 70% coverage of the dish surface by cells). Cell growth was monitored by optical microscopy. Once near-confluent, cells were passaged following ATCC recommendations. Cell culture medium was replaced every two - three days by aspirating all but 5 mL of culture medium from the dishes. Cells were dislodged from the dish with a cell scraper, aspirated and appropriate aliquots of the cell suspension was added into new culture vessel in ratio of 1:3 or 1:6 by the addition of 12-15 mL

of pre-warmed to 37°C fresh medium. For seeding density, cells were counted using a haemocytometer (Laboratory Supplies).

### 4.2.13.    Bacterial cultures

This protocol is taken from Rosa Catania's PhD dissertation. *Salmonella enterica* subsp. e*nterica* serovar Typhimurium DsRed2 (SL1344 transformed with a DsRed2 expression plasmid) was kindly made available by Dr Alan Huett (School of Life Sciences, Nottingham). Bacteria were preserved at -80°C in glycerol at a final concentration of 20% (v/v) until use. For bacterial seeding, a small amount of bacteria was scraped off the glycerol stock. The loop was wiped at the top end of a fresh agarose agar plate moving in a zig-zag horizontal pattern until 1/3 of the plate was covered. The plate was rotated about 60 degrees and the bacteria were spread from the end of the first streak into a second area. This procedure was repeated to spread the bacteria in a third area of the plate. The plate was incubated in incubator overnight at 37°C.

### 4.2.14.    *Salmonella* killing study in RAW 264.7 cells

This protocol is taken from Rosa Catania's PhD dissertation. The day before the experiment, RAW 264.7 cells were seeded in a 48 well plate with a density of 2 x $10^4$ cells/mL per well and the plate was incubated overnight at 37°C. In parallel, two - three colonies of SL1344 DsRed2 were scraped off the agar plate of a culture using a disposable sterile loop. The colonies were suspended in 4 mL of Luria-Bertani (LB) broth supplemented with 100 µg/mL ampicillin. The culture was incubated overnight in a shaking incubator (250 rpm) at 37°C. After 16 hours, bacteria were collected by centrifugation (1500 x g for 15 min) and

resuspended in 4 mL of PBS. Bacteria were diluted in Gentamicin Free Medium (GFM) with a final $OD_{600nm}$ of 0.025. Cultured RAWs 264.7 were infected by the addition of 0.2 mL per well of SL1344 DsRed2 in GFM. The plate was centrifuged (700 x g for 10 min) and incubated for 20 min at 37°C. Then, medium was aspirated, each well was rinsed and then incubated with 0.2 mL of High Gentamicin Medium (100 µg/mL) for 30 min in order to kill extracellular bacteria. After the incubation with HGM, each well was washed 3 times with 0.2 mL of PBS.

Formulations were prepared by suspending freeze dried, empty and IDR 1018-sodium usnate complexes -loaded $IND_{20}:IND_{20}$-*b*-$HEA_{240}$ 8:2 nanoparticles in a 0.01% acetic acid solution containing 0.2% BSA at a final concentration of 2 mg/mL. RP-HPLC analysis on a small aliquot of the complexes-loaded nanoparticles suspension allowed to estimate a concentration of 54.8 µg/mL of IDR 1018 and of 61 µg/mL of usnic acid. Control IDR 1018 solution was prepared by dissolving IDR 1018 in 0.01% acetic acid/0.2% BSA at IDR 1018 concentration of 54.8 µg/mL. Control usnic acid was prepared by pre-dissolving usnic acid in acetone at 2.0 mg/mL concentration and then diluting it in 0.01% acetic acid/0.2% BSA for a final concentration of 61 µg/mL. IDR 1018-sodium usnate complexes solution was prepared by pre-dissolving the complex in DMSO at a concentration corresponding to 5.8 mg/mL of IDR 1018. The solution was then diluted in 0.01% acetic acid/0.2% BSA for a final IDR 1018 concentration of 54.8 µg/mL.

These solutions were diluted in Gentamicin Free Medium for final formulations with concentrations reported in Table 4.5. 0.2 mL of each formulation was applied, and cells incubated with Normal Gentamicin Medium (20 µg/mL) were used as a control. The cells were incubated for 4 hours at 37 °C. Then, cells were rinsed with PBS and incubated for 6 additional hours with Normal Gentamicin Medium (NGM). After this time, the cells were washed three times with PBS, and the surviving intracellular bacteria were harvested by lysis of the cells with 1 % Triton X-100 in PBS. The supernatants were immediately serially diluted with PBS and spread onto LB agar plates. After incubation for 16 h at 37°C, the numbers of bacterial colonies for each sample were counted and expressed as colony-forming units (CFU) per mL. Data were normalised to $10^3$ cells.

NB: N=1, n=3 with N = numbers of replicates (experiment performed in different days, same conditions) and n = numbers of repetition (different measurements during the same experiment).

Table 4.6: final concentrations of usnic acid and peptide IDR 1018 on formulations that were applied on RAW 264.7 cells.

| | Amount of IDR 1018 (µg/mL) | Amount of Usnic Acid (µg/mL) | Amount of NPs (µg/mL) |
|---|---|---|---|
| Unloaded NPs | - | - | 200 |
| Loaded NPs | 5 | 5.5 | 200 |
| IDR-1018 | 5 | - | - |
| Usnic Acid | - | 5.5 | - |
| IDR 1018-sodium usnate complex | 4 | 5 | - |

## 4.3. Results and discussion

As discussed in Chapter 3, the synthesis of $IND_{10}$-based block copolymers was complicated by the partial lack of reactivity of $IND_{10}$ oligomer, as a RAFT agent. Results suggested that part of the oligomeric macro-CTA RAFT agent was unable to mediate the copolymerization of *N*-hydroxyethylacrylamide. As a result, for $IND_{10}$-*b*-$HEA_n$ copolymers the final $HEA_n$ chain length was found to be approximately 25% longer than expected from theoretical values, as assessed by $^1$H NMR.

Interestingly, removal of the unreacted $IND_{10}$ macro transfer agent from the final $IND_{10}$-*b*-$HEA_n$ copolymerisation mixtures, proved to be difficult. When, after the copolymerization, the copolymers were for the first time dissolved in an aqueous solution, a milky, yet homogeneous suspension was observed. SEC analysis revealed that some of the initial $IND_{10}$ oligomer was still present and suggested that $IND_{10}$ was responsible for the milky suspension observed in water. We hypothesised that it was potentially self-assembling and that the resulting nanoparticles could be of potential use for drug encapsulation and release.

$IND_{10}$ self-assembling in water was investigated, together with that of a longer IND-oligomer, $IND_{20}$, to understand if and how the length of the hydrophobic indole chain could influence the final size of nanoparticles and their dispersity. Oligomer $IND_{20}$ was synthesised from monomer IND (also prepared in Chapter 3) through RAFT polymerization following the same conditions used for $IND_{10}$, except for a higher [monomer]:[CTA] ratio (Scheme 4.3). As it was observed for

IND$_{10}$, also for the synthesis IND$_{20}$, polymerisation rate was very slow, requiring

3-4 further additions of AIBN initiator over 48 h to reach 80% conversion. As it

was hypothesised for IND$_{10}$, it is possible that partial indole-driven aggregation

of the growing chain in DMF could have been responsible for this behaviour.

Chemical identity and molar mass distribution of IND$_{20}$ were assessed by $^1$H

NMR and SEC. (Table 4.6).



IND$_{20}$ M$_{n,THEO}$: 5.40 kDa M$_{n,SEC}$:8.40 kDa Đ=1.13
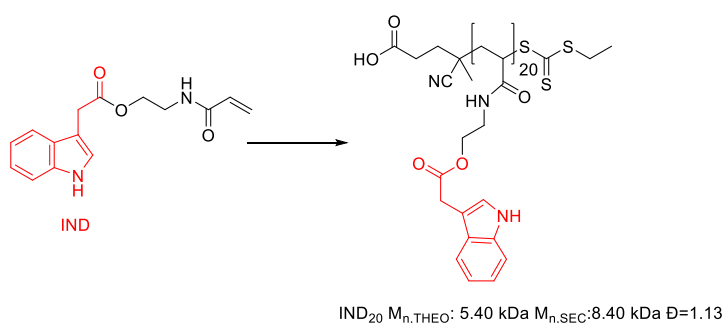
Scheme 4.3: Synthesis of IND$_{20}$ oligomer. *Reagents and conditions*: AIBN, CTA (**10**), DMF, 80°C.

Table 4.7: Composition, M$_n$, and dispersity of the hydrophobic-oligomers prepared in this study.

| Name | Hydrophobic monomer units, m | Hydrophilic monomer units, n | M$_{n,THEO}$[a] (KDa) | M$_{n,NMR}$ (KDa) | M$_{nSEC}$ (KDa) | Đ |
|---|---|---|---|---|---|---|
| IND$_{10}$ | 10 | 0 | 3.00 | [b] | 1.56[c] | 1.12 |
| IND$_{20}$ | 20 | 0 | 5.70 | [b] | 8.40[d] | 1.13 |

[a]Calculated from initial [HEA]$_0$:[CTA]$_0$ and final monomer conversion. [b]Number of repeating units of IND monomers could not be calculated as there were not visible peaks from CTA (**10**) to be compared with the NH of IND repeating units. [c]Obtained from SEC analysis in THF (PS standards). [d]Obtained from SEC analysis in DMF + 0.1% LiBr (PMMA standards).

## 4.3.1. Nanoparticles preparation

The simplest method for the preparation of polymeric nanoparticles is the

solvent displacement method, also known as nanoprecipitation method. This

method was introduced by Fessi et al. in 1989, and it is based on polymer self-

assembling following the addition of a non-solvent to a polymer solution[23, 24].

Among other approaches for the assembly of nanoparticles, nanoprecipitation stands out for its simplicity, generally narrow size distribution of the resulting particles, and because no additives are required[25, 26]. This technique was successfully employed for the preparation of procaine-loaded PLGA-based nanoparticles of sub-micron size (≤210 nm) and low polydispersity[27]. Doxorubicin-loaded PLGA nanoparticles were also prepared by nanoprecipitation, resulting in spherical particles of 230 nm size and 5% wt doxorubicin loading[28]. Recently, polymersomes assembly by nanoprecipitation was accomplished by our group, by dissolving PEG acrylate-2-(acryloyloxy)ethyl-3-chloro-4-hydroxybenzoate (ACH) or 2-(3-chloro-4-hydroxybenzamido)ethyl acrylate (CHB) di-block copolymers in DMSO, diluting the solution by dropwise addition of water and final dialysis in water for 24 h. The resulting vesicles possessed hydrodynamic radii in the 70 - 170 nm range, depending on the polymer employed[29].

A similar method was followed here for nanoprecipitation of $IND_{10}$ and $IND_{20}$. The oligomers were first dissolved in DMSO at a concentration of 10 mg/mL. Water was then added dropwise, under vigorous stirring, using a syringe pump, at a flow rate of 0.5 ml/min (Fig. 4.6). The addition of water induced immediate aggregation of the oligomers. The resulting milky suspension was dialysed against water for 24 h, and the resulting nanoparticles suspension was finally analysed by DLS (Fig. 4.7).
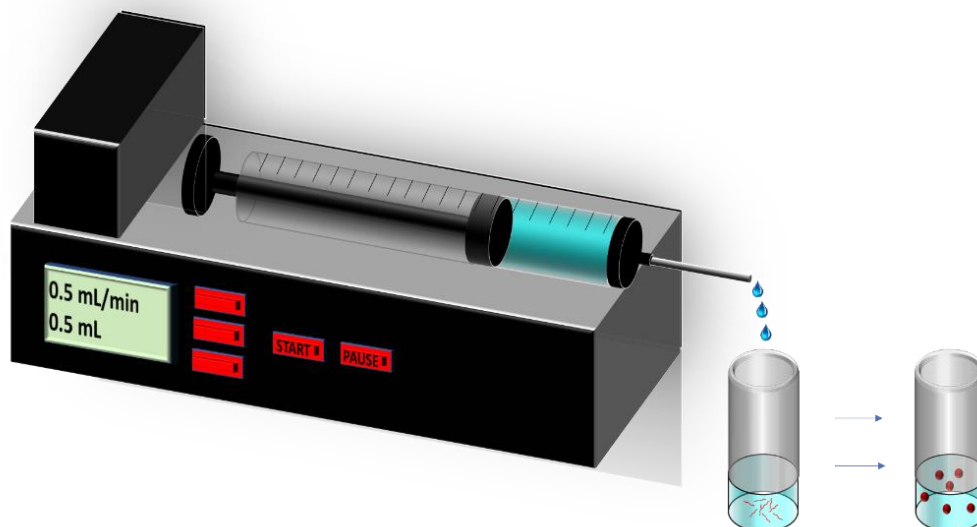
Figure 4.6: Schematic representation of the nanoprecipitation method employed in this chapter. Through a syringe pump, 500 μL of water were added dropwise, at flow rate of 0.5 mL/min, to a 500 μL of a 10 mg/mL polymer solution in DMSO, under vigorous stirring. The addition of water resulted in immediate polymer self-assembly. DMSO was subsequently removed by dialysis.
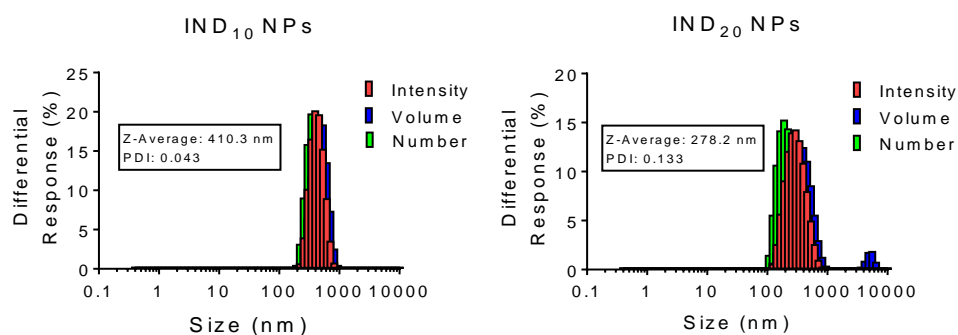


Figure 4.7: $IND_{10}$ and $IND_{20}$ nanoparticles size peak distribution in water, displayed by intensity, volume and number. The oligomers were analysed after dialysis at a concentration of 1 mg/mL in water.

DLS confirmed the presence of a single population of nanoparticles, with size of around 400 nm for $IND_{10}$ and 300 nm for $IND_{20}$, and polydispersity ≤0.15 for both formulations. Encouraged by the narrow size distribution, encapsulation

of IDR 1018-sodium usnate complexes into $IND_{10}$ and $IND_{20}$ nanoparticles using the nanoprecipitation method was attempted.

## 4.3.2. Preparation of IDR 1018-sodium usnate complexes

A method for the complexation and co-precipitation of IDR 1018 and sodium usnate was developed. In Prud'homme *et al.*'s work[14], a range of amphiphilic molecules, bearing acid functionalities were screened as counter ions to evaluate their ability to form ion-pairs with basic functionalities present in antimicrobial, macrocyclic peptide polymyxin B. Water-soluble salt of the acids, and the hydrophilic polymyxin B peptide, were separately dissolved in water. The two solutions were mixed to achieve a 1:1 acid:peptide charge ratio, and the formation of a precipitate from the resulting mixtures was visually verified. Generally, amphiphilic molecules with high hydrophobicity (LogP ≥2) and strong acidity (pKa ≤1) were the most efficient in inducing peptide precipitation. Very hydrophobic molecules, such as sodium oleate with a LogP=7.58, still led to efficient precipitation of the peptide, despite a high pKa=5.0[14].

In this chapter, a similar method was followed to verify the formation of ion pairs between usnic acid and IDR 1018. Usnic acid has three acidic hydroxyl groups, with pKas of 4.4, 8.8 and 10.7 (Fig. 4.8)[30], and its experimental LogP in octanol-water is 2.88[31]. Comparing these values with those of molecules used by Prud'homme *et al*.[14], the hydroxyl with the lowest pKa appeared the most likely to electrostatically interact with IDR 1018. As IDR 1018 has five basic amino groups on its backbone (4 arginine and 1 N-Ter), it was reasonable to

hypothesise that an excess of usnic acid would be necessary to induce IDR 1018 precipitation.
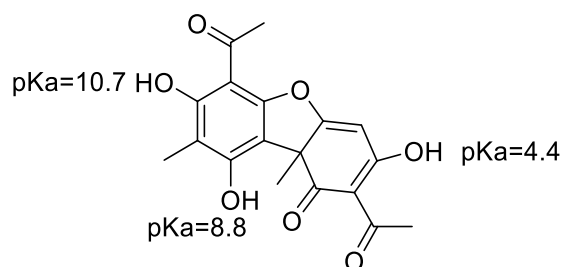


Figure 4.8: Chemical structure of usnic acid, and pKas of its three hydroxyl groups.

### 4.3.2.1. Sodium usnate preparation

Due to its hydrophobicity, usnic acid is poorly soluble in water (3 µg/mL)[32, 33]. Its low solubility would make ion pairing with IDR 1018 peptide in water quite problematic. Thus, a water suspension of usnic acid was first treated with 2 equivalents of NaOH. The resulting sodium salt, sodium usnate readily dissolved in water, and was separated from the residual insoluble usnic acid by filtration. Sodium usnate was then lyophilised, and the resulting fully water-soluble yellow dry powder used for subsequent ion pairing experiments.

### 4.3.2.2. Optimization of precipitation of IDR 1018-sodium usnate complexes

Stock solutions of peptide and sodium usnate were mixed together at appropriate molar ratios. The immediate formation of insoluble aggregates confirmed that the two molecules were electrostatically interacting. To identify the optimal sodium usnate:IDR 1018 molar ratio for complete IDR 1018 precipitation, sodium usnate was dissolved in water at different

concentrations, and mixed with a 1 mM IDR 1018 solution in water, to obtain

mixtures with a final IDR 1018 concentration of 0.05 mM and 1:1, 2:2 and 4:1

usnate:IDR 1018 molar ratios. The precipitated complexes were removed by

centrifugation and the supernatant was analysed by RP-HPLC, to detect the

amount of IDR 1018 left in solution (Fig. 4.9).
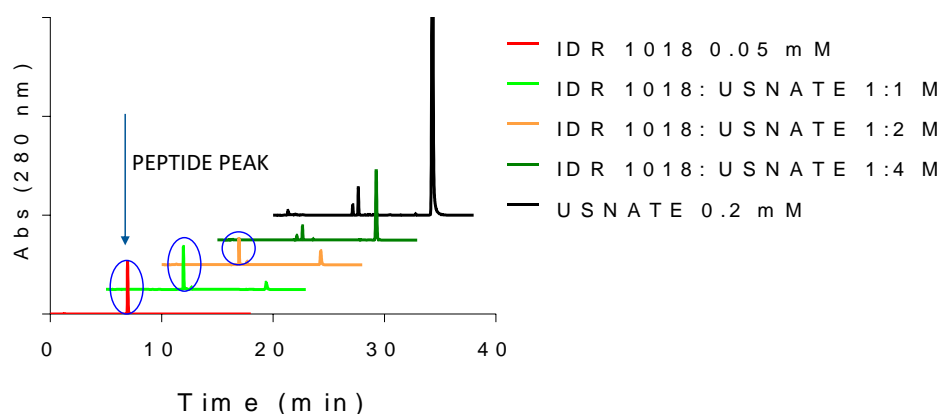


Figure 4.9: C18 RP-HPLC analyses of different sodium usnate:IDR 1018 mixtures. IDR 1018 was dissolved in water a 0.05 mM concentration. Sodium usnate was mixed with IDR 1018 at 1:1, 2:1 and 4:1 usnate:IDR 1018 molar ratio. Samples were eluted using a 25-90% acetonitrile gradient in water with 0.1% of TFA. Complexation between the two species and subsequent complex precipitation was monitored by observing the disappearance of IDR 1018 peak (UV detection, λ=280 nm) at increasing usnate concentrations.

The disappearance of free IDR 1018, as the usnate:peptide molar ratio

increased, was monitored by RP-HPLC analysis of the supernatant, using UV

detection (λ= 280 nm). A 4:1 usnate: IDR 1018 molar ratio was found to be

sufficient to induce full peptide precipitation and was therefore utilised for all

subsequent preparations of IDR 1018-sodium usnate complexes. The insoluble

complexes were washed multiple times with water to remove the excess of

uncomplexed sodium usnate and IDR 1018, and finally lyophilised and stored

at 4°C. To identify the best solvent method for IDR 1018-sodium usnate

complex encapsulation into IND-oligomers nanoparticles, the solubility of

complexes in a range of different solvents: THF, CHCl$_3$, DCM, MeOH and DMSO, was assessed. MeOH proved to be able to at least partially dissolve the IDR 1018-sodium usnate complex but was discarded as it could not solubilise the hydrophobic IND-based oligomers. Thus, DMSO was chosen, due to its ability to dissolve both the complexes and the polymers. A 10 mg/mL stock solution of complex in DMSO was therefore prepared, to be used for the encapsulation experiments.

### 4.3.3. IDR 1018-Sodium Usnate Loading and encapsulation into IND$_{10}$- and IND$_{20}$-based nanoparticles

To incorporate IDR 1018-sodium usnate complexes in IND$_m$-based nanoparticles, complexes were dissolved in DMSO, and added to the IND$_m$ solution in the same solvent, for a final 1 mg/mL complexes concentration, and a 10% w/w ratio between the complex and the IND$_m$ oligomer. Nanoparticles formation was induced again by nanoprecipitation, but this time after dialysis the presence of large, visible aggregates was observed, suggestive of loss of nanoparticles stability upon incorporation of IDR 1018-sodium usnate complexes. A stabiliser was needed to prevent nanoparticles flocculation.

Aggregation is one of the potential drawbacks of nanoparticles formulation. Nanoparticles move in solution by Brownian motion, and there is a high chance that they will collide with each other[34]. According to the DLVO theory, aggregation is regulated by the sum of attractive and repulsive forces. Van der Waals interactions are considered the main attractive force, and are weak interactions that can be established between molecules of two nanoparticles that are at short distance (few nm) one from each other[34]. Conversely, the

repulsion generated by the electrostatic double layer is considered the main repulsive one[34]. This layer is usually generated by presence of ionisable functional groups or by ions adsorption on nanoparticles surface. The ionised nanoparticles surface attracts counter ions, that will form a first, inner layer (Stern Layer), where ions are tightly bound, and an outer one (Diffuse Layer), where ions and counterions are less tightly associated. When the double layers of two nanoparticles overlap, alterations in the Stern layer will cause the two nanoparticles to repel each other. The double layer on each nanoparticle prevents them to come close enough for van der Waals interactions to cause aggregation[35, 36]. Hydrophobic interactions may also lead to NPs aggregation in aqueous media[37]. To overcome the attractive forces that lead to aggregation, hydrophilic polymers can be chemically grafted on nanoparticles surface. These polymers can form a hydrated shell surrounding the nanoparticles core, creating a steric-osmotic repulsive layer that will prevent their aggregation[38]. Grafting will not only improve particles stability, but it will also reduce their interaction with endogenous proteins and reduce their renal clearance[38]. For example, PEG is typically grafted on gold nanoparticles to improve their stability and biocompatibility[39]. The first FDA approval of a PEGylated nanoparticle (NP) product was a PEGylated liposomes system for the delivery of Doxorubicin, Doxil®, in 1995[40].

The addition of amphiphilic surfactants, like block copolymers such as Poloxamers (Pluronic®) and poloxamines (Tetronic®), is a valid alternative to covalent grafting. These surfactants can adsorb on the surface of hydrophobic

nanoparticles, such as PLGA, through the hydrophobic block, leaving the hydrophilic arm(s) floating above the surface, forming a protective shell similarly to grafted polymers[41, 42].

In this thesis project, we synthesised $IND_{10}$-*b*-$HEA_n$ and $IND_{20}$-*b*-$HEA_n$ block copolymers, where the hydrophobic block had the same composition and length of the $IND_{10}$ and $IND_{20}$ oligomers forming the core of the nanoparticles, as potential particle stabilisers. Through their hydrophobic block, these copolymers were expected to interact with $IND_{10}$ and $IND_{20}$ during the nanoprecipitation process, anchoring on the surface of final nanoparticles, an leaving the hydrophilic polyHEA block free to move on the NPs surface with stabilising effects (Fig. 4.10).
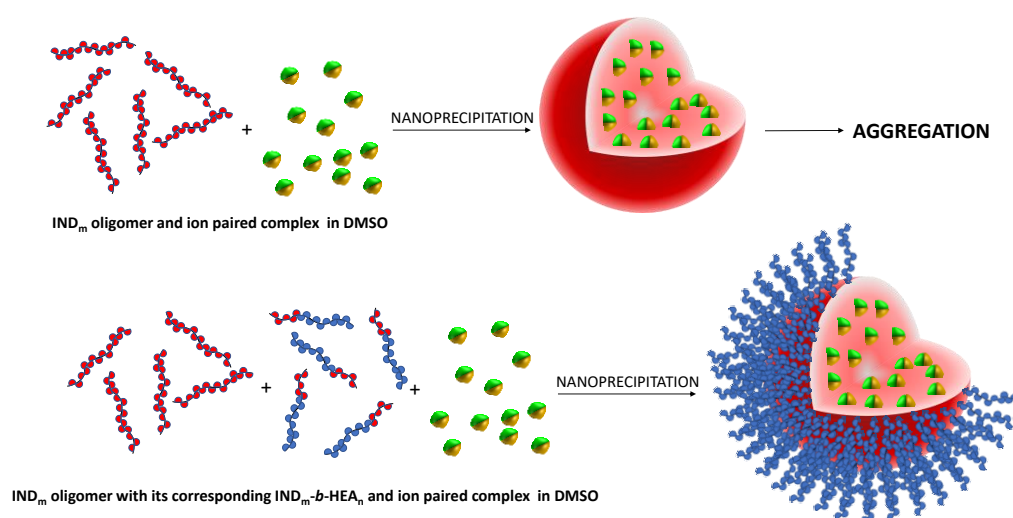


Figure 4.10: (a) $IND_{10}$ and $IND_{20}$ nanoprecipitation in the presence of the IDR 1018-sodium usnate complex resulted in nanoparticles aggregation. (b) $IND_{10}$-*b*-$HEA_n$ and $IND_{20}$-*b*-$HEA_n$ copolymers were mixed with their corresponding $IND_{10}$ and $IND_{20}$ oligomers in DMSO. The hydrophobic block of these copolymers was supposed to anchor on nanoparticles, while the hydrophilic HEA chain was meant to surround and stabilise the nanoparticles surface.

### 4.3.3.1. IND$_{10}$-*b*-HEA$_{95}$ IND$_{10}$-*b*-HEA$_{268}$, IND$_{20}$-*b*-HEA$_{74}$ and IND$_{20}$-*b*-HEA$_{240}$ synthesis and characterisation

Copolymer IND$_{10}$-*b*-HEA$_{95}$ was prepared in Chapter 3. Copolymers IND$_{10}$-*b*-HEA$_{268}$, IND$_{20}$-*b*-HEA$_{74}$ and IND$_{20}$-*b*-HEA$_{240}$ were prepared following the same protocol, using the hydrophobic oligomers IND$_{10}$ and IND$_{20}$ as macro-CTA agents to mediate the RAFT copolymerization of *N*-hydroxyethylacrylamide monomer. Two different chain lengths, with DP 90 and 250, were targeted, to investigate the influence of the size of the polyHEA block on nanoparticle stabilisation (Scheme 4.4).
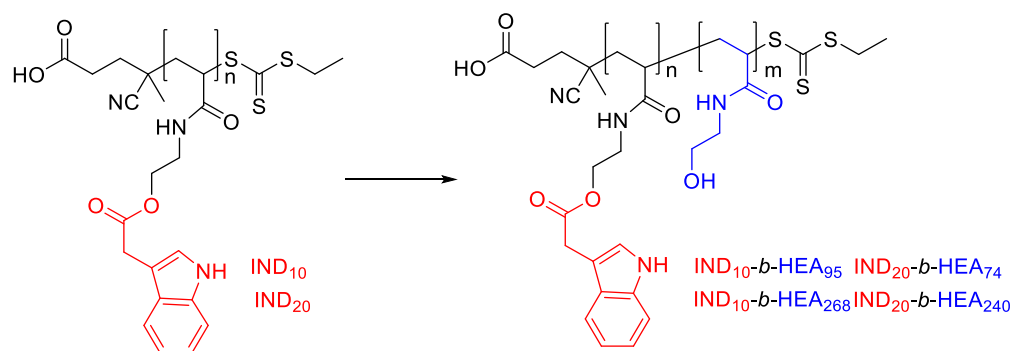


Scheme 4.4: synthesis of copolymers IND$_{10}$-b-HEA$_{95}$, IND$_{10}$-b-HEA$_{268}$, IND$_{20}$-b-HEA$_{74}$ and IND$_{20}$-b-HEA$_{240}$. *Reagents and conditions*: *N*-hydroxyethylacrylamide, V501, DMF at 70 ˚C.

As it in case of IND$_{10}$-based copolymers described in chapter 3, also for these copolymers the final chain length was found to be ~ 25-30% longer than the expected theoretical DP, as assessed by $^1$H NMR, by comparing the integrals of indole aromatic protons between 6.8 and 7.3 ppm, with those of NH and OH groups of the pHEA at 7.5-7.8 and 4.6-5.2 ppm, respectively and those of the polymer backbone between 1 and 2 ppm (see Supporting Information).

As discussed before, the difference may be due to partial aggregation of the hydrophobic block, which may have prevented some of it from reacting during the polymerization. Also, partial removal of the trithiocarbonate moiety from the $IND_m$ oligomers chain end, caused by multiple additions of AIBN radical initiator during the oligomerisation, would explain why a proportion of the chains did not act as macro chain-transfer agent. However, SEC analysis showed again a narrow molar mass distribution, with Đ < 1.25 for all copolymers (Table 4.7, see Fig S4.9 and S4.10 for SEC traces).

Table 4.8: Composition, $M_n$, and dispersity of copolymers $IND_{10}$-b-$HEA_{95}$, $IND_{10}$-b-$HEA_{268}$, $IND_{20}$-b-$HEA_{74}$ and $IND_{20}$-b-$HEA_{240}$ utilised in this study.

| NAME | Hydrophobic monomer | Hydrophobic monomer units, m | Hydrophilic monomer units, n | $M_{nTHEO}^{a}$ (KDa) | $M_{nNMR}^{b}$ (KDa) | $M_{nSEC}^{c}$ (KDa) | $Đ^{c}$ |
|---|---|---|---|---|---|---|---|
| $IND_{10}$-*b*-$HEA_{95}$ | IND | 10 | 95 | 10.5 | $14.1^{d}$ | 10.4 | 1.05 |
| $IND_{10}$-*b*-$HEA_{268}$ | IND | 10 | 268 | 21.3 | $34.4^{b}$ | 32.2 | 1.19 |
| $IND_{20}$-*b*-$HEA_{74}$ | IND | 20 | 74 | 11.5 | $14.3^{c}$ | 12.1 | 1.17 |
| $IND_{20}$-*b*-$HEA_{240}$ | IND | 20 | 240 | 24.4 | $33.8^{d}$ | 27.1 | 1.23 |

[a]Calculated from initial $[HEA]_0:[CTA]_0$ and final monomer conversion. [b]Number of repeating unit of HEA monomers were calculated by ^{1}H NMR by comparing the integral of indole aromatic proton peak with the hydroxyl peak of HEA repeating units. [c]Obtained from SEC analysis in DMF + 0.1% LiBr (PMMA standards).

### 4.3.3.2.    Preparation of $IND_m$:$IND_m$-*b*-$HEA_n$ blends

The synthesised amphiphilic $IND_m$-*b*-$HEA_n$ block copolymers were tested as potential stabilisers for $IND_{10}$- and $IND_{20}$-nanoparticles. In Chapter 3, we had already investigated the self-assembly behaviour of $IND_{10}$-*b*-$HEA_n$ copolymers by DLS, which revealed the presence of particles with size between 10 and 20 nm. An analogous behaviour could be expected from $IND_{10}$-*b*-$HEA_n$ and $IND_{20}$-*b*-$HEA_n$ copolymers synthesised in this chapter.

Self-assembly of $IND_m$-*b*-$HEA_n$ copolymers, together with mixtures of $IND_m$:$IND_m$-*b*-$HEA_n$ at different molar ratios, were investigated. Non-loaded and (IDR 1018-sodium usnate complex)-loaded 100% $IND_m$-based nanoparticles have already been tested, and their characterisation is reported here again for clarity.

Accordingly, mixtures of $IND_{10}$ and $IND_{20}$ oligomers with their corresponding $IND_{10}$-*b*-$HEA_n$ and $IND_{20}$-*b*-$HEA_n$ copolymers were prepared in the presence and in the absence of IDR 1018-sodium usnate complexes, and the resulting nanoparticles were characterised. A range of $IND_m$:$IND_m$-*b*-$HEA_n$ molar ratios, 10:0, 8:2, 6:4, 4:6 and 2:8, were investigated by Dynamic Light Scattering, with a constant 10 mg/mL final mixture concentration in DMSO, and a 10% w/w (IDR 1018-sodium usnate complex)/(oligomer+copolymer) ratio (thus IDR 1018-sodium usnate complex concentration of 0.1 mg/mL).

### 4.3.3.3. PD-10 column purification of IDR1018-Sodium usnate complex loaded-nanoparticles

To remove any trace of unencapsulated complexes from (IDR 1018-sodium usnate complex)-loaded nanoparticles, a further purification step was undertaken, eluting the nanoparticles through a desalting PD-10 column. PD-10 columns are small columns pre-filled with Sephadex G-25 resin, usually used for buffer exchange, desalting and small contaminant removal[43]. With an $M_r$ exclusion limit of 5000 Da, they have been previously used to separate drug-loaded nanoparticles, eluted with the first 3.5 mL of mobile phase, from unencapsulated drugs, which are eluted later or blocked at the top of the column due to poor solubility in the mobile phase[44, 45].

To validate the efficiency of this size-exclusion chromatography step, 8:2 $IND_{20}$:$IND_{20}$-*b*-$HEA_{240}$ blend-IDR 1018-sodium usnate complex-loaded-nanoparticles were analysed by RP-HPLC, after PD-10 column purification. The nanoparticles, suspended in water, were eluted through the PD-10 column and re-collected from the first 3.5 mL. They were then lyophilised and re-dissolved in DMSO at 1 mg/mL before the analysis. In parallel, a negative control was prepared: a 0.1 mg/mL IDR 1018-sodium usnate complex DMSO solution was nanoprecipitated in water in the absence of nanoparticle-forming polymers. The resulting suspension was eluted through PD-10 column and the first 3.5 mL eluted were collected and directly analysed by RP-HPLC (Fig. 4.11). RP-HPLC from the complex-loaded nanoparticles sample showed the presence of two peaks, the first at 7 min, and the second at 16 min, corresponding to IDR 1018 and usnic acid, respectively. By contrast, the first 3.5 mL of mobile phase collected from the control, nanoprecipitated IDR 1018-sodium usnate complex did not show any detectable peak, confirming that neither IDR 1018 nor usnic acid were present. The experiment suggested that the IDR 1018-sodium usnate complex had been loaded into nanoparticles and that PD-10 column elution may be good strategy to remove unencapsulated complex.
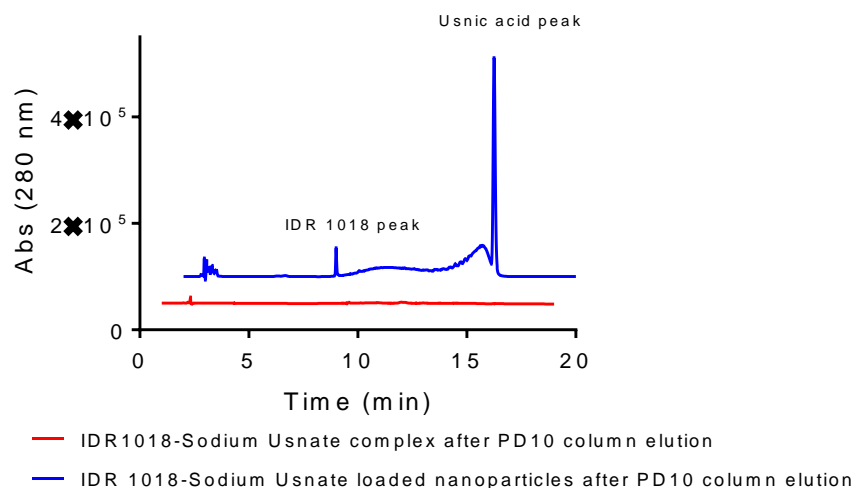
Figure 4.11: C18 RP-HPLC chromatograms of [IND$_{20}$]:[IND$_{20}$-b-HEA$_{240}$] 8:2 - IDR 1018-sodium usnate complex loaded-nanoparticles and nanoprecipitated IDR 1018-sodium usnate complex. Absorbance was recorded at 280 nm. Nanoparticles were lyophilised and re-dissolved in DMSO at 1 mg/mL concentration before RP-HPLC analysis. IDR 1018-sodium usnate complex eluted from PD-10 column was analysed directly.

### 4.3.3.4.        Nanoparticles size characterisation

Experiments discussed above showed that IDR 1018-sodium usnate complex-loaded 100% IND$_{10}$- and 100% IND$_{20}$-based nanoparticles formed large and visible aggregates after nanoprecipitation. Small aggregates, which could be observed upon dialysis, were obtained from complex-loaded 100% IND$_m$-*b*-HEA$_n$-based nanoparticles. DLS analysis highlighted the presence of very disperse particles and confirmed the bad quality of data collected. These preliminary experiments confirmed that both 100% IND$_m$ oligomers and IND$_m$-*b*-HEA$_n$ copolymers are not able to generate sub-micron and narrowly distributed nanoparticles in the presence of the IDR 1018-sodium usnate complexes.

By contrast, nanoparticles formed from blends of $IND_m$ oligomers and $IND_m$-*b*-$HEA_n$ copolymers appeared visually monodisperse, without any large aggregates.

In Figure 4.12 size distribution by intensity, volume and number is displayed for non-loaded and IDR 1018-sodium usnate complex-loaded $IND_{20}$:$IND_{20}$-*b*-$HEA_{240}$ nanoparticles at different $IND_{20}$:$IND_{20}$-*b*-$HEA_{240}$ molar ratios. These specific formulations were used here as a representative example, complete DLS analysis of all formulations is shown in the Supporting Information (Fig. S4.5, S4.6 and S4.7). From non-loaded nanoparticles, increasing proportion of $IND_{20}$-*b*-$HEA_{240}$ caused a reduction in size of resulting nanoparticles. 100% $IND_{20}$-based nanoparticles had average hydrodynamic diameter of 300-350 nm, which was reduced to ~ 230 nm in $IND_{20}$:$IND_{20}$-*b*-$HEA_{240}$ 8:2 blend-nanoparticles and 210 nm in $IND_{20}$:$IND_{20}$-*b*-$HEA_{240}$ 6:4 blend-nanoparticles. At $IND_{20}$:$IND_{20}$-*b*-$HEA_{240}$ 2:8 molar ratio, an aditional distribution centred at ~ 50 nm was observed. The latter was of analogous size of the major distribution observed for 100% $IND_{20}$-*b*-$HEA_{240}$ based-nanoparticles, and could therefore originate from the self-assembly of $IND_{20}$-*b*-$HEA_{240}$.

These results indicate that although $IND_{20}$ and $IND_{20}$-*b*-$HEA_{240}$ form nanoparticles of different size, in mixture of the two polymers at high $IND_{20}$:$IND_{20}$-*b*-$HEA_{240}$ ratios, homogeneous and relatively monodiperse nanoparticles were formed. On the other hand, when $IND_{20}$-*b*-$HEA_{240}$ is present in large excess, a second particle distribution, with lower hydrodynamic

diameter, similar to what formed when $IND_{20}$-$b$-$HEA_{240}$ alone was used, started to appear.

IDR 1018-sodium usnate-loaded nanoparticles showed a similar behaviour, with relatively larger particle size, and narrow size distributions. In particular, $IND_{20}$:$IND_{20}$-$b$-$HEA_{240}$ 8:2 blend- and $IND_{20}$:$IND_{20}$-$b$-$HEA_{240}$ 6:4 blend-nanoparticles showed single populations of size around 260 nm and 215 nm, respectively. Again, lower $IND_{20}$:$IND_{20}$-$b$-$HEA_{240}$ ratios resulted in the appearance of new peaks between 10 and 100 nm, as seen for the non-loaded nanoparticles

The analyses confirmed the stabilising effects of $IND_{20}$-$b$-$HEA_{240}$ on $IND_{20}$.The two polymers together displayed a cooperative behaviour that allowed the incorporation of the IDR 1018-sodium usnate complex.
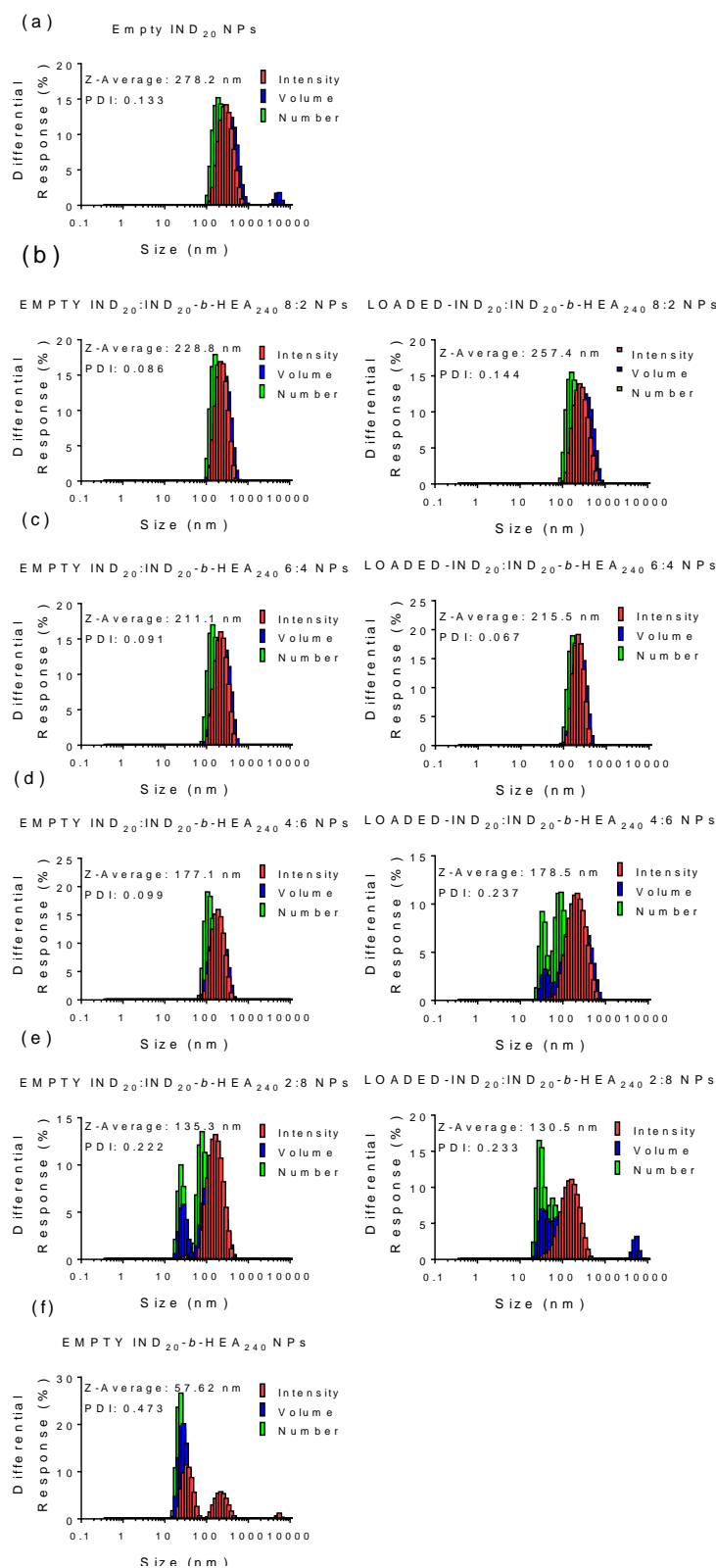
Figure 4.12. size distribution of empty and IDR 1018-sodium usnate complex-loaded IND$_{20}$:IND$_{20}$-b-HEA$_{240}$ blends based-nanoparticles, as assessed by DLS. Sizes are reported as intensity, volume and number % distributions. Nanoparticles were generated from the self-assembly of (a) 100% IND$_{20}$, (b) IND$_{20}$:IND$_{20}$-b-HEA$_{240}$ 8:2 blend, (c) IND$_{20}$:IND$_{20}$-b-HEA$_{240}$ 6:4 blend, (d) IND$_{20}$:IND$_{20}$-b-HEA$_{240}$ 4:6 blend, (e) IND$_{20}$:IND$_{20}$-b-HEA$_{240}$ 2:8 blend and (f) 100 % IND$_{20}$-b-HEA$_{240}$ at a nanoparticle concentration of 1 mg/mL, in water.

Size peaks by volume % for $IND_{20}:IND_{20}$-*b*-$HEA_{240}$ and the other three $IND_m:IND_m$-*b*-$HEA_n$ blends nanoparticles are displayed in Figure 4.13 (complete size distributions by intensity, volume and number can be found in the Supporting Information). In general, DLS analysis confirmed the results obtained from $IND_{20}:IND_{20}$-*b*-$HEA_{240}$ blends. The addition of $IND_m$-*b*-$HEA_n$ copolymers caused a general decrease of nanoparticle size, in a copolymer-concentration dependent manner. 100% $IND_{10}$-based -free nanoparticles had a size peak at around 450 nm, which decreased gradually to 200 nm as increasing amounts of $IND_{10}$-*b*-$HEA_{95}$ were added. A similar effect was observed for $IND_{10}$-*b*-$HEA_{268}$, with the difference that in this case the copolymer appeared more effective in controlling the nanoparticles size, as an $IND_{10}:IND_{10}$-*b*-$HEA_{268}$ ratio of 8:2 was already sufficient to reduce the size of the nanoparticles down to 350 nm.

Loaded IDR 1018-sodium usnate complex-nanoparticles followed a similar profile, with a slight general increase in size. Both $IND_{10}:IND_{10}$-*b*-$HEA_{95}$ and $IND_{10}:IND_{10}$-*b*-$HEA_{268}$ blends behaved similarly to those prepared without incorporation of IDR 1018-sodium usnate complex. Size decreased with increasing proportions of $IND_{10}$-*b*-$HEA_n$ copolymers, from ca. 400 nm of the $IND_{10}:IND_{10}$-*b*-$HEA_n$ 8:2 molar ratio blend, to around 200 nm of $IND_{10}:IND_{10}$-*b*-$HEA_n$ 2:8 molar ratio ones.

Blends between $IND_{20}$ and $IND_{20}$-$HEA_{74}$, possessing a comparatively longer hydrophobic block and shorter hydrophilic segment, displayed a clear size increase upon complex loading. The extent of this increase was dependent on

the $IND_{20}$:$IND_{20}$-$HEA_{74}$ molar ratio. At $IND_{20}$:$IND_{20}$-*b*-$HEA_{74}$ 8:2 molar ratio, size increased from around 300 nm of empty nanoparticles to almost 500 nm of IDR 1018-sodium usnate complex-loaded ones, whilst at 6:4 molar ratio the difference was reduced, as loaded nanoparticles had a size of ca. 400 nm. No difference between unloaded and loaded nanoparticles was observed at lower $IND_{20}$:$IND_{20}$-*b*-$HEA_{74}$ molar ratios.

For all the blends analysed, 100% $IND_m$-*b*-$HEA_n$-based nanoparticles displayed a main size peak between 20 and 30 nm, similarly to the values registered for $IND_{10}$-*b*-$HEA_n$ copolymers in Chapter 3. However, all of them underwent aggregation upon IDR 1018-sodium usnate complex encapsulation.
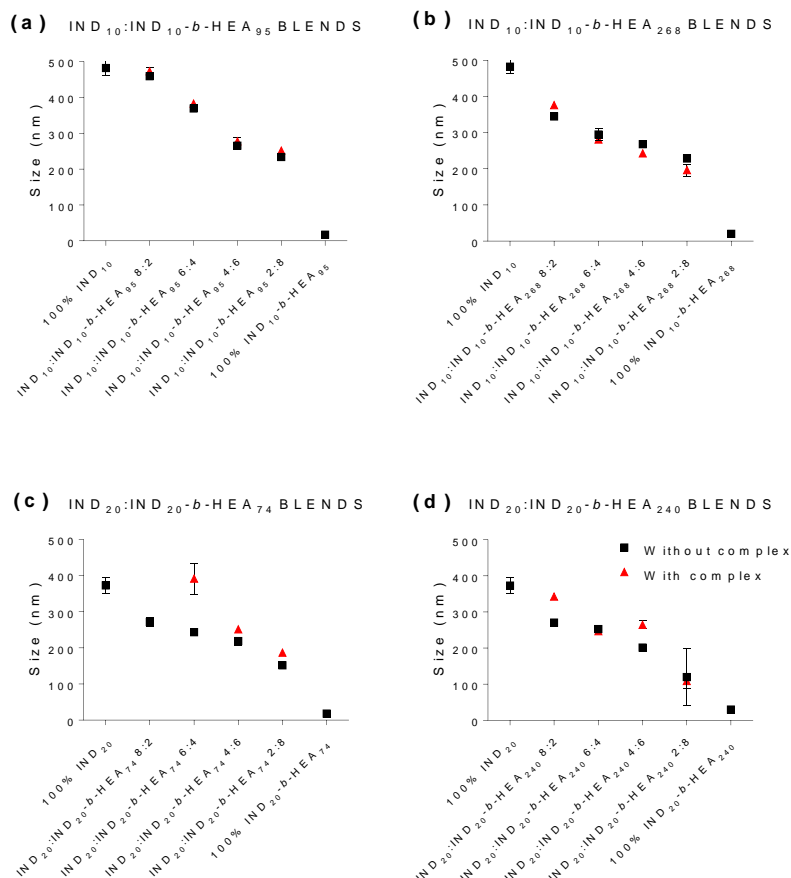
Figure 4.13: Particle size, as assessed by DLS by volume distribution, of free and IDR 1018-sodium usnate complex loaded into (a) $IND_{10}$:$IND_{10}$-b-$HEA_{95}$ blends-nanoparticles, (b) $IND_{10}$:$IND_{10}$-b-$HEA_{268}$ blends-nanoparticles, (c) $IND_{20}$:$IND_{20}$-b-$HEA_{74}$ blends-nanoparticles and (d) $IND_{20}$:$IND_{20}$-b-$HEA_{240}$ blends-nanoparticles. Nanoparticles were generated from the self-assembly of : 100% $IND_m$, $IND_m$:$IND_m$-*b*-$HEA_n$ 8:2 blend, $IND_m$:$IND_m$-*b*-$HEA_n$ 6:4 blend, (d) $IND_m$:$IND_m$-*b*-$HEA_n$ 4:6 blend, $IND_m$:$IND_m$-*b*-$HEA_n$ 2:8 blend and 100 % $IND_m$-*b*-$HEA_n$ at a nanoparticle concentration of 1 mg/mL, in water.

These results indicated that $IND_m$ oligomers and their corresponding $IND_m$-*b*-$HEA_n$ copolymers displayed a cooperative behaviour when mixed together. Addition of appropriate proportion of $IND_m$-*b*-$HEA_n$ allowed to control the size of nanoparticles, avoiding aggregation upon encapsulation of IDR 1018-sodium usnate. In $IND_{20}$:$IND_{20}$-*b*-$HEA_n$ formulations, copolymers with longer polyHEA blocks were more efficient in modulating nanoparticles size. It is reasonable to

hypothesise that a longer hydrophilic block can more efficiently shield the nanoparticles, limiting aggregation, and favouring the formation of homogenous nanoparticle populations.

### 4.3.4. Quantification of IDR 1018-Sodium Usnate complex Loading capacity and Encapsulation efficiency

Quantification of peptide complex encapsulation was carried out by RP-HPLC analysis (UV detection, $\lambda$=280 nm) of samples purified as described previously. Concentration for both IDR 1018 and sodium usnate were calculated from calibration curves previously prepared, and their Loading Capacity and Encapsulation Efficiency quantified separately (Fig. 4.14).

Results indicates that the highest final Loading Capacity and Encapsulation Efficiency values were obtained at $IND_m:IND_m$-$b$-$HEA_n$ 8:2 molar ratio, with Loading Capacity between 2 and 2.5% and Encapsulation Efficiency between 40 and 50% for both IDR 1018 and sodium usnate. A partial expception was $IND_{10}:IND_{10}$-$b$-$HEA_{95}$ 8:2 blend, which presented a higher sodium usnate loading capacity, around 3,5%, and subsequent Encapsulation Efficiency, ca. 60%. The best IDR 1018 incorporation was observed for $IND_{20}:IND_{20}$-$b$-$HEA_{240}$ 8:2 blend, with loading capacity of 2.5% and Encapsulation Eifficiency of 50%. As the $IND_m$ proportion in the blends decreased, both IDR 1018 and sodium usnate incorporation was less efficient, with the lowest loading and encapsulation values observed for $IND_m:IND_m$-$b$-$HEA_n$ 2:8 blends. In particular, in case of $IND_{10}:IND_{10}$-$b$-$HEA_n$ blends, IDR 1018 Loading Capacity decreased from around 2% of the $IND_{10}:IND_{10}$-$b$-$HEA_n$ 8:2 blends to 0% of $IND_{10}:IND_{10}$-$b$-$HEA_n$ 2:8 blends. Sodium usnate displayed a similar behaviour, but higher final values,

with Loading capacity decreasing from initial 2-3% of the 8:2 blends, to 0-0.5% of the blends with the lowest proportion of $IND_{10}$. A similar behaviour was observed with $IND_{20}$:$IND_{20}$-*b*-$HEA_n$ blends, but in this case the decrease of IDR 1018 and sodium usnate incorporation observed at low $IND_{20}$:$IND_{20}$-*b*-$HEA_n$ ratios was less evident: for $IND_{20}$:$IND_{20}$-*b*-$HEA_{74}$ 2:8 blend, loading of IDR 1018 was quantified to be around 1.5%, while that of sodium usnate was calculated to be ca. 2%. In case of $IND_{20}$:$IND_{20}$-*b*-$HEA_{268}$ the reduction of IDR 1018 incorporation was more evident, with final Loading of 0.4% at $IND_{20}$:$IND_{20}$-*b*-$HEA_{268}$ 2:8 ratio.

In general, it was noticed that the decrease of Loading Capacity observed at low $IND_m$:$IND_m$-*b*-$HEA_n$ molar ratios was more evident for $IND_{10}$:$IND_{10}$-*b*-$HEA_n$ blends, and that this decrease affected more IDR 1018 than sodium usnate.

High proportions of $IND_m$ oligomers appear to be necessary for best peptide complex loading capacity and encapsulation efficiency values. $IND_m$-based nanoparticles are therefore more efficient for the incorporation of IDR 1018-sodium usnate complex. However, $IND_m$:$IND_m$-*b*-$HEA_n$ blends are still required to avoid flocculation. Moreover, these studies are to be considered preliminar and will be repeated to confirm the Loading Capacity and Encapsulation Efficiency of each $IND_m$:$IND_m$-*b*-$HEA_n$ blend.
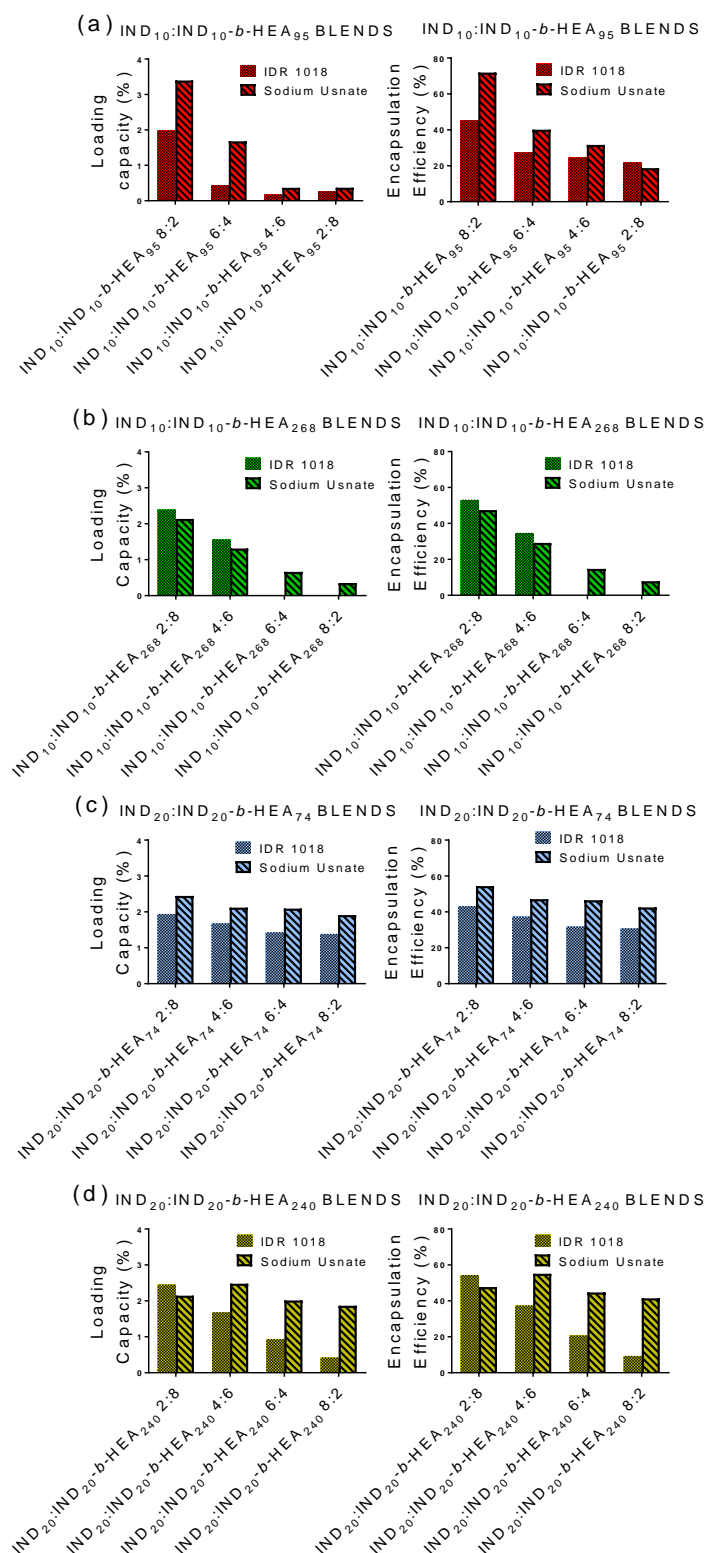
Figure 4.14: Loading capacity and encapsulation efficiency measured for IDR 1018-sodium usnate complex-loaded (a) $IND_{10}$:$IND_{10}$-b-$HEA_{95}$, (b) $IND_{20}$:$IND_{20}$-b-$HEA_{74}$, (c) $IND_{10}$:$IND_{10}$-b-$HEA_{268}$, and (d) $IND_{20}$:$IND_{20}$-b-$HEA_{240}$ blends nanoparticles. Loading capacity and encapsulation efficiency were calculated by C18 RP-HPLC analyses of 1 mg/mL DMSO solutions of IDR 1018-sodium usnate complex -loaded nanoparticles blends, using a 25-90% acetonitrile gradient in water + 0.1% TFA. Absorbance was recorded at 280 nm. For each blend, IDR 1018 and usnic acid were quantified via integration of the peak area of IDR 1018 and usnic acid peaks in the HPLC chromatograms.

### 4.3.5. TEM analysis

TEM imaging was performed to further verify size data obtained from DLS and get more information on nanoparticles shape. Free and IDR 1018-sodium usnate complex loaded $IND_{20}$:$IND_{20}$-*b*-$HEA_{240}$ 8:2 blends-based nanoparticles were selected for this part of the study, due to the high IDR 1018 Loading Capacity obtained for this specific blend. Nanoparticles were stained with 3% uranyl acetate (Fig. 4.15).
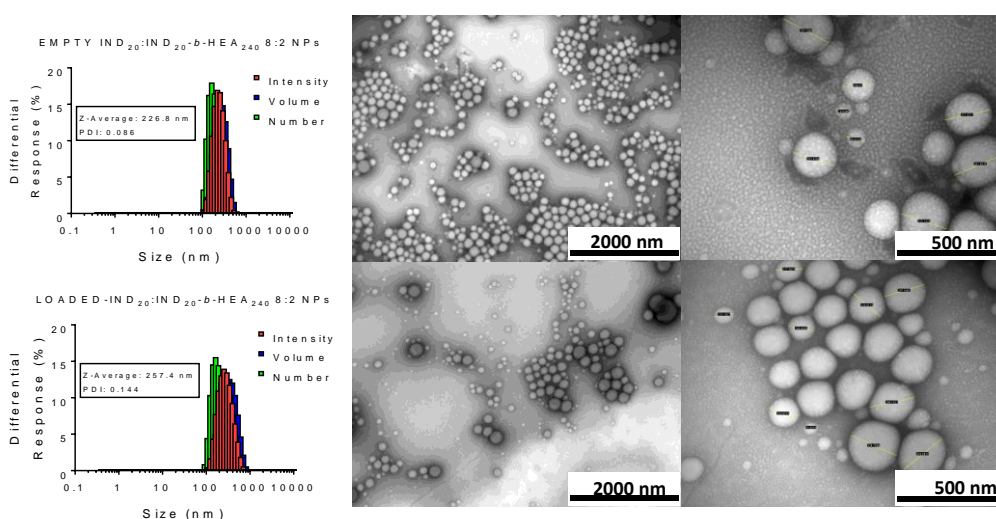


Figure 4.15: TEM images of free and IDR 1018-sodium usnate complex-loaded $IND_{20}$:$IND_{20}$-*b*-$HEA_{240}$ 8:2 blends-based nanoparticles. size-exclusion chromatography on PD-10 columns before TEM. Samples concentration was diluted to 1 mg/mL in water.

The analyses confirmed the presence of nanoparticles of size mostly between 200 and 300 nm, in good agreement with values calculated by DLS.

### 4.3.6. Drug release studies

IDR 1018-sodium usnate complex release study was carried out on $IND_{20}$:$IND_{20}$-$HEA_{210}$ 8:2 molar ratios-based nanoparticles. The investigation aimed at evaluating the release of both usnic acid and IDR 1018. The study was

performed at 37°C using a micro- dialysis device, with MWCO of 3.5 kDa to ensure the passage of both the IDR 1018-sodium usnate complex components, IDR 1018 (molecular weight 1.5 kDa) and usnic acid (molecular weight 0.34 kDa) from the inner to the outer compartment of the dialysis device (Fig. 4.16).



Figure 4.16: The dialysis device employed for the release study. The IDR 1018-sodium usnate complex-loaded-nanoparticles sospension is added to the device, which can be easily fitted into a 2 mL eppendorf. The two released components of the complex, IDR 1018 and sodium usnate, migrate from the dialysis device to the eppendorf through the dialysis membrane located at the bottom of the device.

Potential IDR 1018 aggregation, already discussed in Chapter 3, was a serious experimental limitation. This peptide can self-assemble in a range of buffers and tissue culture media[46], forming large aggregates of increased hydrodynamic size compared to normal, un-aggregated IDR 1018, which could hamper its passage through the dialysis membrane.

Thus, preliminary experiments to evaluate the potential aggregation of IDR 1018 in different media - 10 mM pH 7.2 phosphate buffer, PBS, and two saline solutions of different NaCl concentrations (15.4 and 154 mM NaCl) – were

carried out. The concentration of IDR 1018 in these experiments was 0.20 mM. In 10 mM pH 7.2 phosphate buffer the almost immediate formation of visible aggregates was observed. The aggregation, as explained in Chapter 3, is due to the high amount of salt in solution, whose dissociation releases charged ions that interact with water molecules. Less water molecules are available to interact with charged residues on the peptide backbone with stabilising effects, and subsequently its hydrophobic residues start self-interactions that lead to peptide aggregation and precipitation[47]. The other three solutions, in which no aggregates could be visually observed, were further tested on the mini-dialysis device, to quantify the re-equilibration of the peptide between the two dialysis compartments. 500 µL of starting IDR 1018 solution were added to the inner compartment of the dialysis device, 1500 µL of the same buffer were put in the outer compartment. The peptide was allowed to re-equilibrate between the two compartments over 20 h. IDR 1018 starting concentration in the inner compartment and its concentration in the outer compartment after 20 h were then quantified by RP-HPLC (Fig. 4.17). At complete equilibration, the peptide released from the inner compartment was expected to be 75% of the starting amount.
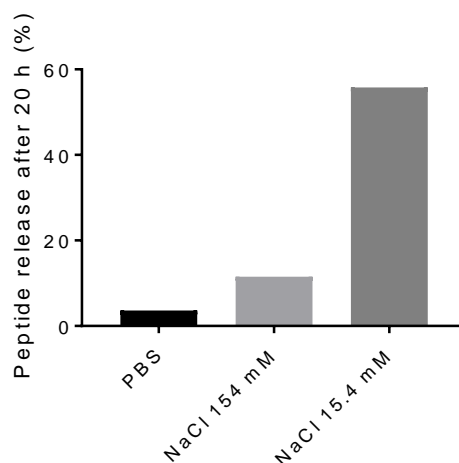
Figure 4.17: amount of IDR 1018 peptide released from the dialysis device shown in Figure 16, after 20 h incubation. Release is expressed as % of the total IDR 1018 present at time 0 in the inner compartment. Peptide quantification were made by C18 RP-HPLC via integration of the AUC of IDR 1018 peak in the HPLC chromatograms, using a 25-90% acetonitrile gradient in water + 0.1% TFA. Absorbance was recorded at 280 nm.

Analyses showed that less then 10% of IDR 1018 crossed the dialysis membrane in PBS, suggesting that under these conditions IDR 1018 may self-assemble to form larger aggregates that cannot easily cross the dialysis membrane. Similarly, release of around 15% IDR 1018 was obtained in 154 mM NaCl. Interestingly, in the diluted 15.4 mM NaCl solution a much higher release of the peptide, was observed. Under these conditions, after 20 h almost 60% of the peptide crossed the dialysis membrane, close to the 75% which would indicate full re-equilibration. Faster release may be ascribed to the fact that the amount of salt in solution has been reduced to 10% compared to 154 mM NaCl, hence also peptide aggregation is minimised.

IDR 1018-sodium usnate complex release from $IND_m$:$IND_m$-*b*-$HEA_n$ polymeric nanoparticles was therefore evaluated in 15.4 mM NaCl. PBS was tested as well. Even if IDR 1018 showed to aggregate in this buffer, we wanted to evaluate the

potential release of usnic acid. Release studies in 100 mM pH 4 acetate buffer were also carried out to evaluate the potential release of the two components of the complexes, IDR 1018 and usnic acid, at acidic pH (Fig. 4.18).
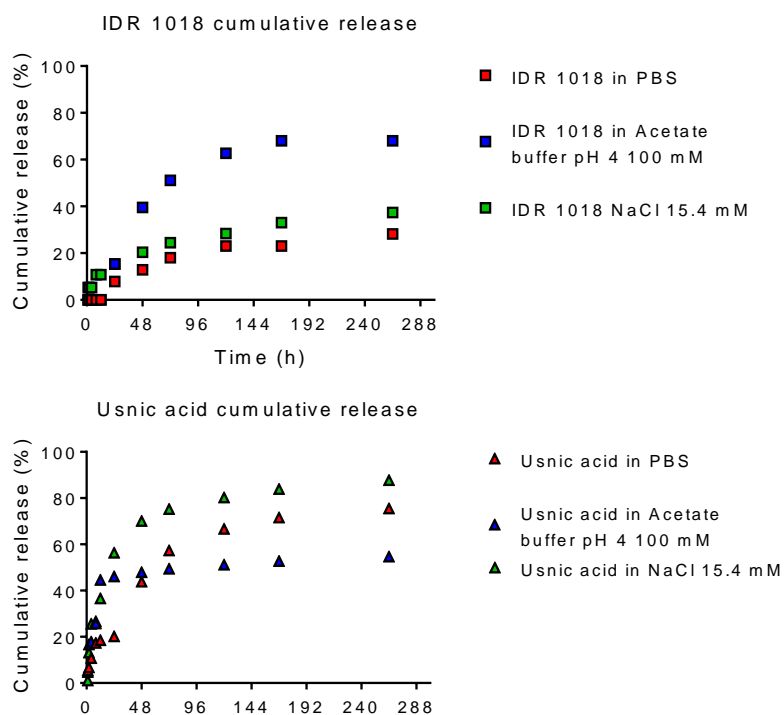


Figure 4.18: Cumulative release of IDR 1018 and usnic acid from (IDR 1018-usnate complex)-loaded nanoparticles, measured in PBS, 15.4 mM NaCl and 100 mM pH 4.0 acetate buffer. The amount of peptide and usnic acid released was calculated from the concentrations quantified in the outer compartment of the release device (Fig. 16) by C18 RP-HPLC at different time points, using a 25-90% acetonitrile gradient in water + 0.1% TFA. Absorbance was recorded at 280 nm. For each buffer, IDR 1018 and usnic acid were quantified via integration of the AUC of IDR 1018 and usnic acid peaks in the HPLC chromatograms.

Results suggested a slow and limited release of peptide IDR 1018 from the nanoparticles, not only in PBS, but also in 15.4 mM NaCl, with around 20 % of IDR 1018 released after 72 h in either medium, and only a small amount released after that. Release in acidic acetate buffer was faster as it reached 40 % after 48 h, and it stabilized at ~ 60% after 144 h.

Compared to IDR 1018, release of usnic acid was faster. In 15.4 mM NaCl 70% release was achieved within 48 h, while in PBS 50% release was achieved between 48 and 72 h. In acidic buffer 45% release was observed in 12 h, but values then reached a maximum of ~ 50% for the subsequent time points.

Overall, a very slow release profile of peptide IDR 1018 was thus observed not only in PBS, where it could be explained by peptide aggregation and slow passage through the dialysis membrane, but also in 15.4 mM NaCl. It is possible that if IDR 1018 were tightly packed inside the nanoparticles, in physiological conditions its release would be limited. As discussed in the previous chapter, this peptide comprises five aminoacids with basic groups (four Arg and one *N*-terminal amine), together with an aggregation-prone, sequence of five aminoacids possessing aliphatic hydrophobic side chains, and one tryptophan[46]. When IDR 1018 is encapsulated inside the nanoparticles, its basic groups may be interacting with usnic acid and then its basic groups would be ion paired and neutralised. Hence, its hydrophobic residues may potentially interact with indolic side chains of $IND_{10}$ and $IND_{20}$ oligomers through hydrophobic interactions, resulting in tighter non-covalent complexation of IDR 1018 in the nanoparticle matrix.

The faster release observed at acidic pH may be ascribed to the protonation of the acidic hydroxyl of usnic acid. With a pKa of 4.4, we could expect ~70% of this hydroxyl to be protonated. Its protonation would disrupt the ion pairing interaction between usnic acid and IDR 1018. Due to the basic arginine on its backbone, free IDR 1018 would be positively charged, and these positive

charges may disrupt the hydrophobic interactions that the peptide has potentially established with $IND_m$ oligomers within the nanoparticles matrix.

By contrast, release of usnic acid appeared much faster in both PBS and 15.4 mM NaCl. Interestingly, acidic buffer 100 mM pH 4.0 acetate buffer induced a significant decrease of its release. After a burst release in the first 12 h, cumulative release stabilised at around 50%. Since at this pH the hydroxyl group of usnic acid is mostly protonated, we can expect a decrease of its water solubility. Even though solubility of usnic acid and sodium usnate at different pHs was not experimentally investigated due to time constraint, precipitation of usnic acid over time in the dialysis inner compartment may be hypothesised as the reason for its slow and limited release. Such a precipitate could not be visually observed, as the nanoparticles suspension was already very cloudy.

### 4.2.7. Antimicrobial activity on *Salmonella enterica* infected macrophages

*Salmonella enterica* is a family of Gram-negative enteropathogenic bacteria which can infect a wide range of animal hosts including humans[48]. These bacteria are amongst the most common causes of foodborne illness worldwide, and are estimated to cause about 1.2 million illnesses, 23,000 hospitalizations, and 450 deaths in the United States every year. [49] Food contamination accounts for about 1 million of these illnesses[50]. Among the clinical manifestations induced by *salmonella* infections, the most important are enteric fever and gastroenteritis[51].

The initial site of infection lies within the distal small intestine. From there, can bacteria penetrate the intestinal epithelium and reach the liver and spleen. Interestingly, they can induce internalisation by host cells. Through a group of bacterial effectors molecules injected into the host cytoplasm, they can trigger radical changes in the host cytoskeleton, which will result in bacteria micropinocytosis[52]. In particular, it has been shown that these bacteria have a preference for infecting host hemophagocytic macrophages, where they can survive after the acute phase of the infection for months or longer, making the macrophage a survival niche for *salmonella* during persistent, chronic infections[53].

Antimicrobial agents such as ampicillin, chloramphenicol and trimethoprim are often used to treat *salmonella*'s infections[51]. Unfortunately, resistance to a range of these antibiotics is becoming increasingly prevalent. A recent study has analysed the development of new antimicrobial resistant strains in the US, 1189 blood isolates of *salmonella* collected between 2003 and 2013 were tested for susceptibility to more than a dozen commonly prescribed antibiotics. 868 were found to be susceptible to all antibiotic agents tested, while 321 were resistant to at least one agent, of which 237 were resistant to first-line treatments[54], indicating that new treatments for *salmonella* infections are urgently needed.

Within our group, a library of liposomes decorated with mannosylated ligands were designed and tested by Dr Rosa Catania, a former PhD student now Research Fellow, as potential antimicrobial delivery systems for the treatment

of *salmonella*-infected macrophages. Liposomes uptake was mediated by the mannose receptor (MR) expressed on macrophages cell membrane.

However, non-targeted nanoparticles uptake by macrophages has also been described in previous studies, with nanoparticles of different types, shapes and size[55]. Nanoparticle internalization by macrophages is usually regulated by phagocytosis. Firstly, specific plasma proteins adsorb on nanoparticles surface (opsonization). The protein "shell" can then interact with specific membrane receptors on macrophages, leading to internalisation into phagosomes, which will then fuse with lysosomes[56]. In the lysosome nanoparticles are subjected to degradation, due to acidic pH and hydrolytic enzymes. In drug delivery, internalisation by macrophages limits nanoparticles circulation and targeting, and it is thus normally considered a loss of nanoparticles and encapsulated drug[56]. Hence, usually different strategies are employed to avoid nanoparticles phagocytosis: for example, PEG grafting provides the nanoparticles with a hydrating layer that will prevent the formation of a proteins-shell, avoiding recognition from macrophages [57].

On the contrary, the internalization of nanoparticles by macrophages can be used to enhance drug internalisation if macrophages are the drug target. This is for example the case of infections of *Mycobacterium tuberculosis*, which, like *salmonella*, resides mainly in macrophages[58]. In a recent study by Kalluru *et al.*, 50-400 nm antimicrobial drug rifampicin-loaded PLGA nanoparticles were applied on infected primary macrophages and found to be significantly more effective in *Mycobacterium tuberculosis* killing than the free rifampicin drug.

The nanoparticles were also loaded with coumarin-6 dye, and the resulting fluorescent particles were tracked by fluorescent microscopy to elucidate their fate after internalisation. The study revealed that nanoparticles remained in the phagolysosome after phagocytosis, where they were slowly degraded over 12 days by acidic pH and hydrolytic enzymes, allowing the free drug to be released in the cytoplasm[59].

In this chapter, *salmonella*-infected macrophages were tested, in collaboration with Dr Rosa Catania, in a preliminary study to assess the uptake and the antimicrobial activity of IDR 1018-sodium usnate complex-loaded nanoparticles. Our previous drug release experiments showed a very slow and overall incomplete release of peptide IDR 1018 from nanoparticles. However, release may be much faster if the nanoparticles are internalised by macrophages, as a result of nanoparticle degradation after internalisation. Lysosome contain hydrolytic enzymes, e.g. esterases, lipases, phosphatases in relatively high concentration[60]. Indole moieties, responsible for the hydrophobic and self-assemblying nature of $IND_{10}$ and $IND_{20}$, are connected to the polyacrylamide backbone through ester bonds. backbone. Hydrolysis of these ester groups would likely result in nanoparticle disassembly, and release of the encapsulated IDR 1018-sodium usnate complex.

Complex loaded-$IND_{20}$:$IND_{20}$-*b*-$HEA_{240}$ 8:2 blend-nanoparticles were chosen for these experiments. Controls of usnic acid, IDR 1018 and corresponding complexes were prepared at the same IDR 1018 and usnic acid concentration

loaded in the nanoparticles. A negative control of non-loaded nanoparticles was also prepared to be applied on macrophages.

The experiment was performed on murine macrophages RAW 264.7 cell line and consisted of several sequential steps. On a 48 well-plate, macrophages were infected using a *salmonella* suspension which was applied to each well. After bacterial internalisation, the wells were washed with gentamicine for 30 min to kill any residual extracellular bacteria. Infected macrophages were finally treated with our samples (concentrations reported in Table 4.1) for 4 h at 37°C. After treatment, the samples-containing medium was replaced with fresh one, and the macrophages left in incubation for 24 h at 37°C. Macrophages were finally lysed, and bacteria recovered from the lysates were seeded on an agar plate. Number of bacteria colonies after 16 h of incubation were visually counted to estimate the antimicrobial efficacy of each sample – that is, the fewer the colonies, the higher the antimicrobial activity. Full description of the experimental procedure is provided in the Figure below.
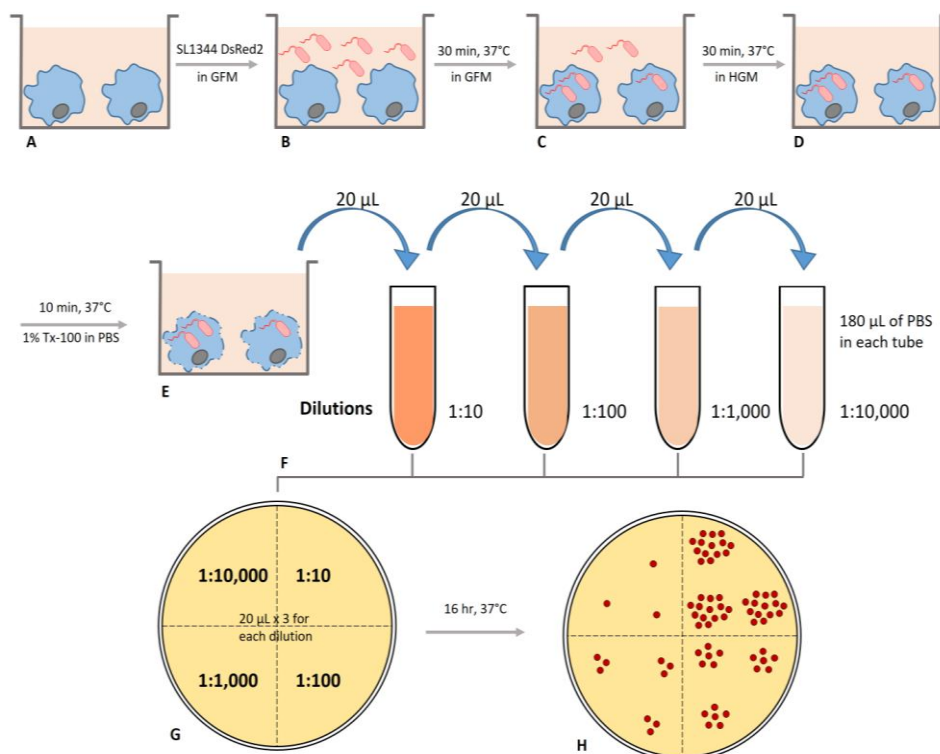
Figure 4.19: schematic representation of the antimicrobial experiment performed on salmonella-infected macrophages. The representation was taken from Dr Rosa Catania's PhD dissertation. (a) Macrophages are seeded on a 48 well-plate, at a density of $2 \times 10^4$ cells/mL per well. (b) After overnight incubation, macrophages are infected by addition of 0.2 mL of bacterial suspension in Gentamicin Free Medium (GFM). (c) Bacteria are allowed to insert into macrophages via 10 minutes centrifugation + 20 min incubation at 37°C. Macrophages are then treated with 0.2 mL of High Gentamicin Medium (100 µg/mL) for 30 min in order to kill extracellular bacteria. (d) Macrophages are finally treated with our samples, dissolved in Gentamicin free Medium, for 4h at 37°C. After treatment, macrophages are lysed with 1 % Triton X-100 in PBS. (e) The lysate is centrifuged and the supernatant is diluted several times and then (g) spread into agar well plates. (h) After 16h at 37°C, the numbers of bacterial colonies for each sample are visually counted and expressed as colony-forming units (CFU)/mL.

The number of bacterial colonies was normalised per $10^3$ of macrophages counted in each well before lysis. Results are reported in Fig. 4.20, expressed as colony-forming units (CFU)/mL.
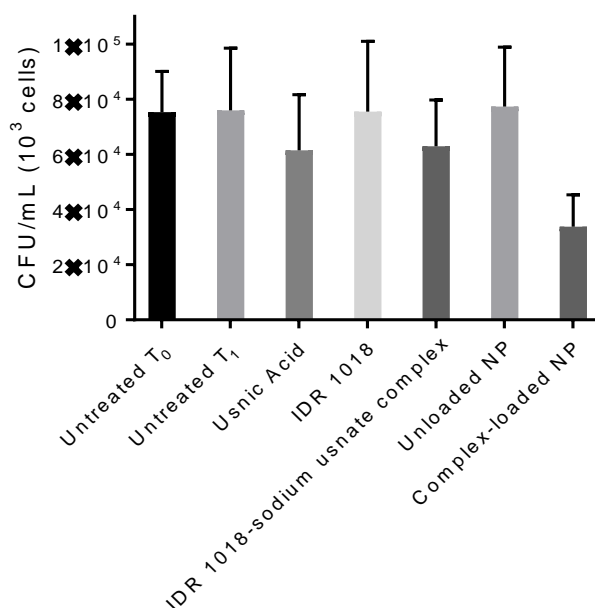
Figure 4.20: bacterial colonies quantified from untreated macrophages, and macrophages treated with our formulations. Colonies were visually quantified and the number of bacterial colonies was normalised per $10^3$ of macrophages counted in each well before lysis.

After infection with *Salmonella*, two different negative controls were tested: the first where macrophages were lysed before the beginning of the treatment (Untreated $T_0$ in Fig. 20), and the second where they were lysed at the end of it (Untreated $T_1$), to verify that during the 4 h treatment bacterial infection did not cause any significant macrophages death, which would cause a reduction of final counted bacterial colonies. The number of bacterial colonies was found to be very similar between untreated macrophages and macrophages treated with the peptide or the empty nanoparticles(~ $7*10^4$ CFU). The lack of efficacy of peptide IDR 1018 under these conditions may be due to poor internalization into macrophages. This was unexpected, as amphipathic peptides like IDR 1018 and other cell-penetrating peptides, containing basic groups like arginine and more hydrophobic amino acids like tryptophan, are believed to be internalised

through the interaction of basic residues on peptides with negatively charged polar heads of phospholipids on cellular membrane, while hydrophobic amino acids can establish hydrophobic interactions with the non-polar part of the membrane[61]. The lack of activity in our assay may be due to peptide aggregation. Although IDR 1018 aggregation was not verified in the gentamicin-free cell medium which was used for the experiment, due to time constraint, it is known (as our previous experiments also showed) that IDR 1018 can aggregate in different buffers and tissue culture media.

A partial reduction of counted colonies was observed with usnic acid and IDR 1018-usnate complexes, with Colony Forming Units (CFU) ~ $6*10^4$, suggesting partial internalization of the formulations. Usnic acid has previously shown antimicrobial activity against *Salmonella*. In a recent study by Stan *et al.* a thin film made of usnic acid-loaded ZnO nanoparticles was prepared. The film was used to coat the wells of a 6-well plate, where a suspension of *Salmonella enterica* was added. The experiment monitored the growth of *Salmonella* biofilm after 24, 48 and 72h in the absence and the presence of the usnic acid-loaded ZnO nanoparticles film. Results showed that after 24h both empty and loaded nanoparticles inhibited by half the biofilm growth. The result was ascribed to ZnO nanoparticles intrinsic antimicrobial activity. However, after 48h only usnic acid-loaded nanoparticles could significantly limit the biofilm growth, suggesting a controlled-release of usnic acid over time[62].

The best results were obtained with 8:2 $IDR_{20}$:$IDR_{20}$-*b*-$HEA_{240}$ nanoparticles incorporating IDR 1018-usnate complexes. Counted colonies were reduced by

50 % compared to the unloaded IDR 1018-sodium usnate complex, with CFU of around $3*10^4$. Although relatively large high experimental standard deviations suggest that definite conclusions should be drawn with caution, these initial results suggest that indeed nanoparticles may be able to enhance IDR 1018-sodium usnate complex internalisation, followed by release of complexes the phagolysosomal compartment and killing of infecting *Salmonella* bacteria. The experiment will be repeated, possibly increasing the amount of complexes applied to macrophages, or the exposure time of macrophages to the formulations.

## 4.3. Final considerations

In this chapter, the self-assembly behavious of two hydrophobic indole-containing short polyacrylamides, $IND_{10}$ and $IND_{20}$, was investigated. We aimed at assembling nanoparticles in the sub-micron range, with a narrow size distribution, to be used as an antimicrobial controlled-delivery system for the simultaneous delivery of two antimicrobial drugs, peptide IDR 1018 and usnic acids, complexed together through electrostatic interactions.

Initial self-assembly of $IND_{10}$ and $IND_{20}$ was achieved by nanoprecipitation, which resulted in nanoparticles with size in the 300-500 nm range with narrow size distribution. Attempts to encapsulate a complex formed with two antimicrobial drugs of opposite charge, usnic acid and IDR 1018 peptide, caused nanoparticles destabilisation and aggregation. Hence, new $IND_m$-*b*-$HEA_n$ block copolymers were synthesised. These copolymers were able to self-assemble into small nanoparticles of around 30-40 nm size but aggregated upon IDR 1018-sodium usnate complex incorporation. However, $IND_m$-*b*-$HEA_n$ were found to stabilise $IND_{10}$ and $IND_{20}$ nanoparticles, most likely by anchoring on their surface and provide steric stabilisation due to a hydrophilic corona formed by their polyHEA blocks . Different blends between the hydrophobic $IND_m$ oligomers and their corresponding $IND_m$-*b*-$HEA_n$ copolymers generated stable 200-400 nm nanoparticles, which were able to load up to 7.5% of IDR 1018-sodium usnate complex.

Drug release study showed that only a limited amount of peptide IDR 1018 was released even after days of incubation, suggesting a tight binding of the peptide

IDR 1018 to the nanoparticles IND$_m$ matrix. In drug delivery, such a slow and partial release can be a disadvantage if the encapsulated drug is supposed to act systemically. However, it can be an advantage if there is a specific therapeutic target, as the drug release is minimised before the target is reached.

For this reason, the nanoparticles were evaluated as antimicrobial delivery system on *Salmonella enterica*-infected macrophages. Nanoparticles were expected to be internalised through phagocytosis. We expected the delivering the IDR 1018-sodium usnate complex inside the macrophages, where the nanoparticles could degrade upon the action of lysosomal enzymes, thus releasing the IDR 1018-sodium usnate complex. Pleasingly, IDR 1018-usnate complex -loaded nanoparticles showed enhanced reduction of the number of bacterial colonies compared by free IDR 1018-usnate complex free IDR 1018 and free usnic acid.

This antimicrobial test will need to be repeated, but these preliminary results are very encouraging and suggest the potential use of these nanoparticles as a co-delivery system of two antimicrobial drugs for bacteria-infected macrophages.

# References

1.       Munita, J. M.; Arias, C. A., Mechanisms of Antibiotic Resistance. *Microbiology spectrum* **2016,** *4* (2), 10.1128/microbiolspec.VMBF-0016-2015.

2.       http://www.who.int/news-room/fact-sheets/detail/antimicrobial-resistance.

3.       The Review on Antimicrobial Resistance, chaired by Jim O'Neill. Antimicrobial Resistance: Tackling a crisis for the health and wealth of nations. **2016**.

4.       Kang, H.-K.; Kim, C.; Seo, C. H.; Park, Y., The therapeutic applications of antimicrobial peptides (AMPs): a patent review. *Journal of Microbiology* **2017,** *55* (1), 1-12.

5.       Mahlapuu, M.; Håkansson, J.; Ringstad, L.; Björn, C., Antimicrobial Peptides: An Emerging Category of Therapeutic Agents. *Frontiers in Cellular and Infection Microbiology* **2016,** *6*, 194.

6.       Powers, J.-P. S.; Hancock, R. E. W., The relationship between peptide structure and antibacterial activity. *Peptides* **2003,** *24* (11), 1681-1691.

7.       Le, C.-F.; Fang, C.-M.; Sekaran, S. D., Intracellular Targeting Mechanisms by Antimicrobial Peptides. *Antimicrobial Agents and Chemotherapy* **2017,** *61* (4).

8.       Benincasa, M.; Zahariev, S.; Pelillo, C.; Milan, A.; Gennaro, R.; Scocchi, M., PEGylation of the peptide Bac7(1–35) reduces renal clearance while retaining antibacterial activity and bacterial cell penetration capacity. *European Journal of Medicinal Chemistry* **2015,** *95*, 210-219.

9.       Guirado, E.; Schlesinger, L. S.; Kaplan, G., Macrophages in tuberculosis: friend or foe. *Seminars in Immunopathology* **2013,** *35* (5), 563-583.

10.      Braun, K.; Pochert, A.; Lindén, M.; Davoudi, M.; Schmidtchen, A.; Nordström, R.; Malmsten, M., Membrane interactions of mesoporous silica nanoparticles as carriers of antimicrobial peptides. *Journal of Colloid and Interface Science* **2016,** *475*, 161-170.

11.      Dong, A.; Zhang, Q.; Wang, T.; Wang, W.; Liu, F.; Gao, G., Immobilization of Cyclic N-Halamine on Polystyrene-Functionalized Silica Nanoparticles: Synthesis, Characterization, and Biocidal Activity. *The Journal of Physical Chemistry C* **2010,** *114* (41), 17298-17303.

12.      d'Angelo, I.; Casciaro, B.; Miro, A.; Quaglia, F.; Mangoni, M. L.; Ungaro, F., Overcoming barriers in Pseudomonas aeruginosa lung infections: Engineered nanoparticles for local delivery of a cationic antimicrobial peptide. *Colloids and Surfaces B: Biointerfaces* **2015,** *135*, 717-725.

13.      Wu, C.; Wu, T.; Fang, Z.; Zheng, J.; Xu, S.; Chen, S.; Hu, Y.; Ye, X., Formation, characterization and release kinetics of chitosan/γ-PGA encapsulated nisin nanoparticles. *RSC Advances* **2016,** *6* (52), 46686-46695.

14.      Lu, H. D.; Rummaneethorn, P.; Ristroph, K. D.; Prud'homme, R. K., Hydrophobic Ion Pairing of Peptide Antibiotics for Processing into Controlled Release Nanocarrier Formulations. *Molecular Pharmaceutics* **2018,** *15* (1), 216-225.

15.      Marcus, Y.; Hefter, G., Ion Pairing. *Chemical Reviews* **2006,** *106* (11), 4585-4621.

16.      Oliveira, M. S.; Goulart, G. C. A.; Ferreira, L. A. M.; Carneiro, G., Hydrophobic ion pairing as a strategy to improve drug encapsulation into lipid nanocarriers for the cancer treatment. *Expert Opinion on Drug Delivery* **2017,** *14* (8), 983-995.

17.      Holmkvist, A. D.; Friberg, A.; Nilsson, U. J.; Schouenborg, J., Hydrophobic ion pairing of a minocycline/Ca2+/AOT complex for preparation of drug-loaded PLGA nanoparticles with improved sustained release. *International Journal of Pharmaceutics* **2016,** *499* (1), 351-357.

18.     Marina Gallarate, L. B., E. Peira, and Michele Trotta Peptide-Loaded Solid Lipid Nanoparticles Prepared through Coacervation Technique. *International Journal of Chemical Engineering,* **2011**.

19.     Wieczorek, M.; Jenssen, H.; Kindrachuk, J.; Scott, W. R. P.; Elliott, M.; Hilpert, K.; Cheng, J. T. J.; Hancock, R. E. W.; Straus, S. K., Structural Studies of a Peptide with Immune Modulating and Direct Antimicrobial Activity. *Chemistry & Biology* **2010**, *17* (9), 970-980.

20.     Ingólfsdóttir, K., Usnic acid. *Phytochemistry* **2002**, *61* (7), 729-736.

21.     Francolini, I.; Norris, P.; Piozzi, A.; Donelli, G.; Stoodley, P., Usnic Acid, a Natural Antimicrobial Agent Able To Inhibit Bacterial Biofilm Formation on Polymer Surfaces. *Antimicrobial Agents and Chemotherapy* **2004**, *48* (11), 4360.

22.     Taresco, V.; Francolini, I.; Padella, F.; Bellusci, M.; Boni, A.; Innocenti, C.; Martinelli, A.; D'Ilario, L.; Piozzi, A., Design and characterization of antimicrobial usnic acid loaded-core/shell magnetic nanoparticles. *Materials Science and Engineering: C* **2015**, *52*, 72-81.

23.     Fessi, H.; Puisieux, F.; Devissaguet, J. P.; Ammoury, N.; Benita, S., Nanocapsule formation by interfacial polymer deposition following solvent displacement. *International Journal of Pharmaceutics* **1989**, *55* (1), R1-R4.

24.     Martínez Rivas, C. J.; Tarhini, M.; Badri, W.; Miladi, K.; Greige-Gerges, H.; Nazari, Q. A.; Galindo Rodríguez, S. A.; Román, R. Á.; Fessi, H.; Elaissari, A., Nanoprecipitation process: From encapsulation to drug delivery. *International Journal of Pharmaceutics* **2017**, *532* (1), 66-81.

25.     Lassalle, V.; Ferreira, M. L., PLA Nano- and Microparticles for Drug Delivery: An Overview of the Methods of Preparation. *Macromolecular Bioscience* **2007**, *7* (6), 767-783.

26.     Hornig, S.; Heinze, T.; Becer, C. R.; Schubert, U. S., Synthetic polymeric nanoparticles by nanoprecipitation. *Journal of Materials Chemistry* **2009**, *19* (23), 3838-3840.

27.     Govender, T.; Stolnik, S.; Garnett, M. C.; Illum, L.; Davis, S. S., PLGA nanoparticles prepared by nanoprecipitation: drug loading and release studies of a water soluble drug. *Journal of Controlled Release* **1999**, *57* (2), 171-185.

28.     Betancourt, T.; Brown, B.; Brannon-Peppas, L., Doxorubicin-loaded PLGA nanoparticles by nanoprecipitation: preparation, characterization and in vitro evaluation. *Nanomedicine* **2007**, *2* (2), 219-232.

29.     Mastrotto, F.; Breen, A. F.; Sicilia, G.; Murdan, S.; Johnstone, A. D.; Marsh, G. E.; Grainger-Boultby, C.; Russell, N. A.; Alexander, C.; Mantovani, G., One-pot RAFT and fast polymersomes assembly: a 'beeline' from monomers to drug-loaded nanovectors. *Polymer Chemistry* **2016**, *7* (44), 6714-6724.

30.     Iolanda Francolini, V. T., Fernanda Crisante, Andrea Martinelli, Lucio D'Ilario, and Antonella Piozzi* Water Soluble Usnic Acid-Polyacrylamide Complexes with Enhanced Antimicrobial Activity against Staphylococcus epidermidis. *Int J Mol Sci* **2015**.

31.     Takai, M.; Uehara, Y.; Beisler, J. A., Usnic acid derivatives as potential antineoplastic agents. *Journal of Medicinal Chemistry* **1979**, *22* (11), 1380-1384.

32.     Jin, J.-q.; Rao, Y.; Bian, X.-l.; Zeng, A.-g.; Yang, G.-d., Solubility of (+)-Usnic Acid in Water, Ethanol, Acetone, Ethyl Acetate and n-Hexane. *Journal of Solution Chemistry* **2013**, *42* (5), 1018-1027.

33.     Lukáč, M.; Prokipčák, I.; Lacko, I.; Devínsky, F., Solubilisation of (+)-Usnic Acid in Aqueous Micellar Solutions of Gemini and Heterogemini Surfactants and their Equimolar Mixture. *European Pharmaceutical Journal* **2012**, *59* (2), 36-43.

34.     Iijima, M.; Kamiya, H., Surface Modification for Improving the Stability of Nanoparticles in Liquid Media. *KONA Powder and Particle Journal* **2009**, *27*, 119-129.

35.    Hotze EM1, P. T., Lowry GV. Nanoparticle aggregation: challenges to understanding transport and reactivity in the environment. *J Environ Qual.* **2010**.

36.    Doukkali, M.; Patel, R. B.; Stepanov, V.; Hadim, H., The Effect of Ionic Strength and pH on the Electrostatic Stabilization of NanoRDX. *Propellants, Explosives, Pyrotechnics* **2017,** *42* (9), 1066-1071.

37.    Wu, W.; Giese, R. F.; van Oss, C. J., Stability versus flocculation of particle suspensions in water—correlation with the extended DLVO approach for aqueous systems, compared with classical DLVO theory. *Colloids and Surfaces B: Biointerfaces* **1999,** *14* (1), 47-55.

38.    Gal, N.; Schroffenegger, M.; Reimhult, E., Stealth Nanoparticles Grafted with Dense Polymer Brushes Display Adsorption of Serum Protein Investigated by Isothermal Titration Calorimetry. *The Journal of Physical Chemistry B* **2018,** *122* (22), 5820-5834.

39.    Uz, M.; Bulmus, V.; Alsoy Altinkaya, S., Effect of PEG Grafting Density and Hydrodynamic Volume on Gold Nanoparticle–Cell Interactions: An Investigation on Cell Cycle, Apoptosis, and DNA Damage. *Langmuir* **2016,** *32* (23), 5997-6009.

40.    Suk, J. S.; Xu, Q.; Kim, N.; Hanes, J.; Ensign, L. M., PEGylation as a strategy for improving nanoparticle-based drug and gene delivery. *Advanced drug delivery reviews* **2016,** *99* (Pt A), 28-51.

41.    Moghimi, S. M.; Hunter, A. C., Poloxamers and poloxamines in nanoparticle engineering and experimental medicine. *Trends in Biotechnology* **2000,** *18* (10), 412-420.

42.    Santander-Ortega, M. J.; Jódar-Reyes, A. B.; Csaba, N.; Bastos-González, D.; Ortega-Vinuesa, J. L., Colloidal stability of Pluronic F68-coated PLGA nanoparticles: A variety of stabilisation mechanisms. *Journal of Colloid and Interface Science* **2006,** *302* (2), 522-529.

43.    https://www.gelifesciences.com/en/us/shop/chromatography/prepacked-columns/desalting-and-buffer-exchange/sephadex-g-25-in-pd-10-desalting-columns-p-05778.

44.    Modi, S.; Anderson, B. D., Determination of Drug Release Kinetics from Nanoparticles: Overcoming Pitfalls of the Dynamic Dialysis Method. *Molecular Pharmaceutics* **2013,** *10* (8), 3076-3089.

45.    Fugit, K. D.; Anderson, B. D., Dynamic, Nonsink Method for the Simultaneous Determination of Drug Permeability and Binding Coefficients in Liposomes. *Molecular Pharmaceutics* **2014,** *11* (4), 1314-1325.

46.    Haney, E. F.; Wu, B.; Lee, K.; Hilchie, A. L.; Hancock, R. E. W., Aggregation and Its Influence on the Immunomodulatory Activity of Synthetic Innate Defense Regulator Peptides. *Cell Chemical Biology* **2017,** *24* (8), 969-980.e4.

47.    Hyde, A. M.; Zultanski, S. L.; Waldman, J. H.; Zhong, Y.-L.; Shevlin, M.; Peng, F., General Principles and Strategies for Salting-Out Informed by the Hofmeister Series. *Organic Process Research & Development* **2017,** *21* (9), 1355-1370.

48.    Ohl, M. E.; Miller, S. I., Salmonella: A Model for Bacterial Pathogenesis. *Annual Review of Medicine* **2001,** *52* (1), 259-274.

49.    http://www.who.int/foodsafety/areas_work/foodborne-diseases/salmonella/en/.

50.    https://www.cdc.gov/salmonella/.

51.    Eng, S.-K.; Pusparajah, P.; Ab Mutalib, N.-S.; Ser, H.-L.; Chan, K.-G.; Lee, L.-H., Salmonella: A review on pathogenesis, epidemiology and antibiotic resistance. *Frontiers in Life Science* **2015,** *8* (3), 284-293.

52.    Ly, K. T.; Casanova, J. E., Mechanisms of Salmonella entry into host cells. *Cellular Microbiology* **2007,** *9* (9), 2103-2111.

53.    Nix, R. N.;  Altschuler, S. E.;  Henson, P. M.; Detweiler, C. S., Hemophagocytic Macrophages Harbor Salmonella enterica during Persistent Infection. *PLOS Pathogens* **2007,** *3* (12), e193.

54.    Angelo, K. M.;  Reynolds, J.;  Karp, B. E.;  Hoekstra, R. M.;  Scheel, C. M.; Friedman, C., Antimicrobial Resistance Among Nontyphoidal Salmonella Isolated From Blood in the United States, 2003–2013. *The Journal of Infectious Diseases* **2016,** *214* (10), 1565-1570.

55.    Terada, K. H. a. H. Endocytosis of Particle Formulations by Macrophages and Its         Application         to         Clinical         Treatment. *IntechOpen* **2012**.

56.    Blanco, E.;  Shen, H.; Ferrari, M., Principles of nanoparticle design for overcoming biological barriers to drug delivery. *Nature Biotechnology* **2015,** *33*, 941.

57.    Kou, L.;  Sun, J.;  Zhai, Y.; He, Z., The endocytosis and intracellular fate of nanomedicines: Implication for rational design. *Asian Journal of Pharmaceutical Sciences* **2013,** *8* (1), 1-10.

58.    Pieters, J., Mycobacterium tuberculosis and the Macrophage: Maintaining a Balance. *Cell Host & Microbe* **2008,** *3* (6), 399-407.

59.    Kalluru, R.;  Fenaroli, F.;  Westmoreland, D.;  Ulanova, L.;  Maleki, A.;  Roos, N.; Paulsen Madsen, M.;  Koster, G.;  Egge-Jacobsen, W.;  Wilson, S.;  Roberg-Larsen, H.; Khuller, G. K.;  Singh, A.;  Nyström, B.; Griffiths, G., Poly(lactide-co-glycolide)-rifampicin nanoparticles efficiently clear Mycobacterium bovis BCG infection in macrophages and remain membrane-bound in phago-lysosomes. *Journal of Cell Science* **2013,** *126* (14), 3043.

60.    Lübke, T.;  Lobel, P.; Sleat, D. E., Proteomics of the lysosome. *Biochimica et Biophysica Acta (BBA) - Molecular Cell Research* **2009,** *1793* (4), 625-635.

61.    Fatemeh Madani, S. L., Ülo Langel, Shiroh Futaki, and Astrid Gräslund., Mechanisms of Cellular Uptake of Cell-Penetrating Peptides. *Journal of Biophysics*, **2011**.

62.    Stan, M. S.;  Constanda, S.;  Grumezescu, V.;  Andronescu, E.;  Ene, A. M.; Holban, A. M.;  Vasile, B. S.;  Mogoantă, L.;  Bălşeanu, T.-A.;  Mogoşanu, G. D.;  Socol, G.;  Grumezescu, A. M.;  Dinischiotu, A.;  Lazar, V.; Chifiriuc, M. C., Thin coatings based on ZnO@C18-usnic acid nanoparticles prepared by MAPLE inhibit the development of Salmonella enterica early biofilm growth. *Applied Surface Science* **2016,** *374*, 318-325.

# Supporting Information Chapter 4

$^1$H and $^{13}$C NMR spectra were recorded on a Bruker DPX400 UltraShield™ Spectrometer and processed with MestReNova 12.0© 2017 Mestrelab Research S.L. All chemical shifts are reported in ppm ($\delta$) relative to tetramethylsilane or referenced to the chemical shifts of residual solvent resonances.

ESI TOF Mass spectrometry analyses were conducted on a Bruker microTOF II.

FT-IR spectra were recorded using an Agilent Cary630.

Polymer SEC analyses were performed on a Polymer Laboratories GPC 50 system equipped with a refractive index detector, using a system made of two PLgel Mixed-D (5 µm bead, 7.8 × 300 mm) columns and a matching guard (7.8 × 50 mm). Analyses were performed in DMF at a flow rate of 1 mg/mL with 0.1% w/v LiBR. Narrow PMMA standards were used for calibration.

HPLC experiments were performed on a Shimadzu HPLC (LC-20AD pump) equipped with a SPD-M20A UV detector and SIL-20A autosampler. Reverse phase analyses were completed using a C18 Zorbax Eclipse Plus C18 column (3.5 µm, 95 Å, 4.6 × 12.5 mm).

Dynamic light scattering was performed using a Nano-Zs from Malvern Instruments, UK, equipped with a 633 nm laser at a fixed angle of 173°. The size was measured at 25 ˚C. Analyses were repeated 3 times for each sample, and a minimum of 10 measurements was performed for each analysis.

Transmission Electron Microscopy (TEM) analyses were conducted on a FEI

TecnaiTM 12 Biotwin transmission electron microscope.
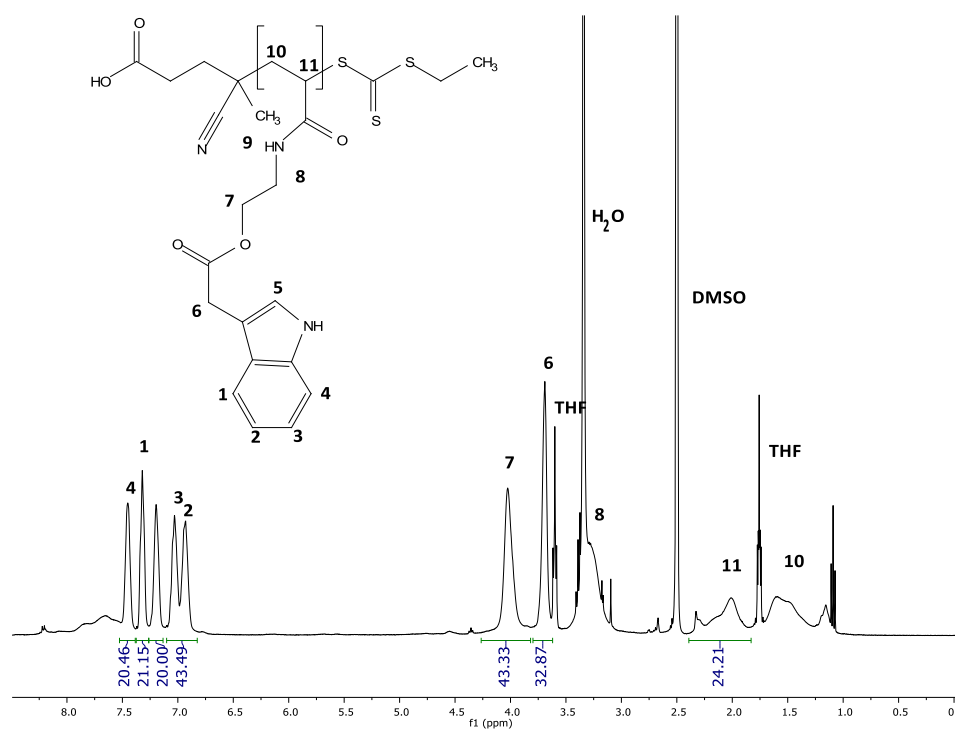


FIgure S4.1: $^1$H NMR spectrum of oligomer IND$_{20}$ in d$_6$-DMSO.
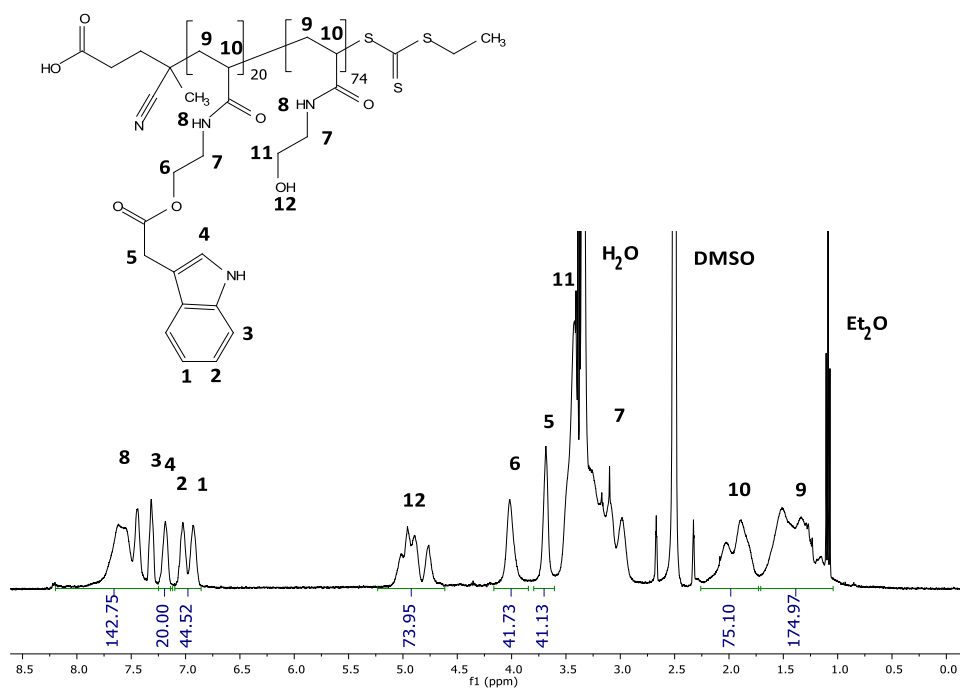
Figure S4.2: $^1$H NMR spectrum of copolymer IND$_{20}$-*b*-HEA$_{74}$ in d$_6$-DMSO.
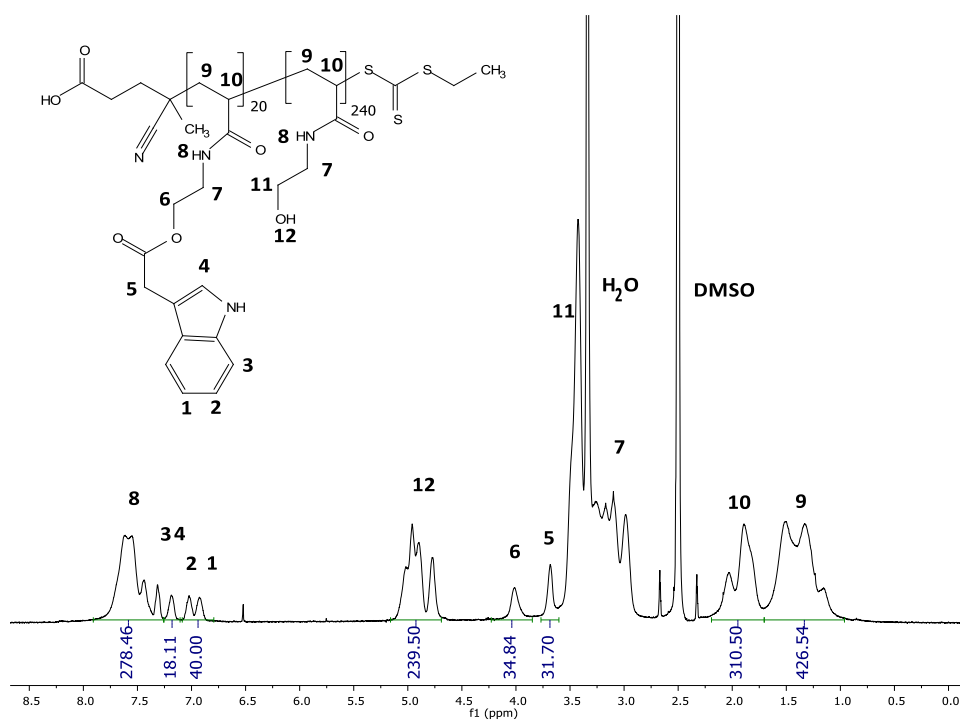


Figure S4.3: $^1$H NMR spectrum of copolymer IND$_{20}$-*b*-HEA$_{240}$ in d$_6$-DMSO.
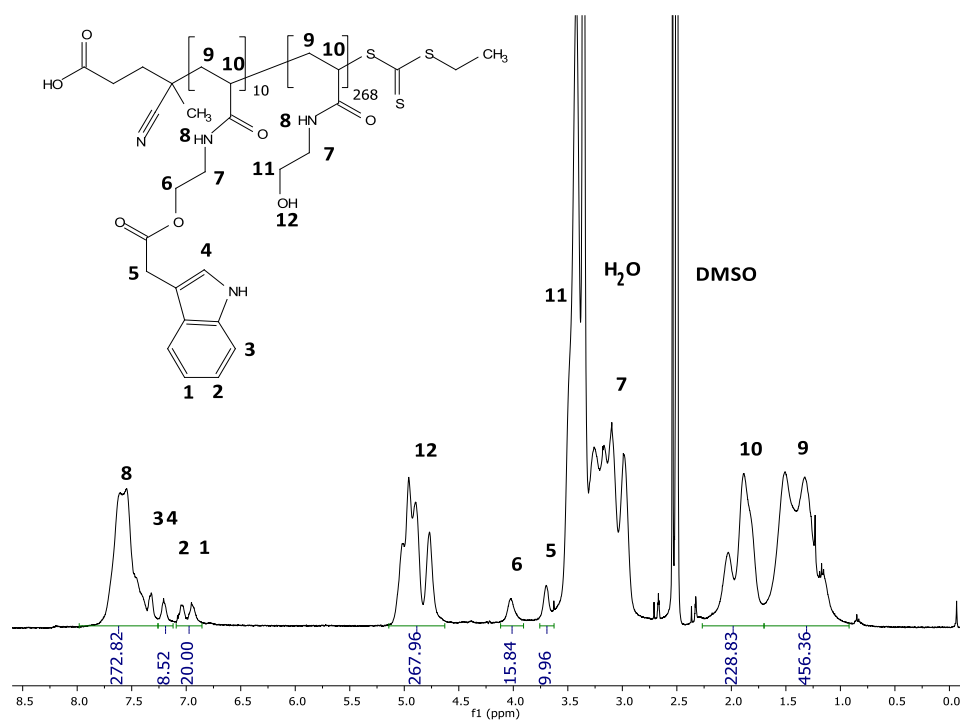
Figure S4.4: $^1$H NMR spectrum of copolymer IND$_{10}$-*b*-HEA$_{268}$ in d$_6$-DMSO.
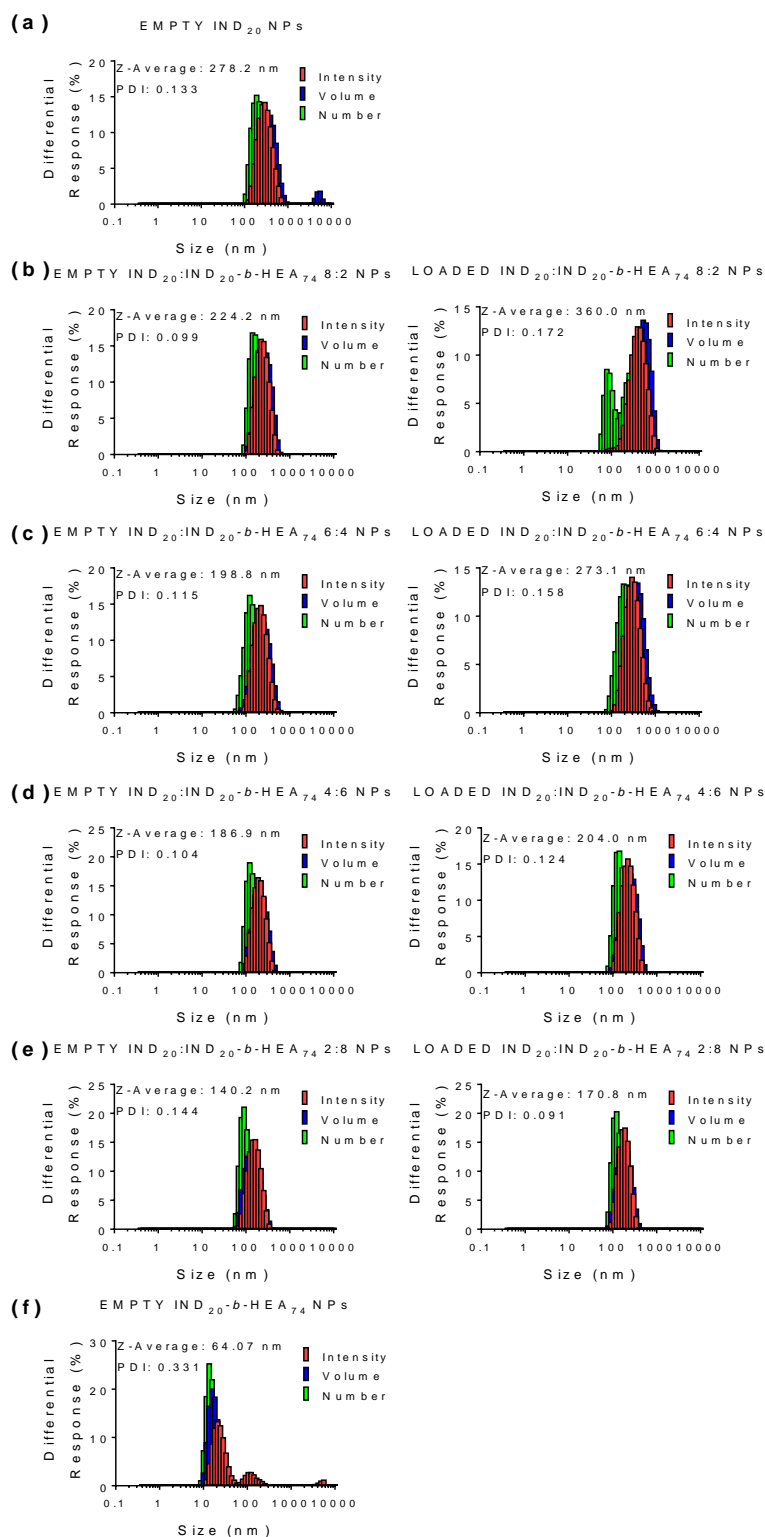
Figure S4.5: DLS size distribution of empty and IDR 1018-sodium usnate complex-loaded IND$_{20}$:IND$_{20}$-*b*-HEA$_{74}$ blends based-nanoparticles. Sizes are reported as intensity, volume and number % distributions. Nanoparticles were generated from the self-assembly of (a) 100% IND$_{20}$, (b) IND$_{20}$:IND$_{20}$-*b*-HEA$_{74}$ 8:2 blend, (c) IND$_{20}$:IND$_{20}$-*b*-HEA$_{74}$ 6:4 blend, (d) IND$_{20}$:IND$_{20}$-*b*-HEA$_{74}$ 4:6 blend, (e) IND$_{20}$:IND$_{20}$-*b*-HEA$_{74}$ 2:8 blend and (f) 100 % IND$_{20}$-*b*-HEA$_{74}$ at a nanoparticle concentration of 1 mg/mL, in water.
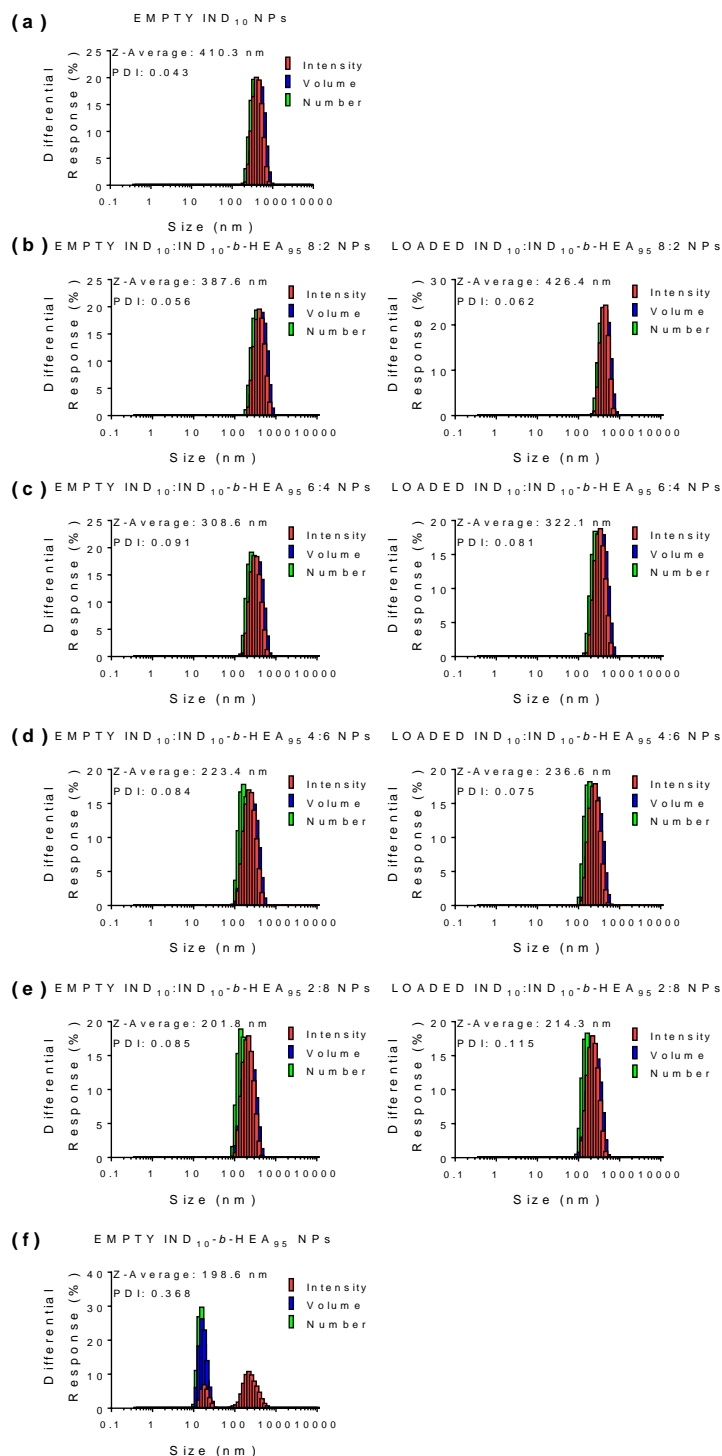
Figure S4. 6: DLS size distribution of empty and IDR 1018-sodium usnate complex-loaded IND$_{10}$:IND$_{10}$-*b*-HEA$_{95}$ blends based-nanoparticles. Sizes are reported as intensity, volume and number % distributions. Nanoparticles were generated from the self-assembly of (a) 100% IND$_{20}$, (b) IND$_{10}$:IND$_{10}$-*b*-HEA$_{95}$ 8:2 blend, (c) IND$_{10}$:IND$_{10}$-*b*-HEA$_{95}$ 6:4 blend, (d) IND$_{10}$:IND$_{10}$-*b*-HEA$_{95}$ 4:6 blend, (e) IND$_{10}$:IND$_{10}$-*b*-HEA$_{95}$ 2:8 blend and (f) 100 % IND$_{10}$-*b*-HEA$_{95}$ at a nanoparticle concentration of 1 mg/mL, in water.
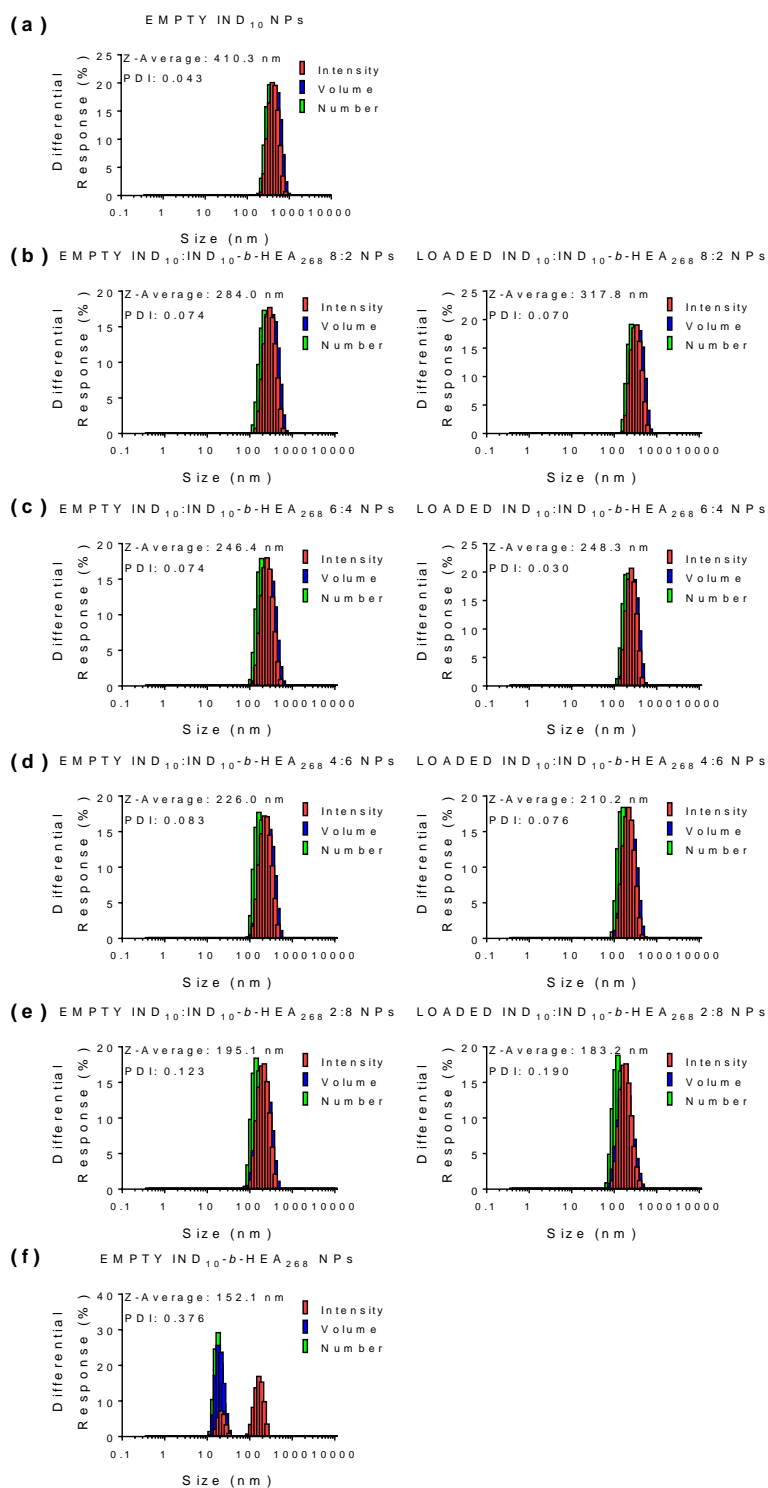
Figure S4.7: DLS size distribution of empty and IDR 1018-sodium usnate complex-loaded $IND_{10}:IND_{10}\text{-}b\text{-}HEA_{268}$ blends based-nanoparticles. Sizes are reported as intensity, volume and number % distributions. Nanoparticles were generated from the self-assembly of (a) 100% $IND_{20}$, (b) $IND_{10}:IND_{10}\text{-}b\text{-}HEA_{268}$ 8:2 blend, (c) $IND_{10}:IND_{10}\text{-}b\text{-}HEA_{268}$ 6:4 blend, (d) $IND_{10}:IND_{10}\text{-}b\text{-}HEA_{268}$ 4:6 blend, (e) $IND_{10}:IND_{10}\text{-}b\text{-}HEA_{268}$ 2:8 blend and (f) 100 % $IND_{10}\text{-}b\text{-}HEA_{268}$ at a nanoparticle concentration of 1 mg/mL, in water.
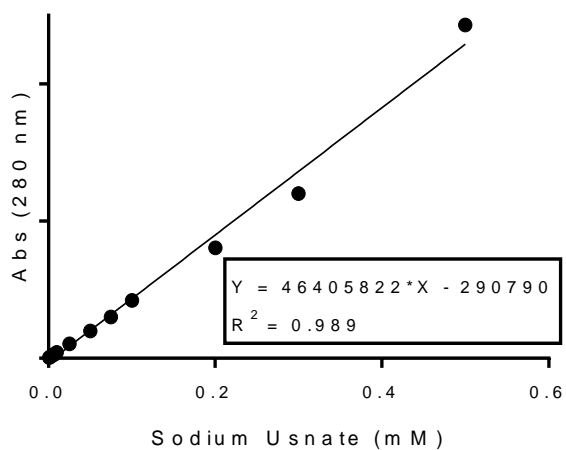
Figure S4.8: Sodium Usnate calibration curve. Sodium Usnate was dissolved in deionised water at different concentrations in the 0.001-0.5 mM range. The samples were analysed in triplicates by RP-HPLC, using a 75-90% MeCN gradient in Milli-q water + 0.1 % TFA. Absorbance was recorded at 280 nm. The area under Sodium Usnate peak was calculated for each concentration.
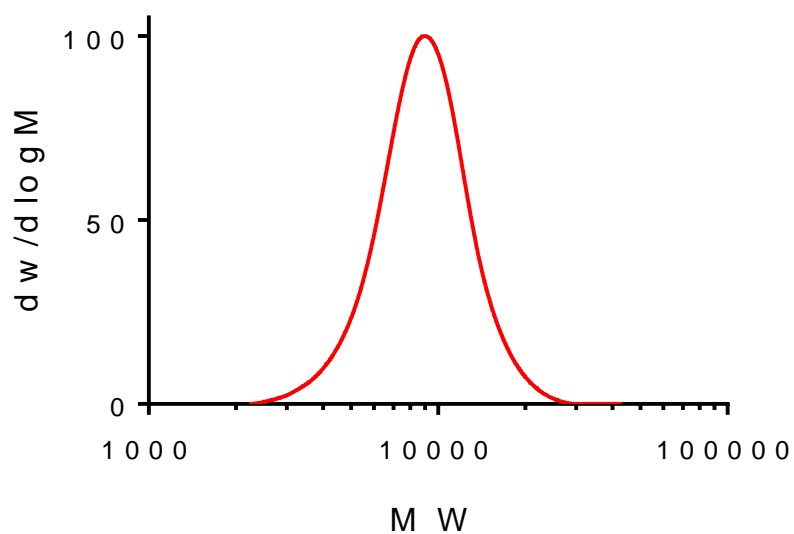


Figure S4.9: SEC trace of $IND_{20}$. SEC analysis was performed in DMF + 0.1 % LiBr (PMMA standards).
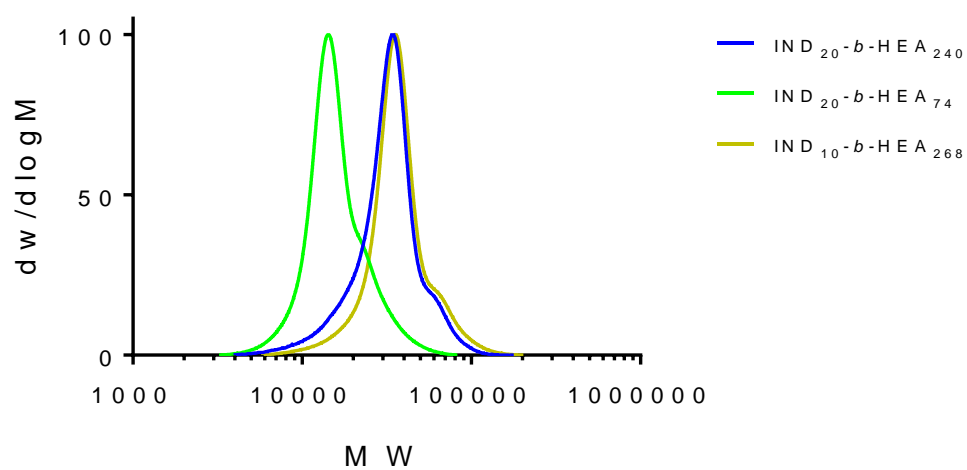
Figure S4.10: normalised SEC traces of IND$_{10}$-*b*-HEA$_{268}$, IND$_{20}$-*b*-HEA$_{74}$ and IND$_{20}$-*b*-HEA$_{240}$. SEC analyses were performed in DMF + 0.1 % LiBr (PMMA standards).

# Chapter 5

**Cholanic-polyacrylamides as tools for the delivery of protein therapeutics**

_____

## 5.1. Introduction

Non-covalent protein-polymer complexation is emerging an attractive alternative to covalent conjugation, to improve solubility, stability and bioavailability of potential protein therapeutics. Drawbacks of covalent polymer conjugation to proteins include chemical modifications of key amino acids in protein binding sites or enzymatic pockets, or steric shielding of their active site, thus reducing their efficacy[1]. In chapter 2 and 3 we have improved protein stability and solubility through non-covalent, hydrophobic interactions between different proteins/peptides and polymers incorporating hydrophobic peptides or peptidomimetic functional groups. The water solubility of these hydrophobic groups was conveniently increased through their copolymerization with the commercial monomer *N*-hydroxyethylacrylamide. Encouraged by these positive results, we focused our attention to cholanic acid, a bile acid molecule, and its precursor cholesterol.

Cholesterol and its analogues play a key role in digestion and processing of adsorbed fats, and are chemically characterised by a common steroid nucleus, made of a saturated tetracyclic hydrocarbon perhydrocyclopentanophenanthrene system[2] (Fig. 5.1).
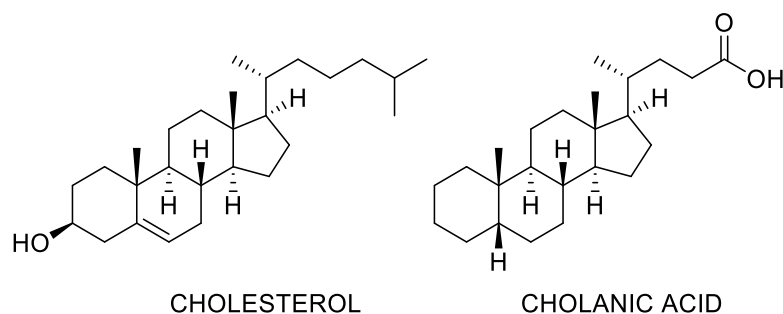
Figure 5.1: chemical structures of cholesterol and cholanic acid.

Cholesterol is also an essential component of cellular membranes, where it enhances the membrane stability and prevents phospholipids hydrophobic chains from crystallizing. Cholesterol is an amphipathic molecule, with a small polar head containing its OH group, and four hydrophobic fused rings. In cell membranes the hydrophilic area locates close to the polar head of phospholipids, while the four rings partition among their hydrocarbon chains[3]. The hydrophobic section of cholesterol is generally divided into two different faces, named α and β (Fig. 5.2), where the planar α face can establish CH-π interactions with protein aromatic residues, while the methyl groups on the β face can interact with leucine and valine residues[4]. These features allow cholesterol to interact with different types of proteins, such as transmembrane proteins[1] [5], but also other water soluble proteins, such as Human and Bovine Serum Albumin and Cytochrome P450[6, 7].
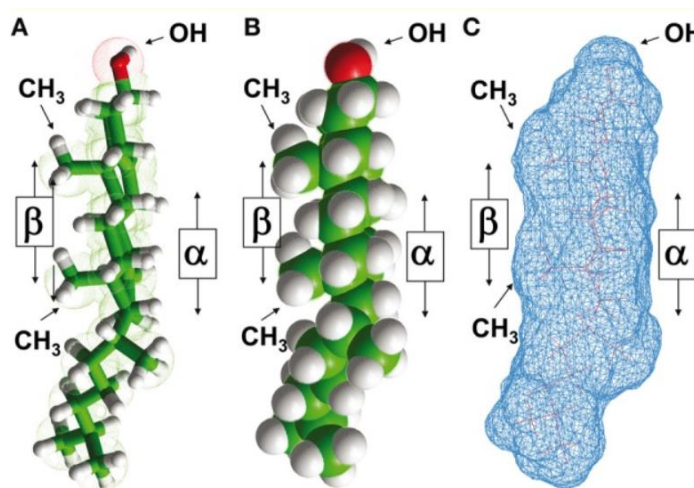
Figure 5.2: the α- and β-faces of cholesterol[4].

Thus, the hydrophobic part of bile acids could be conventiently used to establish non-covalent interactions with protein hydrophobic regions. In a previous work, the polysaccharide pullulan was derivatised with varying cholesterol units. This induced pullulan self-aggregation into hydrogel nanoparticles, which efficiently encapsulated both hydrophobic and water-soluble proteins[8]. More recently, cholanic acid-modified glycol chitosan nanoparticles have been successfully used to incorporate the peptide RGD, with potential antitumoral applications[9].

Cholanic acid interaction with proteins has been further investigated by the Salmaso and Caliceti group, for reversible non-covalent protein PEGylation. Accordingly, cholanic acid-terminated PEGs with different Mn (5, 10, and 20 kDa) were synthesised and tested on two proteins, recombinant human growth hormone (rh-GH) and recombinant human granulocyte colony stimulating factor (rh-G-CSF). Both proteins were found to form nano-complexes with all cholanic-PEGs. The corresponding formulations were tested on rats, where

pharmacokinetic studies highlighted how the complex was able to ensure a slow release of the proteins from the site of injection. The maximal concentration was lower compared to the uncomplexed proteins, but the half-life was significantly longer, with prolonged effects of the two hormones on rat growth [10, 11].

PEG-cholanes were subsequently tested on amphotericin B, as relatively low molecular weight poorly soluble model drug. PEG-cholanes were able to efficiently self-assemble in 30 nm micelles incorporating amphotericin B, increasing its solubility by over three orders of magnitude[12].

In this part of our work, a family of cholanic- and cholesterol-terminating polyacrylamides was developed as potential macromolecular tools for non-covalent protein conjugation. Here, we aimed at extending the initial work in the literature which utilised only commercially available PEGs to a range of different synthetic polymers. To this aim, a new family of six conjugating polymers were synthesised by RAFT polymerisation, using *N*-hydroxyethylacrylamide as a model hydrophilic monomer, and cholanic acid and cholesterol-containing RAFT agents.

The polymers ability to associate with proteins was investigated using Bovine Serum Albumin and Bovine Pancreatic Insulin as model proteins. The interaction was evaluated by Size Exclusion Chromatography, Isothermal Titration Calorimetry, Circular Dichroism, solubility studies and gel electrophoresis.

## 5.2. Materials and Methods

### 5.2.1. Materials

Isopropanol, methanol, dichloromethane (DCM), ethyl acetate, diethyl ether, chloroform, tetrahydrofuran, petroleum ether, *N,N*-dimethylformamide (DMF) and acetone were purchased from Fisher Scientific (Bishop Meadow Rd, Loughborough, UK). Bovine Serum Albumin (BSA) (≥99%), Bovine pancreatic Insulin, DPBS buffer, DIPEA (≥99%), 5β-cholanic acid (99%), TEA (≥99%), VA-501 (≥98%), DMTMM (96%), ethylene-dioxy-bis-ethylamine (98%) and di-*tert*-butyl dicarbonate were obtained from Sigma-Aldrich (St. Louis, Missouri, United States).

### 5.2.2. Synthesis of CTA agent (20)
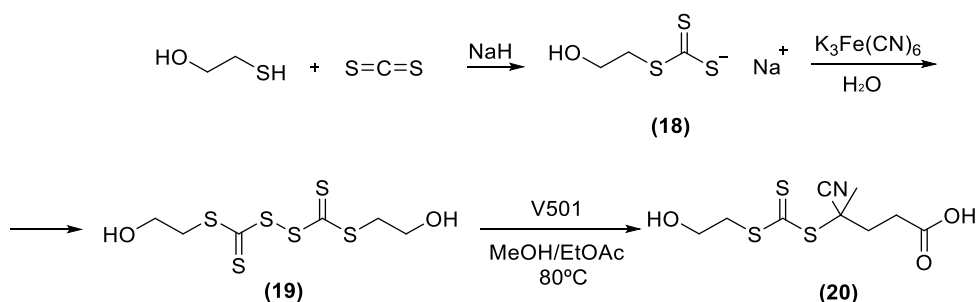


Scheme 5.1: synthesis of CTA **(20)**.

**Sodium 2-hydroxyethyl carbonotrithioate (18).** NaH (60 wt % in mineral oil, 2.82 g, 70.4 mmol, 1.1 eq.) was dispersed in 50 mL of diethyl ether and cooled to 5°C in an ice bath. Mercaptoethanol (4.5 mL, 64 mmol, 1 eq.) was added dropwise under stirring to the organic suspension and the mixture was stirred for 10 minutes, then CS$_2$ (5.8 mL, 96 mmol, 1.5 eq.) was added dropwise to the suspension and the reaction was stirred at room temperature for 1 h. The

resulting suspension was filtered, and the precipitate washed with diethyl ether. After filtration and removal of the solvent under reduced pressure, trithiocarbonate salt **(18)** was isolated as a yellow solid. Yield: 91%.

$^{1}$H NMR (400 MHz, d$_6$-DMSO, δ, ppm): 3.67 (t, *J*=7.2 Hz, 2H, HOC*H$_2$*CH$_2$S), 3.49 (t, *J*=7.2 Hz, 2H, HOCH$_2$C*H$_2$*S) (Fig. S5.1).

$^{13}$C NMR (101 MHz, d$_6$-DMSO, δ, ppm): 230.71 (CS$_3$), 59.37 (HO*C*H$_2$CH$_2$S), 44.10 (HOCH$_2$*C*H$_2$S) (Fig. S5.2).

FT-IR: 3312 cm$^{-1}$ (υ$_{O-H}$).

**Dithiobis-2-hydroxyethyl carbonotrithioate disulfide (19).** Sodium 2-hydroxyethyl carbonotrithioate **(18)** (7.0 g, 0.045 mol, 1 eq.) was dissolved in a solution of K$_3$Fe (CN)$_6$ (16 g, 0.048 mol, 1.1 eq.) in 100 mL of water. The resulting orange precipitate was extracted from the aqueous layer with diethyl ether (4 X 500 mL). The organic fractions were combined and dried with MgSO$_4$. After filtration, the solvent was removed under reduced pressure, affording dithiobis-2-hydroxyethyl carbonotrithioate disulfide **(12)** as an orange oily residue which was utilised for the following step without further purification.

Yield: 86%.

$^{1}$H NMR (400 MHz, d$_6$-DMSO, δ, ppm): 3.67 (t, *J*=6.1 Hz, 2H, HOC*H$_2$*CH$_2$S), 3.49 (t, *J*=6.1 Hz, 2H, HOCH$_2$C*H$_2$*S) (Fig. S5.3).

$^{13}$C NMR (101 MHz, d$_6$-DMSO, δ, ppm): 221.39 (C=S), 57.83 (HO*C*H$_2$CH$_2$S), 41.00 (HOCH$_2$*C*H$_2$S) (Fig. S5.4).

FT-IR: 3306.3 cm$^{-1}$ (υ$_{O-H}$).

ESI-TOF mass spectrometry: expected m/z [ [M+Na]$^+$ 328.9, found 328.9 [M+Na]$^+$.

**2-hydroxyethyl carbonotrithioate cyanovaleric acid (20).** Dithiobis-2-hydroxyethyl carbonotrithioate disulfide **(19)** (4 g, 0.01 mol, 1 eq.) and V501 (5.4 g, 19 mmol, 1.4 eq.) were dissolved in ethyl acetate and methanol (40 mL each). The resulting solution was degassed for 30 min by argon bubbling, under stirring, then heated to reflux for 17 h. Organic solvent was then removed under reduced pressure and the resulting yellow oily residue was purified by silica gel flash chromatography, using Pet. Ether/Et$_2$O 4:6 v/v as the eluent, affording **(20)** as a yellow solid Yield:55%.

$^1$H NMR (400 MHz, CDCl$_3$, δ, ppm): 4.11 (t, *J*=6.0 Hz, 2H, HOC*H$_2$*CH$_2$S), 3.89 (t, *J*=5.9 Hz, 2H, HOCH$_2$C*H$_2$*S), 2.67 (m, 2H, CH$_2$C*H$_2$*COOH), 2.42-2.54 (m, C*H$_2$*CH$_2$COOH), 1.89 (s, CH$_3$) (Fig. S5.5).

$^{13}$C NMR (101 MHz, d$_6$-DMSO, δ, ppm): 218.01 (C=S), 172.22 (C=O), 118.91 (CN), 57.91(HOC*H$_2$*CH$_2$S), 46.63(HOCH$_2$C*H$_2$*S), 32.90 (CH$_2$*C*H$_2$COOH), 28.95 (C*H$_2$*CH$_2$COOH), 23.55 (CH$_3$) (Fig. S5.6).

FT-IR: 3186 cm$^{-1}$ (υ$_{O-H}$), 2115 cm$^{-1}$ (υ$_{CN}$), 1691 cm$^{-1}$ (υ$_{C=O}$).

ESI-TOF mass spectrometry: expected m/z [M+H]$^+$ 280.01, found 280.01.

## 5.2.3. Synthesis of Boc-amine (21)
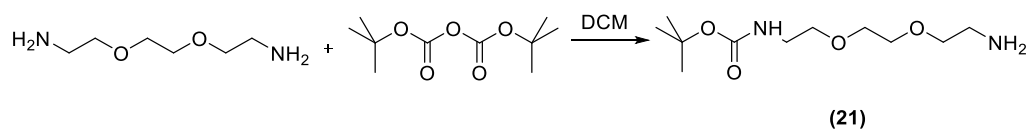


Scheme 5.2: synthesis of Boc-amine **(21)**.

A solution of 2,2-(ethylenedioxy)bis(ethylamine) (23.4 mL, 160 mmol, 1 eq.) in DCM (400 mL) was added to $Boc_2O$ (5.2 g, 24 mmol, 0.15 eq.) at 0 °C, and the resulting mixture stirred at this temperature for 5 h and then left stirring for 18 h at room temperature. The organic phase was washed twice with water (100 mL), dried over $MgSO_4$, filtered, and the solvent removed under reduced pressure to give the Boc-amine **(21)** as a colourless oil. Yield: 67%.

$^1$H NMR (400 MHz, $d_6$-DMSO, δ, ppm): 3.48-3.34 (m, 8H, $CH_2CH_2O$), 3.05 (q, $J$=6.0 Hz, 2H, NHC$H_2$), 2.63 (t, $J$=5.8 Hz, 2H, C$H_2$NH$_2$), 1.37 (s, 9H, $CH_3$) (Fig. S5.7).

$^{13}$C NMR (101 MHz, $d_6$-DMSO, δ, ppm): 155.84 (CONH), 77.98 ($(CH_3)_3$C-O), 73.53 ($CH_2CH_2NH_2$), 69.87 ($CH_2CH_2O$), 41.66 ($CH_2CH_2NH_2$), 28.64 ($CH_3$) (Fig. S5.8).

FT-IR: 3375 cm$^{-1}$ ($\upsilon_{N-H2}$), 2867 cm$^{-1}$), 1701 cm$^{-1}$ ($\upsilon_{C=O}$), 1104 cm$^{-1}$ ($\upsilon_{CH2OCH2}$).

ESI-TOF mass spectrometry: expected m/z [M+H]$^+$ 249.17, found 249.18.

### 5.2.4. Synthesis of Cholanic-amine (22)
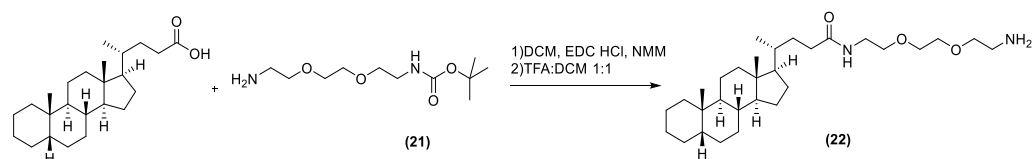


Scheme 5.3: synthesis of cholanic-amine **(22)**.

To a stirred solution of cholanic acid (500 mg, 1.39 mmol, 1 eq.), Boc-amine **(21)** (379 mg, 1.53 mmol, 1.1 eq.) and *N*-methylmorpholine (383 µL, 3.48 mmol, 2.5 eq.) in dry DCM (20 mL) under nitrogen was added N-(3-dimethylaminopropyl)-N'-ethylcarbodiimide hydrochloride (EDC-HCl, 274 mg, 1.43 mmol, 1.03 eq.). The reaction mixture was stirred at room temperature overnight and then diluted with DCM (30 mL), washed twice with 2M HCl (50 mL) and once with brine (50 mL). The mixture was finally dried with $MgSO_4$, filtered, and the volatiles evaporated under reduced pressure.

The product was re-dissolved in a 1:1 v/v mixture of TFA and DCM (20 mL) at room temperature and the resulting solution stirred for 16 h. The volatiles were removed under reduced pressure, and the resulting residue purified by flash chromatography using Pet.Et/EtoAc 2:8 v/v as the eluent.

$^1$H NMR (400 MHz, d$_6$-DMSO, δ, ppm): 3.54-3.38 (m, 8H, $CH_2OCH_2CH_2OCH_2$), 3.17 (q, *J*=6.1 Hz, 2H, C$H_2$NH), 2.97 (m, 2H, $NH_2$C$H_2$), 0.87 (s, 6H, $CH_3$), 0.6 (s, 3H, $CH_3$) (Fig. S5.9).

$^{13}$C NMR (101 MHz, d$_6$-DMSO, δ, ppm): 173.17 (CONH), 42.74 ($CH_2NH_2$), 20.90 ($CH_3$), 18.78 ($CH_3$), 12.36 ($CH_3$) (Fig. S5.10).

FT-IR: 3280.9 cm$^{-1}$ ($\upsilon_{N-H2}$), 1675.4 cm$^{-1}$ ($\upsilon_{C=O}$), 1125.4 cm$^{-1}$ ($\upsilon_{CH2OCH2}$).

ESI-TOF mass spectrometry: expected m/z [M+H]$^+$ 491.41, found 491.42.

## 5.2.5. Synthesis of RAFT agent (23)
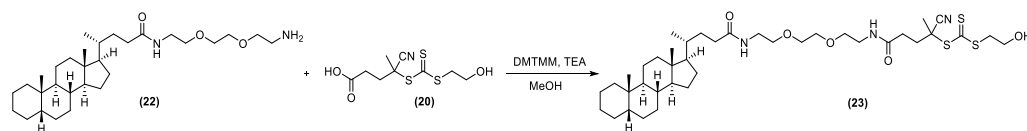


Scheme 5.4: synthesis of RAFT agent **(23).**

CTA **(20)** (271 mg, 0.972 mmol, 1.2 eq.) was dissolved in methanol (50 mL), followed by DMTMM (448 mg, 1.62 mmol, 2 eq.). A solution of triethylamine (169 µL, 1.21 mmol, 1.5 eq.) in methanol (10 mL) was then added dropwise at 0˚C under stirring. The reaction was left under stirring for 24 h at room temperature and monitored by TLC. The solvent was then removed under reduced pressure and the residue purified by silica gel flash chromatography, using EtOAc/MeOH 9/1 v:v as the eluent. Yield: 30%.

$^1$H NMR (400 MHz, d$_6$-DMSO, δ, ppm): 6.32 (t, *J*=6.3 Hz, 1H, NH), 5.94 (t, *J*=6.0 Hz, 1H, NH), 3.93 (t, *J*=5.9 Hz, 2H, OH*CH$_2$*CH$_2$S), 3.63-3.57 (m, 6H, OCH$_2$CH$_2$O and OHCH$_2$C*H$_2$*S), 3.48 (m, 4H, NHC*H$_2$* and C*H$_2$*NH), 2.51 (m, 4H, CH$_2$CH$_2$CO), 0.93 (s, 6H, CH$_3$), 0.69 (s, 3H, CH$_3$) (Fig.5.3).

$^{13}$C NMR (101 MHz, d$_6$-DMSO, δ, ppm): 217.26 (C=S), 174.17 (CONH), 170.51 (NHCO) 119.18 (CN), 20.85 (CH$_3$), 18.44 (CH$_3$), 12.11 (CH$_3$) (Fig. S5.11).

FT-IR: 3285.9 cm$^{-1}$ ($\upsilon_{N-H2}$), 1646.7cm$^{-1}$ ($\upsilon_{C=O}$), 1063.1 cm$^{-1}$ ($\upsilon_{CH2OCH2}$).

ESI-TOF mass spectrometry: expected m/z $[M+H]^+$ 752.42 and $[M+Na]^+$ 774.40,

found 752.42 and 774.40.

## 5.2.6. Cholanic- and cholesterol-polyacrylamides: typical polymerisation conditions
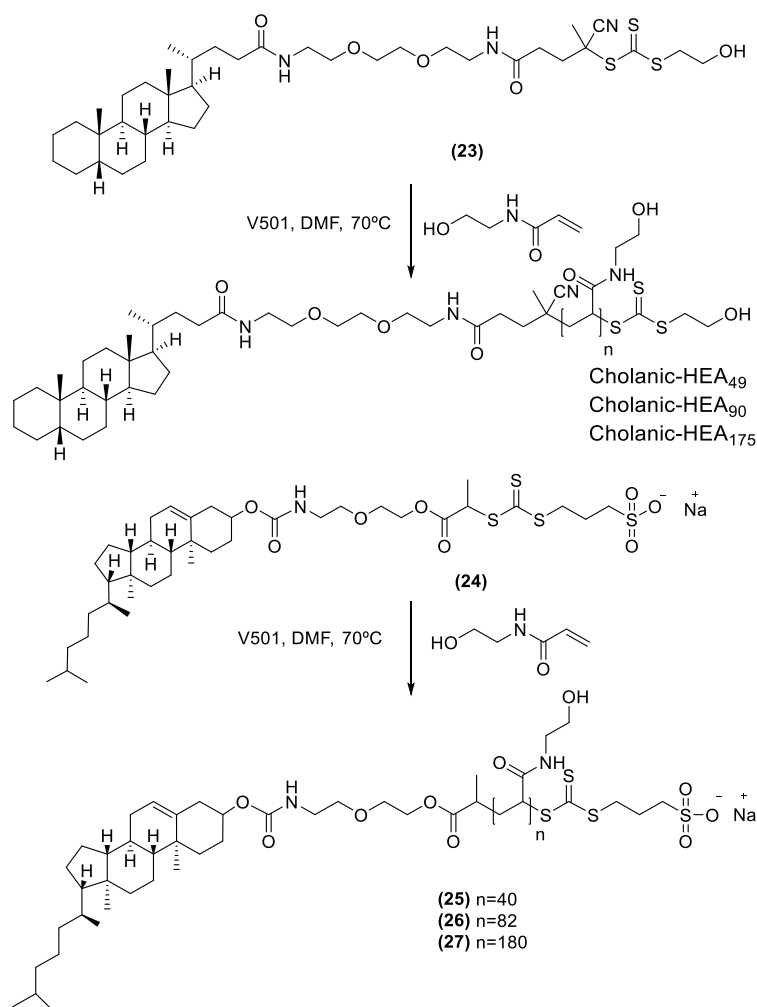


Scheme 5.5: synthesis of Cholanic-HEA$_{49}$, Cholanic-HEA$_{90}$, Cholanic-HEA$_{175}$ and Cholesterol-HEAs **(25)**, **(26)** and **(27)**.

Typical procedure for RAFT polymerisation of HEA: RAFT agent **(23)** (1

equivalent, 75 mg, 0.10 mmol, for cholanic-HEA$_{49}$, 50 mg, 0.066 mmol, for

cholanic-HEA$_{90}$ and cholanic-HEA$_{179}$), RAFT agent **(24)** (1 equivalent, 150 mg,

0.146 mmol, for cholesterol-HEA **(25)**, 0.10g, 0.096 mmol, for cholesterol-HEA

**(26)** and 50 mg, 0.048 mmol for cholesterol-HEA **(27)**) were dissolved in DMF

together with the monomer *N*-hydroxyethylacrylamide (575 mg, 5.00 mmol, 50 eq., for cholanic-HEA$_{49}$, 760 mg, 6.6 mmol, 100 eq., for cholanic HEA$_{90}$, 1520 mg, 13.2 mmol, 200 eq. for cholanic-HEA$_{175}$, 840 mg, 7.3 mmol, 50 eq., for cholesterol-HEA **(25)**, 1100 mg, 9.6 mmol, 100 eq., for cholesterol-HEA **(26)**, 1100 mg, 9.6 mmol, 200 eq., for cholesterol-HEA **(27)**) to reach a final 3.0 M monomer concentration. The mixtures were transferred into small schlenk tubes equipped with a magnetic stirrer, which were put in ice. Initiator V 501 (0.1 eq.), previously dissolved in DMF was added to each tube. The mixtures were degassed under Argon in ice for 30 min, and finally put on a paraffin oil bath at 70 ˚C. The reactions were monitored by $^1$H NMR, checking the disappearance of acrylamide monomer peaks into the 5-6.5 ppm region, until ca. 80% conversion was reached.

See Table below for reaction times and conversions.

Table 5. 1: Reaction times and conversions of cholanic- and cholesterol-polymers.

| POLYMER | REACTION TIME (h) | CONVERSION (%) |
|---|---|---|
| cholanic-HEA$_{49}$ | 3 | 86 |
| cholanic-HEA$_{90}$ | 1 | 69 |
| cholanic-HEA$_{179}$ | 2 | 77 |
| cholesterol-HEA **(25)** | 3 | 76 |
| cholesterol-HEA **(26)** | 1.5 | 54 |
| cholesterol-HEA **(27)** | 3 | 80 |

The polymers were then precipitated in THF, re-dissolved in water, dialysed against water for 48 h and finally freeze-dried. Polymers were analysed by $^1$H NMR and SEC in DMF with 0.1% LiBr. $M_{n,NMR}$ was determined by comparing the integrals of cholanic/cholesterol methyl groups at 0.6 and 0.9 ppm, to those of NH and OH groups of the pHEA at 7.5-7.8 and 4.6-5.2 ppm, respectively.

Cholanic-HEA$_{49}$ Yield: 77%. $^1$H NMR (400 MHz, d$_6$-DMSO, δ, ppm): 7.80-7.40 (m, 49H, polyacrylamide NH), 5.10-4.80 (m, 49H, polyacrylamide OH), 2.10-1.70 (m, 49H, polyacrylamide C*H*CH$_2$) 1.60-1.20 (m, 98H, polyacrylamide CHC*H$_2$*), 0.91 (s, 6H, CH$_3$), 0.62 (s, 3H, CH$_3$) (Fig. 5.4). M$_{n,NMR:}$ 6.4 kDa. M$_{n,SEC(DMF)}$ 8.0 kDa, Đ=1.13.

Cholanic-HEA$_{90}$ Yield: 64%. $^1$H NMR (400 MHz, d$_6$-DMSO, δ, ppm): 7.80-7.40 (m, 90H, polyacrylamide NH), 5.10-4.80 (m, 90H, polyacrylamide OH), 2.10-1.70 (m, 90H, polyacrylamide C*H*CH$_2$) 1.60-1.20 (m, 180H, polyacrylamide CHC*H$_2$*), 0.91 (s, 6H, CH$_3$), 0.62 (s, 3H, CH$_3$) (Fig. S5.12). M$_{n,NMR:}$ 11.9 kDa. M$_{n,SEC(DMF)}$ 12 kDa, Đ=1.09.

Cholanic-HEA$_{175}$ Yield: 81%. $^1$H NMR (400 MHz, d$_6$-DMSO, δ, ppm): 7.80-7.40 (m, 175H, polyacrylamide NH), 5.10-4.80 (m, 175H, polyacrylamide OH), 2.10-1.70 (m, 175H, polyacrylamide C*H*CH$_2$) 1.60-1.20 (m, 350H, polyacrylamide CHC*H$_2$*), 0.91 (s, 6H, CH$_3$), 0.62 (s, 3H, CH$_3$) (Fig. S5.13). M$_{n,NMR:}$ 21.4 kDa. M$_{n,SEC(DMF)}$ 16.4 kDa, Đ=1.14.

SEC traces are displayed in Fig. S5.26.

Cholesterol-HEA **(25)** Yield: 75%. $^1$H NMR (400 MHz, d$_6$-DMSO, δ, ppm): 7.80-7.40 (m, 40H, polyacrylamide NH), 2.10-1.70 (m, 40H, polyacrylamide C*H*CH$_2$) 1.60-1.20 (m, 80H, polyacrylamide CHC*H$_2$*), 0.62 (s, 3H, CH$_3$). M$_{n,NMR:}$ 5.8 kDa. M$_{n,SEC(DMF)}$ 7.5 kDa, Đ=1.12.

Cholesterol-HEA **(26)** Yield: 80%. $^1$H NMR (400 MHz, d$_6$-DMSO, δ, ppm): 7.80-7.40 (m, 82H, polyacrylamide NH), 2.10-1.70 (m, 82H, polyacrylamide C*H*CH$_2$)

1.60-1.20 (m, 164H, polyacrylamide CHC$H_2$), 0.62 (s, 3H, CH₃). $M_{n,NMR}$: 10.4 kDa.

$M_{n,SEC(DMF)}$ 10.9 kDa, Đ=1.16.

Cholesterol-HEA **(27)** Yield: 86%. $^1$H NMR (400 MHz, d₆-DMSO, δ, ppm): 7.80-

7.40 (m, 180H, polyacrylamide NH), 2.10-1.70 (m, 180H, polyacrylamide C$H$CH₂)

1.60-1.20 (m, 360H, polyacrylamide CHC$H_2$), 0.62 (s, 3H, CH₃). $M_{n,NMR}$: 21.9 kDa.

$M_{n,SEC(DMF)}$ 18.5 kDa, Đ=1.28.

## 5.2.7. RAFT removal from Cholesterol-pHEAs: synthesis of final cholesterol-HEAs
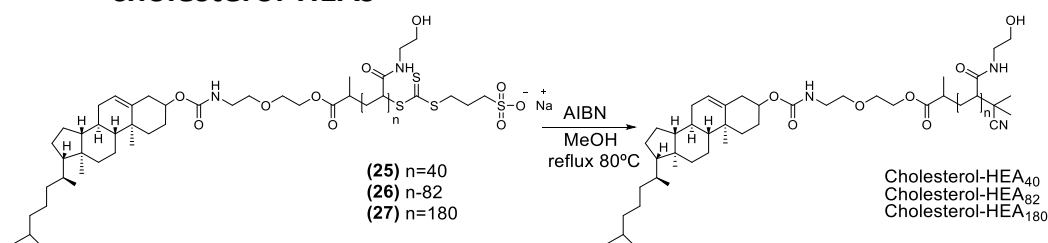


Scheme 5.6: synthesis of Cholesterol-HEA₄₀, Cholesterol-HEA₈₂ and Cholesterol-HEA₁₈₀.

The polymers (Cholesterol-HEA **(25)** 500 mg, 0.086 mmol, Cholesterol-HEA **(26)**

700 mg, 0.067 mmol, Cholesterol-HEA **(27)** 700 mg, 0.03 mmol) were dissolved

in methanol (5 mL), 80 equivalents of initiator AIBN (1128 mg, 6.88 mmol, for

Cholesterol-HEA₄₀, 879 mg, 5.36 mmol, for Cholesterol-HEA₈₂ and 393.6 mg,

2.40 mmol, for Cholesterol-HEA₁₈₀) were added to the polymers solutions. The

mixtures were degassed in ice for 30 min, and then put on an oil bath at 80 ˚C

under reflux overnight. The polymers were then dissolved in methanol and

reprecipitated in THF 3 times, and finally dissolved in water and freeze-dried.

Efficiency of removal of the trithiocarbonate RAFT chain-end from the polymers

was estimated by UV spectrophotometry on final isolated polymers, measuring

the decrease of the band at λ$_{max}$=310 nm, which is characteristic of the

trithiocarbonate group (Fig S5.30). Polymers were analysed by SEC in DMF with 0.1% LiBr. $M_{n,NMR}$ was determined by comparing the integrals of cholesterol methyl groups at 0.6 and 0.9 ppm, to those of NH and OH groups of the pHEA at 7.5-7.8 and 4.6-5.2 ppm, respectively.

Cholesterol-HEA$_{40}$ Yield: 77%. $^1$H NMR (400 MHz, d$_6$-DMSO, δ, ppm): 7.80-7.40 (m, 40H, polyacrylamide NH), 5.10-4.80 (m, 40H, polyacrylamide OH), 2.10-1.70 (m, 80H, polyacrylamide C*H*CH$_2$) 1.60-1.20 (m, 80H, polyacrylamide CHC*H$_2$*), 0.62 (s, 3H, CH$_3$) (Fig. S5.14). $M_{n,NMR}$: 5.8 kDa. $M_{n,SEC(DMF)}$ 7.5 kDa, Đ=1.13.

Cholesterol-HEA$_{82}$ Yield: 89%. $^1$H NMR (400 MHz, d$_6$-DMSO, δ, ppm): 7.80-7.40 (m, 82H, polyacrylamide NH), 5.10-4.80 (m, 82H, polyacrylamide OH), 2.10-1.70 (m, 82H, polyacrylamide C*H*CH$_2$) 1.60-1.20 (m, 164H, polyacrylamide CHC*H$_2$*), 0.62 (s, 3H, CH$_3$) (Fig. S5.15). $M_{n,NMR}$: 10.4 kDa. $M_{n,SEC(DMF)}$ 11.0 kDa, Đ=1.15.

Cholesterol-HEA$_{180}$ Yield: 87%. $^1$H NMR (400 MHz, d$_6$-DMSO, δ, ppm): 7.80-7.40 (m, 180H, polyacrylamide NH), 5.10-4.80 (m, 180H, polyacrylamide OH), 2.10-1.70 (m, 180H, polyacrylamide C*H*CH$_2$) 1.60-1.20 (m, 360H, polyacrylamide CHC*H$_2$*), 0.62 (s, 3H, CH$_3$) (Fig. S5.16). $M_{n,NMR}$: 21.9 kDa. $M_{n,SEC(DMF)}$ 16.9 kDa, Đ=1.34.

SEC traces are displayed in Fig.S5.27.

### 5.2.8. Synthesis of control polymers HEA$_{42}$, HEA$_{105}$ and HEA$_{166}$
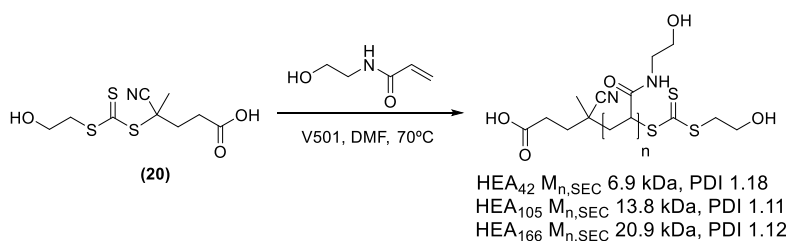


Scheme 5.7: Synthesis of control polymers HEA$_{42}$, HEA$_{105}$ and HEA$_{166}$.

CTA agent **(20)** (150 mg, 0.53 mmol, 1 eq.) was dissolved in DMF together with the monomer *N*-hydroxyethylacrylamide (3100 mg, 27.1 mmol, 50 eq., for HEA$_{42}$, 6200 mg, 54.2 mmol, 100 eq., for HEA$_{105}$ and 12400 mg, 108.4 mmol, 200 eq., for HEA$_{166}$) for final 3.0 M monomer concentration, and the mixtures transferred into glass tubes equipped with a magnetic stirrer, which were put in ice. Initiator V 501 (0.1 eq.), previously dissolved in DMF (100 µL), was added to each tube. The mixtures were degassed under Argon in ice for 30 min, and finally put on a paraffin oil bath at 70 ˚C. The reactions were monitored by $^1$H NMR, checking the disappearance of acrylamide monomer peaks into the 5-6.5 ppm region, until ~ 80% conversion was reached.

See Table below for reaction times and conversions.

Table 5. 2: Reaction times and conversions of cholanic- and cholesterol-polymers.

| POLYMER | REACTION TIME (h) | CONVERSION (%) |
|---------|-------------------|----------------|
| HEA$_{42}$ | 2 | 59 |
| HEA$_{105}$ | 1.5 | 90 |
| HEA$_{166}$ | 1.5 | 89 |

The polymers were then precipitated in THF, re-dissolved in water, dialysed against water for 48 h and finally freeze-dried. Polymers were analysed by $^1$H NMR and SEC in DMF with 0.1% LiBr.

HEA$_{42}$ Yield: 86%. $^1$H NMR (400 MHz, d$_6$-DMSO, δ, ppm): 7.80-7.40 (m, 42H, polyacrylamide N*H*), 5.10-4.80 (m, 42H, polyacrylamide O*H*), 2.10-1.70 (m, 42H, polyacrylamide C*H*CH$_2$) 1.60-1.20 (m, 84H, polyacrylamide CHC*H$_2$*) (Fig. S5.17). M$_{n,SEC}$ 7.5 kDa, Đ=1.08.

HEA$_{105}$ Yield: 74%. $^1$H NMR (400 MHz, d$_6$-DMSO, δ, ppm): 7.80-7.40 (m, 105H, polyacrylamide N*H*), 5.10-4.80 (m, 105H, polyacrylamide O*H*), 2.10-1.70 (m, 105H, polyacrylamide C*H*CH$_2$) 1.60-1.20 (m, 210H, polyacrylamide CHC*H$_2$*) (Fig. S5.23). M$_{n,SEC}$ 14.0 kDa, Đ=1.10.

HEA$_{166}$ Yield: 83%. $^1$H NMR (400 MHz, d$_6$-DMSO, δ, ppm): 7.80-7.40 (m, 166H, polyacrylamide N*H*), 5.10-4.80 (m, 166H polyacrylamide O*H*), 2.10-1.70 (m, 166H, polyacrylamide C*H*CH$_2$) 1.60-1.20 (m, 332H, polyacrylamide CHC*H$_2$*) (Fig. S5.24). M$_{n,SEC}$ 19.0 kDa, Đ=1.17.

SEC traces are reported in Fig.S5.29.

### 5.2.9. Synthesis of 8-O-Carboxymethylpyranine (CM-Pyranine) (28)
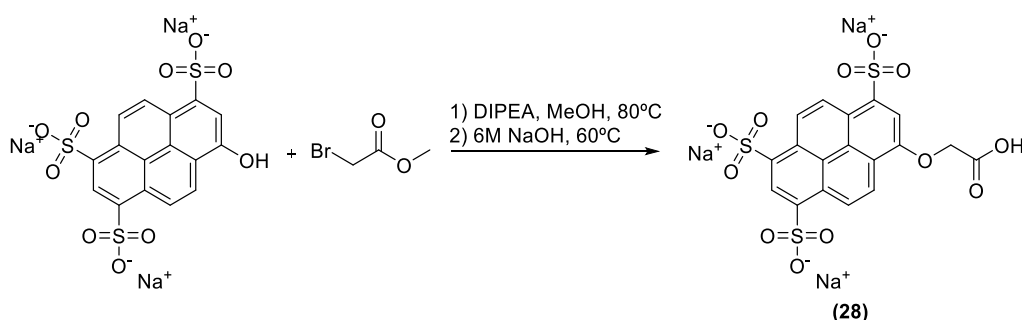


Scheme 5.8: Synthesis of 8-O-Carboxymethylpyranine (CM-Pyranine) **(28)**.

To a refluxing solution of pyranine (1 g, 1.91 mmol, 1 eq.) in MeOH (60 mL), methylbromoacetate (1.1 g, 7.24 mmol, 3.8 eq.) and DIPEA (0.69 g, 5.32 mmol, 2.8 eq.) dissolved in MeOH (8 mL) were added in aliquots of 2 mL over 5 h. The reaction was monitored by $^1$H NMR and finally left to cool down to room temperature. The solution was concentrated under vacuum and diluted in isopropanol. The methyl ester intermediate was collected by filtration, re-dissolved in 20 mL of 6 M aqueous sodium hydroxide, and left stirring at 60°C for 2 h. The solution was then cooled to room temperature and acidified to pH 7 with HCl 2M. The product **(28)** was finally precipitated in isopropanol and recovered by centrifugation. Final yield: 63%.

$^1$H NMR (400 MHz, D$_2$O, δ, ppm): 9.3-8.9 (m, 5H, CH aromatic), 8.26 (s, 1H, CH aromatic), 5.06 (s, 2H, C*H$_2$*COOH) (Fig. S5.18).

FT-IR: 3448.4 cm$^{-1}$ ($\upsilon_{O-H}$), 1176.4 cm$^{-1}$ ($\upsilon_{C-O}$).

ESI-TOF mass spectrometry: expected m/z [M$^-$. 580.89, found 580.89.

## 5.2.10. Synthesis of Cascade Blue-amine (29)
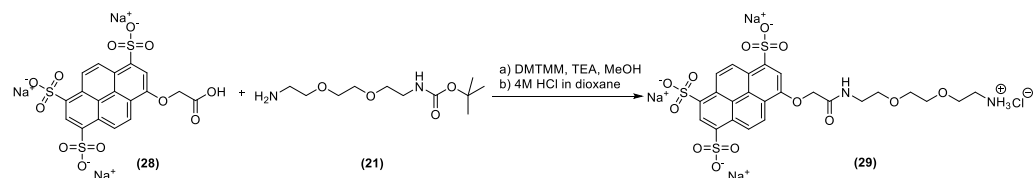


Scheme 5.9: synthesis of Cascade Blue amine **(29)**.

To a stirred suspension of **(28)** (500 mg, 0.86 mmol, 1 eq.), Boc-amine **(21)** (256 mg, 1.032 mmol, 1.2 eq.) and triethylamine (299 µL, 2.15 mmol, 2.5 eq.) in

methanol (40 mL) was added DMTMM (476 mg, 1.72 mmol, 2 eq.). The reaction mixture, which turned into a solution, was stirred at room temperature overnight. The volume was then reduced under pressure, and the intermediate precipitated in isopropanol.

The intermediate was re-dissolved in a 4M HCl solution in dioxane (10 mL) at room temperature, and the resulting mixture was stirred for 6 h. The volatiles were removed under reduced pressure, and the resulting residue used directly for the next step without any further purification. Yield: 82%.

^{1}H NMR (400 MHz, d$_6$-DMSO, δ, ppm): 9.17 (d, *J*=9.6 Hz, 1H, CH aromatic), 9.1-8.9 (m, 3H, CH aromatic), 8.14 (s, 1H, CH aromatic), 4.90 (s, 2H, CH$_2$COO), 3.65-3.40 (m, 8H, CH$_2$OCH$_2$CH$_2$OCH$_2$), 3.40-3.30 (m, 2H, C*H*$_2$NH), 2.91 (t, *J*=5.3Hz, 2H, NH$_2$C*H*$_2$) (Fig. S5.9).

FT-IR: 3417.9 cm$^{-1}$ ($\upsilon_{O-H}$), 1171.3 cm$^{-1}$ ($\upsilon_{C-O}$).

ESI-TOF mass spectrometry: expected m/z [M-H]$^+$. 713.01, found 713.01.

### 5.2.11. Synthesis of Cascade Blue-acrylamide (30)
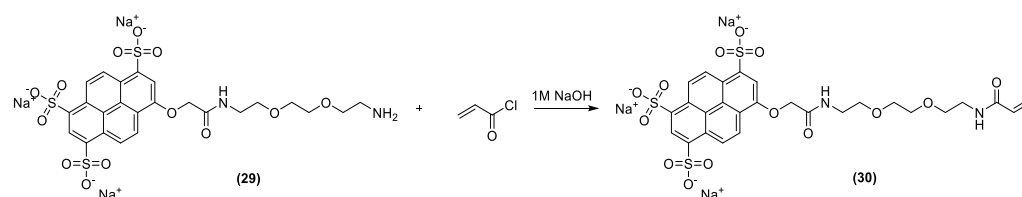


Scheme 5.10: synthesis of Cascade Blue-acrylamide **(30)**.

Product **(29)** (450 mg, 0.63 mmol, 1 eq.) was dissolved in 1M aqueous NaOH (30 mL). Acryloyl chloride (171.06 mg, 1.89 mmol, 3 eq.) was added dropwise at 0°C. After the addition the solution was left stirring at room temperature for

further 2h. The volume was then reduced under vacuum, and the product precipitated in isopropanol.

The crude product was finally purified by flash chromatography using DCM/MeOH 1:1 v/v as the eluent. Yield: 60%.

$^1$H NMR (400 MHz, d$_6$-DMSO, δ, ppm): 9.17 (d, $J$=9.6 Hz, 1H, CH aromatic), 9.1-8.9 (m, 3H, CH aromatic), 8.53 (d, $J$=9.6Hz, 1H, CH aromatic) 8.12 (s, 1H, CH aromatic), 6.26 (dd, $J$=17.1, 10.2Hz, 1H, $CH$=CH$_2$), 6.05 (dd, $J$=17.1, 2.2Hz, 1H, CH=C$H$H), 5.54 (dd, $J$=10.2, 2.2Hz, 1H, CH=CH$H$), 4.87 (s, 2H, CH$_2$COO), 3.70-3.40 (m, 8H, CH$_2$OCH$_2$CH$_2$OCH$_2$), 3.40-3.30 (m, 2H, C$H_2$NH) (Fig. S5.20).

## 5.2.12. Synthesis of CholanicFLUO-HEA$_{80}$
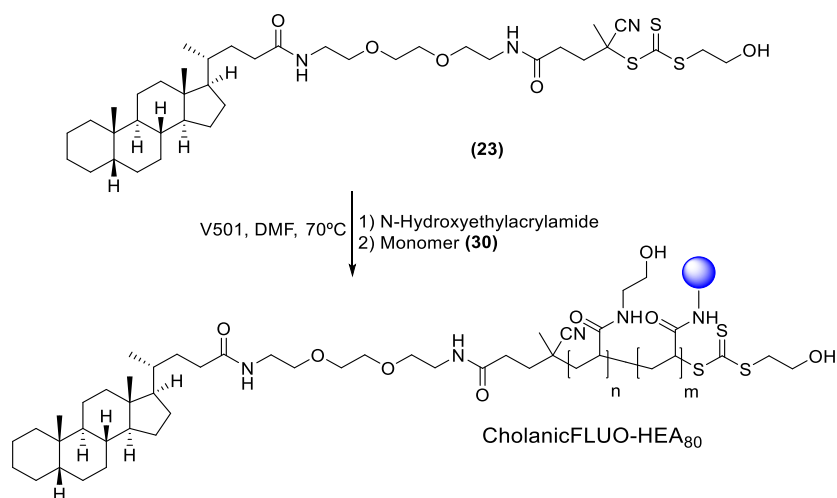


Scheme 5.11: synthesis of CholanicFLUO-HEA$_{65}$.

RAFT agent **(23)** (50 mg, 0.066 mmol, 1 eq.) was dissolved in DMF (1.5 mL) together with *N*-hydroxyethylacrylamide (760 mg, 6.6 mmol, 100 eq.) and the mixture transferred into a small schlenk tube equipped with a magnetic stirrer, which was put in ice. Initiator V 501 (1.8 mg, 0.0066 mmol, 0.1 eq.), previously dissolved in DMF, was added to the tube. The mixture was degassed for 30 min,

and finally put on a paraffin oil bath at 70 ˚C. The reaction was monitored by $^1$H NMR for 90 minutes, checking the disappearance of acrylamide monomer peaks into the 5-6.5 ppm region, until 60% conversion was reached. The polymerization was then stopped, and the monomer cascade blue acrylamide **(30)** (60 mg, 0.08 mmol, 1.2 eq.) previously dissolved in water (200 µL) was added to the solution in the tube. Again, Initiator V 501 (1.8 mg, 0.0066 mmol, 0.1 eq.), previously dissolved in DMF, was added to the tube. The mixture was degassed under Argon in ice for 30 min, and finally put on a paraffin oil bath at 70 ˚C. The reaction was monitored by $^1$H NMR for 3h until 80% conversion was reached.  The polymer was then precipitated in THF, re-dissolved in water, dialysed against water for 48 h and finally freeze dried. The polymer was analysed by $^1$H NMR and SEC in DMF with 0.1 % LiBr.

Yield: 64%. $^1$H NMR (400 MHz, d$_6$-DMSO, δ, ppm): 8.00-7.20 (m, 80H, polyacrylamide N*H*), 5.30-4.70 (m, 80H, polyacrylamide O*H*), 2.10-1.70 (m, 80H, polyacrylamide C*H*CH$_2$) 1.70-1.00 (m, 160H, polyacrylamide CHC*H$_2$*), 0.90 (s, 6H, C*H$_3$*), 0.61 (s, 3H, C*H$_3$*) (Fig. S5.21). M$_{n,NMR:}$ 10.0 kDa. M$_{n,SEC(DMF)}$ 10 kDa, Đ=1.20.

### 5.2.13. Synthesis of CholanicFLUO-HEA$_{80}$-*b*-MAN$_{20}$
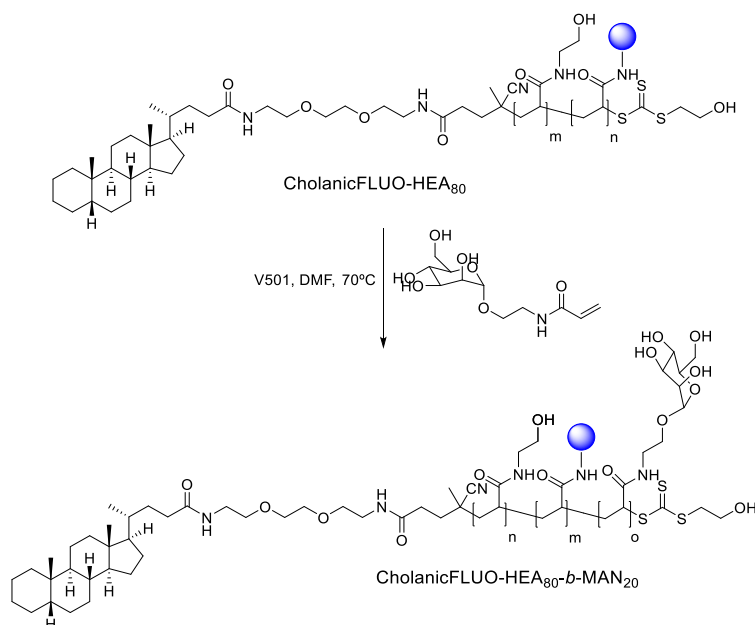


Scheme 5.12: synthesis of CholanicFLUO-HEA$_{65}$-b-MAN$_{15}$.

To a solution of CholanicFLUO-HEA$_{80}$ (1 eq., 150 mg, 0.018 mmol) in DMF (300 μL), a solution of mannose acrylamide (20 eq., 94 mg, 0.36mmol) in water (200 μL) was added. The mixture was transferred into small schlenk tube equipped with a magnetic stirrer, which was put in ice. Initiator V 501 (0.1 eq.), previously dissolved in DMF (100 μL), was added to the tube. The mixture was degassed for 30 min, and finally put on a paraffin oil bath at 70 ˚C. The reaction was monitored by $^1$H NMR, checking the disappearance of acrylamide monomer peaks into the 5-6.5 ppm region, until ~ 80% conversion was reached. The polymer was then precipitated in THF, dialysed against water for 48 h and finally freeze dried. The copolymer was analysed $^1$H NMR and SEC in DMF with 0.1 % LiBr.

Yield: 42%. $^1$H NMR (400 MHz, d$_6$-DMSO, δ, ppm): 8.00-7.20 (m, 100H, polyacrylamide and mannose acrylamide NH), 5.30-4.70 (m, 180H, polyacrylamide and mannose OH), 2.10-1.70 (m, 100H, polyacrylamide C*H*CH$_2$) 1.70-1.00 (m, 200H, polyacrylamide CHC*H$_2$*), 0.90 (s, 6H, CH$_3$), 0.61 (s, 3H, CH$_3$) (Fig. S5.22). M$_{n,NMR:}$ 16.0 kDa. M$_{n,SEC(DMF)}$ 10.6 kDa, Đ=1.23.

SEC traces are reported in Fig. S5.28.

## 5.2.14.     Binding of polymers to BSA: SEC studies

A BSA stock solution was first prepared by dissolving the protein in DPBS buffer at a concentration of 1.0 mg/mL (0.015 mM). Polymers stock solutions were prepared by dissolving various amounts of the polymers in PBS buffer. Different amounts of BSA and polymers stock solutions were mixed to have a final polymer/protein molar ratio of 5:1, 10:1, 20:1 and 40:1. After mixing, polymer/protein solutions were let under gentle stirring overnight at room temperature and then analysed by size exclusion chromatography (SEC) using a TSKgel® G3000SW$_{XL}$ column and DPBS buffer as the mobile phase, at a flow rate of 0.5 mL/min.

## 5.2.15.     Binding of Cholanic-HEA$_{49}$ to BSA: ITC studies

ITC analyses were performed by Valentina Andreetto, a postgraduate researcher at University of Padua. Isothermal titration calorimetry (ITC) was carried out using MSC-ITC equipment from Microcal Inc. (Northampton, MA). Every 5 min, 5 μL of 1.0 mM cholanic-HEA$_{49}$ were automatically injected into the reference calorimetric cell, containing 1.5 mL PBS 20 mM, 154 mM NaCl, pH 7.4. The same procedure was followed injecting Cholanic-HEA$_{49}$ into the

measurement cell, containing 1.5 mL of 0.664 mg/mL ($1.00*10^{-2}$ mM) BSA solution in the same buffer. The cells were maintained through stirring at 351 rpm, and the analyses were performed at 25 °C.

All measurements were replicated three times and data processing was performed with the Microcal Origin 3.5 software.

### 5.2.16. Binding of cholanic-HEA$_{49}$, cholanic-HEA$_{90}$, cholesterol-HEA$_{40}$ and cholesterol-HEA$_{82}$ to BSA: Circular Dichroism study

CD spectra were recorded on an Applied Photo-physics Chirascan circular dichroism spectropolarimeter using a 1 mm path length quartz cuvette. CD measurements were performed at 25°C over a range of 180-280 nm using a response time of 1 s, 1 nm pitch and 0.5 nm bandwidth. The recorded spectra represent a smoothed of the original scan. A BSA stock solution was first prepared by dissolving the protein in DPBS buffer at a concentration of 1.0 mg/mL (0.015 mM). Polymers-BSA mixtures were prepared in PBS as described above and with a final BSA concentration of 0.5 mg/mL and polymer:BSA molar ratios of 5:1 and 10:1.

### 5.2.17. Binding of Cholanic- and Cholesterol-HEAs to insulin: solubility studies

An insulin stock solution was prepared by dissolving the protein in 10 mM phosphate buffer pH 2 at a concentration of 4.0 mg/mL. Polymer stock solutions were prepared by dissolving various amounts of polymers in the same buffer. Different amounts of insulin and polymer stock solutions were mixed to have a final protein concentration of 2.0 mg/mL and polymer:protein molar

ratio of 5:1 and 10:1 in a final volume of 485 µL. After mixing, polymer/protein solutions were let under stirring for 2 h. The pH was then raised to 5.3 by adding 15 µL of NaOH 0.5 M solution to each of the polymers/protein mixtures. The precipitated insulin was left decanting overnight. After centrifugation, 200 µL of the supernatant were then withdrawn, diluted to 1 mL with water and finally analysed by analytical RP-HPLC, using a Zorbax Eclipse Plus C18 column (3.5 µm, 95 Å, 4.6 × 12.5 mm), with a linear gradient of 20-90% acetonitrile in Milli-q water with 0.1% TFA.

### 5.2.18. Binding of Cholanic- and Cholesterol-HEAs to insulin: NATIVE PAGE

Polymer-insulin mixtures were prepared as described above in 10 mM pH 2 phosphate buffer with final insulin concentration of 0.50 mg/mL and polymers:insulin molar ratios of 5:1, 10:1 and 20:1 in a final volume of 480 µL. After mixing, polymer/protein solutions were let under stirring for 2 h. The pH was then raised to 7.4 by adding around 20 µL of NaOH 0.50 M solution to each of the polymers/protein mixtures. Samples were then mixed with 500 µL of sample buffer solution, prepared mixing 1.55 ml of 2M pH 7.5 Tris-HCl buffer, 0.25 ml of a 1% solution of bromophenol blue, 0.70 ml of water and 0.25 ml of glycerol. 10 µL of this final solution were finally loaded onto a 10% acrylamide/bis-acrylamide gel. The gel was run with a 40 mM TRIS base, 20 mM acetic acid, pH 7.5 running buffer at 160 mV. The resulting gel was stained with Coomassie blue and visualised on an ultraviolet transilluminator.

### 5.2.19. Preparation and purification of mono-labelled TRITC-Insulin

Bovine pancreatic insulin (20 mg, 0.0035 mmol, 1 eq.) was dissolved in 0.1 M pH 8.5 sodium tetraborate buffer (2 mL). Tetramethylrhodamine (TRITC) Isothiocyanate (4.6 mg, 0.0105 mmol, 3 eq.) was dissolved in DMSO (200 µL) and the resulting solution added to the insulin solution, which was left stirring for 5 h, protected from light. TRITC-Insulin was then dialysed for 7 days against water (MWCO 3.5 kDa), again protected from light, and finally freeze dried. The recovered powder was re-dissolved in 10 mM pH 2 phosphate buffer, and purified by semi-preparative HPLC, using a Phenomenex Jupiter C18 column (10 µm, 300 Å, 10 × 250 mm), with a linear gradient of 30-60% acetonitrile in water. The purified mono-labelled TRITC insulin was characterised by ESI-MS and analytical HPLC, using a Phenomenex Jupiter C18 column (10 µm, 300 Å, 250 × 4.6 mm), with the same gradient used for semi-preparative purification.

RP HPLC: r.t 14 min. Purity:94%, measured by UV-VIS (Abs=280 nm).

ESI-TOF mass spectrometry: expected m/z [M-4H]$^{4+}$. 1030.5, [M-5H]$^{5+}$. 1236.4, [M-6H]$^{6+}$ 1545.3, found 1030.3, 1236.4 and 1545.3, respectively.

## 5.3. **Results and discussion**

Recent studies have been investigating the formation of supramolecular complexes between different proteins and PEG-cholane polymers.[10, 11]. The interaction has been proposed to involve hydrophobic interactions between the cholane moiety and hydrophobic pockets in proteins folded structure. The resulting nano-complexes were able to prolong the circulation half-life and increase the bioavailability of the complexed proteins.

In this study, we aimed at applying these initial findings to develop a synthetic and versatile route to a wider range of cholanic-incorporating polymeric materials for non-covalent protein complexation. Accordingly, a general synthetic route to cholanic-polymers was designed, through incorporation of cholanic acid into a RAFT agent which was used to mediate the polymerisation of a range of functional monomers. Structurally analogous cholesterol-terminated polymers were also synthesised to investigate the effect of the nature of the hydrophobic polycyclic polymer chain-end on protein complexation. Initially, *N*-Hydroxyethylacrylamide was used as a model hydrophilic monomer, and the chain length of the resulting polyacrylamides was systematically varied to investigate the influence of the polymer size on protein-polymer interactions.

### 5.3.1. Synthesis of Cholanic- RAFT agent (23).

Synthesis of CTA agent **(20)** was accomplished following the same procedure adopted for CTA agent **(10)** in Chapter 2 (Scheme 5.13). Mercaptoethanol was first treated with NaH and carbon disulfide, to give sodium 2-hydroxyethyl

carbonotrithioate salt **(18)**. This was then oxidised with $K_3Fe(CN)_6$, resulting in

dithiobis-2-hydroxyethyl carbonotrithioate disulfide **(19)**, which was treated

with V-501 radical initiator in refluxing ethyl acetate, affording the CTA agent

**(20).**

To assemble the second part of the cholanic-containing RAFT agent, a mono-

Boc-protected bis-amine was first prepared by reacting di-tert-butyl

dicarbonate with an excess of 2,2'-(ethylenedioxy)bis(ethylamine). The

resulting mono-amine intermediate **(21)** was coupled to cholanic acid, and Boc

removal with TFA afforded cholanic-amine **(22)**. Coupling of **(22)** with

previously prepared RAFT agent **(20)** mediated by DMTMM, a coupling agent

which allows selective amidation even in the presence of unprotected alcohols,

resulted in the final Cholanic-RAFT agent **(23)**.
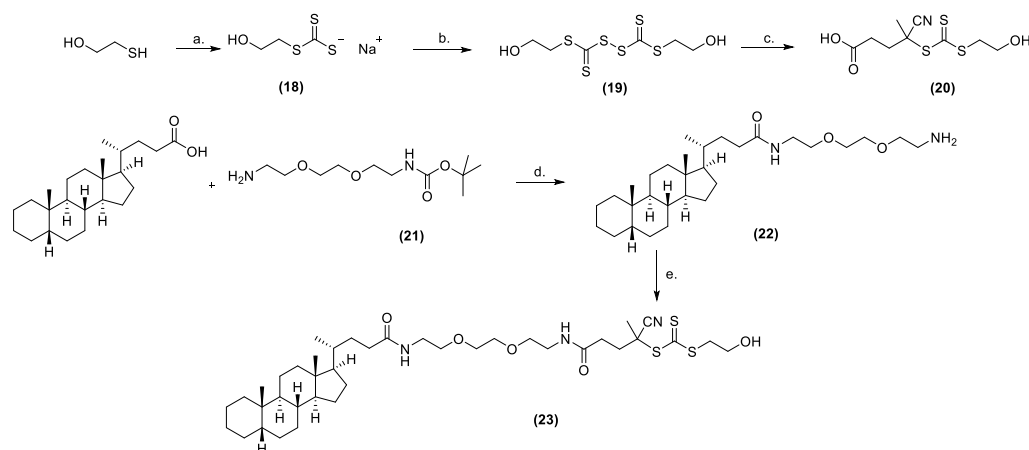


Scheme 5.13: Synthesis of Cholanic RAFT agent **(23)**. *Reagents and conditions*: (a) i. NaH, $Et_2O$, room temperature; ii. $CS_2$. (b) $K_3Fe(CN)_6$, $H_2O$, room temperature. (c) V501, MeOH, ethyl acetate, 80ºC. (d) i. NMN, DCI, DCM at room temperature; ii. TFA/DCM 1/1 v/v at room temperature (e) **(20)**, DMTMM, TEA, MeOH, room temperature.

^{1}H NMR of **(23)** is shown in Figure 5.3. The integration of cholanic methyl peaks

matched that of the other groups of the RAFT agent **(20)** fragment, and that of

the bis-amide backbone, thus confirming the successful synthesis and purification of CTA **(23)**. The cholesterol-RAFT agent **(24)** was kindly donated by Rosa Catania, a former PhD student now Research Fellow within our group.
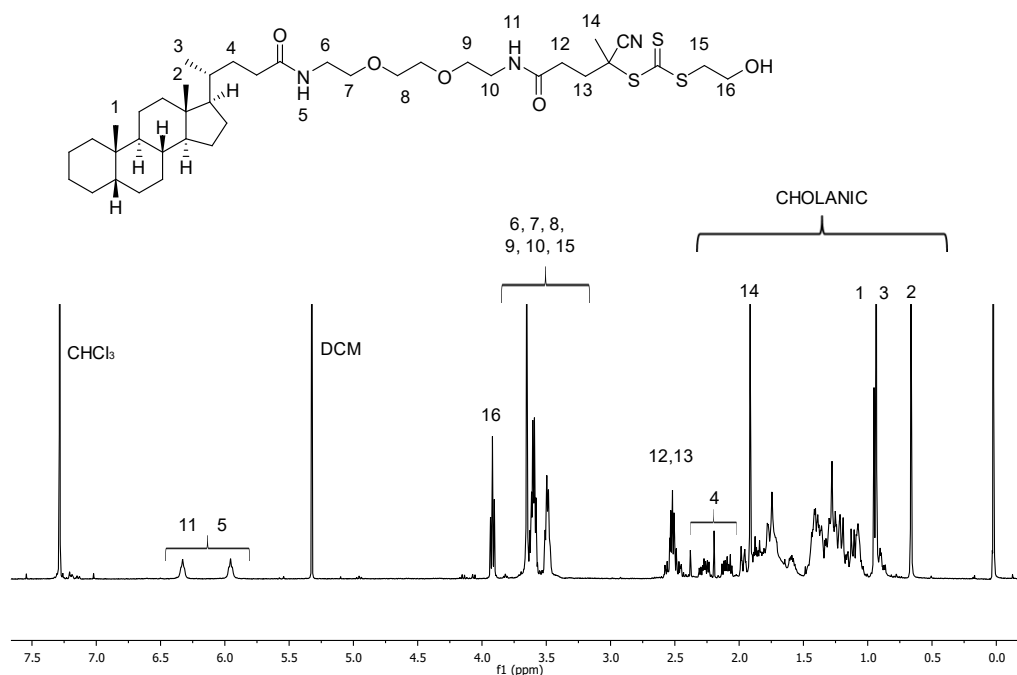


Figure 5.3: $^1$H NMR spectrum of cholanic RAFT agent **(23)** in CDCl$_3$.

## 5.3.2. Synthesis of Cholesterol-and Cholanic-poly-*N* hydroxyethylacrylamides

The two RAFT agents were used to synthesise three cholanic-terminating poly-*N*-hydroxyethylacrylamides, Cholanic-HEA$_{49}$, Cholanic-HEA$_{90}$ and Cholanic-HEA$_{175}$ and three cholesterol-terminating poly-N-hydroxyethylacrylamides, Cholesterol-HEAs **(25)**, **(26)** and **(27)**, with a targeted polyacrylamide molecular weight of 5, 10 and 20 kDa (Schemes 5.14 and 5.15). To avoid potential electrostatic interaction between cholesterol polymers **(25)**, **(26)** and **(27)** and positively charged amino acid residues on the complexed protein, the sulfonic acid salt-containing trithiocarbonate chain ends were removed by treatment

with an excess of AIBN at 80°C, following the Perrier's protocol[13]. This allowed

to generate the final Cholesterol-HEA$_{40}$, Cholesterol-HEA$_{82}$ and Cholesterol-

HEA$_{180}$.



Cholanic-HEA$_{49}$ n = 49, M$_{n,NMR}$ 6.4 kDa, M$_{n,SEC}$ 8 kDa, Đ 1.13
Cholanic-HEA$_{90}$ n = 90, M$_{n,NMR}$ 11.3 kDa, M$_{n,SEC}$ 11.9 kDa, Đ 1.09
Cholanic-HEA$_{175}$ n = 175, M$_{n,NMR}$ 21.9 kDa, M$_{n,SEC}$ 16.4 kDa, Đ 1.14
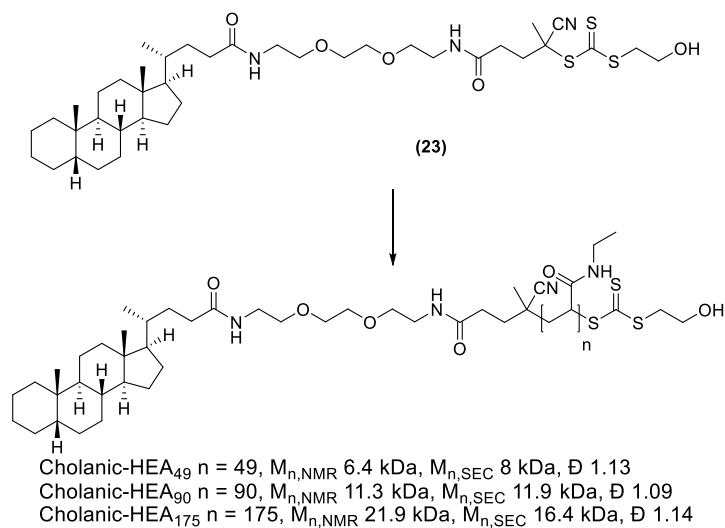
Scheme 5.14: Synthesis of Cholanic-HEA$_{49}$, Cholanic-HEA$_{90}$ and Cholanic-HEA$_{175}$ . *Reagents and conditions*: *N*-Hydroxyethylacrylamide, V501, DMF at 70 ˚C.



Cholesterol-HEA$_{40}$ n = 40, M$_{n,NMR}$ 5.8 kDa, M$_{n,SEC}$ 7.5 kDa, Đ 1.12
Cholesterol-HEA$_{82}$ n = 82, M$_{n,NMR}$ 10.4 kDa, M$_{n,SEC}$ 10.9 kDa, Đ 1.16
Cholesterol-HEA$_{180}$ n = 180, M$_{n,NMR}$ 23.2 kDa, M$_{n,SEC}$ 16.9 kDa, Đ 1.34
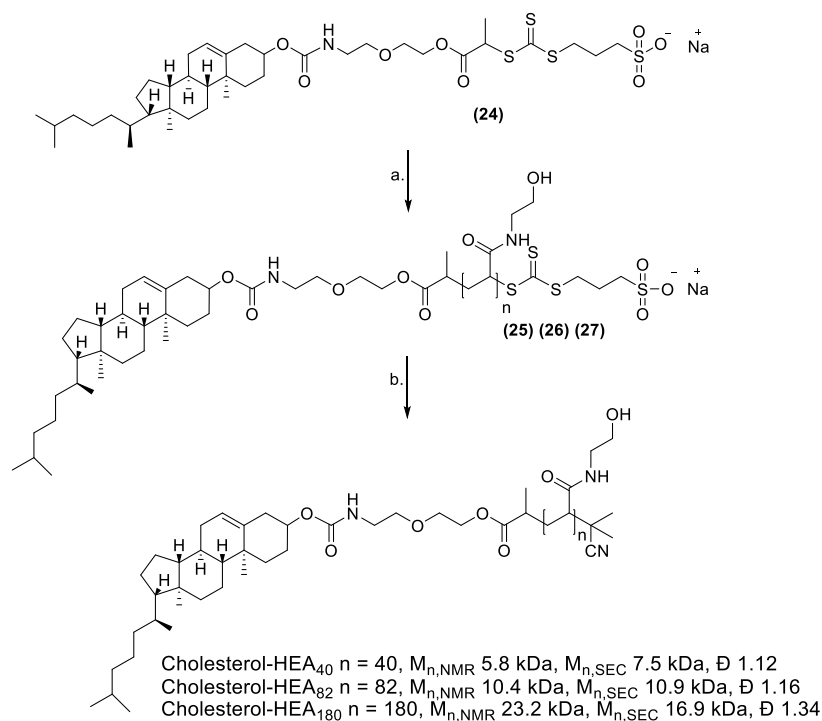
Scheme 5.15: Synthesis of Cholesterol-HEA$_{40}$, Cholesterol-HEA$_{82}$ and Cholesterol-HEA$_{180}$. *Reagents and conditions*: (a) *N*-Hydroxyethylacrylamide, V501, DMF at 70 ˚C. (b) AIBN, DMF at 80°C.

The polymers were characterised by $^1$H NMR in DMSO-d$_6$, and SEC, using DMF + 0.1% LiBr as the mobile phase (see Table 5.1 and the Supporting Information). A representative $^1$H NMR of one of these polymers, Cholanic-HEA$_{49}$, is shown in Figure 5.4. M$_{n,NMR}$ were calculated by comparing the integral of the cholanic acid/cholesterol methyl groups in the 0.5-1.0 ppm region, with that of the polymer OH groups. Values were found to be in good agreement with the theoretical ones, calculated from the initial [monomer]$_0$:[CTA]$_0$ ratios and final monomer conversion, and were found to be close to the expected 5, 10 and 20 kDa targeted molecular weight. SEC analyses indicated apparent M$_n$ values close to those calculated by $^1$H NMR and showed a narrow molar mass distribution, with Đ < 1.2, for all polymers except for Cholesterol-HEA$_{180}$, that had a Đ of 1.34. As for the previous chapters, The discrepancy between M$_{n,SEC}$ and the expected ones may be ascribed to differences between the hydrodynamic volumes of the oligomeric CTAs and those of the narrow PMMA standards used to calibrate the SEC (see Fig S5.26, S5.27 and S5.29 for SEC traces).

Complete trithiocarbonate chain-end removal from cholesterol-pHEAs was confirmed by UV spectroscopy, by monitoring the disappearing of the trithiocarbonate band at λ$_{max}$=310 nm (see Supporting Information).

**Figure 5.4:** $^1H$ NMR spectrum of Cholanic-HEA$_{49}$ in d$_6$-DMSO. M$_{n,NMR}$ was determined by comparing the integrals of cholanic methyl groups at 0.6 and 0.9 ppm, to those of NH and OH groups of the pHEA at 7.5-7.8 and 4.6-5.2 ppm, respectively. For this polymer this allowed to estimate a DP = 49 and M$_{n,NMR}$ of 6.4 kDa (M$_{n,THEO}$ = 6.6 kDa, calculated from a [HEA]$_0$:[CTA]$_0$ = 57 and final monomer conversion of 88%).

Three control polymers were synthesised using CTA **(20)** as RAFT agent and *N*-Hydroxyethylacrylamide as the monomer (Scheme 5.16). The resulting 5 kDa, 10 kDa and 20 kDa HEA$_{42}$, HEA$_{105}$ and HEA$_{166}$ lacking the cholesterol/ cholanic moieties at the chain end, were used as controls in protein-polymers association experiments.



**Scheme 5.16:** synthesis of 5kDa, 10 kDa and 20 kDa pHEA. *Reagents and conditions*: N-Hydroxyethylacrylamide, V501, DMF at 70 °C.

Table 5.3: Composition, $M_n$, and polydispersity of the polymers prepared in this study.

| Polymer | $M_{nTheo(kDa)}$[a] | $M_{n,NMR}$ (kDa)[b] | $M_{n,SEC}$ (kDa)[c] | $Đ_{SEC}$ | $DP_{Theo}$[a] | $DP_{NMR}$[b] |
|---|---|---|---|---|---|---|
| Cholanic-HEA$_{49}$ | 6.6 | 6.4 | 8 | 1.13 | 50 | 49 |
| Cholanic-HEA$_{90}$ | 11.6 | 11.3 | 11.9 | 1.09 | 93 | 90 |
| Cholanic-HEA$_{175}$ | 19.3 | 21.9 | 16.4 | 1.14 | 159 | 175 |
| Cholesterol-HEA$_{40}$ | 5.2 | 5.8 | 7.5 | 1.12 | 37 | 40 |
| Cholesterol-HEA$_{82}$ | 8.6 | 10.4 | 10.9 | 1.16 | 66 | 82 |
| Cholesterol-HEA$_{180}$ | 21.8 | 23.2 | 16.9 | 1.34 | 179 | 180 |
| HEA$_{42}$ | 5.3 | -[d] | 7.5 | 1.08 | 42 | -[d] |
| HEA$_{105}$ | 12.3 | -[d] | 14.0 | 1.10 | 105 | -[d] |
| HEA$_{166}$ | 19.5 | -[d] | 19.0 | 1.17 | 166 | [d] |

[a]Calculated from initial [HEA]$_0$:[CTA]$_0$ and final monomer conversion. [b]Number of repeating unit of HEA monomers, were calculated by ^{1}H NMR by comparing the integral of cholanic/cholesterol methyl groups with the NH and the OH of HEA repeating units. [c]Obtained from SEC analysis in DMF + 0.1% LiBr (PMMA standards). [d] Number of repeating units of HEA monomers could not be calculated as there are not visible peaks from CTA **(20)** to be compared with the NH and the OH of HEA repeating units.

## 5.3.3. BSA-polymers complexes
### 5.3.3.1. Size Exclusion Chromatography analyses

To check the ability of the cholanic- and cholesterol-HEA polymers to complex proteins, Bovine Serum Albumin (BSA), was initially chosen as a model substrate. BSA is a 583 aminoacid, 66.5 kDa protein possessing hydrophobic clefts which are responsible for its ability to bind and transport hydrophobic molecules such as fatty acids *in vivo* [14]. The formation of protein-polymer associates was initially evaluated by Size Exclusion Chromatography (SEC) analyses of BSA/polymers mixtures at different polymers:BSA molar ratios. Since SEC can separate macromolecules according to their size[15], we reasoned that it should have allowed us to detect protein-polymer nano-complexes, provided that they were sufficiently stable under the conditions employed for the analysis. As such complexes would be larger than native BSA, they were

expected to be eluted at shorter retention times. SEC profiles are reported in

Figure 5.5.
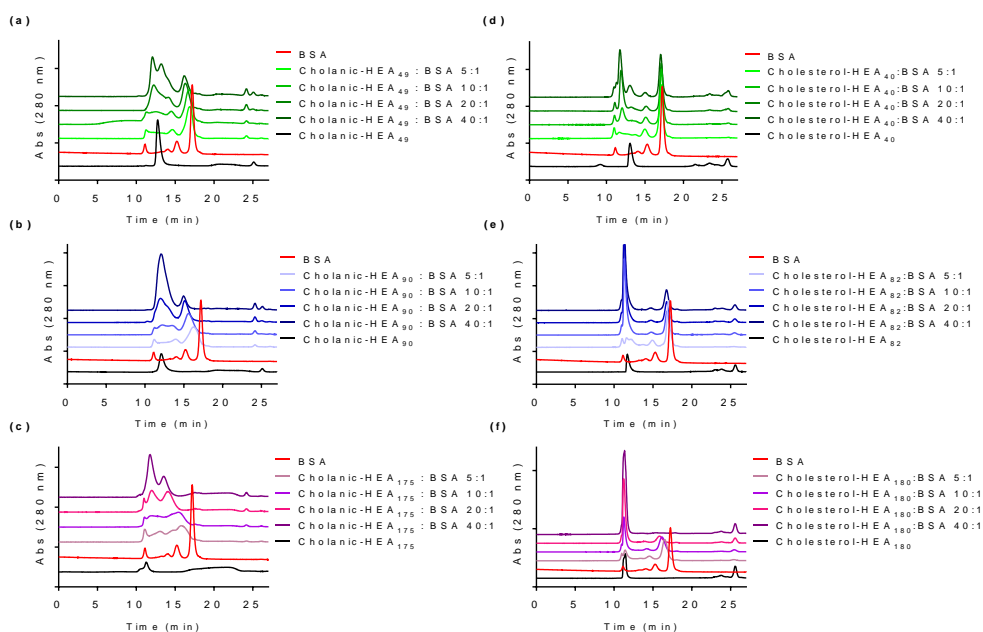


Figure 5.5 (a-f): Size Exclusion Chromatography profiles of BSA, cholanic- and cholesterol-terminating polymers, and mixtures between the polymers and the protein at different polymer:protein molar ratios. BSA was eluted at a concentration of 0.5 mg/mL, polymers were added at 5, 10, 20 and 40:1 polymer-protein molar ratios. The polymers were eluted alone at the same concentration used for the 40:1 mixture. Samples were eluted at 0.5 mL/min using DPBS as mobile phase. Absorbance was recorded at λ=280 nm.

Native BSA was eluted at 17 min, with characteristic smaller peaks at earlier

retention times due to the presence of dimers and trimers[15].

SEC traces of cholesterol- and cholanic-HEA polymers alone using DPBS as the

mobile phase showed a main first peak eluted almost immediately, and minor

peaks eluted later, at higher retention times. This behaviour is likely due to the

fact that the polymers partitioned between large aggregates, which are eluted

almost immediately, and unimeric, non-associated polymer chains (Figure 3).

Formation of micelles can be expected by these polymers, since they are made of a hydrophilic chain terminating with a hydrophobic moiety. As already discussed in Chapter 2, amphiphilic polymers form micelles at concentrations above the so-called Critical Micellar Concentration (CMC), when the polymer chains associate and the hydrophobic parts are located in the micellar core, to minimise contact with the aqueous environment[16].

The behaviour the polymers have shown in SEC is in agreement with what previously described by Grubišć-Gallot *et. al*, who for SEC of polystyrene-block-poly(methylmethacrylate) copolymers described distinct peaks for polymer micelles and unimers. The ratio between the two peaks was found to be dependent on different factors, such as the specific composition of the mobile phase or the sample concentration[17].

For the cholanic-polyHEAs in the absence of BSA, the area of the peak associated to polymer aggregates was found to be inversely proportional to the polymer chain length, in the order Cholanic-HEA$_{49}$ > Cholanic-HEA$_{90}$ > Cholanic-HEA$_{175}$ (Figure 5.5a-c). This may suggest that as the polymer chain length increases, these supramolecular constructs are more easily disassembled as they go through the column stationary phase. In case of cholesterol-polyHEAs, the micellar peak appears to be less affected by the chain length of hydrophilic pHEA (Figure 5.5d-f). The observed differences between cholanic- and cholesterol-polymers could be explained by the opposite orientation of the cholesterol polycyclic structures in the two polymers families, as cholanic acid is derivatised through the carboxyl at the end of its hydrocarbon tail, while cholesterol is linked at the hydroxyl in position 3. The different orientation of

the two hydrophobic moieties may have an influence on how they interact and assemble in solution, thus affecting the stability of the micelles, and also on how they fit in or interact with proteins hydrophobic pockets.

In the presence of 5 kDa $HEA_{42}$ negative control polymer, no BSA complexes could be detected, showing that the poly(*N*-hydroxyacrylamide) chain alone was not able to interact with the protein (see Fig. S5.31). In samples where cholanic-polyHEAs were incubated with BSA, the chromatograms showed a clear decrease and a shift of BSA main peak as the polymer:protein molar ratio increases. The shift is more evident with polymers of higher $M_n$. Meanwhile, at 20:1 and 40:1 polymers:protein molar ratios a new broad peak appears at around 11-12 min r.t., the same retention time where the polymer micellar peak is eluted

In principle, two different hypotheses could be made to describe the interaction occurring between these end-functionalised pHEAs and BSA. In the first case, few polymer molecules are fitting, through the cholanic moiety, into BSA hydrophobic pockets. Albumin possesses six binding sites for hydrophobic molecules like fatty acids and cholesterol[18, 19]. This first type of interaction would be responsible for the initial shift of the original BSA peak in the SEC chromatogram, towards higher molecular weight species. When the polymer:protein ratio further increases, larger supramolecular aggregates start to form, as detected by SEC analysis. BSA is known to aggregate in a range of different conditions[20, 21], and in this case aggregation may be triggered by the large excess of polymer. We have already introduced in Chapter 3 the concept of macromolecular crowding and its potential effect on protein solubility and

stability. The polymer occupies a specific volume, which becomes unavailable to the protein, and is for this reason called "excluded volume". The protein is forced to occupy a reduced volume in solution, its concentration will locally increase, with reduced solubility and higher chances of aggregation and precipitation[22, 23].

In the case of cholesterol-polyHEAs, the decrease and shift of BSA main peak observed with cholanic-polyHEAs is less evident, even when the polymer:protein molar ratio increases . By contrast, similarly to cholanic polymers, at 20:1 and 40:1 polymers:protein molar ratios a new broad peak appears, suggesting again that at higher concentrations the polymers may be inducing BSA aggregation. The reduced shift of the albumin peak at lower polymer:protein ratios may suggest a weaker affinity of cholesterol for albumin binding sites. The reduced affinity could be related again to the different orientation of the cholane/cholesterol chain end between the two families of polymers, which may affect the strength of interaction with the chosen protein. Previous studies have investigated the affinity of bile salts and fatty acids for BSA and report, and measured an affinity constant $K_a=(12.4 \pm 1.1) \, 10^4 \, M^{-1}$ for cholanic acid salt (cholanate). In another work that of cholesterol has been estimated to be two orders of magnitude lower, $(1.12 \pm 0.40) \times 10^3 \, M^{-1}$, thus indicating a tighter binding of cholanic acid for BSA[18, 24].

### 5.3.3.2. ITC analysis

To further confirm this hypothesis, the interaction between Cholanic-HEA$_{49}$ and BSA was analysed using Isothermal Titration Calorimetry (ITC), by Valentina Andreetto, a postgraduate student at University of Padua (Fig. 5.6). This

technique measures the heat released or absorbed upon interaction of two molecules in isothermal conditions, thus providing information on affinity, stoichiometry, enthalpy, and entropy of the binding events[25]. Every 5 minutes, 5 µL of a 1.0 mM cholanic-HEA$_{49}$ solution in PBS were automatically injected into the reference calorimetric cell containing 1.5 mL of a 10 µM BSA solution in the same buffer. The heat generated or adsorbed as a result of the interaction between the two macromolecules was measured till the protein got saturated. Heat expressed as Kcal/mol of injectant was plotted against polymer:protein molar ratio. From the resulting sigmoidal curve, $K_a=1/K_d$ was calculated as the slope at the inflection point, the stoichiometry of the binding n as the polymer:protein molar ratio at the inflection point.

The analysis confirmed the association between the two macromolecules and revealed that, on average, BSA-(Cholanic-HEA$_{49}$) complexes consist of 2.2 molecules of polymer per one molecule of BSA. The calculated Kd was found to be in the micromolar range (3.7 µM), in agreement with what reported in the literature for other molecules that establish hydrophobic interactions with human or bovine serum albumin[18, 24, 26, 27].
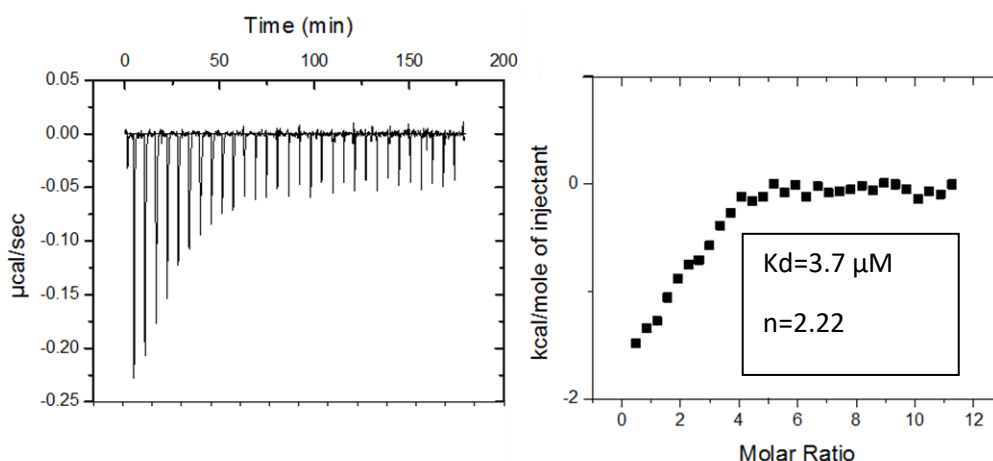
Figure 5.6: ITC analysis of Cholanic-HEA$_{49}$ binding to BSA. On the left the raw data of the heat pulses resulting from the titration of a BSA solution (10 µM in PBS) in the calorimetric cell with a 5 µL injection of a 1.0 mM solution of cholanic-HEA$_{49}$ in the same buffer. On the right the integrated heat pulses, normalized per mol of injectant as a function of the molar ratio between BSA and the injected Cholanic-HEA$_{49}$.

### 5.3.3.3. Circular Dichroism analysis of BSA and BSA-polymer conjugates.

Potential alteration of BSA secondary structure upon polymers complexation was evaluated by Circular Dichroism (CD). Cholanic-HEA$_{49}$, Cholanic-HEA$_{90}$, Cholesterol-HEA$_{40}$ and Cholesterol-HEA$_{82}$ were mixed with BSA in DPBS at 5:1 and 10:1 polymer:BSA molar ratios and subsequently analysed (Fig. 5.7). Analyses of 20:1 and 40:1 molar ratios were not performed due to the poor signal quality, caused by the strong absorptivity of the polymers.

The CD profile of native BSA showed two distinct negative peaks at 208 nm and 222 nm. This profile is typical of proteins with high prevalence of α-helix secondary structures[28] and it has been previously reported for BSA[29]. It is in accordance with BSA high α-helical content, which has been reported to be around 66% in aqueous environment[30].
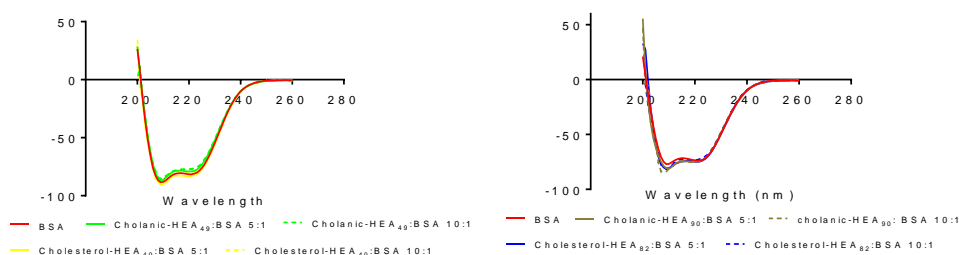
Figure 5.7: CD profiles of BSA, and mixtures between the BSA and (a) Cholanic-HEA$_{49}$/Cholesterol-HEA$_{40}$ and (b) Cholanic-HEA$_{90}$/Cholesterol-HEA$_{82}$ at 5:1 and 10:1 molar ratio. BSA was dissolved at a concentration of 0.50 mg/mL in DPBS.

The CD profiles of the different polymers-BSA mixtures were almost identical to that of BSA alone, indicating that the protein α-helix content remained unchanged following polymer complexation, under the experimental conditions investigated.

## 5.3.4. Polymers self-association and CMC analysis

The SEC profiles of cholanic- and cholesterol-HEAs in the absence of BSA suggested a potential supramolecular aggregation of the two families of polymers. Self-assembly of PEG-cholane polymers into micelles has been described by Caliceti *et al* [11] . Initial studies to investigate the self-assembly modalities of the polymers prepared in this part of this work were carried out by dynamic light scattering (Table 5.2).

Table 5.4: Size, calculated in volume distribution by dynamic light scattering, of cholanic- and cholesterol-polyHEAs polymers, 1.0 mg/mL, in DI water.

| POLYMER | CHOLANIC-HEA$_{49}$ | CHOLANIC-HEA$_{90}$ | CHOLANIC-HEA$_{175}$ | CHOLESTEROL-HEA$_{40}$ | CHOLESTEROL-HEA$_{82}$ | CHOLESTEROL-HEA$_{180}$ |
|---|---|---|---|---|---|---|
| SIZE (nm) | 15.9 | 21.9 | 20.3 | 14.1 | 14.8 | 23.0 |
| PDI | 0.430 | 1.31 | 5.01 | 0.850 | 1.15 | 0.180 |

DLS analysis revealed the presence of particles of size between 15 and 25 nm for all polymers, confirming the self-aggregation of the polymers into small nanoparticles.

Observing the high ratio between the size of the HEA hydrophilic block and that of hydrophobic cholanic/cholesterol groups, micelles could be suggested as the type of self-aggregates made by the polymers. However, at this stage of our work the exact morphology has not been identified yet. Future DLS studies are planned to identify their Critical Aggregation Concentration[31].

### 5.3.5. Insulin-polymers complexes
#### 5.3.5.1. Solubility studies

The second model protein utilised for complexation studies was bovine pancreatic insulin. The formation of nano-complexes between insulin and the cholanic- and cholesterol-polyHEA polymers was initially assessed as described in Chapter 3. Briefly, insulin was dissolved at a concentration of 2.0 mg/mL in 10 mM pH2 phosphate buffer and mixed with 5 and 10 molar excess of polymers in the same buffer.

When the pH was raised to 5.3, the mixtures were left stirring for 2h and then centrifuged to precipitate the aggregated insulin. The precipitate was then re-dissolved in acidic buffer and analysed by RP-HPLC. The concentration of precipitated insulin was calculated integrating the area under insulin peak in the HPLC chromatogram for every insulin:copolymer blend, referring to a calibration curve previously prepared analysing different dilutions of insulin in the 0.1-2 mg/mL range (see Fig. S5.32).

The concentration of residual insulin in solution was then calculated by difference between starting insulin concentration and concentration of precipitated insulin (Fig. 5.8). Due to low solubility at the concentrations required for the experiment (approximately 60 mg/mL), Cholanic-HEA$_{175}$ and Cholesterol-HEA$_{180}$ were not employed for this study.

As shown in Figure 5.8, only a small amount, around 0.3-0.4 mg/mL, of untreated protein remained in solution at pH 5.3. The negative controls HEA$_{42}$ and HEA$_{105}$ had no impact on protein solubility.
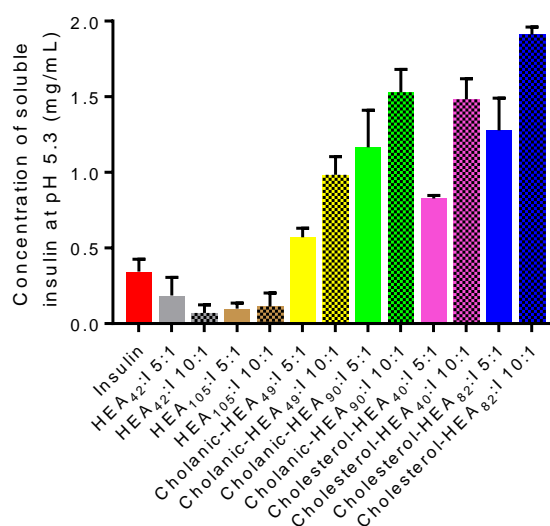


Figure 5.8: Insulin solubility studies. The concentration of soluble insulin at pH 5.3 is reported for native insulin and insulin mixed with cholanic- and cholesterol-HEAs polymers. Samples were prepared in 10 mM phosphate buffer pH 2 at a final insulin concentration of 2 mg/mL and copolymers:insulin molar ratios of 5:1 and 10:1. After the pH was shifted to 5.3, precipitated insulin was re-dissolved in 1 mL of 10 mM phosphate buffer pH 2. The concentration of precipitated insulin, expressed in mg/mL, was calculated by RP-HPLC. HPLC measurements were performed with a linear gradient from 20–90% MeCN in water containing 0.1% TFA over 18 min at a flow rate of 1 mL/ min. Absorbance was recorded at 280 nm. For each sample, the precipitated insulin was quantified via integration of the peak area of insulin in the HPLC chromatograms. Concentration of solubilised insulin was calculated by subtracting the concentration of the precipitated insulin from the starting concentration.

By contrast, both Cholanic- and Cholesterol-polyHEAs increased insulin solubility at least twice, in a concentration-dependent manner, confirming the

association between the polymers and the protein. Some differences could be noticed between the polymers utilised in this study, as a significantly higher solubilisation effect was obtained as the polymer size increased. Moreover, Cholesterol-HEAs appeared to be more effective. In particular, Cholanic-HEA$_{49}$ increased insulin solubility to around 1 mg/mL at 10:1 polymer:protein molar ratio, whereas cholesterol-HEA$_{40}$ was able to keep in solution 1.4 mg/mL of protein. Cholanic-HEA$_{90}$ and Cholesterol-HEA$_{82}$ were more effective keeping it soluble at 1.5 m/mL and 1.7 mg/mL respectively.

Compared to BSA, size and structure of insulin are considerably different. In particular, insulin is a significantly smaller protein, thus the way the polymers associate to the protein could significantly change. While in case of BSA a specific number of polymer chains can insert their chain-end into its hydrophobic clefts, with insulin the polymers may potentially be able to incorporate it within micelle-like polymer aggregates. This hypothesis would be in agreement with Dynamic Light Scattering experiments, which showed the self-assembly of the polymers into small nanoparticles of size comprised between 10 and 20 nm. If that was the case, then longer acrylamide chains may more efficiently protect insulin macromolecules, thus preventing extensive precipitation, explaining why longer cholanic- and cholesterol-HEAs are more efficient in increasing insulin solubility. As discussed already in Chapter 2, the overall net charge of insulin in the 5-6.5 pH range is close to zero, as the positive charges of its basic residues are counterbalanced by those of its acidic ones[32, 33]. Most of the other residues are either aliphatic hydrophobic (luecine, glycine, valine and alanine) or aromatic (3 phenylalanine and 4 tyrosine)[33] residues, and

both types may establish hydrophobic interactions with cholesterol and cholanic acid: aromatic amino acids through cholesterol/cholanic planar α face, aliphatic amino acid through the methyl groups on the β face[4].

### 5.3.5.2. Native Polyacrylamide Gel Electrophoresis

Electrophoretic Mobility Shift Assay (EMSA) is an electrophoretic technique typically employed to confirm Protein (or polymer)-Nucleic Acid interactions. In a typical experiment, the protein (or polymer) and DNA (or RNA) are mixed and the resulting complexes are subjected to polyacrylamide- or agarose-gel electrophoresis. Complexes are expected to migrate more slowly than their free uncomplexed components[34]. In previous studies within our group, the complexation of hen egg lysozyme by negatively charged mPEG-poly(glutamic acid) copolymers through electrostatic interactions was successfully proved using Agarose Gel Electrophoresis[35].

In this thesis work, the interaction between insulin and the polymers was further investigated by Native Polyacrylamide Gel Electrophoresis (PAGE), working close to physiological conditions, at neutral pH. In typical SDS-PAGE electrophoresis, proteins are treated with SDS, a negatively charged surfactant that that will surround proteins and turn their overall charge negative. When an electric field is applied to the gel, proteins migrate through the gel towards the anode, at speed dependent only on their size. Further addition of a reducing agent, such as dithiothreitol (DTT) will break potential disulphide bridges within the protein. These modifications result in a strong improvement of resolution and separation of proteins during electrophoresis[36]. For our experiment, we preferred to perform a Native PAGE, where the use of SDS and DTT is avoided

and the speed at which proteins migrate through the gel depends both on their isoelectric point and their size[37]: as insulin was the only protein analysed, high resolution and good separation were not our most important parameters, because we wanted to assess its interactions with the polymers in native conditions, avoiding any structure alteration. For the same reason, both the running buffer and the buffer used to prepare the polyacrylamide gel were prepared at pH 7.5. Insulin was mixed with the polymers, at 5:1, 10:1 and 20:1 polymer:insulin molar ratios, in 10 mM pH 2 phosphate buffer and a final insulin concentration of 0.5 mg/mL. The pH was then raised to 7.4, and an aliquot from each mixture analysed by Native PAGE. As a control, free insulin was run alongside with polymer-insulin mixtures. Mixtures of insulin with negative control polyacrylamides were also tested, to demonstrate that cholanic acid and cholesterol are essential to establish any insulin-polymer interaction (Fig. 5.9).

**5 KDa POLYMERS**

5:1  10:1  20:1  5:1  10:1  20:1  5:1  10:1  20:1

Insulin (I)  Cholanic-HEA₄₉ : I   Cholesterol-HEA₄₀ : I   HEA₄₀ : I

**10 KDa POLYMERS**

5:1  10:1  20:1  5:1  10:1  20:1  5:1  10:1  20:1

Insulin (I)  Cholanic-HEA₉₀ : I   Cholesterol-HEA₈₂ : I   HEA₁₀₅ : I

**20 KDa POLYMERS**

5:1  10:1  20:1  5:1  10:1  20:1  5:1  10:1  20:1

Insulin (I)  Cholanic-HEA₁₇₅ : I   Cholesterol-HEA₁₈₀ : I   HEA₁₆₆ : I
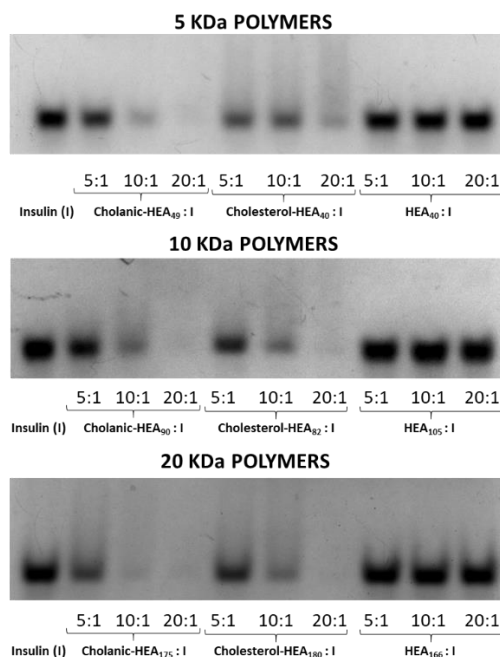
Figure 5.9: Native PAGE analyses of native insulin and insulin mixed with (a) 5kDa polymers, (b) 10kDa polymers and (c) 20kDa polymers. In all gels, native insulin is the first band on the left, followed by complexes of insulin with cholanic-HEAs, complexes with cholesterol-HEAs, and finally mixtures with control poly($N$-hydroxyethylacrylamides). Three different polymer:protein molar ratios, 5:1, 10:1 and 20:1, were utilised for each polymer. 25 ug of insulin were loaded into each well. The gel was run at 120 mV.

Native insulin is the first band on the left of all gels. On the far right of the 3 gels, negative control polyacrylamides $HEA_{42}$-, $HEA_{105}$- and $HEA_{166}$-insulin mixtures were run and no significant difference in insulin band intensity was observed, even at 20:1 polyacrylamide:insulin ratio, proving that a simple polyacrylamide does not interact with insulin under these conditions. However, all six cholanic/cholesterol-terminating polymers, significantly reduced the migration of insulin (resulting in a decrease of the intensity of the insulin band on the gel), in a concentration-dependent manner. No other bands appeared on the gels, suggesting that complexes between the polymers and the protein were retained in the loading wells. Complexation at physiological pH was thus confirmed, as the polymers were able to prevent insulin migration through the gel. From the gels, it can be noticed that more insulin gets retained as the poly-

HEA hydrophilic chain length increases. This is in accordance with the previous solubility study performed at pH 5.3, and may again suggest that a longer hydrophilic chain can more effectively surround and shield the protein, making the complex more stable.

## 5.3.6. Future/preliminary cell uptake studies

As the polymers developed in this study were found to be able to complex proteins under physiological conditions, it was decided to assess their potential ability to enhance protein intracellular uptake. To track polymer internalization, a fluorescently labelled cholanic-terminating polymer was synthesised, using a fluorescent monomer prepared from dye pyranine. We also decided to covalently link to the polymer chain a targeting agent, to induce receptor intracellular uptake.

Mannose receptor is an endocytic receptor, normally present on the surface of macrophages and dendritic cells, which presents two carbohydrates-binding domains, one of which can recognise mannose and analogous sugars[38]. Its expression on macrophages has been exploited for the development of targeted delivery systems, which take advantage of MR-mediated uptake by macrophages in target tissues during infections[39]. In particular, antimicrobial drugs-nanocarriers such as liposomes have been successfully mannosylated to enhance drug uptake by alveolar macrophages in the treatment of tuberculosis[40]. Within our group, this receptor is targeted on macrophages and mammalian cells to mediate the intracellular uptake of mannosylated polymers. The expression of this receptor has been genetically induced on

mammalian Chinese Hamster Ovary cells (CHO) by Luisa Martinez Pomares'

laboratory. Thus, in this present study we decided to attach a short sequence

of mannoses to our fluorescent polymer, to be tested on MR⁺CHO cell line.

The fluorescently labelled cholanic-terminating polymer was used as macro-

CTA RAFT agent, to mediate the polymerisation of a mannose-containing

acrylamide monomer, kindly provided by Joshua Petch, a PhD student in our

lab. A short block of around 20 mannose monomers was subsequently built on

the polyacrylamide chain, creating a targeted block copolymer to be used for

targeted cellular internalization of insulin. To monitor insulin uptake, the

protein was labelled with the dye Tetramethyl Rhodamine isothiocyanate

(TRITC), affording mono-labelled TRITC-insulin, to be used in the uptake studies.

### 5.3.6.1.Synthesis of fluorescent monomer Cascade Blue Acrylamide

The fluorescent monomer was synthesised from the commercially available dye

Pyranine. The first part of the synthesis followed an already established

procedure[41]: pyranine was treated with methyl bromoacetate under reflux to

give the intermediate  methyl ester, which was then hydrolysed in aqueous

NaOH resulting in 8-O-carboxymethylpyranine **(28)**.

8-O-Carboxymethylpyranine **(28)** was coupled to the previously synthesised

Boc-amine **(21)**, using a modified version of an existing procedure[42], followed

by Boc deprotection which afforded the Cascade Blue amine product **(29)**.

Product **(29)** was finally treated with the monomer acryloyl chloride to

generate the final molecule Cascade blue acrylamide **(30)** ($\lambda_{ex}$=405 nm; $\lambda_{em}$=420

nm in water) (Scheme 5.17). Each synthetic step was monitored by $^1$H NMR,

ESI-MS and FT-IR.
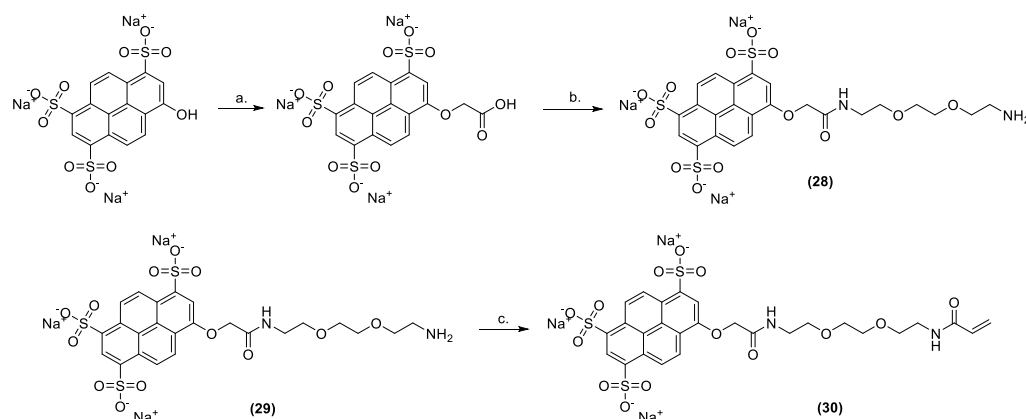


Scheme 5.17: Synthesis of monomer Cascade blue acrylamide. *Reagents and conditions*: (a) i. DIPEA, methyl bromoacetate, MeOH, reflux; ii. 1M NaOH 60°C. (b) i. BOC-amine **(21)**, TEA, DMTMM, MeOH at room temperature; ii. HCl 4M in dioxane, room temperature. (c) Acryloyl chloride, NaOH 1M, room temperature.

### 5.3.6.2. Synthesis of fluorescent polymer CholanicFLUO-HEA$_{80}$-MAN$_{20}$

The cholanic RAFT agent **(23)** was used to synthesise a new cholanic-terminating poly(*N*-hydroxyethylacrylamide), CholanicFLUO-HEA$_{80}$ with a theoretical molecular weight of 10 kDa. Together with commercial monomer *N*-hydroxyethylacrylamide, monomer, Cascade Blue acrylamide **(30)** was added to the polymerization in a 1:1.2 CTA:monomer molar ratio, to achieve the final ratio of 1 fluorescent monomer per polymer chain. The dye monomer was not added immediately, but after *N*-hydroxyethylacrylamide conversion had reached ca. 60%, to prevent the dye to be polymerized too close to the cholanic functional group, as we feared that a potential interaction between the two groups, (Cascade Blue acrylamide **(30)** monomer is significantly larger than *N*-hydroxyethylacrylamide), could hamper cholanic complexing ability. The synthesis of the polymer was verified by $^1$H NMR and SEC, performed in DMF

with 0.1% LiBr. SEC analyses indicated apparent $M_n$ value of 10 kDa identical to that calculated by $^1$H NMR of 10 kDa, and showed a narrow molar mass distribution, Đ =1.20.

The amount of dye monomer which had polymerised per polymer chain was calculated by UV absorption, measuring the absorbance at λ=380 nm of a 1.0 mg/mL polymer solution in methanol, using a calibration curve built with Cascade Blue acrylamide **(30)** monomer in the same solvent (see Fig S5.33). It was found that an average of 0.66 Cascade Blue acrylamide **(30)** molecules had polymerised per polymer chain, that is, on average every three polymer chains, two incorporated a fluorescent repeating unit.

Part of CholanicFLUO-HEA$_{80}$ was finally used as macro-CTA RAFT agent to mediate the polymerisation of the monomer mannose acrylamide, affording CholanicFLUO-*b*-HEA$_{80}$-MAN$_{20}$ (Scheme 5.18). The synthesis of the copolymer was verified by $^1$H NMR and SEC, performed in DMF with 0.1% LiBr. SEC analyses indicated apparent Mn value of 10.6 kDa, close to that calculated by $^1$H NMR of 16.0 kDa, and showed a narrow molar mass distribution, with Đ =1.23 see Fig. S5.28 for SEC traces).
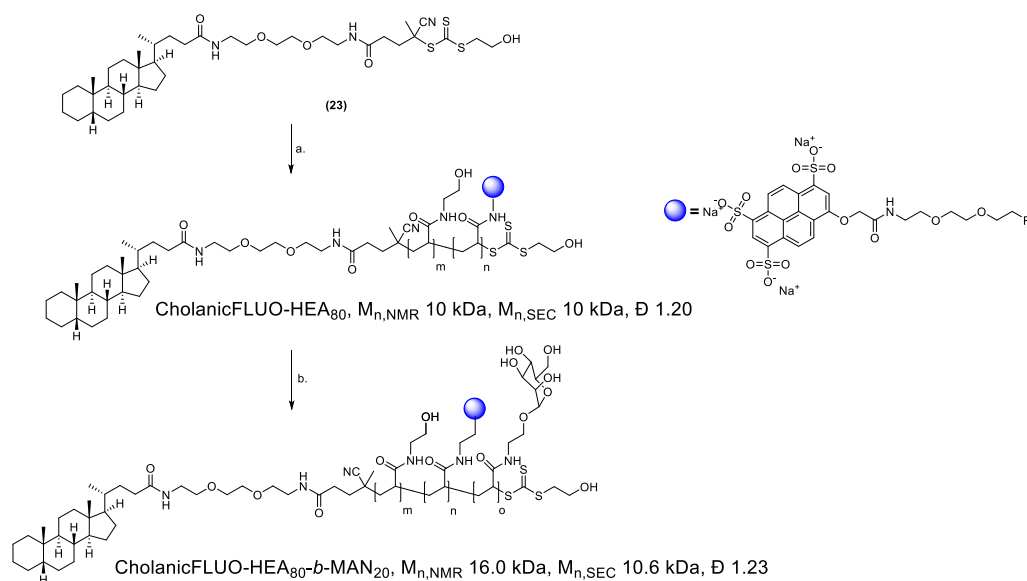
Scheme 5.18: synthesis of CholanicFLUO-HEA$_{80}$ and CholanicFLUO-HEA$_{80}$-*b*-MAN$_{20}$. *Reagents and conditions*: (a) N-Hydroxyethylacrylamide, V501, Cascade Blue acrylamide **(30)**, DMF at 70 ˚C. (b) Mannose acrylamide, V501, DMF at 70 ˚C.

### 5.3.6.3. Synthesis and purification of mono-labelled TRITC-insulin

Insulin was fluorescently labelled with tetramethyl rhodamine isothiocyanate (TRITC) using a modified version of a commercially available protocol[43]. The protein was treated with 3 equivalents of dye in 0.1 M pH 8.5 sodium tetraborate buffer for 5h. RP-HPLC analysis of a sample taken after 5h revealed that a group of n-labelled insulins had formed. Due to concerns that an excessive number of dye molecules covalently linked to insulin could alter its native structure and influence its interactions with the copolymer, mono-labelled TRITC-insulin was purified on semi-PREP RP-HPLC. Successful purification was verified by RP-HPLC and ESI-MS (Fig. 5.10). Analyses confirmed the correct labelling of the protein, and the good purity (94%) of the mono-labelled product.
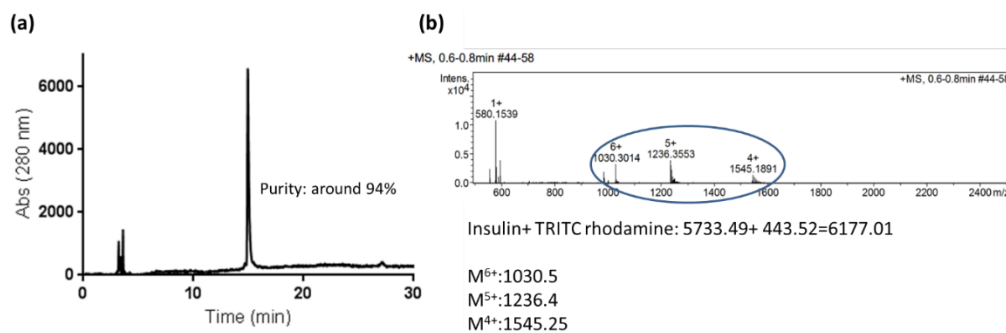
Figure 5.10: (a) C18 RP-HPLC chromatogram of purified mono-labelled TRITC-insulin. The protein was analysed using a 30%-60% MeCN linear gradient. (b) ESI-MS analysis of purified mono-labelled TRITC-insulin. Three peaks are identified: peak at 1030.5 m/z corresponds to [M+6H]$^{6+}$, that at 1236.4 to [M+5H]$^{5+}$, finally peak at 1545.3 corresponds to [M+4H]$^{4+}$.

The purified protein was finally lyophilised. Future studies will be dedicated to the complexation of fluorescent TRITC-insulin into CholanicFLUO-*b*-HEA$_{80}$-MAN$_{20}$, and its potential enhanced intracellular uptake into MR$^+$CHO cells.

## 5.4. Final considerations

In this chapter, a group of three cholanic acid- and three cholesterol-terminating polyacrylamides were successfully synthesised by RAFT polymerization, to be used as synthetic excipients for protein formulations. We wanted to highlight RAFT polymerization as a versatile technique for the development of protein-complexing agents.

The polymers were tested with two different model proteins, BSA and insulin, using various techniques, resulting in the formation of protein-polymer nano-complexes.

In particular, SEC analyses of BSA/polymers mixtures showed the formation of nanocomplexes. According to the polymers:BSA molar ratio employed, two different types of interaction between the polymers and the protein were noticed. At 5:1 and 10:1 polymer:protein molar ratio the polymers mainly inserted into some of BSA hydrophobic pockets, which are already known for their interaction with cholesterol[24]. Further investigation at these molar ratios was accomplished by circular dichroism, which confirmed that up to 10:1 polymers:protein ratios the interaction does not induce any change on protein secondary structure. ITC studies performed with the shortest cholanic-polyacrylamide confirmed the formation of protein complexes with an average of 2 polymer chains per protein macromolecule. SEC analysis performed at 20:1 and 40:1 polymer:protein molar ratios showed the formation of large

aggregates that may be resulting from BSA aggregation, induced at high polymers:BSA ratios.

SEC analysis of cholanic/cholesterol polymers in the absence of BSA also indicate the cholanic/cholesterol polymers self-assemble into supramolecular aggregates[17]. Aggregation was verified by DLS analysis, which revealed the presence of nanoparticles with size between 15 and 25 nm.

Protein complexation was further studied on insulin. Insulin complexation was confirmed at pH 5.3, where protein solubility was drastically increased by the polymers. The interaction was also successfully assessed at physiological pH through Native PAGE electrophoresis, where the formation of a complex between insulin and the polymers prevented the protein to migrate across the gel.

Results confirmed that the cholanic- and cholesterol-HEAs are successfully able to complex different proteins in a range of different conditions. Thus, they indicated that these polymers may be used, like the original PEG-cholane, for the potential controlled delivery of therapeutic proteins.

These promising results prompted us to test their potential ability to enhance protein intracellular uptake by receptor mediated endocytosis. A new fluorescent cholanic-polymer was prepared, containing a short block with an average of 20 mannose repeating units, to be tested for targeted insulin delivery onto an endocytic mannose receptor-expressing cell line. A

fluorescently labelled insulin was prepared to monitor the protein uptake. Due to time constraint, the uptake studies have not been finalised as yet, but are is currently being investigated with the collaboration of another PhD student in our lab.

# References

1. Zhang, F.; Liu, M.-r.; Wan, H.-t., Discussion about Several Potential Drawbacks of PEGylated Therapeutic Proteins. *Biological and Pharmaceutical Bulletin* **2014,** *37* (3), 335-339.
2. Monte, M. J.; Marin, J. J. G.; Antelo, A.; Vazquez-Tato, J., Bile acids: Chemistry, physiology, and pathophysiology. *World Journal of Gastroenterology : WJG* **2009,** *15* (7), 804-816.
3. Alberts B, J. A., Lewis J, et al. The Lipid Bilayer. *Molecular Biology of the Cell. 4th edition* **2012**.
4. Fantini, J.; Barrantes, F. J., How cholesterol interacts with membrane proteins: an exploration of cholesterol-binding sites including CRAC, CARC, and tilted domains. *Frontiers in Physiology* **2013,** *4*, 31.
5. Epand, R. M., Proteins and cholesterol-rich domains. *Biochimica et Biophysica Acta (BBA) - Biomembranes* **2008,** *1778* (7), 1576-1582.
6. Sankaranarayanan, S.; de la Llera-Moya, M.; Drazul-Schrader, D.; Phillips, M. C.; Kellner-Weibel, G.; Rothblat, G. H., Serum albumin acts as a shuttle to enhance cholesterol efflux from cells. *Journal of Lipid Research* **2013,** *54* (3), 671-676.
7. Bukiya, A. N.; Dopico, A. M., Common structural features of cholesterol binding sites in crystallized soluble proteins. *Journal of Lipid Research* **2017,** *58* (6), 1044-1054.
8. Akiyoshi, K.; Sunamoto, J., Supramolecular assembly of hydrophobized polysaccharides. *Supramolecular Science* **1996,** *3* (1), 157-163.
9. Park, J. H.; Kwon, S.; Nam, J.-O.; Park, R.-W.; Chung, H.; Seo, S. B.; Kim, I.-S.; Kwon, I. C.; Jeong, S. Y., Self-assembled nanoparticles based on glycol chitosan bearing 5β-cholanic acid for RGD peptide delivery. *Journal of Controlled Release* **2004,** *95* (3), 579-588.
10. Salmaso, S.; Bersani, S.; Scomparin, A.; Balasso, A.; Brazzale, C.; Barattin, M.; Caliceti, P., A novel soluble supramolecular system for sustained rh-GH delivery. *Journal of Controlled Release* **2014,** *194*, 168-177.
11. Salmaso, S.; Bersani, S.; Mastrotto, F.; Tonon, G.; Schrepfer, R.; Genovese, S.; Caliceti, P., Self-assembling nanocomposites for protein delivery: Supramolecular interactions between PEG-cholane and rh-G-CSF. *Journal of Controlled Release* **2012,** *162* (1), 176-184.
12. Luengo-Alonso, C.; Torrado, J. J.; Ballesteros, M. P.; Malfanti, A.; Bersani, S.; Salmaso, S.; Caliceti, P., A novel performing PEG-cholane nanoformulation for Amphotericin B delivery. *International Journal of Pharmaceutics* **2015,** *495* (1), 41-51.
13. Perrier, S.; Takolpuckdee, P.; Mars, C. A., Reversible Addition–Fragmentation Chain Transfer Polymerization: End Group Modification for Functionalized Polymers and Chain Transfer Agent Recovery. *Macromolecules* **2005,** *38* (6), 2033-2036.
14. Steinhardt, J.; Krijn, J.; Leidy, J. G., Differences between bovine and human serum albumins. Binding isotherms, optical rotatory dispersion, viscosity, hydrogen ion titration, and fluorescence effects. *Biochemistry* **1971,** *10* (22), 4005-4015.
15. Hong, P.; Koza, S.; Bouvier, E. S. P., Size-Exclusion Chromatography for the Analysis of Protein Biotherapeutics and their Aggregates. *Journal of Liquid Chromatography & Related Technologies* **2012,** *35* (20), 2923-2950.
16. Jones, M.-C.; Leroux, J.-C., Polymeric micelles – a new generation of colloidal drug carriers. *European Journal of Pharmaceutics and Biopharmaceutics* **1999,** *48* (2), 101-111.
17. Grubišć-Gallot, Z.; Gallot, Y.; Sedláček, J., Study of polystyrene-block-poly(methyl methacrylate) micelles by size exclusion chromatography/low-angle laser

light scattering, 1. Influence of copolymer concentration and flow rate. *Macromolecular Chemistry and Physics* **1994,** *195* (2), 781-791.

18.     Charbonneau, D. M.; Tajmir-Riahi, H.-A., Study on the Interaction of Cationic Lipids with Bovine Serum Albumin. *The Journal of Physical Chemistry B* **2010,** *114* (2), 1148-1155.

19.     Spector, A. A.; John, K.; Fletcher, J. E., Binding of long-chain fatty acids to bovine serum albumin. *Journal of Lipid Research* **1969,** *10* (1), 56-67.

20.     Borzova VA, M. K., Chebotareva NA, Kleymenov SY, Poliansky NB, Muranov KO, et al Kinetics of Thermal Denaturation and Aggregation of Bovine Serum Albumin. *PLoS ONE* **2016** 11(4).

21.     Li, R.; Wu, Z.; Wangb, Y.; Ding, L.; Wang, Y., Role of pH-induced structural change in protein aggregation in foam fractionation of bovine serum albumin. *Biotechnology Reports* **2016,** *9*, 46-52.

22.     Kuznetsova, M. I.; Zaslavsky, Y. B.; Breydo, L.; Turoverov, K. K.; Uversky, N. V., Beyond the Excluded Volume Effects: Mechanistic Complexity of the Crowded Milieu. *Molecules* **2015,** *20* (1).

23.     Kuznetsova, M. I.; Turoverov, K. K.; Uversky, N. V., What Macromolecular Crowding Can Do to a Protein. *International Journal of Molecular Sciences* **2014,** *15* (12).

24.     Pico, G. A.; Houssier, C., Bile salts-bovine serum albumin binding: spectroscopic and thermodynamic studies. *Biochimica et Biophysica Acta (BBA) - Protein Structure and Molecular Enzymology* **1989,** *999* (2), 128-134.

25.     Raju, B. B.; Winnik, F. M.; Morishima, Y., A Look at the Thermodynamics of the Association of Amphiphilic Polyelectrolytes in Aqueous Solutions: Strengths and Limitations of Isothermal Titration Calorimetry. *Langmuir* **2001,** *17* (14), 4416-4421.

26.     Möller, M.; Denicola, A., Study of protein-ligand binding by fluorescence. *Biochemistry and Molecular Biology Education* **2006,** *30* (5), 309-312.

27.     Fasano, M.; Curry, S.; Terreno, E.; Galliano, M.; Fanali, G.; Narciso, P.; Notari, S.; Ascenzi, P., The extraordinary ligand binding properties of human serum albumin. *IUBMB Life* **2008,** *57* (12), 787-796.

28.     Greenfield, N. J., Using circular dichroism spectra to estimate protein secondary structure. *Nature protocols* **2006,** *1* (6), 2876-2890.

29.     Gao, X.; Zhou, P.; Yang, R.; Yang, D.; Zhang, N., Protein-loaded comb-shape copolymer-based pH-responsive nanoparticles to improve the stability of proteins. *Journal of Materials Chemistry B* **2013,** *1* (38), 4992-5002.

30.     Wang, C. H.; Chen, W., Raman Characterizing Disulfide Bonds and Secondary Structure of Bovine Serum Albumin. *AIP Conference Proceedings* **2010,** *1267* (1), 346-347.

31.     Shi, Y.; Zhou, H.; Zhang, X.; Wang, J.; Long, J.; Yang, Z.; Ding, D., Self-assembling choline mimics with enhanced binding affinities to C-LytA protein. *Scientific Reports* **2014,** *4*, 6621.

32.     Iyire, A.; Alaayedi, M.; Mohammed, A. R., Pre-formulation and systematic evaluation of amino acid assisted permeability of insulin across in vitro buccal cell layers. *Scientific Reports* **2016,** *6*, 32498.

33.     Tah, B.; Pal, P.; Roy, S.; Dutta, D.; Mishra, S.; Ghosh, M.; Talapatra, G. B., Quantum-mechanical DFT calculation supported Raman spectroscopic study of some amino acids in bovine insulin. *Spectrochimica Acta Part A: Molecular and Biomolecular Spectroscopy* **2014,** *129*, 345-351.

34.     Hellman, L. M.; Fried, M. G., Electrophoretic mobility shift assay (EMSA) for detecting protein–nucleic acid interactions. *Nature Protocols* **2007,** *2*, 1849.

35.     Nieto-Orellana, A.; Di Antonio, M.; Conte, C.; Falcone, F. H.; Bosquillon, C.; Childerhouse, N.; Mantovani, G.; Stolnik, S., Effect of polymer topology on non-

covalent polymer–protein complexation: miktoarm versus linear mPEG-poly(glutamic acid) copolymers. *Polymer Chemistry* **2017,** *8* (14), 2210-2220.

36.     Svasti, J.; Panijpan, B., SDS-polyacrylamide gel electrophoresis. A simple explanation of why it works. *Journal of Chemical Education* **1977,** *54* (9), 560.

37.     Arndt C., K. S., Bartsch H., Bachmann M. Native Polyacrylamide Gels. *Methods in Molecular Biology (Methods and Protocols)* **2012**.

38.     Martinez-Pomares, L., The mannose receptor. *Journal of Leukocyte Biology* **2012,** *92* (6), 1177-1186.

39.     Azad AK, R. M., Schlesinger LS. Exploitation of the Macrophage Mannose Receptor (CD206) in Infectious Disease Diagnostics and Therapeutics. *J Cytol Molecul Biol.* **2014**;1(1): 5.

40.     Lyubov Yu. Filatova and Natalia, L. K. a. E. V. K., Targeted delivery of anti-tuberculosis drugs to macrophages: targeting mannose receptors. *Russian Chemical Reviews* **2018,** *87* (4), 374.

41.     Legenzov, E. A.;  Dirda, N. D. A.;  Hagen, B. M.; Kao, J. P. Y., Synthesis and Characterization of 8-O-Carboxymethylpyranine (CM-Pyranine) as a Bright, Violet-Emitting, Fluid-Phase Fluorescent Marker in Cell Biology. *PLoS ONE* **2015,** *10* (7), e0133518.

42.     Nyren-Erickson, E. K.;  Haldar, M. K.;  Gu, Y.;  Qian, S. Y.;  Friesner, D. L.; Mallik, S., Fluorescent Liposomes for Differential Interactions with Glycosaminoglycans. *Analytical Chemistry* **2011,** *83* (15), 5989-5995.

43.     https://www.thermofisher.com/uk/en/home/references/protocols/cell-and-tissue-analysis/labeling-chemistry-protocols/amine-reactive-probe-labeling-protocol.html.

# Supporting Information Chapter 5

$^1$H and $^{13}$C NMR spectra were recorded on a Bruker DPX400 UltraShield™ Spectrometer and processed with MestReNova 12.0© 2017 Mestrelab Research S.L. All chemical shifts are reported in ppm ($\delta$) relative to tetramethylsilane or referenced to the chemical shifts of residual solvent resonances.

ESI TOF Mass spectrometry analyses were conducted on a Bruker microTOF II.

FT-IR spectra were recorded using an Agilent Cary630.

Purification of $IND_m$, $PHEN_m$ and $MTB_m$ oligomers (from m=2 to m=6) was performed on an Agilent 971-FP Flash Purification System using a BIOTAGE KP-C18-HS 12 g column.

Polymer SEC analyses were performed on a Polymer Laboratories GPC 50 system equipped with a refractive index detector, using a system made of two PLgel Mixed-D (5 μm bead, 7.8 × 300 mm) columns and a matching guard (7.8 × 50 mm). Analyses were performed in DMF at a flow rate of 1 mg/mL with 0.1% w/v LiBR. Narrow PMMA standards were used for calibration.

HPLC experiments were performed on a Shimadzu HPLC (LC-20AD pump) equipped with a SPD-M20A UV detector and SIL-20A autosampler. Reverse phase analyses were completed using a C18 Zorbax Eclipse Plus C18 column (3.5 μm, 95 Å, 4.6 × 12.5 mm).

Size Exclusion analyses for the evaluation of Cholanic/cholesterol-HEA polymers:BSA complexes were performed using a TSKgel® G3000SW$_{XL}$ column (I.D. 30 cm × 7.8 mm, 5 µm particle size).

Dynamic light scattering was performed using a Nano-Zs from Malvern Instruments, UK, equipped with a 633 nm laser at a fixed angle of 173°. The size was measured at 25 ˚C. Analyses were repeated 3 times for each sample, and a minimum of 10 measurements was performed for each analysis.

Semi-preparative RP-HPLC for the purification of TRITC insulin was performed on a Waters Prep HPLC, using a Phenomenex Jupiter C18 column (10 µm, 300 Å, 10 × 250 mm).
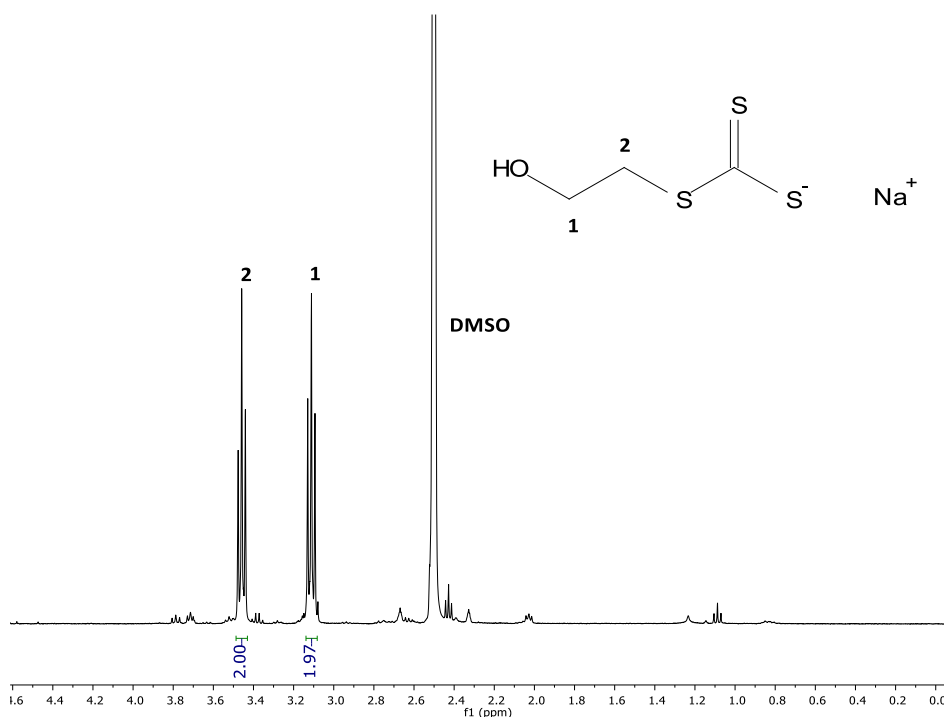


Figure S5.1:$^1$H NMR spectrum of Sodium 2-hydroxyethyl carbonotrithioate **(11)** in d$_6$-DMSO.
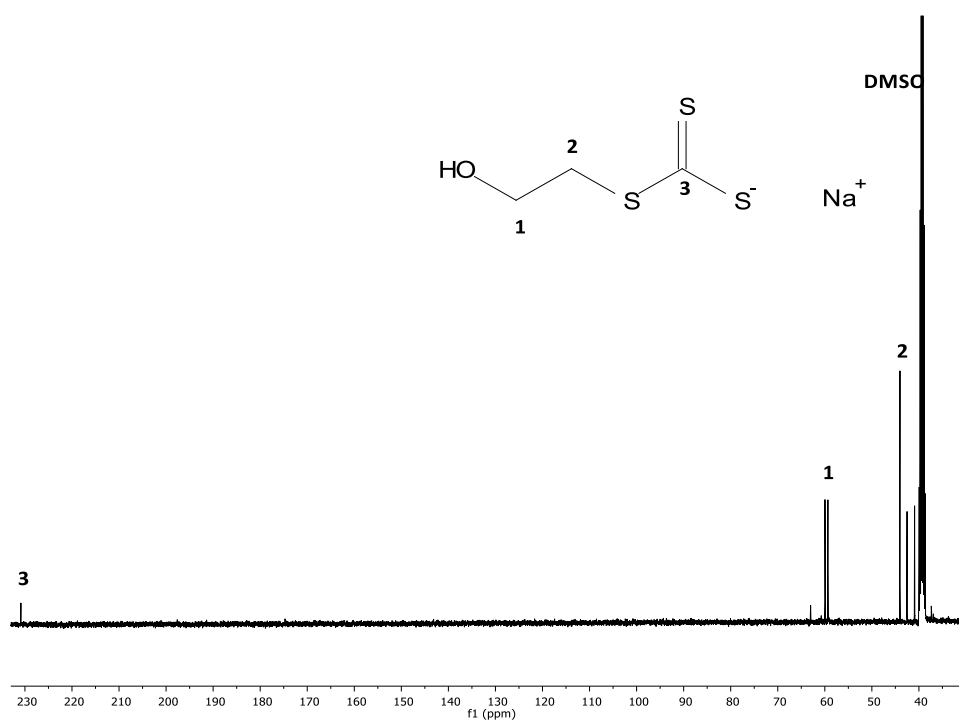
Figure S5.2: $^{13}C$ NMR spectrum of Sodium 2-hydroxyethyl carbonotrithioate **(11)** in $d_6$-DMSO.
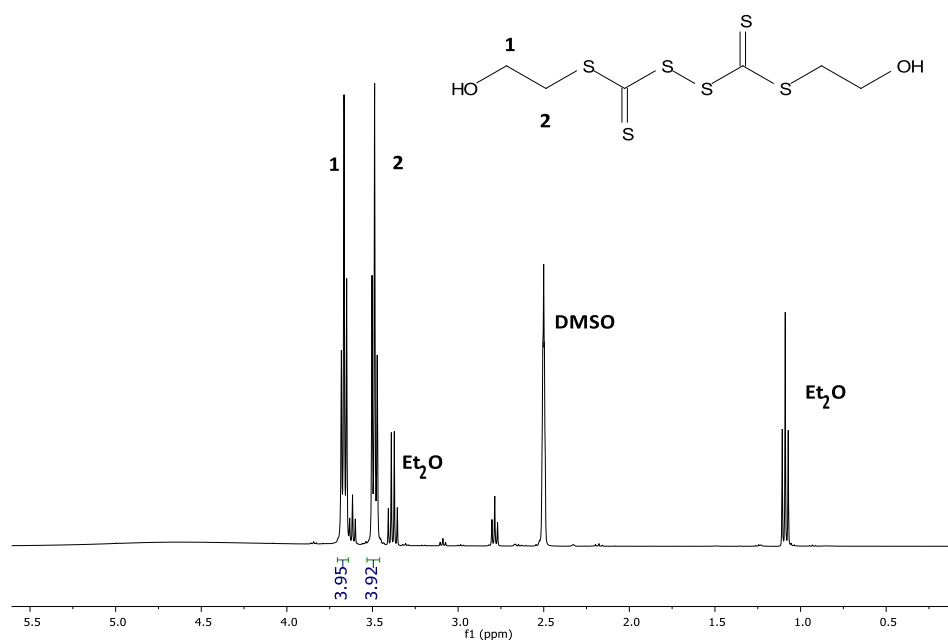


Figure S5.3: $^1H$ NMR spectrum of Dithiobis-2-hydroxyethyl carbonotrithioate disulfide **(12)** in $d_6$-DMSO.
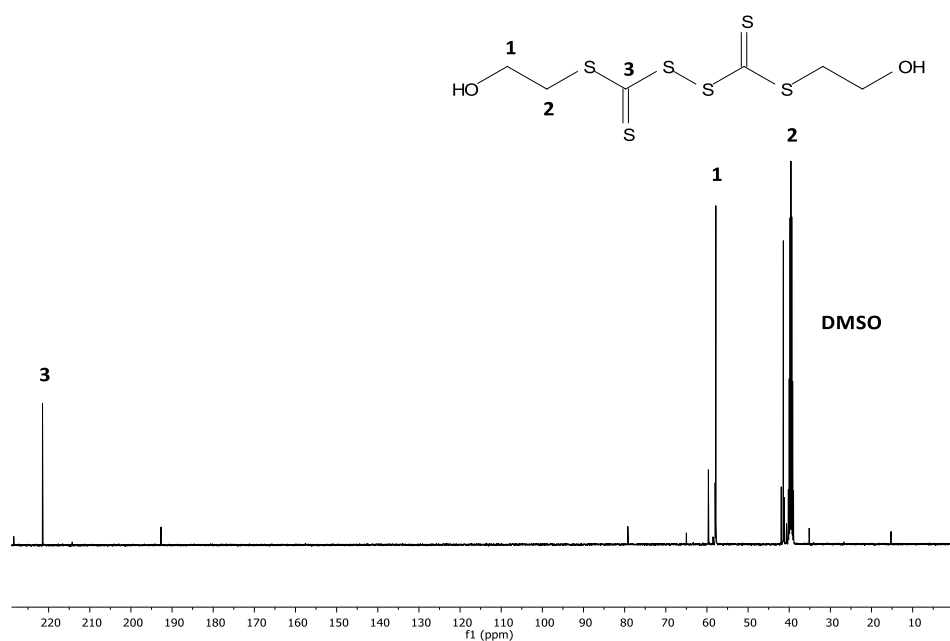
Figure S5.4: $^{13}$C NMR spectrum of Dithiobis-2-hydroxyethyl carbonotrithioate disulfide **(12)** in d$_6$-DMSO.
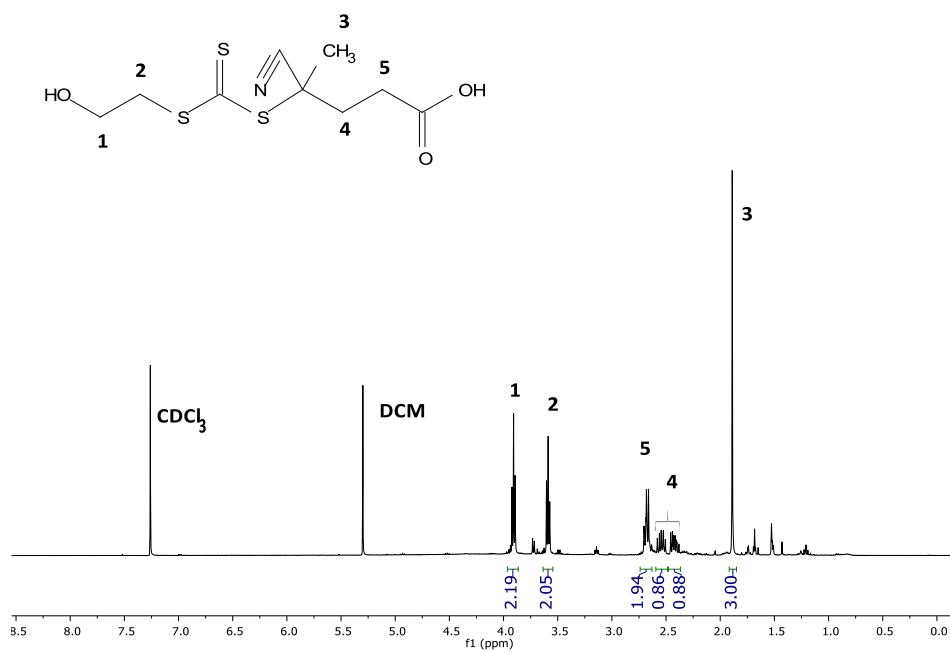


Figure S5.5: $^1$H NMR spectrum of CTA **(13)** in CDCl$_3$.
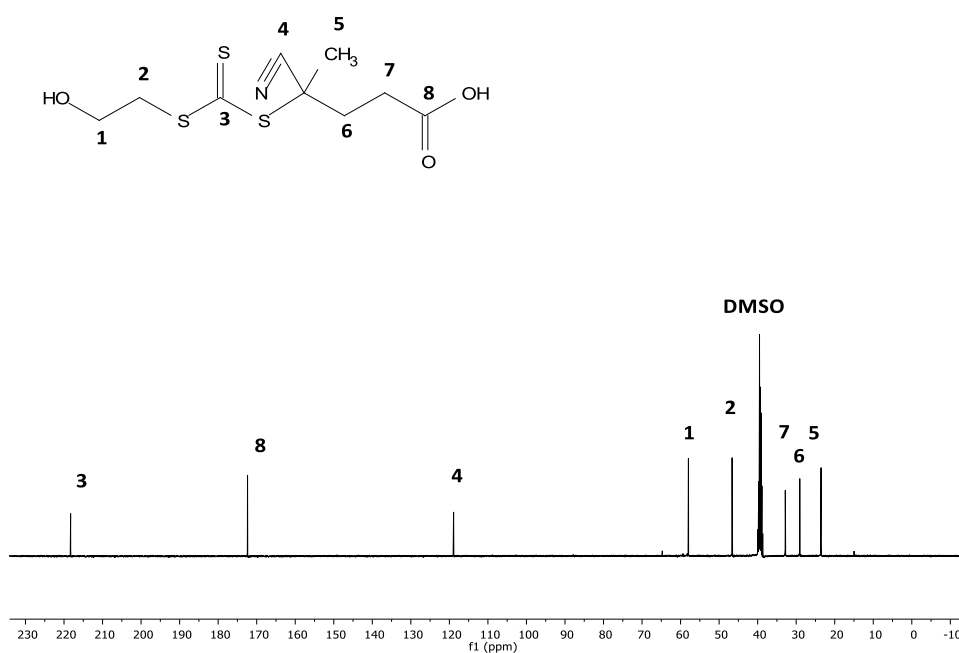
Figure S5.6: $^{13}$C NMR spectrum of CTA **(13)** in d$_6$-DMSO.
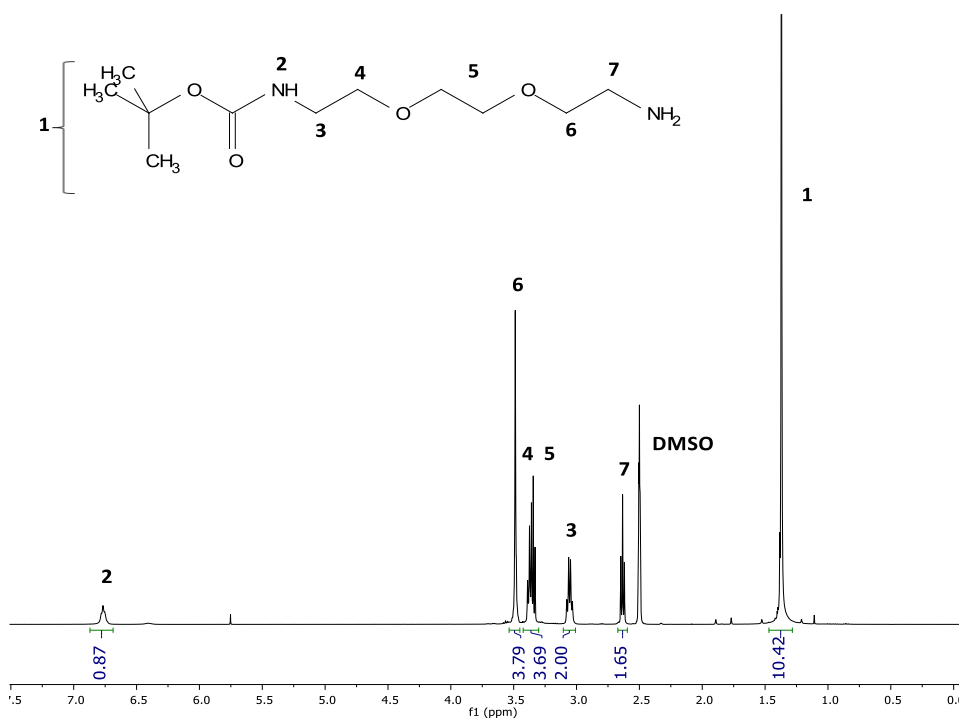


Figure S5.7: $^1$H NMR spectrum of Boc-Amine **(14)** in d$_6$-DMSO.
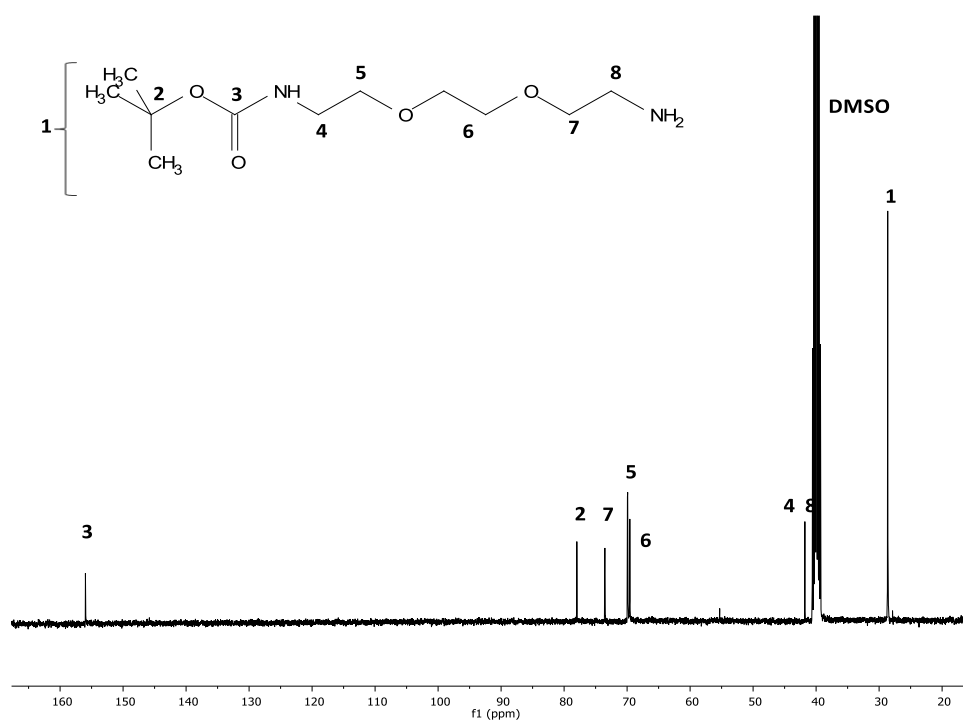
Figure S5.8: $^{13}$C NMR spectrum of Boc-amine **(14)** in d$_6$-DMSO.
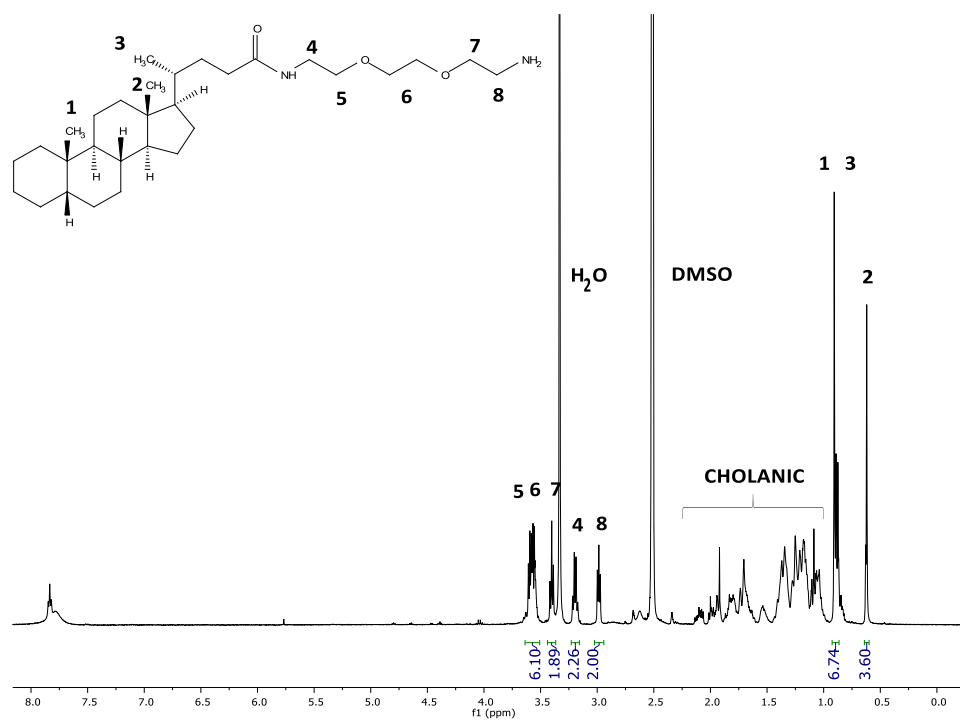


Figure S5.9: $^1$H NMR spectrum of Cholanic-amine **(15)** in d$_6$-DMSO.
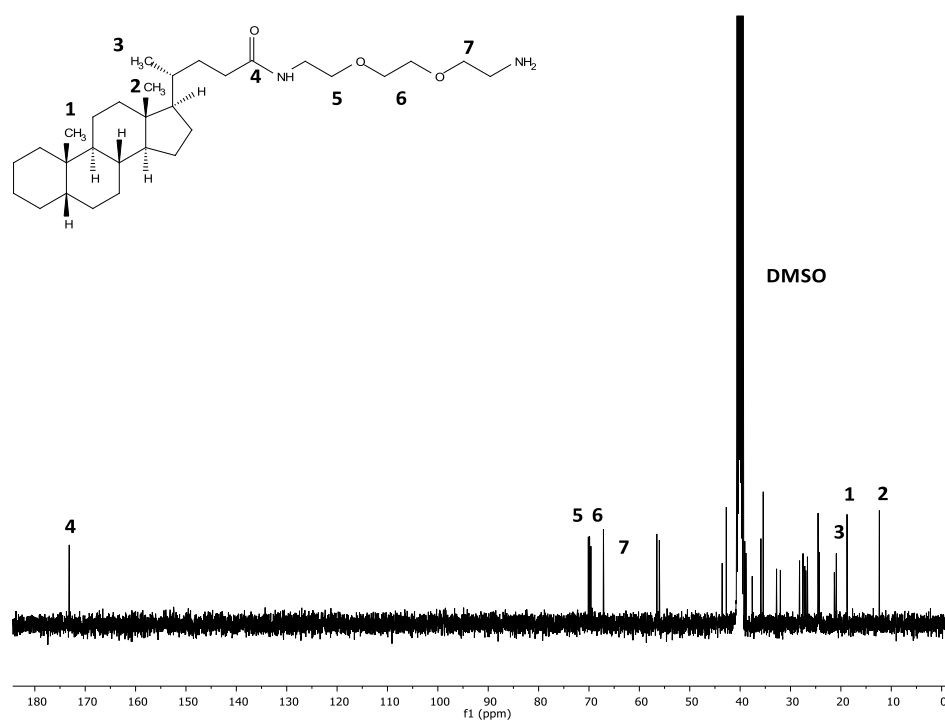
Figure S5.10: $^{13}$C NMR spectrum of Cholanic-amine **(15)** in d$_6$-DMSO.
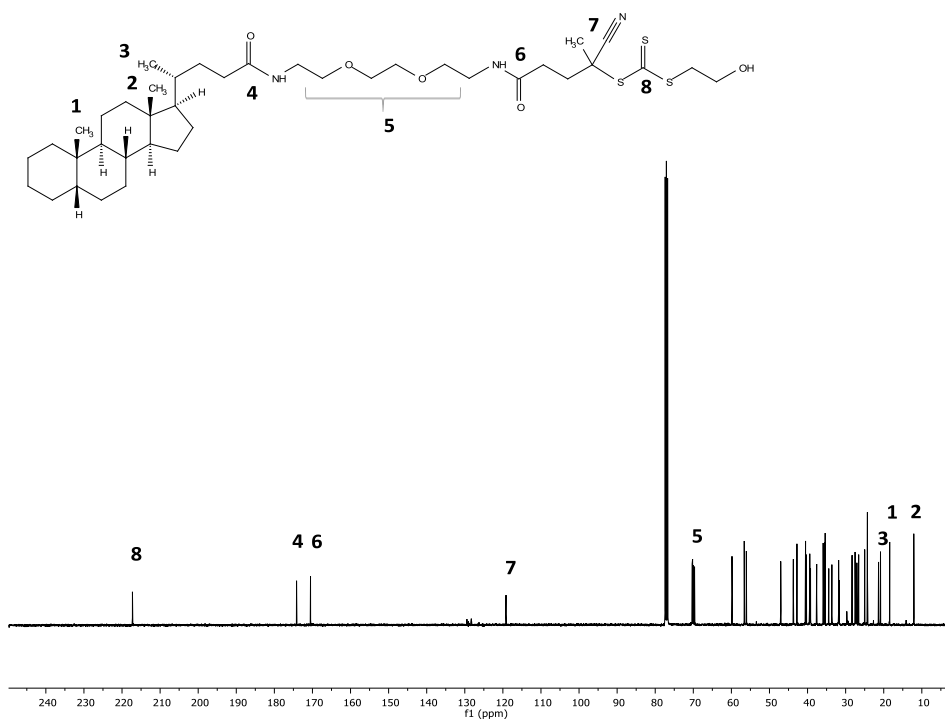


Figure S5.11: $^{13}$C NMR spectrum of RAFT agent **(16)** in d$_6$-DMSO.
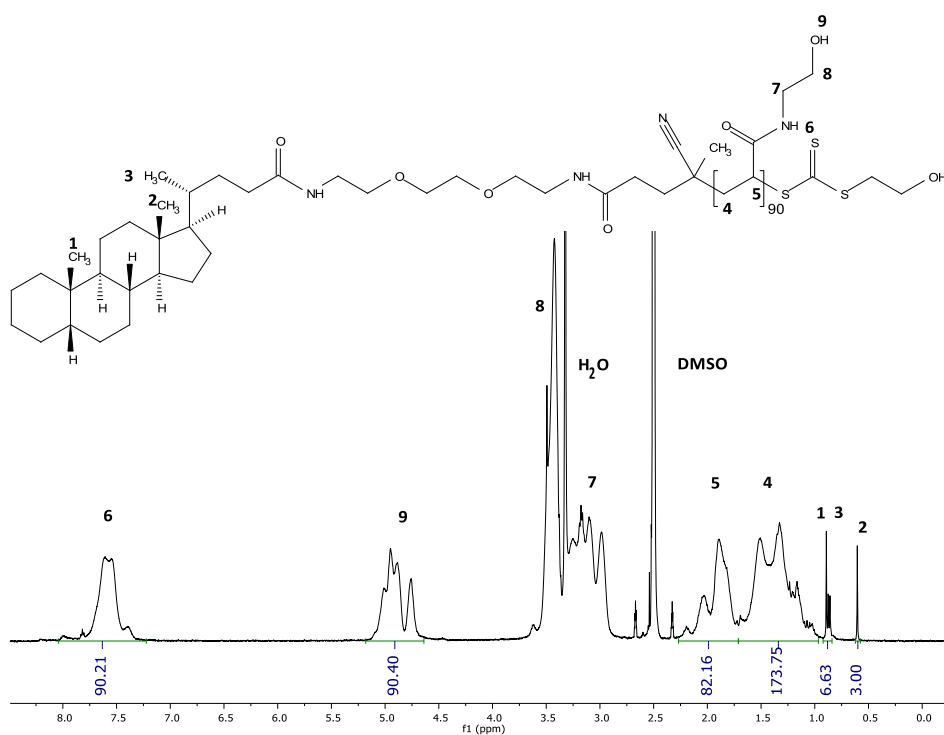
Figure S5.12: $^1$H NMR spectrum of Cholanic-HEA$_{90}$ in d$_6$-DMSO.
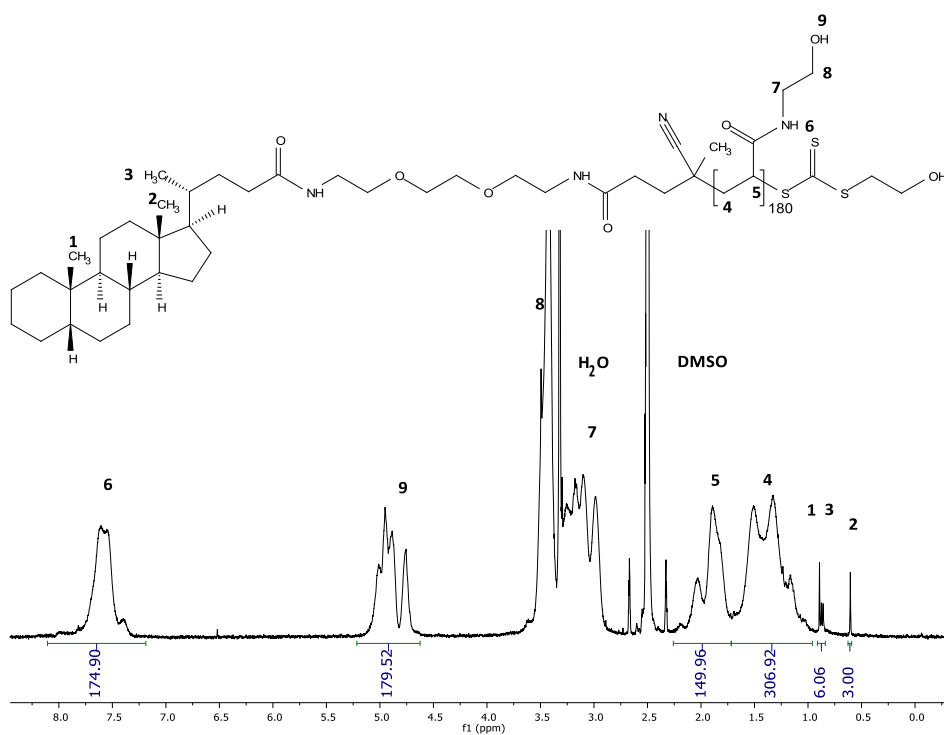


Figure S5.13: $^1$H NMR spectrum of Cholanic-HEA$_{180}$ in d$_6$-DMSO.

375
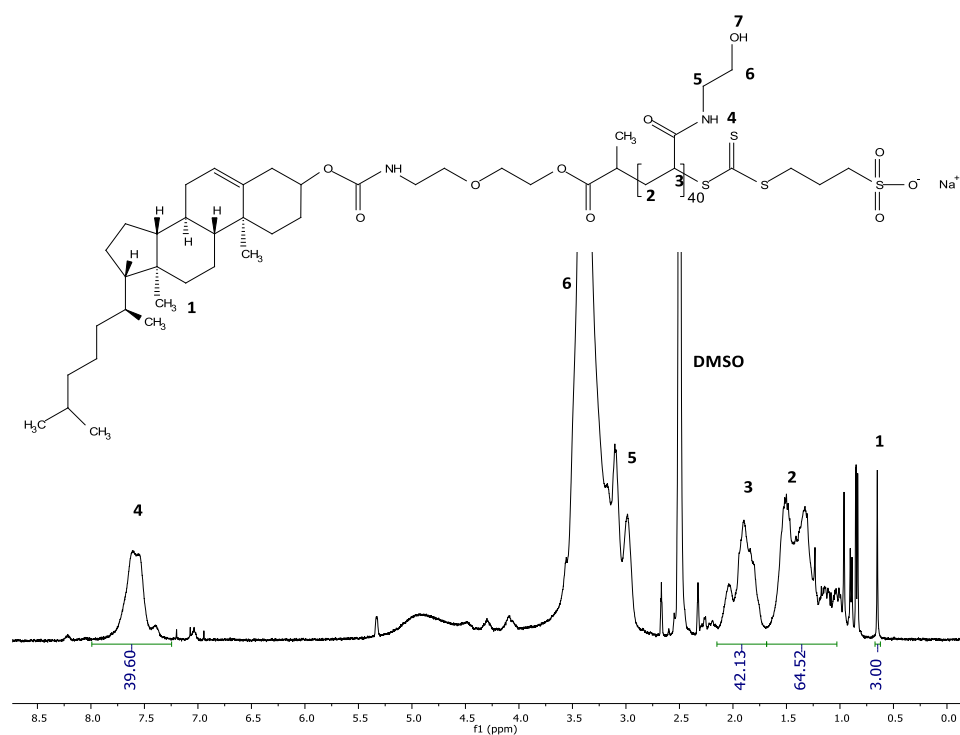
Figure S5.14: $^1$H NMR spectrum of Cholesterol-HEA$_{40}$ in d$_6$-DMSO.
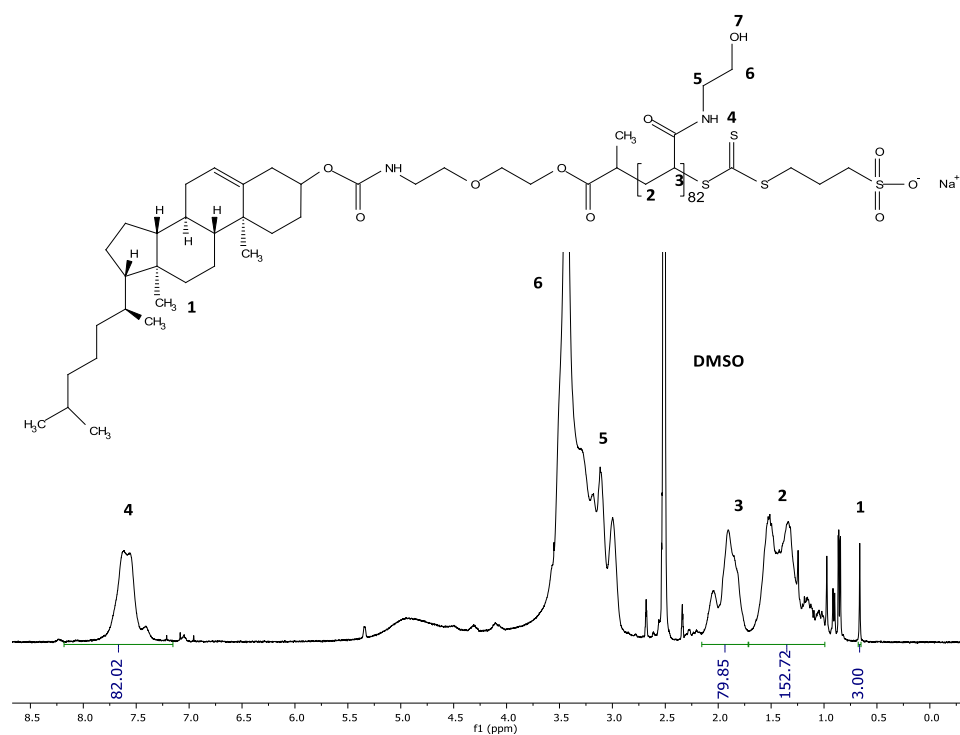


Figure S5.15: $^1$H NMR spectrum of Cholesterol-HEA$_{82}$ in d$_6$-DMSO.
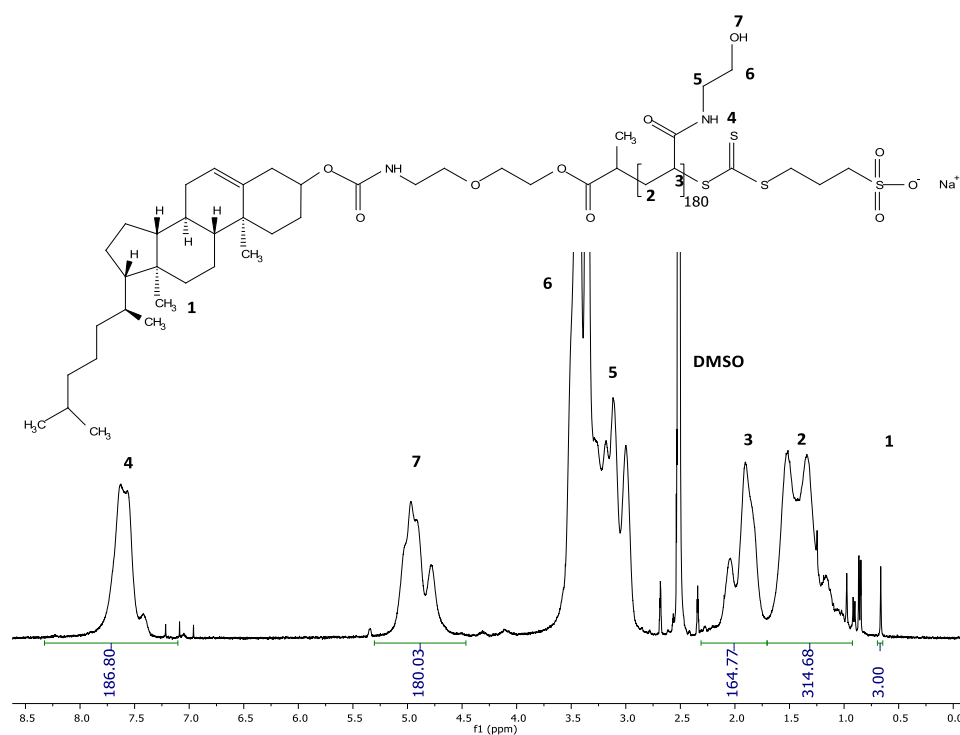
Figure S5.16: $^1$H NMR spectrum of Cholesterol-HEA$_{180}$ in d$_6$-DMSO.
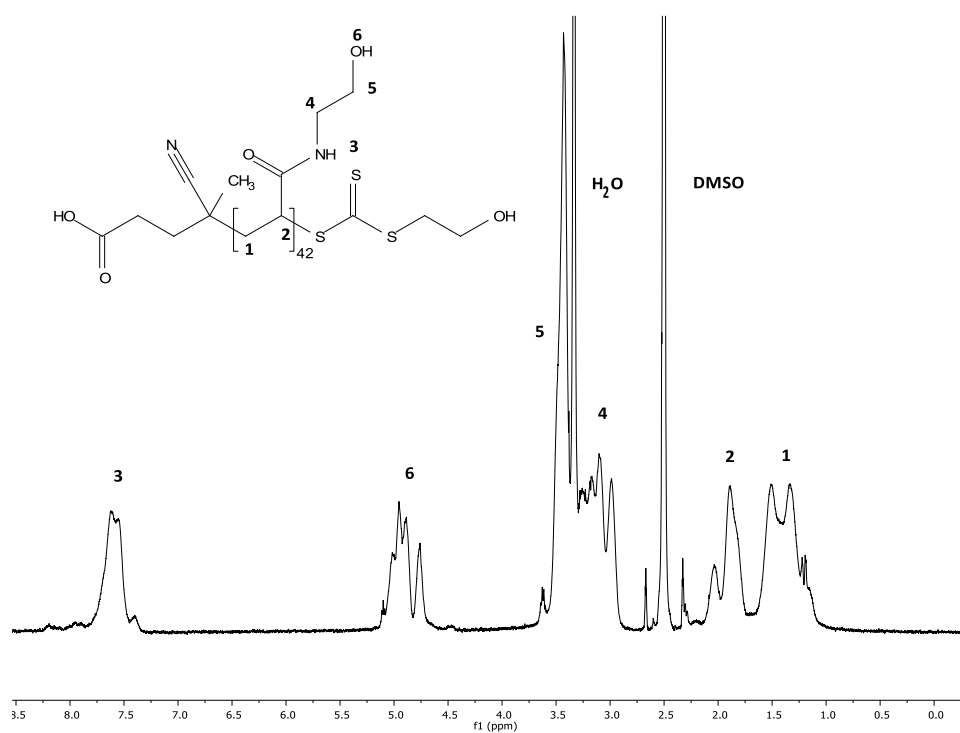


Figure S5.17: $^1$H NMR spectrum of HEA$_{42}$ in d$_6$-DMSO.
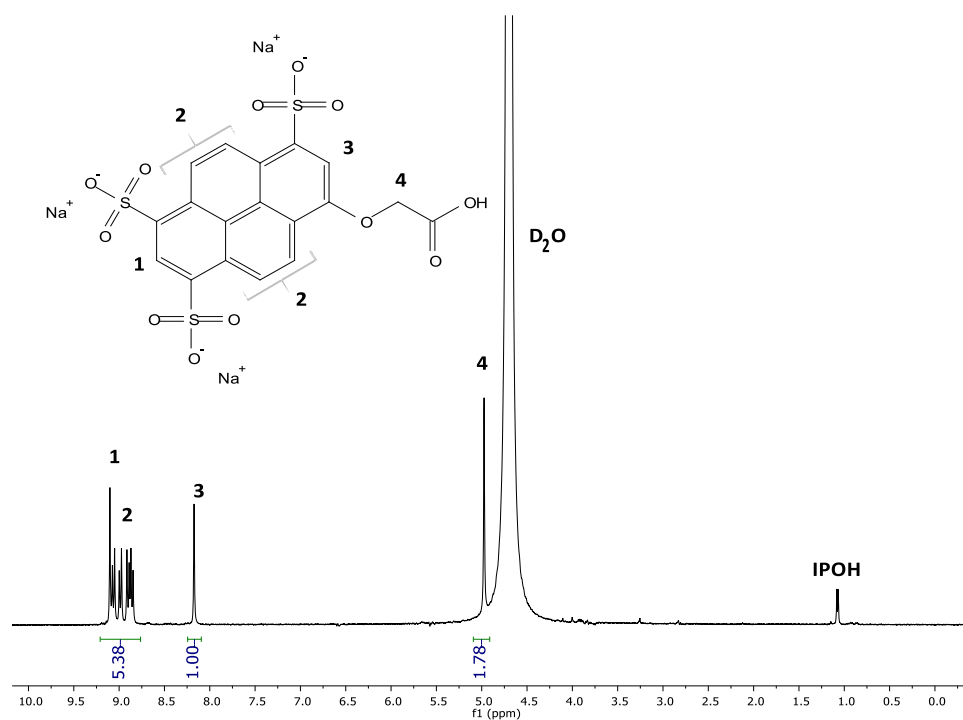
Figure S5.18: $^1$H NMR spectrum of 8-O-Carboxymethylpyranine (CM-Pyranine) **(21)** in D$_2$O.
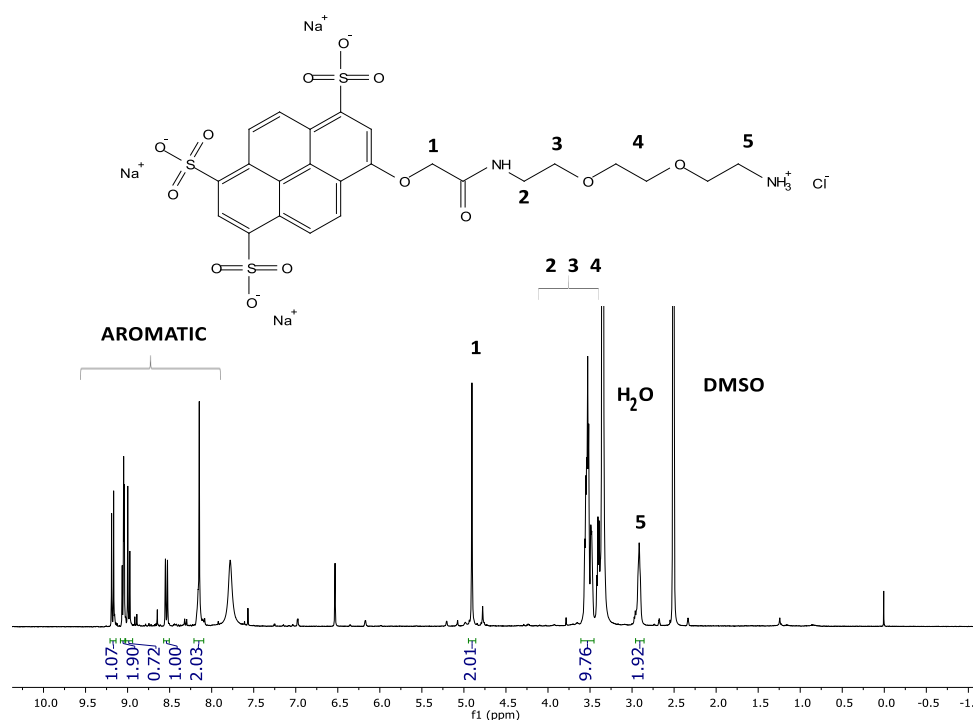


Figure S5.19: $^1$H NMR spectrum of Cascade Blue-amine **(22)** in d$_6$-DMSO.

378
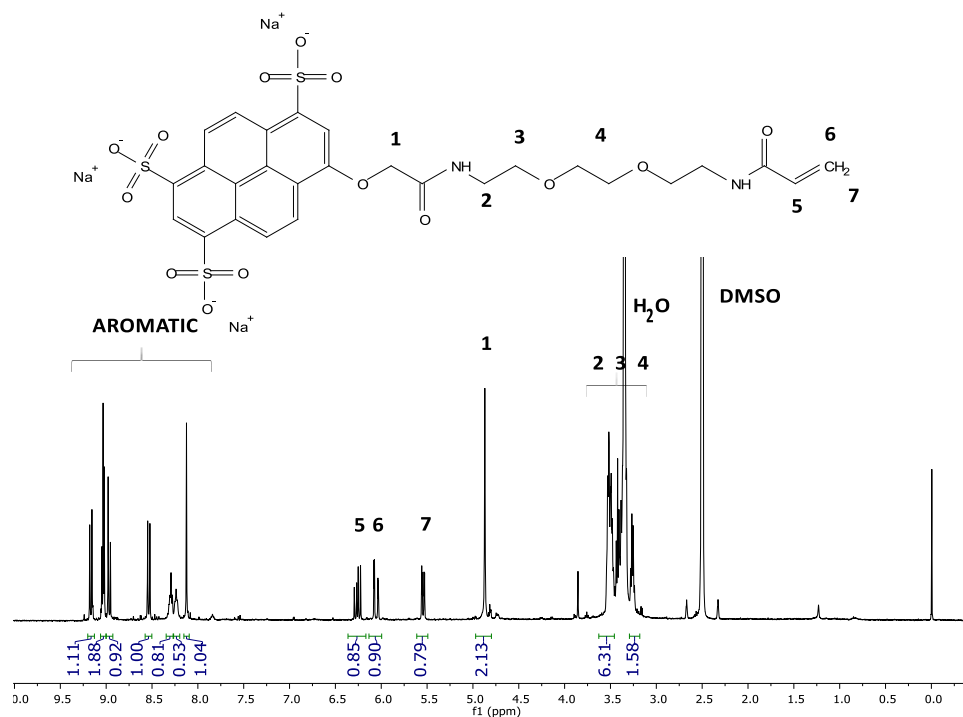
Figure S5.20: ¹H NMR spectrum of Cascade Blue-acrylamide **(23)** in d₆-DMSO.
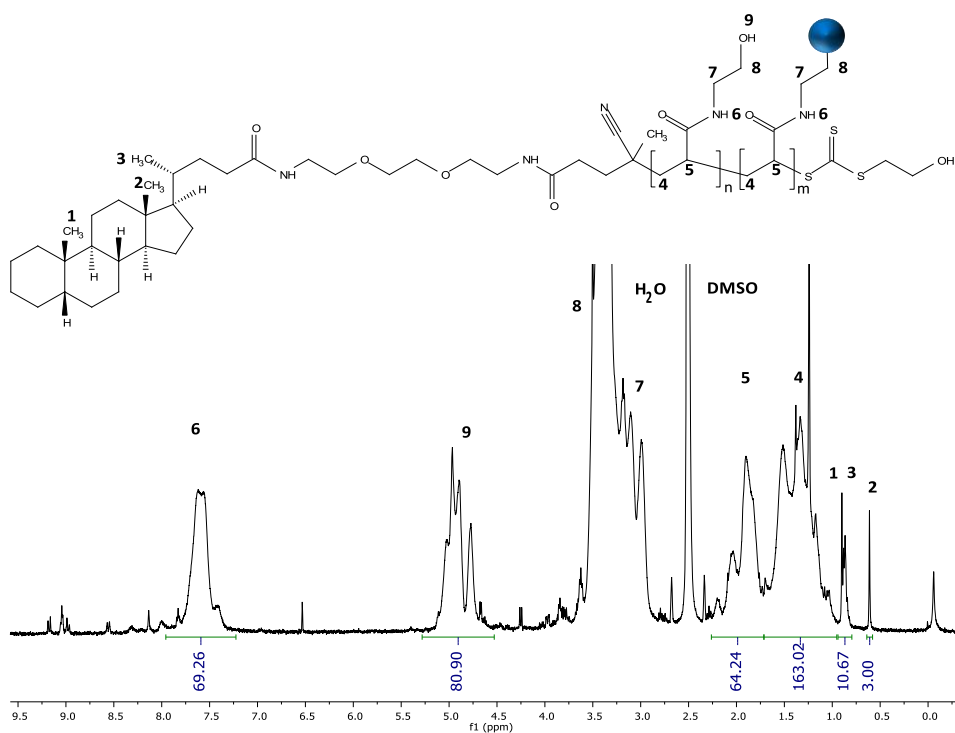


Figure S5.21: ¹H NMR spectrum of CholanicFLUO-HEA₈₀ in d₆-DMSO.
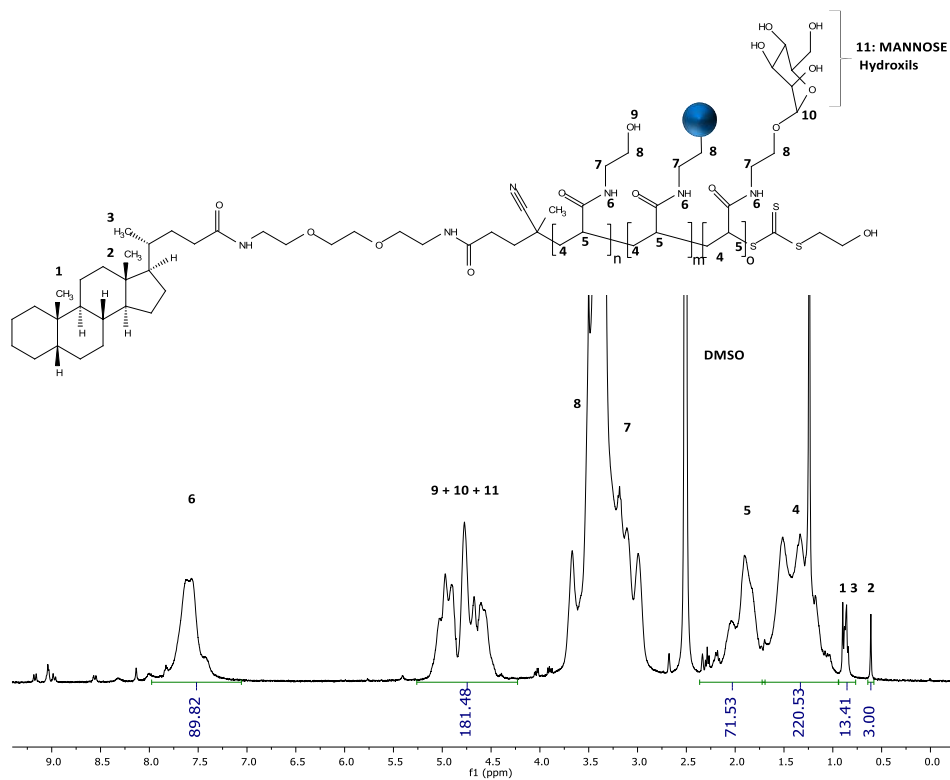
Figure S5.22: $^1$H NMR spectrum of CholanicFLUO-HEA$_{80}$-$b$-MAN$_{20}$ in d$_6$-DMSO.
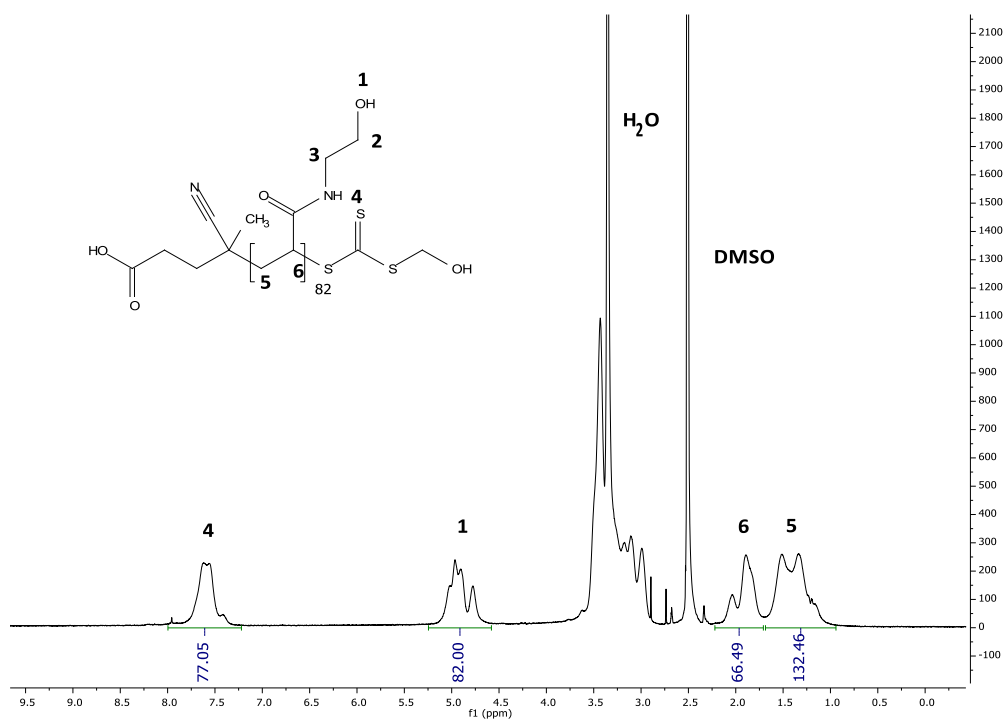


Figure S5. 23: $^1$H NMR spectrum of HEA$_{82}$ in d$_6$-DMSO.
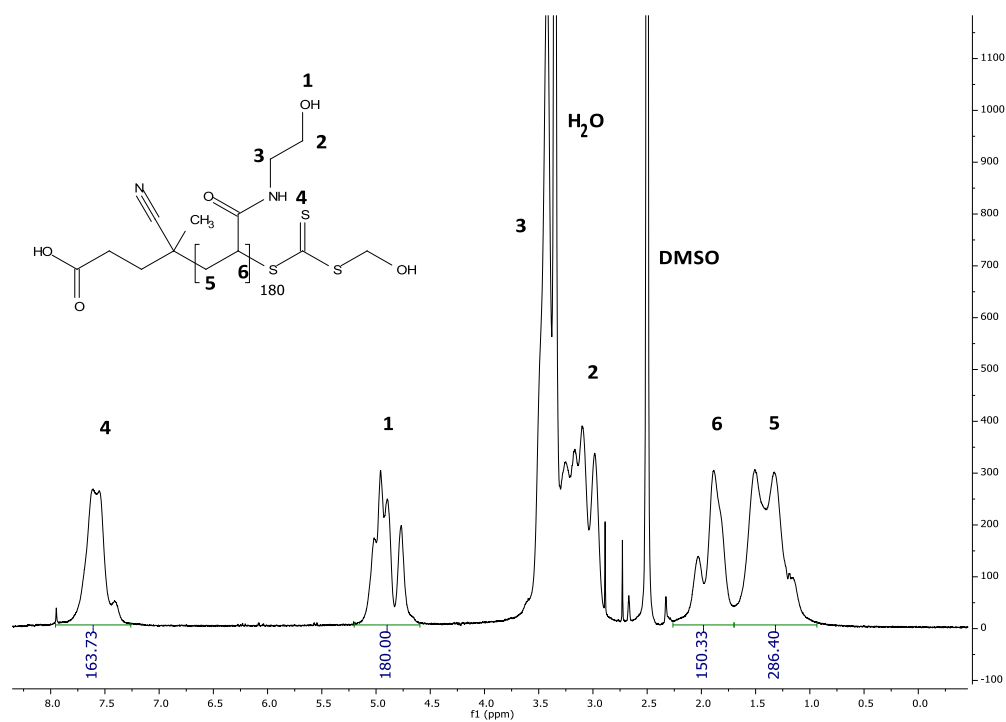
Figure S5.:24: Figure S5. 25: $^1$H NMR spectrum of HEA$_{180}$ in d$_6$-DMSO.
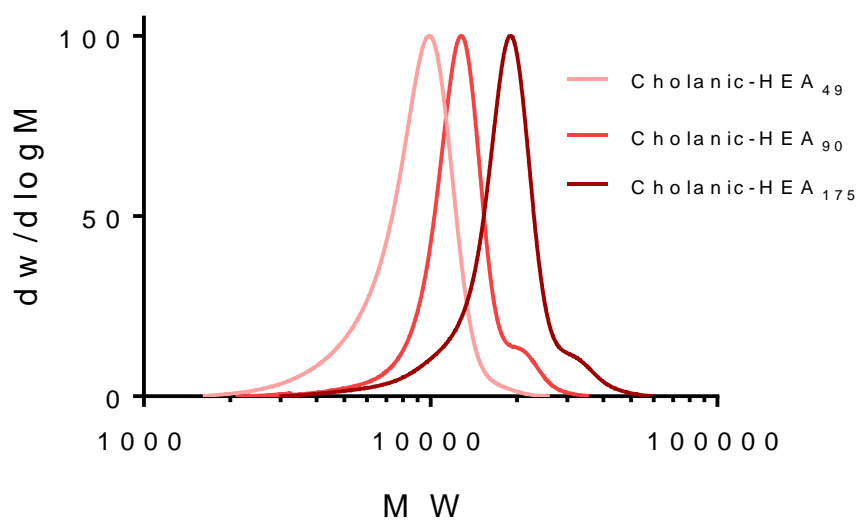


Figure S5.26: normalised SEC traces of Cholanic-poly(HEA) polymers. SEC analyses were performed in DMF + 0.1 % LiBr (PMMA standards).
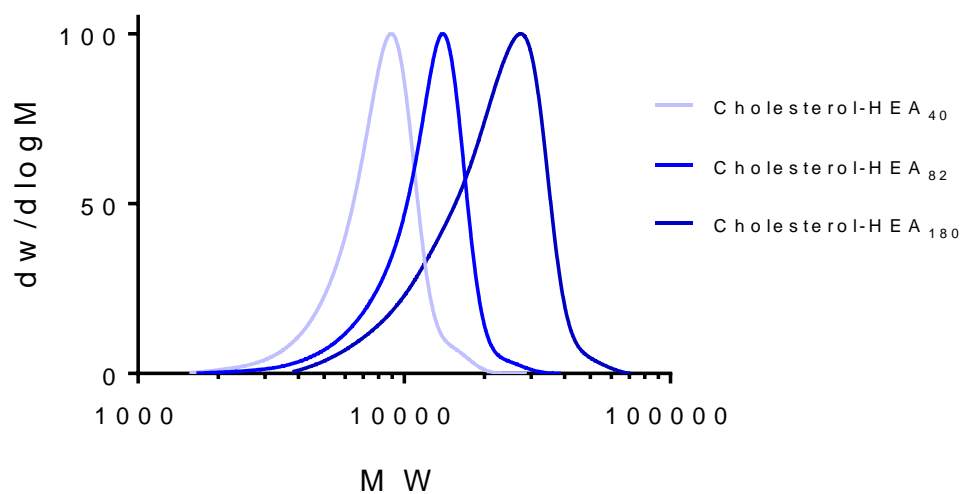
Figure S5.27: normalised SEC traces of Cholesterol-HEAs polymers. SEC analyses were performed in DMF + 0.1 % LiBr (PMMA standards).
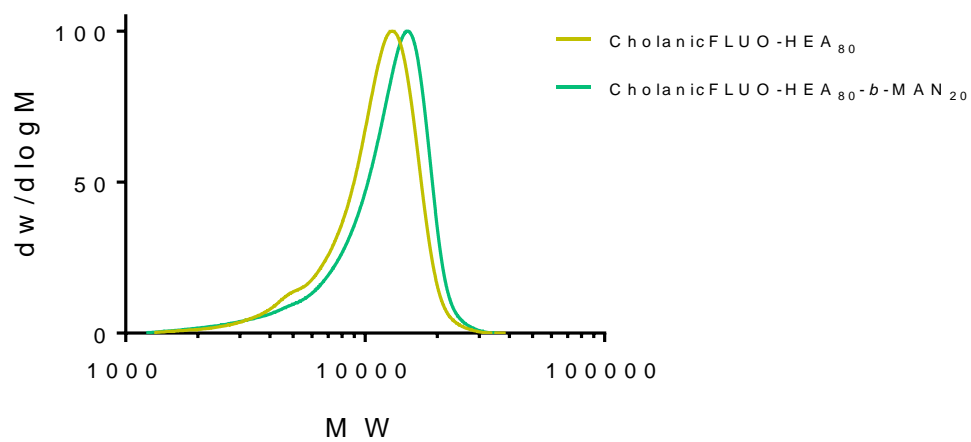


Figure S5.28: normalised SEC traces of CholanicFLUO-HEA$_{80}$ and CholanicFLUO-HEA$_{80}$-b-MAN$_{20}$. SEC analyses were performed in DMF + 0.1 % LiBr (PMMA standards).
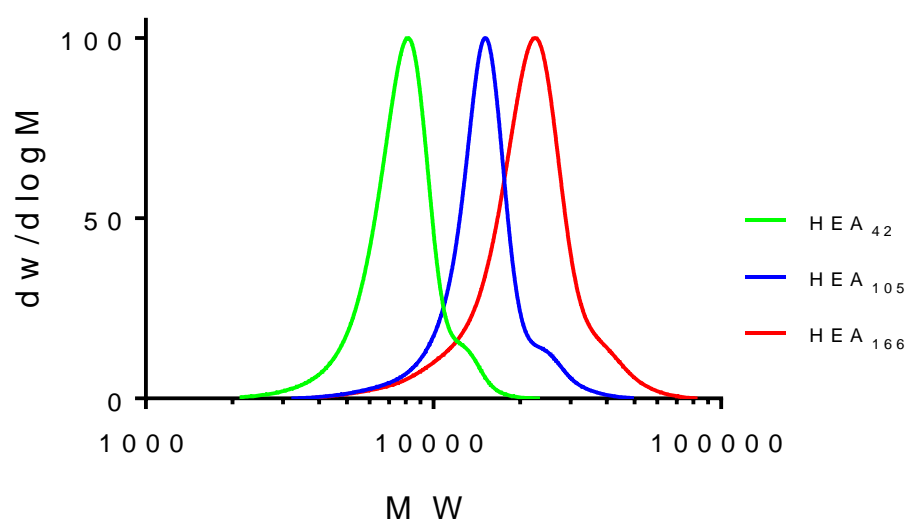
Figure S5.29: normalised SEC traces of controls HEA$_{42}$, HEA$_{105}$ and HEA$_{166}$. SEC analyses were performed in DMF + 0.1 % LiBr (PMMA standards).
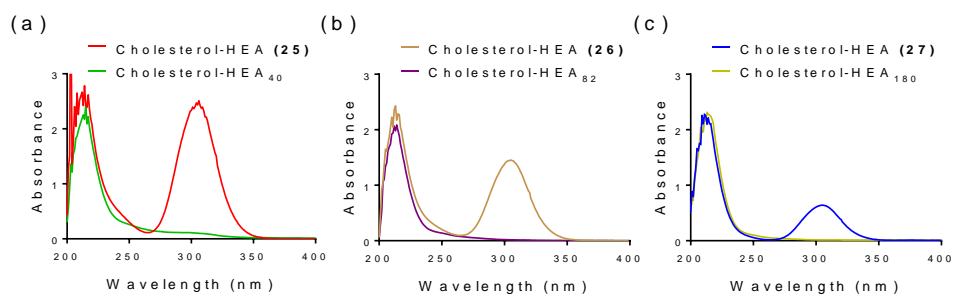


Figure S5.30: Removal of trithiocarbonate polymer chain-ends. UV spectra of (a) Cholesterol-HEA **(25)**, (b) Cholesterol-HEA **(26)** and (c) Cholesterol-HEA **(27)** (before removal of the trithiocarbonate moiety), and (a) Cholesterol-HEA$_{40}$, (b) Cholesterol-HEA$_{82}$ and (c) Cholesterol-HEA$_{180}$ (after removal). The progress of the reaction was followed by monitoring the disappearance of the band at $\lambda_{max} \sim 310$ nm.
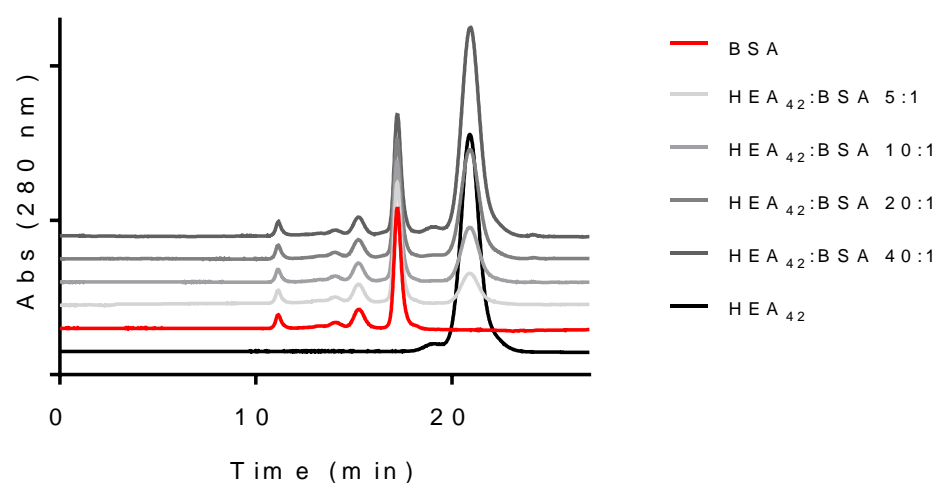
Figure S5.31: Size Exclusion Chromatography profiles of BSA, HEA$_{42}$, and mixtures between the polymer and the protein at different polymer:protein molar ratios. BSA was eluted at a concentration of 0.5 mg/mL, HEA$_{42}$ was added at 5, 10, 20 and 40:1 polymer-protein molar ratios. The polymer was eluted alone at the same concentration used for the 40:1 mixture. Samples were eluted at 0.5 mL/min using DPBS as mobile phase.
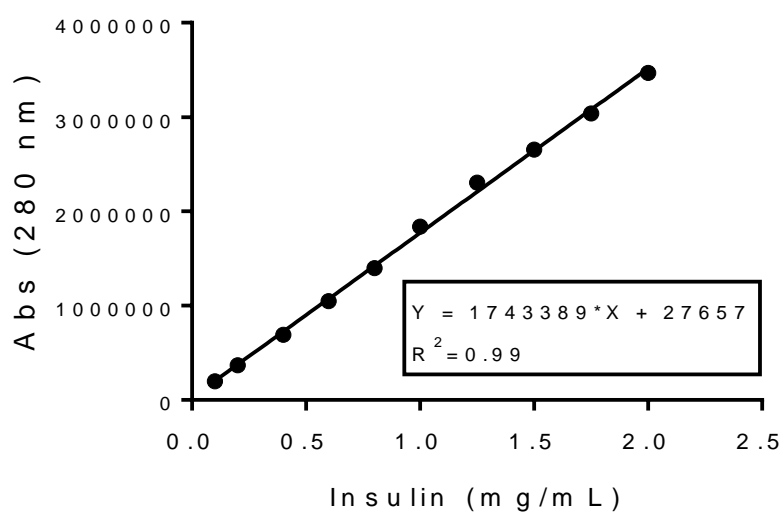


Figure S5.32: insulin calibration curve. Insulin was dissolved in 10 mM pH2 phosphate buffer at different concentrations in the 0.1-2 mg/mL range. The samples were analysed in triplicates by RP-HPLC, using a 20-80% MeCN gradient in Milli-q water + 0.1 % TFA. Absorbance was recorded at 280 nm. The area under insulin peak was calculated for each concentration.
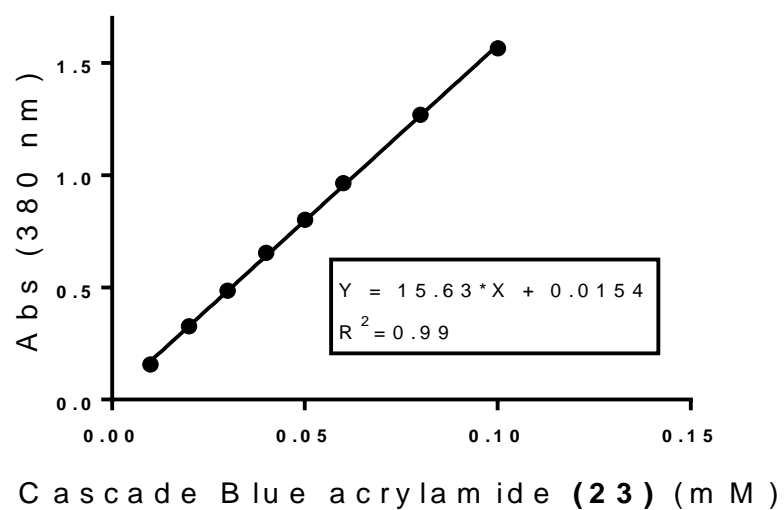
Figure S5.33: Cascade Blue acrylamide **(23)** calibration curve. Cascade Blue acrylamide **(23)** was dissolved in methanol at different concentrations in the 0.01-0.1 mM range. Absorbance was recorded at 380 nm.

# Chapter 6

**Triazolyl methacrylates glycopolymers as unimolecular vectors for hydrophobic drugs**

_____

*This chapter is presented in a form of a draft paper, and it is the continuation of a work from a previous PhD student, Joao Madeira Do O. Joao was responsible for the synthesis of the glycopolymers utilised in this chapter. He also was the first to notice the interaction occurring between small hydrophobic probes and these polymers. During my PhD, I have investigated this interaction using Nile Red as a model for hydrophobic drug incorporation. Francesca Mastrotto, former Research Fellow within our group, performed the cell culture uptake studies. Gokhan Yilmaz, current Research Fellow within our group, performed the Con A- and PNA- affinity studies. Taylor Dispersion analyses were conducted in Malvern, UK, by Dr. Patrick King and Rachael Xerri, PhD student within our group.*

Unimolecular micelles have gained increasing attention as efficient alternative to self-assembling macromolecules for drug delivery applications. Being based on individual polymer chains, these unimolecular carriers do not disassemble at low concentrations upon *in vivo* administration, at it may happen to traditional nanoparticles-based systems. Here, we describe the reversible incorporation of small hydrophobic probes into linear and 4-arm glycopolymer chains. Poly(propargyl methacrylate)s of well-defined molecular weight and low molar mass dispersity were synthesised by ATRP and then functionalised with appropriate sugar azides by copper-catalysed alkyne-azyde cycoaddition (CuAAC), obtaining final sugar triazolyl methacrylates glycopolymers. Nile Red and DCJV dyes were employed to demonstrate the ability of these glycopolymers to incorporate hydrophobic drugs. In particular, incorporation of Nile Red was assessed by fluorescence analysis of polymers-Nile Red mixtures at different Nile Red:polymers molar ratios. The unimolecular behaviour of the glycopolymers was confirmed as no Critical Aggregation Concentration (CAC) could be detected by Surface Tension, Dynamic Light Scattering (DLS) and Nile Red fluorescence analysis. The size of the single polymeric chains, in the absence and presence of Nile Red, was further analysed

by DLS and Taylor Dispersion Analysis, revealing size between 3 and 5 nm, compatible with the presence of singular polymers chain. The potential application of these glycopolymers as unimolecular vectors for targeted drug delivery was confirmed by affinity chromatography assays. Taken together, these results show that sugar triazolyl methacrylates glycopolymers can act as unimolecular micelles, reversibly incorporating small hydrophobic drugs, with potential applications for drug delivery.

## Introduction

In recent years, the development of synthetic single-chain macromolecular devices has been the subject of a considerable research effort. One notable example of this are single-chain polymeric nanoparticles (SCPNs), where polymer chains are designed to fold at predefined points of their repeating units sequence,[1] mimicking in concept the formation of folded structures in natural proteins. SCPNs can be obtained following the formation of covalent or non-covalent intramolecular interactions.[2-5] Accordingly, concerted effort between macromolecular chemists and biophysicists has provided access to increasingly sophisticated single-chain molecular devices with potential applications in catalysis, sensors, nanoreactors, and nanomedicine.[4-6]

Lemcoff,[7-9] Pomposo[10] and Zimmerman's[11] groups engineered single-chain metal−organic nanocatalysts sharing key structural and functional similarity with metalloenzymes. In biomedical settings, the size of nanovectors can affect their ability to cross biological barriers. For example, whilst sub-100-nm micellar nanostructures are able to permeate hypervascular solid tumours, only sub-50-nm nanocarriers can extravasate and penetrate poorly permeable

hypovascular tumours.[12, 13] Thus, possibility of scaling their size down to that of individual polymer chains has the potential to result in considerable clinical benefit.

Unimolecular micelles are molecular devices where polymers chains are designed to possess a core–shell morphology mimicking that of self-assembled micelles.[14, 15] Being based on individual polymer chains, unimolecular micelles possess the advantage of not unfolding or disassembling at low concentrations such as those encountered in clinical settings *in vivo*, which is key for potential applications in drug delivery and (bio)imaging.[16-21] Such molecular devices often include a hydrophobic core with hyperbranched or dendrimeric structure which can non-covalently complex hydrophobic drugs, and an external multi-chain hydrophilic corona.[18, 22, 23] Alternative structures have also been described, such as the 'polysoaps' assembled by McCormick and co-workers by statistical RAFT copolymerization of 2- acrylamido-2-methylpropane sulfonic acid (AMPS) and *n*-dodecyl acrylamide (DDAM) at specific molar ratios.[22]

Jenkins and co-workers have utilised a peptide transporter, K16ApoE, to non-covalently bind a range of protein cargoes through polyionic interactions, and transport them through the blood brain barrier through its LDLR-binding domain of apolipoprotein E (ApoE).[24, 25]

Inspired by these examples, here we explore a minimalistic approach to single-chain vectors, where guest molecules are reversibly incorporated within individual linear and 4-arm glycopolymer chains - as opposed to self-assembled

and/or hyperbranced-like structures - and pendant functionalities are used to provide recognition to specific biological targets.

# Results and discussion

**Sugar poly(triazolyl methacrylate)s: interaction with hydrophobic fluorescent probes.** The linear and 4-arm star triazolyl methacrylate glycopolymers investigated in this work), were prepared by copper-catalysed alkyne-azyde cycoaddition (CuAAC) functionalisation of preformed poly(glycerol methacrylate)s with appropriate sugar azides, as first reported by Haddleton and us.[26, 27] Importantly for this study, this approach allows to prepare libraries of glycopolymers starting from the same functionalisable 'master polymer precursor', leading to families of glycopolymers which only differ for the nature of the pendant carbohydrate units, but share all the other macromolecular characteristics – i.e. degree of polymerisation (DP), macromolecular topology (e.g. linear *vs.* branched), and molecular weight dispersity (Đ).



**(1)MAN** DP_NMR 66,
M_n,SEC 24.9 kDa, Đ_SEC = 1.22

**(2)MAN** DP_NMR 77,
M_n,NMR 29.5 kDa, Đ_SEC = 1.25
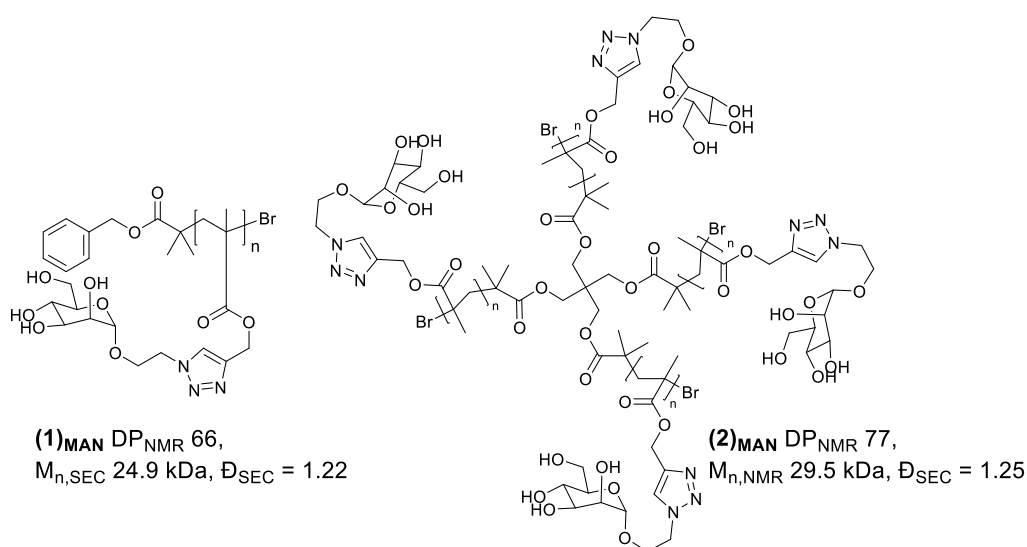
Figure 6.1: Mannosylated linear **(1)MAN AND** 4-arm star **(2)MAN** glycopolymers investigated in this study.

This work focusses primarily on mannosylated materials **(1)**MAN and **(2)**MAN (Figure 6.1), although analogous glycopolymers bearing different pendant carbohydrate units – galactose, lactose and trehalose - were also investigated to identify the general structure-activity relationships of these materials (*vide infra*). Linear **(1)**MAN and 4-arm star **(2)**MAN polymers were made with similar degrees of polymerisation – DP 66 and 77, respectively - to allow to identify the effect of the macromolecular topology on their physico-chemical properties, and on their ability to interact with host molecules.

During a previous study focussed on the use of glycopolymers as modulators of monoclonal antibodies aggregation,[28] we observed that polarity-responsive extrinsic fluorescent dyes Nile Red and SYPRO-Orange interacted with triazolyl methacrylate glycopolymers in aqueous media, resulting in highly fluorescent solutions (data not shown). Both these fluorophores possess low quantum yields in aqueous media, resulting in a low fluorescence intensity, which increases in more non-polar environments.[29, 30] Sugar triazolyl methacrylates glycopolymers have been extensively investigated.[31-42] Yet, to the best of our knowledge, this behaviour, suggestive of their surfactant-like properties and of their ability to non-covalently bind hydrophobic probes under aqueous conditions, has never been described. This present study addresses this gap, by investigating the mechanism and modalities of glycopolymer:probe host-guest interactions, and suggests potential routes for the use of these materials as nanovectors for targeted drug delivery.

Although some possible structures have been suggested,[27, 30] the absolute molecular identity of SYPRO-Orange has not yet been disclosed. Thus, to allow a meaningful investigation on glycopolymer:probe interactions, in this study Nile Red was selected as the hydrophobic fluorophore of choice.

In initial experiments, a solution of Nile Red in THF, was added to DI water to achieve a theoretical final concentration of 20 µg mL$^{-1}$. After evaporation of THF cosolvent, in the absence of glycopolymers **(1)MAN** and **(1)MAN**, Nile Red was found to form a mixture consisting of red-pink precipitate in a colourless-very lightly pink liquid phase (Figure 6.2B), which is consistent with the very low solubility reported for Nile Red in water (< 1 µg mL$^{-1}$).[43] In the presence of triazolyl glycopolymers **(1)MAN** and **(2)MAN** (0, 50, 100, 1000 µg mL$^{-1}$) a visible pink coloration, with intensity increasing with polymer concentration, was observed.

Next, solutions of **(1)MAN** in deionised water (10 and 100 µg mL$^{-1}$) were treated with increasing concentrations of Nile Red (50-1000 µg mL$^{-1}$).The observed fluorescence was found to reach its maximum at approximately 0.5-1 molecules of Nile Red per polymer chain (Figure 6.2C). Interestingly in the experiments with the highest concentration of glycopolymer **(1)MAN** (100 µg mL$^{-1}$) a clear decrease of fluorescence was observed at high [Nile Red]:[**(1)MAN**] ratios. This could be explained with the fact that in aqueous media Nile Red is known to form non-emissive H-type dimers and aggregates through π–π stacking interactions.[44, 45] As expected, this effect was more evident in the set of samples with the highest concentration of glycopolymer **(1)MAN** (100 µg mL$^{-}$

$^1$), which required larger amounts of Nile Red to achieve the same [Nile Red]:[**(1)**$_{MAN}$] ratios. Samples prepared in PBS at the same polymer concentrations resulted in analogous fluorescence vs. concentration profiles (Figure S6.3), hence for the subsequent experiments deionised water was used as the dispersing medium.
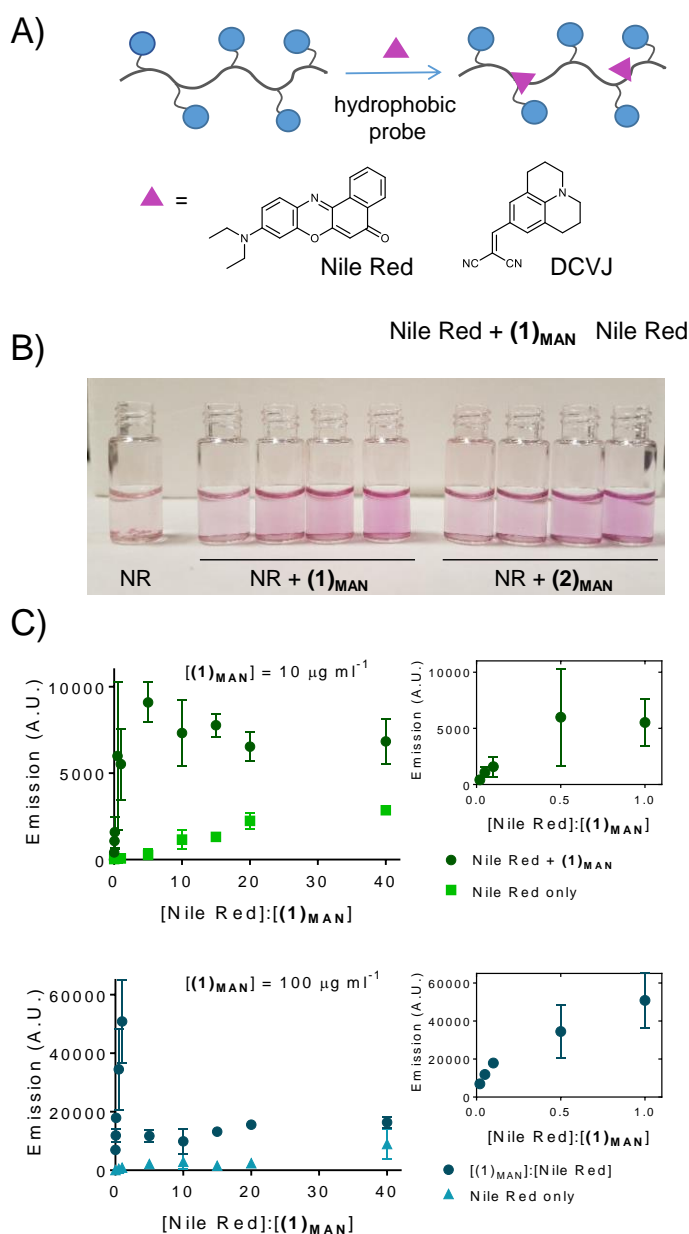


Figure 6.2 interaction of triazolyl methacrylate glycopolymers with hydrophobic fluorescent probes: A) graphical illustration of single chain-probe interaction, and chemical structure of hydrophobic fluorophores utilised in this study – Nile Red and DCVJ. B) Left: Nile Red (NR), 20 µg mL$^{-1}$ in DI H$_2$O. Centre and right: 20 µg mL$^{-1}$ NR + linear **(1)**$_{MAN}$ (centre) and 4-arm star **(2)**$_{MAN}$ (right) at increasing concentration of glycopolymers (0, 50, 100, 1000 µg mL$^{-1}$). C) Fluorescence readings ($\lambda_{ex}$ 550 nm, $\lambda_{em}$ 630 nm) of Nile Red – **(1)**$_{MAN}$ samples at variable [Nile Red]:[polymer chains] molar ratios, in DI H$_2$O. Insets: magnification of the 0-1.0 [Nile Red]:[**(1)**$_{MAN}$] region.

**Sugar poly(triazolyl methacrylates): unimolecular micelles *vs.* higher order assemblies.** To investigate the potential aggregation behaviour of polymers **(1)**$_{MAN}$ and **(2)**$_{MAN}$ – that is, whether or not they are able to form supramolecular assemblies in aqueous solution – surface tension studies were undertaken.

Surface tension ($\gamma$) of aqueous media is reduced in the presence of chemical species able to adsorb at air/water the interface, i.e. surfactants.[46] Typical $\gamma$ vs. [surfactant] plots are sigmoidal curves with three distinct zones. At low concentrations, the air/water interface is scarcely populated by surfactant molecules, which in turn induces only relatively small changes of surface tension.[46, 47] As the concentration of surfactant increases, cooperativity among the adsorbed surfactant molecules at the interface induces a sharp decrease of $\gamma$, until saturation (or quasi-saturation) of the interface is reached.[46, 47] After this point - the onset of aggregation (critical micellar concentration (CMC) if micelles are formed) - any further added surfactant results in the formation supramolecular assemblies, and does not induce any further significant decrease of surface tension.

In this study, for aqueous solutions of both **(1)**$_{MAN}$ and **(2)**$_{MAN}$ the surface tension was found to steadily decrease as the polymer concentration increased, without reaching a plateau, throughout the range of concentrations tested (0.020-5.0 mg mL$^{-1}$) (Figure 6.3A). This suggested that, under these conditions, these materials exist in solution as individual polymeric chains. An analogous behaviour - that is, $\gamma$ *vs.* [surfactant] plots lacking the third zone, the plateau which is used to identify the CMC - has been described in previous studies for

unimolecular micelles macromolecules designed with topologies resembling those of self-assembled micelles. For example, Uhrich and co-workers utilised surface tension measurements to prove that encapsulation of hydrophobic payload lidocaine into mucic acid-fatty acids-PEG branched polymers was caused by individual unimolecular micelles.[48] McCormick's group showed that random copolymers with selected molar ratios of 2- acrylamido-2-methylpropane sulfonic acid (AMPS) and *n*-dodecyl acrylamide (DDAM) possessed unimolecular micellar features, and, similarly to what observed in our work, induced a continuous decrease of surface tension in the range of concentrations investigated (up to 10 mg mL$^{-1}$).

In terms of structure-function relationship, 4-arm star **(2)$_{MAN}$** induced a larger drop in surface tension γ compared to its linear counterpart **(1)$_{MAN}$**, 66.5 vs. 70.2 mN/m at the highest concentration tested, respectively (Figure 6.3A).

The observed surfactant-like properties of triazolyl methacrylates **(1)$_{MAN}$** and **(2)$_{MAN}$** suggested a partial orientation of the hydrophobic polymer backbone towards air at the water-gas interphase. To gain further insight on how the balance between the hydrophilic sugar pendant units and the more hydrophobic polymer backbone affects the surfactant-like behaviour of these materials, these experiments were repeated using analogous linear and 4-arm star polymers bearing larger sugar units, namely D-lactose and α,α-trehalose disaccharides, **(1)$_{LAC}$** and **(2)$_{LAC}$**, and **(1)$_{TRE}$** and **(2)$_{TRE}$**, respectively (Chart S6.4). As these were prepared from the same 'master polymer precursors',[28] they possessed the same macromolecular features – average number of repeating

units (DP), dispersity (Đ), and topology (linear and star) – as **(1)**MAN and **(2)**MAN, and thus allowed to dissect the contribution of the nature of the carbohydrate pendant units on the surfactant-like behaviour of the corresponding glycopolymers. Results indicated that: *i)* glycopolymers with larger hydrophilic sugar pendant units induced a lower overall decrease in surface tension γ, compared to **(1)**MAN and **(2)**MAN, showing that the hydrophobic/hydrophilic balance between the polymer backbone and the carbohydrate pendant units affects the surfactant-like properties of these materials; *ii)* 4-arm star polymers still induced a larger decrease in γ, which is in line with what already observed for **(1)**MAN and **(2)**MAN, and *iii)* again, no CMC could be observed (Figure S6.5). Taken together, surface tension analysis of these glycopolymers suggested that, in the range of concentrations and conditions investigated, they could exist as non-aggregated individual polymer chains.

Next, the aggregation behaviour of poly (triazolyl methacrylates) **(1)**MAN and **(2)**MAN was probed by dynamic light scattering (DLS), by following the profile of the intensity of scattering as the concentration of glycopolymers increased. This method relies on the fact that that micelles or other self-assembled aggregates scatter light orders of magnitude more strongly than their smaller individual component, such as free surfactant molecules,[49] which can be used to identify the onset of surfactant aggregation (CMC). In this study, DLS measurements with **(1)**MAN and **(2)**MAN showed a linear increase of scattering in the 0.0010-2.0 mg mL$^{-1}$ range of concentrations investigated (Figure 6.3B), and, again, no CMC could be identified. in agreement with the results obtained in the surface tension experiments.

However, whilst surface tension and DLS particle count experiments suggested that glycopolymers **(1)MAN** and **(2)MAN** exist as individual chains in solution, in principle the presence of a hydrophobic probe may favour self-assembly. For example, Mohr and co-workers showed that Nile Red can promote the formation of dye-loaded SDS, CTAB and Triton X micelles already at submicellar surfactant concentrations.[45]

To investigate this possibility, the ability of these materials to interact with Nile Red model hydrophobic probe was initially investigated by fluorescence spectroscopy ($\lambda_{ex}$ = 550 nm). The working hypothesis was that that if above a certain polymer concentration micelles or higher order assemblies with a hydrophobic core were formed, a significant increase of fluorescence due to more efficient dye incorporation would have been observed (though we were aware that dye H-dimerization/aggregation within these polymer assemblies could have potentially affected the final fluorescence readings). First, a constant amount of Nile Red, equivalent to a potential final dye concentration of 2.0 μM, was added to solutions of glycopolymers **(1)MAN** and **(2)MAN** in deionised water in a range of concentrations - 0.0050-2.0 mg mL$^{-1}$, corresponding to a [polymer]:[dye] = 0.10-40 for **(1)MAN**, and 0.084-34 for **(2)MAN**. These experiments aimed at looking for discontinuity in the emission intensity *vs.* concentration plot, which could suggest the formation of self-assembled structures with a hydrophobic core able to enhance Nile Red incorporation. Sample fluorescence was found to increase almost linearly as the concentration of glycopolymers increased, with a tailing at higher concentrations for the star polymer **(2)MAN** (Figure 6.3C). As the amount of

added dye was the same for all samples, this enhancement could simply be due to the ability of increasing number of glycopolymers chains to keep in solution larger amounts of Nile Red molecules. An additional contribution might come from the fact that at low concentration of solubilising glycopolymers, low fluorescence may be due to higher proportion of non-emissive dye H-dimers/aggregates, either in aqueous solution, or within the polymer carrier.[45] Nile Red is known to undergo a blue shift of the maximum of emission as the polarity of the surrounding (micro)environment decreases.[43, 50, 51] In these experiments we observed a shift from 650 nm, close to that of Nile Red in water, at the lowest [polymer]:[dye] ratios (0.010 and 0.0084 for linear **(1)**MAN, and star **(2)**MAN, respectively), to 632-634 nm, starting from [polymer]:[dye] ~ 0.5-1 (Figure S6.6). This agrees with what observed by Alexiev and co-workers[51] and Mohr's group[45] for polyglycerol-based core-multishell nanotransporters, and lipid micelles, respectively, where a blue shift of fluorescence emission was ascribed to the incorporation of the dye within hydrophobic domains of their nanocarriers.
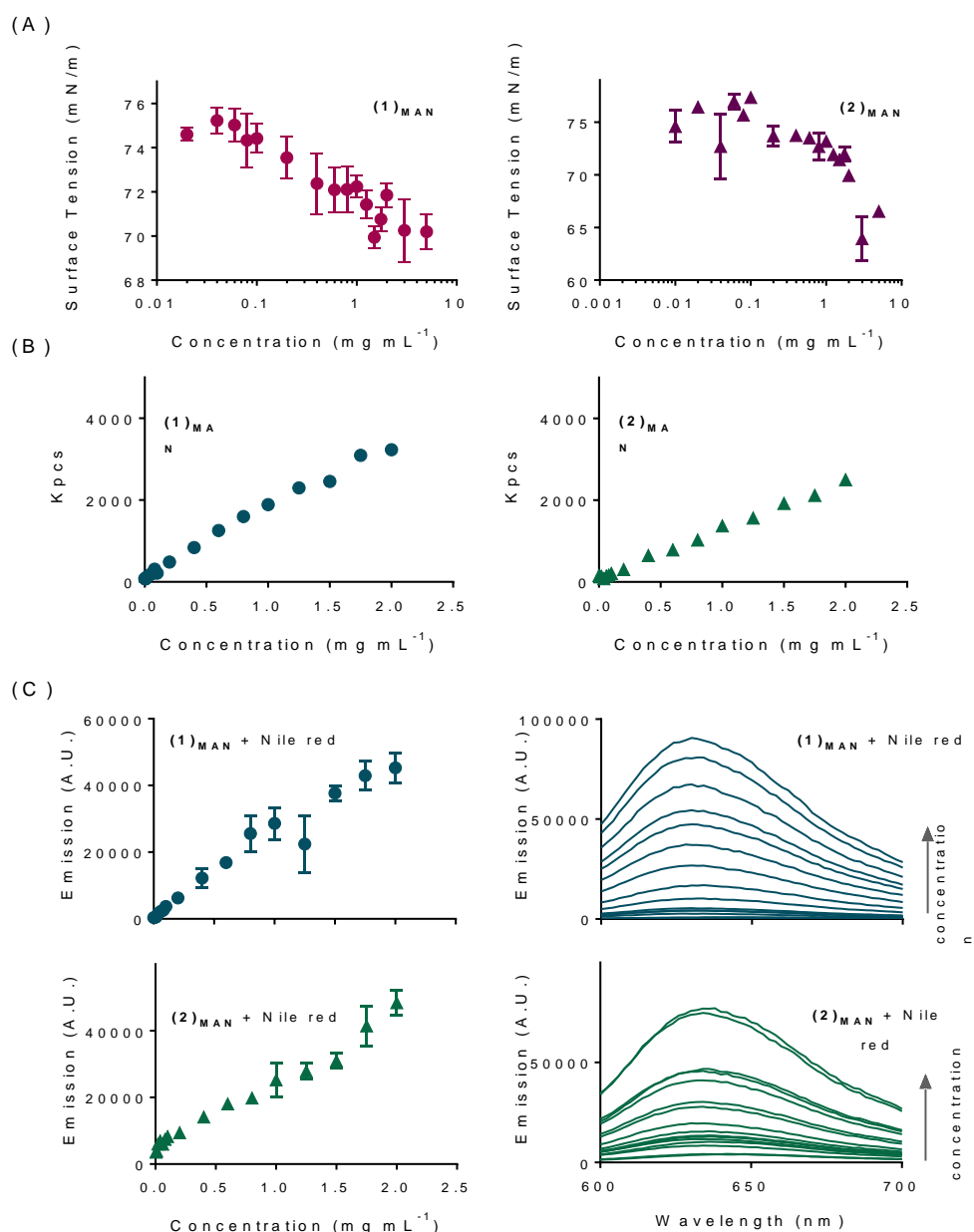
Figure 6.3: A) Surface tension of solutions of linear **(1)**MAN and 4-arm star **(2)**MAN glycopolymers in DI H$_2$O at increasing concentrations (n=2, triplicates). B) Intensity of light scattering as a function of glycopolymer concentration, as measured by dynamic light scattering (DLS) analysis **(1)**MAN and **(2)**MAN. C) Left: fluorescence ($\lambda_{em}$ = 630 nm) vs. concentration profiles for samples containing Nile Red (equivalent to a theoretical final dye concentration of 2.0 µM) and solutions of **(1)**MAN and **(2)**MAN at increasing polymer concentrations. Right: emission spectra of these samples, at $\lambda_{ex}$ = 550 nm.

The aggregation propensity of **(1)**MAN and **(2)**MAN was then investigated by DLS,

by assessing the hydrodynamic volume of the species present in their aqueous

solutions (Figures 6.4A). Results showed a hydrodynamic diameter of ~4.5 nm

for linear **(1)**$_{MAN}$ at 10 mg mL$^{-1}$, without added Nile Red. Upon Nile Red addition, at a 0.1 [dye]:[polymer] molar ratio, large aggregates of size between 300 and 400 nm were observed (Fig. S6.7). Here, our hypothesis was that the aggregates observed consisted mainly of Nile Red aggregates that had not been incorporated into the polymer chains, rather then larger Nile Red-glycopolymer complexes. To confirm this hypothesis, the Nile Red-**(1)**$_{MAN}$ complex solution was filtered using a 0.22 µm PVDF filter. The filtrate, analysed by DLS, showed a hydrodynamic diameter of ~3.5 nm, consistent with the previous analysis performed before Nile Red addition (Fig. 6.4B). In parallel, fluorescence of the filtered solution was investigated, and confirmed the presence of residual Nile Red in solution. A control sample, where Nile Red was sospended in plain water and the sospension filtered with the same 0.22 µm filter, did not show any significant fluorescence, confirming that in the absence of glycopolymer **(1)**$_{MAN}$ Nile Red was virtually insoluble in DI water (Fig. 6.4C). To confirm that in the presence of Nile Red **(1)**$_{MAN}$ did not self-assemble into ≥100 nm particles, a 10 mg mL$^{-1}$ **(1)**$_{MAN}$ solution was prepared in D$_2$O, and Nile Red, previously dissolved in THF, added for a final 1:1 Nile Red:**(1)**$_{MAN}$ molar ratio. To the solution, monomer *N*-hydroxyethylacryalmide (HEA) was added as internal standard for NMR analysis, and the sample, after THF evaporation, filtered with a 0.10 µm PVDF filter. A small and hydrophilic molecule, HEA can freely pass through the filter membrane, thus it can be used an an internal standard to assess any decrease of concentration of polymer **(1)**$_{MAN}$ following filtration through the 0.10 µm filter. The [HEA]:[ **(1)**$_{MAN}$] molar ratio calculated by $^1$H NMR before and after filtration was found to be unchanged, indicating that **(1)**$_{MAN}$ was not

retained by the filter membrane (Fig. S6.8). This further confirmed the hypothesis that Nile Red did not induce **(1)**$_{MAN}$ self-assembly into large (≥100 nm) particles, and suggested that the aggregates observed on the unfiltered solution were due to unicorporated, aggregated dye molecules.
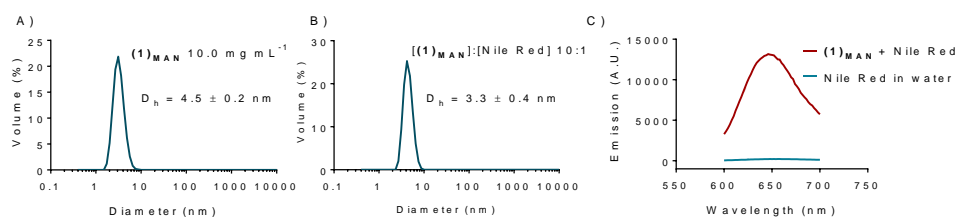


Figure 6.4: A) DLS Size distribution of a 10 mg mL$^{-1}$ water solution of linear mannose poly(triazolyl methacrylate) **(1)**$_{MAN}$ alone. B) DLS Size distribution of **(1)**$_{MAN}$-Nile Red complexes after filtration with a 0.22 μm PVDF filter. [**1)**$_{MAN}$]= 10 mg mL$^{-1}$, the polymer and Nile Red were mixed at **(1)**$_{MAN}$:Nile Red 10:1 molar ratio. C) emission spectra of filtered **(1)**$_{MAN}$-Nile Red complexes and filtered control Nile Red dispersion in water, at λ$_{ex}$ = 550 nm.

The hydrodynamic diameters observed for **(1)**$_{MAN}$ and **(2)**$_{MAN}$ by DLS analysis were close to the lower size detection limit for DLS, hence Taylor dispersion analysis (TDA) of **(1)**$_{MAN}$ was undertaken to get a more accurate estimation of its hydrodynamic size. TDA is an absolute method to determine the diffusion coefficients (D), and thus the hydrodynamic radii (R$_h$), of molecules in solution,[52, 53] based on the dispersion of a solute plug through a uniform cylindrical tube under laminar Poiseuille flow.[54] Following injection, the UV absorbance (λ = 214 nm) of the species in solution was recorded at two detection windows positioned along the capillary windows 1 and 2, (Figure 6.5). The diffusion coefficient of the injected solute(s) can be derived by fitting Taylor's solution to the concentration profile (taylorgram) of the solute(s). In turn, this can be used to assess the size of molecules or particles with hydrodynamic diameter (2R$_h$) from angstroms to submicron size,[55, 56] typically

in the 0.4-100 nm range. Hawe *et al.* showed that for peptide hormone and neuropeptide oxytocin, with a hydrodynamic radius $R_h$=0.9-1.1 nm, not too dissimilar from that expected for our polymers **(1)**$_{MAN}$ and **(2)**$_{MAN}$, TDA was far superior to DLS to estimate the peptide size. The size of oxytocin is towards the lowest size limit for detection of conventional DLS analysis, thus the DLS measurement was dominated by the presence of trace amounts of contaminants and/or dust, resulting in a significant overestimation of the size of oxitoxin, especially under diluted conditions.[54]

Importantly for our study, deconvolution of Taylorgrams from mixtures of species in solution allows to estimate the hydrodynamic radii of their individual components and their relative proportions,[52, 57] and has been used to investigate the aggregation of macromolecules in solution.[53, 54] For example, Latunde-Dada *et al.* estimated accurately size and relative proportion of bovine serum albumin (BSA) monomer and thermally-induced aggregates in BSA:(BSA aggregates) in the 3-100% range.[53] Initial experiments were carried out at a concentration of linear **(1)**$_{MAN}$ of 2.0 mg mL$^{-1}$ and variable [polymer]:[dye] molar ratios (Figure 6.5). Samples were filtered with a 0.22 µm PVDF filter prior the analyses to remove un-incorporated Nile Red.

In all samples only one species in solution could be detected, with hydrodynamic radius ($R_h$) in the 2.0-2.2 nm range, corresponding to a diameter of 4.0-4.4 nm, which again is indicative of the presence of unimolecular polymer chains in solution.

| [(1)MAN]:[Nile Red] | Rh (nm) |
|---|---|
| (1)MAN only | 2.20 |
| 10:1 | 2.07 |
| 4:1 | 2.07 |
| 2:1 | 2.00 |
| 1:1 | 2.08 |
| 1:3 | 2.00 |
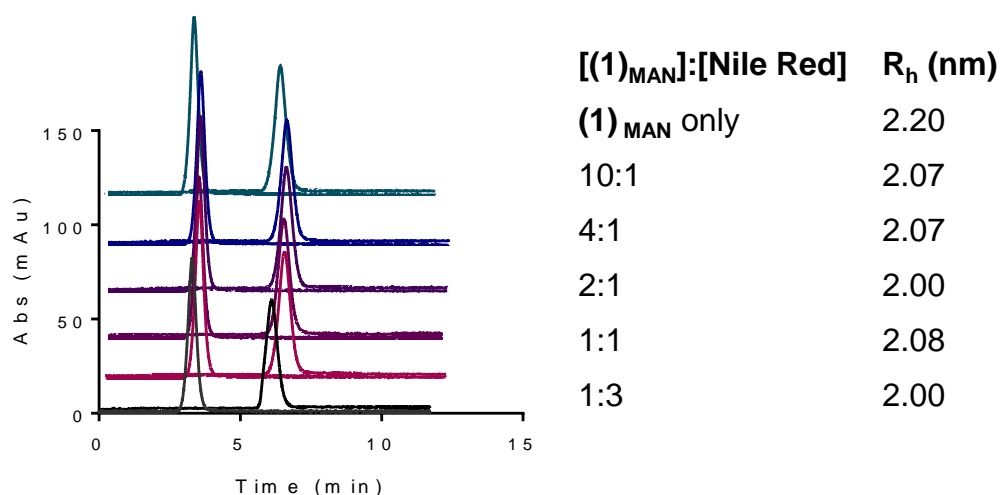
Figure 6.5: Taylor dispersion analysis of (1)MAN alone and (1)MAN-Nile Red complexes. Broadening of concentration profile due to axial spreading of the solute pulse observed between two detection windows is used to estimate the hydrodynamic radii.

**Effect of the nature of polymer backbone on guest molecule incorporation.**

The surface tension experiments showed that for the same clicked propargyl methacrylate backbone, the nature and size of the pendant carbohydrate units have a direct effect on the hydrophilic:hydrophobic balance of these materials, and thus affect their surfactant-type properties. Here, we aimed at investigating the effect of the nature of the polymer backbone on the ability of these glycopolymers to incorporate hydrophobic fluorescent probes. To this aim linear and 4-arm star poly(N-ethylacrylamidoyl-α-D-mannopyranoside) (3)MAN and (4)MAN (Figure 6.6A), respectively, analogous to (1)MAN and (2)MAN, were synthesised by SET LRP and tested. In the first set of experiments a fixed amount of Nile Red was added to solutions of polymers (1)-(4)MAN at increasing concentration (0.050-1.0 mg mL$^{-1}$), and the fluorescence of the solubilised probe was recorded (Figure 6.6B). Results clearly showed that whilst mannose triazolyl methacrylates (1)MAN and (2)MAN were able to interact with Nile Red and incorporate it already at the lowest concentration tested in this set of

experiments (50 µg mL$^{-1}$), linear and start mannose acrylamide **(3)**$_{MAN}$ and

**(4)**$_{MAN}$, except for a small increase for linear **(3)**$_{MAN}$ at the highest concentration

tested (1.00 mg mL$^{-1}$), showed no detectable polymer-dye interaction. It should

be noted that the increase of fluorescence is used here only for a qualitative

assessment of relative amounts of Nile Red, as a proportion of molecules of

fluorophore incorporated within carriers could still interact with each other and

form non-fluorescent dimers and H-type aggregates through π–π stacking

interactions.[45] 9-(2,2-Dicyanovinyl)julolidine (DCVJ, Figure 6.2A) was then

tested as the hydrophobic probe (Figure 6.6C). DCVJ belongs to a class of

fluorophores known as molecular rotors, whose fluorescence depends on the

velocity of rotation of a specific bond, presenting maximal fluorescence when

the molecule is in a fully planar conformation. Upon irradiation, fluorescent

molecular rotors undergo twisted intramolecular charge transfer (TICT), and

relax via the nonradiative torsional relaxation pathway.[58] The fluorescence of

molecular rotors is therefore more sensitive to changes in microenviroments

which restrict rotation around key bonds – e.g. increase of local viscosity or

inclusion within tightly packed complexes – than to the polarity of the medium

the fluorophore is dissolved in.[59] Thus DCVJ here served two purposes: *i)*

demonstrate that glycopolymers based on clicked propargyl methacrylates are

capable of incorporating a range of different hydrophobic molecules, and *ii)*

gather some initial information on the molecular mobility of the entrapped

guest molecule within polymer:dye complexes. As for the previous tests, only

mannose triazolyl methacrylates **(1)**$_{MAN}$ and **(2)**$_{MAN}$ showed an increase in

fluorescence, although at higher polymer concentrations compared to

experiments with Nile Red, suggesting a certain degree of steric rotational restriction of the gest molecule DCVJ within the polymer-dye complex.
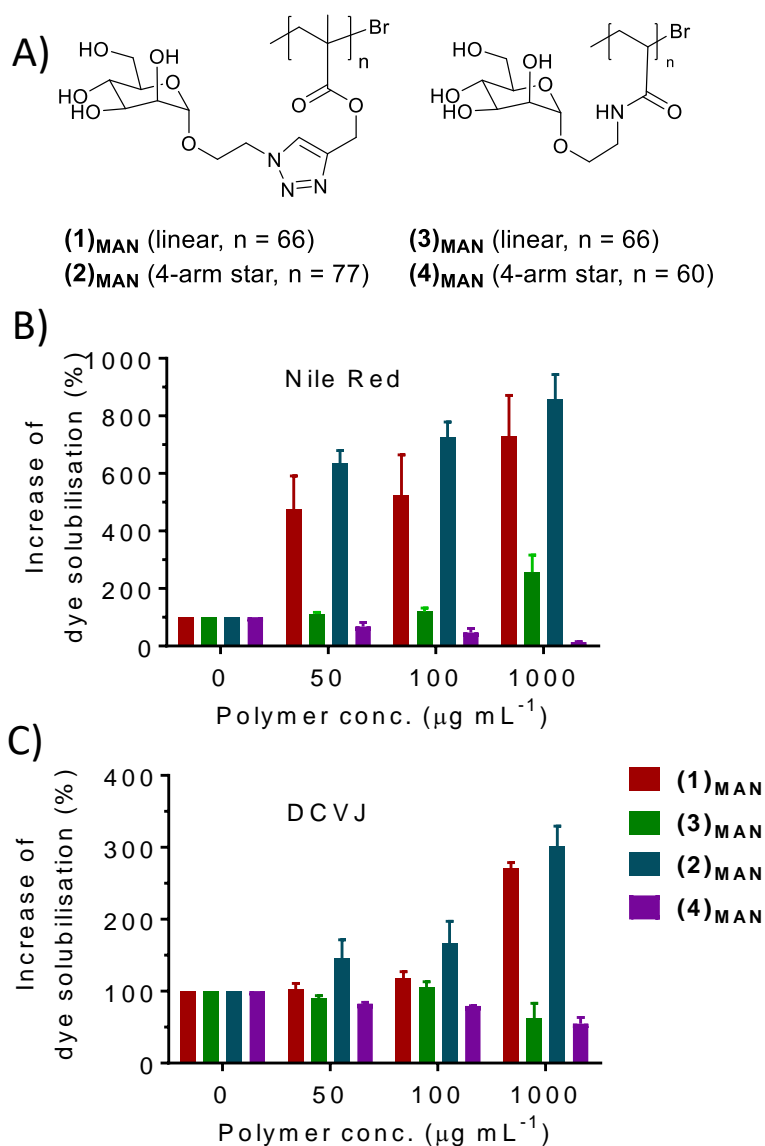


Figure 6.6: A) Mannosylated linear **(1)**MAN and **(3)**MAN and 4-arm star **(2)**MAN and 3)MAN glycopolymers used in this experiment. B) Nile Red and C) DCVJ solubilised in the presence of different amounts of linear and 4-arm star 1,2,3-triazole **(1)**MAN and **(2)**MAN and non-triazole containing **(3)**MAN and **(4)**MAN glycopolymers. Amount of dye in was quantified by RT-HPLC and expressed as % increase compared to control samples prepared in the absence of glycopolymers. Results were obtained from two independent runs (N=2) with sample triplicates (n=3). Nile Red and DCVJ were added from stock solutions in acetonitrile, achieving a theoretical concentration of 20 µg mL-1 (63 µM and 80 µM, respectively) before potential precipitates were removed by centrifugation.

Finally the guest probe release profiles were tested using Nile red-**(1)MAN** /

**(2)MAN** complexes in deionised water (1.00 mg mL-1 of -**(1)MAN** or **(2)MAN**, 1.0 mg

mL$^{-1}$. Nile Red 20 µg mL$^{-1}$, 63 µM) through a 5 kDa MWCO membrane, under

sink conditions. Consistent with an overall relatively weak and reversible

polymer-probe interaction, near complete Nile Red release was observed

already after 4 hours (Figure S6.9).

**Towards targeted guest molecule delivery.**

Following initial characterisation of glycopolymer-Nile Red non-covalent

conjugates, the ability of these supramolecular complexes to recognise

carbohydrate-binding proteins (lectins) was investigated. In nature

carbohydrates are involved in the regulation of a plethora of biological

processes such as cell differentiation, proliferation and adhesion,

inflammation, and immunological response, [60] thus targeted drug delivery

through sugar-binding receptors to modulate these key processes both *in vitro*

and *in vivo*, would be particularly attractive. To this end, an assay based on the

known interaction of mannose with concanavalin-A [61, 62] was developed, in

analogy to a previous study by Haddleton and co-workers. [63] Concanavalin- A

(Con A) is a lectin isolated from the jackbean (*Canavalia ensiformis*) plant. It

exists predominantly as a homotetramer at pH 7, with each unit presenting one

sugar binding site. [64] The binding sites are located at a 65 Å distance from each

other and bind pyranose forms of D-mannose, D-glucose, D-*N*-acetyl

glucosamine, and Lactose. [65] By possessing four sugar binding sites in its

tetrameric form, Con A is frequently used as to crosslink glucose and mannose-containing macromolecules and nano- and micro-objects. [66]

In the first part of the assay, increasing amounts of Con A were added to solution of glycopolymers-Nile Red complexes (1.00 mg mL$^{-1}$ and 20 μg mL$^{-1}$, 63 μM, respectively), resulting in the formation of insoluble Con A-glycopolymer clusters. The highest Con A concentration, 1.00 μg mL$^{-1}$, corresponds to one molecule of con A monomer per 2 polymer chains. The fluorescence at λ$_{em}$ 630 nm was found to decrease steadily as the concentration of Con A crosslinking agent increased from 0 to 1.00 mg mL$^{-1}$ (Figure 6.7). This can be explained in terms of *i)* a Con A-induced precipitation of fluorescent glycopolymers-Nile Red complexes, *ii)* a sequestration of glycopolymers by the added Con A lectin crosslinker, followed by precipitation of Nile Red due to the lack of polymer chains able to solubilise it, or *iii)* a combination of these two effects.

In the second part of the assay, the reversibility of this process was evaluated. The release of glycopolymers from the clusters formed at 1.00 mg mL$^{-1}$ Con A concentration was tested by adding an excess of D-mannose, which can act as a competitive monovalent ligand for Con A. An increase in fluorescence, dependent on the amount of monovalent mannose ligand added, was observed, indicating that Nile Red was retained within the mannose glycopolymers, or re-complexed, according to the mechanism ii) above, following decomplexation, from Con A lectin.
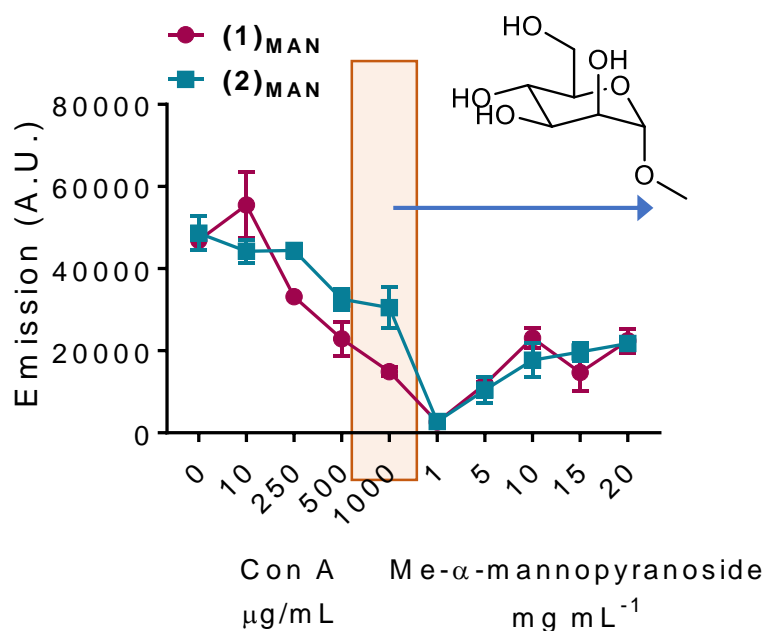
Figure 6.7: Binding of **(1)MAN**-Nile Red non-covalent conjugates to mannose-specific model lectins. Left: Con A agglutination assay. To a polymer solution (1.0 mg mL$^{-1}$ in 20 mM HEPES buffer (pH 7.4 with 50 mM NaCl, 5 mM CaCl$_2$ and 5 mM MnCl$_2$), Nile Red was added [final concentration 12.6 μg/mL, 1:1 polymer:dye molar ratio], and the fluorescence at λ$_{ex}$=630 nm (λ$_{ex}$=550 nm) was recorded. Upon addition of Con A, decrease of fluorescence due to formation of insoluble of Con A-(**(1)MAN**-Nile Red) was recorded. Reversible agglutination: the solid precipitate obtained from the 1000 μg mL$^{-1}$ Con A experiment was re-dissolved by addition of different concentrations of Me-α-mannopyranoside, and recovery of fluorescence due to re-dissolution (or re-formation) of **(1)MAN**-Nile Red complexes was measured.

To elucidate this point, the ability of these glycopolymers to mediate selective targeting to lectin-functionalised surfaces was investigated. To this aim, commercially available 45-165 μm agarose beads functionalised with mannose-binding Con A and galactose-binding peanut agglutinin (PNA) were utilised, along with linear galactose glycopolymer **(1)GAL** analogous to Mannosylated **(1)MAN**. Lectin beads were treated with **(1)MAN**- and **(1)GAL**-Nile Red complexes (1:1 glycopolymer:dye ratio) solutions in the 0.10-1.0 mg mL$^{-1}$ range of polymer concentrations. Upon centrifugation and removal of the supernatant, followed by several washing cycles, the beads were suspended in HEPES buffer and analysed by fluorescence microscopy (Figure 6.8). Pleasingly, selective

recognition of **(1)MAN**- and **(1)GAL**-Nile Red complexes to Con A and PNA, respectively, was observed. No binding to 'mismatched' lectins – that is, **(1)MAN** to PNA, and **(1)GAL** to Con A – was detected, thus ruling out any significant binding to the lectin surfaces due to physical absorption or other non-specific binding mechanisms.
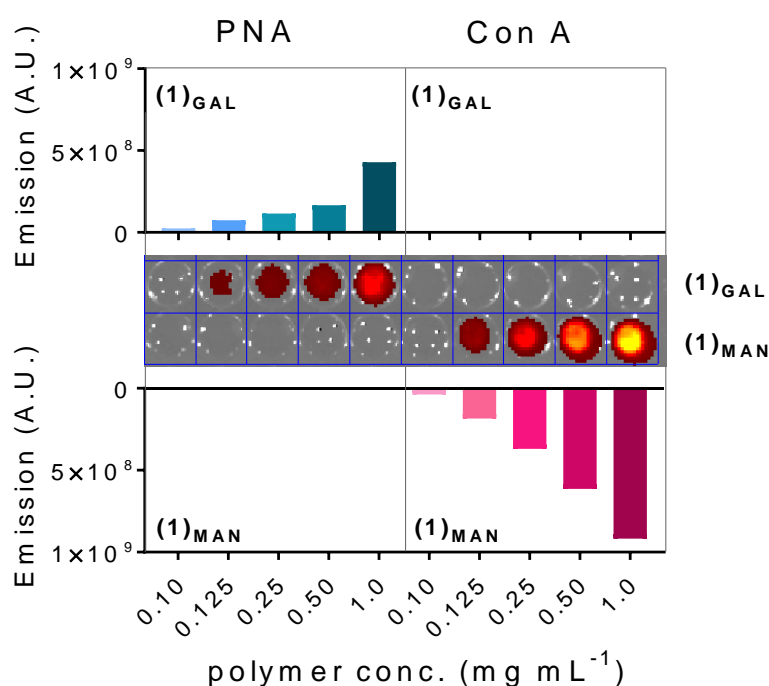


Figure 6.8: Agarose-bound lectin beads were treated with different amounts of **(1)MAN**- and **(1)GAL**-Nile Red complexes (1:1 polymer:dye molar ratio). After extensive rinsing with 20 mM HEPES buffer, the samples were seeded on a 96-well plate and the fluorescence recorded.

Con A and PNA agarose beads were also utilised as stationary phases for affinity chromatography of **(1)MAN**–Nile Red complexes (Figures 6.9 and S6.10 and S6.11). Following elution with 20 mM HEPES buffer at pH 7.4, the polymer-dye complex was found to be retained by Con A, while it was readily eluted from the PNA column. This showed that **(1)MAN** was able to efficiently transport Nile Red through this stationary phase, without significant loss of its fluorescent

payload. Treatment of with a 10 mg mL$^{-1}$ aqueous solution of methyl-α-mannopyranoside (a monovalent competitive ligand for Con A) resulted in the elution of the **(1)MAN**–Nile Red complex from the Con A column, confirming that **(1)MAN** here acted as a targeted nanoscale vector for Nile Red. Repeating this experiment using **(1)GAL,** an identical linear glycopolymers displaying galactose binding units, resulted in analogous results, with selective binding of **(1)GAL**-Nile Red complexes to PNA and not to Con A. Taken together, this part of our study showed that upon complexation of Nile Red, glycopolymers conserved their ability to reversibly bind model lectins Con A and PNA, whilst at the same time retaining Nile Red molecules within their supramolecular non-covalent structure.
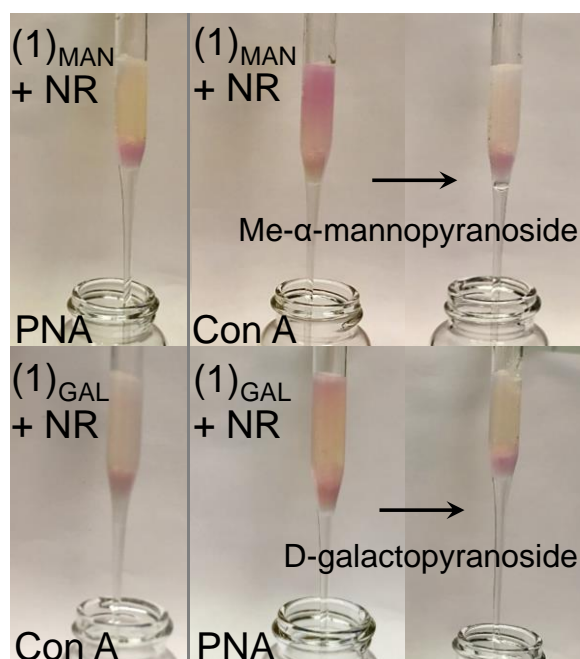


Figure 6.9: Affinity chromatography assay. Con A- and PNA-immobilised beads were utilised as stationary phases for affinity chromatography on **(1)MAN**- and **(1)GAL**-Nile Red complexes (1:1 polymer:dye molar ratio), eluting with HEPES buffer. **(1)MAN**-Nile Red was found to selectively bind to Con A, **(1)GAL**-Nile Red to PNA. These complexes could be eluted from the lectin stationary phase by addition of a mobile phase containing an excess of monovalent competitive ligands, Me-α-mannopyranoside, and D-galactopyranoside, respectively.

Whilst not within the main scope of this work, the possibility of using these single-chain vectors for targeted delivery of a model cargo, Nile Red, to cells presenting endocytic lectin receptors was explored. Chinese Hamster Ovary (CHO) cells were selected due to the availability of a mutant cell line expressing Mannose Receptor (MR, CD206), an endocytic receptor expressed in subpopulations of dendritic cells (DCs), macrophages, and selected endothelial cells, and which plays a role in both innate and adaptive immunity.[67, 68] Importantly, in a separate study, we had already shown that these cells can efficiently internalise fluorescent mannose-containing glycopolymers in a dose-dependent manner (data not shown). Accordingly, MR$^+$-CHO cells were incubated for 30 minutes with glycopolymer:Nile Red-containing solutions at polymer concentrations in the 50-1000 µg mL$^{-1}$, and Nile Red at a theoretical concentration of 10 µM (if all of it were solubilised). Dye cell internalisation was studied by flow cytometry (FACS), and was found to be significantly increased in the presence of **(1)$_{MAN}$** and **(2)$_{MAN}$**, and to be dependent on the concentration of the added glycopolymers (Figure 6.10A).
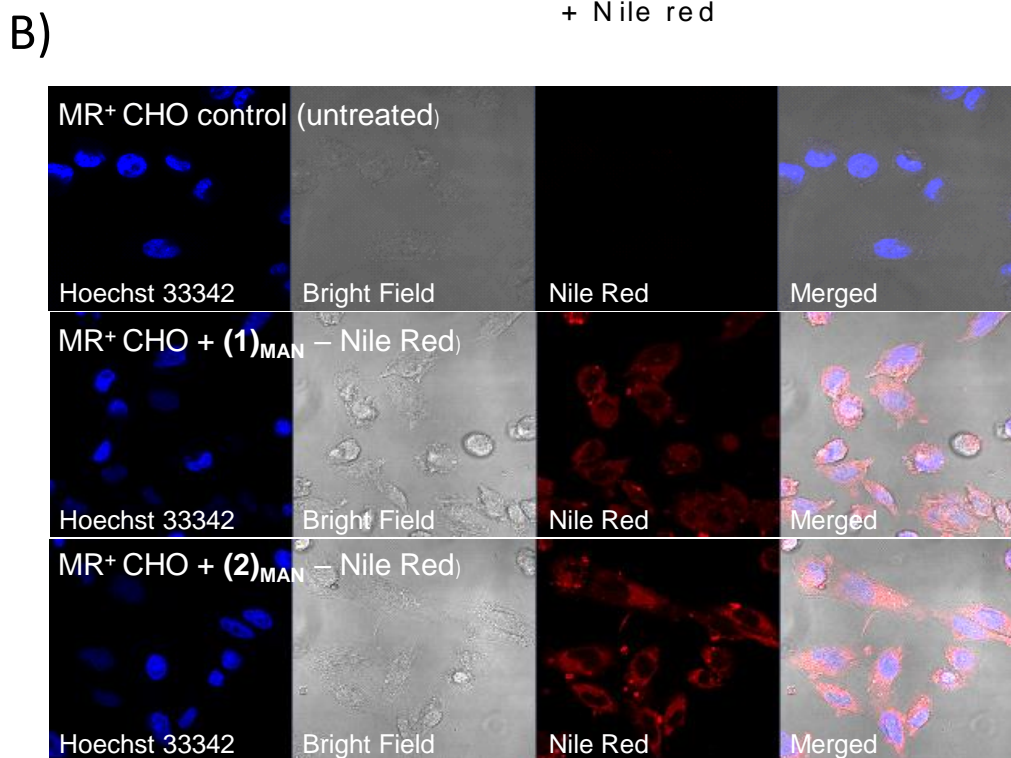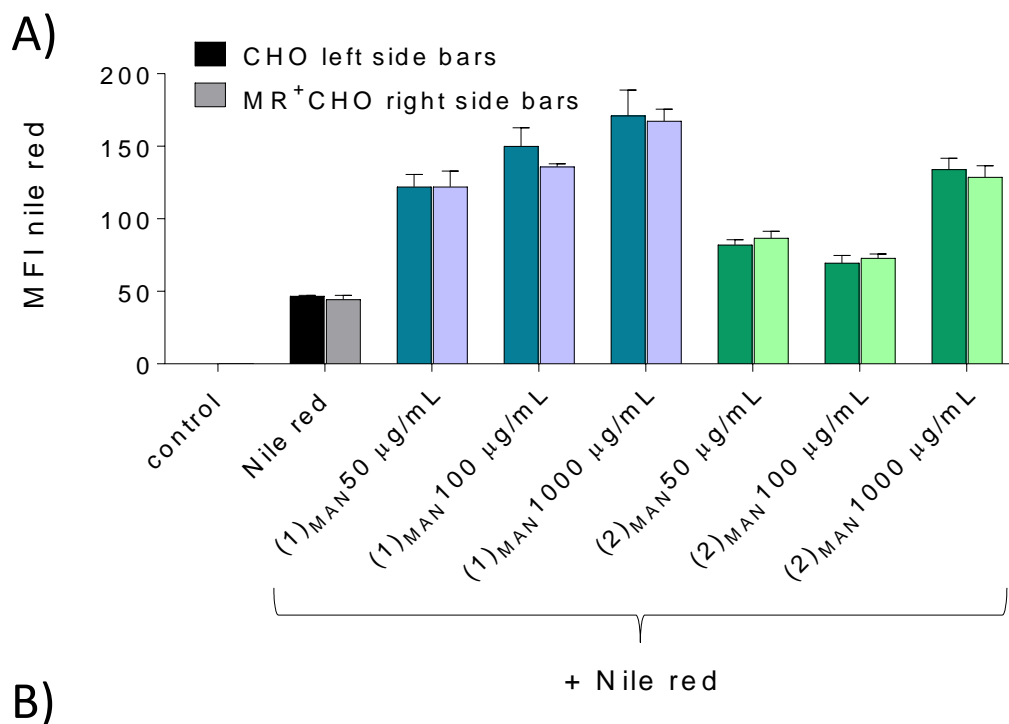
Figure 6.10: A) Flow cytometry quantification of uptake of Nile Red by MR⁺CHO cells incubated with **(1)**MAN- and **(2)**MAN-Nile Red complexes. B) Confocal microscopy analysis of these samples: Top. MR⁺CHO untreated cells (negative control). Middle. MR⁺CHO cells treated with 1.00 mg mL$^{-1}$ **(1)**MAN + 10 mM Nile Red, and Bottom MR⁺CHO cells treated with 1.00 mg mL$^{-1}$ **(2)**MAN + 10 µM Nile Red, for 30 min.

Interestingly, uptake was also found to be not significantly different than that on MR⁻CHO negative control cells. Several studies have described Nile Red transfer from nanoparticle systems to hydrophobic acceptors.[69-72] Thus, our results could be explained in terms of an equilibrium between Nile Red reversibly complexed to the glycopolymers, and the unbound fraction being able to enter through CHO cells by diffusion through the plasma membrane, or other mechanisms, e.g. nanoparticle-cell contact-mediated transfer. Confocal analysis of cells following treatment with Nile Red and **(1)MAN** or **(2)MAN** showed diffuse intracellular cytosolic fluorescence, with a few punctuated spots (Figure 6.10B). This is in line with analogous fluorophore distribution patterns described by Snipstad *et al.* who showed that using Nile Red-loaded poly(butylcyanoacrylate nanoparticles, dye uptake by human prostate adenocarcinoma cells (PC3) did not occur by endocytosis, but rather by nanoparticle-cell contact-mediated transfer directly to the cytosol and, to a lesser extent, release of payload into the medium, followed by diffusion into cells.[69]

Thus, these initial cell experiments, whilst not suitable to probe lectin-mediated targeted cell delivery, confirmed the ability of triazolyl methacrylates **(1)MAN** and **(2)MAN** to act as unimolecular carriers for Nile Red and enhance their cellular uptake.

# Conclusions

In this study the incorporation of small hydrophobic molecules into linear and 4-arm sugar triazolyl methacrylates glycopolymers through guest molecule-single polymer chain interaction was investigated. The polymers were synthesised from linear and 4-arm star poly(propargyl methacrylate) precursors, to which various sugar azides were clicked by copper-catalysed alkyne-azyde cycoaddition (CuAAC). The reaction afforded different glycopolymers that shared the same topology, degree of polymerisation and dispersity. Incorporation of small hydrophobic probes, such as Nile Red and DCJV, into linear and multi arm mannose polymers was confirmed by fluorescence studies performed at different probe:polymer molar ratios. The aggregation propensity of these two polymers was then investigated by Surface tension measurements, fluorescence studies and Dynamic Light Scattering. No detectable Critical Micelle Concentration could be identified for both polymers, confirming that they do not self-assemble into supramolecular aggregates. Results were further confirmed by Taylor Dispersion Analysis, conducted in the absence and in the presence of Nile Red, which revealed an average hydrodynamic radius of 2 nm, which were attributed to the single polymer chain. The results indicate that these glycopolymers act as unimolecular micelles which incorporate hydrophobic molecules on the polymer backbone. Affinity chromatography experiments suggest the potential employment of these polymers as unimolecular vector fot targeted drug delivery, through the pendant mannose functionalities as targeting agent. Preliminary cells uptake studies displayed enhanced Nile Red uptake, which was mainly attributed to

the ability of the polymers to reversibly complexe the dye molecules, largely increasing its solubility.  Overall, these results confirm the ability of triazolyl methacrylates glycopolymers to incorporate small hydrophobic molecules as unimolecular micelles, and suggest the potential application of these glycopolymers in drug delivery.

# References

1.      Lutz, J.-F.;  Ouchi, M.;  Liu, D. R.; Sawamoto, M., Sequence-Controlled Polymers. *Science* **2013,** *341* (6146).

2.      Gonzalez-Burgos, M.;  Latorre-Sanchez, A.; Pomposo, J. A., Advances in single chain technology. *Chemical Society Reviews* **2015,** *44* (17), 6122-6142.

3.      Hanlon, A. M.;  Lyon, C. K.; Berda, E. B., What Is Next in Single-Chain Nanoparticles? *Macromolecules* **2016,** *49* (1), 2-14.

4.      Altintas, O.; Barner-Kowollik, C., Single Chain Folding of Synthetic Polymers by Covalent and Non-Covalent Interactions: Current Status and Future Perspectives. *Macromolecular Rapid Communications* **2012,** *33* (11), 958-971.

5.      Altintas, O.; Barner-Kowollik, C., Single-Chain Folding of Synthetic Polymers: A Critical Update. *Macromolecular Rapid Communications* **2016,** *37* (1), 29-46.

6.      Lyon, C. K.;  Prasher, A.;  Hanlon, A. M.;  Tuten, B. T.;  Tooley, C. A.;  Frank, P. G.; Berda, E. B., A brief user's guide to single-chain nanoparticles. *Polymer Chemistry* **2015,** *6* (2), 181-197.

7.      Berkovich, I.;  Mavila, S.;  Iliashevsky, O.;  Kozuch, S.; Lemcoff, N. G., Single-chain polybutadiene organometallic nanoparticles: an experimental and theoretical study.  *Chemical Science* **2016,** *7* (3), 1773-1778.

8.      Mavila, S.;  Diesendruck, C. E.;  Linde, S.;  Amir, L.;  Shikler, R.; Lemcoff, N. G., Polycyclooctadiene Complexes of Rhodium(I): Direct Access to Organometallic Nanoparticles. *Angewandte Chemie International Edition* **2013,** *52* (22), 5767-5770.

9.      Mavila, S.;  Rozenberg, I.; Lemcoff, N. G., A general approach to mono- and bimetallic organometallic nanoparticles. *Chemical Science* **2014,** *5* (11), 4196-4203.

10.     Sanchez-Sanchez, A.;  Arbe, A.;  Colmenero, J.; Pomposo, J. A., Metallo-Folded Single-Chain Nanoparticles with Catalytic Selectivity. *ACS Macro Letters* **2014,** *3* (5), 439-443.

11.     Bai, Y.;  Feng, X.;  Xing, H.;  Xu, Y.;  Kim, B. K.;  Baig, N.;  Zhou, T.;  Gewirth, A. A.;  Lu, Y.;  Oldfield, E.; Zimmerman, S. C., A Highly Efficient Single-Chain Metal–Organic Nanoparticle Catalyst for Alkyne–Azide "Click" Reactions in Water and in Cells. *Journal of the American Chemical Society* **2016,** *138* (35), 11077-11080.

12.     Quader, S.; Kataoka, K., Nanomaterial-Enabled Cancer Therapy. *Molecular Therapy* **2017,** *25* (7), 1501-1513.

13.     Cabral, H.;  Matsumoto, Y.;  Mizuno, K.;  Chen, Q.;  Murakami, M.;  Kimura, M.;  Terada, Y.;  Kano, M. R.;  Miyazono, K.;  Uesaka, M.;  Nishiyama, N.; Kataoka, K., Accumulation of sub-100 nm polymeric micelles in poorly permeable tumours depends on size. *Nature Nanotechnology* **2011,** *6*, 815.

14.     Chen, G.;  Wang, Y.;  Xie, R.; Gong, S., A review on core–shell structured unimolecular nanoparticles for biomedical applications. *Advanced Drug Delivery Reviews* **2018**.

15.     Fan, X.;  Li, Z.; Loh, X. J., Recent development of unimolecular micelles as functional materials and applications. *Polymer Chemistry* **2016,** *7* (38), 5898-5919.

16.     Wang, Y.;  Qi, G.; He, J., Unimolecular Micelles from Layered Amphiphilic Dendrimer-Like Block Copolymers. *ACS Macro Letters* **2016,** *5* (4), 547-551.

17.     Liu, G.;  Gao, H.;  Zuo, Y.;  Zeng, X.;  Tao, W.;  Tsai, H.-i.; Mei, L., DACHPt-Loaded Unimolecular Micelles Based on Hydrophilic Dendritic Block Copolymers for Enhanced Therapy of Lung Cancer. *ACS Applied Materials & Interfaces* **2017,** *9* (1), 112-119.

18.     Fan, X.;  Hu, Z.; Wang, G., Synthesis and unimolecular micelles of amphiphilic copolymer with dendritic poly(l-lactide) core and poly(ethylene oxide) shell for drug delivery. *RSC Advances* **2015,** *5* (122), 100816-100823.

19.    Chen, G.; Wang, L.; Cordie, T.; Vokoun, C.; Eliceiri, K. W.; Gong, S., Multi-Functional Self-Fluorescent Unimolecular Micelles for Tumor-Targeted Drug Delivery and Bioimaging. *Biomaterials* **2015,** *0*, 41-50.

20.    Xiao, Y.; Hong, H.; Javadi, A.; Engle, J. W.; Xu, W.; Yang, Y.; Zhang, Y.; Barnhart, T. E.; Cai, W.; Gong, S., Multifunctional unimolecular micelles for cancer-targeted drug delivery and positron emission tomography imaging(). *Biomaterials* **2012,** *33* (11), 3071-3082.

21.    Popeney, C. S.; Lukowiak, M. C.; Böttcher, C.; Schade, B.; Welker, P.; Mangoldt, D.; Gunkel, G.; Guan, Z.; Haag, R., Tandem Coordination, Ring-Opening, Hyperbranched Polymerization for the Synthesis of Water-Soluble Core–Shell Unimolecular Transporters. *ACS Macro Letters* **2012,** *1* (5), 564-567.

22.    Porsch, C.; Zhang, Y.; Ducani, C.; Vilaplana, F.; Nordstierna, L.; Nyström, A. M.; Malmström, E., Toward unimolecular micelles with tunable dimensions using hyperbranched dendritic-linear polymers. *Biomacromolecules* **2014,** *15* (6), 2235-2245.

23.    Xu, J.; Luo, S.; Shi, W.; Liu, S., Two-Stage Collapse of Unimolecular Micelles with Double Thermoresponsive Coronas. *Langmuir* **2006,** *22* (3), 989-997.

24.    Sarkar, G.; Curran, G. L.; Sarkaria, J. N.; Lowe, V. J.; Jenkins, R. B., Peptide Carrier-Mediated Non-Covalent Delivery of Unmodified Cisplatin, Methotrexate and Other Agents via Intravenous Route to the Brain. *PLOS ONE* **2014,** *9* (5), e97655.

25.    Sarkar, G.; Curran, G. L.; Mahlum, E.; Decklever, T.; Wengenack, T. M.; Blahnik, A.; Hoesley, B.; Lowe, V. J.; Poduslo, J. F.; Jenkins, R. B., A Carrier for Non-Covalent Delivery of Functional Beta-Galactosidase and Antibodies against Amyloid Plaques and IgM to the Brain. *PLOS ONE* **2011,** *6* (12), e28881.

26.    Ladmiral, V.; Mantovani, G.; Clarkson, G. J.; Cauet, S.; Irwin, J. L.; Haddleton, D. M., Synthesis of Neoglycopolymers by a Combination of "Click Chemistry" and Living Radical Polymerization. *Journal of the American Chemical Society* **2006,** *128* (14), 4823-4830.

27.    Geng, J.; Mantovani, G.; Tao, L.; Nicolas, J.; Chen, G.; Wallis, R.; Mitchell, D. A.; Johnson, B. R. G.; Evans, S. D.; Haddleton, D. M., Site-Directed Conjugation of "Clicked" Glycopolymers To Form Glycoprotein Mimics: Binding to Mammalian Lectin and Induction of Immunological Function. *Journal of the American Chemical Society* **2007,** *129* (49), 15156-15163.

28.    Madeira do O, J.; Mastrotto, F.; Francini, N.; Allen, S.; van der Walle, C. F.; Stolnik, S.; Mantovani, G., Synthetic glycopolymers as modulators of protein aggregation: influences of chemical composition, topology and concentration. *Journal of Materials Chemistry B* **2018,** *6* (7), 1044-1054.

29.    Jose, J.; Burgess, K., Syntheses and Properties of Water-Soluble Nile Red Derivatives. *The Journal of Organic Chemistry* **2006,** *71* (20), 7835-7839.

30.    Kroeger, T.; Frieg, B.; Zhang, T.; Hansen, F. K.; Marmann, A.; Proksch, P.; Nagel-Steger, L.; Groth, G.; Smits, S. H. J.; Gohlke, H., EDTA aggregates induce SYPRO orange-based fluorescence in thermal shift assay. *PLOS ONE* **2017,** *12* (5), e0177024.

31.    Becer, C. R.; Gibson, M. I.; Geng, J.; Ilyas, R.; Wallis, R.; Mitchell, D. A.; Haddleton, D. M., High-Affinity Glycopolymer Binding to Human DC-SIGN and Disruption of DC-SIGN Interactions with HIV Envelope Glycoprotein. *J. Am. Chem. Soc.* **2010,** *132* (43), 15130-15132.

32.    Chen, J.; Travelet, C.; Borsali, R.; Halila, S., Hemicellulosic Polysaccharides Mimics: Synthesis of Tailored Bottlebrush-Like Xyloglucan Oligosaccharide Glycopolymers as Binders of Nanocrystalline Cellulose. *Biomacromolecules* **2017,** *18* (10), 3410-3417.

33.    Geng, J.; Mantovani, G.; Tao, L.; Nicolas, J.; Chen, G.; Wallis, R.; Mitchell, D. A.; Johnson, B. R. G.; Evans, S. D.; Haddleton, D. M., Site-Directed Conjugation of

"Clicked" Glycopolymers To Form Glycoprotein Mimics: Binding to Mammalian Lectin and Induction of Immunological Function. *J. Am. Chem. Soc.* **2007,** *129* (49), 15156-15163.

34.     Gou, Y.; Geng, J.; Richards, S.-J.; Burns, J.; Remzi Becer, C.; Haddleton, D. M., A detailed study on understanding glycopolymer library and Con A interactions. *J. Polym. Sci., Part A: Polym. Chem.* **2013,** *51* (12), 2588-2597.

35.     Gou, Y.; Slavin, S.; Geng, J.; Voorhaar, L.; Haddleton, D. M.; Becer, C. R., Controlled Alternate Layer-by-Layer Assembly of Lectins and Glycopolymers Using QCM-D. *ACS Macro Lett.* **2012,** *1* (1), 180-183.

36.     Jono, K.; Nagao, M.; Oh, T.; Sonoda, S.; Hoshino, Y.; Miura, Y., Controlling the lectin recognition of glycopolymers via distance arrangement of sugar blocks. *Chem. Commun. (Cambridge, U. K.)* **2018,** *54* (1), 82-85.

37.     Ladmiral, V.; Mantovani, G.; Clarkson, G. J.; Cauet, S.; Irwin, J. L.; Haddleton, D. M., Synthesis of Neoglycopolymers by a Combination of "Click Chemistry" and Living Radical Polymerization. *J. Am. Chem. Soc.* **2006,** *128* (14), 4823-4830.

38.     Nurmi, L.; Lindqvist, J.; Randev, R.; Syrett, J.; Haddleton, D. M., Glycopolymers via catalytic chain transfer polymerisation (CCTP), Huisgens cycloaddition and thiol-ene double click reactions. *Chem. Commun. (Cambridge, U. K.)* **2009,** (19), 2727-2729.

39.     Tanaka, J.; Gleinich, A. S.; Zhang, Q.; Whitfield, R.; Kempe, K.; Haddleton, D. M.; Davis, T. P.; Perrier, S.; Mitchell, D. A.; Wilson, P., Specific and Differential Binding of N-Acetylgalactosamine Glycopolymers to the Human Macrophage Galactose Lectin and Asialoglycoprotein Receptor. *Biomacromolecules* **2017,** *18* (5), 1624-1633.

40.     Zhao, Y.; Zhang, Y.; Wang, C.; Chen, G.; Jiang, M., Role of Protecting Groups in Synthesis and Self-Assembly of Glycopolymers. *Biomacromolecules* **2017,** *18* (2), 568-575.

41.     Babiuch, K.; Dag, A.; Zhao, J.; Lu, H.; Stenzel, M. H., Carbohydrate-Specific Uptake of Fucosylated Polymeric Micelles by Different Cancer Cell Lines. *Biomacromolecules* **2015,** *16* (7), 1948-1957.

42.     Geng, J.; Lindqvist, J.; Mantovani, G.; Chen, G.; Sayers, C. T.; Clarkson, G. J.; Haddleton, D. M., Well-defined poly(N-glycosyl 1,2,3-triazole) multivalent ligands: design, synthesis and lectin binding studies. *QSAR Comb. Sci.* **2007,** *26* (11-12), 1220-1228.

43.     Greenspan, P.; Fowler, S. D., Spectrofluorometric studies of the lipid probe, nile red. *Journal of Lipid Research* **1985,** *26* (7), 781-789.

44.     Eisfeld, A.; Briggs, J. S., The J- and H-bands of organic dye aggregates. *Chemical Physics* **2006,** *324* (2), 376-384.

45.     Kurniasih, I. N.; Liang, H.; Mohr, P. C.; Khot, G.; Rabe, J. P.; Mohr, A., Nile Red Dye in Aqueous Surfactant and Micellar Solution. *Langmuir* **2015,** *31* (9), 2639-2648.

46.     Mukherjee, I.; Moulik, S. P.; Rakshit, A. K., Tensiometric determination of Gibbs surface excess and micelle point: A critical revisit. *Journal of Colloid and Interface Science* **2013,** *394*, 329-336.

47.     Pan, A.; Rakshit, A. K.; Moulik, S. P., Dwelling on the adsorption of surfactant at the air/water interface in relation to its states in the bulk: A comprehensive analysis. *Colloids and Surfaces A: Physicochemical and Engineering Aspects* **2015,** *464*, 8-16.

48.     Liu, H.; Jiang, A.; Guo, J.; Uhrich Kathryn, E., Unimolecular micelles: Synthesis and characterization of amphiphilic polymer systems. *Journal of Polymer Science Part A: Polymer Chemistry* **2000,** *37* (6), 703-711.

49.     Sutherland, E.; Mercer, S. M.; Everist, M.; Leaist, D. G., Diffusion in Solutions of Micelles. What Does Dynamic Light Scattering Measure? *Journal of Chemical & Engineering Data* **2009,** *54* (2), 272-278.

50.     Rei, A.; Ferreira, M. I. C.; Hungerford, G., Nile Red Synchronous Scan Fluorescence Spectroscopy to Follow Matrix Modification in Sol–Gel Derived Media

and its Effect on the Peroxidase Activity of cytochrome c. *Journal of Fluorescence* **2008,** *18* (6), 1083-1091.

51.     Boreham, A.; Pfaff, M.; Fleige, E.; Haag, R.; Alexiev, U., Nanodynamics of Dendritic Core–Multishell Nanocarriers. *Langmuir* **2014,** *30* (6), 1686-1695.

52.     Latunde-Dada, S.; Bott, R.; Hampton, K.; Patel, J.; Leszczyszyn, O. I., Methodologies for the Taylor dispersion analysis for mixtures, aggregates and the mitigation of buffer mismatch effects. *Analytical Methods* **2015,** *7* (24), 10312-10321.

53.     Latunde-Dada, S.; Bott, R.; Barker, D.; Leszczyszyn, O. I., Methodologies for the rapid determination of the diffusion interaction parameter using Taylor dispersion analysis. *Analytical Methods* **2016,** *8* (2), 386-392.

54.     Hawe, A.; Hulse, W. L.; Jiskoot, W.; Forbes, R. T., Taylor Dispersion Analysis Compared to Dynamic Light Scattering for the Size Analysis of Therapeutic Peptides and Proteins and Their Aggregates. *Pharmaceutical Research* **2011,** *28* (9), 2302-2310.

55.     Cottet, H.; Biron, J.-P.; Martin, M., On the optimization of operating conditions for Taylor dispersion analysis of mixtures. *Analyst* **2014,** *139* (14), 3552-3562.

56.     Cipelletti, L.; Biron, J.-P.; Martin, M.; Cottet, H., Measuring Arbitrary Diffusion Coefficient Distributions of Nano-Objects by Taylor Dispersion Analysis. *Analytical Chemistry* **2015,** *87* (16), 8489-8496.

57.     Cottet, H.; Biron, J.-P.; Martin, M., Taylor Dispersion Analysis of Mixtures. *Analytical Chemistry* **2007,** *79* (23), 9066-9073.

58.     Goh, W. L.; Lee, M. Y.; Joseph, T. L.; Quah, S. T.; Brown, C. J.; Verma, C.; Brenner, S.; Ghadessy, F. J.; Teo, Y. N., Molecular Rotors As Conditionally Fluorescent Labels for Rapid Detection of Biomolecular Interactions. *Journal of the American Chemical Society* **2014,** *136* (17), 6159-6162.

59.     Hawe, A.; Filipe, V.; Jiskoot, W., Fluorescent Molecular Rotors as Dyes to Characterize Polysorbate-Containing IgG Formulations. *Pharmaceutical Research* **2010,** *27* (2), 314-326.

60.     Delbianco, M.; Bharate, P.; Varela-Aramburu; Seeberger, P., Carbohydrates in Supramolecular. *Chem Rev* **2016,** *116*, 1693-1752.

61.     Surolia, A.; Bishayee, S.; Ahmad, A.; Balasubramanian, K.; Thambi-Dorai, D.; Podder, S.; Bachhawat, B., Studies on the interaction of concanavalin A with glycoproteins. *Adv Exp Med Biol* **1975,** *55*, 95-115.

62.     Papp, I.; Dernedde, J.; Enders, S.; Riese, S.; Shiao, T.; Roy, R.; Haag, R., Multivalent presentation of mannose on hyperbranched polyglycerol and their interaction with concanavalin A lectin. *Chembiochem* **2011,** *12* (7), 1075-83.

63.     Gou, Y.; Geng, J.; Richards, S.-j.; Burns, J.; Becer, C. R.; Haddleton, D., A detailed study on understanding glycopolymer library and Con A interactions. *J Polym Sci A Polym Chem.* **2013,** *51* (12), 2588-2597.

64.     Mangold, S.; Cloninger, M., Binding of monomeric and dimeric Concanavalin A to mannose-functionalized dendrimers. *Org Biomol Chem* **2006,** *4* (12), 2458-65.

65.     Bittiger, H.; Schnebli, H., Concanavalin A as a Tool. *John Wiley & Sons* **1976**.

66.     Yilmaz, G.; Becer, C. R., Glycopolymer code based on well-defined glycopolyners or glyconanomaterials and their biomolecular recognition. *Front Bioeng Biotechnol* **2014,** *2* (39).

67.     Taylor, P. R.; Gordon, S.; Martinez-Pomares, L., The mannose receptor: linking homeostasis and immunity through sugar recognition. *Trends in Immunology* **2005,** *26* (2), 104-110.

68.     Martinez-Pomares, L., The mannose receptor. *Journal of Leukocyte Biology* **2012,** *92* (6), 1177-1186.

69.     Snipstad, S.; Westrøm, S.; Mørch, Y.; Afadzi, M.; Åslund, A. K. O.; de Lange Davies, C., Contact-mediated intracellular delivery of hydrophobic drugs from polymeric nanoparticles. *Cancer Nanotechnology* **2014,** *5* (1), 8.

70.     Snipstad, S.;  Hak, S.;  Baghirov, H.;  Sulheim, E.;  Mørch, Ý.;  Lélu, S.;  von Haartman, E.;  Bäck, M.;  Nilsson, K. P. R.;  Klymchenko Andrey, S.;  de Lange Davies, C.;  Åslund Andreas, K. O., Labeling nanoparticles: Dye leakage and altered cellular uptake. *Cytometry Part A* **2016,** *91* (8), 760-766.

71.     Bastiat, G.;  Pritz, C. O.;  Roider, C.;  Fouchet, F.;  Lignières, E.;  Jesacher, A.;  Glueckert, R.;  Ritsch-Marte, M.;  Schrott-Fischer, A.;  Saulnier, P.; Benoit, J.-P., A new tool to ensure the fluorescent dye labeling stability of nanocarriers: A real challenge for fluorescence imaging. *Journal of Controlled Release* **2013,** *170* (3), 334-342.

72.     Petersen, S.;  Fahr, A.; Bunjes, H., Flow Cytometry as a New Approach To Investigate Drug Transfer between Lipid Particles. *Molecular Pharmaceutics* **2010,** *7* (2), 350-363.

# Supporting Information Chapter 6
# Materials and methods.

Synthesis and characterisation of Sugar poly(triazolyl methacrylates) linear **(1)**MAN, **(1)**GAL, **(1)**LAC, **(1)**TRE, and 4-arm star **(2)**MAN, **(2)**GAL, **(2)**LAC, **(2)**TRE, are described in Madeira do O *et al*. *J. Mat. Chem. B* 2018, 6, 1044-1054.[1] Monofunctional **(D)**[2] and tetrafunctional **(E)**[1] initiators were synthesised according to literature methods. Agarose-bound Concanavalin A (Con A) and Peanut Agglutinin (PAN) (45-165 μm agarose beads) were purchased from Vector Laboratories, Peterborough, UK. All other reagents and solvents were obtained at the highest purity available from Aldrich Chemical Company or Fischer Scientific and used without further purification unless otherwise stated.

[1]H and [13]C Nuclear Magnetic Resonance (NMR) analysis was carried out using a Bruker DPX400 UltraShield™ Spectrometer. The spectra were processed with MestReNova 6.0.2© 2009 Mestrelab Research S.L. All chemical shifts are reported in ppm ($\delta$) relative to tetramethylsilane, referenced to the chemical shifts of residual solvents resonances. Peak multiplicities are defined by the following abbreviations: s = singlet, br = broad, d = doublet, t = triplet, m =multiplet. FT-IR spectra were recorded with an Attenuated Total Reflection spectrophotometer (Agilent Technologies Cary 630 FTIR) equipped with a diamond single reflection ATR unit. Spectra were acquired with a resolution of 4 cm$^{-1}$, in the range 4000-650 cm$^{-1}$ by recording 32 interferograms. Mass Spectroscopy was carried out using a Micromass LCT KC453 spectrometer. Data were processed with OpenLynx software. Samples were prepared in suitable solvent with sodium trifluoroacetate added to them.

Aqueous SEC analysis of glycopolymers **(3)MAN** and **(4)MAN** was carried with a Wyatt dawn 8+ 1200 Infinity series, with RI detection, in a system calibrated with PEO narrow standards. Standard Dulbecco's Phosphate Buffered Saline (DPBS) was used as the mobile phase, at a flow rate of 1 ml min$^{-1}$.

*Flow cytometry.* Samples were analysed with a Beckman Coulter FC500 Series equipped with tetraCXP SYSTEM Software. At least 2x10$^3$ cells were analysed for each sample. All experiments were performed in duplicates and repeated a minimum of two times.

## Synthesis of glycopolymers (3)MAN and (4)MAN
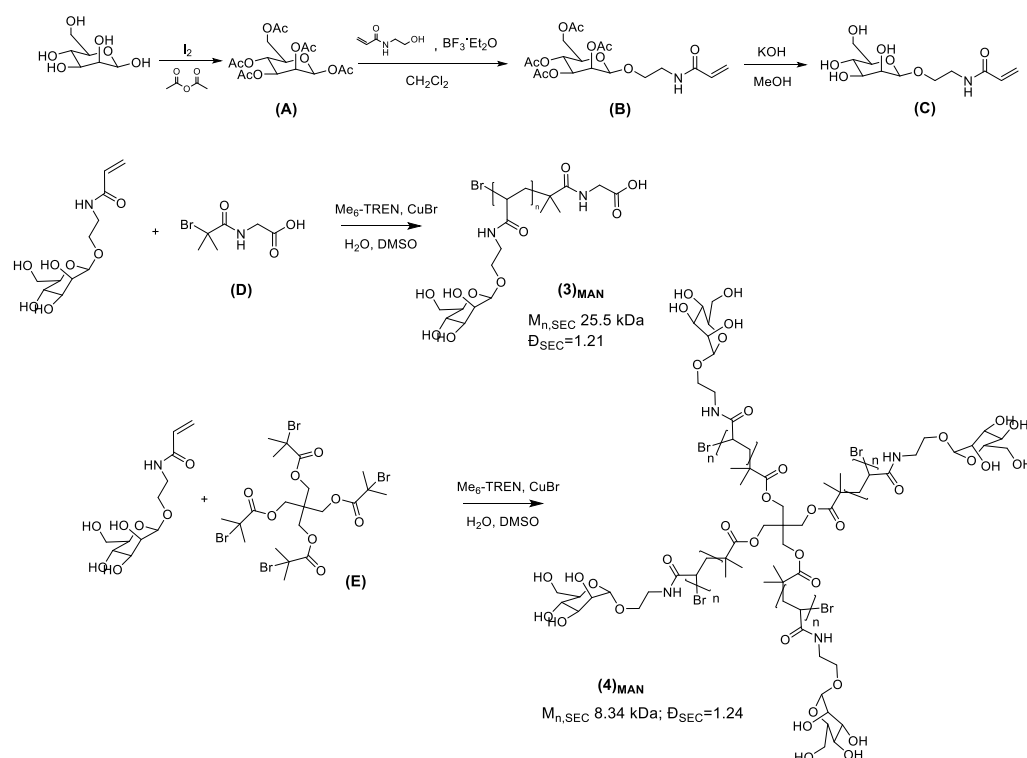


Figure S6.1: Synthesis of glycopolymers **(3)MAN** and **(4)MAN**. Full synthesis description can be found in Joao Madeira do O PhD dissertation.

**Fluorescence spectroscopy analysis of [Nile Red]:[(1)MAN] complexes at variable dye:polymer ratios.** Two stock solutions of linear **(1)MAN** glycopolymer

were prepared in water (or PBS) at 10 µg mL$^{-1}$ and 100 µg mL$^{-1}$ concentrations. A 1.3 mg mL$^{-1}$ Nile Red stock solution was prepared in THF. Different dilutions in THF were made from this stock solution. For each dilution, 8 µL were taken and added to 200 µL of a 100 µg mL$^{-1}$ polymer water solution, for final Nile Red:polymer molar ratios of 0.02:1, 0.05:1, 0.1:1, 0.5:1, 1:1, 5:1, 10:1, 15:1, 20:1 and 40:1 (0.02:1, 0.05:1, 0.075:1, 0.1:1, 0.2:1, 0.3:1, 0.5:1, 0.75:1, 1:1 and 2:1 for the experiments at narrower molar ratio range, Figure S1). For each ratio, the experiment was performed in triplicate.

The Nile Red stock solution was then diluted 10 times, for a final Nile Red concentration of 0.13 mg mL$^{-1}$. Different dilutions in THF were prepared from this stock solution. For each dilution, 8 µL were taken and added to 200 µL of a 10 µg mL$^{-1}$ polymer water solution, for final Nile Red:polymer molar ratios of 0.02:1, 0.05:1, 0.1:1, 0.5:1, 1:1, 5:1, 10:1, 15:1, 20:1 and 40:1 (0.02:1, 0.05:1, 0.075:1, 0.1:1, 0.2:1, 0.3:1, 0.5:1, 0.75:1, 1:1 and 2:1 for the experiments at narrower molar ratio range, Figure S1). For each ratio, the experiment was performed in triplicate.

The samples were left for 5h protected from light to let the THF evaporate. 50 µL were then taken from each sample and transferred into a Corning black 384-well plate. Samples were analysed on a TECAN Spark 10M Multi-function Plate reader. Fluorescence was read from 580 to 700 nm, with $\lambda_{ex}$=550 nm.
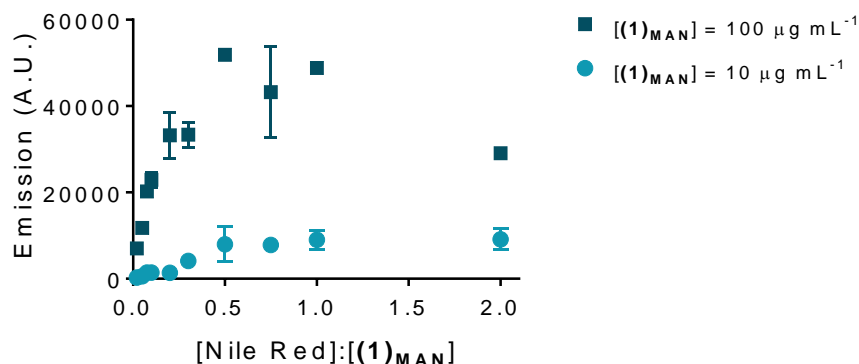
Figure S6.2: Fluorescence readings ($\lambda_{ex}$ 550 nm, $\lambda_{em}$ 630 nm) of Nile Red – (1)$_{MAN}$ samples at variable [Nile Red]:[polymer chains] molar ratios, in DI $H_2O$. The experiment is analogous to that shown in Figure 1, but focuses on the 0-2.0 [Nile Red]:[(1)$_{MAN}$] range of molar ratios, with additional data points.
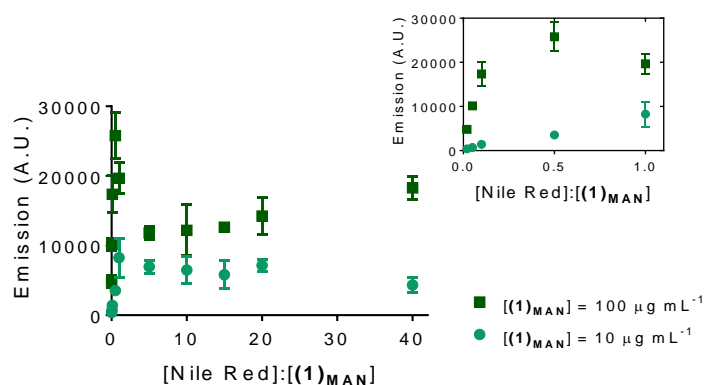


Figure S6.3: Fluorescence readings ($\lambda_{ex}$ 550 nm, $\lambda_{em}$ 630 nm) of Nile Red – (1)$_{MAN}$ samples at variable [Nile Red]:[polymer chains] molar ratios, in PBS. Insets: magnification of the 0-1.0 [Nile Red]:[(1)$_{MAN}$] region.

**Surface tension analysis.** A DSA 100 Drop Shape Analyser with DSA 4 software (Kruss GmbH, Germany) was used. The pendant drop method at room temperature with Laplace–Young computational method was employed for surface tension analysis. Measurements were taken immediately after droplet formation. Samples were measured in triplicates, from two independent solutions.

**(1)MAN** n= 66, $M_{n,theo}$ 24.9 kDa, $M_{n,SEC}$ 23.9 kDa, Đ = 1.22  **(2)MAN** n= 77, $M_{n,theo}$ 29.5 kDa, $M_{n,SEC}$ 27.2 kDa, Đ = 1.25
**(1)LAC** n= 66, $M_{n,theo}$ 35.6 kDa, $M_{n,SEC}$ 25.5 kDa, Đ = 1.25  **(2)LAC** n= 77, $M_{n,theo}$ 42.0 kDa, $M_{n,SEC}$ 42.6 kDa, Đ = 1.29
**(1)TRE** n= 66, $M_{n,theo}$ 36.5 kDa, $M_{n,SEC}$ 37.6 kDa, Đ = 1.18  **(2)TRE** n= 77, $M_{n,theo}$ 43.0 kDa, $M_{n,SEC}$ 55.9 kDa, Đ = 1.17

mannose
(MAN)

lactose
(LAC)

trehalose
(TRE)
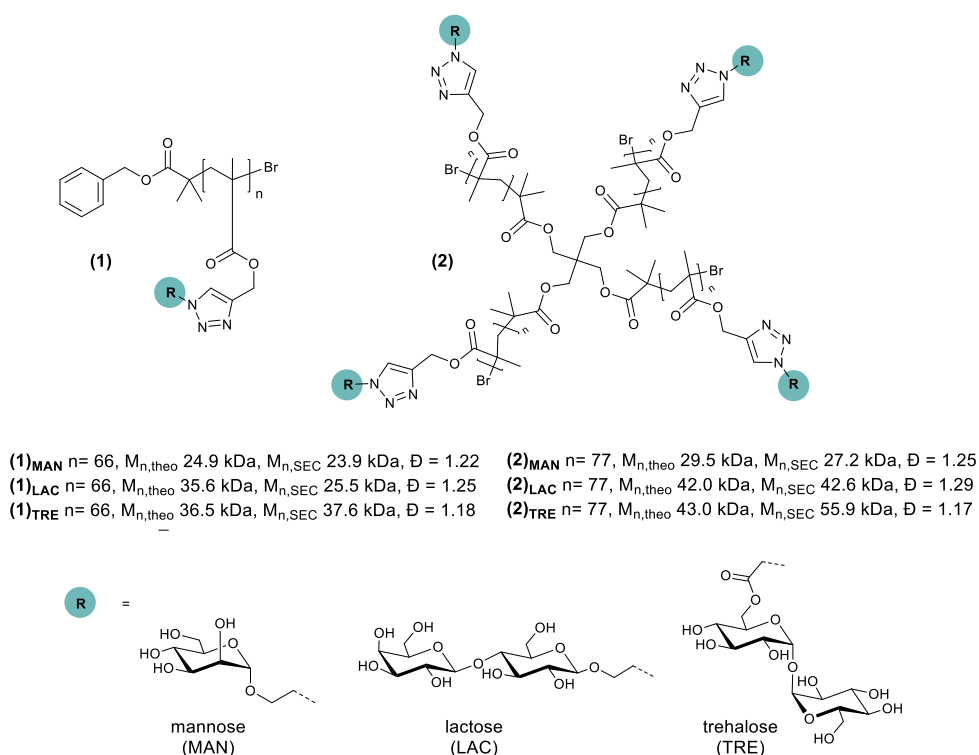
Figure S6.4: Glycopolymers utilised for the surface tension analysis measurements. Synthesis and characterisation of these materials are described in Madeira do O et al. J. Mat. Chem. B 2018, 6, 1044-1054.[1]
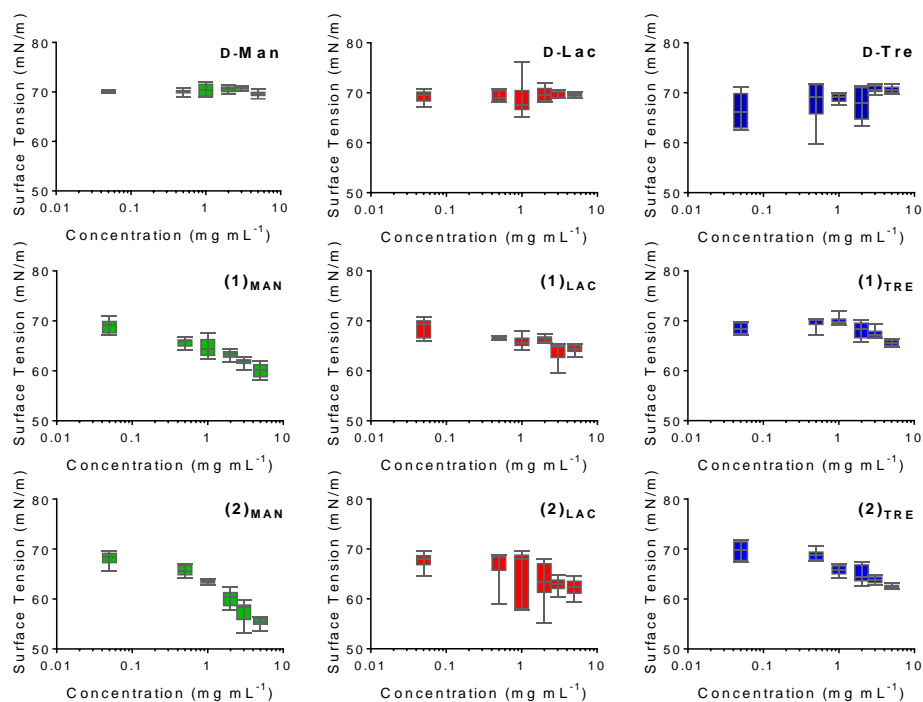


Figure S6.5: Surface tension analysis of solutions of mono- and disaccharides - mannose, and lactose and trehalose, respectively – (top line); and the corresponding linear (middle line), and star (bottom line) glycopolymers. Surface tension of sugar and polymer solutions (N=2, triplicates). Boxes represent median values, 25th and 75th percentile. Whiskers represent

maximum and minimum values. All solutions were prepared in deionised water. The experiment is part of Joao Madeira do O PhD dissertation.

(A)



(B)
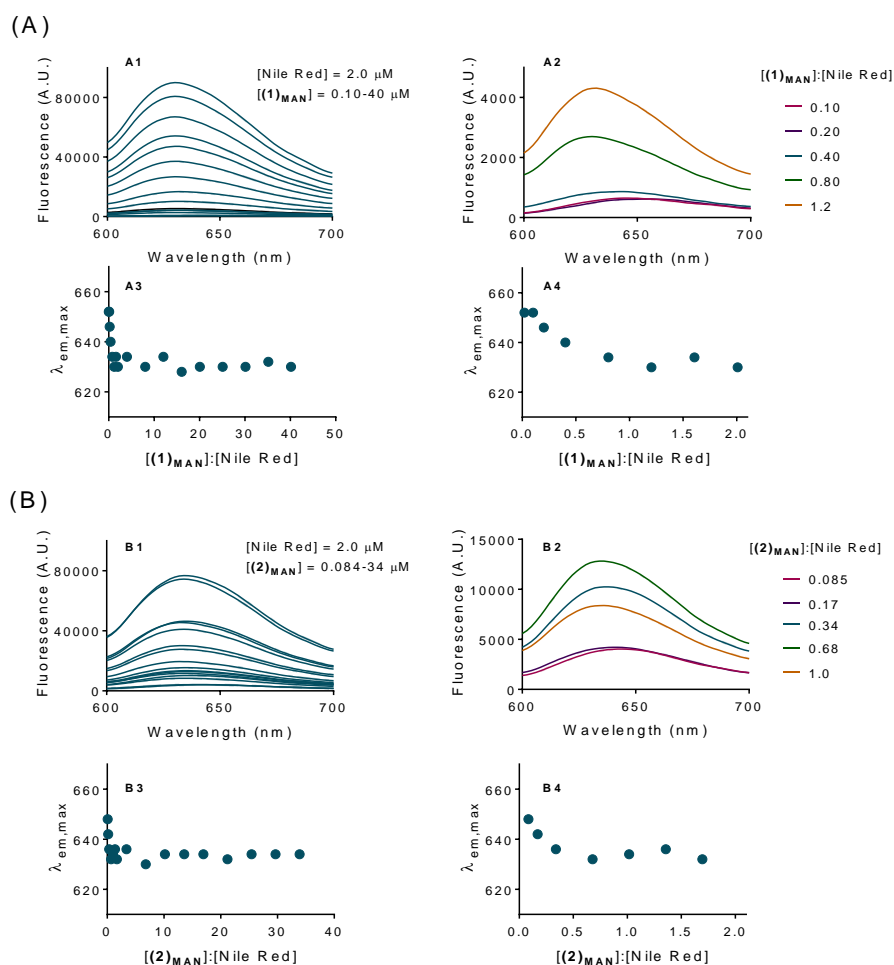


Figure S6.6: Fluorescence spectroscopy analysis of samples of Nile Red and **(1)**MAN (A), and **(2)**MAN (B) in deionised water. Nile Red was added from a stock solution in THF (targeting a theoretical [Nile Red]= 2.0 μM in each sample) to solutions of **(1)**MAN (A) and **(2)**MAN in deionised water, and samples were analysed following evaporation of THF. A1 and B1: emission spectra ($\lambda_{ex}$ = 550 nm) for 0.0050-2.0 mg mL$^{-1}$ solutions of **(1)**MAN, and **(2)**MAN. A2 and B2: emission spectra for polymer samples in the 0.0050-0.060 mg mL$^{-1}$ range. A3 and B3: overall shift in $\lambda_{em,max}$ vs. concentration of glycopolymer. A4 and B4: magnification of graphs A3 and B3 in the 0.0050-0.10 mg mL$^{-1}$ concentration range.

**DLS analysis.** DLS measurements were taken using a Zetasizer Nano (Malvern Panalytical, United Kingdom). A **(1)**MAN 10 mg mL$^{-1}$ solution was prepared in filtered Milli-Q water and analysed by DLS to confirm the absence of polymer aggregates. Nile Red was dissolved in THF at a starting concentration of 1 mg mL$^{-1}$. From this stock solution, 12.7 μL were added to 1 mL of the 10 mg mL$^{-1}$

**(1)**$_{MAN}$ solution, for a final **(1)**$_{MAN}$:Nile Red 10:1 molar ratio. The solution was left for 5h protected from light to evaporate the THF, and finally analysed by DLS. The solution was then filtered with a 0.22 PVDF filter and the DLS analysis repeated.

A negative control was prepared by adding 12.7 μL of Nile Red stock solution to 1 mL of filtered Milli-Q water. After THF evaporation, the suspension was filtered with a 0.22 PVDF filter. The two filtered solutions were analysed on a TECAN Spark 10M Multi-function Plate reader. Fluorescence was read from 580 to 700 nm, with $\lambda_{ex}$=550 nm.
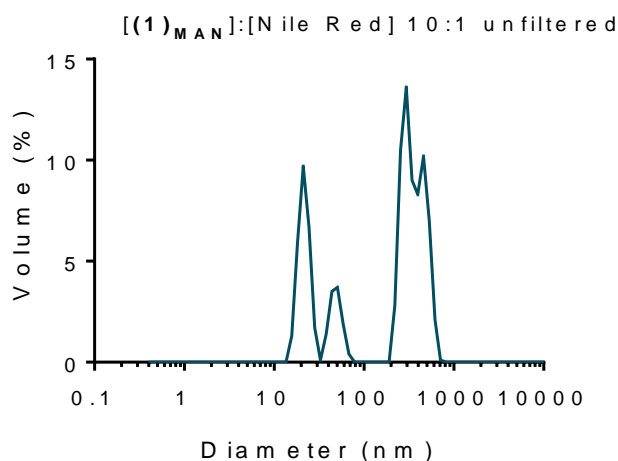


Figure S6.7: DLS Size distribution of **(1)**$_{MAN}$-Nile Red complexes before filtration. [**1)**$_{MAN}$]= 10 mg mL$^{-1}$, the polymer and Nile Red were mixed for a final **(1)**$_{MAN}$:Nile Red 10:1 molar ratio.

(a)



(b)
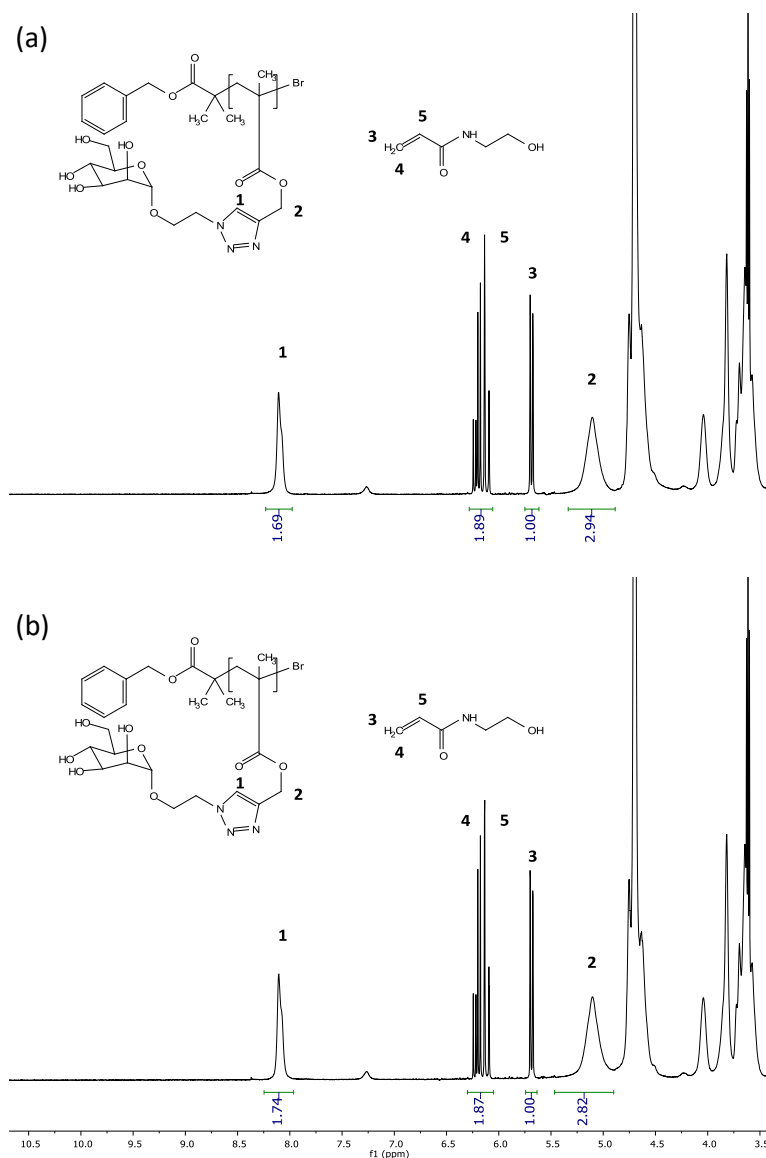


Figure S6.8: ^{1}H NMR of a mixture of **(1)**MAN, monomer *N*-hydroxyethylacrylamide (HEA) and Nile Red in D$_2$O (a)before and (b) after filtration with a 0.100 μm PVDF filter. This experiment was performed by Gokhan Yilmaz. Monomer HEA was used as internal standard to verify the amount of residual polymer after filtration. The mixture was prepared by dissolving 20 mg of **(1)**MAN and 2 mg of HEA in 2 mL of D$_2$O. The solution was splitted into two fractions of 1 mL each. 50 μL of a 0.38 mg mL$^{-1}$ Nile Red solution in THF were added to each fraction, for a final **(1)**MAN:Nile Red 1:1 molar ratio. The solutions were left overnight to evaporate the THF. ^{1}H NMR was then performed on one solution, while the other one was filtered using a 0.1 μm PVDF filter and finally analysed by ^{1}H NMR as well. The [**(1)**MAN]:[HEA] molar ratio was calculated by comparing the integrals of HEA monomeric peaks in the 6.5-5.5 ppm range with the triazolic proton of **(1)**MAN at 8 ppm, and it was estimated to be ~1.7 before filtration. No change in [**(1)**MAN]:[HEA] molar ratio was observed after filtration, suggesting that Nile Red did not induce **(1)**MAN self-assembling into nanoparticles of size ≥100 nm and that subsequently **(1)**MAN could entirely pass through the filter membrane.

**Taylor Dispersion analysis of [Nile Red]:[(1)MAN] complexes at variable dye:polymer ratios.** A 2 mg mL$^{-1}$ linear **(1)**MAN glycopolymer solution was

prepared in Milli-Q water. A 0.26 mg mL$^{-1}$ Nile Red stock solution was prepared in THF. Different dilutions in THF were made from this stock solution. For each dilution, 12 µL were taken and added to 300 µL of the 2 mg mL$^{-1}$ polymer water solution, for final Nile Red: **(1)$_{MAN}$** molar ratios of 1:10, 1:4, 1:2, 1:1 and 3:1.

The samples were left for 5h protected from light to let the THF evaporate, and finally filtered using a 0.22 µm PVDF filter. 200 µL were then taken from each filtered sample and analysed on a Viscosizer (Malvern, UK), to determine the hydrodynamic radius of the different **(1)$_{MAN}$**-Nile Red blends. 6 µl were injected and analysed per sample. Absorbance was recorded at λ= 214 nm.

**Sample preparation for dye quantification through RP- HPLC.** This experiment is part of Joao Madeira do O PhD dissertation. 1.00 mL of solutions were prepared at different concentrations (50 µg mL$^{-1}$, 100 µg mL$^{-1}$ and 1000 µg mL$^{-1}$) in commercial available RPMI buffer. Nile Red and DCVJ stock solutions in acetonitrile at 1000 µg mL$^{-1}$ were also prepared. Subsequently, 20 µL of the dye stock solution were added to the vials containing the glycopolymer solutions. The resulting mixtures were centrifuged for 5 minutes at 14000 RPM to remove non-polymer entrapped dye. 40 µL of the supernatant were then collected and mixed with 80 µL of acetonitrile in a HPLC vial. 100 µL of the samples were injected and quantity of dye present was quantified via fluorescence detection (λ$_{ex,max}$ 530 nm, λ$_{em,max}$ 630 nm for Nile Red and λ$_{ex,max}$ 430 nm, λ$_{em,max}$ 500 nm for DCVJ).

**Release of Nile Red from (1)$_{MAN}$ - and (2)$_{MAN}$ –Nile Red complexes.** This experiment is part of Joao Madeira do O PhD dissertation. Solutions of **(1)$_{MAN}$**-

and **(2)**MAN-Nile Red complexes were introduced into a float-a-lyzer dialysis tubing (MWCO 5 kDa), and dialysed against PBS under gentle stirring. Released Nile Red was quantified by fluorescence spectroscopy analysis of the external dialysis medium, at regular intervals of time.
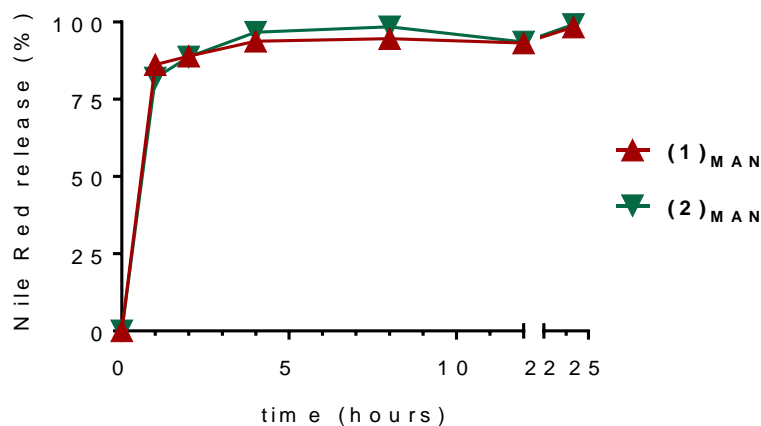


Figure S6.9: Release profile of Nile Red assessed by dialysis against PBS. Experiment was undertaken at room temperature and in sink conditions. Fluorescence readings of the sample were taken immediately before dialysis and values were taken as 100%, and were used for subsequent dye release quantification. Glycopolymers concentration: 1.0 mg mL$^{-1}$. Nile Red concentration of 20 µg mL$^{-1}$, 63 µM.

**Reversible agglutination assay.** This experiment was performed by Dr. Gokhan Yilmaz. A 2.0 mg mL$^{-1}$ stock solution of Con A was prepared in 20 mM HEPES buffer (pH 7.4 with 50 mM NaCl, 5 mM CaCl$_2$ and 5 mM MnCl$_2$). Several aliquots of this stock solution were transferred into Eppendorf vials containing a 100 µL of **(1)**MAN- and **(2)**MAN-Nile Red complexes (1:1 polymer:dye molar ratio) at a polymer concentration of 2.0 mg mL$^{-1}$ in 20 mM HEPES buffer at pH 7.4. Concentration of Con A in these Eppendorf vials were 0, 10, 250, 500, 1000 µg mL$^{-1}$. The addition of the Con A immediately resulted in the formation of a cloudy suspension due to the formation of insoluble glycopolymer-Con A

clusters. The solutions were centrifuged for 2 min at 1000 rpm, and the supernatant was collected and analysed fluorescence spectroscopy ($\lambda_{ex}$ 550 nm, emission recorded the 520-700 nm region) to obtain an estimation of residual **(1)$_{MAN}$**- and **(2)$_{MAN}$**-Nile Red complexes in solution. The precipitates from the 1000 µg mL$^{-1}$ Con A experiment were redissolved in a solution of methyl-α-mannopyranoside at different concentrations (200 µL, 1-20 mg mL$^{-1}$) and, the fluorescence of the samples was recorded again.

**Binding of (1)$_{MAN}$- and (1)$_{GAL}$-Nile Red complexes to immobilised Con A and PNA lectins.** This experiment was performed by Dr. Gokhan Yilmaz. Agarose lectin beads (Con A and PNA beads) were washed with cold 20 mM HEPES buffer (pH 7.4 with 50mM NaCl, 5 mM CaCl$_2$ and 5 mM MnCl$_2$) five times in order to remove sugar added to stabilize the lectins during storage. 100 µL aliquots of a 2 mg mL$^{-1}$ lectin bead suspension was transferred into eppendorfs. To these, different amounts of linear **(1)$_{MAN}$**- and **(1)$_{GAL}$**-Nile Red complexes (1:1 polymer:dye molar ratio) were added to achieve final polymer concentrations of 0.10, 0.125, 0.25, 0.50, 1.0 mg mL$^{-1}$. The suspensions were gently mixed with a vortex. After 20 min, the suspensions were centrifuged for 1 min at 1200 rpm, followed by careful removal of the supernatants. The resulting pellets were resuspended in HEPES buffer again, and the centrifugation-washing cycle was repeated three times. The suspensions were then transferred into a 96-well plate for fluorescence imaging using an In Vivo Imaging System (IVIS) (excitation: 550 nm, detection 640 nm).

**Affinity chromatography assay using Con A- and PNA stationary phases.** This experiment was performed by Dr. Gokhan Yilmaz. Agarose lectin beads (Con A and PNA beads) were washed with cold 20 mM HEPES buffer (pH 7.4 with 50mM NaCl, 5 mM $CaCl_2$ and 5 mM $MnCl_2$) five times in order to remove sugar added to stabilize the lectins during storage. The lectin beads were resuspended in 1 mL of buffer solution, and transferred to Pasteur pipettes previously fitted with small piece of cottonwool to ensure that the resin is retained in the pipette. Following elution of the excess of suspending buffer from the column, 1.0 mL aliquots of of a 2.0 mg $mL^{-1}$ linear **(1)$_{MAN}$**- and **(1)$_{GAL}$**-Nile Red complexes (1:1 polymer:dye molar ratio) in 20 mM HEPES buffer at pH 7.4 were added to the pipettes and again allowed to drain through the lectin beads under gravity. Next, the columns were eluted with 10-12 mL of HEPES buffer solution. Subsequently, 3-4 mL of 10 mg $mL^{-1}$ methyl-α-mannopyranoside and D-galactopyranoside solution in HEPES buffer was ran through Con A and PNA bead columns, respectively, followed by 5 mL of HEPES buffer solution.

| Con A | PNA |

Addition of **(1)MAN** + Nile Red

Elution with 10-12 mL of HEPES buffer, pH 7.4

Elution with 3 mL of 10 mg mL$^{-1}$ methyl-α-mannopyranoside

Figure S6.10: Affinity chromatography assay. 1 mL of **(1)MAN-** Nile Red complex (1:1 polymer:dye molar ratio, polymer concentration 2 mg ml$^{-1}$ ) was added to Con A- and PNA-immobilised beads on a glass pipette, followed by 10-12 mL of HEPES buffer. **(1)MAN-**Nile Red complex was retained by the Con A-immobilised beads, while it was eluted immediately from the PNA-immobilised beads-containing pipette. The complex was finally eluted from the Con A stationary phase by addition of a 3-4 mL 10 mg mL$^{-1}$ methyl-α-mannopyranoside solution in HEPES buffer.

Con A        PNA

Addition of **(1)**$_{MAN}$ + Nile Red

Elution with 10-12 mL of HEPES buffer, pH 7.4
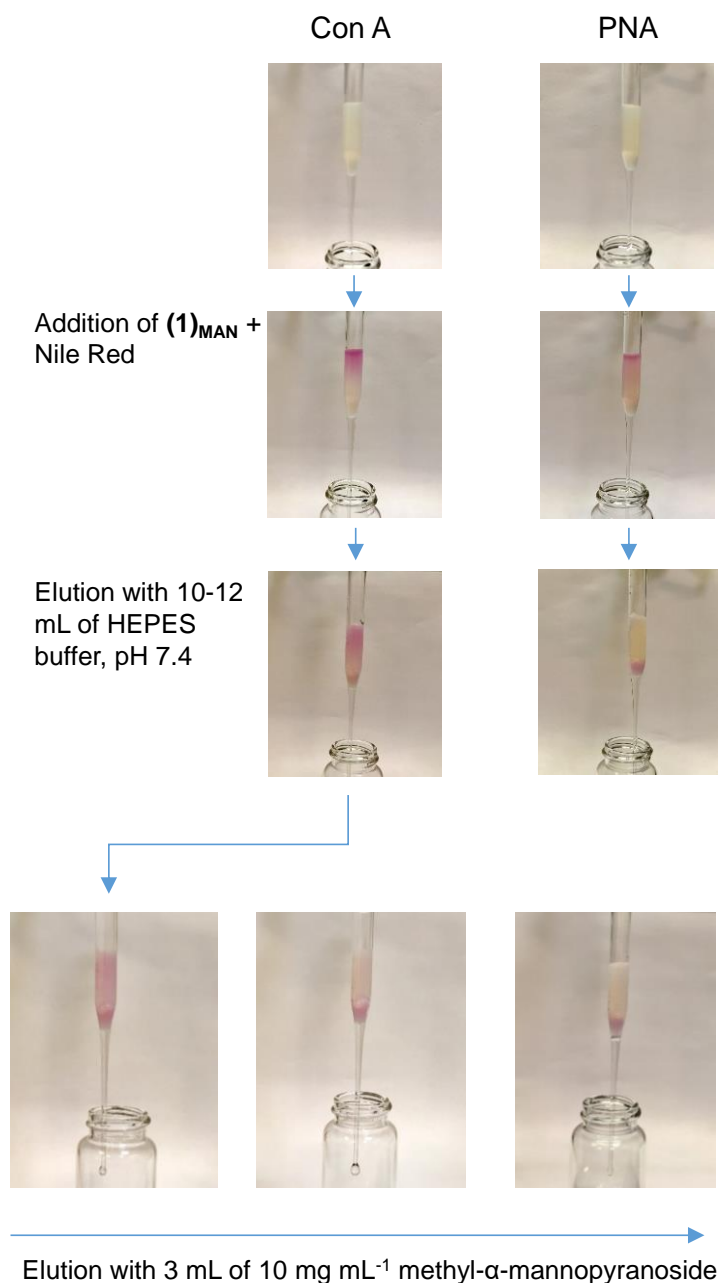
Elution with 3 mL of 10 mg mL$^{-1}$ D-galactopyranoside

Figure S6.11: Affinity chromatography assay. 1 mL of **(1)**$_{GAL}$- Nile Red complex (1:1 polymer:dye molar ratio, polymer concentration 2 mg ml$^{-1}$ ) was added to Con A- and PNA-immobilised beads on a glass pipette, followed by 10-12 mL of HEPES buffer. **(1)**$_{GAL}$-Nile Red complex was retained by the PNA-immobilised beads, while it was eluted immediately from the Con A-immobilised beads-containing pipette. The complex was finally eluted from the PNA stationary phase by addition of a 3-4 mL 10 mg mL$^{-1}$ methyl-α-mannopyranoside solution in HEPES buffer.
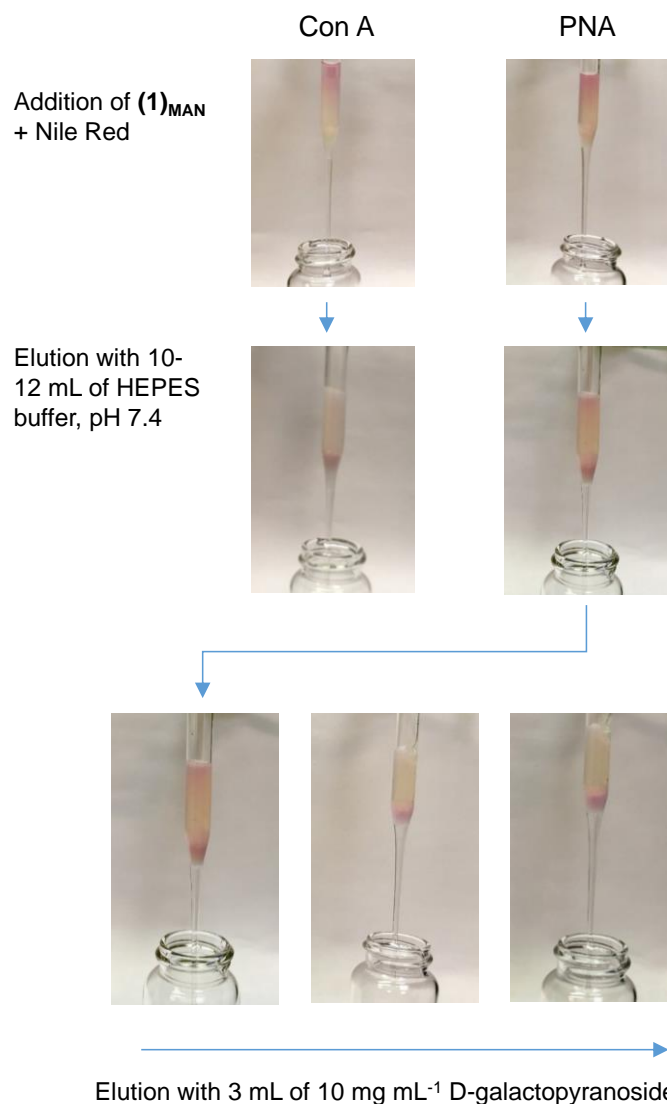
## Cell uptake studies

This experiment was perfomed by Dr. Francesca Mastrotto and is part of Joao Madeira do O PhD dissertation. Chinese Hamster Ovary expressing Mannose Receptor (CHO-MR) cell lines were cultured in   containing 10% Foetal Bovine Serum (FBS) (Sigma Aldrich, UK), 2 mM L-glutamine, 100 U/mL penicillin and 100 µg mL$^{-1}$ streptomycin (Sigma Aldrich, UK), at 37°C, 5% $CO_2$ and 95% relative humidity.  CHO-MR stable transductants were selected by addition of 0.6 mg mL$^{-1}$ geneticin (Sigma Aldrich, UK) in the culture medium.

Mannosylated linear **(1)**$_{MAN}$ or **(2)**$_{MAN}$ star glycopolymers-Nile Red solutions were prepared by dissolving the two polymers in RPMI at 50, 100 and 1000 µg mL$^{-1}$ concentrations. To 1 mL of each solution, 20 µL of a 1 mg mL$^{-1}$ Nile Red solution in Acetonitrile were added, for a final Nile Red concentration of 20 µg mL$^{-1}$ (62.82 µM).

Chinese Hamster Ovary (CHO) or Chinese Hamster Ovary expressing Mannose Receptor (CHO-MR) were seeded in 24 wells plate ($20 \times 10^4$ cells/well) and incubated overnight at 37°C, 5% $CO_2$ (DMEM/F12 medium). The medium was removed, cells were washed with 2x1 mL of PBS and incubate for 30 minutes with RPMI W/O phenol red, 5% $CO_2$. The media was then replaced with mannosylated linear **(1)**$_{MAN}$ or **(2)**$_{MAN}$ star glycopolymers-Nile Red solutions, and cells were incubated at 37°C, 5% $CO_2$ for further 30 minutes. Subsequently, wells were rinsed with PBS (3x1 mL), the cells harvested using trypsin/EDTA solution diluted 1:1 in PBS and fixed with 2% paraformaldehyde in PBS. Cells treated with media only were analysed as controls. The medium was then

replaced with the glycopolymers-Nile Red solutions and cells are incubated for further 30 minutes at 37°C, 5% $CO_2$ in the dark. Wells were rinsed with 3x1mL PBS, cells were harvested by treatment with tripsin/PBS 1:1 and fixed in 2% paraformaldehyde. Samples were subsequently analysed by flow cytometry (FACS).
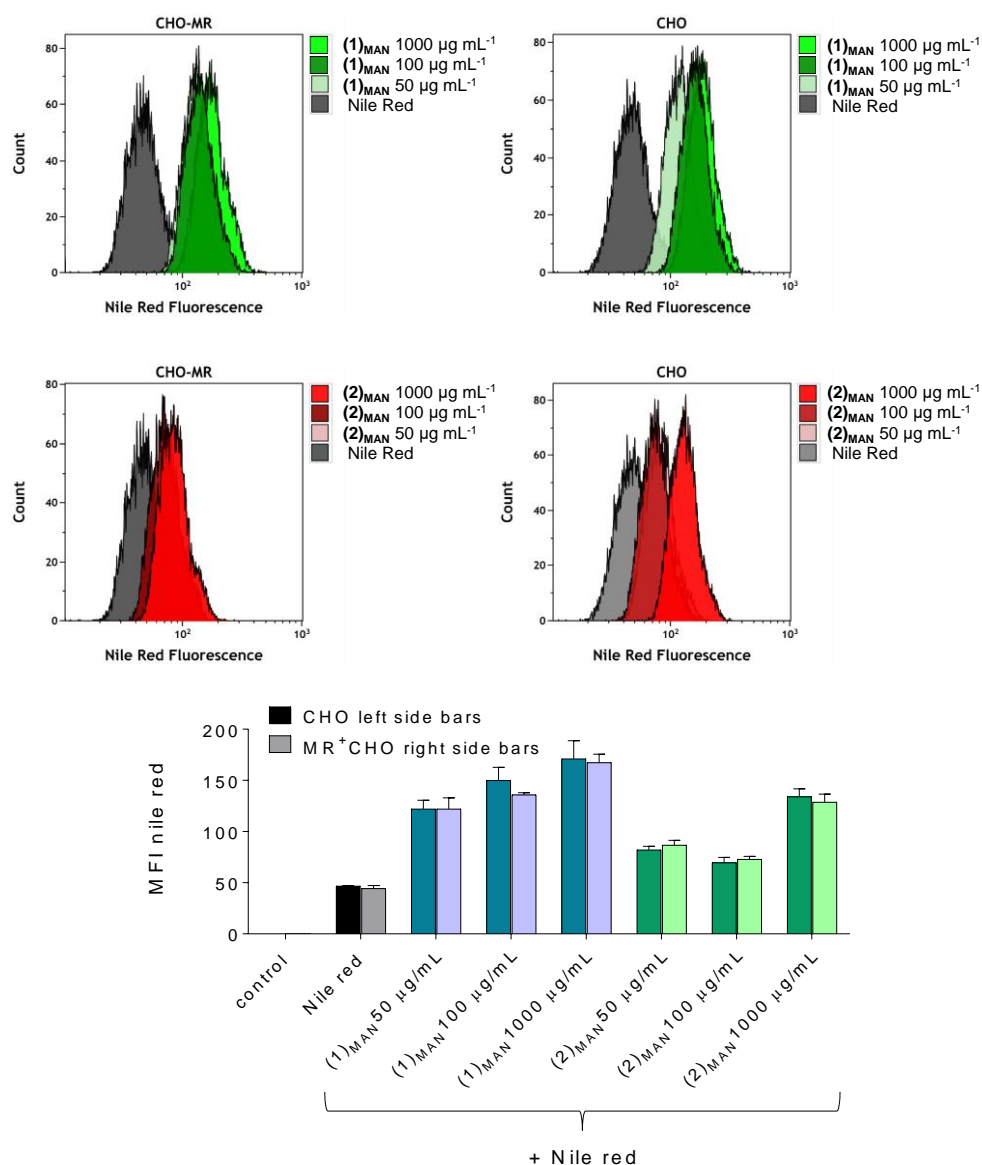


Figure S612: Nile Red uptake on CHO and MR⁺CHO cells, assessed by Flow Cytometry.

1.      Madeira do O, J.;  Mastrotto, F.;  Francini, N.;  Allen, S.;  van der Walle, C. F.;  Stolnik, S.;  Mantovani, G., Synthetic glycopolymers as modulators of protein aggregation: influences of chemical composition, topology and concentration. *Journal of Materials Chemistry B* **2018,** *6* (7), 1044-1054.

2.      Murata, H.;  Cummings, C. S.;  Koepsel, R. R.;  Russell, A. J., Polymer-Based Protein Engineering Can Rationally Tune Enzyme Activity, pH-Dependence, and Stability. *Biomacromolecules* **2013,** *14* (6), 1919-1926.

3.      Simula, A.;  Nurumbetov, G.;  Anastasaki, A.;  Wilson, P.; Haddleton, D. M., Synthesis and reactivity of α,ω-homotelechelic polymers by Cu(0)-mediated living radical polymerization. *European Polymer Journal* **2015,** *62*, 294-303.

4.      Zhang, Q.; Wilson, P.; Li, Z.; McHale, R.; Godfrey, J.; Anastasaki, A.; Waldron, C.; Haddleton, D. M., Aqueous Copper-Mediated Living Polymerization: Exploiting Rapid Disproportionation of CuBr with Me6TREN. *Journal of the American Chemical Society* **2013,** *135* (19), 7355-7363.

# Chapter 7

## Summary and future directions

_____

## 7.1. Overall summary

Biotherapeutics are the fastest growing class of pharmaceuticals[1], with over 200 protein therapeutics that have been commercialised (2016). Biotherapeutics currently make up for 30% of pharmaceuticals under development[2], and have reached US$ 228 billion in global sales in 2016[3].

However, the development of proteins as pharmaceuticals is hampered by a serious of challenges, one of which is proteins poor stability in the different steps of manifacturing, purification and formulation. A number of excipients have been employed so far to improve proteins stability and prevent their aggregation: direct covalent conjugation of polymers, such as polyethyleneglycole, has been successfully used to sterically shield proteins, preventing them from coming into contact and aggregate. However, problems have arisen which involved loss of proteins activity and increased protein immunogenicity, that have highlighted the need for less invasive, non-covalent protein-polymer interactions. Another strategy relied on β-sheet breakers, small peptides which derives from the Aggregation Prone Regions of specific proteins, conveniently modified to interact with their target APR and block it from starting the aggregation process. β-sheet breakers so far have been designed to block the aggregation of specific proteins and generally require chemical modifications that improve their aqueous solubility.

In this thesis, the stabilisation of proteins through non-covalent interactions was attempted using hydrophobic, self-aggregating β-sheet breakers-like moieties, which were incorporated into amphiphilic block copolymers to

mediate the stabilising effect of hydrophilic polymeric chains. We aimed at developing a new type of non-covalent conjugation and at the same time greatly improving the aqueous solubility of these peptidomimetic sequences. Moreover, while the first peptidomimetic sequences were developed from lysozyme Aggregation Prone Region, in the following chapters we prepared more generic hydrophobic blocks, easier to synthesise and active on a broader range of proteins. different families of potential protein stabilisers were developed. A subset of these stabilisers was further investigated, to understand if the interactions that they established with proteins could be further used to develop systems for protein delivery and controlled-release.

In particular, in Chapter 2, different peptide analogues were developed from hen egg lysozyme Aggregation Prone Region. Here, the working hypothesis was that a synthetic APR analogue could interact with its homologue or with other hydrophobic sequences on the protein backbone, thus masking these protein regions, suppressing protein aggregation. Our synthesised APR copolymer was found to be able to significantly delay the onset of lysozyme aggregation and the amount of final protein aggregate.

In the following Chapter, we extended our approach from specific APRs to more generic, hydrophobic, oligomers containing amino acid-like moieties, which were block-copolymerised with hydrophilic monomer *N*-hydroxyethylacrylamide. The resulting block copolymers were tested on different proteins. Block copolymers incorporating indole oligomers as hydrophobic block could successfully prevent the aggregation of bovine

pancreatic insulin and the antimicrobial peptide IDR 1018. The stabilising effect was ascribed to the hydrophobic interactions that indole, as tryptophan side chain, can establish with proteins hydrophobic residues.

Encouraged by these results, in Chapter 4 we evaluated these indole oligomers as potential delivery systems for peptide IDR 1018. Controlled self-assembly of these oligomers was achieved by nanoprecipitation into nanoparticles of size between 300 and 400 nm and narrow polydispersity. IDR 1018 was conveniently ion paired with antimicrobial molecule usnic acid, obtaining a hydrophobic complex between the two molecules that was successfully incorporated into the indole-based nanoparticles.

In chapter 5, cholanic acid was incorporated into a RAFT agent which was used to mediate the polymerization of *N*-hydroxyethylacrylamide. The resulting cholanic-polyacrylamides were tested as protein complexing agents on using bovine serum albunin and bovine pancreatic insulin as model proteins. Protein complexation was successfully achieved through non-covalent hydrophobic interactions between cholanic acid and hydrophobic patches on proteins.

Finally, in Chapter 6, we investigated non-covalent, hydrophobic interactions between the small hydrophobic dye Nile Red and different linear and multi-arm glycopolymers, synthesised by a former PhD student within our group. Interestingly, we found the dye incorporation to be reversible, and driven by dye molecule-single polymer chain interactions, suggesting that the polymers may act as unimolecular micelles instead of high-order supramolecular assemblies.

To conclude, results show that some of the different polymeric materials prepared during this PhD act on proteins with stabilising effects, developed through non-covalent, hydrophobic interactions that these materials can establish with proteins. It has been proven that generic hydrophobic blocks, derived from specific amino acids naturally involved in proteins-β-sheet breakers interactions, can be used to interact with a wider range of proteins. Their incorporation into amphiphilic block copolymers appears necessary to improve their solubility.

## 7.2.  Future directions

More studies would be needed to evaluate these non-covalent stabilisers on a wider range of proteins. The stabilising effects may vary according to the protein tested. More tests should be conducted on commercialised biotherapeutics, such as, for example, antibodies. As mentioned in Chapter 1, various Aggregation Prone Regions have been identified on commercialised antibodies. These APRs could be a potential target of our $IND_m$-$b$-$HEA_n$ copolymers.

Moreover, further studies are required to elucidate any alteration that these materials may induce on proteins structure. Even though aggregation is prevented, the non-covalent interactions observed may still induce changes in proteins native conformations, with subsequent loss of proteins functionality.

The self-assembly behaviour displayed in Chapter 4 by hydrophobic indole oligomers suggests a potential application of these oligomers as carriers for the delivery of not only therapeutic proteins, but also small hydrophobic drugs.

More antimicrobial tests are currently ongoing with ion paired, encapsulated antimicrobial peptide IDR 1018, to confirm the applicability of this delivery system on *Salmonella* infected macrophages. Repetitions of Loading and controlled release experiments will also be performed. Finally, the ability of cholanic polymers to induce protein complexation suggest their potential use for protein targeted intracellular delivery. Further experiments are planned for the targeted delivery of fluorescent insulin using a mannosylated, fluorescent cholanic polyacrylamide.

# References

1.      Pedro H. Oliveira, J. M., Paula M. Alves, Alvaro R. Lara, and Cleo Kontoravdi Advances in the Development of Biotherapeutics. *BioMed Research International*, **2015**.

2.      Acri, K. M. L. The Biologics Revolution in the Production of Drugs, *Fraser Institute,* **2016**.

3.      Moorkens, E.; Meuwissen, N.; Huys, I.; Declerck, P.; Vulto, A. G.; Simoens, S., The Market of Biopharmaceutical Medicines: A Snapshot of a Diverse Industrial Landscape. *Front Pharmacol*, **2017**, 8, 314.